BULETINUL INSTITUTULUI POLITEHNIC DIN IAŞI

BULETINUL INSTITUTULUI POLITEHNIC DIN IAŞI

ŞTIINŢA ŞI INGINERIA MATERIALELOR

ŞTIINŢA ŞI INGINERIA MATERIALELOR

SUMAR

MATERIALS SCIENCE AND ENGINEERING

C O N T E N T S

NUMERICAL PREDICTIONS AND EXPERIMENTAL VALIDATION OF THE VOLTAGE INDUCED IN A COIL BY DYNAMICALLY LOADED NiMnGa SPECIMENS

BY

NICKOLAUS M. BRUNO*, **CONSTANTIN CIOCANEL**
and HEIDI P. FEIGENBAUM

Northern Arizona University, USA
Department of Mechanical Engineering

Abstract. Magnetic shape memory alloys (MSMAs) are materials that when exposed to a magnetic field may exhibit up to 10% extension strain due to martensitic variants reorientation. When a fully strained MSMA element is compressed, while exposed to a bias magnetic field, a change in the material's magnetization occurs. The magnitude of this change is dependent on the strength of the bias magnetic field and material properties and can be quantified using a pick-up coil surrounding the MSMA element. Accordingly, the material may be used for energy harvesting and sensing applications. The work herein presents experimental measurements and theoretical predictions of the electromotive force (emf) produced by a Ni-Mn-Ga specimen loaded cyclically in compression while exposed to a bias magnetic field oriented normal to the compression direction. The theoretical predictions use the thermodynamic based constitutive model developed by Kiefer and Lagoudas. Emf predictions correlate well with experimental data suggesting that one may rely solely on theoretical modeling for the design of power harvesting or sensing applications.

Key words: magnetic shape memory alloys, power harvesting, sensing.

---

* Corresponding author; *e-mail:*

1. Introduction

Magnetic shape memory alloys (MSMA) are materials that exhibit the shape memory effect in the presence of a magnetic field. When a MSMA specimen, formerly exposed to a magnetic field, is subjected to a mechanical compressive load, the material deforms, and when it does so, the substructure reorients altering the material's magnetization, thus altering the surrounding magnetic field. This alteration in the magnetic field represents the transformation of energy from mechanical to magnetic, which in turn can be easily transformed into electrical energy by means of an inductor whose core is the MSMA element.

The prevailing theory for the magnetic shape memory effect states that the martensite crystal, after transformation from cubic austenite, consists of the mixture of tetragonal martensite variants, having different magnetic easy axis (often called the *c*-axis) orientations, separated by twin boundaries that are highly mobile. These variants have different magnetic and crystallographic orientations. When the MSMA is exposed to an external magnetic field the twins in a favorable orientation relative to the field direction "grow" at the expense of other twins, i.e. the twin boundaries move in the material so that the amount of twin variants of "preferable" orientation increases. Similarly, when the MSMA is exposed to an external mechanical load the twins in a favorable orientation relative to the load direction "grow" at the expense of other twins.

Martensite variants within the MSMA are normally assumed to exhibit uniaxial symmetry with their magneto-crystalline anisotropy energy, which is defined as the energy stored in the MSMA required to de-twin its crystallographic microstructure. This de-twinning produces rotation of the magnetization away from the easy axis, thus creating a measurable change in mass magnetization and presents the opportunity of using the material as a sensor or source of harvestable power. The rotation of magnetic easy axis induced by martensite reorientation is considered a thermodynamically reversible process[1,2], and therefore the internal state of the material is completely recoverable under proper loading. Since changes in magnetization within MSMAs are fully recoverable, this material is a viable candidate for power harvesting and sensing applications.

The idea of using the martensitic reorientation mechanism for energy harvesting has been explored in the past[3,4]. Karaman *et al.* conducted research on energy harvesting using $Ni_{50}Mn_{28.5}Ga_{21.5}$ and proposed a simple mathematical model for the prediction of harvestable power based on experimental data. Their model predicts that a specimen loaded at a frequency of 10Hz, under an optimum bias magnetic field of $1.2T$[3], to experience a 5% reorientation strain, produces approximately 260mV captured by a coil

surrounding the specimen. An attempt at using a demagnetizing factor in the voltage calculation leads to a significant reduction in the predicted voltage. Concurrently, Kiefer and Lagoudas developed a phenomenological constitutive model based on the MSMAs free energy and internal thermodynamic state[1,2]. This model accurately predicts the magneto-mechanical response of the MSMAs under variable stress-constant field loading conditions, and can be used to replace the simple mathematical model produced by Karaman *et al.,* which explicitly uses Faraday's law of induction.

Faraday's law of magnetic induction (Equation 1) states that the time rate of change of the magnetic induction creates a corresponding electric field in the surrounding media. If the surrounding material is conductive, electron displacement is produced and an electromotive force (emf) can be measured using a conductor. In this study, a coil of approximately 1000 turns surrounding the specimen is used as the conductor (see Fig. 1).

$$\vec{\nabla} \times \vec{E} = -\frac{\partial B}{\partial t} \tag{1}$$

According to Karaman *et al*., the right hand side of Equation (1) can be replaced with a sinusoidal inductance term which is a function of reversible magnetic inductance, volume fraction of martensite reorientation, and frequency of excitation. The simplicity of assuming a sinusoidal inductance produces surprisingly accurate results. However, this approach doesn't account for the magneto-mechanical response of the material; this is why the constitutive model proposed by Kiefer and Lagoudas[2] is implemented in the algorithm used for the power harvesting output capabilities of these materials.
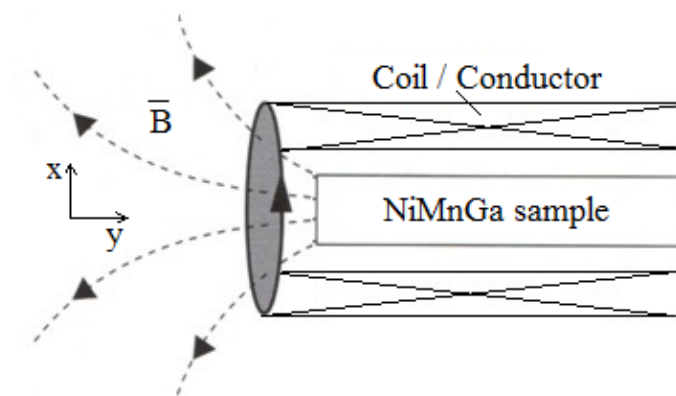
Fig. 1 – Pickup coil surrounding a MSMA specimen that produces a changing magnetic inductance. This changing magnetic inductance forms an electric field.

2. Modeling Approach

2.1. General Framework

In this study, the magneto-mechanical response of the material is simulated using the phenomenological model developed by Kiefer and Lagoudas[2]. This model provides the framework for the evaluation of the specimen magnetization in the y-direction, M_y, by specifying an evolution equation for the volume fraction of the martensitic variants ξ. According to Equation (1), the y-direction magnetization is dependent on material properties, *i.e.* M^{sat} – saturation magnetization, ρK_1 – effective magneto-crystalline anisotropy energy, the magnetic field experienced by the specimen in the x direction, the magnetic permeability of the free space, μ_0, and the martensitic variants volume fraction, ξ.

$$M_y = (1 - \xi) \cdot M^{sat} \sqrt{1 - \left(\frac{\mu_0 M^{sat} H_x}{2 \rho K_1} \right)^2} \qquad (2)$$

magnetization is then used to calculate the magnetic induction B, required by Faraday's law (see Equation 1) to estimate the voltage output, using the following equations:

$$B = \mu_0 M(\xi) \qquad (3)$$

where $M(\xi)$ is the specimen magnetization that depends on the martensitic volume fraction. Note that only the y component of the magnetic induction will be used for the voltage calculation.

The experimental results reported here were obtained using a position control method for the loading-unloading of the MSMA specimen; accordingly, the implementation of the constitutive model was done to simulate the equivalent of the position control experiments. This is being mentioned because, most often, the model is implemented in a stress controlled or magnetic field controlled mode. The choice of position control tests was made because the hydraulic test rig used for the experiments was not able to control tightly the applied load on the specimen due to the fast time response of the material (*i.e.* fast variant reorientation over a very narrow stress window).

2.2. Position Controlled Mode

In the constitutive model, the total strain of the specimen is defined as the combination of multiple strains. When temperature is held constant, only the elastic and reorientation, $\varepsilon^T = \varepsilon^{el} + \varepsilon^{re}$, contribute to the total strain. The elastic strain, ε^{el}, is due to the Young's modulus of the specimen, and in this case is assumed constant. The reorientation strain, ε^{re}, is produced when the applied stress is large enough to initiate twin boundary motion. Using Hooke's law for isotropic materials and the definition for reorientation strain[2], Equation (4) defines total strain as:

$$\varepsilon^T = \sigma \cdot S_{const} + \varepsilon^{r,\max} \cdot \xi \tag{4}$$

where σ is the applied compressive stress, S_{const} is the compliance of the specimen (assumed constant), and $\varepsilon^{r,\max}$ is the maximum reorientation strain.

In position controlled tests, the total strain is assumed to be the input parameter for the constitutive model, which means that the stress as well as the variant volume fraction must be determined from it. The stress and variant volume fraction are defined depending on the reorientation direction and whether the driving force is significant enough to produce reorientation. Accordingly, the stress and variant volume fraction are evaluated by solving simultaneously equations (5) for variant 2 to variant 1 reorientation, or equation (6) for variant 1 to variant 2 reorientation. In Equations (5) and (6), A, B_1, B_2, Y, and C are model parameters, H^* is the magnetic field used for calibration, and $\xi^{(1,2)}$ ($\xi^{(2,1)}$) is the volume fraction of variant 2. The flowchart shown in Fig. 2 shows the required steps for an iterative solver.

$$\left. \begin{aligned} \sigma \cdot S_{const} + \varepsilon^{r,\max} \cdot \xi - \varepsilon^T = 0 \\[2mm] \sigma \varepsilon^{r,\max} + \mu_0 M^{sat} H - \frac{(\mu_0 M^{sat})^2}{4\rho K_1} H^2 - B_1 - B_2 - Y^\xi - \xi^{(1,2)} A = 0 \end{aligned} \right\} \tag{5}$$

$$\left. \begin{aligned} \sigma \cdot S_{const} + \varepsilon^{r,\max} \cdot \xi - \varepsilon^T = 0 \\[2mm] \sigma \varepsilon^{r,\max} + \mu_0 M^{sat} H - \frac{(\mu_0 M^{sat})^2}{4\rho K_1} H^2 - B_1 + B_2 + Y^\xi - \xi^{(2,1)} C = 0 \end{aligned} \right\} \tag{6}$$
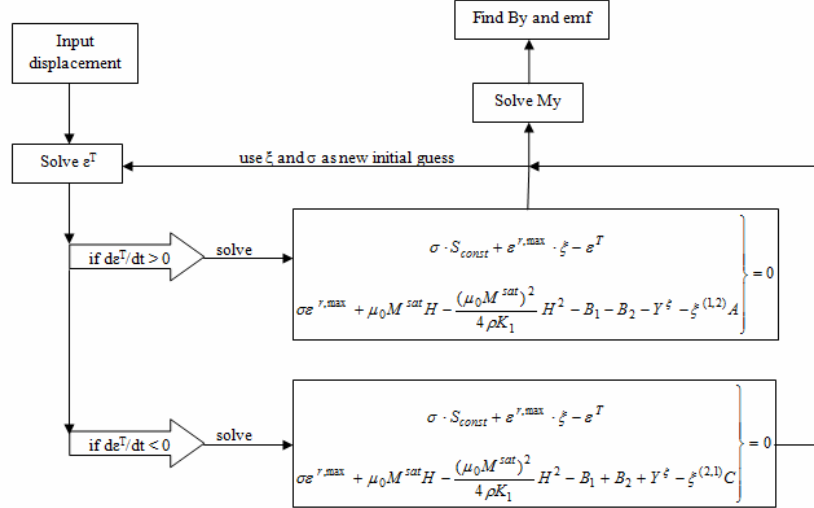
Fig. 2 – Flowchart for an iteratively solved position controlled method.

When solving Equations (5) and (6), ξ must be saturated to a limiting value specific to the material being tested. Each new value of ξ and σ offers an initial guess for the iterative solver and can be used to first determine magnetization using Equation (2), then the magnetic inductance using Equation (3), and finally the coil generated voltage using Equation (1). The simulated results produced with this approach are presented in the next section.

3. Result

3.1. Model Validation

The model was implemented in MATLAB Simulink, where extrinsic embedded MATLAB (eml) functions were used to solve the iterative sequence shown in Fig. 3. The model calibration constants, together with the MSMA specimen geometry and properties, are given in Table 1.

Table 1
Material Specifications and Model Calibration Values

Specimen	$\sigma^{s\,(1,2)}$ MPa	$\sigma^{f\,(1,2)}$ MPa	$\sigma^{s\,(2,1)}$ MPa	$\sigma^{f\,(2,1)}$ MPa	E GPa	ρK_1 J/m^3	M^{sat} A/m	$\varepsilon^{r,max}$ %	Dimensions mm	D_{xx}, D_{yy}[1]
Ni$_{50}$ Mn$_{28.5}$Ga$_{21.5}$	1.9	0.85	3.6	4.8	18.5	1.9e5	572,49	6.1	2.88 x 2.96 x 20.15	0.48, 0.04

The results summarized in Fig. 3 indicate that implementation of the Kiefer and Lagoudas model, in the equivalent of a position control test, accurately predicts stress-strain hysteresis as well as the strain evolution over

time when a sinusoidal displacement at a frequency of 5 Hz is considered as input excitation. While the model captures the trend of the stress evolution over time, it is considered that addition of dynamic effects associated with the variants reorientation may lead to improved dynamic stress predictions. Simulated and experimental results compare well for the entire frequency range tested, *i.e.* 0 to 10Hz, but are not reported here due to space limitations.

The experimental data shown in Fig. 3*d* indicates a local maximum for the voltage at an applied field of 0.8 Tesla during the 5 Hz tests with a reorientation strain of 5%. This local maximum corresponds to the applied magnetic field that causes the greatest change in the material magnetization during the reorientation process.
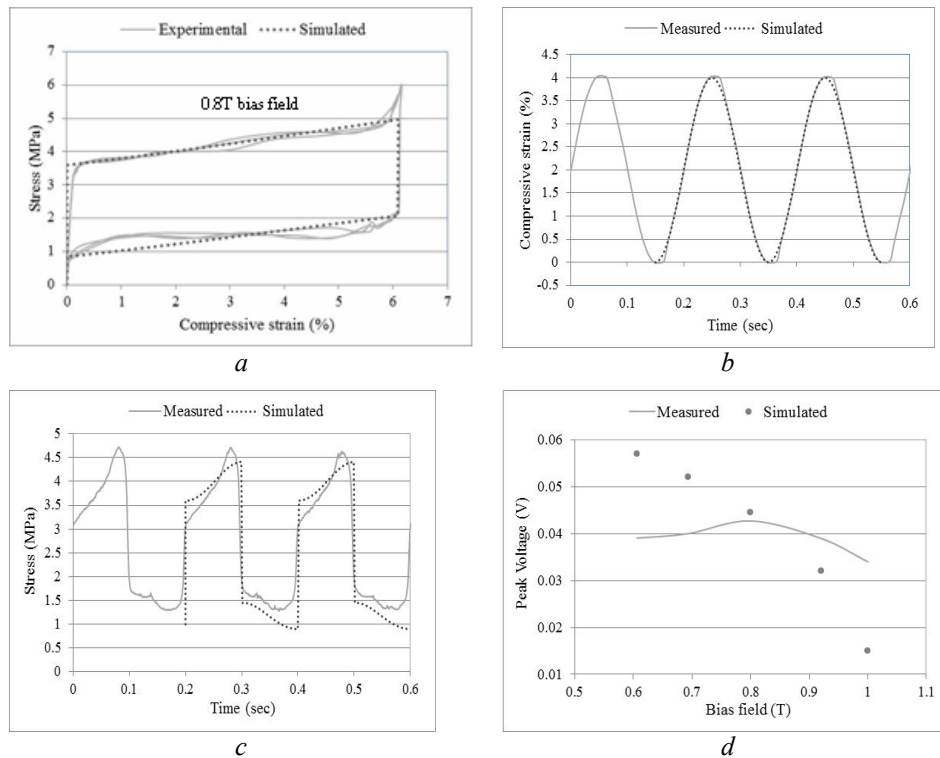
Fig. 3 – *a*) Stress-strain response of the specimen described in Table 1, for full martensitic reorientation at 0.8T bias field; *b*– Strain vs. time during a test performed at 5 Hz for 4% reorientation strain; *c* – Stress vs. time during a test performed at 5 Hz for 4% reorientation strain; *d* – Voltage produced during 5 Hz cyclic tests with a controlled 5% reorientation strain, as a function of bias field.

As seen in Fig. 3*d*, the model is not able to accurately predict the voltage output over the range of the applied magnetic fields. The model predicts fairly accurately the voltage output at 0.8T bias field, while for all the other

fields is either over- or under-estimating the voltage output. This may be due to the fact that all model predictions were made using model parameters determined from the magneto-mechanical response of the material at 0.8T. Another reason for this mismatch may be the equation used to model the material magnetization (*i.e.* Equation 2); this equation predicts that an increase in the applied magnetic field causes a decrease in material magnetization, which the trend is shown by the simulated voltage data. However, this doesn't seem to be confirmed by experiments, so a closer look at this equation is required.

Tests and simulations were not performed at fields lower than 0.6T as preliminary investigations indicated that fields below 0.6T will not initiate enough nucleation of martensite variants to produce reorientation strains close to 5%. Accordingly, further tests were only performed at a bias field of 0.8T for several frequency and strain values.

3.2. Experimental and Numerical Voltage Data

As inferred from the previous section, for the tested specimen, a bias magnetic field of 0.8T will facilitate the production of the maximum voltage (electro motive force - emf) output. As a result, all the tests results discussed in this section will assume a 0.8T bias magnetic field.

The experimental emf was measured by placing a coil of approximately 1000 turns of AWG 36 insulated magnet wire around the specimen; a schematic of this layout is shown in Fig. 1. A virtual instrument developed in LabVIEW was used to measure the voltage output through a PCMCIA DAQCard-6024E analog to digital converter and a SCB-68 I/O connection box. Different reorientation strains were tested at the following frequencies of excitation: 1, 3, 5, and 10 Hz.

The results are summarized in Fig. 4 *a* through 4 *d*; the experimental voltage output data was filtered to minimize the noise interference. Overall, the plots show a good correlation between the simulated and experimental data, indicating that an increase in frequency of excitation leads to an increase in the magnitude of the output voltage.
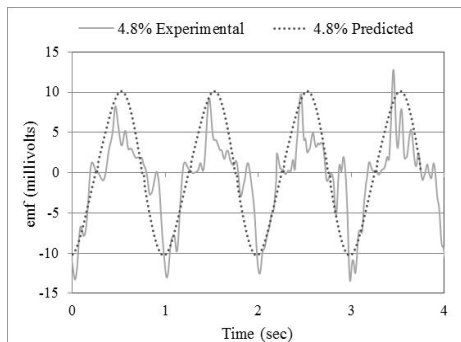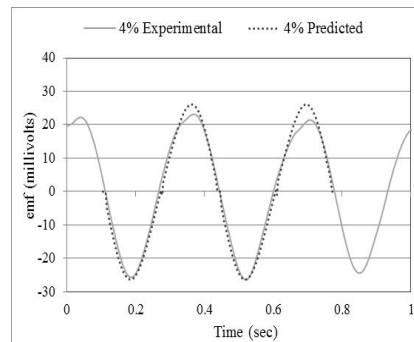
a   *b*
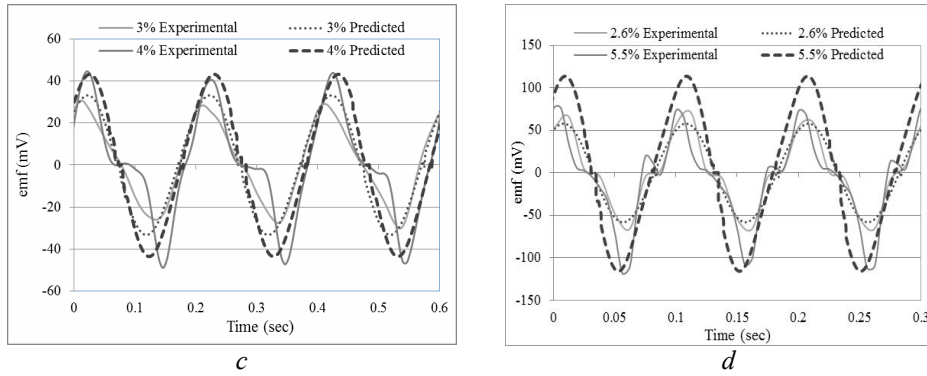
Fig. 4 – *a*) 1 Hz emf vs. time; *b*) 3 Hz emf vs. time; *c*) 5 Hz emf vs. time; *d*) 10 Hz emf vs. time.

The plots shown in Fig. 5 are intended to illustrate the trend of the voltage output in relation to the amount of strain experienced by the specimen and the frequency of excitation. This information may be useful to one evaluating the suitability of these materials for actuation applications.

The results plotted in Fig. 5 indicate that the implementation of the constitutive model combined with Faraday's law of induction under-predicts the voltage induced in the coil during martensitic variants reorientation. The difference between the experimental and simulated data ranges between 0% and 20%, depending on the magnitude of loading parameters, with the difference increasing with the increase in the test frequency (see the 10Hz, 20Hz, and beyond data sets).
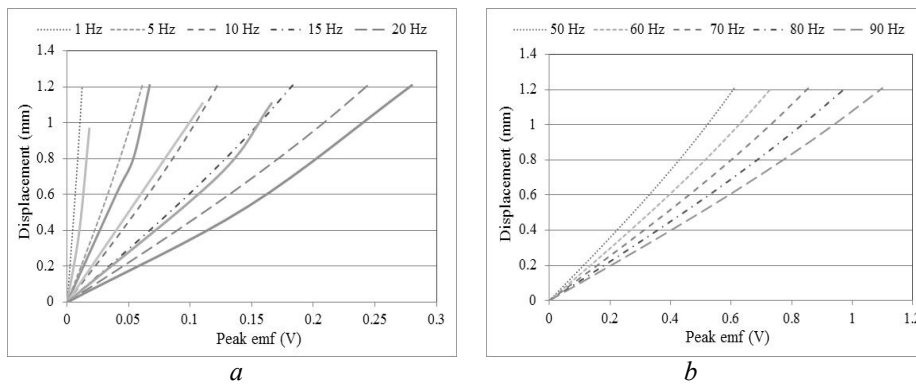
Fig. 5 – *a* – Experimental displacement vs. peak emf for 0.8T applied field (solid-experimental, dashed-simulated); *b* – simulated displacement vs. peak emf for 0.8T applied field.

This may be explained by the fact that the model was calibrated against data acquired at 0.8T bias magnetic field, 5% reorientation strain, and 5Hz

loading frequency, where the dynamic effects play a low to moderate effect on the reorientation mechanism. Accordingly, at low frequencies, the model does a good job predicting experimental data. However, as the frequency increases, and the dynamic effects become more significant, the difference between results increases. As a theoretical exercise, voltage predictions during loading with 1.2mm total displacement up to 90Hz frequency have been plotted in Fig. 5*b*. These results indicate that a peak voltage of 1000 mV may be achieved at the highest frequency; considering that the model under-predicts the voltage as the frequency increases, this indicates that the possible voltage output may be significantly larger that 1V during actual test conditions. However, it has to be mentioned that verifying these predictions is going to be a challenging task as, usually, high amplitudes of displacement and high frequencies are very hard to be achieved simultaneously without specialized testing equipment. Also, the predictions are only valid for a MSMA specimen with the properties defined in Table 1. Specimens with different saturation magnetization, or mass densities, and different effective magnetic anisotropy energy will produce more or less voltage depending on the applied field and amplitude of displacement. Furthermore, the coil used in these experiments had approximately 1000turns, and its geometry as well as the number of turns were not optimized for this application.

4. Conclusion

This study confirmed the suitability of using MSMA specimens for power harvesting and sensing applications and illustrated that voltage prediction can be made using the model developed by Kiefer and Lagoudas to describe the magneto-mechanical response of the material. The implementation of the model leads to voltage predictions that are acceptable at low to moderate frequency levels (i.e. below 15Hz) which is considered to be due to the limited impact of the dynamic effects on the martensitic reorientation mechanism. However, as the frequency level increases (*i.e.* above 20Hz), the model implementation starts to under-predict voltage output. Model predictions could potentially be improved by accounting for inertial effects in future implementations.

REFERENCES

Feigenbaum H.P., Ciocanel C., *Experiments and Modeling of the Magneto-Mechanical Response of Magnetic Shape Memory Alloys.* Proceedings of the ASME Conference on Smart Materials, Adaptive Structures and Intelligent Systems, SMASIS 2009, Paper #1354, 2009.

Karaman I., Basaran B., Karaca H.E., Karsilayan A.I., Chumlyakov Y.I., *Energy Harvesting Using Martensite Variant Reorientation Mechanism in NiMnGa Shape Memory Alloy*. Applied Physics Letters, *90*, 172505 (2007).

Kiefer B., Lagoudas D.C., *Magnetic Field-Induced Martensitic Variant Reorientation in Magnetic Shape Memory Alloys*, Philosophical Magazine, **85**, *33-35*, 4289-4329 (2005).

Kiefer B., Lagoudas D.C., *Modeling the Coupled Strain and Magnetization Response of Magnetic Shape Memory Alloys under Magnetomechanical Loading*. Journal of Intelligent Material Systems and Structures, *20*, 143-170 (2009).

REZULTATE NUMERICE ŞI VALIDARE EXPERIMENTALĂ A VOLTAJULUI INDUS ÎNTR-O BOBINĂ ÎN TIMPUL ÎNCĂRCĂRII DINAMICE A UNUI SPECIMEN DE ALIAJ MAGNETIC CU MEMORIA FORMEI

(Rezumat)

Lucrarea prezintă rezultate numerice şi experimentale privind evaluarea voltajului indus într-o bobină, în timpul reorientării martensitice cauzate din încărcarea dinamică a unui specimen prismatic de aliaj magnetic cu memoria formei. Rezultatele numerice sunt calculate cu ajutorul programului MATLAB combinând un model constitutiv dezvoltat de Kiefer şi Lagoudas cu legea lui Faraday a inducţiei magnetice. Rezultatele numerice sunt apropiate de cele experimentale pentru frecvenţe de până la 15Hz. Pentru frecvenţe peste 15Hz, rezultatele simulate diferă cu până la 20% de cele experimentale; această diferenţă este atribuită efectelor dinamice care sunt mai pronunţate la frecvenţe ridicate şi care nu sunt anticipate cu acurateţe de către modelul folosit în acest studiu.

INDICES FOR THE EQUIVALENT AND OVERALL ASSESSMENT OF THE ECO-SOCIO-ECONOMIC EVENTS IN METALLURGY

BY

AVRAM NICOLAE[1]*, STROE BOGDAN[2], EMANUELA STOICA[1] and MARIA NICOLAE[1]

[1] Politehnica University of Bucharest,
[2] IJP Dolj, Craiova

Abstract. The sustainable development is the result of the interactions between natural (environmental), social and economic systems. For analysing the events in such a situation, we should use aggregate indices for the equivalent and overall assessment. We examined the indices relating to consumption (contents) of primary energy, primary substance and primary negentropy. Hereinafter, we present the methods used to calculate the primary energy and primary substance consumptions. Also, qualitative assessments are made on the consumption of primary negentropy.

Key words: indices, primary energy, primary substance, primary negentropy.

1. Introduction

The concept of sustainable development implemented in industry deals with the modern society as a *eco-socio-economic* (mega)system *(SESE)*, resulted from the interactions and interconditionings of the three fundamental

---

* Corresponding author; *e-mail:*

sections: *the natural system* (the natural environment system), *the social system* and *the economic system*. It is thought that these three systems (not only the natural system) have ecological origin and functions because, within the SESE, the energy, material and information inputs, as well the absorption, by dissipating entropy into the environment, of the majority of waste, are provided by components from the natural system ponds. Such an assertion concerns the important role of the natural environment in the correlations between the three systems, *i.e.*:

–   It provides material and energy inputs for the social and economic systems, using feedback type information on opposite flows; this capacity of the natural environment is the most important condition to optimize the processes of *economic metabolism (industrial)*;

–   It provides the natural absorption and regeneration of most of the waste produced by human activities.

To analyse SESE, as a result of the interactions between the three component systems, we need *methodological tools*, able to:

•   unitary characterize and equalize (through aggregation or globalization possibilities) the interactions among the events carried out in SESE;

•   offer information about the capacity of the natural ponds to provide the material (substance), energy and information required for the human activities;

•   emanating from natural ponds, these three elements are represented in the economic and social analyses of the *primary substance (material), primary energy* and *primary negentropy* (Nicolae *et al.,* 2009).

The application of new equivalence, aggregation and globalisation methodological tools are also justified by the fact that now there are required (Vădineanu, 2004):

–   the replacement of the sectoral assessment techniques with complex and efficient techniques, with high resolution power;

–   the sharing of information regarding the flows of material, energy and information;

–   a methodology able to analyse the SESE-wide metabolism.

Based on the above, the present paper examines the possible use of new indices that can be employed in the metal materials industry, *i.e. the specific consumptions of primary energy, primary substance and primary negentropy*.

2. Specific Consumption of Primary Energy

The primary energy is the energy contained (stored) in the natural deposits of primary fuels (fossil fuels), which are coal, natural gas and oil.

The analyses regarding the primary energy consumptions are made by using the index $I_{s.c.p.e}$, called *specific consumption of primary energy*. It represents the amount of primary energy consumed to obtain a unit of material:

$$I_{s.c.p.e} = \frac{E_p}{Q_s}, \quad \frac{[MJ]_p}{t.steel} \tag{1}$$

In the above relation, Q_s represents the quantity of steel made in the metallurgical furnace. In some papers (especially economic sciences), $I_{s.c.p.e}$ is assimilated with the *primary energy content* of the product obtained in the industrial processes (Nicolae *et al.,* 2005).

The primary energy equivalent of various forms of energy, E_p (expressed in $[MJ]_p$), that depends on the energy E_i recorded in a particular consumer, is calculated using the relation:

$$E_p = eE_i, \quad\quad [Kwh]_p \tag{2}$$

where: E_i is the consumption recorded in the EAFs (expressed in $[kWh]_i$) and in the combustion units (expressed in $[MJ]_i$).

In the above relations, e represents the primary energy equivalent coefficients of the various types of energies used in the metallurgical unit. The currently recommended values for these coefficients are: $e_{n.g.} = 1[MJ]_p/[MJ]_i$ (for coal and natural gas), $e_p = 1.1[MJ]_p/[MJ]_i$ (for fuel oil), $e_k = 1.2[MJ]_p/[MJ]_i$ (for coke) and $e_{e.e} = 10[MJ]_p/[kWh]_i$ (for electric energy).

To understand the essence of the transformation of energy consumptions recorded in the metallurgical thermal facility, it is recommended to see the diagram presented in Fig. 1*a*, which presents the case of an electric arc furnace (EAF) used for steelmaking that consumes the electric energy (EE) produced in power stations (PS) fuelled with natural gas extracted from the deposit (*Z*). The transportation of natural gases and electric energy is carried out on the routes T_1 and T_2. In Fig. 1*b*, we presented the case of a combustion furnace supplied with natural gas directly from ore. (In this case, the possible losses on the transportation route are not born by the metallurgical consumer).
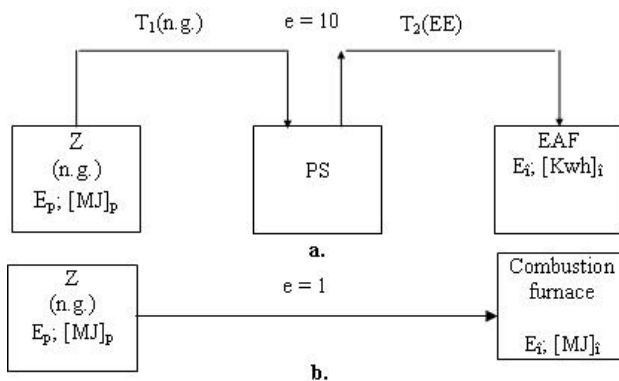
Fig. 1 – Diagram for the interpretation of the equivalent coefficients "e" (Nicolae *et al.,* 2006).

The analysis performed at the EAF must take into account that:

- the extraction and transport *(T₁)* of the natural gases require energy consumptions and losses expressed in percentage through the yield p_1;

- the transformation of the n.g. in electric energy in the PS (power stations) is realised with the yield p_2 (in Romania, the PS yield is about 30…40%);

- the transport *(T2)* means the consumptions and losses measured through the yield p_3;

- the consumption *(E_i)* recorded in the EAF, expressed in *Kwh*, must be multiplied by 3.6 to be obtained in *MJ*.

Based on the above observations, we obtain:

$$E_{p(z)} = 3.6 \frac{E_{i(EAF)}}{p_1 \cdot p_2 \cdot p_3} \tag{3}$$

It can be concluded that:

$$e_{e.e} = \frac{3,6}{p_1 \cdot p_2 \cdot p_3} \tag{4}$$

Considering that $p_1 = p_3 \cong 1$ and taking into account only p_2 with the value 0.35, it results:

$$e_{ee} = \frac{3.6}{0.35} \cong 10 [MJ]_p / [kwh]_i \tag{5}$$

3. Consumption of Primary Substance

The primary substance is the matter (substance) existent in the natural deposits, to be used in industrial processes. For example, the primary substance is the iron transported by the iron ore from the deposit (mine) in the process of obtaining steel sheet. In metallurgy, in addition to the primary energy consumption, we should know the primary substance consumption.

This becomes more and more necessary, as, at present, the cost-benefit analysis assigns costs to extraction and transformation of raw materials, but not for the internal value of the fuel, ore etc. In order to compensate for this deficit, a new ecological index, $I_{c.s.p.p}$, called *content in primary substance of the product,* shall be proposed for definition and description. These considering, the following shall be put forward:

The $I_{c.s.p.p}$ index provides information on the quantity of primary substance to be extracted from the primary substance deposit, in order for the metallurgical product to contain a certain quantity of *useful substance*, $M_{s.u,}$

which, in the iron and steel metallurgy, represents *the quantity of iron* contained in the product obtained based on the transformation chain shown under Fig.2.
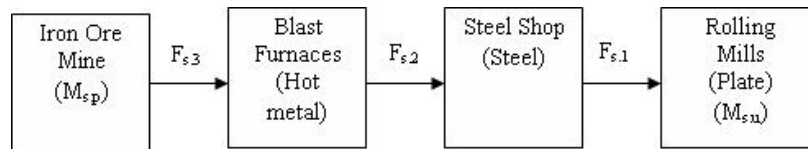
Fig. 2 – Diagram of an inbuilt metallurgical flow.

For engineering needs, this index can be replaced with the *specific consumption of primary substance*.

The index definition and calculation equation is:

$$I_{c.s.p.p} = \frac{M_{s.p}}{Q_p} = \frac{M_{s.u}}{\Pi F_{s_i} \cdot Q_p}; \text{ [kg primary substance/kg plate]} \quad (6)$$

In the above equation, $M_{s.p}$ is the quantity of primary substance (for example, the iron ore required for plate; the coal required for coke etc.) in [kg primary substance; kg iron ore], Q_p is the production of steel [kg steel; kg plate], $M_{s.u}$ is the quantity of useful substance [kg iron/kg plate] and $F_{s.i}$ are the substance transformation subunit factors on the chain in Fig. 2.

- The F_{s_i} factors shall be consecutively measured in [kg iron/kg steel], [kg steel/kg hot metal], [kg hot metal/kg ore].

- The substance transferred from the raw material to the product shall be called *content in primary substance M_p,* of the metallurgical product.

- The transfer of substance from the raw material into the product results in the increase in the sequencing rate (decrease in the random rate) of the processed material, meaning the decline of the *S entropy* or rise of the *nS negentropy* occur.

Further to the above, there may be ascertained that the quantity of primary substance contained in the product is given by the increase of the raw material negentropies:

$$M_{p.s} \text{ or } M_{u.s} = f\left(\sum nS_i\right) \quad (7)$$

In the above relation, nS_i is the negentropy increase recorded in each phase of the global flow.

4. The Consumption of the Primary Negentropy

The econological analyses regarding the primary negentropy consumptions are based on the aspects which will be presented as follows.

By means of its components, among which iron ore, natural resources represent the ranking states of the matter. Thus, it can be asserted that the environment is a storage megasystem of negentropy. In such context, it is valid the statement according to which in nature there is a *primary negentropy storage, nS_p,* where the negentropy of the natural resources is also part of, $nS_{n.r.}$ The existence of living organisms consists of efforts made in order to constantly maintain *the level of the quality of life,* that is of the own entropy (or negentropy). These efforts require large demands of negentropy from outside.

The economic-productive process through which goods required by social needs are produced, is a matter-ranking process, a proven fact that the negentropy of the steel plate is bigger than that of the iron ore taken from nature. According to the first principle of thermodynamics, this transformation cannot be performed unless there is consumption of nS_p from outside the outline of the operating process.

As a whole, the human activity means:
- the consumption of natural resources' negentropy, $nS_{n.r.}$;
- the production of negentropy, S_n, within operating processes, $S_{o.p.}$;
- the release of specific secondary materials (toxic wastes) in the environment is made together with the release of the entropy, S_w, because the alteration states of the ranking matter is increased;
- the transformation of the negentropy of the initial good, resulted from the operating process in entropy of the wastes is accompanied by wastage, which can be both *physical* and *moral;*
- recovering negentropy, $S_{r.n.}$, based on activities of reintegrating wastes (recirculation, recycling, regeneration).

The history of human production shows that the positive reserve $(nS_n + nS_{r.d})$ does not cover the quantum in absolute values $\left[nS_{r.n} + |S_w| \right]$. Thus, the human activity based on a social purpose has to appeal to nS_p, which therefore will decrease.

A diagram representing the variation of the (neg)entropy in mega system may be the one described in Fig. 3.

The above finding is sustained by an assertion according to which what comes in the economic process consists of *valuable natural resources,* and what goes out represent *useless wastes.* Thermodynamically speaking, this means that both matter and energy absorbed by the economic-productive process are in a *state of negentropy*, and what is discharged is in a *state of entropy..*

To conclude, the following aspects are notable:
– performing activities of sustaining social needs presupposes nS_p consumption; thus, maintaining the entropic level within a social outline causes a decrease of negentropy somewhere else;
– the operationalization of the concept of sustainable development has to consider first of all the reduction of rates (speeds) of decreasing nS_p.
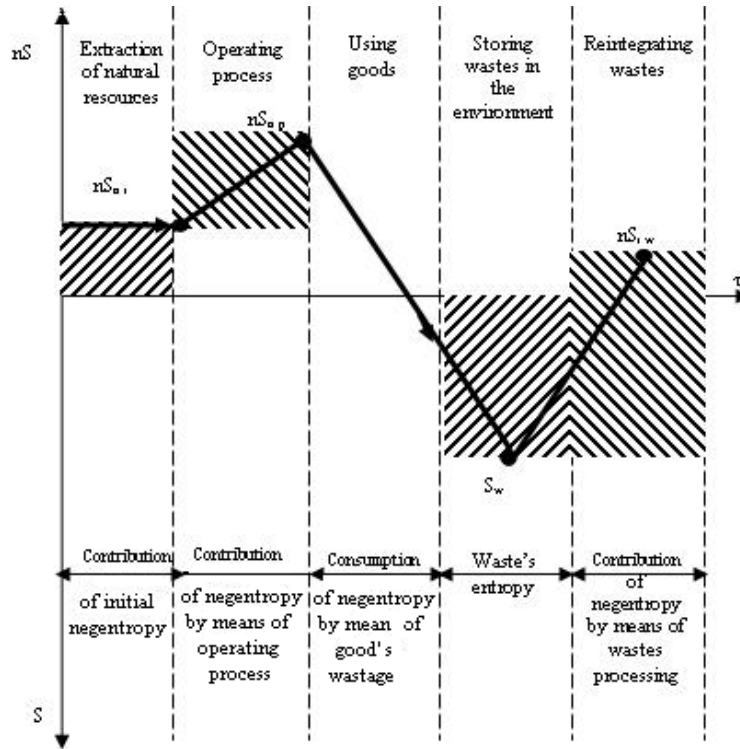
Fig. 3 – Variation of (neg)entropy within the megasystem of natural resources –
operating process – using goods – reintegrating wastes.

The deficit of primary negentropy $\Delta(nS_p)$ is:

$$\Delta(nS_p) = \left[nS_{r.n} + |S_w| \right] - (nS_t + nS_{r.w}) \tag{8}$$

Further to the above, it can be stated that the *technology-sociology* connection, in the sense that the first factor influences the other one, should be analyzed considering the reserves of negentropy. As it is known, the quality of life, as social object, may be improved through modern technological means, as mechanization, automation, etc. However, it should also be taken into account that the mechanization of agriculture, for example, by replacing the ox as an instrument of gaulage for the plough with the tractor, causes an increase in the consumption of initial negentropy due to the manufacture of the tractor and due to the necessary resources for its operation and workers' social needs.

5. Conclusions

The analysis of the eco-socio-economic events resulting from the interaction of natural, social and economic systems needs aggregate indices

with equivalence and globalization role. Important in this respect may be the indices that characterize, in the industrial processes, the specific consumption of primary energy, primary substance and primary negentropy.

The calculation methods presented in this paper can be used for complete engineering analyses regarding the consumptions of primary energy and primary substance.

In terms of consumption of primary negentropy, the information presented in the paper shows the qualitative character of the analyses. We are going to settle the possibilities of quantitative assessment.

REFERENCES

Nicolae A., Borş I., Predescu C., Nicolae M., Şerban V., Predescu Andra, Predescu A., Berbecaru A., *Metallurgical Econology*. (in Romanian), "Printech" Publishing House, Bucharest, 2009.

Nicolae A., Predescu C., Nicolae M., Vizureanu P., Vasiliu A., Minea A.A., *Operationalisation of SD Concept in Siderurgy*. (in Romanian), "Printech" Publishing House, Bucharest, 2006.

Nicolae M., Pană C., Ionescu C.B., Proc. *Sustainable Development in Romania*. (in Romanian), "Expert" Publishing House, Bucharest, 55-100 (2005).

Vădineanu A., *Management of Development*. (in Romanian), "Ars Docendi" Publishing House, Bucharest, 2004,

INDICI PENTRU EVALUAREA ECHIVALENTĂ ŞI GLOBALĂ A EVENIMENTELOR ECOSOCIOECONOMICE ÎN METALURGIE

(Rezumat)

Dezvoltarea sustenabilă este rezultatul interacţiunilor între sistemele natural (de mediu), social şi economic. Într-o astfel de situaţie pentru analiza evenimentelor se impune adoptarea unor indici agregat pentru evaluarea echivalentă şi globală. Se analizează indicii referitori la consumurile de energie primară, substanţa primară şi negentropie primară. Se prezintă metode de calcul pentru consumurile de energie primară şi substanţă primară. Se fac aprecieri calitative referitoare la consumurile de negentropie primară.

IMPLEMENTATION AND PROMOTION OF SOCIAL RESPONSIBLE BEHAVIOR IN ORGANIZATIONS IN THE CONTEXT OF ISO

BY

STELUŢA NISIPEANU[1]*, RALUCA STEPA[2], RUXANDRA CHIURTU[1] and MARIA HAIDUCU[1]

[1] The National R&D Instiute on Occupational Safety,
INCDPM Alexandru Darabont Bucharest
[2] Kooperationsstelle Hamburg IFE GmbH Germany

Abstract. On November 1, 2010 was officially launched in Geneva, ISO 26000 under the name ISO 26000 "Guidance on Social Responsibility", which provides guidance on social responsibility, both for private sector organizations, as well as the public sector, taking into account the principles, key topics and issues of social responsibility. Thus, in this paper there are identified numerous opportunities and benefits that implementation and promotion of social responsibility behaviour could provide for organizations and society, namely: contributing to sustainable development and poverty reduction, development and generalization of a sustainable business model, pursuing excellence and long-term success, the widespread involvement of any type of organization in achieving sustainable development objectives etc. Currently, in Romanian companies there is a strong tendency to relate to international requirements on social responsibility activities.

Key words: social responsibility, implementation, sustainable development.

---

* Corresponding author; *e-mail:* nisipeanusteluta@yahoo.com;

1. Introduction

Corporate social responsibility is a mean by which organizations make a statement of their own principles and values for both employees and external organizations. Many aspects of corporate social responsibility (CSR) have been an integrated part of economic activity long before the current debate on social responsibility. Business concerns regarding the increasingly complex relationships between business activities and society are more obvious than ever. Today organizations are expanding their responsibility for social problems by integrating the latter in their own activity, as to increase competitiveness and to prevent any crisis.

This paper presents some of the results obtained in the national R&D project entitled *"Corporate social responsibility in terms of Europeanization and globalization. Opportunities and constraints for the Romanian economy",* implemented by INCDPM- Alexandru Darabont Bucharest, together with six national partners, in the *Partnership Programme - Competition 2008,* in order to emphasize the current state of development of the corporate social responsibility (CSR) concept on national scale, with the view to implement and promote a social responsible behaviour.

The project has a special significance, by anticipating the necessary framework for the European Commission regulation, announced on 29.11.2010, on CSR compulsory reporting starting with 2011; on this matter, the European Commission had launched a public consultation for a legislative pack on the social responsibility reporting at Member States level (Communication from the European Commission, 2010).

What is more, social responsibility is an integrated part of the 2020 Strategy, by the "Enterprise 2020" initiative, which aims to support companies in achieving sustainable competitiveness, by providing a platform for innovation and change, and to strengthen Europe's leadership at a global level, by means of collaboration with the European Union and a wide range of international partners (OECD, ILO, ONU etc.) (www.csreurope.org).

2. Chapter 1 Aspects Regarding ISO 26000 Standard

On November 1, 2010, one of the most anticipated international standards: ISO 26000 "Guidance on Social Responsibility", was officially launched in Geneva. This standard provides guidance on social responsibility, both for private sector organizations, as well as for the public ones.

The development of ISO 26000 international standard is a concentration of international expertise on social responsibility. For the first time, a standardization process is led by representatives of organizations from a broad social spectrum, both in the developed countries and developing countries, through an initiative that did not belong to governments or

international organizations, such as United Nations. Introducing ISO 26000 will involve a radical change in terms of social responsibility practices, primarily because it would require common terminology and implementation for all organizations in all spheres of activity.

ISO 26000 adds value to existing activities on social responsibility (SR) and will extend the understanding and implementation of RS, owed to the fact that it:

- presents an international consensus on what SR means and what subjects must the organization cover; provides guidance for processing;
- provides guidance for transforming principles into effective action;
- includes the best practices already established and disseminates them worldwide for the international community benefit.

The standard is designed for organizations of all types, public or private sector, in developed countries, developing or in transition. ISO 26000 contains recommendations, not requirements, and is not used for certification (2010).

For organizations, sustainable development means not only providing products and services to satisfy the customer and their implementation without affecting the environment, but also acting in a manner governed by social responsibility. European Commission considers CSR as *"a concept that defines the way in which companies voluntarily include and integrate social and environmental concerns in their strategies, business activities and their relations with the stakeholders"* (2007).

For many years the European Union has given a high strategic priority to promote CSR, as shown in the 2006 Commission's strategy "to make Europe a pole of excellence in this field. Moreover, the European Commission supports a series of initiatives taken by companies to promote CSR projects, noting in particular the European Alliance for CSR, and the European multilateral quorum for facilitating the dialogue in the field.

In this context, it is worth highlighting the recently launched initiative - October 2010 CSR Europe under the name 'Enterprise 2020', which aims to:

- Support companies in achieving sustainable competitiveness, providing a platform for innovation and change;
- Cultivate a collaborative operation between companies and their stakeholders, exploring new ways of working together towards a sustainable future;

Strengthen Europe's global leadership in CSR, working with EU institutions and a wide range of international partners (www.csreurope.org).

3. Chapter 2 CSR Concept Knowledge Level in Romania

CSR is a relatively new concept in Romania and we can't be specified

an exact number of organizations implementing or evaluating their involvement in CSR. Even if there is a series of events and workshops on CSR, Business Ethics Conference, International Conference on Corporate Social Responsibility, celebrating its 3rd edition, Romanian PR Award, however, we cannot speak about a centralization of all existing programs.

However, during the last years there have been concerns from this point of view and these positive trends could contribute to increased attention on social responsibility, because the implementation of CSR activities is a global trend.

One of the broad issues of CSR, which generally exists at the international level, not only in Romania, is the lack of understanding of these concepts and also the small number of professionals. Companies should be able to distinguish between social responsibility, philanthropy and marketing, as these things are put together by the Romanian. The concepts are new to Romania and, consequently, there are efforts to recover lost time.

CSR practices are met especially in the multinationals companies. However, they have the ability to boost social engagement, providing models of firms in Romania, or even being the originators of joint projects, where even public authorities or institutions should be involved.

Looking at these problems and constraints of the current situation in Romania, we therefore welcome the emergence of ISO 26000, which is one of the main indicators of economic responsibility, social and also environmental, for any company that understands the need for its implementation. It is clear that the number of companies developing CSR projects in Romania is increasing. But what is questionable is the real motivation that leads firms to get involved in CSR (economic or charity), how these costs are represented in terms of accounting in reports, if you may talk about being a specialist CSR in Romania. In Romania, CSR is growing, as the economy becomes more stable. According to an estimate by Saga Business & Community, a company specialized in environmental and social services in 2005, companies have invested about 10 million euros in CSR activities (Saga Business&Community Newsletter, 2010).

4. Chapter 3 Implementing and Promoting Social Responsible in Organizations from Romania

In our R&D project a field investigation has been conducted, with the help of our national partners INCSMPS Bucharest, CURS Bucharest and ICEMENERG Bucharest, which aims to determine the current level of standard *ISO 26000- "Guidance on Social Responsibility"* knowledge and implementation by organizations in Romania, companies perceptions and attitude towards its content, structure and utility for the Romanian companies,

practices and ways in which CSR is monitoring impact assessment and reporting. Based on data from the survey results, there will be an assessment of the impact of implementing this standard in Romania and will make proposals and recommendations for improving CSR activity in Romania, in accordance with the requirements of standard ISO 26000.

The field investigation revealed the differences between large and small companies in developing and implementing CSR projects. The relationship between CSR and company size is an issue intensely debated and quite controversial. Internationally speaking, we can see less involvement of small and medium companies regarding specific CSR activities, thus reducing the scope of CSR policies and programs at large companies, enterprise groups or multinationals companies. This is also the reason for which now there are sought methods and means of persuasion and support for the companies with fewer employees to include initiatives, actions and CSR programs in their activity (Capron, 2010).

The companies investigated by us in this study agree that CSR activity in every organization is very important and that all companies, regardless of their size should be involved in CSR programs. But, there are differences existing between small and large companies regarding their development and the scale and complexity of the programs discussed. There are also differences in terms of complexity measures for implementation, monitoring and evaluating the results of those actions as required by ISO 26000, small firms are less willing to devote time and funds for such activities.

We also identified opportunities in ISO 26000 implementation in Romania, some of them are:
- the multinationals companies entry on the market, that caused a sort of pressure, in terms of identifying appropriate ways to enhance corporate image and reputation;
- participation in auctions or partnering with serious companies are subject to the implementation of management standards;
- charitable activities of an enterprise increase together with the increase in profits;
- discrimination based on sex, religion, social, age is not as extensive as in other countries;
- more organizations provide employee training;
- existence of public campaigns against corruption and the unmasking of a person;
- increasingly more companies involved in local community life;

Some of the major constraints that stop the implementation of ISO 26000 in Romania are:
- the use of "moonlighting" labour and even minors labour;
- often, quality is not the key criterion, but the price;

- national recycling and waste management are just theoretical concepts;
- several managers' lack of basic knowledge on the existance or the benefits of CSR;
- many companies do not report adequately their impact on the environment and ignore or aggravate environmental problems.

5. Conclusion

Our study and field investigation reveals that in Romania there is interest and openness to the implementation of CSR programs, but there is now a phase shift between the Romanian and the foreign companies (multinational companies) in the application of specific methodologies for monitoring, evaluation and reporting of CSR, expressed in ISO 26000.

Thus, in Romania we may talk about a landing of multinational companies that constantly promote CSR projects and programs, which are included in long-term strategies of the companies and apply CSR models in countries of origin, adapted to conditions in Romania. Intense media coverage and publication of their annual CSR reports help enrich the experience of Romanian companies in the field of CSR.

Analysis of the organizational structure of the CSR activities of state-owned companies reveals the existence of weaknesses such as lack of a special division for CSR activities and an interest insufficient to assess CSR activities (notably those carried out at Community level) and reporting to work according to international standards.

As the study conducted in this phase of research was exploratory in nature, further investigation by conducting a nationally representative survey to assess the specific information needs to implement CSR programs according to ISO 26000 standard requirements, as well as the in-depth study of some companies' experience, companies that have CSR standard specific activity and strong coverage of this practice in companies with a weaker experience in this field.

REFERENCES

* * *CSR Report Starting with 2011.* (Transl. from English), Communication from the European Commission, November 2010, 136.
* * *ISO 26000 - Guidance on Social Responsibility.*Transl. from English, November 2010, 5-7.
* * *Responsabilité sociale des entreprises Politiques publiques nationales dans l'Union européenne.* (Transl. from French), Commission européenne: Direction

générale de l'emploi, des affaires sociales et de l'égalité des chances Unité D.2, 2007, 23;

* * Saga Business&Community Newsletter, March 2010;

* * www.csreurope.org/enterprise2020 (Transl. from English).

Capron M., *La responsabilité sociale des entreprises (RSE) est positive pour la société, l'environnement et l'activité économique. C'est pourquoi la Commission européenne mène des activités en sa faveur dans divers secteurs industriels, (transl. from French).* Les concepts de la RSE et de developpement durable *IAE Gustave Eiffel* –Créteil, Avril 2010, France, 11.

IMPLEMENTAREA ŞI PROMOVAREA UNUI COMPORTAMENT SOCIAL RESPONSABIL ÎN ORGANIZAŢII, ÎN CONTEXTUL APARIŢIEI STANDARDULUI ISO 26000

(Rezumat)

La data de 1 noiembrie 2010 a fost lansat oficial, la Geneva, standardul ISO 26000 cu denumirea ***ISO 26000, Guidance on social responsability***, care furnizează linii directoare privind responsabilitatea socială, atât pentru organizaţiile din sectorul privat, cât şi pentru cele din sectorul public, ţinând cont de principiile, subiectele cheie şi problematicile responsabilităţii sociale. În acest sens, în acest articol sunt identificate numeroase oportunităţi şi beneficii pe care le poate oferi implementarea şi promovarea comportamentului responsabilităţii sociale pentru organizaţii şi pentru societate şi anume: contribuţia la dezvoltarea sustenabilă şi scăderea sărăciei, dezvoltarea şi generalizarea unui model durabil de a face afaceri, urmărind excelenţa şi succesul pe termen lung, implicarea pe scară largă a oricărui tip de organizaţie în atingerea obiectivelor dezvoltării durabile etc. În prezent, la nivelul firmelor din România, se manifestă o tendinţă pronunţată de racordare la cerinţele internaţionale privind activitatea de responsabilitate socială.

BEHAVIOR OF DIELECTRIC PROPERTIES OF NANO-CONDUCTIVE POLYMER FILMS

BY

MARIUS OLARIU[1]*, SEBASTIAN ARĂDOAEI[1], SUAT CETINER[2], ROMEO CIOBANU[1] and SEZAI A. SARAC[2]

[1]"Gheorghe Asachi" Technical University of Iaşi,
Department of Electrical measurements and Materials
[2]Istanbul Technical University,
Department of Textile Engineering

Abstract. Dielectric properties of polyacrylonitrile composite films in the presence of pyrrole derivatives are reported in this paper. The composite films were fabricated by oxidative polymerization of pyrrole, N-methyl pyrrole and N-phenyl pyrrole by cerium (IV) on polyacrylonitrile matrix. The effect of temperature on the dielectric properties was studied in the frequency range from 0.05 Hz up to 10 MHz and in the temperature range from 0°C up to 250°C. The conductivity increased with the temperature due to increased mobility of charge carriers in the composite films. By increasing the temperature the dipoles became free and respond to the applied electric field in composite structure, thus, the polarization and dielectric constant increased as well. Tan delta was shifted to higher frequencies when the temperature was reached to 100°C. PNPhPy-PAN composite films exhibited the highest dielectric constant, AC conductivity and tan delta.

Key words: conductive composite film, temperature dependence on dielectrics, AC conductivity, pyrrole derivatives.

---

* Corresponding author; *e-mail:* molariu@ee.tuiasi.ro

1. Introduction

Conducting polymers are a new class of materials with an extensive delocalization of p-electrons conjugated network opening the way to new applications in the fields of energy storage, microelectronics, textiles, sensors, electroluminescence and electromagnetic interference (EMI) shielding. The essential feature of the conducting polymers is the one of providing p-bands of delocalizet molecular orbital within which full range of semiconductors and metal behavior can be achieved through the control of the degree of band filling (Dhawan *et al.,* 2002; Hakansson *et al.,* 2006). Among the conducting polymers, polypyrrole (PPy) has attracted much attention in particular thanks to its high conductivity, redox properties, environmental stability and easy preparation as a film or powder by both electrochemical and chemical methods under various conditions (Ping *et al.,* 2009; Li F. *et al.,* 2009). Development of textiles with new properties and applications has received great attention during the last years. One of these properties is the electrical conductivity in textiles. The reason is that electrostatic and electromagnetic interference became common place because of human lifestyle changes and the increasing sophistication of industrial technology. Intrinsically conducting polymers (ICP) with relatively high conductivity and dielectric constant are promising materials for EMI shielding applications (Lee *et al.,* 2001). By varying the electrical conductivities or the dielectric constants of conjugated polymers the materials EMI shielding performance can be controlled (Kim *et al.,* 2002). Saafan *et al.* (2006) investigated the temperature effect on the dielectric properties of polypyrrole which dielectric constant increases with increasing temperature at lower frequencies due to the thermally activated nature of charge transport in PPy resembling semiconductor. Harun *et al.* (2008) studied polyvinyl alcohol-polypyrrole (PVA-PPy) composite films; the AC conductivity was measured at different temperatures in frequency range starting from 20 Hz up to 1 MHz. By increasing the temperature the AC conductivity of composite films increased as well due to free charges mobility. Abthagir & Saraswathi, (2005) investigated the effect of temperature on conductivity of the electrochemically prepared polypyrrole. The mobility of charge carriers in conjugated polymers increased by increasing temperature leading to higher conductivity; at room's temperature, the measured conductivity as 5.7×10^{-2} S/cm. Oh *et al.* (2004) studied the electrical properties of electrochemically synthesized polypyrrole films at different temperatures. Conductivity's augmentation was due to the molecular chains of polymers which were fully rearranged by heating and offering a flowing route to electrons.

In the present paper, composite films were fabricated by the oxidative polymerization of pyrrole, N-methyl pyrrole and N-phenyl pyrrole with

cerium (IV) on polyacrylonitrile matrix to observe the effect of substitution. The effect of temperature on the dielectric properties was studied in a frequency range starting from 0.05 Hz up to 10 MHz and in a temperature range from 0°C up to 250°C.

2. Experimental

2.1. Materials

Cerium Ammonium (IV) Nitrate $(NH_4)_2[Ce(NO_3)_6]$ (CAN), nitric acid (HNO_3), dimethylformamide (DMF) and oxalic acid were all Merck reagents. Acrylonitrile was supplied by Aksa, Turkey. Pyrrole, n-methyl pyrrole and n-phenyl pyrrole were all Aldrich reagents. All these chemicals and monomers were used as received. Distilled water was used for preparing solutions and stock solutions.

2.2. Fabrication of Conducting PPy/PAN Composite Thin Films

The polymerized PAN (polymerization conditions were given in our previous work) (Cetiner *et al.,* in press) was dissolved in DMF and pyrrole with initial mass ratio (40 wt%) was added into the solution. After mixing the solution for one hour at room temperature, Ce(IV) (30% amount of Py) was added in order to polymerize pyrrole; the temperature was increased up to 80°C to obtain a viscous PPy/PAN solution. Viscous solutions were casted as films on a 5×5 cm^2 glass substrate and were dried in a 600 mmHg vacuum stove for 24 hours at 60°C. The composite films with thicknesses between 40 and 80 μm were obtained. The same aforementioned procedure was used for preparing the conducting PNMPy/PAN and PNPhPy/PAN composite films.

2.3. Characterization of Composite Thin Films

The dielectric measurements by using a Novocontrol Broadband Dielectric Spectrometer (Alpha-A High Performance Frequency Analyzer, frequency domain 0.001Hz to 3GHz). The samples were sandwiched between two gold electrodes with a diameter of 20 mm. The temperature variation and controlling was realized using nitrogen gas cryostat which assured a temperature stability of 0.1°C and the applied AC voltage was equal to 1.5V.

3. Results and Discussion

3.1. Dielectric Spectroscopic Analysis

3.1.1. *Dielectric Constant.* Figs. 1 *a…c* shows the frequency dependence of dielectric constant (ε') of the composite films at different

temperatures including 40 wt% Py, NMPy and NPhPy.

The dielectric properties of the samples were evaluated on the basis of dielectric constant (ε') which is decreasing while increasing the frequency and of dielectric losses (ε'') which may exhibit one or more peaks on the frequency characteristic. The decrease of dielectric constant with increasing frequency is an expected behavior in most dielectric materials, but the difference between the values at low and high frequencies are significant if referring to conductive polymers. More than that, at lower frequencies when the temperature increases, the side groups or small units of main chains may be able to move and follow the variation of the field and therefore may contribute to the polarization. While the frequency is increased, those side groups or small units of main chains lose gradually their ability to follow the field and consequently their contribution to the polarization ceases (Saafan *et al.,* 2006). At low frequencies and higher temperature, the increased values of the dielectric constant can be explained by the thermally activated transport of charges in the composite.
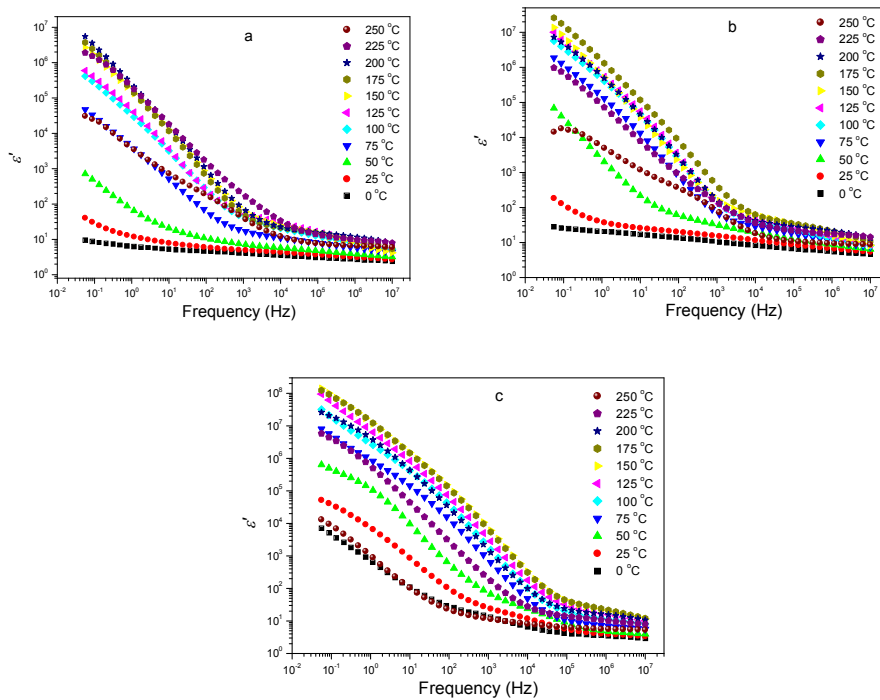
Fig. 1 – Dielectric constant change with increasing frequency of composite films polymerized with (*a*) Py, (*b*) NMPy, (*c*) NPhPy.

The high values of dielectric constant at low frequencies are due to Maxwell/Wagner and/or electrode polarization which can be observed when

the electric field is applied and when the charges are moving to the interface between the conjugated polymer and the matrix (Fig. 1) or towards the electrode-polymer interface. At lower temperatures, as the dipoles are rigidly fixed in the composites, the field can not change the condition of dipoles. As the temperature increases, the dipoles comparatively become free and they respond to the applied electric field in composite film structures. Thus, polarization increases and hence dielectric constant is also increased with the increase of temperature (Saafan *et al.,* 2006; Suri *et al.,* 2003).

Fig. 2 presents dielectric constant comparison of composite films at different temperatures for 1 Hz.
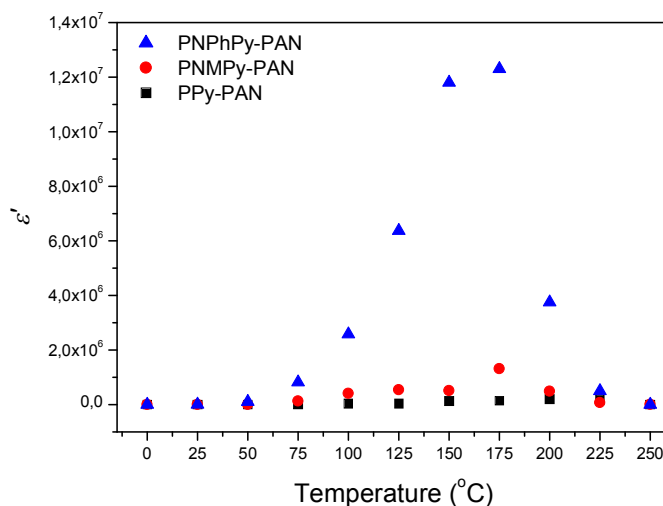
Fig. 2 – Dielectric constant comparison of composite
films at different temperatures for 1 Hz.

When the temperature was increased up to 175°C for NMPy and NPhPy based composite films a maximum was observed for NPhPy and NMPy, and a decrease of the dielectric constant can be noticed after this maximum (Fig. 2).

3.1.2. *AC Conductivity.* The initial increase of conductivity can be considered by the fact that molecular chains of polymers are fully rearranged by heating and offer a flowing route to electrons. The conductivity augmentation with the frequency and temperature is a polymeric semiconductors response which is due to the increase of the charge carriers' mobility in the composite films. An obvious conductivity increase between 1-10 MHz and conductivity is reached the highest value at 10 MHz in all composite films. In PNPhPy-PAN composite films, the temperature

dependence is more evident if comparing with the Py and NMPy. For the PPy films doped with DBSA the conductivity increased as temperature is increased up to 150°C while in case of the PPy doped with NSA the conductivity is incresing up to 200°C and then is swiftly decreasing (Oh, 2004). Referring to our results, for the composite films prepared with NMPy and NPhPy the conductivity is augmenting as the temperature is increased up to around 175°C and then is decreasing, whereas the conductivity of the composite film prepared with Py started to decrease as the temperature reached to 200°C (Fig. 3). The iron oxide-polypyrrole nanocomposites having 15% pyrrole exhibited the polypyrrole degradation at lower temperatures ranging from 120-200°C (Suri *et al.,* 2003). Polypyrrole decomposition temperatures were found between 180°-237°C by thermal gravimetric analysis (Akram *et al.,* 2005). Thus, conductivity decrease might be due to the decomposition of pyrrole derivatives at temperatures ranging from 175-200°C for our composite films (Fig. 3).
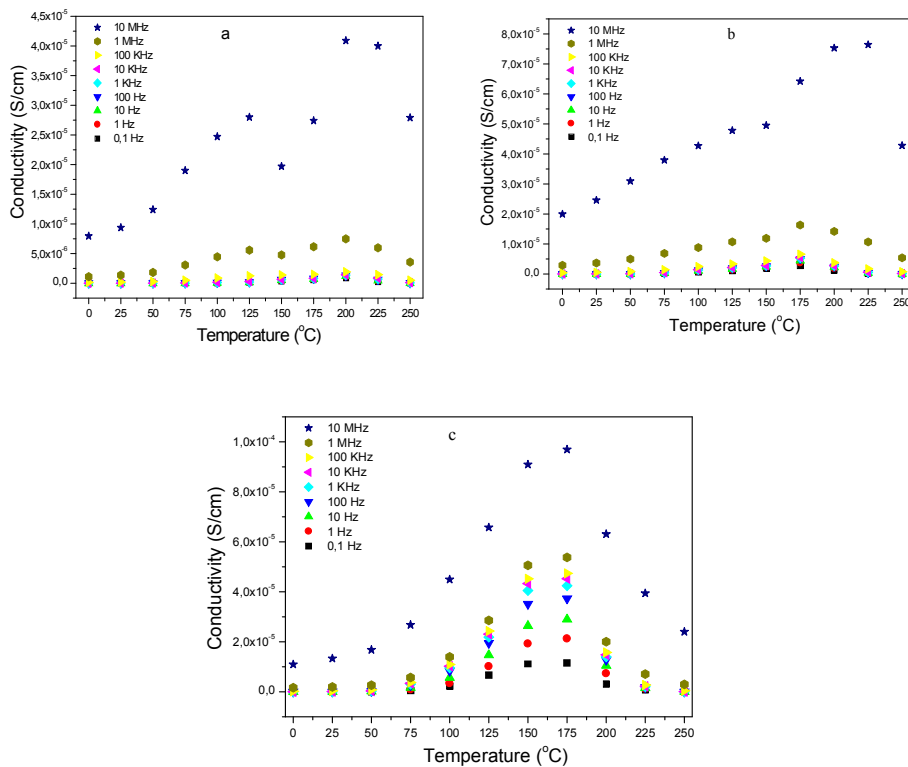
Fig. 3 – Conductivity change with increasing temperature of composite films polymerized with (*a*) Py, (*b*) NMPy, (*c*) NPhPy.

Conductivity maxima were attributed to the relaxation processes in the polymer chains. The charges mobility is expected to increase while increasing the temperature in the conjugated polymers. This may lead to an increase in the energy of activation and also a higher resistance toward inter and intra-chain charge transports due to the increased distance between the neighboring domains. The conductivity maximum occurs at a temperature close to the end temperature of the dielectric relaxation (Abthagir & Saraswathi, 2005).

Fig. 4 presents a comparison among the conductivity of composite films at different temperatures at 10^6 Hz. Especially at higher temperatures, the band gap between the valence band and conduction band is reduced and providing easiness for electrons to hopping from valence band to conduction band (especially for NPhPy) and thus, higher conductivity values are obtained compared to lower temperatures. Intrinsically conducting polymers (ICP) with relatively high conductivity and dielectric constant are promising materials for EMI shielding applications (Lee *et al.*, 2001). According to the absorption mechanism of EMI shielding, the shield (*i.e.*, composite film) material should have electric or magnetic dipoles (Chung, 2000).
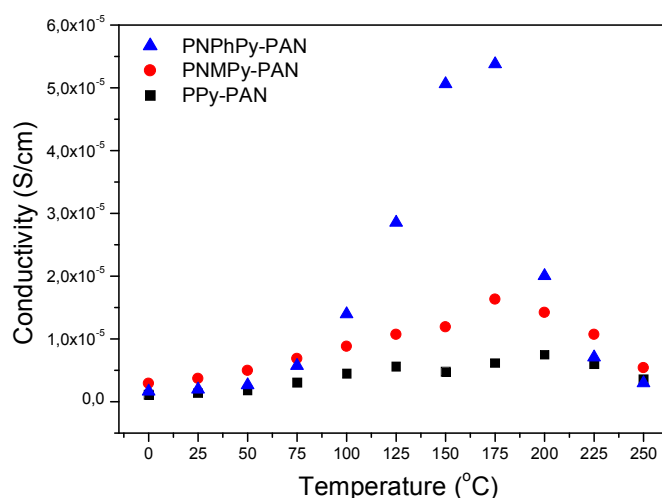
Fig. 4 – Conductivity comparison of composite films at
different temperatures for 10^6 Hz.

In the presence of phenyl pyrrole, composite films have the higher dielectric constant and conductivity values compared to pyrrole and methyl pyrrole at lower frequencies (Figs. 4, 6). Thus, PNPhPy-PAN composite films can be a candidate for absorbent panels and EMI shielding applications.

3.3.3. *Tan Delta.* The variation of tan δ (*dissipation factor or dielectric losses*) with frequency for Py, NMPy and NPhPy at selected temperatures (a=25°C, b=100°C) is presented Fig. 5*a* and 5*b*.

Fig. 5*a* presents the relaxations at room temperature. The Py and NMPy are exhibiting the first relaxations at lower frequencies, below 10^{-2} Hz, while for the NPhPy sample the relaxation appeared at higher frequencies, around 10-100Hz. The second relaxation (at frequencies around 10-100 kHz) is very weak for Py and NMPy and is more visible on the descending ramp in the presence of NPhPy. At 100°C the relaxations are movong to higher frequencies by changing pyrrole substitution (Fig. 5*b*). The temperature and the type of Py substitute has a significant influence on the dipole dimensions of conjugated polymers in PAN matrix, so that the dipoles for the NPhPy are bigger than the ones observed for the Py.
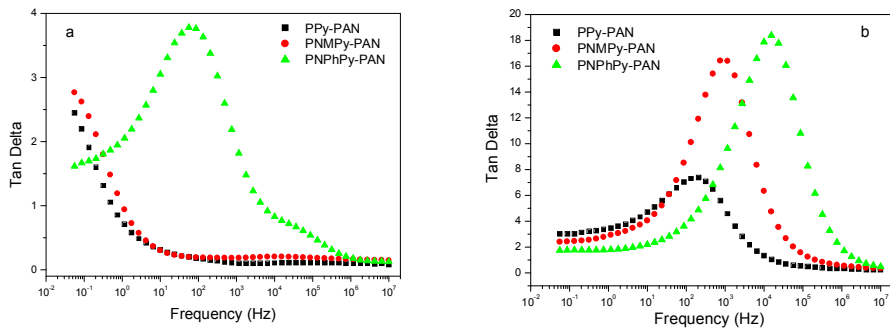
Fig. 5 – Variation of tan δ of the composite films as a function of frequency for different pyrrole derivatives at 25°C (*a*) and 100°C (*b*).

The composites exhibited high dielectric constant and dissipation factor(=tan delta) in the low and radio frequency ranges, so they can be utilized in charge storing devices, decoupling capacitors and electromagnetic interference (EMI) shielding applications (Panwar & Mehra, 2008). In our results, the high values of tan delta make NPhPy suitable for these applications at higher frequencies.

4. Conclusion

Conductivity increased with the temperature due to increasing the mobility of charge carriers in the composite films. The dielectric constant augmented while increasing the temperature at lower frequencies, fact that can be linked with the thermally activated transport of charges in the composites

resembling semiconductor. Conductivity and dielectric maxima were attributed to the relaxation processes in the polymer chains. The mobility of the charges are expected to increase while increasing the temperature in the PPy chain leading to an increase in the energy of activation and a higher resistance toward inter and intra-chain charge transports due to the increased distance between the neighbouring domains. Tan delta moved to higher frequencies when the temperature reached 100°C. PNPhPy-PAN composite films exhibited higher dielectric constant, AC conductivity and tan delta values, and thus, they can be candidate for absorbent panels, decoupling capacitors and EMI shielding applications.

REFERENCES

Abthagir P.S., Saraswathi R., *Materials Chemistry and Physics. 92*, 21 (2005).

Akram M., Javed A., Rizvi T.Z., *Turk J Phys*, *29*, 355 (2005).

Biswas M., Roy A., *Journal of Applied Polymer Science*, *51*, 1575 (1993).

Cetiner S., Karakas H., Ciobanu R., Olariu M., Kaya N.U., Unsal C., Kalaoglu F., Sarac A.S., *Synthetic Metals*-in press.

Chung D.D.L., *Journal of Materials Engineering and Performance*, *9*, 350 (2000).

Dhawan S.K., Singh N., Venkatachalam S., *Synthetic Metals. 129*, 261 (2002).

Hakansson E., Amiet A., Kaynak A., *Synthetic Metals.* 156, 917 (2006).

Harun M.H., Saion E., Kassim A., Hussain M., Mustafa I.S., Omer M.A.A., *Malaysian Polymer Jounal*, *3*, 24 (2008).

Kim M.S., Kim H.K., Byun S.W., Jeong S.H., Hong Y.K., Joo J.S., Song K.T., J.K. Kim, Lee C.J., Lee J.Y., *Synthetic Metals. 126*, 233 (2002).

Lee C.Y., Lee D.E., Joo J., Kim M.S., Lee J.Y., Jeong S.H,, Byun S.W., *Synthetic Metals.119*, 429 (2001).

Li F., Tingyang D., Yun L., *Synthetic Metals.* 159, 2101 (2009).

Oh K.W., Park H.J., Kim S.H., *Journal of Applied Polymer Science.* 91, 3659 (2004).

Panwar V., Mehra R.M., *European Polymer Journal*, *44*, 2367 (2008).

Ping X., Xijiang H., Bin Z., Nathan H. M., Sea-Ho J., Hsing-Lin W., *Polymer.* 50, 2624 (2009).

Saafan S.A., El-Nimr M.K., El-Ghazzawy E.H., *Journal of Applied Polymer Science*, 99, 3370 (2006).

Suri K., Annapoorni S., Tandon R.P., Rath C., Aggrawal V.K., *Current Applied Physics*. *3*, 209 (2003).

EVOLUŢIA PROPRIETĂŢILOR DIELECTRICE A UNOR FILME POLIMERICE
NANOCONDUCTIVE

(Rezumat)

În această lucrare este prezentată evoluţia proprietăţilor dielectrice ale filmelor compozite din poliacrilonitril în prezenţa derivaţilor pirolului. Filmele compozite au fost fabricate prin polimerizarea oxidativă a pirolului, N-metil pirolului şi a N-fenil pirolului cu ceriu (IV) în matrice de poliacrilonitril. Efectul temperaturii asupra proprietăţilor dielectrice a fost analizat într-un domeniu de frecvenţă de la 0.05 Hz până la 10 MHz şi într-un domeniu de temperatură cuprins între 0°C şi 250°C.

PIEZO SENSORS IN MONITORING THE BONDED ZONE COMPOSITES-METALLIC STRUCTURES

BY

S. OPRIŞAN[1]*, A. BUZAIANU[2], N. CONSTANTIN[3], S. RUSU[4], C. BANU[2] and I. RUSU[4]

[1] STRAERO S.A., Bucharest,
[2] METAV-R&D S.A., Bucharest,
[3] University "Politehnica" Bucharest,
[4] "Gheorghe Asachi" Technical University of Iaşi.

Abstract. The paper approaches the complex aspects related to the health monitoring of aluminum alloy aeronautical structures bonded with composite based on prepreg and epoxy adhesives. Crack detection with piezoelectric wafer active sensors (PWAS) is an effective and powerful technique in structural health monitoring (SHM). Although quite fragile, piezo MEMS prove to be satisfactorily endurable to environmental factors (temperature, corrosion etc.) and can be applied with success if measures are taken to physically protect the sensors.

Key words: health monitoring, piezo MEMS, Lamb wave, hybrid composites, SHM.

1. Introduction

The new concepts on the design and maintenance of structures involving composite materials should also take into account the need for a rapid

---

* Corresponding author; *e-mail:* sorin.oprisan@straero.ro

diagnosis of the different types of defects that may appear in composite bonding whiz metallic structures. Their advancement would increase the reliability of the so called "smart composites" with piezoelectric sensors in repair interventions. The piezo-MEMS devices are capable to detect, in real time, certain types of loads to which composite type aeronautical structures respond. As a result, significant investments are being made to develop technologies that enable the health monitoring of composite structures with minimum costs. They allow the selection of the right time for repair, the assessment of the repair work quality and the monitoring of the repaired structure behavior in service. When inserted into the composite patches, under the action of the loads in the material, MEMS can offer information on the local area deformation and structural degradation appearing in the monitored area. The advantage is that the sensor may be embedded in different interest areas to monitor changes due to strain or fatigue. An "in situ" microprocessor may be embedded in the repaired structure so as to supply data, in real time, on the structural integrity of the composite. These sensor types also have the advantage to function without another energy source. They are able to supply information upon request and can be attached or embedded in the structure after repair. In order to set up a structural health monitoring system, one also needs instruments for the activation of the electric field, as well as equipment for the acquisition, processing and interpretation of data. To enable easy monitoring, the investigation devices must be small. The areas selected for the piezo-sensors location should be protected, especially if piezoelectric film sensors are replaced with ceramic plate sensors.

2. Theoretical Framework

Damage detection in bonded hybrid structures depends on both the characteristics of the associated materials and on the characteristics of the attachment type performed, which may vary within a very large range, function of the type of intervention in which the composite material is used.

To this purpose, a brief reference to the Lamb wave transmission will be made, as the experiment further detailed is based on it. In 1917, the English mathematician Horace Lamb published an analysis of the elastic wave propagation in flat solids and defined the propagation manner of these types of acoustic waves (Lamb, 1917). Lamb shows that an infinite medium supports just two wave modes traveling at unique velocities; but plates support two infinite sets of Lamb wave modes, whose velocities depend on the relationship between the wavelength and the plate thickness. Lamb's equations were derived by setting up formalism for a solid plate having infinite extent in the x and y directions, and thickness d in the z direction. Sinusoidal solutions to the wave equation were postulated, having x and z displacements of the form. Since the 1990's, the understanding and utilization of Lamb waves has advanced greatly, thanks to the rapid increase in the availability of computing power. Lamb's

theoretical formulations have found substantial practical application, especially in the field of nondestructive testing (Viktorov, 1967).

3. Experimental Investigations

The special test samples were manufactured from aluminum alloy panels in which crack type damages on different directions were induced by milling. The defective areas have been repaired with prepreg composite patches to which piezo-MEMS of transducer type have been attached. The main physical and mechanical characteristics of the composite materials end the adhesive used in technological testing are presented in Table 1. Fig. 1 illustrates the transducers' positioning as well as the manner in which they were set onto the composite patch.

Table 1
Characteristics of Composite Materials Used in Panel Repair

Characteristics	Composite based on carbon fiber prepregs (60%)	Composite based on fiberglass prepregs (50%) type E	Epoxy resin
Density (g/ cm^3)	1,8	2,6	1,3
Specific heat (kJ kg $^{-1}$ K $^{-1}$, la 20°C)	1200	-	1700
Thermal conductivity (W/ m . K)	0,8-1,5	0,1-0,3	0,20
Tensile strength (MPa)	800	600	35
Coefficient of thermal expansion (°C^{-1})	5 x 10^{-5}	10x 10^{-5}	3 x 10^{-6}

The Lamb waves emission/reception is made through transducers located in pairs. The positioning solution for the wafer transducers was selected so as to best cover the composite repaired area monitored by piezo-MEMS. When stretched or compressed, the latter produce a voltage, due to the piezoelectric effect, and therefore require no power to operate.

Fig. 1 –Experimental device for studying the interraction of Lamb wave modes. Piezo-MEMS (wafer transducers) positioning on the test panel bondind with composite patch to definitive the amplacement and frquency sensor.

The monitoring of Lamb wave propagation is based on a comparative approach. First, the wave transmission in a recently repaired (undamaged) panel is monitored, then in panels with different damage degrees, in order to see how the existing flaws influence the different wave propagation A0 and S0 modes. The wave propagation modes were determined in panels repaired with composite patches reinforced with fiberglass or carbon fibers, as shown in Table 1. In order to prepare the tests on the panel behavior, numerical simulations were made, using the finite element method. In the beginning, using the ANSYS program, 2D models were developed, followed by 3D models. At the same time, the most appropriate testing conditions were studied, mainly focused on two interest directions: the case when the PZT-type MEMS to be used for the Lamb wave inspection method could be positioned right at the respective interface, thus becoming in themselves a cause for disbonding initiation, or, the case when fissures are created at the interface due to a deficient repair technology.

In this purpose, a numerical model was taken into account to simulate the overlapping area formed by a 3-layer composite patch applied over an aluminum substrate of the same thickness. A laminate hybrid aluminum/composite plate was thus created, with the total thickness of 2.4mm, from a 1.2 aluminum foil and 3 equally thick layers of GFRP 0°/90°/0°, for which the lamina properties at 0° are: $E_1 = 109.34$ GPa; $E_2 = 8.12$ GPa; $E_3 = 8.12$ GPa; $G_{12} = 4.32$ GPa; $G_{23} = 3.2$ GPa; $G_{13} = 4.32$ GPa; $\nu_{12} = 0.342$; $\nu_{23} = 0.26$; $\nu_{13} = 0.342$; (MAJOR Poisson ratio); $\rho = 1580$ kg/m^3. For the aluminum plate, the following dimensions were considered: $E = 70$ GPa; $\nu = 0,33$ and $\rho = 2700$ kg/m^3. To generate the signal, a Velleman signal generator was used, with a PCLAB 2000 programme, as per Fig. 2.
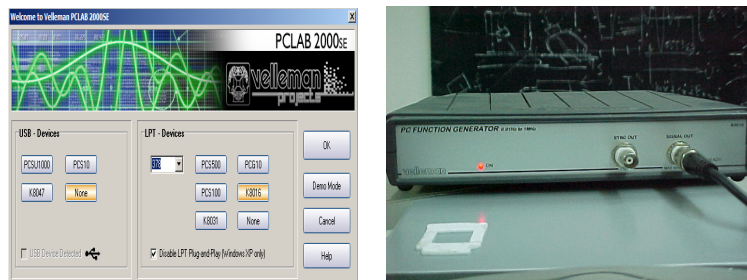
Fig. 2 – The Echipament Valleman to signal generator with
PCLAB 2000, program (STRAERO data-acquisition system).

The signal is generated based on a text file. Different types of propagation modes and different base frequencies were tried. Two solutions were tested: a program written in LabView mode and a program written for a computer connected functions' generator. The second solution was adopted

because it delivers better results for higher frequencies, due to better definition of the signal form. (Parameters A_0 – maximum amplitude, n_0 – number of cycles, f_0 frequency).

For maximum sensitivity, the transducer length must be thoroughly chosen. Unlike in isotropic plates or symmetrical composites, in hybrid plates there exist multi-mode Lamb waves for which the symmetry/anti-symmetry is perturbed. The frequency and the signal shape should be thus selected as to generate certain modes corresponding to non-dispersive wave propagation intervals (Fig.3).
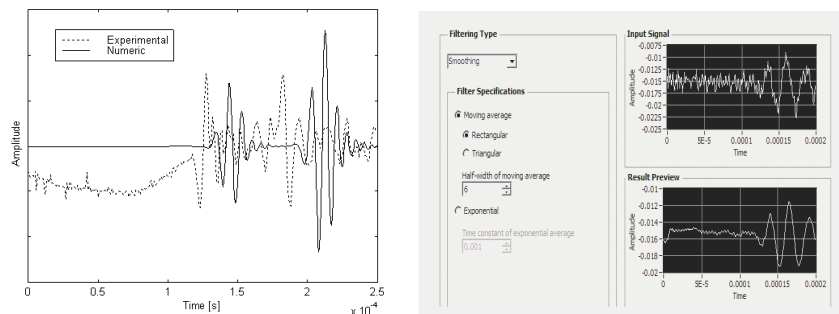
Fig. 3 – Exemplification of numerical and experimental curves for the wafer transducer for the tests device under study and optimization sensor (above - non-filtered signal; below - filtered signal). A descresid reference represents a disbond of panel.

The data were numerically filtered in the LabView program. In general, the data filtering method that seemed to be efficient was based on the computation of mean values. Measurement is triggered by the excitation signal reaching a certain level. The measurement chain consists of an amplifier and, possibly, of a signal conditioning system and the generation-reception signal is measured by a computer acquisition control for a time interval sufficiently long to enable the signal to travel the distance between the excitation element and the receiver device, but, at the same time, sufficiently short to prevent boundary reflected waves to overlap the received signal. An amplifier was used for the generated signal as well as a conditioning device for the signal taken over by the receiving PZT transducers which send it to the data acquisition system in a ready to process form. A voltage amplifier was used for certain measurements so as to enable the excitation pulse voltage to rise above 10V. Piezoelectric devices generally accommodate high voltages but high pulse voltage is limitative in aeronautical applications (Giurgiutiu, 2003).

4. Results and Discussion

There are two propagating modes that display clearly different characteristics. The S0 mode has the highest group velocity and shows particle

displacements mostly in the x direction. There is little dilatation and expansion in the y direction, which is symmetrical about the center of the plate; this arises due to the Poisson effect. The slower wave is the A0 mode, which shows particle displacements that are mostly in the y direction and are asymmetrical about the center of the panel.
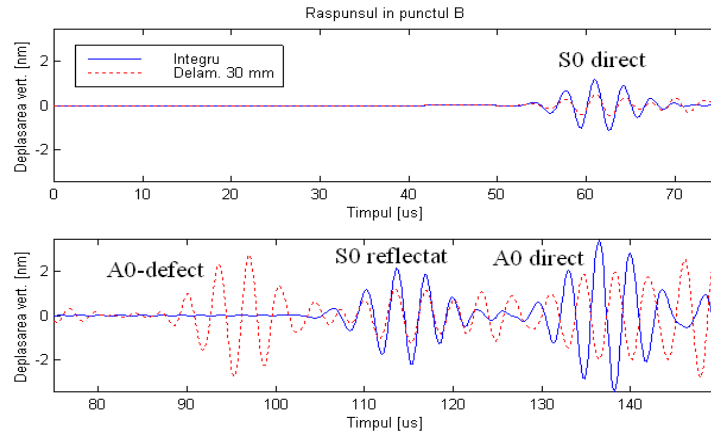
Fig. 4 - Comparative signals recorded for vertical displacements in the two modes: continuous curve for the undamaged composite and discontinue curve for the delaminated composite. Comparative plot of axial wave and flexural wave transmission in A0 and S0 response modes in sensitivity to detect the delamination damage.

The propagation velocity of the A0 mode is less than that of the S0 mode and depends significantly on frequency. Qualitatively, it appears that the relative magnitudes of the A0 and S0 modes vary, as presented in Figure 4.Modes A0 and S0 have approximate wavelengths λ_{A0} = 6 mm and λ_{S0} = 20 mm and represent group velocities with approximate values of v_{gA0} = 2400 m/s and v_{gS0} = 5700 m/s. Taking into account the dimensions of the analyzed panel, a pulse-type excitation was used. This is relatively long as compared to the low frequency waves below 100kHz.

The "Hanning window" excitation type used can be described by the equation:

$$F(t) = \begin{cases} 0.5F_0 \left[1 - \cos\left(\dfrac{2\pi f_0 t}{n_0}\right)\right] \sin(2\pi f_0 t); & if \ t \leq \dfrac{n_0}{f_0} \\ 0; & if \quad t > \dfrac{n_0}{f_0} \end{cases} \tag{1}$$

where f_0 is the central generated frequency, n_0 is the pulse generated number of cycles and F_0 is the maximum amplitude of the force. For F_0 = 500 N/m, n_0 =

5 and f_0 = 300 kHz, the excitation form is represented in Fig. 5, and one can notice that the signal duration is of 16,7 s. The Hanning window is a general purpose window for the analysis of continuous signals and should be used in most cases, because it has the best overall filter characteristic. The Hanning window may also be used for system analysis (frequency response measurements) for both excitation and response signal when a random excitation signal is used. The pulse behavior of the Lamb wave is represented by the calculated curves in dispersion diagrams for the tested hybrid composites (Fig. 5, *a*, *b*).
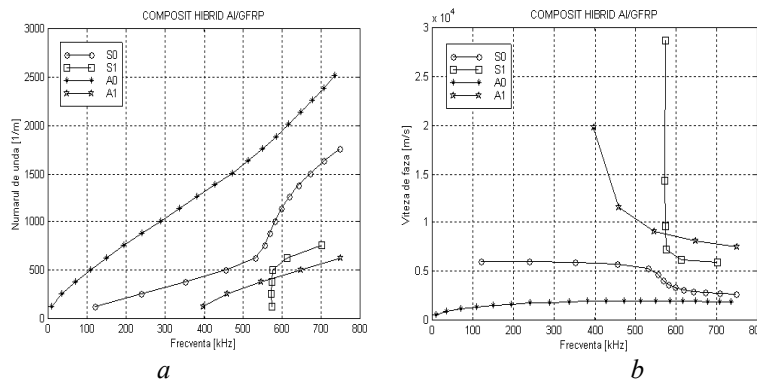
Fig. 5 – Experimental dispersion diagrams for test hybrid composites:
a) Lamb wavelength (1/λ). The horizontal axis represents frequency;
b) Lamb Phase velocity. The horizontal axis represents frequency.

In the experiment, two different types of delaminations are taken into consideration: slip delaminations, in which noncontact boundary conditions are assumed only for shear displacement and stress, and stress-free delaminations, in which no contact boundary conditions are assumed for all mechanical displacements and stresses. The calculations, which are based on a modal decomposition method, show that delaminations in absorptive bilayers result in a considerable change of the normal displacement amplitude at the bilayer surfaces inside the delamination region, and for an incident mode A0. Stress-free and slip delaminations can be distinguished exploiting their different effect on the steel-like A0 and S0 modes (Fig.4).

The simulation analysis of the Lamb wave detection of defects on the panel-type model was carried out with a specialized solver, based on the dependency relation between the wavelength and the transducer response time, using the finite element model FEMLAB 3.0.

Simulations were performed for several modes, with separate calculations for the Lamb wave transmission patterns in the panel in modes A0 and S0, according to Fig. 7*a* and 7*b*, but also for the Lamb wave transmission patterns in modes A1 and S1, according to Fig.7*c* and 7*d*.
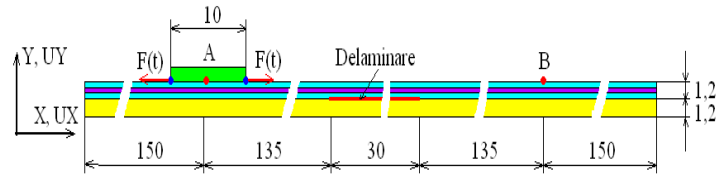
Fig. 6 – The theoretical part calculates- Model analysis for Lamb wave propagation.
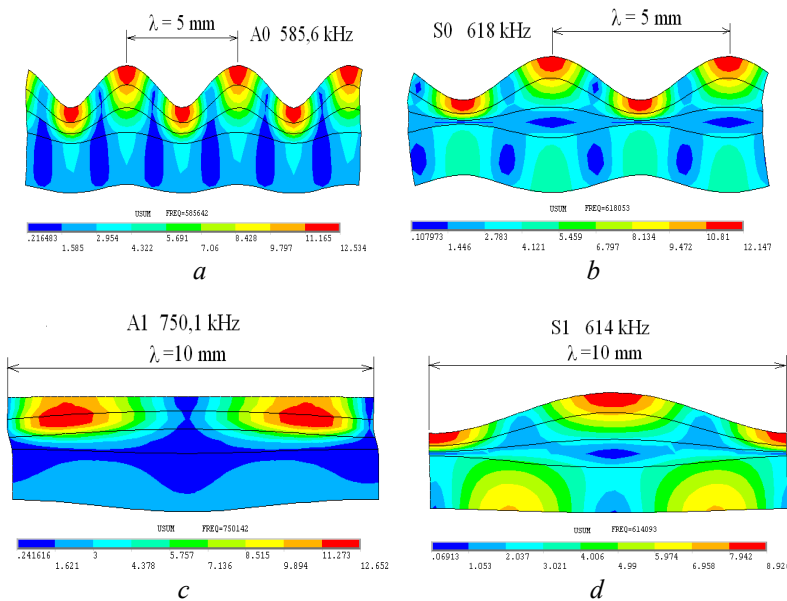
Fig. 7 – The simulation of Lamb wave transmission modes in the hybrid plate.
Distribution of total wave displacements as represented in the analysis of the model
simulating the induced deformation – the dispersion curves.

Real aspect of the dispersion curves Fig. 8 show the measurement results at two time intervals: 25 and 50 microseconds from simulation, at a frequency range between 600-650 kHz. The waves are generated symmetrically about the panel stress axis [9]. **LIPSA IN BIBLIOGRAFIE**

The colors in these figures indicate the Von Mises stress (Chungang *et al.*, 2007) and the arrows indicate the vector particle displacement from the equilibrium (initial) position. Von Mises stress evaluation as their sole yield failure criterion for mild structures is assessed with 3-D finite element analysis.

If the Von Mises stress is greater than the Yield Strength of the material, there will theoretically be a permanent deformation in the part. If the Von Mises stress is greater than the Ultimate Tensile Strength, the material will theoretically break (Luo & Tong, 2002; (Yazdi, 2007).

Time [s]	Composite Type	Deformation amplified 200 000 times and values of total displacements - experimental signal
25	Delaminate carbon composite. Disbonding modeling in sensor region	
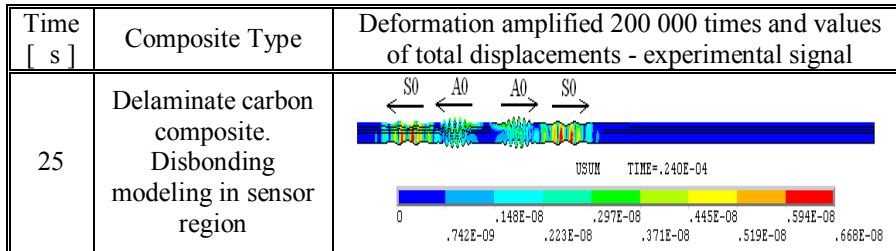
Fig. 8 – Results of received signals of A0 and S0 waves at 25 s. Real aspect of the experimental signal processing indicates different aspects for the intact panel versus the delaminated panel when the response time increases form 25 to 50 s. (Success identification-the signal changes are significant).

Time [s]	Composite Type	Deformation amplified 200 000 times and values of total displacements - experimental signal
50	Intact fiber glass composite	
50	Delaminate fiber glass composite. Disbonding modeling in sensor region.	

Fig. 9 – Results of received signals of A0 and S0 waves at 50 s. Real aspect of the experimental signal processing indicates different aspects for the intact panel versus the delaminated panel when the response time increases form 25 to 50 s. (Success identification-the signal changes are significant).

5. Conclusion

1. The paper presents an inspection method suitable for monitoring the health status of hybrid metal-epoxy/prepreg composites, based on Lamb wave detection techniques, with applications in the aeronautical industry.

2. The basic data thus obtained may assist in developing a technology that relies on composite material compatible inspection methods, through the use of piezo MEMS and Lamb waves.

3. The applicative potential of the Lamb wave method was evidenced, as an on line method, suitable for the case when no other parasite sources of close frequency waves exist. Cross-inspections become more efficient,

especially when the same transducers can be used to generate vibrations with frequency ranges between frequency 500-700 kHz and response times above 50 microseconds of the signal changes.

REFERENCES

Lamb H., *On Waves in an Elastic Plate*. Proc. Roy. Soc. London, Ser. **A 93**, 114–128 (1917).

Viktorov I.A., 1967, *Rayleigh and Lamb Waves: Physical Theory and Applications*. Plenum Press, New York.

Giurgiutiu V., *Lamb Wave Generation with Piezoelectric Wafer Active Sensors for Structural Health Monitoring*. Journal of Intelligent Materials Systems and Structures, **111**, 959-975 (2003).

Wilkie W.K., *et al.*, *Low-Cost Piezocomposite Actuator for Structural Control Applications*. proceedings, SPIE 7th Annual International Symposium on Smart Structures amd Materials, Newport Beach,CA, March 2000.

Chungang Zhuang, Zhenhua Xiong, Xiangyang Zhu, Han Ding, *Von Mises Stress and Level Set Method based Structural Topology Optimization with Multi-Phase Materials*. in Automation Science and Engineering, CASE 2007, IEEE International Conference. **I**, 945-949 (2007).

Gorinevsky D., Body S., Stein G., *Optimization-Based Tuning of Low-Bandwidth Control in Spatially Distributed System*. June 2003, American Control Conference, Denver, CO, **3**, 2658-2663 (2003).

Luo Q.T, Tong L., *Exact Static Solution to Piezoelectric Smart Beams Including Peel Stresses*. Int. J.Solid Struct., **39**, 4677-4695, (2002).

Yazdi A.A., *Flutter of Perforated Metallic Plates Repaired With a Composite/Piezoelectric Patch*. MS Thesis, Department of Mechanical Engineering, Fedowsi University of Mashhad, Iran, 2007.

PIEZO SENZORI ÎN MONITORIZAREA ZONELOR DE ÎMBINARE COMPOZITE – STRUCTURI METALICE

(Rezumat)

Lucrarea abordează aspectele complexe in ceea ce priveşte monitorizarea calităţii îmbinărilor aliajelor structurilor aeronautice unite cu un compozit pe bază de prepreg şi adeziv epoxidic. Detectarea fisurilor cu senzori piezoelectrici activi plăci (PWAS), este o tehnică eficientă şi puternică în monitorizarea integrităţii structurale (SHM). Deşi destul de fragilă, piezo MEMS s-a dovedit a fi destul de rezistentă la factorii de mediu (temperatură, coroziune etc.) şi pot fi aplicate cu succes dacă sunt luate măsuri pentru a proteja fizic senzorii.

PIEZO MEMS APPLICATIONS IN THE HEALTH HYBRID COMPOSITE AERONAUTICAL STRUCTURES

BY

S. OPRIŞAN[1]*, S. RUSU[2], A. BUZAIANU[3], N. CONSTANTIN[4], C. BANU[1] and I. RUSU[2]

[1] STRAERO S.A., Bucharest
[2] "Gheorghe Asachi" Technical University of Iaşi
[3] METAV-R&D S.A., Bucharest
[4] University "Politehnica" Bucharest

Abstract. The paper points out certain aspects related to the health monitoring of aluminum alloy aeronautical structures repaired with composite patches based on prepreg and epoxy adhesives. The effort behaviour of these metal-composite hybrid structures was monitored with ceramic piezoelectric micro-devices MEMS, positioned at the intervention areas to check the repair integrity.

Key words: hybrid composites, health monitoring, piezo MEMS, Lamb wave.

1. Introduction

Due to the constant need to improve the reliability and maintainability of composite repair structures, a health monitoring method based on the application of piezoelectric micro-sensors seems promising, especially for

---

* Corresponding author; *e-mail:* sorin.oprisan@straero.ro

monitoring fissures, non-adherence and composite material disbonding. The technique introduces the use of piezoelectric polyvinyldiene fluoride films (PVDF), suitable for utilization below 80°C, or ceramic patch devices, with extended applicability, up to 120°C. Their main purpose is to detect and monitor the defects appearing in the structure of composite materials applied over metallic substrates, such as aircraft aluminum alloy panels repaired with fiberglass, carbon fiber or boron fiber prepregs. The idea is to combine, during the manufacture or repair processes, the use of the different composite laminates with some distinctly designed areas meant to shelter Lamb wave guided couples of piezo-ceramic micro-electro-mechanical devices (MEMS). To ensure health monitoring, these devices can be embedded "in situ", during manufacture, or subsequent to manufacture, "ex situ", thus creating systems that can be ranged in the "smart composites"category.

The new concepts on the design and maintenance of structures involving composite materials should also take into account the need for a rapid diagnosis of the different types of defects that may appear in composite structures. Their advancement would increase the reliability of the so called "smart composites" with piezoelectric sensors in repair interventions. PWAS devices are capable to detect, in real time, certain types of loads to which composite type aeronautical structures respond. As a result, significant investments are being made to develop technologies that enable the health monitoring of composite structures with minimum costs.

2. Theoretical Framwork

Damage detection in bonded hybrid structures depends on both the characteristics of the associated materials and on the characteristics of the attachment type performed, which may vary within a very large range, function of the type of intervention in which the composite material is used. A defect of the types presented in Fig.1 makes the material properties in the affected area be different from the properties of the remaining material and thus affects the propagation of electrical, thermal and acoustic signals in the respective area.

| Delamination | Cracks | Fibre fractures |
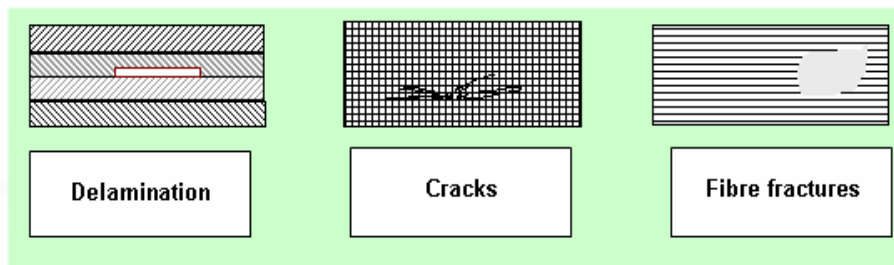
Fig. 1 – Most frequent damage types affecting composite materials.

In order to establish the optimum damage monitoring technology in this case, it is useful to refer to the manner in which sound propagates into the examined object and to know the way in which damage affects the sound propagation and the wave field propagation in the area. To this purpose, a brief reference to the Lamb wave transmission will be made, as the experiment further detailed is based on it. In 1917, the English mathematician Horace Lamb published an analysis of the elastic wave propagation in flat solids and defined the propagation manner of these types of acoustic waves (Lamb, 1917). Lamb shows that an infinite medium supports just two wave modes traveling at unique velocities; but plates support two infinite sets of Lamb wave modes, whose velocities depend on the relationship between the wavelength and the plate thickness. Lamb's equations were derived by setting up formalism for a solid plate having infinite extent in the *x* and *y* directions, and thickness *d* in the *z* direction. Sinusoidal solutions to the wave equation were postulated, having x and z displacements of the form.

$$\xi = A_x f_x(z) e^{i(\omega t - kx)} \tag{1}$$

$$\zeta = A_x f_x(z) e^{i(\omega t - kx)} \tag{2}$$

This form represents sinusoidal waves propagating in the *x* direction with wavelength $2\pi/k$ and frequency $\omega/2\pi$. Displacement is a function of *x, z, t* only; there is no displacement in the *y* direction and no variation of any physical quantities in the *y* direction. Inherent in these equations is a relationship between the angular frequency ω and the wave number k. Numerical methods are used to find the phase velocity $c_p = f\lambda = \omega/k$, and the group velocity $c_g = d\omega/dk$, as functions of d/λ or *fd*. c_l and c_t are the longitudinal wave and share wave velocities respectively (Viktorov, 1967). Lamb's characteristic equations were established for waves propagating in an infinite plate: a homogenous, isotropic solid bounded by two parallel planes beyond which no wave energy can propagate. In formulating his problem, Lamb confined the components of particle motion to the direction of the plate normal (*z*-direction) and the direction of wave propagation (*x*-direction) (Achenbach, 1984). By definition, Lamb waves have no particle motion in the *y*-direction. Since the 1990's, the understanding and utilization of Lamb waves has advanced greatly, thanks to the rapid increase in the availability of computing power. Lamb's theoretical formulations have found substantial practical application, especially in the field of nondestructive testing (Baker *et al.*, 2003).
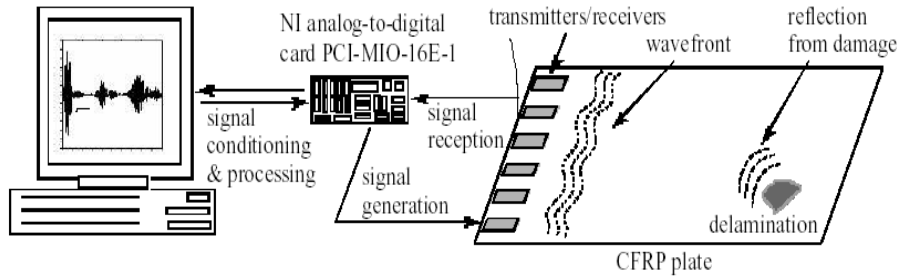
Fig. 2 − Schematic diagram of the experimental setup.

The schematic diagram in Fig. 2 defines a classical actuation design meant to study and demonstrate that a piezoelectric wafer transducer can be used to detect flaws in panels in which piezoelectric wafer active sensors are used to transmit and receive Lamb waves (Zhu & Rose, 1999). In this paper, we combine finite element simulation and experimental studies to further explore the operation of the wafer transducer.

3. Experimental Investigations

The special test samples were manufactured from aluminum alloy panels in which crack type damages on different directions were induced by milling. The defective areas have been repaired with prepreg composite patches to which piezo-MEMS of transducer type have been attached. The main physical and mechanical characteristics of the composite materials end the adhesive used in technological testing are presented in Table 1.

Table 1
Characteristics of Composite Materials Used in Panel Repair

Characteristics	Composite based on carbon fiber prepregs (60%)	Composite based on fiberglass prepregs (50%) type E	Epoxy resin
Density (g/ cm^3)	1,8	2,6	1,3
Specific heat (kJ kg^{-1} K^{-1}, la 20°C)	1200	-	1700
Thermal conductivity (W/m . K)	0,8-1,5	0,1-0,3	0,20
Tensile strength (MPa)	800	600	35
Coefficient of thermal expansion (°C^{-1})	5 x 10^{-5}	10x 10^{-5}	3 x 10^{-6}

Fig. 3 – Scheme of the experimental
aluminum alloy panel.

Fig. 4 – Experimental panel repaired by the
composite patch method.

The panel with the dimensions 200x140x1.2 mm exhibits an artificially induced damage in the central area, under the form of a 25mm long by 0.4 m thick crack (Figs. 3, 4). The piezoelectric devices have a circular shape and are encapsulated in epoxy resin.
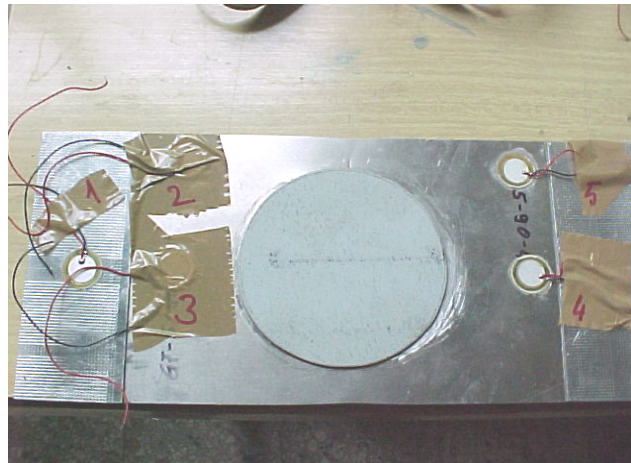
Fig. 5 - Experimental device for studying the interaction of Lamb
wave modes. Piezo-MEMS positioning on the test panel repaired
with composite patch to definitive the emplacement and frequency sensor.

Fig. 5 illustrates the transducers' positioning as well as the manner in which they were set onto the composite patch. The Lamb waves emission/reception is made through transducers located in pairs. The positioning solution for the wafer transducers was selected so as to best cover the composite repaired area monitored by piezo-MEMS. When stretched or compressed, the latter produce a voltage, due to the piezoelectric effect, and therefore require no power to operate.

The monitoring of Lamb wave propagation is based on a comparative approach. First, the wave transmission in a recently repaired (undamaged) panel is monitored, then in panels with different damage degrees, in order to see how the existing flaws influence the different wave propagation A0 and S0 modes. The wave propagation modes were determined in panels repaired with composite patches reinforced with fiberglass or carbon fibers, as shown in Table 1. In order to prepare the tests on the panel behavior, numerical simulations were made, using the finite element method. In the beginning, using the ANSYS program, 2D models were developed, followed by 3D models. At the same time, the most appropriate testing conditions were studied, mainly focused on two interest directions: the case when the PZT-type MEMS to be used for the Lamb wave inspection method could be positioned right at the respective interface, thus becoming in themselves a cause for disbonding initiation, or, the case when fissures are created at the interface due to a deficient repair technology.

In this purpose, a numerical model was taken into account to simulate the overlapping area formed by a 3-layer composite patch applied over an aluminum substrate of the same thickness. A laminate hybrid aluminum/composite plate was thus created, with the total thickness of 2.4 mm, from a 1.2 aluminum foil and 3 equally thick layers of GFRP 0°/90°/0°, for which the lamina properties at 0 are: $E_1 = 109.34$ GPa; $E_2 = 8.12$ GPa; $E_3 = 8.12$ GPa; $G_{12} = 4.32$ GPa; $G_{23} = 3.2$ GPa; $G_{13} = 4.32$ GPa; $\nu_{12} = 0.342$; $\nu_{23} = 0.26$; $\nu_{13} = 0.342$; (MAJOR Poisson ratio); $\rho = 1580$ kg/m^3. For the aluminum plate, the following dimensions were considered: $E = 70$ GPa; $\nu = 0,33$ and $\rho = 2700$ kg/m^3.

This panel may contain delaminations, mainly centrally located, between the aluminum plate and the composite laminate. The research work is focused on the possibility to detect such defects by analyzing the Lamb wave propagation mode through the panel. In order to select the signals due to A0 and S0 modes at an output transducer, as a function of pulse center frequency, one should first know the dispersion curves.

The programs are meant to generate adequate excitation signals for the piezoelectric transmitter and to make possible the signal acquisition by the piezoelectric receiver. The excitation signal should be produced in certain conditions. Its duration must be small (of only several sinusoids (the so-called "burst signal", Fig. 7), so as the generated waves should not interfere with those reflected by different geometrical discontinuities (panel boundaries, abrupt thickness variations, lap bonded joints etc.).

For maximum sensitivity, the transducer length must be thoroughly chosen. Unlike in isotropic plates or symmetrical composites, in hybrid plates there exist multi-mode Lamb waves for which the symmetry/anti-symmetry is perturbed. The frequency and the signal shape should be thus selected as to generate certain modes corresponding to non-dispersive wave propagation intervals (Fig.7).
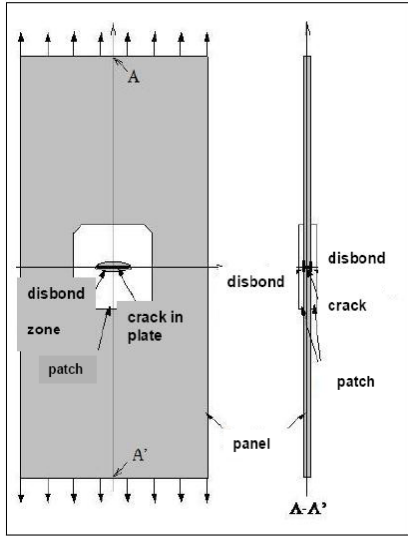
Fig. 6 – Damage-tolerant and safe-life
zone in a repair bonded panel.
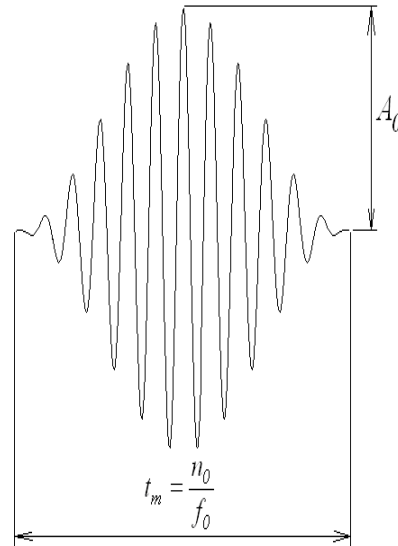
Fig. 7 – Theoretical and typical excitation
mode signal (amplitude-time).
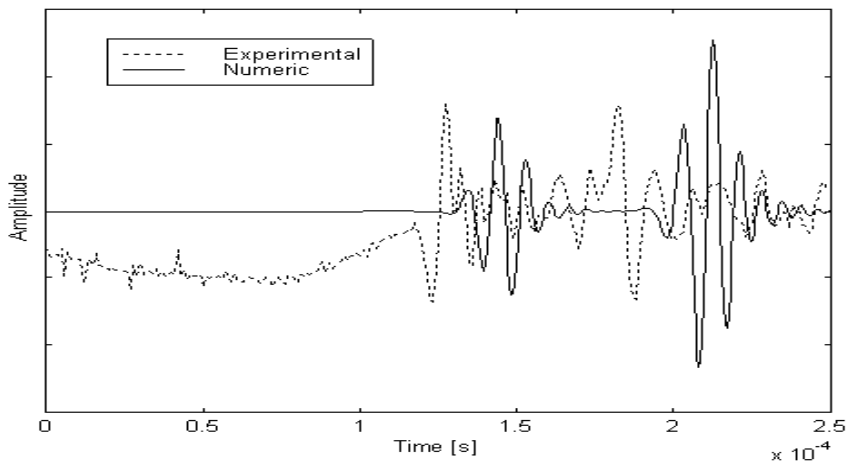
Fig. 8 – Exemplification of numerical and experimental curves for the wafer transducer
for the tests device under study and optimization sensor (above-non-filtered signal;
below-filtered signal). A decreased reference represents a disbond of panel.

They enable the waves to travel long distances, thus ensuring a large range of action for the nondestructive inspection. An amplifier was used for the generated signal as well as a conditioning device for the signal taken over by the receiving PZT transducers which send it to the data acquisition system in a ready to process form.

A voltage amplifier was used for certain measurements so as to enable the excitation pulse voltage to rise above 10V. Piezoelectric devices generally accommodate high voltages but high pulse voltage is limitative in aeronautical applications (Giurgiutiu, 2003; Wilkie, *et al*., 2000).

4. Results and Discussion

The analysis of the dispersion curves for the frequencies between 300-350 KHz, reveal the structure puts in evidence the A0 and S0 modes only. To simplify analysis, the central excitation frequency of 300Khz was selected. This is weakly dispersive for both modes. Modes A0 and S0 have approximate wavelengths λ_{A0} = 6 mm and λ_{S0} = 20 mm and represent group velocities with approximate values of v_{gA0} = 2400 m/s and v_{gS0} = 5700 m/s. Taking into account the dimensions of the analyzed panel, a pulse-type excitation was used. This is relatively long as compared to the low frequency waves below 100kHz.

The calculations, which are based on a modal decomposition method (Fig. 9), show that delaminations in absorptive bilayers result in a considerable change of the normal displacement amplitude at the bilayer surfaces inside the delamination region, and for an incident mode A0. Stress-free and slip delaminations can be distinguished exploiting their different effect on the steel-like A0 and S0 modes (Fig.10).
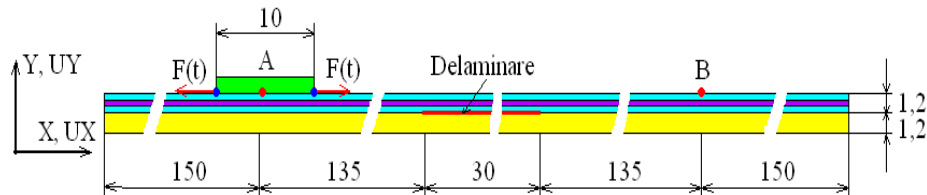
Fig. 9 – The theoretical part calculates- Model analysis for Lamb wave propagation.

Real aspect of the dispersion curves Figure 10 show the measurement results at two time intervals: 50 microseconds from simulation, at a frequency range between 600-650 kHz.

The waves are generated symmetrically about the panel stress axis. The colors in these figures indicate the Von Misses stress and the arrows indicate the vector particle displacement from the equilibrium (initial) position. Von Misses stress evaluation as their sole yield failure criterion for mild structures is assessed with 3-D finite element analysis.

If the Von Misses stress is greater than the Yield Strength of the material, there will theoretically be a permanent deformation in the part. If the Von Misses stress is greater than the Ultimate Tensile Strength, the material will theoretically break.

Time [s]	Composite Type	Deformation amplified 200 000 times and values of total displacements- experimental signal
50	Intact fiber glass composite	
50	Delaminate fiber glass composite. Disbonding modeling in sensor region.	
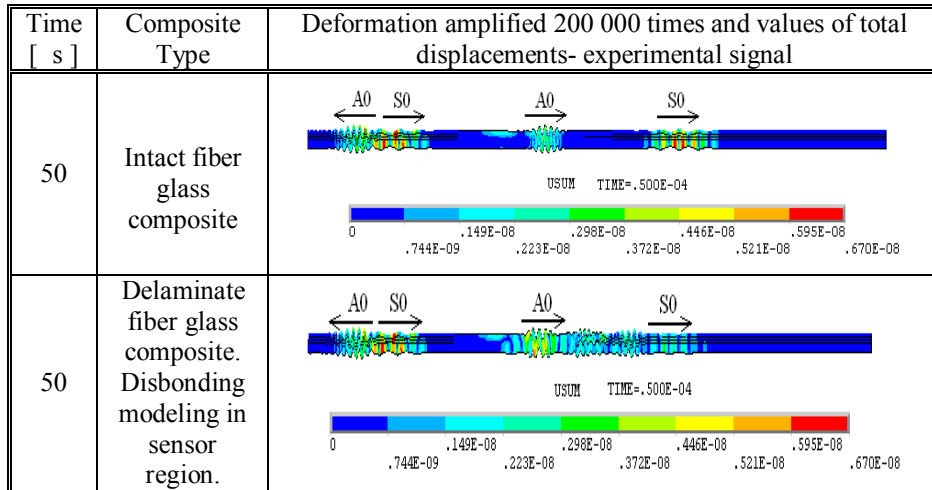
Fig. 10 − Results of received signals of A0 and S0 waves at 50 s. Real aspect of the experimental signal processing indicates similar aspects for both panel inspection cases. (Success identification of the intact versus damaged panels-the signal changes are significant).

5. Conclusion

1. The paper presents an inspection method suitable for monitoring the health status of hybrid metal-epoxy/prepreg composites, based on Lamb wave detection techniques, with applications in the aeronautical industry.

2. The basic data thus obtained may assist in developing a technology that relies on composite material compatible inspection methods, through the use of piezo MEMS and Lamb waves.

REFERENCES

Lamb H., *On Waves in an Elastic Plate*. Proc. Roy. Soc. London, Ser., **A 93**, 114–128 (1917).

Viktorov I.A., *Rayleigh and Lamb Waves: Physical Theory and Applications*. Plenum Press, New York, 1967.

Achenbach J.D., *Wave Propagation in Elastic Solids*. New York, Elsevier, 1984.

Baker A.A., Rose F., Jons R., *Advances in the Bonded Composite Repair of Metallic Aircraft Structure*. Elsevier., **1**, 2003.

Zhu M., J.L. Rose, *Lamb Wave Generation and Reception with Time-Delay Periodic Linear Arrays: A BEM Simulation and Experimental Study*. IEEE Trans. Ultrason.,Ferroelec., and Freq. Control., **46**, 654-664 (1999).

Giurgiutiu V., *Lamb Wave Generation with Piezoelectric Wafer Active Sensors for Structural Health Monitoring*. Journal of Intelligent Materials Systems and Structures, **111**, 959-975 (2003).

Wilkie W.K., *et al*., *Low-Cost Piezocomposite Actuator for Structural Control Applications*. proceedings, SPIE 7th Annual International Symposium on Smart Structures and Materials, Newport Beach,CA, March 2000.

APLICAȚII ALE PIEZO-MEMSURILOR ÎN CONTROLUL COMPOZITELOR HIBRIDE UTILIZATE ÎN STRUCTURILE AERONAUTICE

(Rezumat)

Lucrarea tratează câteva aspecte în ceea ce privește monitorizarea calității îmbinărilor aliajelor structurilor aeronautice unite cu un compozit pe bază de prepreg și adeziv epoxidic. Comportamentul la efort a acestor structuri hibride metal-compozit a fost monitorizată cu microdispozitive piezoelectrice MEMS, poziționate în zonele de intervenție pentru a verifica integritatea.

STRUCTURAL AND MAGNETIC PROPERTIES OF ALNICO-TYPE THIN FILMS

BY

DELIA PATROI*, **DIONEZIE BOJIN, EROS-ALEXANDRU PATROI,
MIRELA MARIA CODESCU and CĂTĂLIN CONSTANTINESCU**

Politehnica University of Bucharest

Abstract. Thin films having a chemical composition close to Alnico-type hard magnets have been prepared on ceramic substrates using the Pulsed Laser Deposition technique. Different annealing treatments have been applied onto the obtained thin films aiming to obtain a high coercive field comparable to the conventional bulk Alnico. Furthermore, a series of structural characterization techniques (XRD, SEM) were used to analyze the structural transformation of the samples, from the as-obtained amorphous structure to the nanocrystalline arrangement emerging after annealing. Finally, the magnetic behavior of the thin films has been characterized through AGFM, before and after the sequence of thermal treatments in direct connectivity with structural changes.

Key words: thin films, magnetism, permanent magnetic materials.

1. Introduction

Even after so many years, since 1931, when Mishima discovered the first modern permanent magnet, Alnico play an important role in developing many applications (Buchow, 1991). Today, the technology requires materials at

---

* Corresponding author; *e-mail:* patroidelia@yahoo.it

small scale in order to integrate them in various applications like those of micro-electro-mechanical systems (MEMS). In order to satisfy this condition with no loose of the bulk's properties many researches were devoted to obtain also magnetic thin films with structural and magnetic related properties similar or even better like those already obtained for the bulk materials. Because the difficulties of obtaining rare earth based thin films and preventing them of the oxidization, knowing the costs of obtaining Fe-Co and Fe-Pt thin films and making use of the excellent corrosion stability of Alnico alloys, some of the researches were devoted to obtain similar properties of the thin films like in bulk Alnico 5. Ganzha *et al.,* (1975) reported on the production of films of Fe-Ni-Al-Co by vacuum evaporation on quartz, NaCl or ceramic substrate. They concluded that the films have inferior high-coercively characteristics than the bulk, but also they report a difference in film composition (in terms of aluminium), which can be responsible of a different mechanism of phase transformations with respect to the bulk material. More recently, (Akdogan & Hadjipanayis, 2010) tried to obtain such films on silicon substrates by sputtering starting from a commercial Alnico 5 magnet. They reported higher coercivity with respect to the bulk, but – as reported by the author himself – this result is of difficult to explain, because the source of such a high coercivity can not be related with the low anisotropy of the crystalline phases formed after the annealing treatments. Therefore, in order to appreciate any development occurring in the production of Alnico thin films, it is necessary to understand the mechanisms of both magnetization processes and phase formation starting from the knowledge already developed on the corresponding bulk material.

2. Experimental

Alnico type thin films were prepared by pulsed laser deposition using a Nd:YAG laser working at a repetition rate of 10 Hz; 266 nm wavelength (5–7 ns per pulse) and an incident fluence (*i.e.* the radiative flux integrated over time) of 1,6 J/cm^2. The target used in order to obtain the desired thin films was made by conventional casting method starting from raw elements. The target composition was calculated to obtain a little imbalance in Fe-Co-Al elements with respect to the commercial Alnico 5 as a means to optimize appropriately the composition of the produced films. The ceramic substrates, 1cm^2 area, were placed at a distance of 4 cm from the target. The substrates were held at room temperature during deposition. The number of applied pulses was in the range of 6.000-100.000. In order to have a uniform ablation, the target was rotated and the laser beam was scanned on the target surface, during all the experiments. The depositions took place in vacuum at low pressures, namely at 6.9x10-6 mbar and 9x10-6 mbar.

After producing, the obtained Alnico type thin films were submitted to a sequence of thermal treatments, a simple annealing at 900°C for 1h, and

subsequently a tempering treatment for 20h at 600°C, and 650°C, in order to obtain a similar structure like in bulk material (*i.e.* a soft magnetic matrix containing finely divided particles of a second phase- hard magnetic one). After each annealing treatment both structural and magnetic behaviors were studied.

Structural characterization was carried by X-ray diffraction (XRD), Co Kα radiation in a parallel beam configuration, in order to minimize the substrate contribution to the observed diffracted intensities. The angle of incidence of the x-ray beam on the sample surface was fixed at 1°. The evaluation of the thickness of the obtained films was made by using X-ray reflectometry (XRR) technique which allows the measurement of thin films having the roughness less than 5nm and integrates all the surface "illuminated" by the incident beam. Scanning electron microscopy (SEM) was used in order to evaluate the structural behaviour of the films after a sequence of thermal treatments. SEM (Scanning Electron Microscopy) observations were made at NanoFacility Piemonte, INRIM, a laboratory supported by the Italian "Compagnia San Paolo".

Magnetic properties were evidenced using the Alternating Gradient Force Magnetometry (AGFM), in a magnetic field applied along to the film plane.

3. Results and Discussion

There were taken into account two different thicknesses of the obtained films that showed important changes in structural and magnetic properties after the sequences of annealing treatment.
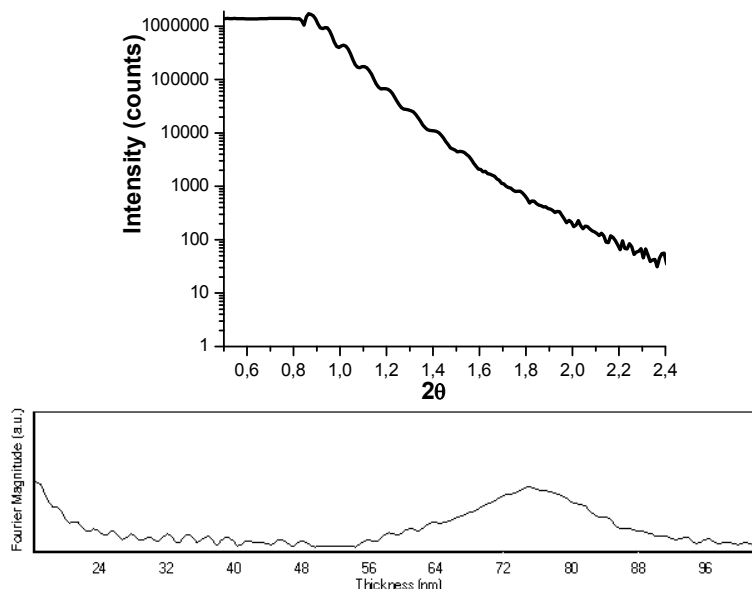
Fig. 1 − XRR spectra and Fourier transform for the evaluation of the film thickness.

This two thickness were evaluated by XRR technique and are of 75 and 150 nm. In the Fig. 1 it is presented the XRR spectra, together with the Fourier transform for the film of 75 nm thickness. The distance between two successive fringes correlated with the maximum obtained using Fourier transform indicates the thickness of the measured film.

XRD analysis (see Fig. 2) on as made films independently of thickness reveals amorphous structure, with small and rare crystalline nuclei most probably of α-Fe, Co and Ni. This observation could confirm the existence of a preliminary α-phase, as previously mentioned in literature (Hetherington *et al.,* 1984). After annealing at 900°C there were developed crystalline phases of body centered FeCo and face centered FeNi or body centered AlNi; that means there were developed the both structural phases which could be responsible for at list a semi-hard magnetic behavior.
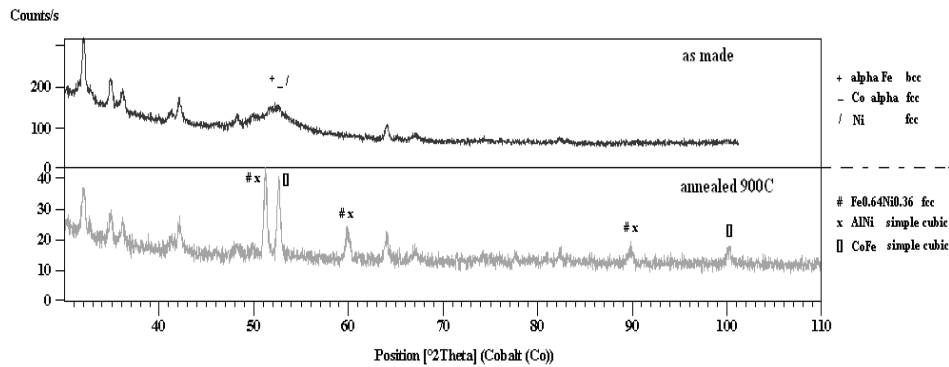
Fig. 2 – XRD patterns of a film on ceramic substrate (thickness = 130 nm) before and after the simple annealing treatment at 900°C for 1h.

SEM images (Fig. 3 *a*, *b*) too evidenced an amorphous structure and no granular arrangements for the as made films independently of thickness; additionally by means of quantitative microanalysis and backscattered electrons images (BSE), it was possible to detect the presence of all the elements coming from the initial target composition. After the simple annealing treatment at 900°C a granular structure is developing, having a strong interconnectivity between the formed crystalline phases evidenced by BSE images (Fig. 3 *c, d, e, f*).

Furthermore, after the subsequent tempering treatments at 600°C and 650°C for 20h in high vacuum atmosphere, nanometric needle shaped precipitates are forming with a relieved composition rich in Fe and Co elements (Fig. 3 *g, h*). These needle shaped precipitates have no preferential orientation devoted also of the amorphous ceramic substrate.

a

b

c

d

e

f

g

h
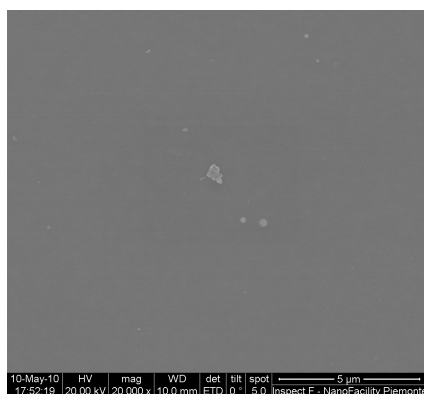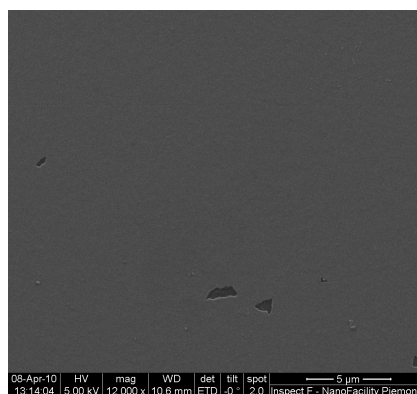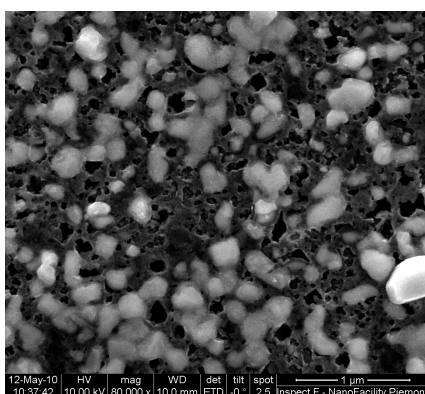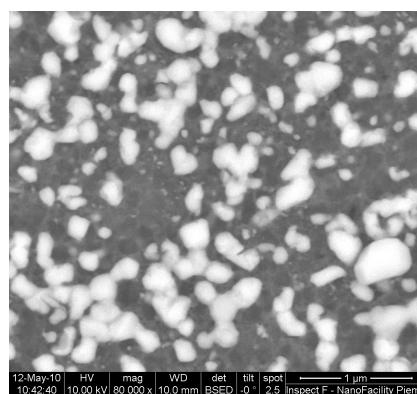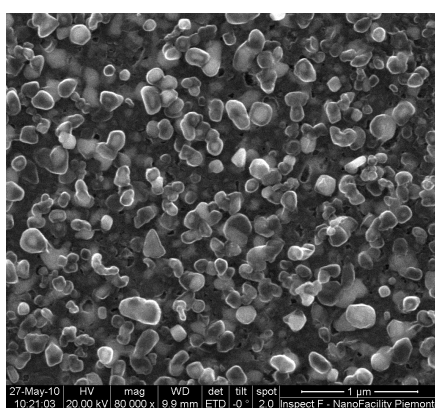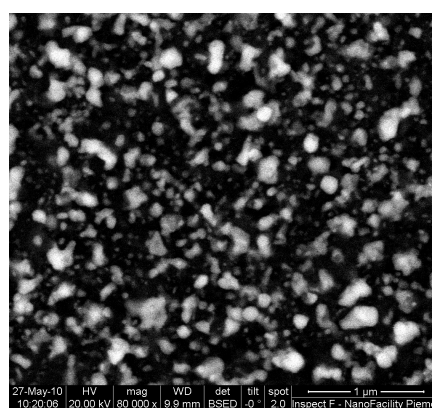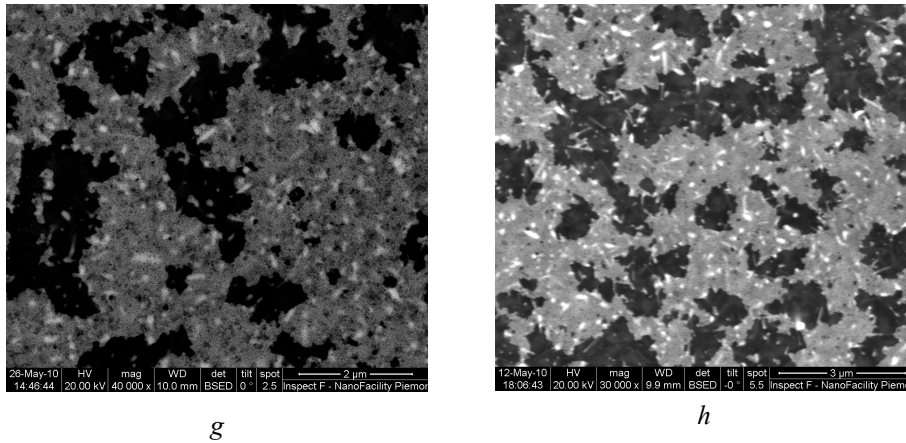
Fig. 3 - SEM images of the films deposited on ceramic substrate
SE images: *a* − as obtained film of thickness = 150 nm, *b* − as obtained film of
thickness = 75 nm, c − film of thickness = 150 nm annealed at 900°C, *e* − film of
thickness = 75nm, annealed at 900°C, 1h BSE images: *d* −film of thickness = 150 nm
annealed at 900°C, 1h, *f* − film of thickness = 75nm, annealed at 900°C, 1h, *g* − film of
thickness = 150 nm annealed at 900°C, 1h and tempered at 600°C, 20h; *h* − film of
thickness = 754nm, annealed at 900°C, 1h and tempered at 650°C, 20h.

These precipitates could be responsible of a high coercive field, but the direct interconnectivity between this precipitates, behaving like hard magnetic phase, and the matrix, behaving like a soft magnetic phase turns into low values of coercivity evaluated through AGFM measurements (Fig. 4).

a
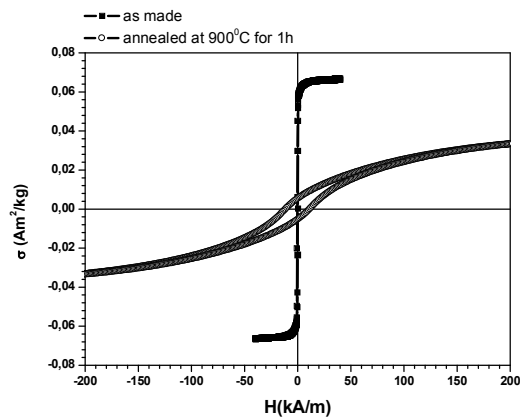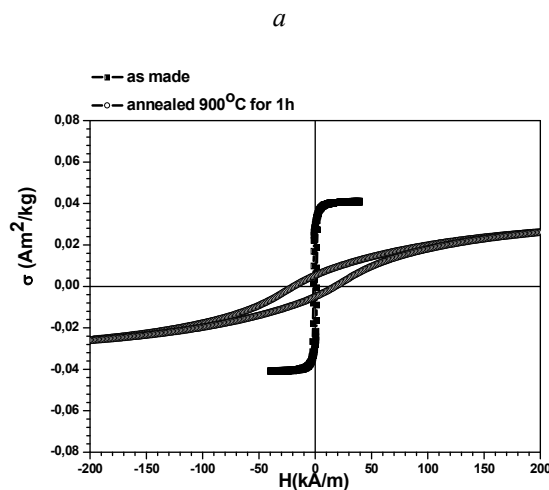
b

Fig. 4 – In plane hysteresis loops (normalized mass
magnetization vs. applied field) of the films on
ceramic substrate; *a* – thickness = 130nm;
b – thickness =74nm) before and after the
annealing treatment at 900°C for 1h.

4. Conclusion

Even the annealed film exhibits a similar structure with the bulk one, having small precipitates immersed into a matrix, it is not allays a happy condition in order to achieve the desired coercive filed, close to the bulk material. It matters maybe also the ratio between the hard magnetic phase and the soft magnetic or non magnetic one, but in the case of the films studied in this paper it has to be noticed also that the disorder of the needle shaped precipitated is responsible also for such a low coercivity taking into account also the unfavorable surrounding matrix which is a soft magnetic one.

REFERENCES

Buchow K.H.J. Rep. Prog. Phys. **54**, 1123-1213 (1991).

Ganza R.N., Dolyuk A.V., Laptei D.A., Salanskii N.M., *Magnetic Anisotropy and Coercivity of AlNiCo-Alloy Fims*. Izvestiya Vysshikh Uchebnykh Zavedenii Fizika, *3*, 137-139 (1975).

Akdogan O., Hadjipanayis G., *Alnico Thin Films with High Coercivities up to 6.9kOe*. ICM2009, J. of Physics: Conference Series, *200*, 2010.

Hetherington M.G., Cerezo A., Jakubovics J. P., Smith G.D.W., J. de Physique, suppl., **45**, *12*, 1984.

PROPRIETĂŢI STRUCTURALE ŞI MAGNETICE ALE FILMELOR SUBŢIRI DE TIPUL ALNICO

(Rezumat)

Filme subţiri având compoziţia chimică apropiată de cea a magneţilor permanenţi Alnico au fost obţinute pe substraturi ceramice cu ajutorul tehnicii de depunere cu laser pulsat (PLD). În scopul obţinerii câmpului coercitiv comparabil cu cel al magneţilor Alnico, filmele au fost supuse la diferite tratamente termice. Apoi, o serie de tehnici de caracterizare structurală (XRD, SEM) au fost utilizate în scopul evaluării transformărilor structurale ale filmelor, de la structura amorfă obţinută prin depunere până la structura nanocristalină obţinută în urma tratamentelor termice. În sfârşit, comportamentul magnetic al filmelor subţiri a fost evaluat cu ajutorul tehnicii AGFM, înainte şi după secvenţa de tratamente termice în directă conexiune cu transformările structurale survenite.

COMPARATIVE STUDY REGARDING THE HARDENING OF PLASTIC DEFORMED AND HEAT TREATED ALUMINUM

BY

MANUELA CRISTINA PERJU*, **DRAGOŞ CRISTIAN ACHIŢEI,**
ŞTEFĂNICĂ GABRIELA ROXANA and **LUCHIAN ZAHARIA**

"Gheorghe Asachi" Technical University of Iaşi,
The Faculty of Materials Science and Engineering

Abstract. The use of duralumin in aeronautics, metal cutting industry, becomes an important base for the enhancement of researches on it. The paper presents a comparative study on the hardness evolution of an aluminum alloy, duralumin, from Al-Cu system. The experiment achieved for a set of test bars, deformed by free upset forging with cold-age hardening. The other set of test bars were deformed by free upset forging, solution quenching and artificial ageing.

Key words: duralumin, cold hardening, ageing, hardening.

1. Introduction

Duralumin is a modern alloy for technical applications. Its value is given by the fact that pieces made of duralumin are thrice as lighter as pieces made of steel at an approximative equal resistance.

---

* Corresponding author; *e-mail:* cryss_ela@yahoo.com

The most important uses of duralumin are aeronautics, for which the specific weight is very important, this feature is important for automotives industry too. It is also used for water transportation because it brings a weight diminish, speed increase and finally exploitation saving. Thus, reduction of metallic constructions weight presents an enormous importance for different domains and partial replacement of steel with duralumin would have a huge technical-economic impact, (http://www.e-referate.ro/Aluminiul).

Advantages of cold-hardening process are well known in aerospace industry such as lifetime increase of some components without increasing their weight.

Duralumin is also used in domains such as engineering, equipments industry, interior and exterior architecture, and advertising industry. Duralumin alloys are complex alloys based on Al-Cu alloys and contains some other elements such as Mg, Mn, Fe, Si, Zn, (Starke, 2005; Vermeşan, 1987). They are wrought and are found as sheets, bars, wires and tubes. They are called duralumin due to the characteristics of high resistance close to some mild steels.

Resistance to wear is hardness closely knit and hardness is an important characteristic of aluminum alloys and is linked to their use in practice.

2. Experimental Results

An aluminum alloy from 2xxx class was used for the experiment, precisely AlCu4MgMnSi, according to EN AW 2017. The two set of test bars obtained from laminates cut to the dimensions of Ø30/45mm, corresponding to the upset procedure in order to fulfill the condition $h_0/d_0 = 1,5$.

Duralumin analyzed in terms of chemical composition presented in Table 1. It was determined by quantitative spectral analysis that allows the percentage identification of the chemical elements. Foundry Master spectrometer was used for chemical composition.

Table 1
Chemical Composition of the Duralumin AlCu4MgMnSi, %

Al	Cu	Mg	Si	Fe	Mn	Zn	Pb	Others
91,3	4,44	0,702	0,663	0,623	0,596	0,147	1,12	0,35

Increase of resistance properties for aluminum alloys realize by cold hardening or by solution quenching and ageing, (Alexandru *et al.,*1995), so that, hardness properties were analyzed for both sets.

2.1. Hardness Analysis on Cold Hardening Test Bars Through Free Upset

The modifications of materials properties after cold forging are due to cold hardening. So, resistance properties such as hardness, flow resistance and ultimate stress increase while plasticity properties such as elongation and resilience decrease (Ursache & Chircă, 1982; Zaharia Luchian, 2001).

Achievement of a structure that assures an easy deformability realize through annealing, which eliminates hardening effects of the aluminum alloy. Technology of recrystallization annealing consists in heating up to 420°C, maintain 1 hour and cooling down with the furnace. During heating soluble components pass in solid solution and because of diffusion, it takes place the concentration balancing of alloying components at the grain boundaries. During cooling the solid solution decomposes but chemical compounds separate finished and uniformly distributed in the entire mass of the alloy. Duralumin hardness after recrystallization annealing decreases due to overageing effect.

Upset deformation realized on a hydraulic press type Hydramold, of 75 tf, with three degrees of deformation 12%, 25% and 39%.

The test bars were first analyzed in terms of hardness before they were heat treated, after annealing and after the procedure of free upset.

Table 2
Hardness Values For Upset Deformed Duralumin

Time	Duralumin hardness after drawing		
	98,98 HB		
	Duralumin hardness after annealing		
	54,85 HB		
	Duralumin hardness after upset deformation		
	Deformation degree 12%	Deformation degree 25%	Deformation degree 39%
0,05 h (5 minutes)	57,83 HB	59,16 HB	60,38 HB
48 h (2 days)	58,83 HB	59,73 HB	60,90 HB
336 h (14 days)	60,51 HB	62,23 HB	63,57 HB
2160 h (3 months)	66,16 HB	66,78 HB	67,14 HB
4320 h (6 months)	66,72 HB	67,98 HB	70,02 HB
8760 h (1 year)	67,06 HB	69,79 HB	71,94 HB
13080 h (1 year and 6 months)	67,14 HB	69,90 HB	72,78 HB

Hardness is a mechanical characteristic associated with resistance values, which can be increased by cold hardening. Hardness was verified immediately after deformation and at certain periods (Table 2). The apparatus used for this was a hardness machine type Wolpert. An indenter with steel a steel ball of 2,5 mm diameter, and pressure load of the indenter was of 62,5 daN. Brinell method was used for determinations. The final values present an average of three results and were tabulated in Table 2.
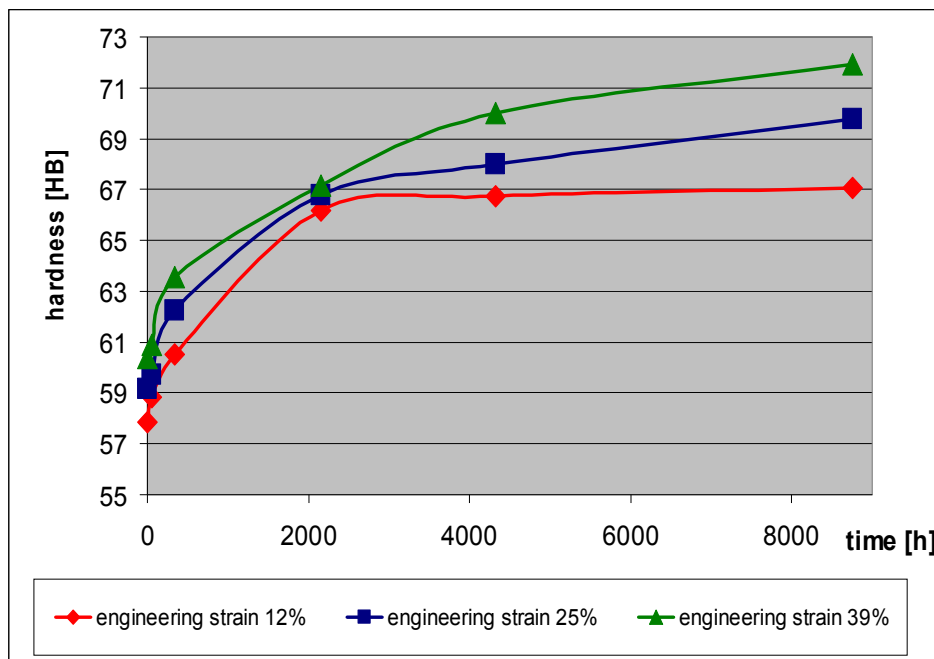
Fig. 1 – Variation of hardness dependent on time of the upset deformed test bars with three deformation degrees 12%, 25% and 39%.

It noticed an increase in hardness immediately after free upset and after some time (Fig. 1), maximum value being achieved at the sample deformed with a degree of 39%. Hardness is only due to cold hardening by the increasing number of barriers that stand in front of the dislocations because after annealing and cold deformation, there are no ageing phenomena and the structure is not oversaturated to produce precipitates.

2.1. Hardness Analysis on Deformed Test Bars Through Upset, Solution Quenching and Ageing

For the second set of test bars, from the same material, with the same chemical composition, upset operation realized for three deformation degrees

12%, 25% and 39%. As seen in the prior case, the test bars supported annealing before deformation. In addition, hardness determined before heat treatment, after annealing and free upset. The increase of hardness, in this case, achieved through solution quenching and artificial ageing (Hopulele *et al.,* 1984).

Hardness achieves in three stages as follows solution quenching of the hardening elements (secondary phase) consists in volatilization, dissolving, solution quenching of the precipitate phases from the structure, rapid cooling to rich a metastable solid solution at ambient temperature; precipitation of the secondary hardening phases through decomposition at high temperatures of the solid solution (artificial ageing), (Suciu V. & Suciu M.-V., 2008).

Table 3
Hardness Values for Deformed and Heat Treated Duralumin

	Duralumin hardness after drawing		
	109,13 HB		
	Duralumin hardness after annealing		
	59,18 HB		
	Duralumin hardness after upset deformation		
	Deformation degree 12%	Deformation degree 25%	Deformation degree 39%
	59,65 HB	61,29 HB	64,49 HB
Duralumin hardness after artificial ageing			
Not deformed test bar	Deformation degree 12%	Deformation degree 25%	Deformation degree 39%
99,84 HB	102,13 HB	105 HB	111,43 HB

Solution quenching consists in heating at 500°C, holding for one hour and water-cooling, and ageing consists in heating at 160°C, holding for eight hours and air-cooling.

The values of the achieved hardness were tabulated in Table 3. After solution quenching, it gets an oversaturated solution, aside from equilibrium, which is soft and plastic. From this reason, it is necessary the ageing heat treatment, when the oversaturated solid solution decomposes into a solid solution and a chemical compound that correspond to equilibrium.

Aluminum alloys contain a series of elements as impurities or as alloying elements, so that in their structure appear other intermetallic phases

that are dissolved in solid solution favoring hardness or are insoluble and place at the grain boundaries.

In Fig. 2 notices an increase in hardness for the pieces deformed through upset at three deformation degrees, pieces that supported solution quenching and ageing. Increase of mechanical resistance at the aged alloys is because coherent precipitates separated from oversaturated solid solution form barriers in the way of dislocations movement.
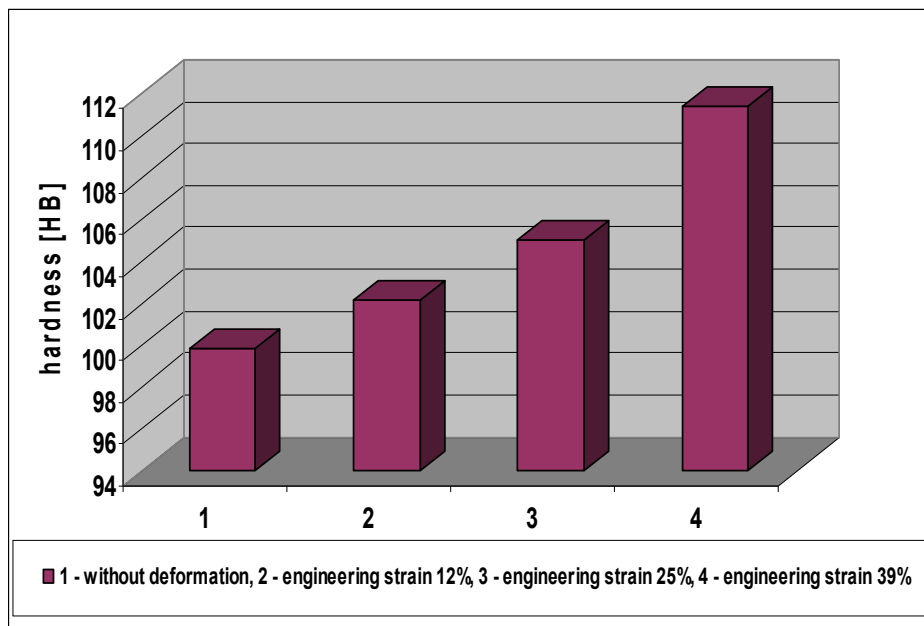
Fig. 2 – Comparative analysis regarding hardness of deformed duralumin through upset with three deformation degrees 12%, 25% and 39%, solution quenched and artificially aged.

3. Conclusion

1. In case of cold deformation, after heat treatment of recrystallization annealing, hardness increases appear when the structure is cold hardening and when slow structure modifications appear. Structure modifications produce by rearrangements when a reduction of intern stresses and the beginning of a regeneration process take place. From this reason, initial hardness increases and stands constant afterwards.

2. Aluminum alloys can support annealing before cold deformation only for deformation degrees up to 50%, after this value, it is recommended solution quenching to avoid breakage risk.

3. High resistant aluminum alloys used in aircrafts construction, submitted to multiple stresses, must present a good combination of mechanical resistance, plasticity, tenacity, fatigue and corrosion resistance. Hence, cold deformed duralumin presents a high hardness through solution quenching and artificial ageing by satisfying all the characteristics required in exploitation.

Hardness values, for deformed and heat treated (solution quenched and artificially aged) samples (for example sample deformed with 39% has a hardness of 111,43 HB), do not present a significant increase towards the hardness values of the sample that did was not deformed or heat treated (99,84 HB).

4. The most effective version in terms of hardness evolution is the one where deformed test bars through free upset supported solution quenching and artificial ageing.

REFERENCES

Alexandru I., Popovici R., Călin M., Bulancea V., Baciu C., Cojocaru V., Carcea I., Poloşanu I., *Alegerea şi utilizarea materialelor metalice*. Editura Didactică şi Pedagogică, Bucureşti, 1995.

Gâdea S., Petrescu M., *Metalurgie fizică şi studiul metalelor*. Editura Didactică şi Pedagogică, Bucureşti, 1983.

Hopulele I., Alexandru I., Găluşcă D.G., *Tratamente termice şi termochimice*. **II**, 1984.

Mantea St., Geru N., Dulămiţă T., Rădulescu M., *Metalurgie fizică*. Editura Tehnică, Bucureşti, 1970.

Suciu V., Suciu M.-V., *Studiul materialelor*. Editura Fair Partners, 2008.

Starke Jr., E. A., *Alloys: Aluminum*. Encyclopedia of Condensed Matter Physics, 18-24 (2005).

Ursache M., Chircă D., *Proprietăţile metalelor*. Editura Didactică şi Pedagogică, Bucureşti, 1982.

Vermeşan G., *Tratamente termice – Îndrumător*. Editura Dacia, Cluj-Napoca, 1987.

Zaharia Luchian, *Teoria deformării plastice*. Editura „Gh.Asachi", Iaşi, 2001.

* * http://www.e-referate.ro/Aluminiul.

STUDIUL COMPARATIV PRIVIND DURIFICAREA DURALUMINIULUI
DEFORMAT PLASTIC ŞI TRATAT TERMIC

(Rezumat)

Utilizarea duraluminiului în industria aeronautică, industria prelucrărilor mecanice face ca importantă intensificarea cercetărilor pentru acest material. Lucrarea

prezintă un studiu comparativ asupra evoluţiei durităţii unui aliaj, tip duraluminiu deformabil din sistemul Al-Cu. Experimentul s-a realizat pentru un lot de epruvete, care au fost supuse deformării plastice prin refulare liberă, cu durificare prin ecruisare şi pentru un alt lot de epruvete, care au fost supuse deformării plastice prin refulare liberă, călire de punere în soluţie şi îmbătrânire artificială.

THE RISK OF WORKERS EXPOSURE AT LOW FREQUENCIES NOISES

BY

MIHAELA PICU* and SILVIU NASTAC

„Dunarea de Jos" University Galaţi

Abstract. An excessive exposure at low frequencies noises causes vibro-acoustic diseases. The most vulnerable are the pilots, the airplane technicians, passenger trains and railway personnel, etc. Low frequencies noise exposure may lead to cardiovascular diseases or psychic diseases (isolation tendencies, depression, irritability, aggression). This paper presents frequency distributions in 100-500 Hz range, of the noise in the metal factory.

Key words: available criteria for low frequencies noises, metal factory, levels of sound, spectrogram of noise

1. Introduction

In order to evaluate the existing LF noise levels there should be an objective criterion (Lederman, http://www.areco.org/LowFreq.pdf; http://www.scotland.gov.uk). This is especially the case when there is a discussion between an annoyed person and the possible cause of the LF noise. Noise-reducing measures can not be founded on the subjective perception of one or more annoyed persons (DeGagne & Lapka, 2007). There are, however, no unambiguous general assessment criteria available (Nuno & Branco 2005). Three in the metal factory situation used LF criteria will be evaluated.

---

* Corresponding author; *e-mail:*

2. The Available Criteria

In the factory three possible criteria are used for the assessment of LF noise, namely: criteria derived from a (STAS 9779-1982; STAS 9783/0-1984; STAS 10009-1988). All three criteria deal with the sound pressure level inside indoor measured in the 1/3-octave bands. Fig. 1 gives an overview of the three available criteria. The difference between these STAS is remarkable.

3. Experimental

This paper studies the propagation of low frequencies sounds in a metal factory hall. Free-field microphone Type 40AN and 4160 and 4180 Brüel & Kjær were used and they were placed at 4m, 10m, 12 and 16m from the noise source (Fig. 2). The measuring method was according to (STAS 7150-1977).
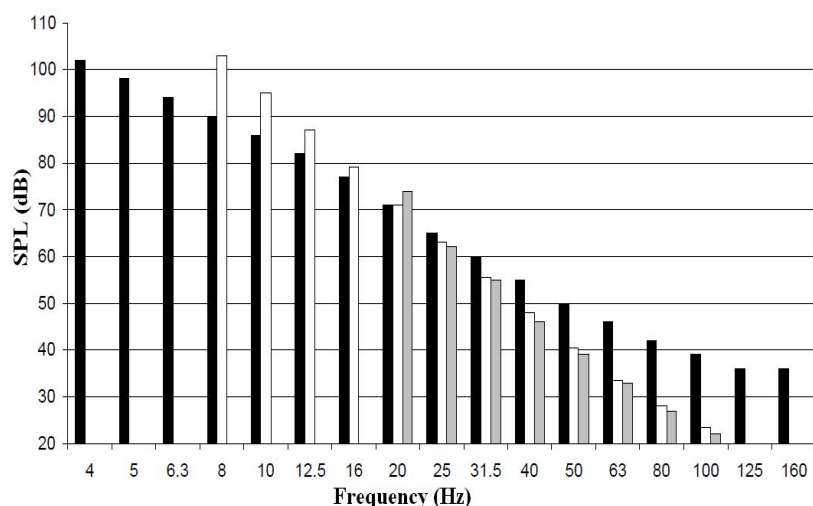
Fig. 1 – Comparison of three noise criteria:
STAS 10009-1988 (■); STAS 9779-1982 (□); STAS 9783/0-1984 (■).

Fig. 3 is a graph drawn from a Wyle Labs program on a low-frequency noise study conducted at metal factory. The thresholds in this figure represent the workers who are directly exposed and represent the nominal levels of sound that would elicit a particular response from occupants inside a hall. An important feature of these figures is the downward-pointing wedge-like region characterized by oppressive response. In this frequency range there is relative little difference between the levels at which a worker detects the noise and at which that noise is perceived as being oppressive (Persson, 2005; Van den Berg, 2005).

Fig. 4 shows a spectrogram during a production process. The color indicates the sound pressure level in dB ref 20 Pa. The production process is placed from around the 5s mark to the 30s mark. The near parallel striations in the upper left portion of the graph, beginning at around 5s, represent the tonal signals characteristic of the noise. The highest sound pressure levels, most noticeable by the darker colors in the 15-20s periods, occur at frequencies below 200Hz.
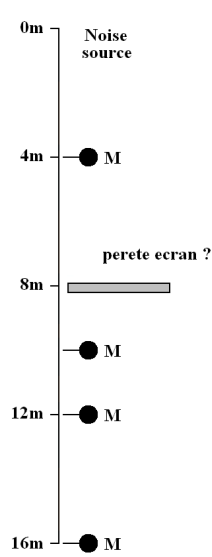
Fig. 2 – Microphone location.   Fig. 3 – The nominal levels of sound.
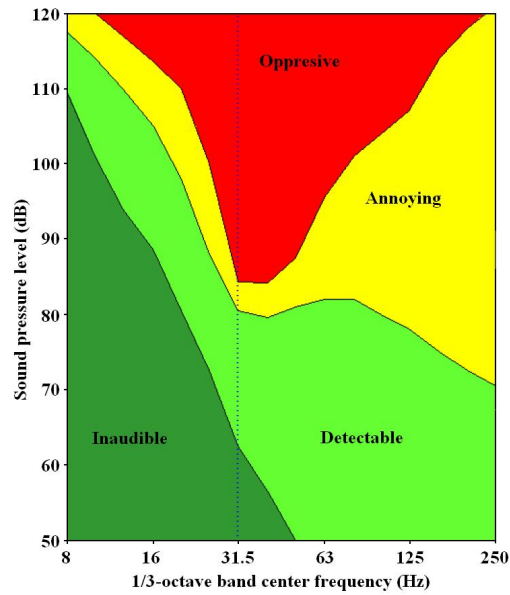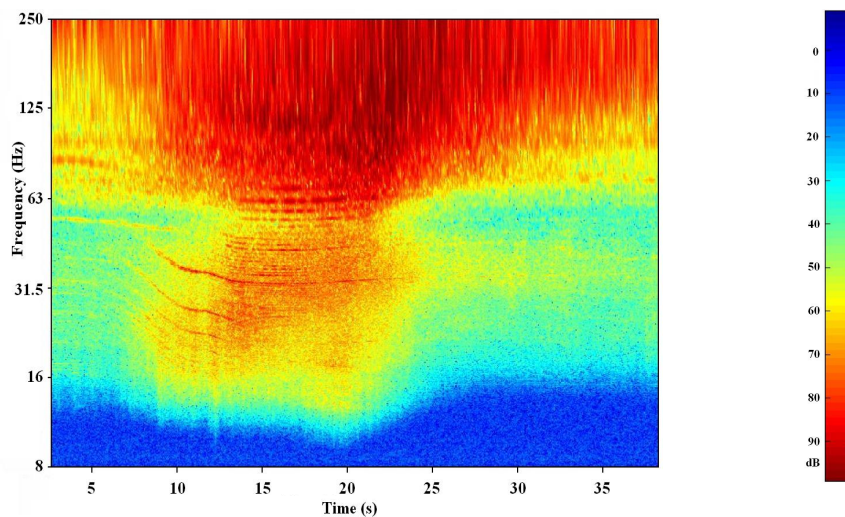
Fig. 4 – Spectrogram of sideline noise during a production process.

4. Discussions

The dependence of the sound level as a frequency function is presented in Fig. 5. The measurements were made for: 8; 16; 31.5; 65 and 125Hz. On the left side of the figure are shown the dependence of the sound levels as a frequency for each microphone.

It can be seen that the sound level registers an important decrease for the 10-16m mark, as opposed to the values measured at 4 m; the decrease is 8,88-22,5% for the used bandwidth.

4m	L_{eq}=-.6497·lnv+105.89 (R^2=0.9682)
10 m	L_{eq}=-2.6462·lnv+86.45 (R^2=0.9774)
12 m	L_{eq}=-.2794·lnv+83.623 (R^2=0.9641)
16 m	L_{eq}=-.0044·lnv+81.503 (R^2=0.9458)
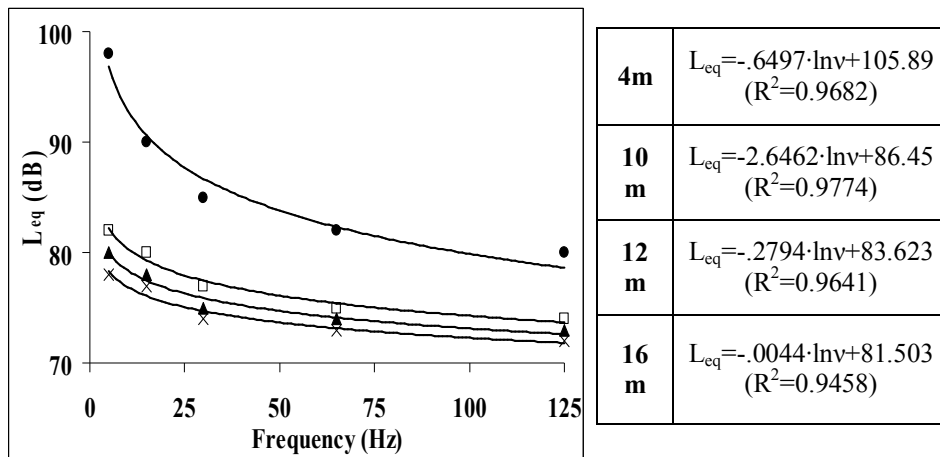
Fig. 5 – The dependence of the sound level as a frequency function
(●) – 4m, (□) – 10m, (▲) – 12m, (x) – 16m

5. Conclusion

The perception of LF noise is individual and depends on:

a. sex: generally women 'suffer' more from LF noise than men;

b. age: elder people often 'suffer' more from LF noise than younger people. This can be explained by the fact that for instance older people usually have a deafness for higher frequencies;

c. state of mind: happy people 'suffer' less from LF noise than more or less unhappy people.

It should be clear that a general LF noise criterion has to deal with these individual aspects. One way to do so is a statistical approach, starting with the LF hearing thresholds. There are, however, not many experimental

data available especially on LF hearing thresholds. Most of the literature derives LF hearing thresholds from 'normal hearing thresholds'.

The requirements for a general, unambiguous LF noise criterion are many, complex and differ widely. This hinders the creation of a general criterion. There is a lack of experimental data on LF hearing thresholds. This makes further investigation on especially LF hearing thresholds necessary. It is however questionable if the make of an unambiguous, general LF noise criterion is possible. One might even ask if it is necessary or desirable.

REFERENCES

* * *DEFRA, Department of the Environment, Northern Ireland Scottish Executive, Report Low Frequency Noise*. 2001, http://www.scotland.gov.uk/ Resource/ Doc/158512/0042973.pdf

* * STAS 10009-1988: *Acustică urbană. Limite admisibile ale nivelului de zgomot.*

* * STAS 7150-1977: *Metode de măsurare a nivelului de zgomot în industrie*.

* * STAS 9779-1982: *Evaluarea efectelor zgomotului asupra omului. Indicaţii generale.*

* * STAS 9783/0 – 1984: *Parametrii pentru proiectarea şi verificarea acustică a sălilor de audiţie publică. Clasificare şi limite admisibile.*

DeGagne D.C., Lapka S.D., *Incorporating Low Frequency Noise Legislation for Energy Industry in Alberta*. Canada, 2007, http://www.windcows.com/files/ low-frequency-noise-ercb-legislation-noise-solutions-inc.pdf

Lederman N., *Report Aviation Low Frequency Noise*. April 13, Oval Window Audio, USA, http://www.areco.org/LowFreq.pdf

Nuno A.A., Branco C., Re*port Low Frequency Noise: A Major Risk Factor in Military Operations*. 2005, http://docs.wind-watch.org/Castelo-Branco-low-frequency-noise-military-operations.pdf

Persson, K., *Adverse Effects on low Frequency Noise in the Occupational Environment.* Department of Environmental Medicine. The Sahlgrenska Academy, Goteborg University, Sweden, 2005, http://www.tc26.ashraeregion 7.org/pastprograms/low-frequency/effects_of_low_freq_noise.pdf

Van den Berg M., *Influence of Low Frequency Noise on Health and Well-being*. Informal document No. GRB-41-8, 22-24 February 2005.

RISCUL EXPUNERII MUNCITORILOR LA ZGOMOTE
DE FRECVENŢĂ MICĂ

(Rezumat)

Expunerea excesivă la zgomote de frecvenţă joasă produce boli vibro-acustice. Cei mai vulnerabili sunt piloţii, tehnicienii de avioane, pasagerii trenurilor şi personalul căilor ferate etc. Zgomotele de frecvenţă joasă pot produce boli cardiovasculare sau psihice (tendinţa de izolare, depresie, iritabilitate, agresiune). Această lucrare prezintă distribuţia frecvenţelor în plaja 100-500 Hz, într-o fabrică metalurgică.

CHARACTERIZATION OF Cu$_x$S POWDER OBTAINED BY PRECIPITATION

BY

ANDREEA EUGENIA POP[*], **MEDINA – NATALIA BATIN**
and VIOLETA POPESCU

Technical University of Cluj - Napoca,

Abstract. Due to its various phases and complex structure, copper sulphide (Cu$_x$S) presents a great interest for the researchers. Literature data show that copper sulphide is a material with excellent semiconducting properties. We obtained copper sulphide powder by chemical precipitation. The chemical reaction solution composed by CuSO$_4$ (copper sulphate), CH$_4$N$_2$S (thiourea), triethanolamine (TEA), sodium hydroxide (NaOH) and bidistilled water, was heated at 60°C for 2 hours for the obtaining of the precipitate. The precipitate was washed, filtered and finally dried at room temperature. In order to study the influence of thermal treatment on the optical properties of copper sulphide, the obtained powders have been treated at 150°C (60 minutes) and 200°C (60 minutes) respectively. The copper sulphide was characterized by UV-VIS spectrometry.

Key words: powder, Cu$_x$S, optical properties, precipitation.

---

[*] Corresponding author; *e-mail:* popandreea_jeni@yahoo.com

1. Introduction

The study of Cu_xS compounds was marked by several controversies related to the structure of obtained copper sulphides. Due to its complex structure and wide range of applications, copper sulphide was widely studied in recent years. Copper sulphide particles are prepared by different methods including solid state reactions, synthesis methods at high temperatures and hydrothermal processes (Kaur *et al.,* 1980; Froment *et al.,* 1997). Although the preparation methods of copper sulphide based on aqueous solutions are well established, however, the literature data concerning the preparation of the solution starting from different copper salts and/ or agents containing sulphur are quite different. The hydrogen sulphide is frequently used as a sulphur source being bubbled into liquid solution containing copper salts (when it is an external source of sulphur) or is generated as a results of some chemical reactions, inside the bath (as an internal source of sulphur) (Silvester *et al.,* 1991; Drunnond *et al.,* 1999). Another method used to obtain copper sulphide films is the immersion of a copper foil in a solution of thiourea (Tu) (Leon & Arjona, 1986).

Cu_xS is a material intensely studied in the literature due to its optical, electrical and photovoltaic properties. The copper sulphide is represented by a family of compounds, among the most known phases being chalcocite (Cu_2S), covellite (CuS), digenite (Cu_9S_5), dijurleite ($Cu_{1,96}S$), anilite ($Cu_{1,75}S$) and yarrowite (Cu_9S_8).

The refining of the chemical methods allowed the formation of copper sulphide powders with various applications in technique. Currently, copper sulphide is used to produce solar cells (Nair & Nair, 1989; Nair *et al.,* 1987a; Nair *et al.,* 1987b; Nair *et al.,* 1988; Nair & Nair, 1987c; Sebastian *et al.,* 1994; Varkey, 1990; Cumberbatch *et al.,* 1986; Bhattacharya R *et al.,* 1997), gas sensors (Sagade & Sharma, 2008), termoreflectant windows (Nair *et al.,* 1989) and last but not least, the creation of memory devices based on Cu_xS (Cruz-Vazquez *et al.,* 1999).

In this paper, we reported the characterization of Cu_xS powders obtained by chemical precipitation of an aqueous solution with the following composition: $CuSO_4*5H_2O$, complexing agent – TEA, NaOH, thiourea (TU-CH_4N_2S) and water.

2. Experimental Details

2.1. Preparation of Cu_xS Powder

Copper sulphide powders were obtained by precipitation of an aqueous

solution consisting of: 10 ml $CuSO_4*5H_2O$, 0,1 M; 1,5 ml complexing agent – TEA, 3,7 M; 5 ml NaOH, 1 M; 3 ml thiourea (TU- CH_4N_2S), 1 M and water up to 50 ml. The addition of the TU determined a change of the solution color from light green to olive green. The prepared solution was heated in a thermostated bath (Arex, Velp SCIENTIFICA) at a constant temperature of 60ºC for 2 hours; in the end a black precipitate was formed.

    The precipitate obtained was filtered with a vacuum pump (707.76 cm Hg) using a 4G ceramic filter and then was rinsed with distilled water and dried at the room temperature, in presence of air. In order to improve the optical properties of the obtained material, the powder was divided in two melting pots and treated in an electric oven at a temperature of 150ºC, for 60 minute (sample b) and at 200ºC for 60 minute (sample c).

2.2. Characterization of Cu_xS Powder

    For the study of the absorption spectra of the samples it's been used a Lambda 35 spectrometer (Perkin Elmer) at a wavelength range of 300– 1100 nm.

3. Results and Discussion

3.1 Optical Properties

    Fig. 1 presents the absorption curves for the Cu_xS powders prepared from $CuSO_4*5H_2O$ at 60°C and a synthesis time of 2 hours.
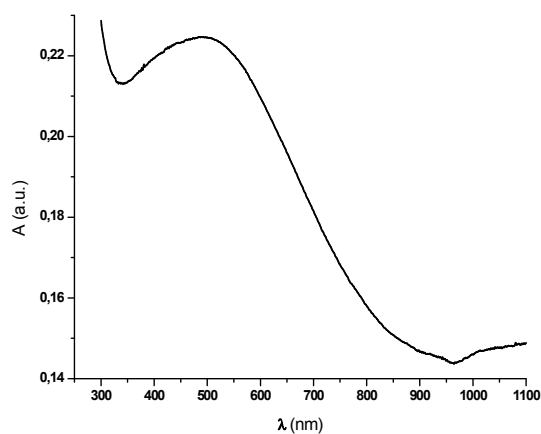
a
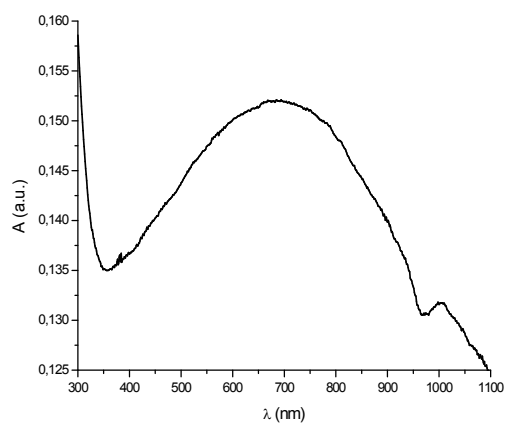
b
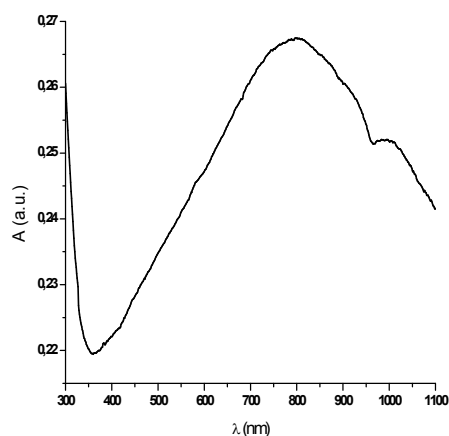
c

Fig. 1 – Absorption spectra for samples of Cu$_x$S powder: *a* – untreated sample,
b – sample treated at 150°C and *c* – sample treated at 200°C.

It can be observed a different allure of the absorption curves. The untreated sample (Fig. 1*a*) has a maximum of absorption at wavelengths of 491nm, after which there is an almost linear decrease in absorbance to 850 nm wavelength. The increase in absorbance at low wavelengths is characteristic for the semiconductor materials (Xiuwen Zheng & Qitu Hu, 2009).

One can observe a shift of the absorption maxima for samples treated at 150°C (Fig. 1*b*) and at 200°C (Fig. 1*c*), which present a maximum at 689.79 nm wavelength and respectively 801,38 nm wavelength. This shift takes place

towards the IR field. H. T. Zhang reported in his paper an increasing of the absorption at wavelength from the IR field which is specific to the covellite (Zhang, *et al.,* 2006).

The energy band gap of the untreated Cu_xS powder (Fig. 2*a*), the sample treated at a temperature of 150ºC (Fig. 2*b*) and the sample treated at a temperature of 200ºC (Fig. 2*c*) was determined from the variation $(\alpha h\nu)^b$ vs. hν, where b= 2 for direct transition, for values of ordinate equal with 0.
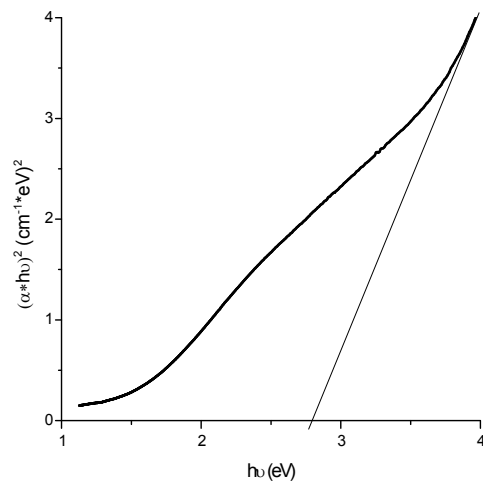
a
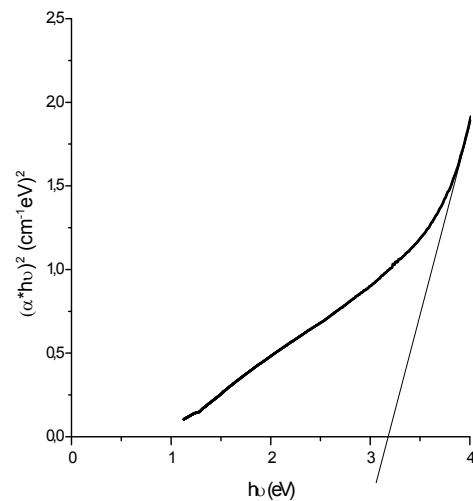
b
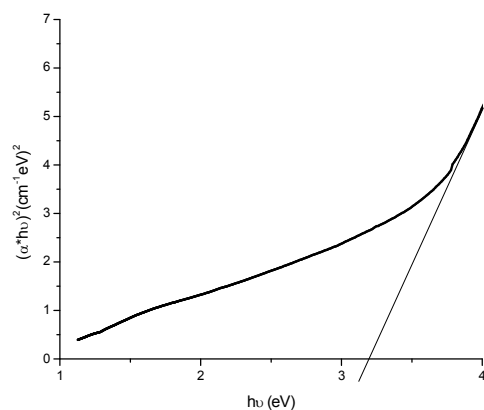
c

Fig. 2 – Variation $(\alpha h\nu)^2 = f(h\nu)$ to powder of Cu_xS a) sample untreated, b) sample treated at 150ºC and c) sample treated at 200ºC.

As can be seen in Table 1, the values of the energy band gap of the copper sulphide powders ranges between 2.79 – 3.19 eV.

Table 1

Temperature Influence on Energy Band Gap of Cu_xS

Sample	untreated	150ºC	200ºC
Energy band gap (Eg)	2.79 eV	3.18 eV	3.19 eV

These increased values of the energy band gap depends on the powder composition and its crystallinity.

We can conclude that the values of the energy band gap for the Cu_xS powders obtained in our laboratory are close to those reported in the literature data (Eg = 0.83 – 3.1) (Table 2).

Tabel 2

Summary of Energy Bands Gaps of the Literature Data

Energy band gap	Reference
0.83 – 1.9	20
2.54 eV	21
2.31 eV	15
2.80 eV	22
2.96 eV	23
2.46 - 3.1 eV	24

4. Conclusion

The study of optical properties of copper sulphur (Cu_xS) obtained by chemical precipitation method, indicate the followings:
- the curve of absorption shows a different allure;
- it was observed a shifting of the maxima absorption at wavelength from the visible field to wavelength from the IR field;
- the values of the indirect energy band gap of the obtained Cu_xS powder determined by extrapolation of the linear region of the graph $(\alpha*h\nu)^2 = f(h\nu)$, were close to those from the literature, 3.18 eV for the powder treated at 150ºC, respectively 3.19 for the powder treated at 200ºC.

REFERENCES

Behboudnia M., Khanbabaee B., *Investigation of Nanocristalline Copper Sulfide Cu_7S_4 Fabricated by Ultrasonic Radiation Technique.*, Journal of Crystal Growth, *304*, 158-162 (2007).

Bhattacharya R. N., Nonfi R., Wang L., PCT Int. Appl. WO 9723,004, 1997.

Cruz-Vazquez C., Inoue M., Inoue M.B., *Characterization of Copper Sulfide Materials.* Superfivies y Vacio 9, December 1999, 219 -221.

Cumberbatch T. J., Parden P.E., Photovoltaic Sol. Energy. Conf., **7**, 675 (1986).

Drunnond D.M., Grieser F., Haly T.W., Silvester E.J., Giersig M., *Steady- State Radiolysis Study of the Reductive Dissolution of Ultrasmall Colloidal CuS.* Lagmuir, *15*, 6637- 6642 (1999).

Froment M., Cachet H., Essaudu H., Maurin G., Cortes R., *Metal Chalcogenides Semiconductors Growth from Aqueous Solutions.* Pure & Applied Chemistry, *69*, 77- 82 (1997).

Isac L., Popovici I., Enesca Al., Duta Anca, *Copper Sulfide (Cu_xS) thin Films as Possible P-Type Absorbers in 3D Solar Cells.* Energy Procedia, *2*, 71-78 (2010).

Kaur I., Pondya D.K., Chopra K.L., *Growth Kinetics and Polymorphism of Chemically Deposited CdS Films.* Journal of the Electrochemical Society, *127*, 943- 948 (1980).

Leon M., Arjona F., *Electron Diffraction Analysis of Cu_xS Films Obtained Through a Sulfurisation Process.* Journal of pysics D: Applied physics, 19, 1529 – 1534 (1986).

Lukashev Pavel, *Crystal and Electronic Structure of Copper Sulfides.* Ianuarie 2007.

Ming Yang, Xiao Yang, Lufeng Huai, Wei Liu, *Synthesis and Characterization of Spherical Hollow Composed of Cu_2S Nanoparticles.* Applied Surface Science 255 1750-1753 (2008).

Nair M.T.S., Nair P.K., *Chemical Bath Deposition of Cu$_x$S Thin Films and Their Prospective Large Applications*. Semicond. Sci. Technol., **4**, 191–199 (1989).

Nair M.T.S., Nair P.K., Compos J., Proc. SPIE 823, 256 (1987a).

Nair P.K., Compos J., Nair M.T.S., *Opto-Electronic Characteristics of Chemically Deposited Cadmium-Sulphide Thin Films*. Semicond Sci.Technol., **3**, 134 (1988).

Nair P.K., Nair M.T.S., Compos J., Sansorex L.E., Soll. Cells, **22**, 211 (1987b).

Nair P.K., Nair M.T.S., Fernandez A., Ocampa M., *Prospects of Chemically Deposited Metal Chalcogonide thin Films for Solar Control Application*. Journal of physics D: Applied physics, **22**, *6*, 1989.

Nair P.K., Nair M.T.S., *Prospects of Chemically Deposited CdS Thin Films in Solar Cell Application*. Sol. Cells., **22**, 103 – 112 (1987c).

Puspitasari Indra, Gujar T.P., Jung Kwang- Deog, Joo Oh-Shim, *Simple Chemical Preparation of CuS Nanowhiskers*. Materials Science and Engineering B 140 199-202 (2007).

Sagade A.A., Sharma R., *Copper Sulphide (Cu$_x$S) as an Ammonia Gas Sensor Working at Room Temperature*. Sensors and actuators B 133, 135-143 (2008).

Sebastian P.J., Gomez–Daza O., Compos J., Banos L., Nair P.K., Sol. Energy Mater., **32**, 159 (1994).

Silvester E.J., Grieser F., Sexton B.A., Healy T.W., *Spectroscopic Studie Son Copper Sulfide Sols*. Langmuir, **7**, 2917 – 2922 (1991).

Varkey A.J., *Prospects for Solution-Grown Cu$_2$S and Ag$_2$S Thin Films in Photovoltaic and Architectural Applications*, Int. Mater. Prod. Technol., **5**, *3*, 264-270 (1990)

Xiuwen Zheng, Qitu Hu, *Facile Synthesis and Phase Control of Copper Chalcogenides with Different Morphologies*. Appl. Phys. **A 94**, 805- 812 (2009).

Zhang H.T., Wu G., Chen X.H., *Controlled Synthesis and Characterization of Covellite (CuS) Nanoflakes*. Materials Chemistry and Physics, *98*, 298–303 (2006).

CARACTERIZAREA PULBERII DE Cu$_x$S OBŢINUTĂ PRIN PRECIPITARE

(Rezumat)

Datorită varietăţii fazelor şi structurii complexe, sulfura de cupru (Cu$_x$S) prezintă un mare interes pentru cercetători. Datele din literatura de specialitate arată că sulfura de cupru este un material cu proprietăţi semiconductoare bune. Pulberi de sulfură de cupru au fost obţinute prin precipitare chimică. Reacţia chimică a amestecului compus din CuSO$_4$ (sulfat de cupru), CH$_4$N$_2$S (thiouree), trietanolamină (TEA), hidroxid de sodiu (NaOH) şi apă bidistilată, a fost realizată la 60ºC timp de 2 ore pentru obţinerea precipitatului. Precipitatul a fost spălat, filtrat şi uscat la temperatura camerei. Pentru a studia influenţa tratamentului termic asupra proprietăţilor optice a sulfurii de cupru, pulberea obţinută a fost tratată la 150ºC (60 de minute) şi 200ºC (60 de minute). Sulfura de cupru a fost caracterizată prin spectrometrie UV-VIS.

OBTAINING OF NANOSTRUCTURED ALUMINIUM BASED MASTER ALLOYS

BY

GABRIELA POPESCU[1*], VICTORIA SOARE[2*], DUMITRU MITRICĂ[2], GHEORGHE IACOB[1], ADINA UŞURELU-CRISTEA[1] and MIHAI BUZATU[1]

[1] University POLITEHNICA of Bucharest,
Materials Science and Engineering Faculty
[2] National Institute of Research and Development for
Non-Ferrous and Rare Metals – INCDMNR - IMNR, Ilfov

Abstract. Attaining of nanocrystalline master alloys for modification and refining of aluminum and its alloys constitute a new research direction in the improvement of aluminum alloys. Nanocrystalline aluminum based master alloys are used to manufacture semi-finished and finished aluminum/aluminum alloys nanostructured products, so necessary in building components and equipment from leading industries (aerospace engineering, military engineering, vehicle construction, etc.) where performances are prevalent in the price of components. The master alloys used in this paper are: Al-Mn (obtained by mechanical alloying), Al-Ti5-B1 (obtained by rapid solidification) and Al-Sr (obtained by electrochemical decomposition). X-ray diffraction and electron microscopy images (SEM) reveal the formation of nanoscale crystallites and intermetallic compounds in aluminum and its alloys structure.

Key words: aluminum master alloys, mechanical alloying, ultra-fast solidification, electrochemical decomposition.

---

[*] Corresponding author; *e-mail:* gabriela.popescu@mail.upb.ro

1. Introduction

Nanostructured metallic materials can be defined as materials having structural constituents in nanometer scale (1-100 nm) and are particular in the field of nanomaterials, by the structural constitution, properties and practical methods of obtaining. The nanostructured alloys have very high mechanical strength and to a certain extent are being successfully applied in aerospace industry, and particularly designed for structural applications. The achievement of nanocrystalline master alloys for modification and grain refining of Al and its alloys constitute a new research direction in the improvement of Al alloys, which, despite having difficulties in production methods and technologies will present characteristics superior to existing conventional materials due to: the large number of crystallization germs - intermetallic stable compounds with nanoscale dimensions, increasing the germination speed at solidification and the more active, immediately and long term effect of modification in metallic melts (Olejnik & Rosochowski, 2005). To obtain a high degree of grain refinement of Al alloys structure it is recommended introducing of micro-alloying elements acting as support of the nucleating alloy grains during solidification process. This process is achieved by introducing modifying elements as master alloys (Moldovan *et al.*, 1998).

The achievement of Al alloys with very fine structures, microcrystalline or nanostructured, with constituents having grit sizes of 30 ÷ 500 nm, using nanocrystalline master alloys for their development, it leads to superior properties: higher yield strength, tensile strength, hardness and elongation, toughness and compactness significantly increased, porosity and solidification micro-cracks level much lower, plastic and mechanical processing technology features improved (Popescu & Cârceanu, 2007; Suryanarayana, 2001; Sfăt & PENCEA, 2009). The master alloys investigated in this paper are: Al-Mn (by mechanical alloying), Al-Ti-B (by rapid solidification) and Al-Sr (by electrochemical decomposition).

The *Al-Mn master alloy* is used in recent years as concentrated tablets form Al-Mn (75/80% Mn), as seen in Fig. 1*a* named compact master alloys, which are used successfully in the development of Al alloys. They provide an effective and economical method of adding not only Mn of but also of other alloying elements (Ti, Fe, Cr, Zn, Ni and Cu) for obtaining high quality alloys.

The *Al5Ti1B master alloy* is used largely as grain refiner in processing of Al alloys in the form of cast products, plates, sheets or wires (Fig. 1*b*). With his addition to the development of Al alloys are improved mechanical properties, homogeneity by obtaining an uniform distribution of fine equiaxed grains, response to heat treatment and processing ability. Al-Ti-B master alloy cause the increasing of grain refinement efficiency of Al-Si alloys due to the very small dimensions of $(AlTi)B_2$ complex boride.

<center>a   b   c</center>
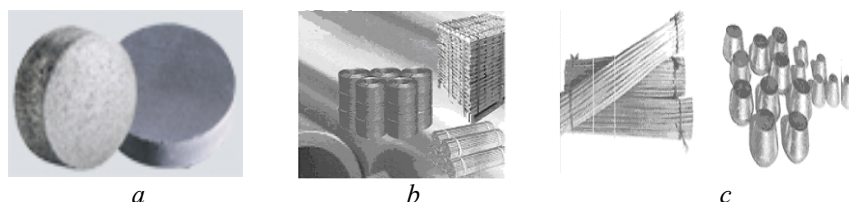
Fig. 1 – Presentation form of Al master alloys: *a*) Al-Mn as concentrated tablets, *b*) Al-Ti-B in various forms, *c*) Al-Sr in various forms.

The *Al-Sr master alloy* change the structure of hypo and hyper eutectics AlSi alloys; its presentation form as thin bars or small ingots is seen in Fig. 1 *c*). Choosing of a good grain refiner and modifier is important in achieving optimum structures and properties, many factors being involved in producing high-quality Al alloys. Given the above, the paper describes three methods for producing nanostructured Al master alloys: mechanical alloying, rapid solidification and electrochemical decomposition techniques.

2. Experiments on Obtaining Nanocrystalline Aluminum Master Alloys

2.1. Obtaining of Nanocrystalline Aluminum Master Alloys by Mechanical Alloying

Advanced grinding and mechanical alloying of metal powders is a complex process involving the optimization of a large number of variables to achieve desired phases and/or to obtain the desired structure. Process parameters are: type mill, milling equipment and grinding jars, balls-to-powder ratio (BPR), speed, grinding time and atmosphere, the degree of filling, the use of process control agents (PCA) (Popescu & Cârceanu, 2007; Suryanarayana, 2001). For experiments we used a planetary mill (Fig. 2) with a maximum rotation speed of 400 rpm, providing an extremely high fineness. It has the possibility to reverse rotation, thus, preventing the powder settlement on the walls of the grinding jars.

<center>a   b   c</center>
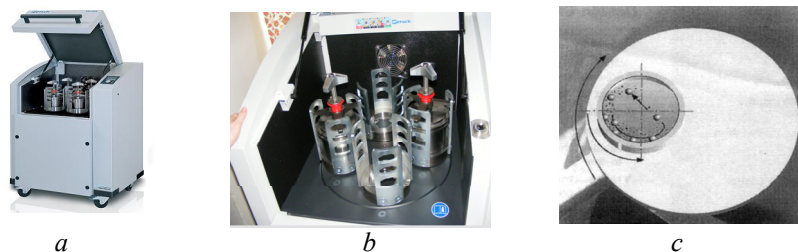
Fig. 2 – RETSCH PM400 planetary mill ball (a), milling vials (b) and schematic depiction of the ball motion inside the vial of a planetary mill.

Table 1

Pressing of Al-Mn Mixture with Different Compression Forces

Sample no.	Press force, [tf]	Height, [mm]	Bulk density, [g/cm³]
1	6,00	3,0	1,81
2	5,00	3,2	1,77
3	4,00	3,8	1,62
4	2,00	4,0	1,44

Al-Mn master alloy was obtained by mechanical alloying of Al and Mn powders with grain size of 325 mesh (44 μm) for 3, 5 and 8 hours using a speed of 300 rpm. Were examined two concentrations of Mn: 65% Mn and respectively 75% Mn. Experiments were conducted at ambient temperature using a BPR of 10:1. Obtained powder mixture was compacted in tablets pressed using a hydraulic press and various pressures (Table 1).

2.2. Obtaining of Nanocrystalline Aluminum Master Alloys by Rapid Solidification

Another series of experiments were the production of aluminum master alloys type Al-Ti5-B1 and Al-Sr10 in nanocrystalline state. Cast Al-Ti5-B1 and electrochemical Al-Sr10 master alloys were amorphised and compacted in the form of tablets.
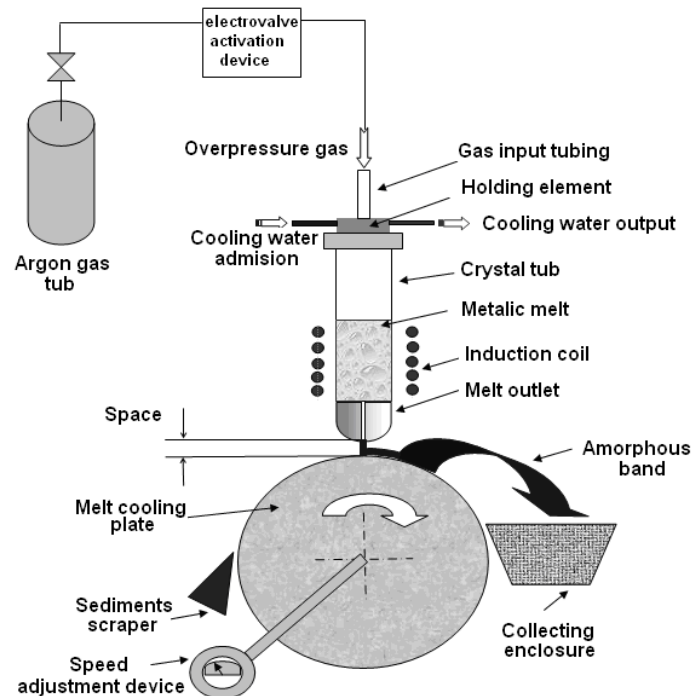
Fig. 3 − Rapid solidification layout of metallic melts, with rotating disk.

Table 2

Rapid Solidification Process Parameters of the Al-Ti5-B1 Master Alloy

Master alloy	Exp. No.	Process Parameters					Band thickness, m	Cooling speed °C/s
		d_{d-t} mm	T_E °C	D_d mm	P_g bar	N_{tamb} rpm		
AlTi5B1	1	1	1200	0,7	1,2	5500	55 m	-
	2	1	1200	0,7	1,2	2500	85 m	-
AlSr10	1	1	1000	1	1,8	2000	55 m	$2,35 \cdot 10^5$
	2	1	1000	1	1,8	4400	45 m	$4,33 \cdot 10^5$

Crystalline Al-Ti5-B1 and Al-Sr10 master alloys were amorphised using a laboratory equipment (Fig. 3), "melt spinning" type, the solidification process parameters being presented in Table 2. Compaction of amorphous bands has been achieved in tablets similarly like Al-Mn master alloys (Table 3). Amorphous bands can be used in treatment processes of Al alloy melts to grain refine the structure (Gadea *et al.,* 1988).

Table 3

Pressing with Different Compression Forces

Sample no.	Compression force, [tf]	Height, [mm]	Apparent density, [g/cm^3]
1	6,00	3,1	1,963
2	5,00	3,4	1,79
3	4,00	3,8	1,6
4	2,00	4,3	1,4

2.3. Obtaining of Nanocrystalline Aluminum Master Alloys by Electrochemical Method

Al-Sr10 master alloy was obtained by electrochemical decomposition of $SrCO_3$ in molten cryolite using the laboratory equipment presented in Fig. 4.

At temperatures of 800-950°C $SrCO_3$ is dissolved in cryolite and dissociates in Sr^{2+} and CO_3^{2-} ions, which under the action of the electric current migrates to the cathode, and respectively anode. Sr^{2+} ions are deposited on the cathode consisting of melted Al and the CO_3^{2-} ions are formed at the anode in the form of gases (CO_2, CO and O_2). By accomplishment of adsorption, neutralization and diffusion kinetic stages, Sr enter and disperse in the molten mass of Al (Li Ji-dong & Zhang Ming-jie, 2005). The cathode, represented by the molten Al is at the bottom of the electrolysis bath, and the anode is made of high-dense graphite cylindrical

shape, having two orifices for evacuation. Influence of process time and current intensity on the master alloy composition and current efficiency are presented in Table 4.
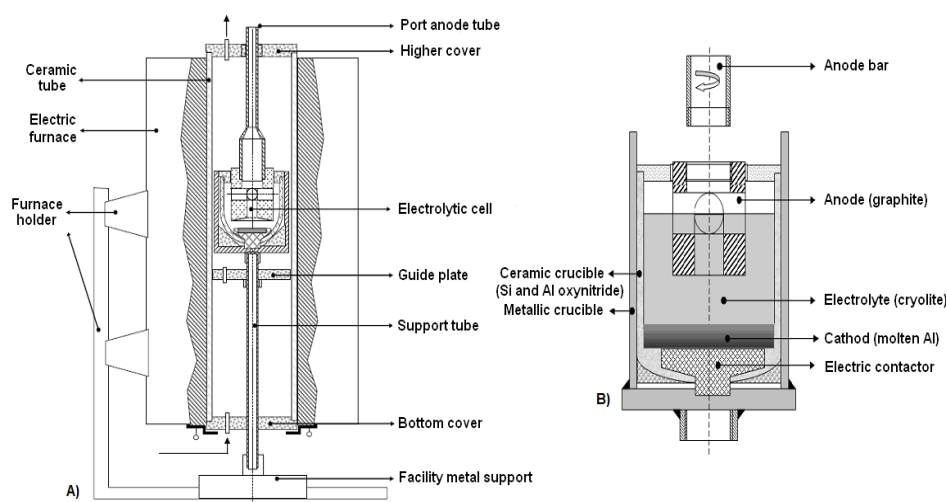
Fig. 4 – Experimental equipment for electrochemical reduction (*a*); Scheme of the electrolysis cell (*b*).

Table 4
Electrolysis Process Parameters

Exp. No.	Process parameters				Master alloy composition %Sr	Current efficiency
	t h	I A	E V	D_{A-K} cm		
1	0,21	5,00	5,00	1,5	0,85	0,75
2	0,28	5,00	5,00	1,5	1,15	0,75
3	0,91	5,00	5,00	1,5	3,70	0,75
4	1,35	5,00	5,00	1,5	5,50	0,75
5	2,45	5,00	5,00	1,5	10,00	0,75
6	2,55	5,00	5,00	1,5	10,40	0,75
7	2,45	4,00	5,00	1,5	6,62	0,63
8	2,45	6,00	5,00	1,5	10,89	0,68

3. Results and Discussion

The powders obtained by mechanical alloying were analyzed and characterized in terms of size, shape crystallites, phase constituents by X-ray diffraction and electron microscopy (SEM).
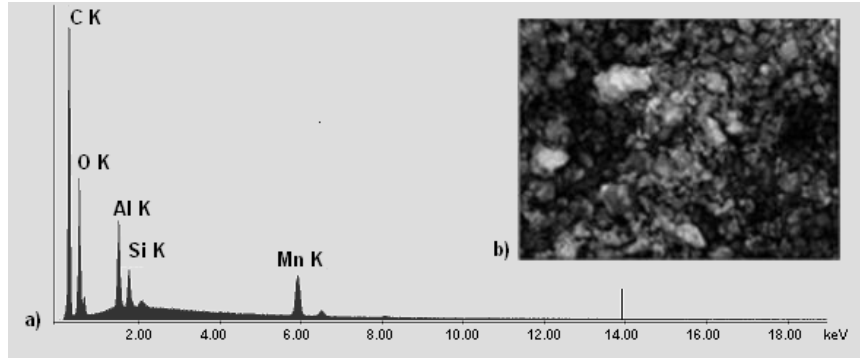
Fig. 5 − EDS analysis and SEI microstructure for Al-65%Mn.

In Fig. 5 and 6 are shown SEI and X-ray images for Al, Mn, Si and O detected in master alloy samples of Al-65% Mn, and Al-75% Mn respectively.
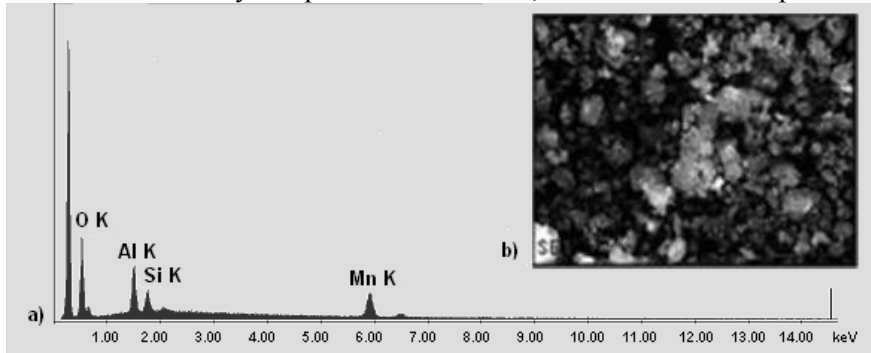
Fig. 6 − EDS analysis and SEI microstructure for Al-75%Mn.

The Si presence is attributed to the consumption of grinding material (SiO$_2$ balls) and the O presence due to the partial oxidation of powder surface. After milling, the powder particle size became very small, the crystallites determined from the diffraction lines having nanometer dimensions as can be observed in Fig. 7. The cristallites decreased with increasing the grinding time. X-ray diffraction also revealed Al$_8$Mn$_5$ and Al$_{15}$Mn$_{11}$ compounds.
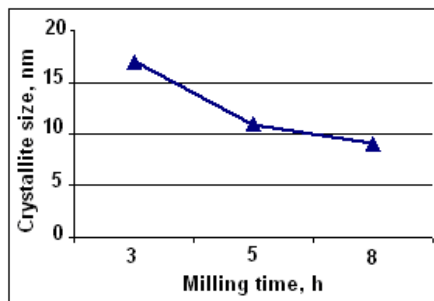
Fig. 7 − Plot of the crystallite size against milling time.

X-ray diffraction of Al-Ti5-B1 master alloy developed by rapid solidification is shown in Fig. 8 *a* and the microstructure of Al-Ti5-B1 master alloy bar in Fig. 8 *b*. There are fine TiAl$_3$ and TiB$_2$ particles inside grains of α-Al solid solution. Amorphous material Al-Ti5-B1 band dimensions have a thickness of 55 m and widths of 1 mm, while Al-Sr10 bands have a thickness of 45 m and widths of 1 mm.

X-ray diffraction of Al-Sr10 master alloy developed by rapid solidification is shown in Fig. 9 *a*.
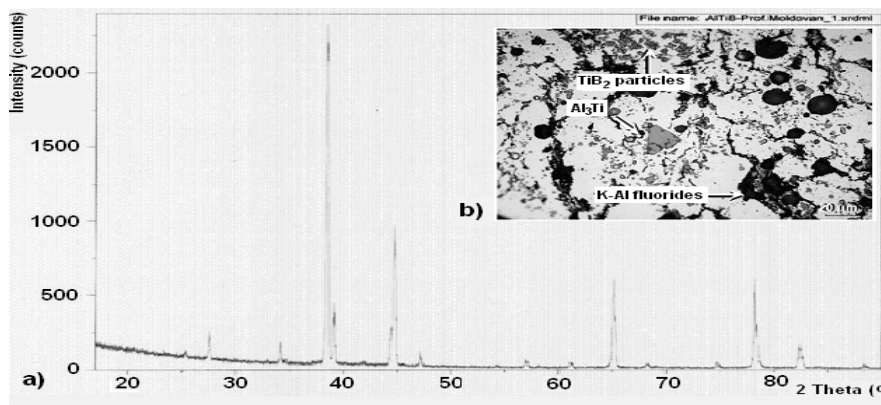
Fig. 8 – Al-Ti5-B1 master alloy: X-ray diffractometry (*a*) and microstructure (*b*).
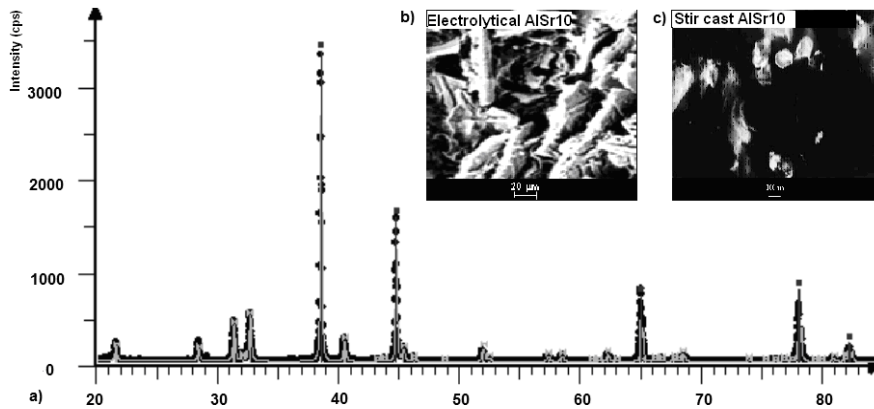
Fig. 9 – Al-SR10 master alloy: XRD diffraction (*a*); SEM images of Al-SR10 master alloy obtained electrolytical (*b*), and by stir casting (*c*).

Analysis by electron microscopy of Al-Sr10 master alloy samples obtained by electrolysis in molten salts (Fig. 9 *b*) revealed that the microstructure of Al-Sr10 master alloy obtained by electrolysis differ

considerably from the microstructure of the master alloy obtained by the classical method of melting and mixing (Fig. 9 *c*).

4. Conclusion

1. Experiments were carried out to obtain Al master alloys with nanocrystalline structure: AlMn65, AlMn75, AlTi5B1 and AlSr10.

2. Al-Mn master alloys were achieved by mechanical alloying determining the correlation of grinding time (3, 5, 8 hours), the degree of grain refined powder sizes and their microstructures, with the appearance of modifiers compounds.

3. Al-Ti5-B1 master alloy was obtain by rapid solidification and analyzed by electron microscopy. It was put in evidence the presence of TiB_2, AlB_2 and $(Ti,Al)B_2$ compounds, and also the presence of Si, Fe and O derived from sponge Ti and working atmosphere of the facility development.

4. AlSr10 master alloy was obtained by electrochemical decomposition of $SrCO_3$, and by mean of electronic microscopy. It was observed Al_4Sr fine phase formation with more complex morphology than that present in the alloys obtained by conventional methods.

REFERENCES

Gadea S., Petrescu M., Petrescu N., *Aliaje amorfe solidificate ultrarapid - sticle metalice.* Editura Ştiintifica şi Enciclopedică, Bucureşti, 1988.

Li Ji-dong, Zhang Ming-jie, *New Process For Preparation Of Al-Sr Alloys By Molten Salt Electrolysis And Its Feeding Study On Period.* Journal of Materials and Metallurgy, **1**, 2005.

Moldovan P., Panait N., Mărginean Şt., *Bazele tratării topiturilor metalice neferoase.* Editura INTACT, Bucureşti, 1998.

Olejnik L., Rosochowski A., *Methods of Fabricating Metals for Nano-Technology.* Bulletin of the Polish Academy of Sciences, Technical Sciences, **53**, *4*, 2005.

Popescu G., Cârceanu I., *Alierea mecanică - Principii mecanisme şi aplicaţii.* Ed. Printech, Bucureşti, 2007.

Sfăt E.C., PENCEA I., *Aliaje de aluminiu amorfe şi nanocristaline.* Ed. Printech, Bucureşti, 2009.

Suryanarayana C., *Mechanical Alloying and Milling.* Progres in Materials Science *46*, 11-32 (2001).

OBŢINEREA DE PREALIAJE NANOSTRUCTURATE PE BAZĂ DE ALUMINIU

(Rezumat)

Realizarea prealiajelor nanocristaline pentru modificarea şi finisarea aluminiului şi aliajelor sale constituie o direcţie nouă de cercetare în perfecţionarea aliajelor de aluminiu. Prealiajele nanocristaline pe bază de aluminiu sunt folosite la fabricarea semiproduselor şi produselor din aluminiu şi/sau aliaje de aluminiu nanostructurate, atât de necesare în construcţia de componente şi echipamente din industriile de vârf (construcţii aerospaţiale, tehnica militară, construcţia de autovehicule etc.), în care performanţele sunt predominante în raport cu preţul componentelor. Prealiajele folosite în această lucrare sunt: Al-Mn (obţinut prin aliere mecanică), Al-Ti5-B1 (obţinut prin solidificare ultrarapidă) şi Al-Sr10 (obţinut prin descompunere electrochimică). Difracţiile de raze X şi imaginile de microscopie electronică (SEM) pun în evidenţă formarea cristalitelor nanometrice şi a compuşilor intermetalici care realizează finisarea structurii în aluminiu şi aliajelor sale.

THE TRIBOLOGICAL ASPECTS OF CHROMED OLC45 STEEL TO DRY FRICTION AND HIGH TEMPERATURE

BY

MARIAN POPESCU[1*], NICOLAE POPA[1], RADU NICOLAE DOBRESCU[1] and JEAN DENAPE[2*]

[1]University of Pitesti,
Department of Applied Mechanics
[2]ENI Tarbes (France)

Abstract. Numbers of modern technologies of mechanical properties changing are used in industry because some traditional materials cannot offer the superior mechanical and tribological proprieties. The paper shows the very good tribological properties of the chromed OLC45 steel at the 4000˚C temperature.

Key words: OLC45, dry friction, pion-disc, worn.

1. Introduction

Numbers of modern technologies of mechanical properties changing are used in industry field due to the fact that frequently used traditional materials cannot offer superior mechanical properties. Chrome plating is a pretty hard cover process and it is applied to a large scale of basic materials, including stainless steel, cast iron, aluminium, titan, copper, bronze, nickel alloys. The study we present is on quality carbon steel which will be used in automobile industry at the speed gear.

---

* Corresponding author; *e-mail:* pmt_ig@yahoo.fr; denape@enit.fr

The hard chrome plating process advantages are the following:
- Obtaining a high hardness (~ 100 HV);
- Very good tribological properties: low friction coeficient, wear resistance (200 times approximely) comparing with other hardness treatments especially in dry friction conditions;
- High protection level against corrosion;
- Long exploitation timing and product life prolongation;
- Costs reduction comparing with other technologies.

2. Materials Used and Applied Technology

The material we used was XC45. The samples which are hard chrome plated have the geometrical form of a disc having exterior diameter of ф 37mm. For chrome plating we used 22 samples, 10 of which for chrome plating at 30 µm thickness and 11 for chrome plating at 50 µm. One witness sample was left for each group.

3. Testing Conditions

The tribometer we used for tests was made of Adamou (Adamou, 2005) in the Tribology laboraty of ENI Tarbes (Fig.1). The contact configuration is pawn-disc type.
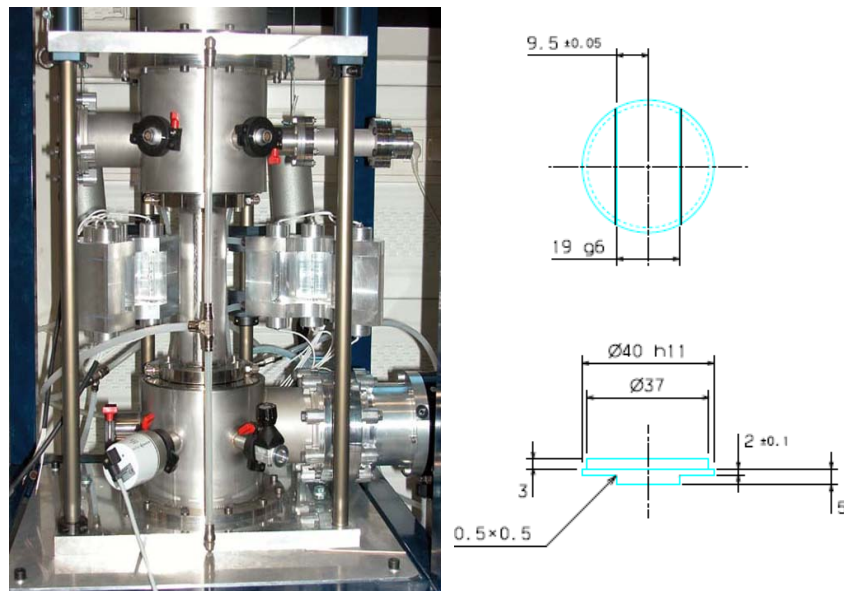
Fig. 1 – Testing device and the samples and pawn dimensions.

This tribometer answer at the following technical specifications:
- The contact configuration is plane fixed pawn – revolving disc type
- Voided room at 10-6 mbar having the possibility of gas introduction;
- The samples temperature is forecasted to vary between 200 and 900°C;
- Normal load is from 1 to 100 N;
- The sliding speed may vary between 0,01 and 1,5 m/0.
- The samples are fitted up at the two coaxial vertical shafts extremities.
- The cylindrical pawn and the disc have the 6 mm, respectively 37 mm diameters.

The contact surface is of 28 mm². The pawn lenght is of 15mm. The loading is made by gravity (pointed masses) at the upper part of the tribometer, out of the device. The direct checking is made using a extension-compression force pick-up, put between the pawn and the disc for marking the load before the tests are done (Fig.2).
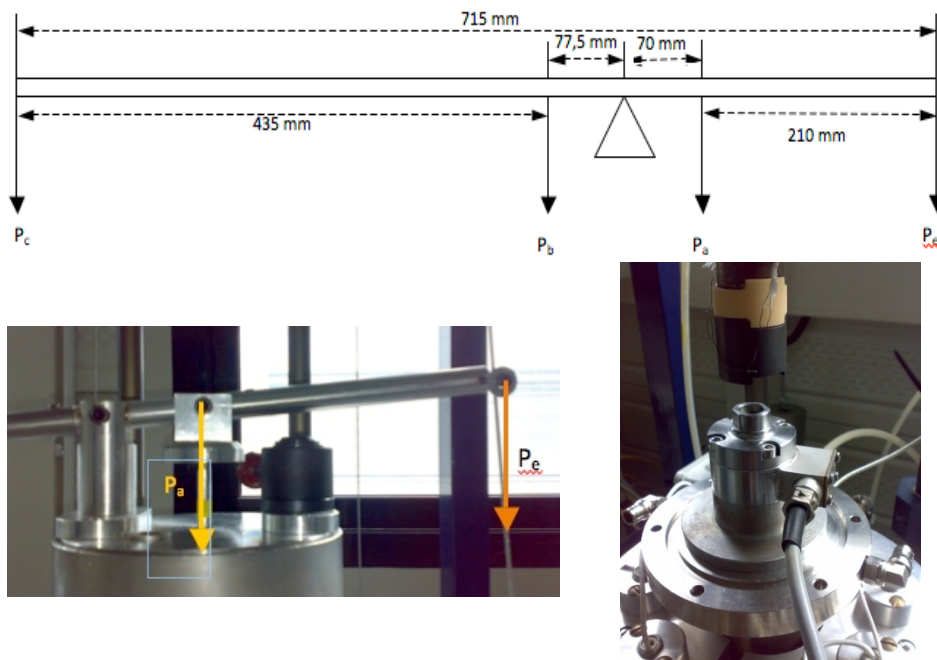
Fig. 2 – The lever arm and the axal load computing chart (Pa).

The data acquisition is continuously make with a HBM type SPIDER 8 console help collateral linked to a PC.
The test took place in the following conditions:

● first test (Fig. 3)
- temperature: 400°C± 5°C;
- speed: constant of 0,25 m/s;
- load: cumulated from 2,5 N to 40 N with levels of 2,5 N, of 300s;
- total timing: 65 min;
- outer relative humidity: approximatively 65 %
● second test (Fig. 4)
- temperature: 400°C ± 5°C;
- speed: cumulated from 0,1 m/s, to 1,5 m/s using levels of 300 s;
- load: constant of 15 N;
- total timing: 35 min.;
- outer relative humidity: approximatively 65 %
During the test, the following parameters are enlisted, with the pick-up help:
- the friction coefficient as ratio between the tangent force and the normal one, in ASCII format under Excel;
- the samples vertical movement represented by the material wear
- the friction coefficient comparing with time;
- the contact surface temperature.
The plane friction surface pawn is made by steel „Stub" X22CrNi17, hardness 247 HV30.
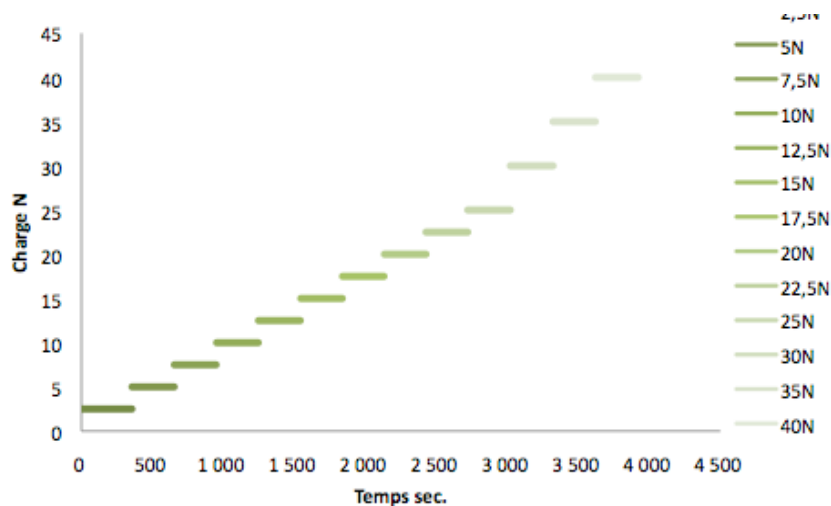
Fig. 4 – The constant charge test.
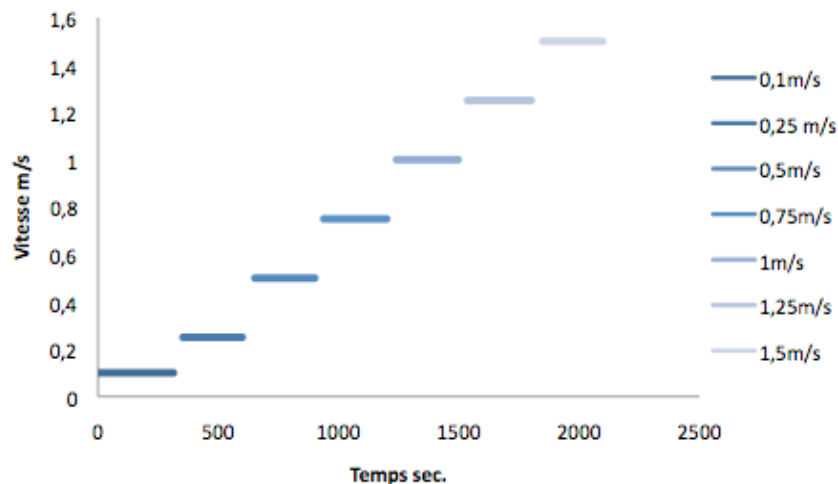
Fig. 5 – The cumulated speed test

The sample heating is made by the internal surface of the collar. The samples temperature raising is very fast (7 minutes from 20 to 900°C). The temperature is homogeneous on all the disc's surfaces. The characterization means we use are the optical microscope (the binocular LEICA), the electronic microscope with the analyser connected to the X energy dispersion one (MEB Philips SEM 515) and the optical profilometer (VEECO NT 1100).

3. Results

A global average value is obtained μ = 0,65 (see also Table 1).

Table 1
The Friction Coefficient Values at the Testing Speeds

	Average
m/s	μ
0,1	0,5008363
0,25	0,5287197
0,5	0,5562374
0,75	0,5671996
1	0,5532789
1,25	0,5667199
1,5	0,5554559

The discs and the pawns after tests observation was made with the binocular microscope NACHET Z45P fitted up on a XCD Sony camera and processed with the Archimed programs from the Microvision Instruments. These observations have permitted knowing the wear process of the surfaces, confirming the presence or absence of the atriped particles and the worn surface dimension.

In order to compute the wear produced during the test, the surface topographic characterization was used. This characterization was made by interferometry with white light VEECO NT 1100 on a disc section. The device permits viewing the surfaces in 2D or 3D and gives the possibility of evaluating the material volumes put on a part and the other from a referential plan

Leaving from the 3D topography the following volumes were computed:

VM = V(-) – V(+) : the wear volume

V(-) : the worn material volume layed under the reference line;

V(+) : the worn material volume layed upon the reference line and lateral from the friction route;

VT = V(-) +V(+) : the total volume (or the damaged material volume)

These calculations are made on small surfaces. The total volume must be related to the whole friction route by a simple relation at the radius r = 13,5 mm, which is the average radius of the route and y – the width of the analyzed surface (Fig.6).

$$V_{total} = V_{masurat} \times \frac{2\pi r}{y} \qquad (1)$$
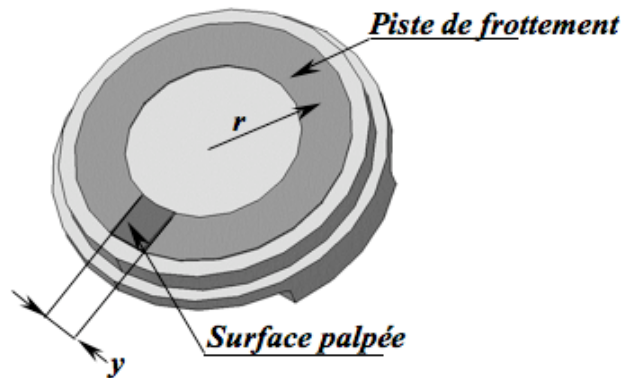
Fig. 6 – The arithmetic chart of the total worn volume.

Taking into consideration that the tests conditions are different (constant loading and cumulated velocities or loading in levels with constant speed), it appears the necessity of introducing the wear percent defined as wear volume related to the normal loading product and the passing distance

expressed in m^3 N-1 m^{-1}. As the wear volumes are negative, we will also express the transfer percent in order to have positive values.

In the case to solve, these transfer percentages correspond to the following relations for a cumulated loading and cumulated velocity:

$$U_{\Sigma F} = \frac{V_{M\,total}}{L_T \cdot \sum_{L=1} F_{Ni}}$$ (2)

$$U_{ZVi} = \frac{V_{M\,total}}{F_N \cdot \sum V_i t_i}$$ (3)

For the test at cumulated loading, L_T is the total sliding lenght, meaning 12x300 (s) x 2,5 (m/s) and F_{Ni} is the level i loading. For the test at cumulated velocities, v_i is the level i speed, t_i is the level i time and F_N is the normal loading of 15 N.

It results a wear percent of 1,6.102m^3 N^{-1} m^{-1} for cumulated loading and sliding velocity of 0,25 m/s, at a global friction coefficient $\mu = 0,64$.

4. Conclusion

This study has permitted the tribological behavior analysis at a temperature of de 400°C for XC45 hard chrome plated material. in the introduction: it assures a better resistance and it is It was observed that it has a lower friction coefficient then an alloyed (Popescu & Alexis, 2010) and also a lower wear

From the chrome plating treatment point of view, we draw the following conclusion related to the advantages specified a future oriented process combined with an advanced environment technology.

REFERENCES

Adamou A.S., PhD Thesis, ì'Institut National Polytechnique de Toulouse, France, 2005.
Dalvemy D., PhD Thesis, ì'Université de Bordeaux, 1998.
Denape J., Introduction à la TRIBOLOGIE. *Frottement et usure des Matériaux*, ENI Tarbes 2008-2009.
Popa N., Dobrescu R.N., Petit A.J., *Tribology elements*. University of Pitesti Publishing House, 2005.
Popescu M.T., Alexis J., *Recherches concernant le comportement des aciers revêtus au frottement sec et a haute température.* Ingineria Automobilului, *14*, March 2010.

ABORDAREA TRIBOLOGICĂ A OŢELULUI OLC45 CROMAT DUR LA
FRECARE USCATĂ ŞI TEMPERATURĂ ÎNALTĂ

(Rezumat)

Numeroase tehnologii moderne de modificare a proprietăţilor mecanice se utilizează în industrie deoarece unele materiale tradiţionale nu pot oferii proprietăţi mecanice şi tribologice superioare. Lucrarea pune în evidenţă proprietăţile tribologice foarte bune ale oţelului OLC 45 cromat dur la temperatura de 4000˚C.

COMPOSITES OBTAINED FROM Cu AND Fe$_3$O$_4$ NANOPOWDERS

BY

ANDREI PREDESCU[1]*, EUGENIU VASILE[2], ROXANA TRUSCA[2] and LIANA MARIA VLADUTIU[1]

[1]Politehnica University of Bucharest
[2]METAV CD Bucharest

Abstract. The paper presents results of research carried out in order to obtain a copper-based nanocomposite reinforced with nanoparticles of magnetite. Nanoscale powders of copper, respectively magnetite, were obtained by chemical methods. These powders are characterized by XRD, SEM, TEM and were used to obtain a Cu-Fe$_3$O$_4$ nanocomposite by conventional methods of powder metallurgy (compacting and sintering).

Key words: intermetallic composite, nanomaterials, powder metallurgy, magnetite.

1. Introduction

The notion of nano scale particle is not so new in the real world as well as in the engineering materials. There are a number of examples of improvement of mechanical properties of structural materials when a microstructure has been developed. In the ferromagnetic materials, the coercive force proved to be maximal when the spherical particles have a diameter approximately equal to 50 nm. When individual molecules are arranged in

---

* Corresponding author; *e-mail:*

defined and controlled nanosystems, they form new structures and acquire new properties. Besides high mechanical properties, high electrical and thermal conductivity properties are more often required. Within this group of materials particularly promising are those of nano - metric size of the matrix hardening phase grains. This paper is concentrated on this problem. Investigations into fabrication, properties and microstructure of a copper matrix - hardened with magnetite - microcomposites are presented.

2. Experimental Procedures

The obtaining of the Fe_3O_4 nanopowders was made by coprecipitation method. Chemical coprecipitation is a simple and economical method of obtaining the magnetite nanoparticles. You can use cheap iron salts with different precipitation agents (NaOH, NH3, urea, mixtures of precipitation). It results nanosize particles of iron oxides in relatively large quantities in a short reaction time, important aspects from economically point. The copper powder was obtained using the polyol reduction process.

There were obtained nanocomposites with $Cu - Fe_3O_4$, containing 5%, 15% and 20% Fe_3O_4. These were obtained by powder metallurgy technique, that is compacting and sintering. The mixtures of powders were compacted at 500 and 700 Mpa at room temperature and than sintering in vacuum at 650° and 850°C for 1 hour was applied. The compacting was realized using a unidirectional press in an antimagnetic matrix. The resulted nanocomposites was examined using SEM, XRD and EDS.

3. Results and Discussions

Results of the examination of microstructure of the Fe_3O_4 powders have shown that size of particles was of an order 5-50 nm. The magnetite nanoparticles were preapared by coprecipitation of ferrous ion (Fe2+) and ferric ion (Fe3+) with NaOH solution. Like many cases of nanoparticles, the agglomeration of particles should be properly controlled. Fig. 1 *a* represents a transmission electron microscope bright field (TEMBF) image. The image shows sferical particles with low sizes, well dispersed. Fig. 1 *b* represents an electron diffraction image that shows the interplanar distances coresponding to the magnetite nanoparticles.

In Fig. 1 *c* (HRTEM image), could be identified in an area of the sample, the interplanar distances (311) si (220), coresponding to magnetite. The obtained magnetite has a crystalin structure and is a face-centered cubic system. The copper powder was obtained by polyol reduction process. The size of the particles is between 10-30 nm and has a concentrations of 99,9% copper. After compacting and sintering, the obtained nanocomposite was taken for the examination of structure properties by SEM, EDAX and XRD.

a   *b*

c
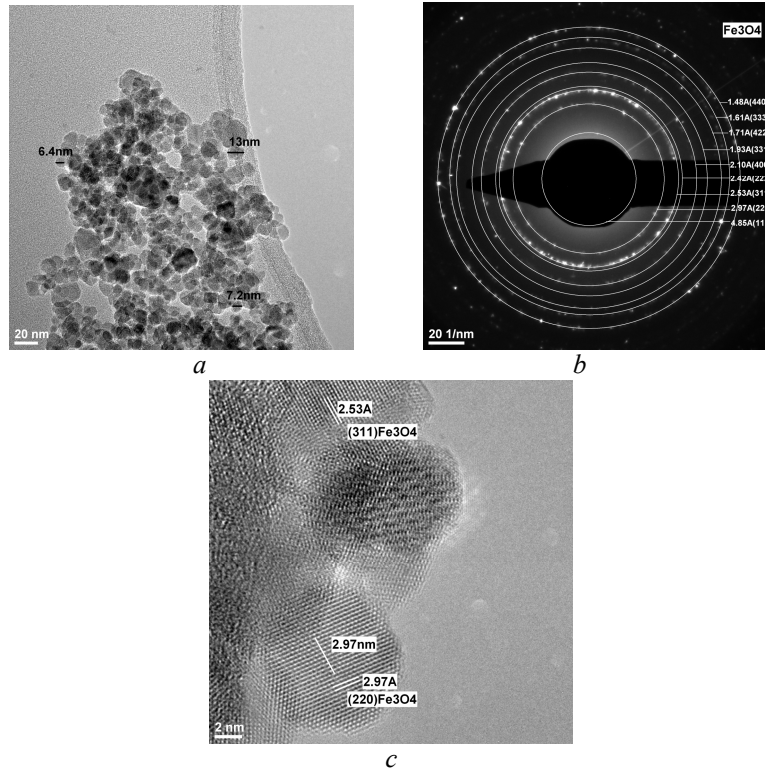
Fig. 1 − *a*) TEM micrograph of Fe3O4 particles; *b*) Electron diffraction pattern;
c) HRTEM image with interplanar distances.

In Fig. 2 is shown SEM microstructure of the nanocomposite with 15% Fe_3O_4 before and after sintering in vacuum at 650°C.

a   *b*
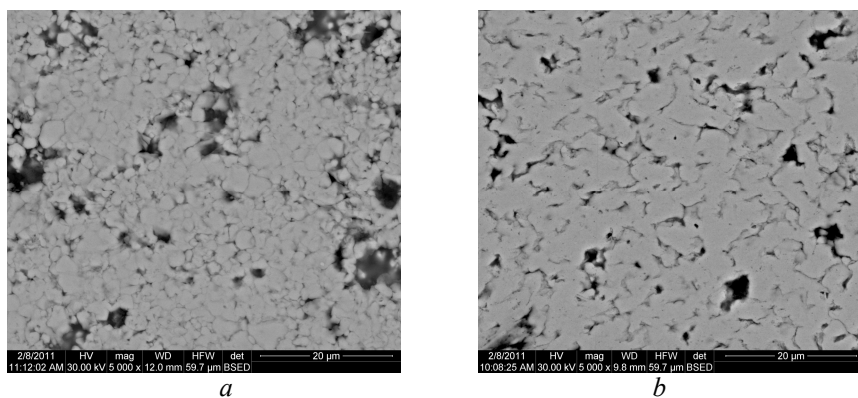
Fig. 2 − SEM microstructure of the Cu-Fe3O4 nanocomposite:
a − before sintering; *b* − after sintering.

The images shows that after sintering the nanocomsites is more compact, but the investigations results have shown that it is difficulty of compacting to high densities, avoiding retained porosity, and at the same time ensuring good powder particle bonding for investigated materials. Agglomeration is a definite problem in consolidated nanopowders.

The X-ray diffraction spectra of the Cu-Fe$_3$O$_4$ with 20% Fe$_3$O$_4$ nanocomposite is shown in Fig. 3. The X-ray powder diffraction patterns of the materials proved its crystalline nature.
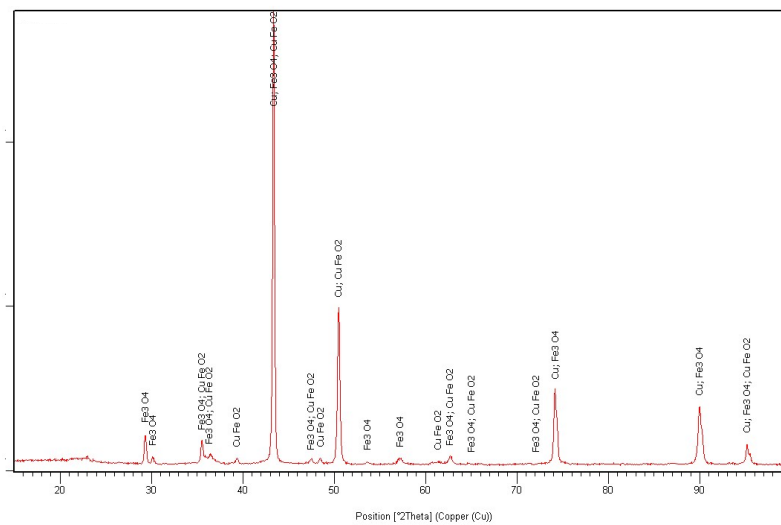
Fig. 3 – XRD Pattern of nanocomposite Cu-Fe$_3$O$_4$.
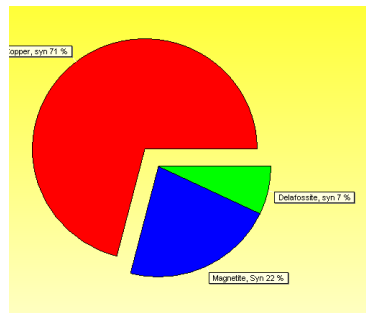
Fig. 4 – Distribution of the newly formed compound (CuFeO$_2$).

All the detected diffraction peaks that were indexed in Fig. 3 and indicate that the particles correspond to magnetite, copper and a newly formed compound during sinterizing, CuFeO$_2$ (coresponds to natural mineral compound known as delafossite). In Fig. 4 is shown the distribution of the identified

compounds according to the XRD semiquatitative analysis. The newly determined compound has 8% in the nanocomposite matrix.

The diffraction spectra showed very broad diffraction lines, in accordance with their small particle size and high specific surface area.

The EDS analysis (Fig. 5) of the nanocomposite $Cu-Fe_3O_4$ with 15% Fe_3O_4 represents the distribution of the elements which forms the matrix. The image shows a irregular dispersion of the magnetite which confirms the tendancy to agglomerate of the nanoparticles.
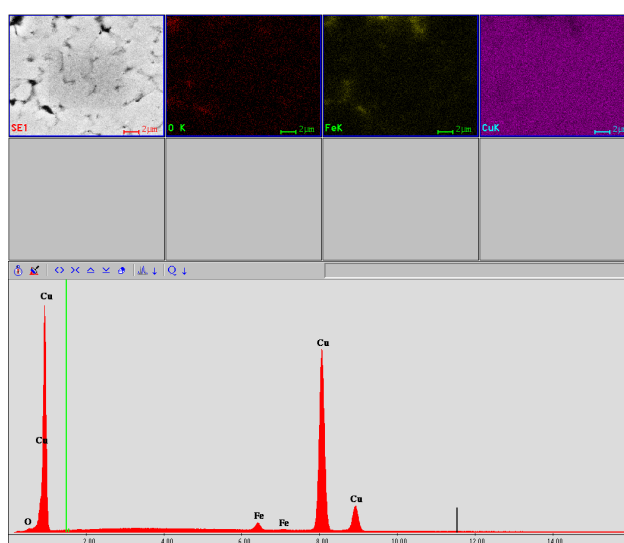
Fig. 5 – EDS distribution of the nanocomposite $Cu-Fe_3O_4$

3. Conclusion

Results of the experiments shows the possibility to obtained a $Cu-Fe_3O_4$ nanocomposite by conventional methods of powder metallurgy (pressing and sintering). The originality of the paper consists in using copper and magnetite nanopowders obtained by chemical methods (solvothermal method for Cu and coprecipitation method for Fe_3O_4). It was obtained a new composite with nanostructure which was structural characterised. After the pressing and sintering, it was identified a new intermetallic compound $CuFeO_2$. The next researches will investigate the magnetic and electrical properties of the $Cu-Fe_3O_4$ nanocomposite. This intermetallic composite reinforced with iron oxide (Fe_3O_4) will be used essentially in aeronautical engineering or in electronic industry. First of all, certain parameters such as sintering time and sintering temperature, percentage of the reinforcement, compact pressure, etc. were evaluated. One purpose of this project will be focused on the improvement of the conductivity and magnetic permeability of this new composite.

LIPSA TRIMITERILE BIBLIOGRAFICE IN TEXT
REFERENCES

[1]. Abrudeanu M., Piticescu R.R., Piticescu R.M., *Wet Synthesis of Ceramic Powders ultradispers*. Editura tehnica, 1999.

[2]. Motoc A. M., Moldovan P., *Research on Influence of Additives on the Characteristics of Nanocomposites Materials Based on Zirconium*. 2007.

[3]. Predescu Andrei, Vladutiu Liana, Moldovan Petru, *Research on the Characteristics Nanopowders Based on Magnetic Iron Oxide*. Structural Analysis of advanced Materials – ICSAAM, 50 (2009).

[4]. Fredika M. Robertson, Mauro Ferrari, *Nanotechnology in Cancer Therapy*. Nat. Rev. Cancer , **5**, *3*, 161-167 (2005).

[5]. Predescu A., *Cercetari privind dimensiunea si distributia nanopulberilor bazate pe oxid de fier magnetic si caracterizarea acestora*. Buletinul Institutului Politehnic din Iasi, **LVI (LX)**, *2*, 95-102 (2010).

[6]. Matei E., Predescu A. M., Predescu A., Vasile E., Predescu C., *Investigations on Nano-Iron Oxides Properties used for Different Industrial Applications*. Optoelectronics and advanced materials – rapid communications, **5**, *3*, 296-301, March 2011.

[7]. Nechifor A.C., Andronescu E., Nechifor G., Rev. Chim., **54**, *8*, 455 (2003).

COMPOZITE OBŢINUTE DIN Cu ŞI NANOPULBERI Fe$_3$O$_4$

(Rezumat)

În lucrare se prezintă rezultatele cercetărilor efectuate în scopul obţinerii unui nanocompozit cu baza cupru armat cu nanoparticule de magnetită. Pulberile nanometrice de cupru şi respectiv magnetită, au fost obţinute prin metode chimice. Aceste pulberi caracterizate prin XRD, SEM, TEM, s-au folosit pentru obţinerea unui nanocompozit Cu-Fe$_3$O$_4$, prin metodele clasice ale metalurgiei pulberilor (presare şi sinterizare).

[1]. (Abrudeanu *et al.,* 1999)
[2]. (Motoc & Moldovan, 2007)
[3]. (Predescu *et al.,* 2009)
[4]. (Fredika *et al.,* (2005)
[5]. (Predescu, 2010)
[6]. (Matei *et al.,* 2011)
[7]. (Nechifor *et al.,* 2003)

RESEARCH REGARDING THE INFLUENCE OF MnS INCLUSIONS ON THE TRAIN AXLES FATIGUE STRENGTH

BY

C. PREDESCU*, E. VASILE, MIRELA SOHACIU, A. BERBECARU and A. PREDESCU

Politehnica University of Bucharest,

Abstract. Our paper aims to present the examinations, checks and tests made on train axles in order to establish the mechanism and causes resulting in breaking after a short period of operation.

Research was realize for breaking surface analysis and its adjacent area and had consisted in: - macroscopic visual examination;

- microscopic examination of fracture surface of the material and its adjacent area by optical stereomicroscopy and scanning electron microscopy (SEM) at low magnification;

- investigation of the material by energy dispersive X-ray microanalysis (EDX) for micro scale composition;

- chemical analysis by optical emission spectrometry on the samples from adjacent fracture surface.

Key words: macroscopic visual, SEM, chemical analysis.

1. Introduction

Mechanical properties of steels are adversely affected by nonmetallic inclusions, because they are discontinuities in the metallic mass reducing active section are local power concentrators, reducing the mobility of dislocations and

---

* Corresponding author; *e-mail:* predescu@ecomet.pub.ro

having effect of indenture. Because are the crack primers and are reducing the strength, plasticity, toughness, resistance to fatigue, corrosion, wear and weld ability.

Mechanical properties are influenced by quantity, chemical composition, shape, size and mode of distribution of nonmetallic inclusions.

Properties are becoming worse and more pronounced under the action of intercrystalline inclusions and also under the coarse intracrystalline inclusions which are in big proportions. Plastic inclusions keep a better grip on the request matrix. The tough, especially rough oxide inclusions favors local concentrations of stress and the occurrence of cracks. Crack propagation speed is influenced by the nature of inclusion: the fragile, which can be broken by the stress field, forming secondary cracks and accelerating crack propagation. Hard inclusions that remains supportive on the matrix, decreases velocity of the crack propagation.

Thermal contraction difference between the mass and inclusion, especially hardening can lead to the emergence of fields of stress or structural discontinuities. Thus, if the coefficient of contraction is low compared with the matrix (Al_2O_3, Cr_2O_3 on steel) appear fields of tension on the surface of inclusion, if it is large (MnS, MnSe on steel) appear goals, with especially negative action requests to fatigue.

MnS inclusions have high melting temperature (1610°C), are a form of primary idiomorf crystals, plastic and steel structure with no preferential distribution.

2. Experimental Investigation on the Causes of Fracture Axle Shaft

Research carried out to establish the causes that led to the breaking of the axle, the analysis focused on breaking the surface and its adjacent area and consisted of:

- Macroscopic visual examination by optical;
- Microscopic examination of fracture surface of the material and its adjacent area by scanning electron microscopy (SEM);
- Investigation of the material by energy dispersive X-ray microanalysis (EDX) for micro scale composition;
- Chemical analysis by optical emission spectrometry on the samples from adjacent fracture surface.

Macrovisual examination of fracture surface of axle shaft shown in figure 1 is presented fracture surface, composed from fragments (samples), cut from the section of shaft in the form of a disk, containing the fracture surface.

Fracture surface aspect is characteristic of a fatigue fracture process with multiple primers. Damage of both breaking surface and edge breaking surface (outside the zone) that took place during the train accident event or in

the process of sampling and preservation of evidence does not allow clear identification of the percussion break.

Surface aspect suggests that the initiation of the breaking process had appeared first in area A (very damaged) and then in area B.

Both breaking processes met in the threshold C, which separates them through level differences. Towards zone D, fracture surface becomes more uneven, which suggests the fracture propagation speed increases until the zone D, where the final rupture took place, with uprooting of material.
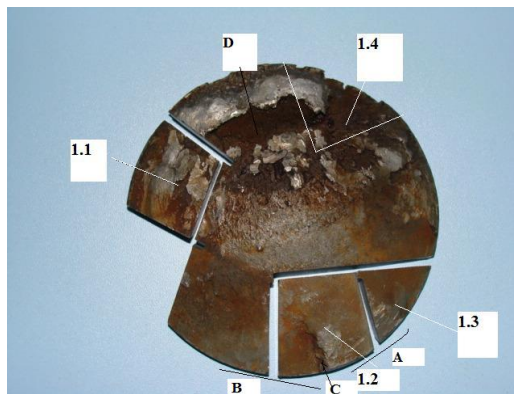
Fig. 1 – Aspect of fracture surface of axle shaft.

Microscopic examination made on scanning electon microscopy had followed microstructure characterization of material and establishes the nature of material weakness (inclusions, thermal influence) using energy dispersive X-ray microanalysis (EDAX) allowing determination of local micro – chemical composition and significant elements distribution interesting micro regions.
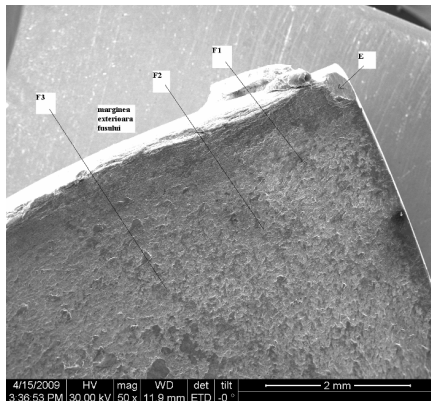
Fig. 2 – Microscopic image of the fracture initiation zone.

Scanning electron microscopy image (Fig. 2) shows a part of the fracture initiation from zone B. In point E (probably one of the primers) existence of visible mechanical damage prevents identification of the primer.

We can see the existence of fronts F1, F2, F3 of changing the propagation fracture rate, characteristic of a fatigue fracture. The edge zone corresponding to circumference of the shaft is deformed mechanically, on a depth of about 0.3-0.4 mm (probably after the rupture on shaft axle) showing cracks and even separation of material to the inner area of the breaking surface.

In Figs. 3,…, 5 we can clearly see microstructure details of the micro – area which presents a variation in diameter of the axle shaft in the breaking zone. Marginal area which corresponds to the narrow zone of the section presents characteristic microstructure aspects of a region with local molten material, with the ferrite – pearlite grains growth directions perpendicular on the longitudinal axis of the axle.

Solidification fronts are seen and the existence of micro – cracks in the material from this micro – area.
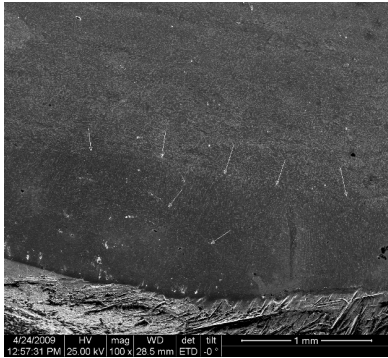
Fig. 3 – Marginal area, highlighting areas of molten material. Arrows indicate the start of the front lines of solidification (x100).
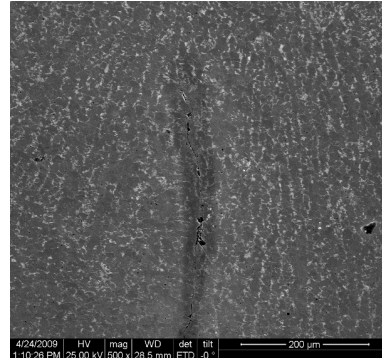
Fig. 4 – Crack parallel with the solidification temperature gradient (x200). Is observed the oriented nature of the material solidified structure.
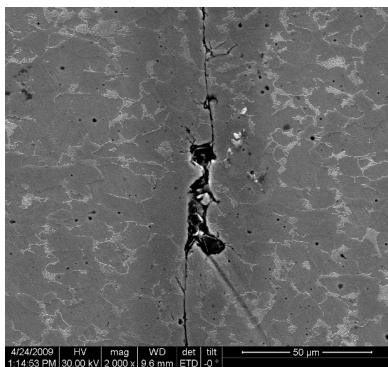
Fig. 5 – Emphasizing higher-order enlargement of the crack propagation intragranulare (X2000).
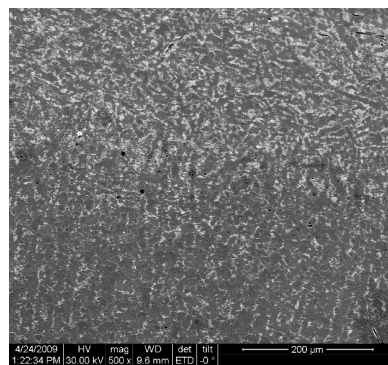
Fig. 6 – Image obtained on the transition from the base material to the molten material (x500).

In Fig. 6 we can observe the orientation differences of the structural formations but also a lower proportion of pearlite in the molten area (due to loss of carbon). We can also observe pores and micro inclusions at the interface between the two volumes of material.

The axle shaft base material microstructure is shown in Figs. 7, 8. The microstructure is oriented in bands, rich areas in perlite alternating with the areas in ferrite. Also are observed the MnS plastic inclusions elongated in the direction of deformation.
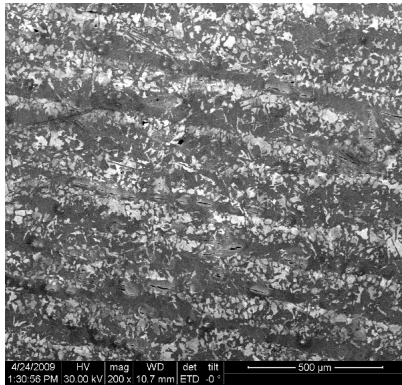
Fig. 7 – Microstructure from the base material of the axle shaft (x200)
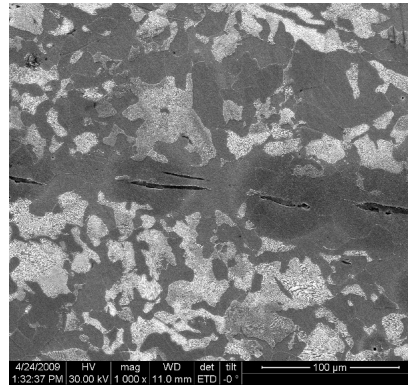
Fig. 8 – Detail of image shown in Fig. 7. Inclusions arranged in the direction of plastic deformation (x1000)

In the thicker zone, is observed a folded of material (on the circumference of the zone) to the fracture surface (Fig. 9). Scanning electron microscopy images from the Figs. 10, 11 reveals clearly elongated microstructure (flow) to the fracture surface.
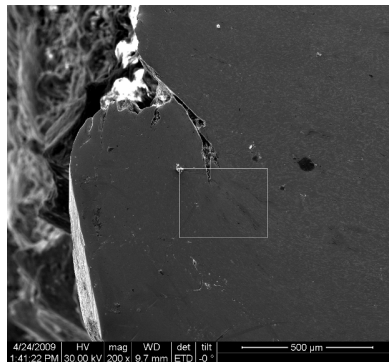
Fig. 9 – ,,Folding" of material observed near the fracture surface (x200).
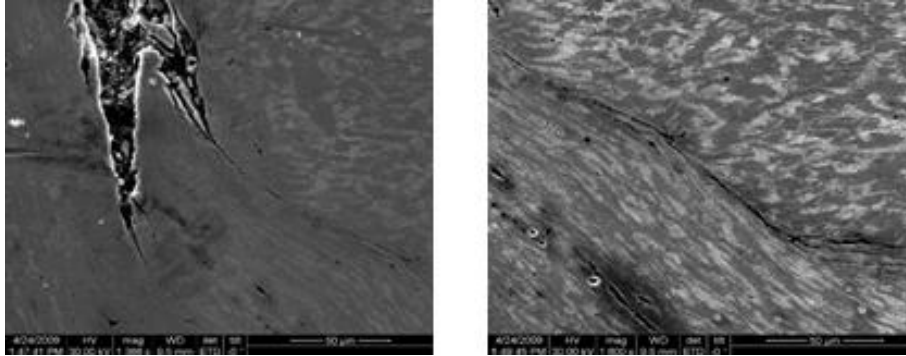
Fig. 10 – Details of the selected area in the image of Fig. 9.

X-ray microanalysis performed on micro area of local melting, micro area of folding the material and the base material (inside micro area) to axle shaft showed no micro structural differences between these micro regions.

Characterization of material microstructure in the adjacent area of breaking surface was performed on the sample 2.1, Fig.11.

Images from Figs. 12,…,15, are images of secondary electrons, presents the material microstructure obtained on the sample 2.1, from fig. 11. The existance of MnS inclusions unevenly distributed in the material is remarkable, on the ferite-perllite microstructure background. Unfavorable to its mechanical properties, these inclusions are typically grouped in discontinuous networks. We observed also the the rows of MnS inclusions existence, which arrive in the axle shaft surface. Such marginal inclusions may be percussion break of those parts that are in service, rows of inclusions that emerge in the area are preferred regions of propagation and development of microcracks.
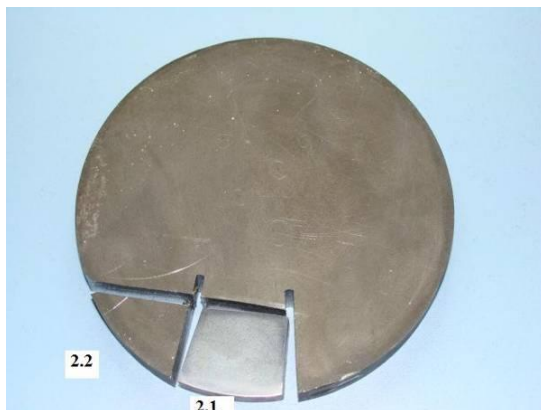
Fig. 11 – Transversal cutting disc from shaft near the surface rupture.
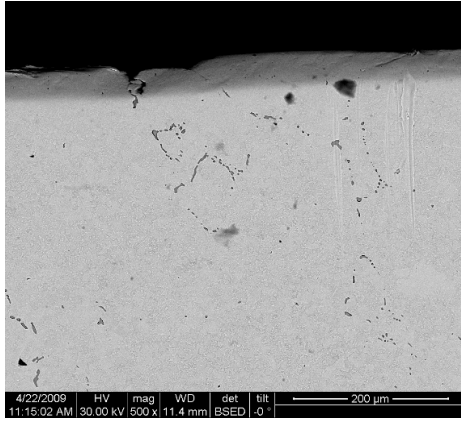
Fig. 12 – Microstructure of axle shaft (image of secondary electron), cross section on shaft (x500). MnS inclusions in both isolated and discontinuous networks, number of inclusions MnS come out in the outer edge of axle shaft.
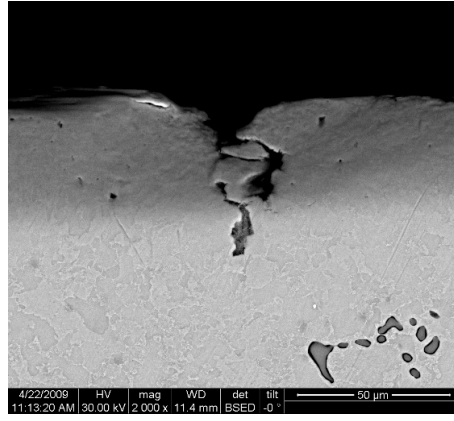
Fig. 13 – Detail from fig. 10a (x 2000)- edge corrosion primer on the sequence on MnS inclusions.
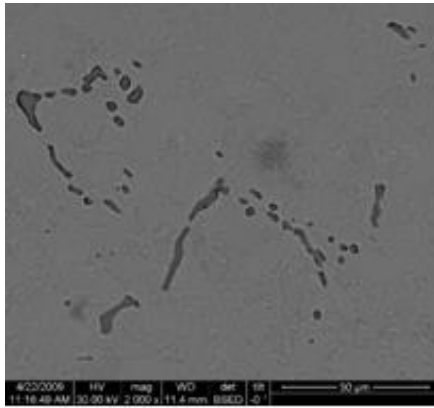
Fig. 14 – Detail from Fig. 10 *a*- discontinuous network of MnS inclusions (x 2000).
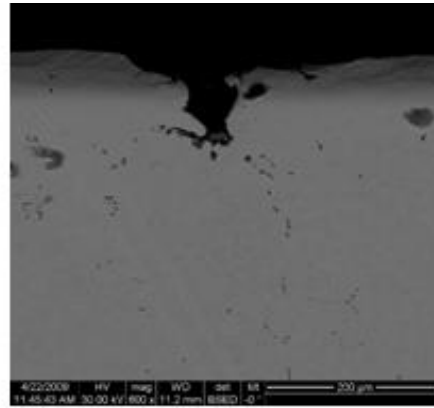
Fig. 15 – Aspect of another edge micro area with corrosion initiated on a network of inclusions (x 600).

Energy dispersive X-ray analysis (EDAX) highlights the nature of microstructural components of interest in the material.

In this way in Fig. 16 is presented the elements distribution like Mn, S and Fe in the micro area shown in the left up corner of the image. It's observed the majority presence of the Mn and S elements in the elongated inclusions (manganese sulfide).
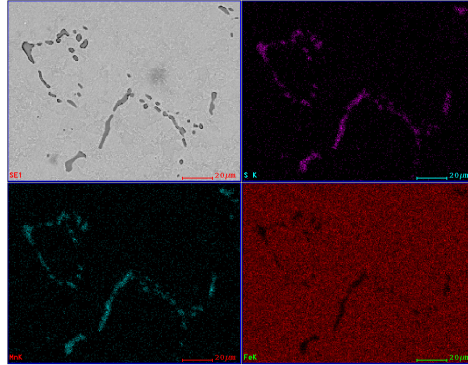
Fig. 16 – Elements distribution of Mn, S
and Fe in the micro area shown in the up
left corner.

Promoting the development of microcracks by strings and
networks of MnS inclusions is demonstrated by the images from Fig. 17.
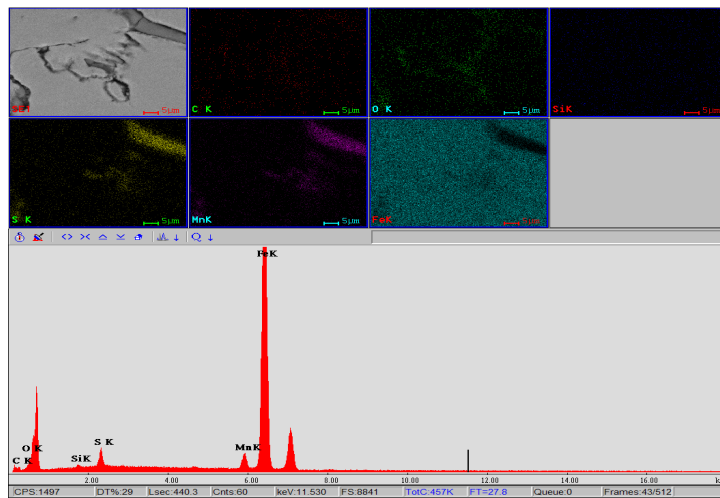
Fig. 17– Distribution of elements evidenced by the EDAX
spectrum in the micro area from the upper left corner. Micro area
is adjacent to the breaking surface and corresponds to sample 1.4
(Fig.1)

Results of micro compositional chemical analysis through optical
emission spectrometry , shows that the percentage of S in samples taken form
the area of rupture surface exceeds the upper limit of permissible concentration
in the material (up 0.04%). Also the percentage of Cu (0.35) exceeds the upper
limit of the maximum permissible concentration (0.3%).

3. Conclusion

The experimental studies performed resulted in following conclusions:

- Visual examination of the fracture surface indicates that it is a fatigue fracture;

- Microscopic examination and investigation by X-ray microanalysis of the material surface area adjacent to the axle shaft beaking highlight the following factors unfavorable in terms of material quality from which the axle was made: a) existence in the cross section of shaft of the discontinues networks of MnS inclusions, negative factor for the mechanical properties of the material; b) existence inclusions rows (observed in transverse section on shaft) that emerge in edge. This may be primers of breaking and corrosion primer of the material.

- Chemical composition analysis shows that sulfur is present in the analyzed samples, in higher concentrations (from 0.05 to 0.06%) than the maximum allowed (0.04%, according to the norm of material). Also the upper limit of the maximum admisible concentration of Cu (0.3%) is exceeded.

Exceeding allowable concentration of sulfure, has the effect of attracting greater amounts of manganese from the ferrite existing in the steel (forming MnS inclusions) with implications for the manganese ferrite depletion and impaired fatigue fracture properties of the material.

Existance of copper (although the upper permitted limit is only slightly exceeded) may be a negative factor. Thus, forging at higher temperatures of 1050°C can lead to the formation of surface cracks, even with a content in Cu of approximately 0.2%, due to melting constituent rich in Cu which is found under the burning layer as a result of steel oxidation and its formation, the immediately steel layer from under the burning layer, thus Cu enriches.

REFERENCES

* * Electron Microscopy. Methods and Protocols-Second Edition-2nd ed./edited by John Kuo,Center for Microscopy and Microanalysis,Crawley,Australia, 2007.

* * *Industrial Applications of Electron Microscopy*. Edited by Zhigang R.Li, DuPont Company,Wilmington, Delaware, U.S.A., 2003.

* * Patent number: RU2415180-C1, Assignee: Novok Metal Comb. Stock Co, Inventors: Alexandrov I.V., Kozyrev N.A., Kuznetsov E.P., *Procedure for Production of Rail Steel, Involves Charging Metal Scrape Into Furnace, and Carrying on Oxidising Period Till Production Steel.*

Cao G.L., Li G.M., Chen S., *et al.*, *In Effects of Deoxidizing Degree on the Pitting Corrosion Behaviour of Carbon and Manganese Steels*. International Journal of Minerals Metallurgy And Materials, **18**, Issue:2, 169-177 (2011).

CERCETĂRI PRIVIND INFLUENȚA INCLUZIUNILOR DE MnS ASPURA REZISTENȚEI LA OBOSEALĂ A OSIILOR DE TREN

(Rezumat)

Lucrarea prezintă examinările, verificările și testele efectuate pe o osie de tren, în scopul de a stabili mecanismul și cauzele care au condus la ruperea acesteia după o scurtă perioadă de funcționare.

Cercetările au fost realizate pe suprafața de rupere și zona adiacentă acesteia și au constat în:

- Examinare macroscopică vizuală;

- Examinare microscopică a suprafeței de rupere a materialului și a zonei adiacente acesteia, prin stereomicroscopie optică și microscopie electronică de baleiaj (SEM);

- Investigare material prin metoda energiei dispersive în radiații X (EDX);

- Analize chimice prin spectrometrie de emisie optică.

APPLICATION OF MICROWAVE THERMAL DESORPTION TO TREAT SOILS CONTAMINATED WITH DANGEROUS CHEMICAL SUBSTANCES

BY

VASILE CĂLIN PRODAN[*], VALER MICLE
and MARIA SZANTO (PRODAN)

Technical University of Cluj-Napoca,
Faculty of Materials Engineering and Enviromental

Abstract. In the large specter of electromagnetic radiations, microwaves occupy the frequency domain from 0,3 to 300 GHz, corresponding wave lenths being situated beween 1 m and 1 mm. Separated from the souce of the microwave, in its propagation, the wave transports energy and interacts with the substance.

Microwave thermal desorption is a method that it's used more and more in the research conducted for the elimination of dangerous chemical substances (pesticides, PCB) from polluted soils. In this article an analysis is being made on the way of application and the characteristics of microwave thermal desorption for soils polluted with dangerous chemical substances.

The main parameters that must be taken into account when this decontamination method is used are: the time of residence of the sample in the oven, microwave iradiation power, soil sample moisture and last but not least the concentration of the pollutant in the sample.

Key words: thermal desorption, microwaves, dangerous chemical substances.

---

[*] Corresponding author; *e-mail:* vasile.prodan@im.utcluj.ro

1. Introduction

Microwaves are electromagnetic oscilations with frequences in the range of $3 \cdot 10^8...3 \cdot 10^{10}$ Hz. In electromagnetic specter, the microwave radiation is situated between infrared radiations and radio waves. The frequencies used in microwave processing domain correspond to the industrial, scientific and medical frequency bands, assigned by the International Telecommunication Union, being called ISM frequencies. In Europe the 2450 MHz, 5800 MHz and 22125 MHz bands are autorized, the most used being the 2450 MHz frequency, its wave length being 12.2 cm (Landini *et al.*, 2000).

The most commonly encountered phenomenon of microwave processing is heating of dielectric materials, due to hysteresis in electrical fields variable in time, which has the effect of converting electromagnetic energy to thermal energy.

Microwave heating is a volumetric heating, whose efficiency depends on the characteristics of the processed material. The thermal process evolves rapidly, the transfer of heat inside the material being independent of the speed of the air flow. The energy concentration in small volumes of material has as an effect important temperature growth, which can modify the properties of the material.

The depth of penetration into the material increases with wave length or with frequency decrease, thus at the frequencies used for microwave processing the depth of penetration is of the order of centimeters and varies depending on the temperature and the properties of the material.

The extraction of organic pollutants using microwave energy was first introduced in 1986 by Ganzler *et. al.* From that moment on, this extraction technique with microwaves was successfully applied for the extraction from soil of different compunds, such as pesticides, polycyclic aromatic hydrocarbons, polychlorbipheniles and phenols.

The extraction using microwave energy is effective because of the reduced time of heating the soil samples by direct effect on the molecules, through ionic conduction and dipole rotation. In principle the dipole rotation is a mechanism by which the energy in the form of electromagnetic radiations is converted into thermal energy (Chen Ligang, *et al.*, 2007).

Organochlorine pesticides were used primarly because of their effectiveness as insecticides. These compounds are forbidden in most of the countries since the 1970s. Also pesticides are chemical substances that bioaccumulate in the environment and living organisms, they're resistant to

natural degradation and present the risc of causing adverse effects on human health (Daura Vega Moreno *et al.*, 2006).

1.1. Dielectric Properties of the Soil

Researchers Hoekstra and Delaney have studies the dielectric properties of sands, muds and clays in the frequency range of 100-26000 MHz. Their data reveal general relations between the dielectric properties, moisture content, temperature and frequency as follows:

• the dielectric constant increases as temperature increases from 5°C to 25°C, but the dielectric loss factor remains constant in this temperature range;

• the dielectric constant and the dielectric loss factor increase with the increase of moisture content in the soil (Gfrerer & Lankmayr, 2005).

Usually, the dielectric constant of soils varies from 2-3 times for dry soils up to 20 times for soils with a moisture content of 0.3 g/ml (Gfrerer & Lankmayr, 2005).

2. The Stage of Application of Thermal Desorption with Microwaves for Treatment of Soils Contaminated with Dangerous Chemical Substances

Following the review of different publications from specialized literature it's observed the development of certain technical aspects (determination of optimal conditions for decontamination, used parameters, temperature, time, iradiation power) necessary for decontamination of soils polluted with dangerous chemical substances.

The summary of the paper is based on date taken from the specialized literature, resulting in the implementation stage of the thermal desorption with microwaves applied to soils contaminated with pesticides, polychlorbipheniles, polycyclic aromatic hydrocarbons and others.

To apply the thermal desorption with microwaves it's very important primarily to know certain characteristics about the soil samples subjected to such treatment.

Before introducing the soil samples into the installation of thermal desorption, they should be subjected to some analysis to determine the samples' characteristics, such as: moisture of soil samples, pollutant concentration, existing pollutant type (Onuska & Terry, 1993). After determining these characteristics, soil samples can be subjected to treatment with microwave thermal desorption, watching the time of keeping the sample in the microwave installation as well as the power of microwave iradiation.

2.1. Microwave Thermal Desorption Applied to Soils Contaminated with Polychlorbiphenile (PCB)

If the soil is contaminated with polychlorbiphenile (PCB) for its remediation according to researchers Kastanek P.and Kastanek F., you can use a facility like the one presented in Fig. 1. Initially the two performed a test in which the soil sample was introduced inside the resonant enclosure and maintained for 2 minutes, applying a power of iradiation with microwaves of 250W. Following this other experimental tests were conducted, heating the soil sample for 5 minutes at a power of 440W, or for 10 minutes at a power of 600W (Kastanek & Kastanek, 2007).

To conduct these experiments P. Kastanek and F. Kastanek used: 100g of contaminated soil, 30g of absorbant for microwaves, 2g of $NaHCO_3$, 8g of NaOH and 25ml of H_2O. The research on a laboratory scale presented above were realised on the facility in Fig. 1 at a temperature of 600°C, temperature necessary and sufficient for the decontamination of soil samples (Kastanek & Kastanek, 2007). Moisture existent in soil is a very important factor, which might affect the final temperature of the heating system with microwaves. Thus the content of water will modify the conductivity and permittivity of the soil, because at temperatures higher than 100°C water turns into vapors, and these vapors can help the desorption process to eliminate the polychlorbipheniles from the soil (Chen Ligang, *et al*., 2007).
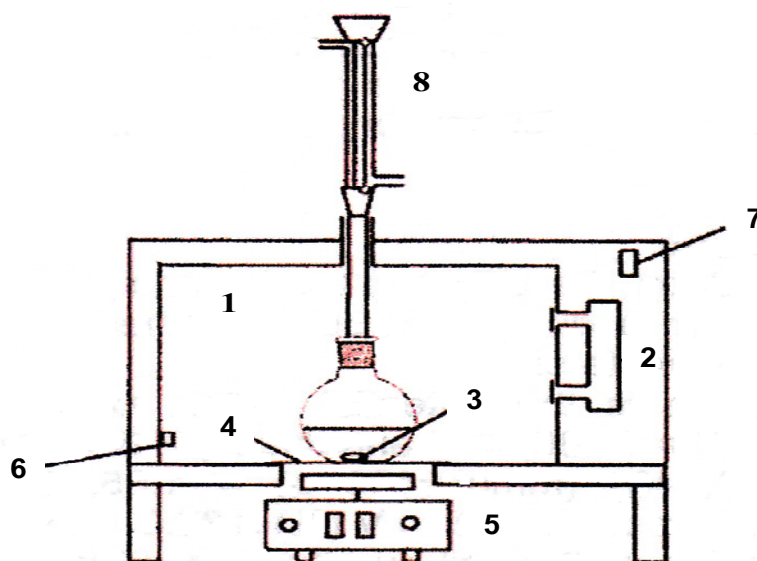
Fig. 1 – Microwave oven scheme: 1 – oven chamber; 2 – magnetron;
3 – magnetic mixer; 4 – sample support; 5 – magnetic stirrer; 6 – IR thermometer;
7 – switch; 8 – cooling water (Kastanek & Kastanek, 2007).

Microwave iradiation is based on the direct effect of microwaves by applying an electromagnetic field upon the ionic molecules, producing a heating

of the entire material from the inside up to the contact surface (Gfrerer & Lankmayr, 2005).

2.2. Microwave Thermal Desorption Applied to Soils Contaminated with Polycyclic Aromatic Hydrocarbons (PAH)

For decontamination of the soil polluted with polycyclic aromatic hydrocarbons you can use a facility like the one presented in Fig. 2. In Fig. 2 it's presented the facility at a laboratory scale, comprising a microwave generator with a power between 0.5 and 1.5 kW providing a microwave frequency of 2.45GHz and a cavity in which the sample of soil is placed.

The installation also comprises of a system of gas input (in this case nitrogen) to ensure a controlled atmosphere, and a gas output system to extract the gases resulted from the thermal desorption process.

Soil salmples having a weight of 25g were placed on a silica bed situated inside a quartz reactor. Positioned like this, the soil sample was occupying the central section of the cavity for a better direct contact between the sample and the beam of microwaves (Robinson *et al*., 2009).

The removal of polycyclic aromatic hydrocarbons from the contaminated soil sample was possible thanks to the microwave thermal desorption at a temperature situated between 100 and 300°C (Robinson *et al*., 2009).
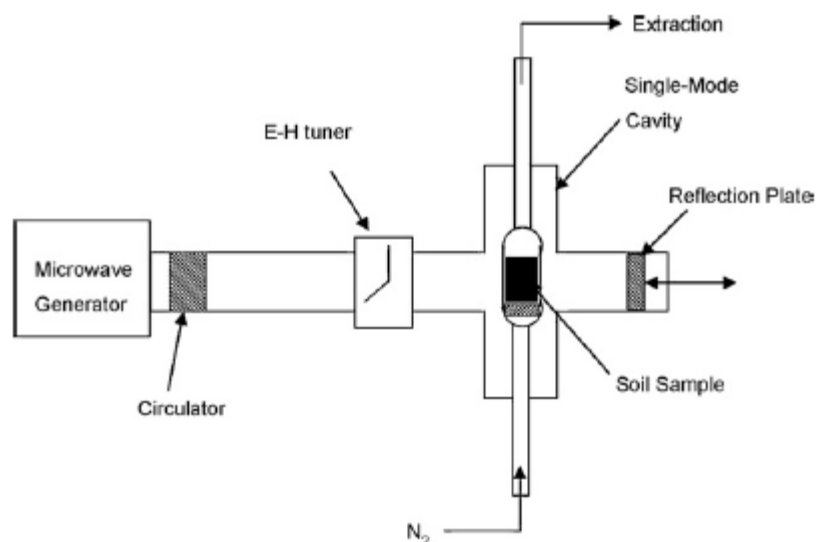
Fig. 2 – Microwave facility scheme for decontamination of soils polluted with polycyclic aromatic hydrocarbons (Robinson *et al*., 2009).

Researchers Onuska F.I. and Terry K.A. made some research regarding microwave desorption applyed to soils contaminated with pesticides and they obtained the following results presented in Table 1, (Onuska & Terry, 1993).

Table 1

The Time of Maintaining and Degree of Recovery of Various Pesticides from the Soil (*Onuska & Terry, 1993*).

Pesticides	Time (minutes)	Recovery degree (%)
Hexachlorbenzene	12,60	91,7±4,8
Lindane	14,03	86,7±4,9
Aldrine	19,22	93,8±4,7
Dieldrine	24,94	88,8±4,1
Endrine	26,12	91,5±4,9
p,p`-DDD	27,66	74,0±3,0
o.p –DDT	27,74	81,7±4,3
p,p`-DDT	29,08	81,6±4,2
Mirex	34,97	81,2±4,0

Advantages:

Microwave thermal desorption advantages compared to incineration are:

- lower investment costs;
- the humic value of the soils remains intact upon decontamination;
- the pollutants from the soil are not destroyed but recovered in a form that allows their recovery;
- rapid decontamination (time of maintaining the soil inside the facility varies between a few seconds to several tens of minutes) (Micle & Neag, (2009; Micle, 2009).

Disadvantages:

One disadvantage of the method would be the fact that microwave thermal desorption has a rather large consumption of electricity.

Also we must take into account the fact that upon the thermal desorption result gases with different pollutants, which must be depolluted before being evacuated into the atmosphere.

The dusting equipment may be humid or dry, comprised of different filters and cyclons, but we must remember that at an industrial scale these installations are pretty expensive.

3. Conclusion

The depollution efficiency for microwave thermal desorption using NaOH was 98.4%. After pre-treatment, the hexachlorbenzene residue present in the soil reached the value of 0.91 mg/kg.

Keeping time in the oven is generally low from a few seconds to a few tens of minutes, according to the contamination degree of the soil, to the moisture of the sample subjected to analisys and to the microwave iradiation power.

The two microwave thermal desorption facilities presented above are executed only at a laboratory stage to be able to closely monitor the thermal desorption process, the parameters and the applying conditions, before it can also be realized at an industrial scale.

REFERENCES

Chen Ligang, Ding Lan, Jin Haiyan, Song Daqian, Zhang Huarong, Li Jiantao, Zhang Kun, Wang Yutang, Zhang Hanqi, *The Determination of Organochlorine Pesticides Based on Dynamic Microwave-Assisted Extraction Coupled with on-Line Solid-Phase Extraction of High-Performance Liquid Chromatography.* 239–246 (2007).

Daura Vega Moreno, Zoraida Sosa Ferrera, Jos´e J. Santana Rodriguez, *Microwave Assisted Micellar Extraction Coupled with Solid Phase Microextraction for the Determination of Organochlorine Pesticides in Soil Samples.* 51–57 (2006).

Gfrerer M., Lankmayr E., *Screening, Optimization and Validation of Microwave-Assisted Extraction for the Determination of Persistent Organochlorine Pesticides.* 203-211 (2005).

Kastanek P., Kastanek F., *Microwave Enhanced Thermal Desorption of Soil Contaminated With Polyhalogenated Biphenyls.* 648-654 (2007).

Landini L., De Araújo Sumair G., Lugão A.B., *Application of Microwave Technology in Rare Earth Elements - a Short Inquiry.* International Nuclear Atlantic Conference - INAC 2007, Santos, SP, Brazil, Associação Brasileira de Energia Nuclear, September 30 to October 5, 2000.

Micle Valer, Neag Gh., *Procedee şi echipamente de depoluare a solurilor şi a apelor subterane.* U.T.PRESS Cluj-Napoca, 185-189 (2009).

Micle Valer, *Refacerea ecologică a zonelor degradate.* U.T.PRESS Cluj-Napoca, 149-153 (2009).

Onuska F.I., Terry K.A., *Extraction of Pesticides from Sediments Using a Microwave Technique.* Chromatographia, **36**, 1993.

Punt M.M., *Microwave-En Hanced Extraction of Organic Contaminants from Soil*. 1997.

Robinson J.P., Kingman S.W., Snape C.E., Shang H., Barranco R., Saeid A., *Separation of Polyaromatic Hydrocarbons from Contaminated Soils Using Microwave Heating*. Separation and Purification Technology, *69*, 249–254 (2009).

APLICAREA DESORBŢIEI TERMICE CU MICROUNDE LA TRATAREA
SOLURILOR CONTAMINATE CU SUBSTANŢE CHIMICE PERICULOASE

(Rezumat)

În spectrul larg al radiaţiilor electromagnetice, microundele ocupă domeniul de frecvenţe 0,3 – 300 GHz, lungimile de undă corespunzătoare situându-se între 1 m şi 1 mm. Desprinsă de sursa care produce microunda, în propagarea sa, unda transportă energie şi interacţionează cu substanţa.

Desorbţia termică cu microunde este o metodă care se foloseşte din ce în ce mai des în cercetările efectuate pentru eliminarea din solurile poluate a substanţelor chimice periculoase (pesticide, PCB). În cadrul articolului se face o analiză privind modul de aplicare şi caracteristicile desorbţiei termice cu microunde pentru solurile poluate cu substanţe chimice periculoase.

Parametrii principali de care trebuie să se ţină seama atunci când se foloseşte această metodă de decontaminare sunt: timpul de staţionare al probei în cuptor, puterea de iradiere cu microunde, umiditatea probei de sol şi nu în ultimul rând concentraţia poluantului existent în probă.

BIREFRINGENCE DISPERSION OF A LIQUID CRYSTALLINE LAYER FROM ALKOXY BENZOIC ACID ESTER IN TETRACHLOROMETHANE DETERMINED BY SPECTRAL METHOD

BY

**ALINA ROGOJANU[∗], CARMEN FELICIA DASCALU
and DANA ORTANSA DOROHOI**

University "Al.I.Cuza", Jassy,
Faculty of Physics

Abstract. The visible birefringence dispersion of a liquid crystalline layer (alkoxy benzoic acid ester in tetra chloromethane) was determined from the channeled spectrum recorded in the absence and in the presence of an external electrostatic field. The increase of the visible birefringence of the liquid crystalline layer in the presence of the electric field was evidenced in this paper. A Wood filter was simulated with Maple program using the experimental data. The knowledge regarding the electric field influence on the birefringence values can help the specialists in designing the electronic display cells containing liquid crystals.

Key words: optical birefringence, channeled spectra, Wood filter.

1. Introduction

Alkoxy benzoic acids are typical representatives of liquid crystals (Ramakrishna *et al*., 2010; Kuz'mina L *et al*., 2009). The polymeric esters of

---

[∗] Corresponding author; *e-mail:* rogojanu_alina@yahoo.com

alkoxy benzoic acids (PEABA) in thermodynamically bad solvent, such as tetra chloromethane (TCM) show a lyotropic liquid crystalline phase, realized by side-chains parallel ordering. The chemical structure of theses is given in Fig. 1.

The PEABA in TCM have potential practical applications in changing the radiation spectral composition. One optical system consisting from one anisotropic layer between two crossed polarizers induces changes in the spectral composition of radiations.
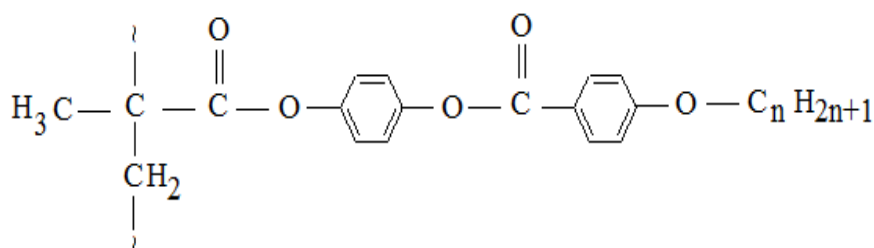
Fig. 1 – The chemical structure of polymeric esters of alkoxy benzoic acid.

The wavenumber of the radiations which pass from this system depends on the birefringence and thickness of the anisotropic layer. The liquid crystalline layer between two electrically charged transparent walls becomes anisotropic with the director perpendicular to the field direction. This kind of layer changes the polarization state of radiation. The monochromatic radiations which keep their polarization state can't pass through the optical device. The radiations with changed polarization state can cross the system. This is the principle of a polarization filter.

The anisotropic liquid crystals uniax shows two values of the refractive index n_o and n_e, the ordinary refractive index and the extraordinary refractive index respectively. The birefringence of the liquid crystals layers is given by the difference of the two refractive indices (equation 1).

$$\Delta n = n_e - n_o \qquad (1)$$

The optical birefringence of the liquid crystalline layer is closely related to the degree of order of the side chains comparing with the main chains. The degree of order in liquid crystalline layer can be improved by applying an external electrical field. The similar studies have been conducted in other liquid crystals such as poly-(phenyl methacrylic) ester of cetyloxybenzoic acid (PPMAECOBA) (Baran *et al*., 2005) and N-(4-methoxybenzilidene)-4-butylaniline (MBBA) (Dumitrascu *et al*., 2006).

The birefringence of the liquid crystals samples increase with the intensity of the electrical field. In the presence of an electrical field within a practical range, the optical birefringence is induced by the liquid crystalline

layer order (Kim *et al*., 2010) and its magnitude can be determined by the equation (2).

$$\Delta n = K C E^2 \tag{2}$$

where Δn is the optical birefringence, C is the concentration of sample, E is the intensity of the applied electrical field, K is the Kerr constant.

2. Experimental Part

The channeled spectra were recorded using a spectrophotometer Specord UV VIS Carl Zeiss Jena in the spectral range [14000 - 23000] cm^{-1}, in absence and in presence of electrostatic field.

The polymeric esters of alkoxy benzoic acids (PEABA) were achieved from Sigma-Aldrich Company and kept in a special cell (Dorohoi, 2010; Dorohoi *et al*., 2001; Dorohoi *et al*., 1999; Pop *et al*., 2006). This cell is placed between two identical crossed polarizer. In the comparison beam of spectrophotometer are introduced two polarizer with their transmission directions parallel. For the application of the external electrical field, the cell is connected by a variable transistor to an electric source. The concentration of liquid crystal is 10-2 g/cm^{3} in TCM and the layer thickness is 14 m.

From the chanelled spectra can be accurately identified the position of two minimum and maximum between them, which can be used to calculate the birefringence according to equation (3).

$$\Delta n = \frac{1}{2L} \frac{v_{2(k+1)} - v_{2k}}{v_{2(k+1)}v_{2k+1} + v_{2k}v_{2k+1} - 2v_{2(k+1)}v_{2k}} \tag{3}$$

where L is the liquid crystalline layer thickness, v_{2k} and $v_{2(k+1)}$ are the wavenumbers corresponding to the consecutive two minima, and v_{2k+1} corresponds to the maximum between them.

Let's consider a device (D) consisting by a PEABA LC with a constant thickness L placed between two crossed polarizers. The main transmission directions of LC are at 45° in relation to the transmission directions of the polarizers (Baran *et al*., 2005). The device (D) can be considered as being a Wood type polarization interferential filter. The transmission factor of the device (D) is express by relation (Dumitrascu *et al*., 2009):

$$T(\lambda_0) = \frac{1}{2} sin^2 \frac{\pi \cdot \Delta n \cdot L}{\lambda} \qquad (4)$$

where Δn is the birefringence of the LC, L is the thickness of the liquid crystal layer λ is the light wavelength.

Using formula (4) the transmission factor of the device (D) was simulated for a thickness of the liquid crystalline layer L=14μm with program Maple 13.

3. Results and Discussions

The birefringence dependence of the wavelength is show in Table 1 in the absence of electric field and in the presence of electrostatic field (E=110kV/m).

Table 1
Birefringece of PEABA in TCM

E=0		E=110kV/m	
λ (nm)	Δn	λ (nm)	Δn
445,632	0,1704	444,839	0,2607
459,558	0,1703	457,038	0,2564
493,096	0,1698	498,008	0,2414
531,914	0,1696	530,785	0,2300
554,323	0,1695	549,450	0,2242
577,367	0,1694	589,622	0,2107
603,864	0,1693	612,745	0,2028
632,911	0,1693	637,755	0,1950
663,129	0,1691	666,666	0,1871
700,280	0,1690	696,378	0,1778

From the Table1 one can be observed that in the absence of electrostatic field, the birefringence values are between 0,1690 - 0,1704. The birefringence values increase (0,1778 - 0,2607) when the external electric field (E=110kV/m) was applied.

The transmission factor vs. birefringence and vs. wavelength of the device consisting of PEABA liquid crystal (with thickness L=14μm) between cross polarizers is given in Fig. 2.
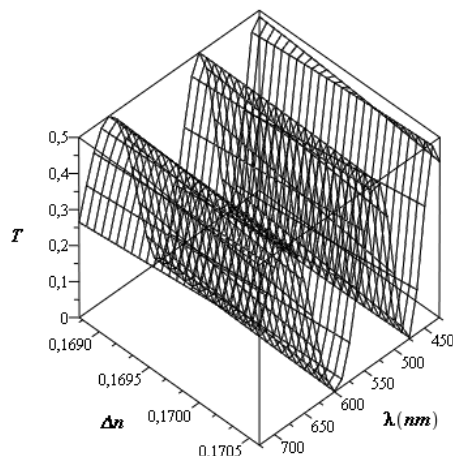
Fig. 2 – Transmission factor (T) vs. birefringence (Δn) vs. wavelength (λ) of device (D).

The value of the transmission factor of device (D) can be estimated for a given birefringence and wavelength from 3D graph (Fig. 3).

4. Conclusion

The values of the PEABA in TCM birefringence are determined from channeled spectra. An external electrostatic field increases the degree of order in liquid crystalline sample determining the increase in the birefringence of PEABA liquid crystal. A decrease of the birefringence (main refractive indices) with the wavelength increasing has been evidenced for PEABA in TCM. The transmission factor of the device (D) has three maximum in the spectral range 425-725nm. The simulation of Wood filters can help the specialists in designing electronic display cells containing liquid crystals.

REFERENCE

Baran J., Postolache M., Postolache M., Journal of Optoelectronics and Advanced Materials, **8**, *4*, 1529 (2005).
Dorohoi D.O., *Fundamental Optics*. Addleton Academic Publisher, New York, 2010.
Dorohoi D.O., Nasta L. Cotlet M., Frunza S., Tonitza O., An. Univ. Al.I.Cuza, Iasi, s. Chimie, **VII**, *1*, 83 (1999).

Dorohoi D.O., Postolache M., Postolache M., MacromoJ., l. Science, part B - Physics, **40**, *2*, 239 (2001).

Dumitrascu I., Dumitrascu,L. Dorohoi D., Journal of Optoelectronics and Advanced Materials, **8**, *3*,1028-1032 (2006).

Dumitrascu L., Dumitrascu I., Dorohoi D. O., Rev. Chim. Bucuresti, **60**, *11*, 2009.

Kim M., Kang B.G., Kim M.S., Kim M.-K, *et al.*, Current Applied Physics, *10*, 118-121 (2010).

Kuz'mina L.G., Kucherepa N.S., Pestov S.M., Kochetov A.N., Rukk N.S., Syrbu S.A., *Crystallography Reports*, **54**, *5*, 862–879 (2009).

Pop V., Angheluta E. Dorohoi D.O., Bull I.P.I, **L(LV)**, *5*, Matematica, Mecanica Teoretica, Fizica, 98 (2006).

Ramakrishna M., Rao N., Datta Prasad P.V., Pisipati V.G.K.M., Mol. Cryst. Liq. Cryst., **528**, 49–63 (2010).

DISPERSIA BIREFRINGENŢEI UNUI STRAT DE CRISTAL LICHID DE ESTER AL ACIDULUI ALCOXIBENZOIC ÎN TETRACLORMETAN DETERMINATĂ PRIN METODĂ SPECTRALĂ

(Rezumat)

Dispersia birefringenţei în domeniul vizibil a stratului de cristal lichid (de ester al acidului alcoxibenzoic în tetraclormetan) a fost determinată din spectrul canelat înregistrat în absenţa şi în prezenţa unui câmp electrostatic extern. În lucrare s-a pus în evidenţă faptul că în prezenţa câmpului electric birefringenţa cristalului lichid creşte. Un filtru de tip Wood a fost simulat utilizând programul Maple şi datele experimentale. Cunoaşterea influenţei câmpului electric asupra birefringenţei poate ajuta specialiştii să proiecteze display-uri cu celule ce conţin cristal lichid.

RESEARCH ON ALUMINUM ALLOY MODIFICATIONS WITH SEVERE PLASTIC DEFORMED AlTi5B1 FINISHING PRE-ALLOY

BY

COSTEL ROMAN[1]*, **ROMEU CHELARIU**[1], **IOAN CARCEA**[1],
RADU COMĂNECI[1], **GABRIELA POPESCU**[2] and **MIHAI AXINTE**[1]

[1] Technical University "Gheorghe Asachi" of Iaşi,
[2] Polytechnic University of Bucharest

Abstract. The present paper presents some preliminary experimental data concerning the severe plastic deformation AlTi5B1 prealloy on one aluminum alloy. The severe plastic deformation of prealloy by ECAP has the more beneficial effect, on the modification of aluminum alloy.

Key words: severe plastic deformation, aluminum alloys.

1. Introduction

Grain finishing of non-ferrous alloys consists in melt treatment before casting or during the solidification process. The metallic material crystals increase having as support the grains. The higher the number of grains (nuclei) is, the higher is the increase of number of crystals and finer they are.

The artificial change process of cast metallic material structure is carried out by adding in the melt of some finishing pre-alloys containing the

---

* Corresponding author; *e-mail:* romancostel2005@yahoo.com

modifying chemical elements before casting.

The modifiers used for finishing the primary dendrites' granulation in aluminum alloys are substances forming difficult fusible particles acting as inoculants of heterogeneous germination. Among the class of these modifiers we may mention boron and a series of transition metals with a high chemical reactivity such as titanium, zirconium, tantalum, vanadium etc.

The nucleating processes have an important role in aluminum alloy solidification, controlling the type of primary structure, the range of dimensions and the spatial distribution of phases. Also, the nucleating effects induce a considerable influence on the solidification microstructure respectively on the grain size, on composition morphology and homogeneity (Moldovan *et al.,* 1998).

2. Experimental Procedure

The severe plastic deformed AlTi5B1 pre-alloys by various procedures (Fig. 1) were used for modifying the AlSi5Cu3 aluminum alloy, according the following table:

Table 1
Experimental Tests

Test no.	Severe deformation procedure of pre-alloy	Addition of pre-alloy, %	Modification temperature, °C
1	-	0	760
2	Non-deformed pre-alloy	4	760
3	Rolled pre-aloy	4	760
4	ECAP pre-alloy	4	760
5	Compressed pre-alloy	4	760

The deformed pre-alloy by various procedures is illustrated in Fig. 1.

Fig. 1 – Severe deformed AlTiB pre-alloy by various procedures.

3. Results and Debates

3.1. Study of AlTiB Pre-Alloy

In the following figures the AlTiB pre-alloy structure and Al_3Ti metallographic constituent dimension distribution are presented.

As we may notice both in graphs and in micrographics, through severe plastic deformation of pre-alloy, the dimensions and form of Al_3Ti compound are modified obtaining a metallographic constituent of smaller average dimensions and a more uniform distribution within the pre-alloy matrix.
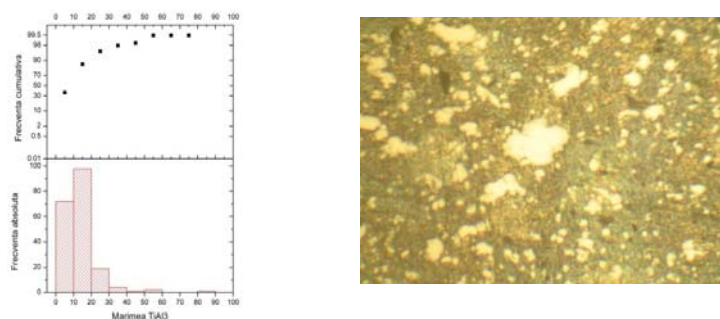
Fig. 2 – Non-deformed pre-alloy. Scale: 1 cm = 50 μm.
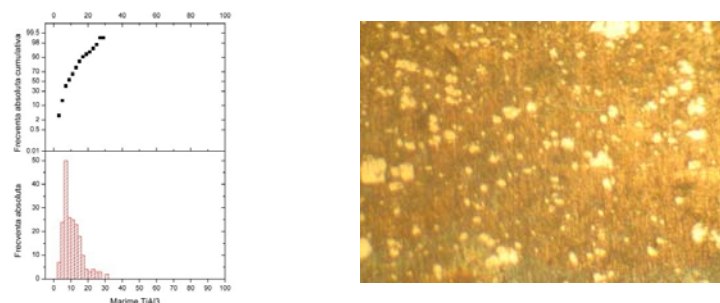
Fig. 3 – Severe deformed pre-alloy by successive rolling. Scale: 1 cm = 50 μm.
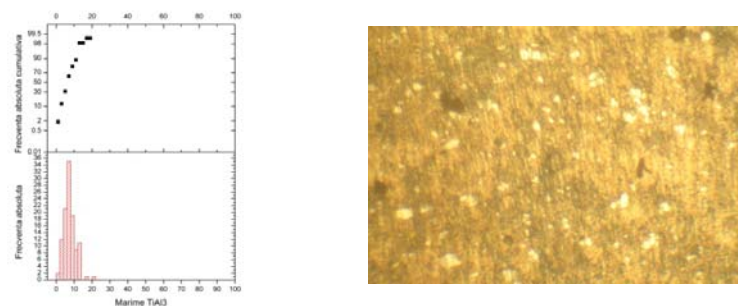
Fig. 4 – Severe deformed pre-alloy by ECAP. Scale: 1 cm = 50 μm.
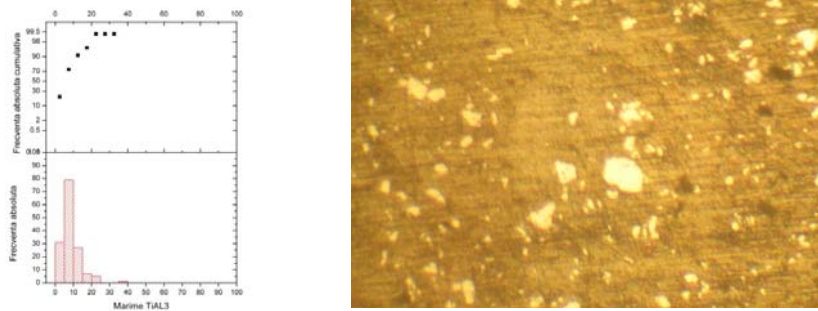
Fig. 5 – Severe deformed pre-alloy by compression. Scale: 1 cm = 50 μm.

As we may notice both in graphs and in micrographics, through severe plastic deformation of pre-alloy, the dimensions and form of Al_3Ti compound are modified obtaining a metallographic constituent of smaller average dimensions and a more uniform distribution within the pre-alloy matrix.

The study of severe deformed pre-alloy samples by the three deformation methods at electronic microscope, shows up the chemical composition of the alloy and its structure.
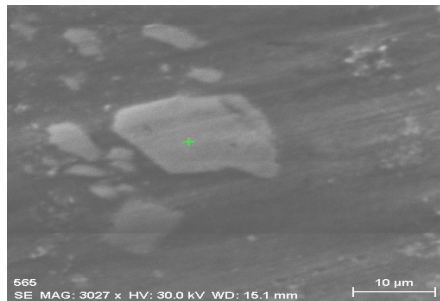
Fig. 6 – Electronic microscopy of AlTiB pre-alloy.

The distribution of Al, B, Ti elements in the studied structures is given below:
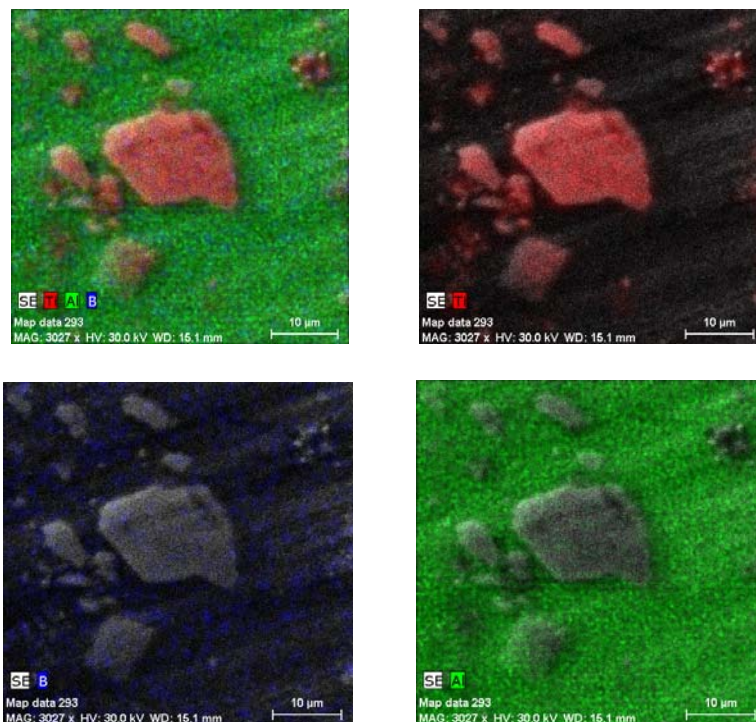
Fig. 7 − Distribution of Al, B, Ti elements AlTiB pre-alloy.

Chemical composition of AlTiB pre-alloy on the point indicated in the above figure is given in Table 2.

Table 2
Chemical Composition of AlTiB Pre-Alloy on the Point Indicated in Fig. 6

Element	AN	series	Net	wt.%	norm. wt.%	norm. at.%	Error in %
Aluminum	13	K-series	114698	49.79564	51.65738	51.94795	2.527021
Titanium	22	K-series	71768	36.35271	37.71185	21.37108	1.031554
Boron	5	K-series	748	10.24764	10.63077	26.68097	2.548676
			Sum:	96.39599	100	100	

The breaking curve of AlTiB pre-alloy is shown in Fig. 8 and the mechanical characteristic properties in Table 3.

Characteristic curve

Sample no.

Deformation
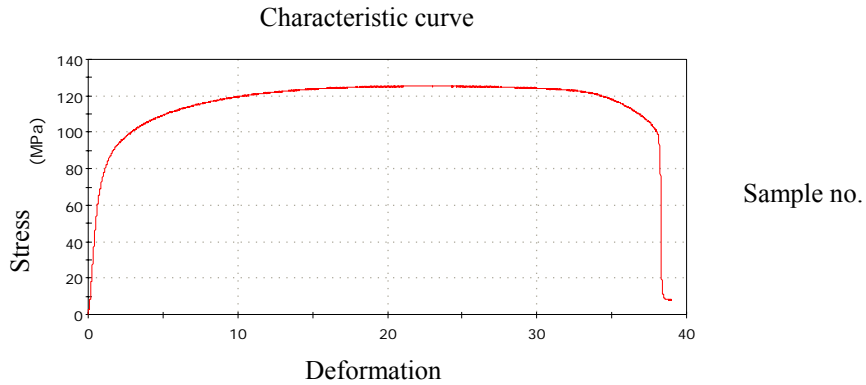
Fig. 8 – Breaking curve of AlTiB pre-alloy.

Table 3
Characteristic Mechanical Properties of AlTi5B1 Master Alloy

Sample	Maximum Load (N)	E-modulus (MPa)	Tensile stress at Tensile Strength (MPa)	Tensile strain at Break (Standard) (%)	Tensile stress at Yield (Offset 0.2 %) (MPa)
AlTi5B1	1,578.51	10,538.51	125.159	38.97	74.643

3.2. Study of Modified Alloys with Severe Deformed AlTiB Pre-Alloy by Various Methods

The smelting of AlSi5Cu3 alloy was performed in an induction melting furnace of 5 kg showing in Fig. 10 and modification with pre-alloy was carried out in the casting ladle according to Table 1.

Fig. 9 – Induction melting furnace.

In the following figures it is presented the ATAlSi5Cu3 alloy structure modified or unmodified with severe plastic deformed AlTiB pre-alloy by various methods.
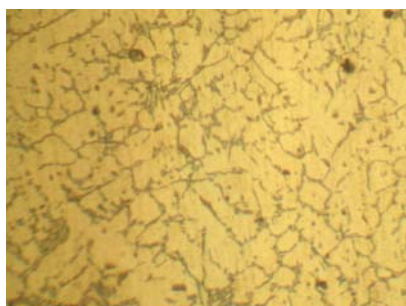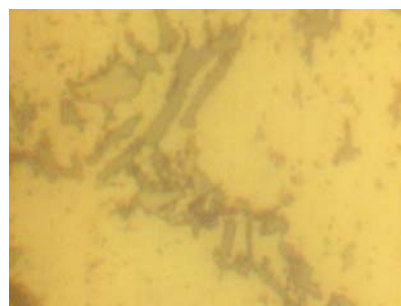
<div align="center">
<i>a</i>   <i>b</i>

The microstructure of cast and unmodified ATAlSi5Cu3 alloy:
<i>a</i>) alpha phase + silicone separations, scale: 1 cm = 60 μm;
<i>b</i>) morphology of silicone separations, scale: 1 cm = 6 μm
</div>

<div align="center">
<i>a</i>   <i>b</i>
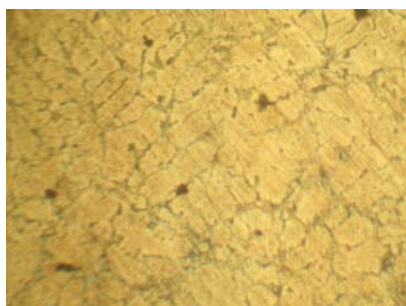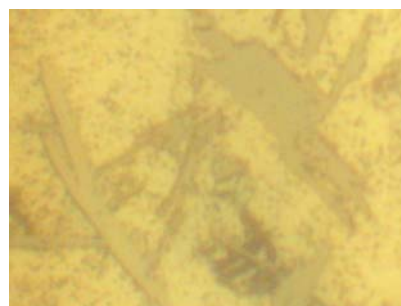
Microstructure of cast and modified ATAlSi5Cu3 alloy non-deformed AlTiB pre-alloy:
<i>a</i>) alpha phase + silicone separations, scale: 1 cm = 60 μm;
<i>b</i>) morphology of silicone separations, scale: 1 cm = 6 μm.
</div>

<div align="center">
<i>a</i>   <i>b</i>
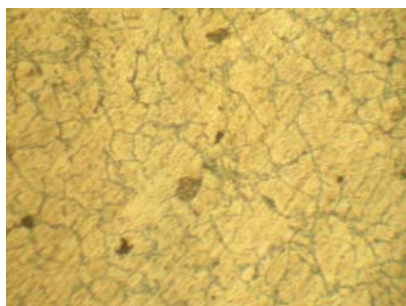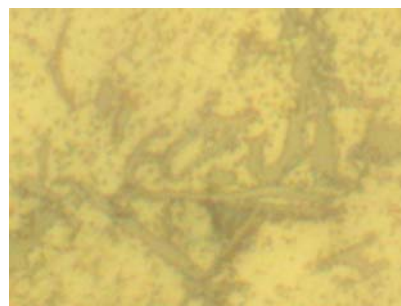
Microstructure of cast and modified ATAlSi5Cu3 alloy AlTiB pre-alloy deformed by
successive rolling: <i>a</i>) alpha phase + silicone separations, scale: 1 cm = 60 μm;
<i>b</i>) morphology of silicone separations, scale: 1 cm = 6 μm.
</div>

a   b
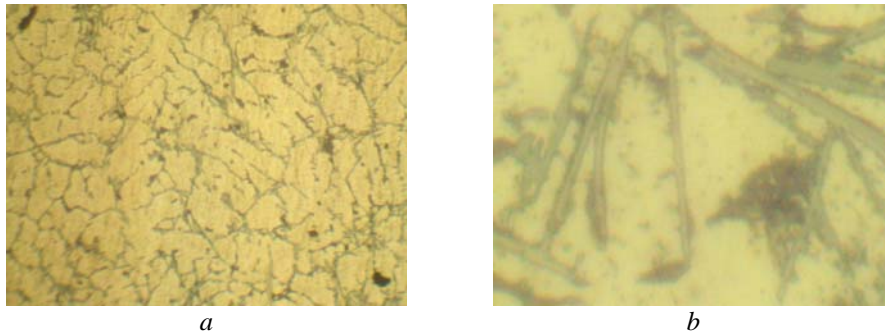
Microstructure of cast and modified ATAlSi5Cu3alloy AlTiB pre-alloy by
ECAP: *a*) alpha phase + silicone separations, scale: 1 cm = 60 μm;
b) morphology of silicone separations, scale: 1 cm = 6 μm.

a   b
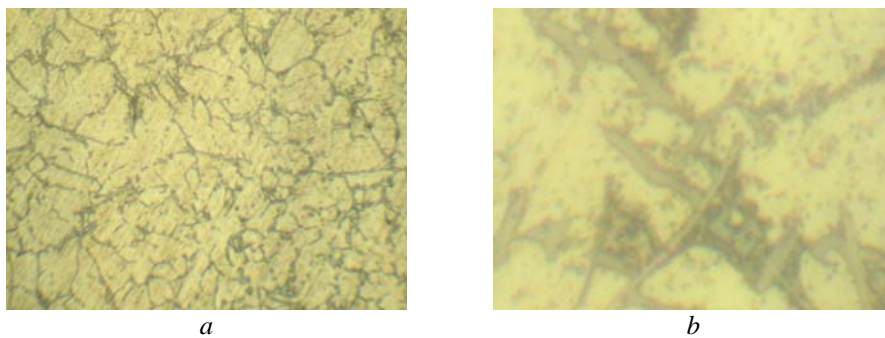
Microstructure of cast and modified ATAlSi5Cu3 alloy AlTiB pre-alloy deformed by
compression: *a*) alpha phase + silicone separations, scale: 1 cm = 60 μm;
b) morphology of silicone separations, scale: 1 cm = 6 μm.

Fig. 10 − Microstructures of cast and modified ATAlSi5Cu3 alloy with severe deformed
AlTiB pre-alloy by various methods.

In order to characterize the structure of unmodified and modified
alloys, there were determined with DeWinter Materials Plus program the
dimensions of alpha phase dendrites and the aspect ratio of silicone (RA=L/l).
These sizes were measured and statistically analyzed in order to be compared.

The statistical analysis shows that between the values of the two sizes
there are significant differences indicating that the modification effects
depends also on the plastic deformation state of the pre-alloy.

The graphical representation of dendrite dimensions that were
determined with the DeWinter Materials Plus program, the dimensions of
alpha phase dendrites and the aspect ratio of silicone (RA=L/l) are presented
in Fig. 11.
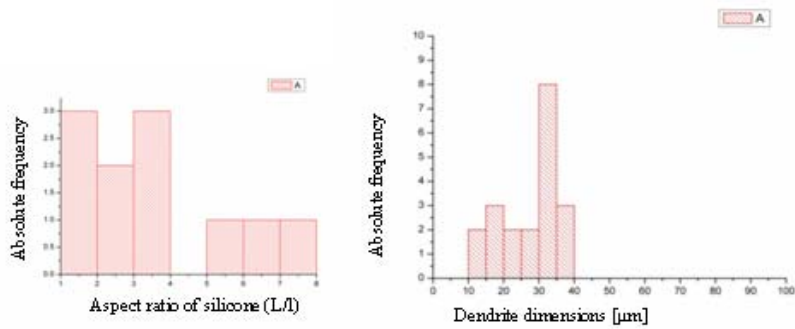
a − Unmodified AlSi5Cu3 alloy
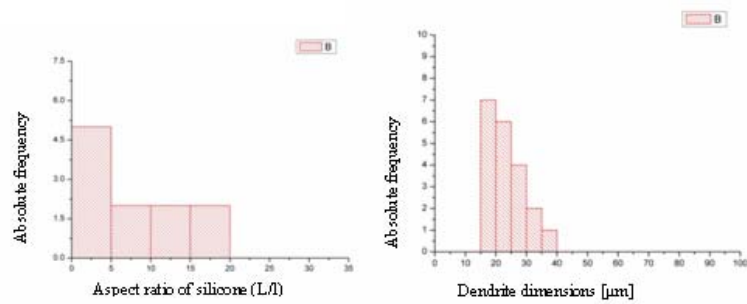
b − Modified AlSi5Cu3 alloy with non-deformed pre-alloy
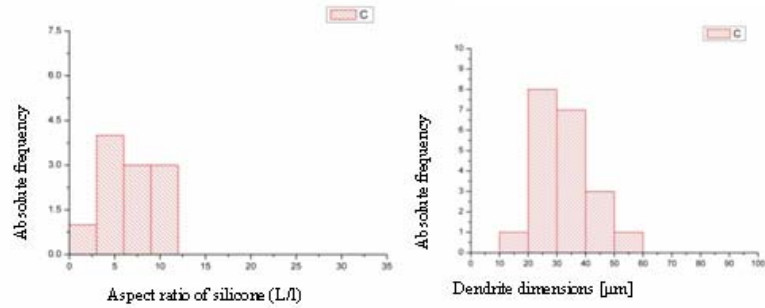
c − Modified AlSi5Cu3 alloy with rolled pre-alloy
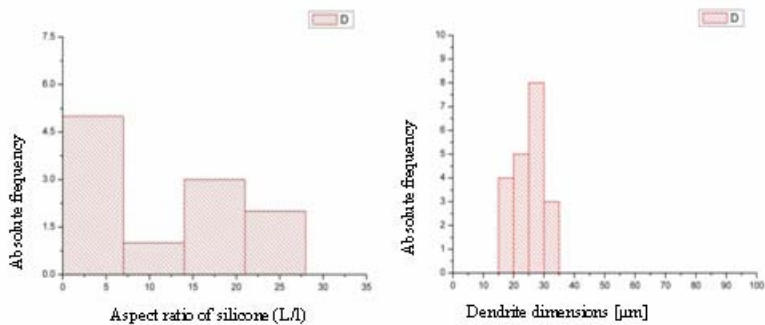
d − Modified AlSi5Cu3 alloy with ECAP pre-alloy
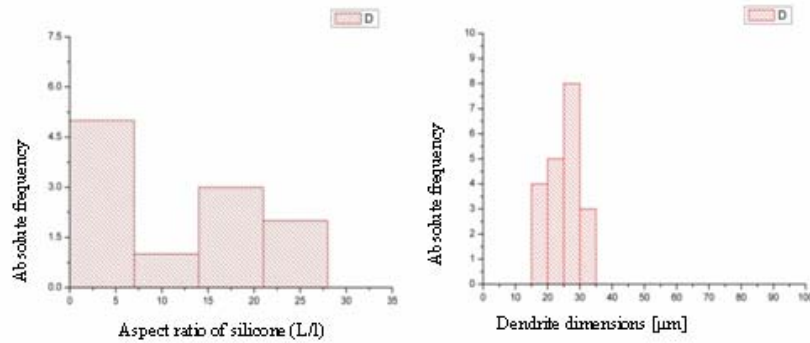
e − Modified AlSi5Cu3 alloy with compressed pre-alloy
Fig. 11 − Dimensions of alpha phase dendrites and aspect ratio of silicone.

4. Conclusions

1. As we may notice both in graphs and micrographics, by severe plastic deformation of the pre-alloy, the dimensions and form of Al_3Ti compound are modified obtaining a metallographic constituent with smaller average dimensions and a more uniform distribution in the pre-alloy matrix.

2. The study of severe deformed pre-alloy samples by the three deformation methods at electronic microscope points out the chemical composition of the alloy and its structure.

3. In order to characterize the structure of unmodified and modified alloys, there were determined with DeWinter Materials Plus program the dimensions of alpha phase dendrites and the aspect ratio of silicone (RA=L/l). These sizes were measured and statistically analyzed in order to be compared. In tables 3 and 4 there are given the values of the two sizes followed by the results of the statistical analysis using the dispersion analysis method.

4. The statistical analysis shows that between the values of the two sizes there are significant differences indicating that the modification effects depends also on the plastic deformation state of the pre-alloy.

5. From the analysis of histograms presented in figure 12, we conclude that the modified alloys with deformed pre-alloy by ECAP method have the L/l silicon ratio within 0-7 value with the highest frequency of about 5.2 and the dimensions of dendrites within 15-35 μm with a frequency range of 3 and 8.2.

NU SE REGASESTE IN TEXT

REFERENCES

Comăneci R., Chelariu R., Zaharia L., Bejinariu C., Roman C., *Experimental Aspects Regarding Equal Channel Angular Pressing of Aluminium and Al-Mg Alloys.*

International Conference on Material Science and Engineering BRAMAT 2007, Braşov, Romania, 22-24 February, Bulletin of the Transilvania University of Braşov, supplement BRAMAT 2007, 141-146 (2007).

Iwahashi Y., Furukawa M., Horita Z., Nemoto M., Langdon T.G., *Microstructural Characteristics of Ultrafine-Grained Aluminum Produced Using Equal-Channel Angular Pressing Metall.* Mater. Trans. 29A, 2245 (1998).

Moldovan P., Panait N., Mărginean Şt., *Foundations of Non-Ferrous Metallic Melt Treatment.* Intact Printing House, Bucharest, 1998.

Richert M., Stüwe H.P., Richert J., Pippan R., Motz Ch., *Characteristic features of microstructure of AlMg5 deformed to large plastic strains*, Materials Science & Engineering, **A 301**, 237-243 (2001).

CERCETĂRI ASUPRA MODIFICĂRII ALIAJELOR DE ALUMINIU CU PREALIAJUL FINISOR AlTi5B1 DEFORMAT PLASTIC SEVER

(Rezumat)

Prezenta lucrare cuprinde câteva date experimentale preliminare privind influenţa deformării plastice severe a prealiajului AlTi5B1 asupra eficienţei modificării unui aliaj de aluminiu. Deformarea plastică severă prin metoda ECAP are efectul benefic cel mai evident.

[1]. (Moldovan *et al.,* 1998)
[2]. (Comăneci *et al.,* 2007)
[3]. (Iwahashi *et al.,* 1998)
[4]. (Richert *et al.,* 2001)

INFLUENCE OF HEAT AND OXYGEN PRESSURE ON THE BEHAVIOR OF AN EVA COMPOUND USED AS CABLES JACKET

BY

CĂTĂLIN RUSU-ZAGĂR[1]*, SIMONA PĂSĂREANU[1], IONEL IORGA[2] and GILDA RUSU-ZAGĂR[2]

[1] S.C. Eurotest S.A.,
[2] National Institute for Research,
Development on Occupational Health and Safety

Abstract. Knowing the state of degradation of electrical insulation materials is important for any type of equipment, but it is imperative in the case of equipment for nuclear plants. A study was conducted to evaluate the use of oxygen under pressure to accelerate thermo-oxidative degradation rate in EVA compound used as cable jacket. In this paper are presented the results of estimating the state of deterioration of insulating EVA compound subjected to accelerated aging simple and combined, thermal and oxygen pressure. Evaluation of degradation was performed using DSC method, and verification of results was done by determining the elongation at break. The paper concludes that the use of DSC allows accurate estimation of activation energy and estimate the lifetime of the material.

Key words: cable jacket, accelerated aging, degradation, lifetime.

1. Introduction

The insulation systems of high-voltage power cables in operation are subject to different kinds of stresses during their service life and thus suffer

---

* Corresponding author; *e-mail:*

degradation and deterioration. These can lead to a reduction of life which in turn can lower the reliability of electrical power systems.

The processes of degradation of electrical insulating materials consist of oxidation reactions (produced acids which shows high electrical conductivity), crosslinking which contributes to reducing the elasticity and plasticity, depolymerization (leading to lower mechanical resistance and the emergence of gaseous inclusions). Add to this the contribution of hydrolysis processes, incompatibility reactions between the constituents or solvent attack.

Under the action of these requests, cable insulation undergoes degradation, which involves changing physico-chemical properties. To estimate the state of degradation and lifetime experiments are performed in laboratory using the accelerated aging method. There are simple and combined stresses, is the most accurate combination (multi-stress) because it best reflects the real operating conditions of the cable insulation. This paper presents the results of accelerated aging of cable insulation compound EVA, being subjected to accelerated thermal aging and aging under simultaneous action of heat and oxygen pressure.

2. Experiments

Two instrumentation and control cables being identified by the serial numbers JE-H (ST) H 2X2X0, 8 BD SI FRNCX and JE-H (ST) H 4x2x0.8 BD SI FR NCX have been subjected to thermal aging and aging under the simultaneous action of heat and oxygen pressure because the simultaneous aging reduces aging time. The preliminary analyses have been performed on single cable jacket type because both cables are the same EVA compound for cable jackets. At the first experiment, after first sampling time, in oxygen aging vessel to observe that many cable segments have been destroyed until 100°C. Thermal aging was performed with the oven temperature control system, monitored by Lab View virtual instrumentation software (Fig. 1).

Fig. 1 – Oven-controlled system using LabView virtual instrumentation program.

The ageing experiment performed on the A-type cable at 100°C and 4 barr oxygen pressure, and for the B-type product, the simultaneous ageing at 135°C and the same oxygen pressure led to the results showed in Fig. 2.

Fig. 2 – A-type cable at the first sampling during the pressurised oxygen ageing experiment (100°C şi 4 bar).

For the first type of cable jacket that we will note A (JE-H(ST)H 2X2X0.8 BD SI FRNCX) have been used DSC method (Differential Scanning Calorimetry), and for the other type (noted with B, the cable with code JE-H(ST)H 4x2x0.8 BD SI FRNCX) have been used RTL method (radio-thermo-luminescence). Equipment which DSC analysis was performed, to allow measurements in a temperature range between – 85 and 600°C is presented in Fig. 3.

Fig. 3 – DSC 204 F1 Phoenix - produced by NETZSCH GERATEBAU GmbH.

The activation energies were determined by chemiluminescence method (CL).

The relative elongation at break is physical parameter which has been used to asses the degradation state of EVA compound for both cable jackets. The degradation criterion used to evaluate the lifetime is the relative elongation at break of 50 %.

The relative elongation at break has been measured with Monsanto T-10/E, device with pneumatic gripping. The tests were carried out using a crosshead speed of 50 mm/min. The test sample gauge length was 20 mm, dumbbell sample having had width in the gauge length of approximately 4 mm. The dumbbells (100 mm long) were obtained from the cable jackets (before and after the aging) by stamping with specific devices.

3. Results and Discussions

DSC curve for this type is shown in the Fig. 4 points in the compound DSC curve. This jacket type has the glass transition temperature of - 26.2°C (inflexion point of curve). At the same time, can be observed partial softening points.

It can be seen that the structure of A compound presents a highly endothermical area between 54 - 70°C, wich indicates a low thermooxidative stabilisation, posibly because of antioxidant lack.

At the same time, the image in Fig. 2 indicates a melting point lower than 100°C. This and the high value of the relative elongation at break and the small value of tensile strength and similar experimental values for B-type compound, indicate a low crosslinking ratio. At B-type compound, as Fig. 9 shows, can be observed a diminishment followed by an increase of relative elongation at break that indicates a post-crosslinking.

The behaviour of the B type (Fig. 9) sugests that the oxygen pressure accelerated the ageing process, this compound being very good. In the same time, the A type compound sugests the cable jacket by reason of the melt (Fig. 9) is not adequates for industrial products.

Tensile strength value is 9.459 MPa (standard deviation being s = 0.305). For the first type of EVA compound, the initial relative elongation at break has an average value of 548.86 % (standard deviation s = 14.146). This determination has been performed on a volume of 16 statistical units.

For the second type of compound, relative elongation at break is 241.875 % (standard deviation being sd = 23.51), and the tensile strength has the value 17.68 MPa (standard deviation being s = 1.088).
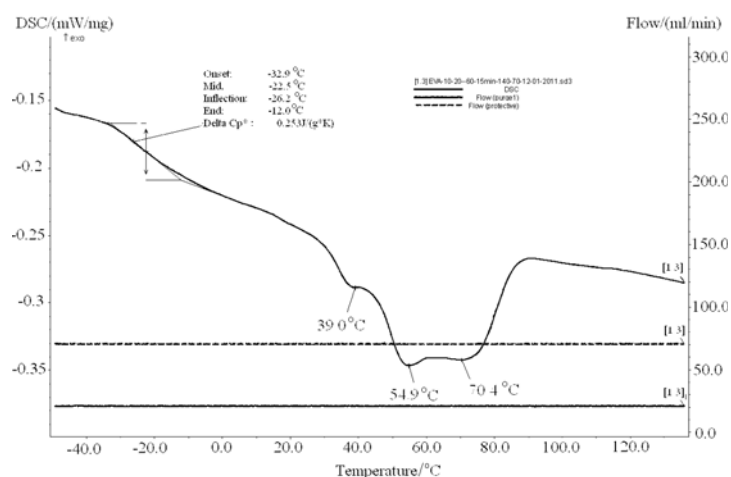
Fig. 4 – DSC curve of EVA compound material A-type.
The heating rate is 10°C / min.

The determination of glass transition temperature was made by RTL method. The RTL curve (Fig. 8) generates two regression lines (red lines). The intersection point of lines defines the glass transition temperature. In agreement with Fig. 8, the intersection point gives a value of −32.15°C for glass transition temperature of second compound type. Other laboratory analyses (*e.g.* TG and DTG) sugest a good thermal stability until 150°C. For this, an ageing experiment havig had ageing factors – heat an oxygen pressure, have been made for both compounds.
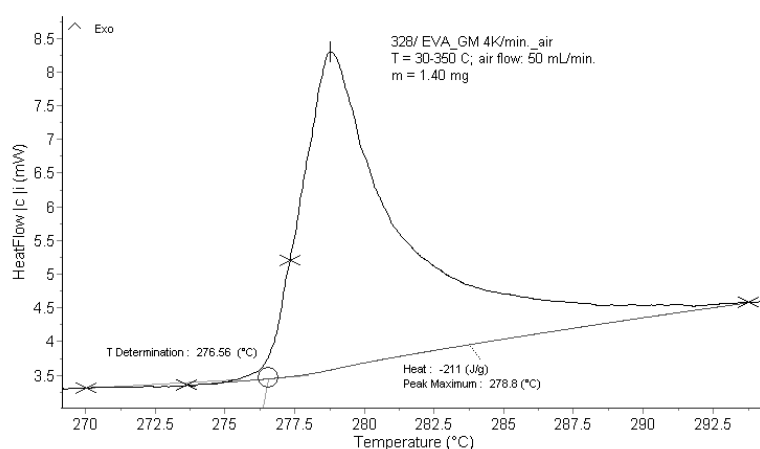
Fig. 5 − Example of calculation of OOT (T determination),
T_m (Peak Maximum) and ΔH (Heat) from a DSC curve.
The oxidation process following the decomposition was considered.
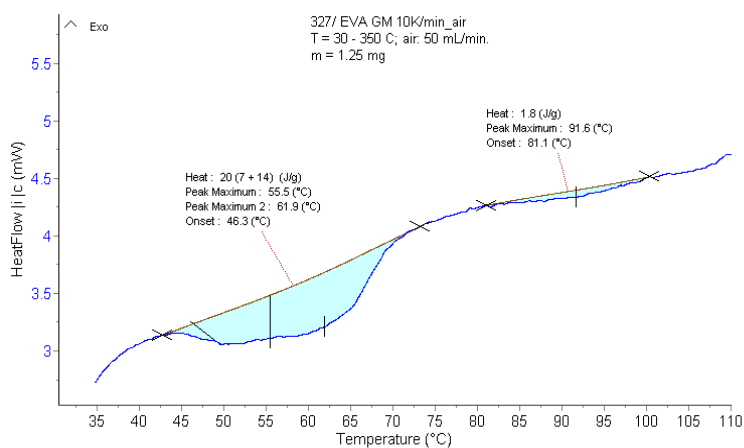
Fig. 6 − DSC curve of EVA based material: focus on the region
assigned to the crystals melting processes.
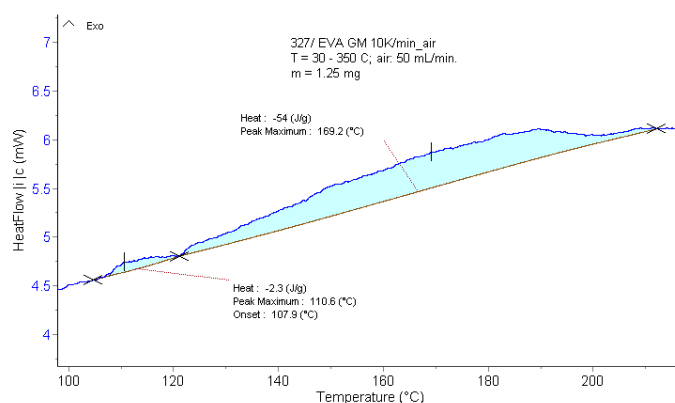
Fig. 7 – DSC curve of EVA based material: focus on the region assigned to the exotherm processes occurring in the range 100 - 200°C (possible crosslinking and hydroperoxides decomposition).
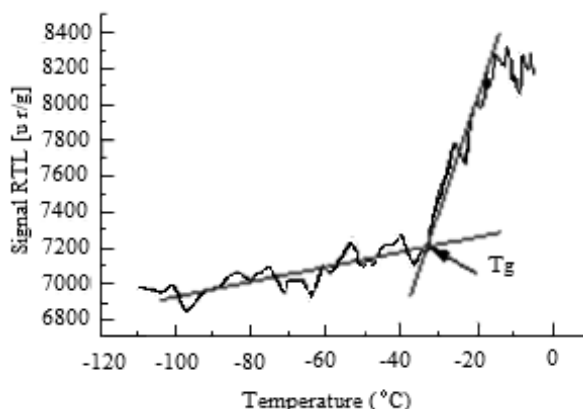
Fig. 8 – RTL curve for the EVA compound used as a coating
for unaged JE-H(ST) H 4X2X0,8 BD SI FRNCX. Sample weight is 0.0262g.

In addition, the same compound has been subjected to other DSC analys for more details (Figs. 4,..., 7). In the first stage can be observed that:
- an endothermic process in the form of a large peak, with at least two maxima, one at approx. 50°C, and the other at approx. 65°C; the peak at 50°C is characteristic for the uncrosslinked polymer, while the appearance of the one at approx. 65°C is related to the crosslinking of the polymer. According to reference (Starink, 1996) the crosslinked polymer, should not present a peak between 20-50°C, and only one at 65°C. Thus, it can be concluded that the material is only partially cross linked, fact confirmed also by the observation that it easily suffers plastic deformation, irreversible (observation made in the laboratory when we tried to place the sample in the crucible) and that it melts

and flows when heated (observation made by direct examination of sample's aspect after the DSC measurement) (Fig. 6);
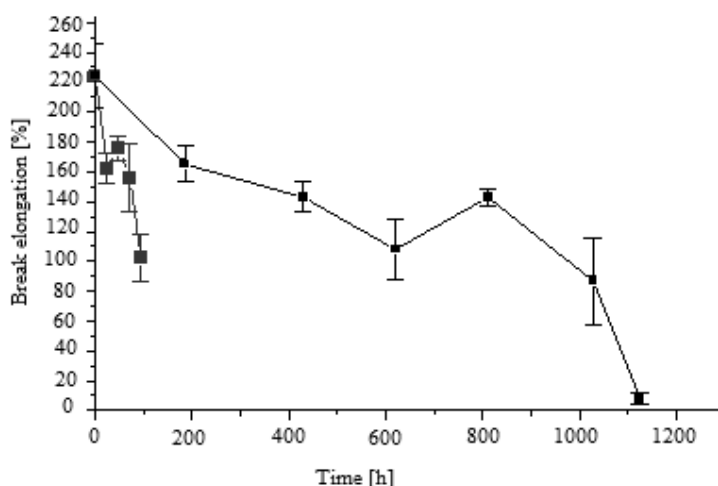
Fig. 9 – Relative elongation at break variation for the EVA compound used as cable jacket for JE-H(ST) H 4X2X0,8 BD SI FRNCX with the ageing time:
- dumbbell air aged at 135°C
- dumbbell oxygen aged at 135°C and 4 bar.

- a second endothermic process at 91-93°C is attributed to the melting of crystals (Vogel & Heinze, 1993); this process is characterized by a low thermal effect, suggesting a low share of this crystalline phase;

- a series of exothermic processes that start at approx. 100°C and extends to beyond 200°C (Fig. 7), that are characteristic for the materials based on uncrosslinked EVA (Starink, 1996). Peaks are observed very broad and the position and number of the maxims differs to some extent from one measurement to another. In addition to the curing processes, it is possible that the thermal effect observed at temperatures of approx. 150°C and contribute to the decomposition of some hydroperoxides accumulated during analyzing;

-an endothermic decomposition process (acetic acid elimination) takes place at approx. 275°C. The thermal effect is very small compared to other studied EVA copolymers (Tab. 1), suggesting a low content of vinyl acetate of the material. The main peak shows a series of adjacent shoulders, which may be due to the fact that the decomposition takes place in several stages, or to a low and uneven thermal conductivity of the material. For the calculation of E_a, from Tm was used only the main peak, ignoring the shoulders (Tab. 2). It should be mentioned that the process of decomposition is preceded by another exothermic process, which begins at approx. 230°C and could be given by the oxidation of ethylene segments.

-a series of exothermic processes, oxidation and decomposition take place in the oxidizing atmosphere.

The exothermic process, immediately following the decomposition, was considered the most important for describing the state of the material regarding the aging processes in order to define the lifetime of material. Therefore, the activation energy was calculated in the comparison with it.

Table 1
Dsc Parameters for Decomposition fnd Oxidation Processes

Process	Heating rate					
	10 K/min			6 K/min		
	Onset (^{o}C)	T_m (^{o}C)	ΔH (J/g)	Onset (^{o}C)	T_m (^{o}C)	ΔH (J/g)
Acid elimination	265.7	276.0	+8	260.4	265.7	+24
Oxidation	287.5	292.0	-183	283.6	285.6	-201
	4 K/min.			2 K/min.		
Acid elimination	255.4	259.5	+5	248.3	249.7	+16
Oxidation	276.6	278.8	-211	269.5	271.0	-135

Table 2
Activation Energy Values Calculated from Decomposition and Oxidation Parameters

Process	DSC parameter	r	A	B	E_a (kJ/mol)
Decomposition	*OOT	-0.98467	22.04	-17476	145
	T_m	-0.99667	19.90	-16566	138
Oxidation	*OOT	-0.99074	33.66	-24713	205
	T_m	-0.99738	28.55	-21998	183

4. Conclusion

The present work evaluate state of degradation of the material subjected to accelerated thermal aging. With this method can determine the activation energy for oxidative processes. Method has confirmed the state of degradation of the two cable insulation.

Evaluating the state of degradation of the materials used as cable jacket by calculating the activation energy is a efficient method. Utilising oxygen under pressure to accelerate thermo-oxidative degradation contributed to

reduced time of experiments and quick assessment of the material resistance to aging. Using DSC and elongation a break can determine the lifetime of this material. The method can help to quick detect manufacturing defects of different batches of cable insulation.

LIPSA TRIMITERILE IN TEXT

REFERENCES

[1]. Reading M., Vaughan A.S., *The Effect of Thermal Ageing on the Rheological, Thermal and Electrical Properties of Poly(Ethylene Oxide).* Electrical Insulation and Dielectric Phenomena (CEIDP), 2010.
[2]. Mares G., Budrugeac P., *Chap. X, Elastomer Technology Handbook.* CRC Press, Boca Raton, London, Tokyo, 1993.
[3]. Mares G., *Polymer Degradation and Stability. 50*, 29-32 (1995).
[4]. Mittemeijer E.J., *Analysis of the Kinetics of Phase Transformation.* Journal of Materials Science, **27**, *15*, 3977-3987 (2010).
[5]. Starink M.J., *A New Method for the Derivation of Activation Energies From Experiments Performed at Constant Heating Rate.* Thermochimica Acta, **288**, *1-2*, 97-104 (1996).
[6]. Vogel J., Heinze C., *Reactive Processing of Polyethylene and Poly(Ethylene-Co-Vinyl Acetate).* Angewandte Makromelekulare Chemie, 157-171 (1993).
[7]. Shi X.M., Zhang J., Li D.R., Chen S.J., *Effect of Damp-Heat Aging on the Structures and Properties of Ethylene-Vinyl Acetate Copolymers with Different Vinyl Acetate Contents.* Journal of Applied Polymer Science, **12**, 2358–2365 (2009).
[8]. Zlatkevich L., *Radiothermoluminescense and transitions in polymers.* Springer-Verlag, 1987.
[9]. Munteanu D., Turcu S., *Evaluation of Kinetic Parameters of the Thermal Decomposition of Polyethylene-Vinyl Acetate Graft Copolymers.* J. Thermal Anal., **20**, 281 (1981).
[10]. Marcilla A., Beltran M., *Kinetic Study of Thermal Decomposition of Polystyrene and EVA Graft Copolymer by Thermogravimetric Analysis.* Polym. Deg. and Sab., 117-124 (1995).
[11]. *∗ Standard Test Method for Oxidation Onset Temperature of Hydrocarbons by Differential Scanning Calorimetry.* ASTM 2009-08.

INFLUENŢA CĂLDURII ŞI OXIGENULUI SUB PRESIUNE ASUPRA COMPORTĂRII UNUI COMPOUND EVA UTILIZAT CA MANTA DE CABLU

(Rezumat)

Cunoaşterea stării de degradare a materialelor folosite pentru izolaţiile cablurilor electrice este importantă pentru orice tip de echipament, dar este imperativ necesară în cazul echipamentelor folosite pentru centralele nucleare. A fost efectuat un

studiu pentru a evalua rata de degradare termo-oxidativă în compound–ul EVA utilizat ca manta de cablu. Sunt prezentate rezultatele estimării stării de deteriorare a izolaţiei supusă la îmbătrânire accelerată, simplă şi combinată, termică şi sub presiune de oxigen. Evaluarea stării de degradare a fost efectuată folosind metoda DSC, iar verificarea rezultatelor s-a realizat prin determinarea alungirii la rupere. Lucrarea concluzionează că utilizarea DSC permite estimarea exactă a energiei de activare o proceselor oxidative şi estimarea duratei de viaţă a materialului.

[1]. (Reading & 2010)
[2]. (Mares & Budrugeac, 1993)
[3]. (Mares, 1995)
[4]. (Mittemeijer, 2010)
[5]. (Starink, 1996)
[6]. (Vogel & Heinze, 1993)
[7]. (Shi *et al.,*2009)
[8]. (Zlatkevich, 1987)
[9]. (Munteanu & Turcu, 1981)
[10]. (Marcilla & Beltran, 1995)
[11]. (ASTM 2009-08)

THE RELATIVISTIC "GUN" EFFECT AND ITS IMPLICATIONS WITHIN LASER MARKING PROCESSES

BY

ŞTEFAN RUSU[*]**, MARICEL AGOP, DAN-GELU GĂLUŞCĂ and IOAN RUSU**

"Gheorghe Asachi" Technical University of Iaşi,
Faculty of Material Science and Engineering

Abstract. The paper aims to explain the implications induced by the stochastic gun effect, within the physical movements dynamics associated with the phenomenology of laser marking processes. For the study of the gun effect, we have adopted a model which implies studying the motion of a charged particle – from the target material, which is simultaneously under the influence of a static magnetic field – generated impact plasma, and an electromagnetic wave (polarized or not) – the laser beam.

Key words: gun effect, laser, marking.

1. Introduction

Regarding the general interest in traceability laser marking (Dusser *et al.,* 2007), from the angle of the process itself for different alloys and super-alloys and the existing experimental results which indicate the formation of micro-cracks at droplets for certain processing parameters, we question the physical theoretical aspect which governs these interactions. We avoid

---

[*] Corresponding author; *e-mail:* rusu.st@gmail.com

analyzing the known phenomena which refer to the laser beam – target – formed plasma interaction, because they are well described within the literature for different types of lasers. Therefore, we turned our attention towards an associate physical phenomenon, for a "commercial" nanosecond laser, but with a high degree of novelty: the "gun" effect. Understanding this is of importance not only to the physicist mind, but also to the engineers and specialist working in fields which imply laser operations (heat treatment, material processing, logistics etc.), because of the optimization possibility for the energy transfer, laser functioning and laser – solid material interaction based processing.

This paper aims to explain the implications induced by the stochastic gun effect, within the physical movements dynamics associated with the phenomenology of laser marking processes.

2. General Considerations Regarding the Relativistic Gun Effect

For the study of the relativistic gun effect, we have adopted a model which implies studying the motion of a charged particle – from the target material, which is simultaneously under the influence of a static magnetic field – generated impact plasma, and an electromagnetic wave (polarized or not) – the laser beam (Dusser *et al.,* 2007). The math for the model consists in combining the relativistic motion equation for a charged particle, located within a static electromagnetic field, with the Maxwell equation system which corresponds to an electromagnetic wave, in order to describe the non-linear interaction between the charged particle, the constant magnetic field and the electromagnetic wave (variable electromagnetic field). We obtain a numerically integrable strongly non-linear equation system (Dusser *et al.,* 2007; Argyris & Ciubotariu, 2000; Antici *et al.,* 2009; Argyris *et al.,* 2007).

The model has been created by numerically integrating a non-linear differentiable equations system, which is capable to describe the generating and evolution of the gun effect (Dusser *et al.,* 2007; Argyris & Ciubotariu, 2000; Argyris *et al.,* 2007).

For numerically solving the non-linear equations system which describes the gun effect, the literature proposed the usage of the order five Runge – Kutta algorithm, with an adaptive step adjustment (Rusu & Găluşcă, 2010). By applying this algorithm, we obtained the 3D numerical solution associated to the effect, respectively to a „multi – gun" cascading effect for the (X, Px, Py) sets of values. The Wolfram Mathematica 7.0 application has been used; it collects processing data generated by a Fortran 9.0 specific algorithm within a designated file. In this way, we have obtained the parameter values for which the "radicalization" by stochastization of the gun effect is generated, as we could analyze the movement "regimes" specified in (Dusser *et al.,* 2007; Argyris & Ciubotariu, 2000; Argyris *et al.,* 2007).

2.1. Generating the Relativistic Chaotic Gun Effect

Research upon the particle acceleration will lead to determining new methods of obtaining high levels of energy which are necessary for exploring the future boundaries of physics. The methods refer to acceleration within the laser plasma, I[st] order Fermi processes ("impact" acceleration, which implies that particles diffuse due to scattering induced slow moving magnetic "irregularities"), to stochastic acceleration (IInd order Fermi processes) and to laser acceleration in vacuum. Within the stochastic mechanism, the particle acceleration is determined by the resonant interaction between the wave and the particle, all within turbulent plasma.

For an efficient acceleration, the free mean path for particle scattering must be less than the turbulence area size. In this way, the particle spatial convection can be approximated by a spatial diffusion. Thus, the kinetic Fokker – Planck equation, which describes the charged particle spectrum, depends exclusively upon the time and E_{cin} kinetic energy and can be expresses by (Ramaty, 1979; Pertosian, 1994):

$$\frac{\partial N}{\partial t} = \frac{\partial^2}{\partial E^2_{cin}} \cdot \left[D \cdot \left(E_{cin}\right) \cdot N \right] - \frac{\partial}{\partial E_{cin}} \cdot \left\{ \left[A\left(E_{cin}\right) - \left|\dot{E}_{cin}\right| \right] \cdot N \right\} - \frac{N}{t_{sc} \cdot \left(E_{cin}\right)} + Q\left(E_{cin}\right) \quad (1)$$

where $N(E_{cin}t)dE_{cin}$ defines the number of particles within the unit of volume for a dE_{cin} time interval, $E_{cin} = \gamma - 1$ is the relativistic kinetic energy in $m_0 c^2$ units, $D(E_{cin})$ is the diffusion rate, $A(E_{cin})$ is the systematic acceleration rate, $\left|\dot{E}_{cin}\right|$ is the energy loss rate due to indirect processes linked to stochastic acceleration or transport effects, $t_{sc}(E_{cin})$ is the particle mean "escape" time towards the outside of the accelerated region, $Q(E_{cin})$ is the source term which can be described by a Maxwell function (Ramaty, 1979; Pertosian, 1994):

$$Q\left(E_{cin}\right) = Q_0 \cdot \frac{2}{\sqrt{\pi}} \cdot \sqrt{\frac{E_{cin}}{KT}} \cdot \exp\left(-\frac{E_{cin}}{KT}\right) \quad (2)$$

where Q_0 is the rate (part./vol./sec.) to which the charged particles from the plasma are accelerated at the T temperature.

The number of "escaped" particles is equal, for a state of equilibrium, to the number of accelerated particles, such as (Ramaty, 1979; Pertosian, 1994):

$$Q_0 = \int dE_{cin} \cdot Q(E_{cin}) = \int dE_{cin} \cdot \frac{N(E_{cin})}{t_{sc}(E_{cin})} \tag{3}$$

The motion of a charged particle within an external uniform magnetic field and within an electromagnetic wave field generated by a charged particle beam produces a chaotic gun effect, as the longitudinal component of the pulse (parallel to the wave vector) suffers a chaotic variation and rises suddenly to a value to which is holds constant, between two circular Larmor orbits. Thus, the Larmor phase or orbit (circle) is defined: the circular trajectory for the (P_x, P_y) system, which is perpendicular to the uniform external magnetic field; the generalization for this effect stands in the Larmor spiral, which occurs along with the increase of the particle energy.

The motion of the charged particles, within a field of waves excited by a beam of charged relativistic particles, which in turn are in motion in a periodic environment, can also spark an interest for the free-electron laser (Gutzwiller, 1998; Argyris *et al.,* 2007). Generally, all chaos indicators (Lyapunov exponents, the entropy, integral correlation, spectral power, the Hausdorff dimension, fractals etc.) show that the motion of a single charged particle from the beam becomes chaotic when the field amplitude satisfies the resonant overlapping condition.

2.2. The Non-Linear Equations for the Charged Particle Beam

We consider a relativistic beam of identical charged particles, which move within an external uniform magnetic field B_0, with the following components (Gutzwiller, 1998; Argyris *et al.,* 2007): $B_0 = \{B_{0x}, B_{0y}, B_{0z}\} = \{0, 0, B_0\}$.

A charged particle which travels under a certain angle compared to the external magnetic field, behaves as a non-linear oscillator which generates an electromagnetic field. One can therefore observe a relativistic beam, composed of oscillators, within a self-sustained electromagnetic field, described by the Maxwell equation system:

$$\nabla \times B_b = \frac{4\pi}{c} \cdot j_b + \frac{1}{c} \cdot \frac{\partial E_b}{\partial t} \tag{4}$$

$$\nabla \times E_b = -\frac{1}{c} \cdot \frac{\partial B_b}{\partial t} \tag{5}$$

$$\nabla \cdot E_b = 4 \cdot \pi \cdot n_b \cdot q \tag{6}$$

$$\nabla \cdot B = 0 \tag{7}$$

The relativistic motion equations afferent to a single particle from the beam, are given by the relations (Argyris & Ciubotariu, 2000; Ramaty, 1979; Pertosian, 1994; Argyris *et al.,* 2007):

$$\frac{dr}{dt} = \frac{1}{m_0\gamma} p = \frac{1}{m_0\gamma}\left(p_c - \frac{q}{c} \cdot A \right) = \frac{q}{m_0\gamma}\left(R_c - \frac{1}{c} \cdot A \right) \equiv v \tag{8}$$

$$\frac{dp}{dt} = q \cdot E_b + \frac{q^2}{c}\frac{R}{m_o\gamma} \times \left(B_b + B_0 \right) \tag{9}$$

The distribution function for the beam particles is (Argyris & Ciubotariu, 2000; Ramaty, 1979; Pertosian, 1994; Argyris *et al.,* 2007):

$$Q_b = n_b \cdot \delta\left(p_{\Box} \right)\frac{\delta\left(p_\perp - p_{b\perp} \right)}{p_\perp} \cdot \delta \cdot \left[\phi - \left(\phi_b + \omega_c t \right) \right] \tag{10}$$

where q and m_0 are the repose charge and mass of the beam particle, ϕ is the angle between $p_\perp$ and the x axis, n_b the beam particle density , $R = \dfrac{p}{q}$ the impulse per charge unit and $p = m_0\delta v$ the relativistic particle impulse.

The following equations describe the non-linear dynamics of the model (Argyris & Ciubotariu, 2000; Ramaty, 1979; Pertosian, 1994; Argyris *et al.,* 2007):

$$\dot{X} := \frac{dX}{dT} = \frac{1}{\gamma} P_x = \frac{1}{\left(1 + P_x^2 + P_y^2 \right)^{1/2}} P_x \tag{11}$$

$$\dot{P}_x := \frac{dP_x}{dT} = \Omega_c \left[\beta \cos\left(X - T \right) + 1 \right] P_y \tag{12}$$

$$\dot{P}_y := \frac{dP_y}{dT} = -\Omega_c \left[\beta \cos\left(X - T \right) + 1 \right] P_x + H \cos\left(X - T \right) \tag{13}$$

3. Numerical Solutions

Considering that there are no efficient analytical methods for describing the stochastic motion components, it is possible to numerically integrate the (11) – (13) equations. We now present the numerical analysis for the aforementioned stochastic processes of beam – particle interaction.

The parameter values taken into consideration for the calculus (Gutzwiller, 1998; Argyris *et al.,* 2007) are:

- cyclotronic frequency: $\Omega_B = 0.5$;

- resonance scale: $n = 4$;

- initial energy: $\gamma_0 = \gamma_4 = 2$;

- initial impulse: $P_{x0} = P_{y0} = \sqrt{1.5}$.

The dynamic (11) – (13) equations system generates a three-dimensional representation within the (P_x, P_y, X) phase space. The numerical solutions have been obtained by applying the order five Runge – Kutta algorithm (with an adaptive step adjustment), which was implemented via the Fortan 9.0 programming environment, which works with the Wolfram Mathematica 7.0 software application. The initial values for [T, P_x, P_y, X] are: [0.001, $\sqrt{1.5}$, $\sqrt{1.5}$, 0.001]. Therefore, when $H = 1.6$, there emerges a strong acceleration and a gun effect is initiated, whereby a sudden expulsion of a particle from the system takes place in a certain distortion – see Fig. 1.
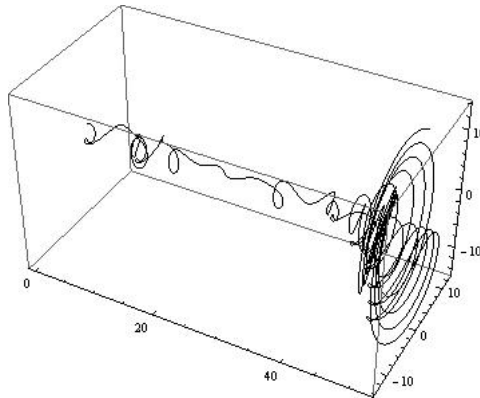
Fig. 1–3D Graphic afferent to H=1.6.

For H=4.6, a multi-gun effect results – see Fig. 2.
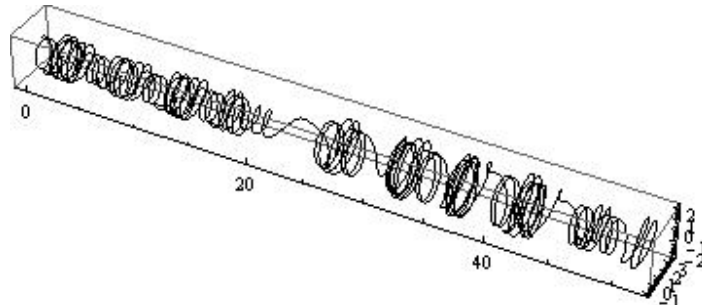
Fig. 2 – 3D Graphic afferent to H=4.6.

For both Figs, 1 and 2, we have shown the three-dimensional (3D) phase space *(X, P_x, P_y)*.

4. Implications and Conclusions

The gun effect can be associated, for laser marking applications, to a supplementation of the existing and demonstrated formation and of droplets and microcracks propagation. Furthermore, where the state of chaos is determined, one can imply that the processing parameters are not at an optimal setting, as the results of the marking are non-qualitative and potentially hazardous, with regard to intense gun particle expulsion, proportional to the laser power, which also raises the droplets formation and microcrack propagation indexes, as the process needs adjusting. This adjustment is achievable in a fine manner via a computerized software prediction system. As a plus, the rise of internal stresses which result from laser processing is also sustained by the successive strong impacts with the gun expulsed particles.

For ultra-fast laser applications, such as femtolaser materials processing (Rusu & Găluşcă, 2010; Rusu Ş. & Rusu I., 2010), the presence of the gun effect is negligible, because of the great speed of the process, which leads to the lack of gun effect specificity, presented within the present paper. Therefore, although the laser power is far superior compared to a commercial laser marking unit, the droplet and microcracks formation is not significant – a situation experimentally proven by the authors in other papers on the matter of laser traceability marking.

The adopted model for studying the relativistic gun effect is: a charged particle (a component of the mark target), a static magnetic field (the plasma formed as a result of the interaction between the laser and the target) and an electromagnetic wave (the laser beam). The particle can undergo "collisions" with the electromagnetic wave, as the system behaves like a collision oscillator.

The beam – particle impact leads to a stochastization of the particle rotation phase within the magnetic field; if the electromagnetic wave amplitude is high enough, a strong acceleration results and the gun effect is initiated: a sudden expulsion of the particle from the system, in a random direction. The energetic contribution becomes significant and an overlapping resonance state is determined. The gun effect can become a highly important element for studying the stability of dense beams composed of charged particles.

REFERENCES

Dusser B., Sagan Z., Bruneel D., Jourlin M., Audouard E., *Laser Deep Marking of Metals And Polymers: Potential Interest for Information Coding*. IOP Publishing Ltd, 2007.

Gutzwiller M.C., *Chaos in Classical and Quantum Mechanics*. Springer-Verlag, New-York, 1990, trad. Ed. Tehnică, Bucureşti, 1998.

Argyris J., Ciubotariu C., *A Chaotic Gun Effect for Relativistic Charged Particles*. Chaos, Solitons and Fractals, 1234 (2000).

Ramaty R., *Particle Acceletation Mechanism in Astrophysics*. In AIP Conf. Proc. **56**, eds. 7. Arons, C. Max and C. McKee. AIP, New York, 135 (1979).

Pertosian V., *Stochastic acceleration*. In AIP Conf. Proc. 294, High-energy Solar Phenomena, eds. 7. M. Ryan and W. T. Vestrand. AIP, New York, P. 162 (1994).

Antici A., Marin C., Agop M., *Haos prin stocasticizare*. Editura Ars Longa, Iaşi, 2009.

Argyris J., Marin C., Ciubotariu C., *Physics of Gravitation and the Universe*. **I**, **II**, Editura Spiru Haret, Iaşi, 2002 şi Editura Tehnica-Info, Chişinău, 2007.

Rusu Ş., Găluşcă D.G., *Laser Marking of Materials: Principles and Processes*. Buletinul Institutului Politehnic Iaşi, **LVI (LX)**, *4*, s. Materials Science and Engineering, 2010.

Rusu Ş., Rusu I., *Laser Technology for Applications in Marking*. Buletinul Institutului Politehnic Iaşi, **LVI (LX)**, *4*, s. Materials Science and Engineering, 2010.

EFECTUL RELATIVIST „GUN" ŞI IMPLICAŢIILE ACESTUIA ÎN PROCESELE DE MARCARE CU LASER

(Rezumat)

Prezenta lucrare are ca scop analiza implicaţiilor induse de efectul stocastic de tip „gun" în dinamica mişcărilor fizice asociate fenomenologiei proceselor de marcare cu laser. În studiul efectului „gun" relativist, a fost adoptat un model ce implică studiul mişcării unei particule cu sarcină – componentă a materialului ţintă, supusă simultan unui câmp magnetic static – plasma formată la impact şi unei unde electromagnetice (polarizate sau nepolarizate) – fasciculul laser.

IMPACTION OF COMPOSITE MATERIALS – CARBON FIBERS WOVEN - POLYPHENYLENESULPHIDE (PPS); THE EFFECT OF TEMPERATURE

BY

PETRICĂ DANIEL SALAVASTRU[1]*, PAUL DORU BĂRSĂNESCU[1], FELIPE SILVA[2], ADRIANA SAVIN[3] and RAIMOND GRIMBERG[3]

[1] “Gheorghe Asachi” Technical University of Iaşi,
[2] School of Engineering, University of Minho, Guimarães,Portugal
[3]National Institute of Research and Development for Technical Physics Iaşi

Abstract. This paper presents the behavior of carbon fiber woven-PPS composites at impacts with low energies occurring at different temperatures. The impacts were made at 20°C, 60°C, 100°C. The analysis of the impact force shows that, in the case of impacts at 20°C, the impacts with energies of 6, 8, 10 and 12J have caused delaminations. The impacts with 2 and 4 J practically have not generated delaminations. In the case of the impacts at 60°C, only impacts with 8, 10 and 12J have caused delaminations; the impacts with low energies only have elastically deformed the materials. In the case of the impacts at 100°C only the impacts with 10 and 12J have caused delaminations. The results have been confirmed by ultrasound and eddy current nondestructive tests.

Key words: carbon fibers Polyphenylene sulphide (PPS), DMA, ultrasound phased array, eddy current testing, impact energy, delaminations.

1. Introduction

The composite carbon fibers Polyphenylene sulphide (PPS) type has start to be used in large scale in the aeronautic industry, practically replacing the

---

* Corresponding author; *e-mail:*

carbon-epoxy composites and, in the same time, certain metallic structures (Morgan, 2005). The special advantages of the matrix consist in its slow thermal degradation meaning higher glass transition temperature (T_g) and activation energy of this transition, smaller quantity of toxic vapours disengaged during an eventually thermal destruction of the matrix, possible to happen in the case of fire at the board of the airship compared with the case of epoxy resins (www.tencate.com).

As all the composites reinforced with long fibers, the carbon fibers woven –PPS is sensitive to impacts, these can produce delaminations with and without fiber breaking.

This paper presents the behavior of carbon fiber woven-PPS composites at impacts with low energies occurring at different temperatures.

2. The Studied Samples

Plates from the composite carbon fiber woven-PPS having dimensions 150x100x4.2mm have been taken into study. The samples contain 12 layers of carbon fiber woven satin 5H type, the fibers being T300JB. The volume ratio is 0.5±0.1. The composite is produced by TenCate Netherlands. The studied samples are presented in Fig. 1.

The principal elastic characteristics of the studied composites are presented in Table 1, the determination being made by procedures shown in (Grimberg *et al.,* 2011).

Table 1
The Principal Elastic Characteristics of the Studied Composites

E_1 [GPa]	E_2 [GPa]	E_3 [GPa]	G_{12} [GPa]	G_{21} [GPa]	$G_{13} = G_{23}$ [GPa]	υ_{12}	υ_{21}	$\upsilon_{13} = \upsilon_{23}$
45.8 ± 0.8	44.8 ± 0.9	11.4 ± 0.5	8.4 ± 0.2	8.4 ± 0.2	5.5 ± 0.1	0.32	0.32	0.03

Fig. 1 – Studied sample.

3. The Experimental Set-Up

The samples impacts were effectuated with the impaction equipment FRACTOVIS PLUS 9350-CEAST-Instron USA using a hemispherical bumper head with 20mm diameter and 2.045kg weight. The impact data were recorded with acquisition system DAS16000-Instron USA, having sampling frequency 1MHz. The samples were mounted on a fixture. In Fig. 2, is presented the impaction equipment and the sample's fixture device.

a   *b*
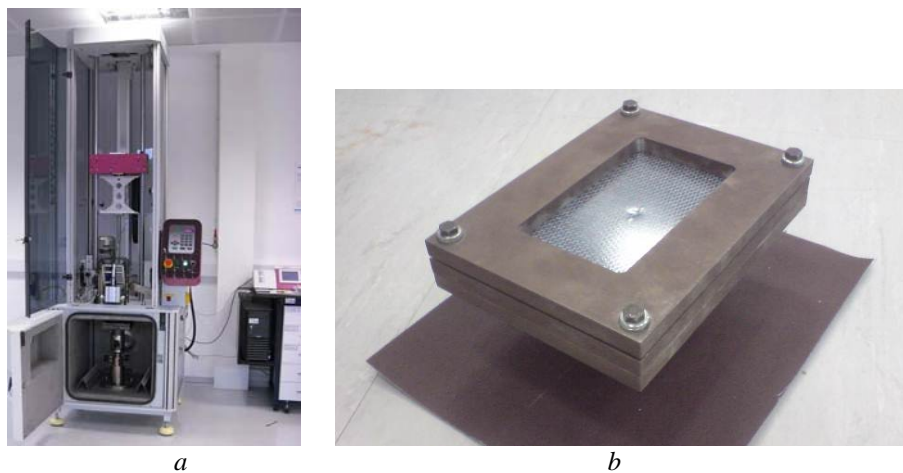
Fig. 2 − Experimental set-up: *a* − the impaction equipment; *b* − fixture device.

The impacts have been made with progressive energies of 2J, 4J, 6J, 8J, 10J, and 12J for the samples at the temperatures 20°C, 60°C and 100°C. In order to have the warranty that the entire mass of the composite has reached the prescribed temperature, the impaction has been effectuated after 30 minutes from the moment when the heating system has indicated the prescribed temperature. It must be mentioned that, for the studied composites, the glass transition temperature, measured with Dynamical Mechanical Analyzer DMA 242°C – Netzsch Germany is 128.5°C, higher than the maximum temperature at which the impact takes place.

The nondestructive evaluation of the composite plates has been effectuated through two procedures

- Ultrasound testing using phased array transducer and the equipment Phasor XS GE –USA

- Eddy current testing using the transducer with orthogonal coils coupled at Network/Spectrum/Impedance Analyzer 4395A Agilent USA and a XY displacing system –Newmark USA.

The control equipment is presented in Fig. 3*a* and *b*.

a   *b*

Fig. 3 − Nondestructive testing equipment: *a* − Ultrasound testing using phased array transducer and the equipment Phasor XS GE –USA; *b* − Eddy current testing using the transducer with orthogonal coils coupled at Network/Spectrum/Impedance Analyzer 4395A Agilent USA.

4. Experimental Results. Discussions

During the impact, the following parameters were determined: the impact force, the impact energy, the deformation of the composite plate in the region of contact and the speed of the impactor.

In Fig. 4 is presented the time dependency of the impact force for all the impact energies and for the three temperatures at which the impaction has taken place.

a

b

c
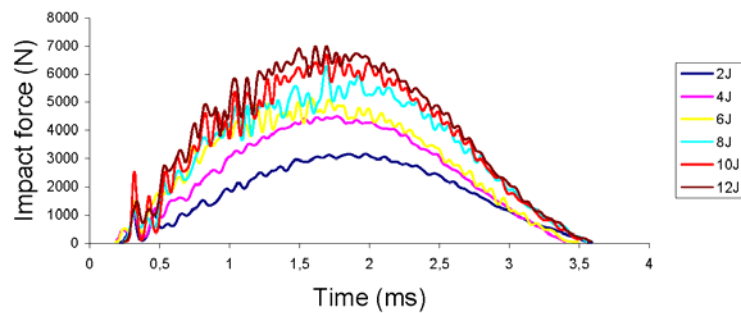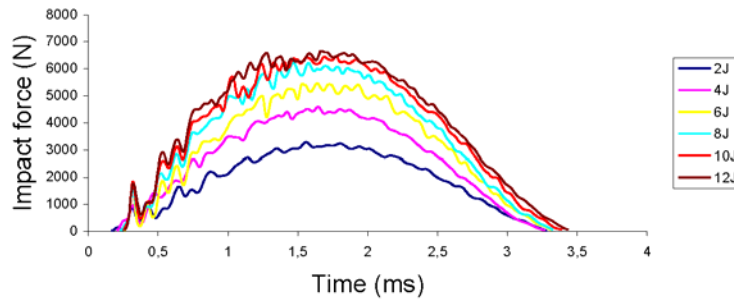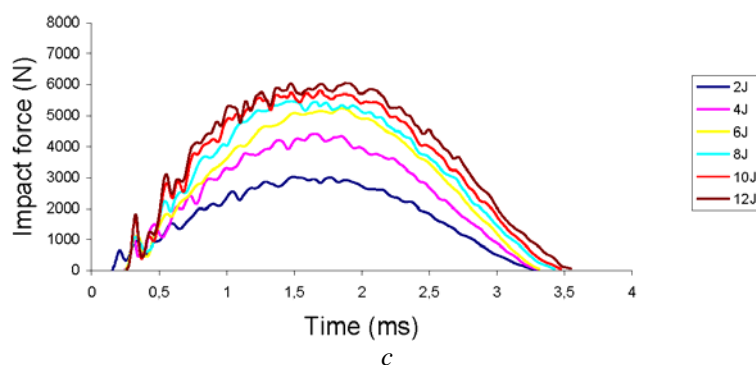
Fig. 4 − Time dependency of the impact force: *a*) 20°C; *b*) 60°C; *c*) 100°C.

Examining the data from Fig. 4, it can be observed that the impact forces at 20°C are greater than those at higher temperature. This is due to the decreasing of transversal stiffness of the composite with the increasing of temperature. For the impact with energies equal with 6J and higher, in the increasing region of the contact force the existence of raw modifications of the force can be observed, suggesting the appearance of delaminations between different laminas.

In Fig. 5 is presented the dependency if the impact force maximum by the impaction energy for the three temperatures.
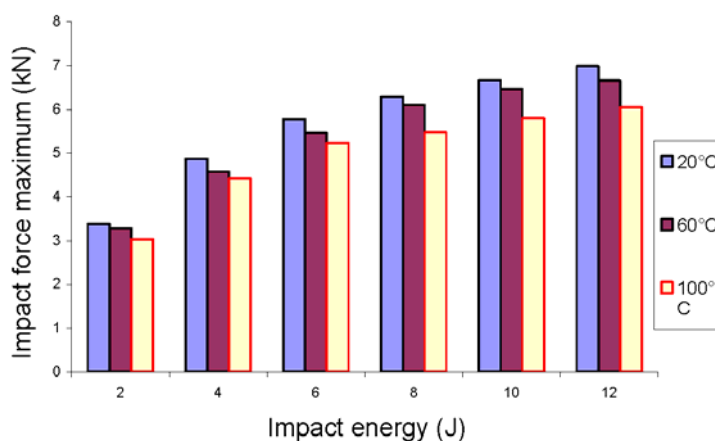
Fig. 5 − Dependency of the maximum impact force by the impact energy.

The data from Fig. 5 confirms the observation about the dependency of the impact force by the temperature for constant energies.

In Fig. 6 is presented the time dependency of the impact energy. Only the impacts with energies that can produce delaminations (according Fig. 4) were taken into consideration.

a

b

c
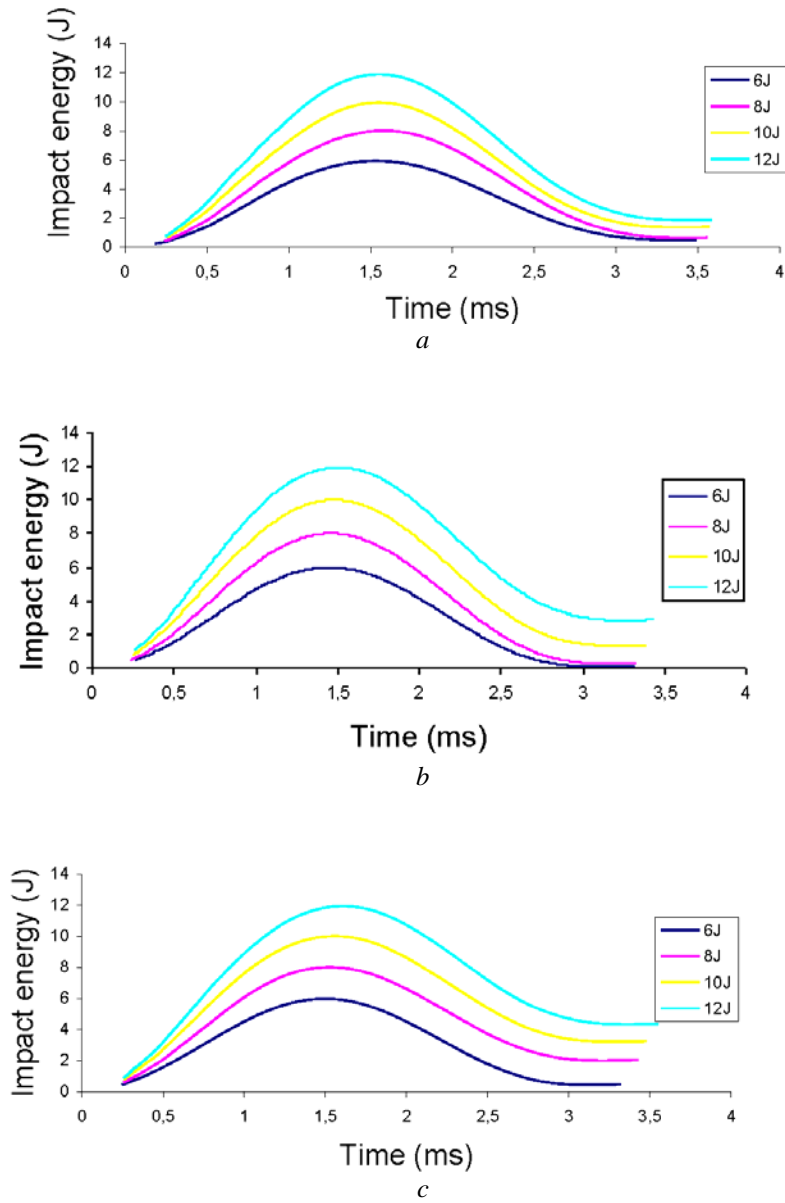
Fig. 6 − Time dependency of the impact energy: *a*) 20°C; *b*) 60°C; *c*) 100°C.

The maximum impact energy can be write as a sum of energies

$$E_{\max_{impact}} = E_{rebounded} + E_{absorbed}$$

The energy absorbed by the composite serves at the plastic deformation of the composite in the contact zone; it is dissipated through internal friction between the matrix's molecules, carbon fibers, matric -carbon fibers as well as at the creation of delaminations.

In Fig. 7 is presented the ratio $\left(E_{absorbed} / E_{\max_{impact}} \right) \cdot 100\%$ in function of the impact energy for the three temperatures.
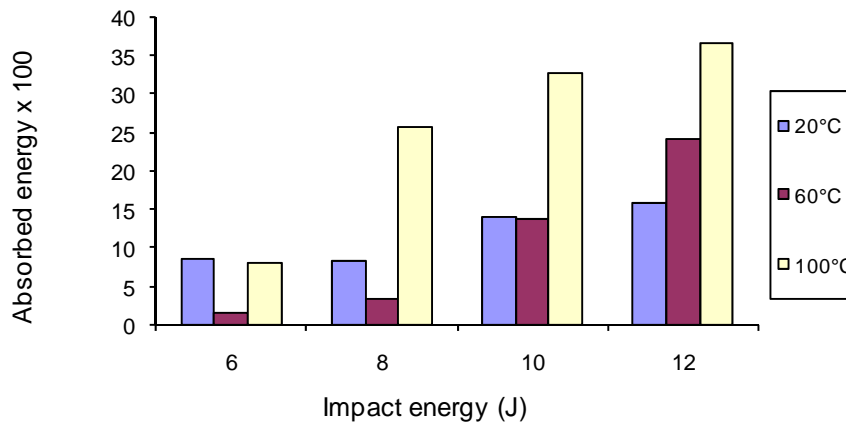
Fig. 7 – The dependence of absorbed energy by the impact energy.

From data in Fig. 7 it can be observed that together with the increasing of the energy impact, also increase the energy absorbed by the composite. It is higher in the case of impacts at 100°C. In order to elucidate this problem, the plastic deformation of the composite in the impact zone has been measured, observing that the deformation increase together with the increasing of the impact energy, being greater in the case of impacts that were made at 100°C, as is presented in Fig. 8.

Despite the absorbed energy has increased with the increasing of temperature, it is possible that the energy that serves at the creation of delaminations by disentanglement of the adherence between the layers of the carbon fibers woven and the matrix might be smaller, fact observable in the data from Fig. 4, the jump of the force diminishing for the same impact energy, together with the increasing of the temperature.

Both nondestructive examination with ultrasound as well as those with eddy current had shown that at impact energies smaller than 6J, the delamination does not appear.
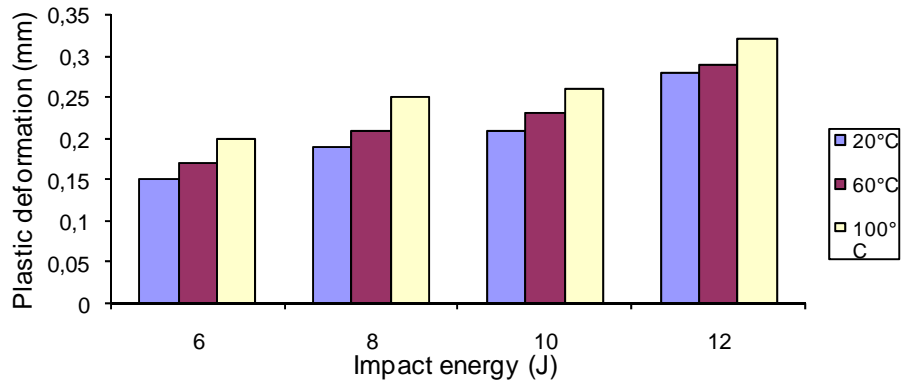
Fig. 8 – Plastic deformation in the impact zone function on the impact energy.

In Fig. 9 *a* and *b* are presented the C-scan images of delaminations due to impacts with 12J energy, and respective 6J at 20°C.

a   b
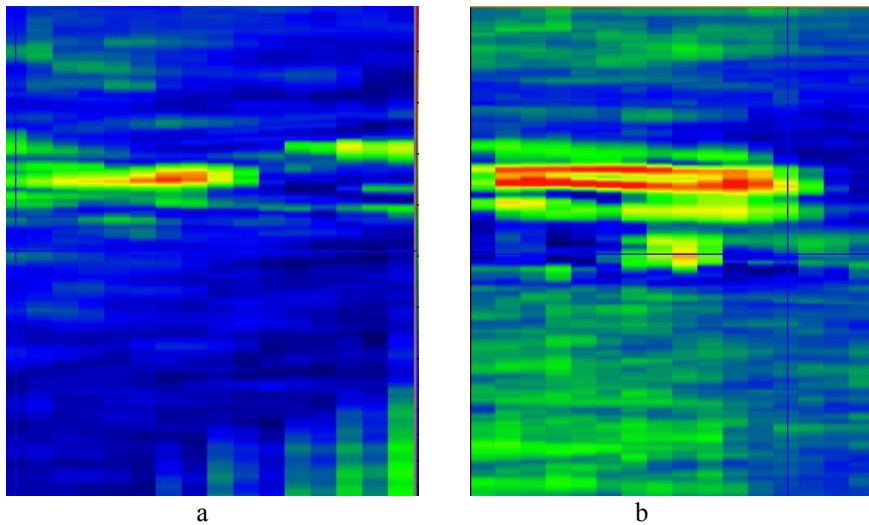
Fig. 9 – C-Scan imaging: *a* – impact at 6J, 20°C; *b* – impact at 12J, 20°C.

It can be observed that with the increasing of the impact energy, the area of the delaminated surface increase.

The same impacts were investigated by eddy current method. The results are presented in Fig. 10 *a* and *b*. the optimal work frequency was 1MHz.

a

b
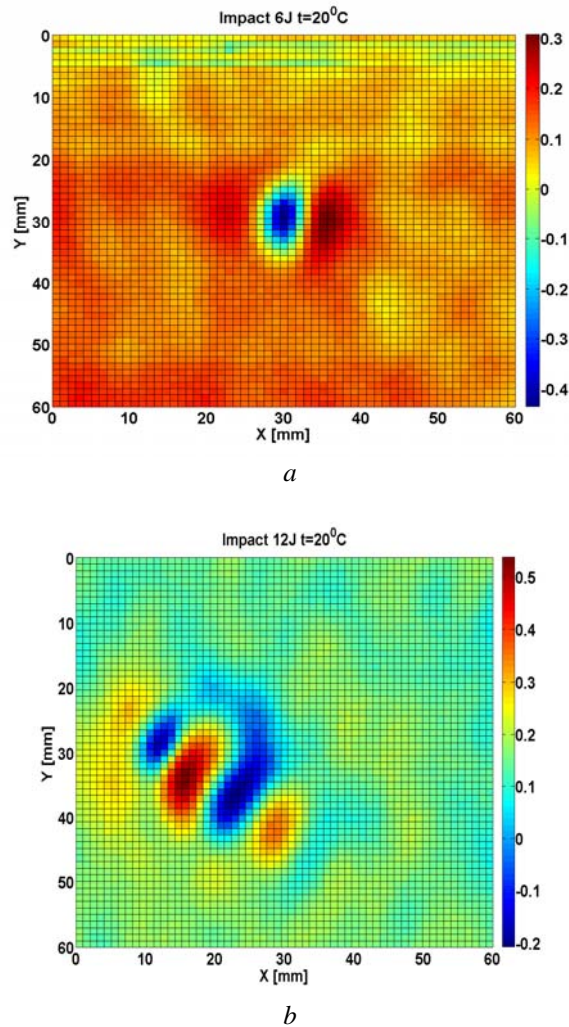
Fig. 10 − Eddy current imaging of delaminations:
a − impact at 6J, 20°C; *b* − impact at 12J, 20°C.

Also, in the case of eddy current nondestructive examination the area of delaminated surface increases with the increasing of the impact energy.

5. Conclusion

The composite materials from carbon fibers woven, 5 harness satin type as reinforcement and polyphenylenesulphide (PPS) is a material relatively sensitive to impact. The impacts with energies till 6J do not create delaminations at none of the impact temperature taken into consideration. The

impacts with energies higher than 6J or equal, respective 8J, 10J and 12J create delaminations of which area increase together with the impact energy. The delaminations can be nondestructive evaluated using C-scan ultrasound using phased array transducers and eddy current method at high frequency using a transducer with orthogonal coils.

REFERENCES

Morgan P., *Carbon Fibers and Their Composites*. Taylor &Francis, NY, 2005.
∗ ∗ www.tencate.com/TenCate/Aerospace_composites/
Grimberg R., Savin A., Steigmann R., Dobrescu G.S., Iftimie N., *Determination of Elastic Tensor of CFRP Through Ultrasound Procedures*. The 8th International Congress in Materials Science and Engineering-ISSIM 2011, 26–29 May 2011 Iaşi–România.

IMPACTELE MATERIALELOR COMPOZITE DIN TESĂTURĂ DE FIBRĂ DE CARBON ŞI POLIFENILENSULFIDĂ; EFECTUL TEMPERATURII

(Rezumat)

Lucrarea prezintă comportamentul compozitelor din tesătură de fibre de carbon şi matrice de polifenilensulfidă ca matrice la impacte cu energii scăzute ce au loc la diferite temperaturi. Impactele au fost efectuate la temperaturi de 20°C, 60°C, 100°C. Analiza forţelor de impact arată că, în cazul impactelor la 20°C, impactele cu 6, 8, 10 şi 12J au cauzat delaminări. În cazul impactelor la 60°C, doar impactele cu 8, 10 şi 12 J au cauzat delaminări, impactele cu energie scăzută creând deformări elastice ale materialului. La 100°C doar impactele cu 10 şi 12 J au creat delamianări. Rezultatele au fost confirmate prin teste nedistructive cu ultrasunete şi prin curenţi turbionari.

EFFECT OF MOISTURE CONTENT ON MECHANICAL PROPERTIES OF GLASS-POLYESTER COMPOSITES

BY

ADRIANA SAVIN[1*], ROZINA STEIGMANN[1], NICOLETA IFTIMIE[1], RAIMOND GRIMBERG[1] and JANEZ GRUM[2]

[1] National Institute of Research,
Development for Technical Physics Iaşi,
[2]University of Žilina, Slovakia

Abstract. In this paper we present the results obtained on glass-polyester samples with different types of polyesters, made by HELIOS GROUP Slovenia. The reinforcement consists in nonwoven fiberglass made by KURARAI – AMERICA Inc. the studied samples were immersed in distilled water at the temperature of 25±1°C. The effect of moisture content over the complex elastic modulus and tanδ was studied, its effect over the Arrhenius activation energy and glass transition temperature being elucidated.

Key words: fiber-glass polyester composite, DMA, activation energy, glass transition.

1. Introduction

Glass fiber reinforced plastics (GFRP) composites is an immensely versatile material that combine lightweight with inherent strength to provide a weather resistant finish, with a variety of surface texture and an unlimited color range available. GFRP was developed in the UK during the Second World War as a replacement for the molded plywood used in aircraft radoms. Its first main

---

* Corresponding author; *e-mail:*

civilian application was for building of boats. GFRP uses also include hot tubs, pipes for drinking water and sewers, office plant display containers and flat roof systems. This type of composites is also used in the telecommunications industry for shrouding the visual appearance of antennas, due to its RF permeability and low signal attenuation properties. Other uses include sheet form made electrical insulators and other structural components commonly found in the power industries. GFRP are also used in the house building market, and for construction of storage tanks (Mayer, 1993).

The mechanical performances of GFRP composites depends on the fiber strength and modulus, the matrix strength and chemical stability, and the effectiveness of interface bonding between the matrix and fiber to enable stress transfer (Erden *et al.,* 2010).

Glass fiber reinforced polyester (GRP) composites are the most "popular" GFRP. The matrix is based on cured thermosetting resin. The raw material is supplied in the form of a viscous liquid comprising the following basic ingredients: linear unsaturated polyester, a cross-linking monomer (curing agent), usually styrene, and an inhibitor to impede cross-linking until resin is to be used by the manufacturer. When the catalyst (initiator) and glass reinforcement are added, the resulting mixture is ready for production of the GRP item. During fabrication, the monomer reacts with the polyester, resulting in cross-linking of the polyester chain and final cure. The ultimate result is a rigid solid material in which the matrix has joined chemically and mechanically with the reinforcing glass fibers to provide a composite structure whose properties are very different from and significantly superior to those of either material alone.

In those application in which GRP composites are subject to a heat and mechanical load, it is essential to determinate the elastic properties using nondestructive methods, the best methods being the ultrasound methods.

GRP using as reinforcement the sheets of ravings (unwoven continuous strands) is an orthotropic composite material, being quasi-isotropic in plane and having other elastic properties out of plane. In this case, GRP is a transversally isotropic material (Lemaitre & Chaboche, 1994).

This paper proposes the determination, by ultrasound methods, of GRP's elastic tensor components. For in-plane components, using the value of propagation speed of fundamentals modes of Lamb waves (Schmerr, 1998), generated and received by air-coupling ultrasound transducers. For out-of-plane components, the propagation speeds of longitudinal and transversal waves are used (Krautkramer & Krautkramer, 1990).

2. Studied Samples

Samples of GRP plates having as reinforcement 5 and 6 sheets of ravings with $250 \pm 50 \text{gm}^{-2}$ density and matrix from different types of unsaturated

Orthophthalic polyester resins, made by COLPOLY Slovenia have been taken into study, Fig. 1.

Fig. 1 − Studied GRP samples.

The characteristics of studied GRP samples are presented in Table 1.

Table 1
Studied GRP Samples

No	Sample name	Matrix	Number of reinf. layers	Fiber volume ratio	Density [kg/m^3]	Observations
1	7201-5l	COLPOLY 7201	5	0.52±0.005	1466±20	medium reactivity resin
2	7201-6l	COLPOLY 7201	6	0.43±0.005	1550±20	medium reactivity resin
3	7524-6l	COLPOLY 7524	6	0.43±0.005	1530±20	Chemical resistance
4	7243-6l	COLPOLY 7243	6	0.57±0.005	1410±20	Preaccelerated thixotropic

3. Experimental Set-Up

A Dynamical Mechanical Analyzer DMA 242C −Netzsch Germany has been used, having the three points bending fixture with the distance between the supports of 40mm, Fig. 2.

a   b

Fig. 2 − Dynamical Mechanical Analyzer: *a* − the equipment;
b − three points bending fixture.

For all the samples, the bulk modulus E', loss modulus E" and $\tan\delta$ ($\tan\delta = E'/E"$) were measured function of the temperature in the range 30°-250°C. In this range, the studied materials do not reach the thermal destruction. The equipment has been set-up with the parameters: heating speed 2°C/minute, amplitude of the down force 6N, the deflection amplitude 30μm. The tests were effectuated at frequencies 1, 3.33, 5, 10, 33.3, 50Hz.

For determination of adsorbed water content, the samples were weighted with a METTLER balance having 1μg precision. The samples were immersed in bi-distillated water at +25°C±1°C for different periods till 60days. The adsorbed water quantity has been calculated as:

$$C(t) = \frac{M(t) - M_0}{M_0} \cdot 100 [\%] \qquad (1)$$

where $M(t)$ represents the weight of the sample after immersion in water during the time t and M_0 the initial weight of the sample.

4. Experimental Results, Discussions

The time dependency of the adsorbed water in the studied composites is presented in Fig. 3.
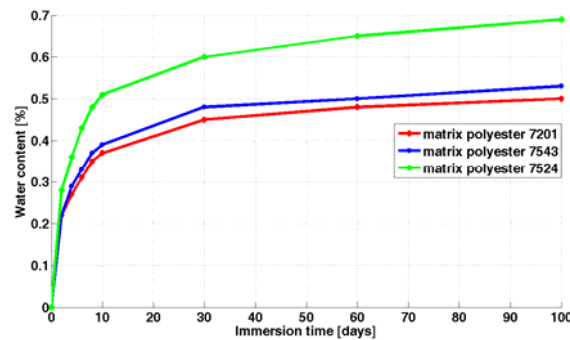
Fig. 3 – The time dependency of adsorbed water.

The shape of the curves from figure suggests that the diffusion of water in the polymer matrix is subdued to the second rule of Fick, expressed as:

$$\frac{\partial C}{\partial t} = D \frac{\partial^2 C}{\partial z^2} \qquad (2)$$

where C is the concentration of water that diffuses into different types of polymers along z axis (axis perpendicularly on the plane of the composite). If

we consider the initial concentration of water as being zero and the composite material is immersed into infinite water-bath, the solution of the eq. (2) become.

$$\frac{m(t)}{m_\infty} = 1 - \frac{8}{\pi^2} \sum_{n=0}^{\infty} \frac{1}{(2n+1)^2} \exp\left[-\frac{\pi^2 (2n+1)^2}{g^2} Dt \right] \tag{3}$$

where $m(t)$ is the weight of water adsorbed at the moment t and m_∞ is the quantity of water adsorbed after a time $t \to \infty$ and g is the thickness of the composite plate.

For ratio of $m(t)/m_\infty \leq 1\%$, the eq. (3) is simplified a lot becoming:

$$\frac{m(t)}{m_\infty} \cong \frac{4}{g} \sqrt{\frac{Dt}{\pi}} \tag{4}$$

Using eq.(4) it can be determined the diffusion coefficient of water in the studied composites, the values being indicated in Table 2.

Table 2
Diffusion Coefficient

Composite's matrix	7201	7543	7524
D[m^{-2}days^{-1}]	$2.52 \cdot 10^{-6}$	$2.69 \cdot 10^{-6}$	$3.51 \cdot 10^{-6}$

The measurements effectuated with DMA emphasized a multiple action of adsorbed water over the elastic and chemical parameters of the composite.
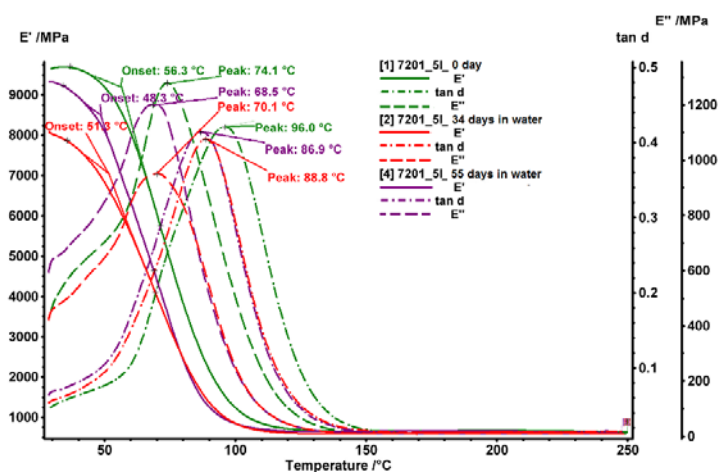
Fig. 4 − Temperature dependency of E', E" and tanδ for different immersion time at the composite with matrix from the resin 7201.

In Fig. 4 is presented, for different types of immersion time, the way in which bulk modulus E', loss modulus E'' and $\tan\delta$ of the glass polyester with the matrix from the resin 7201 behave.

The examination of data from Fig. 5 shows the existence of a glass transition, characterized by the T_g temperature defined as the temperature corresponding to the maximum of $\tan\delta$ peak as well as of a activation energy of this transition, that can be calculated from Arrhenius law (Menard, 1999):

$$K = A \exp\left(\frac{\Delta H}{RT}\right) \qquad\qquad (5)$$

where K is degradation rate for the glass transition process, ΔH is the activation energy (Arrhenius energy), R is the gas constant, T is absolute temperature.

In Fig. 5 and 6 are presented the dependency of glass transition temperature by the immersion time and respective of Arrhenius activation energy determined in the basis of eq. (5) by the Protheus Analysis software.
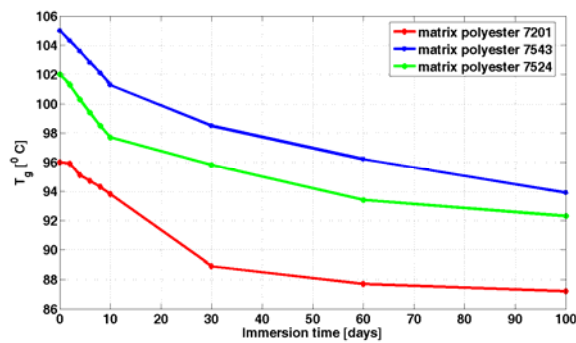
Fig. 5 – The dependency of glass transition
temperature by the immersion time.
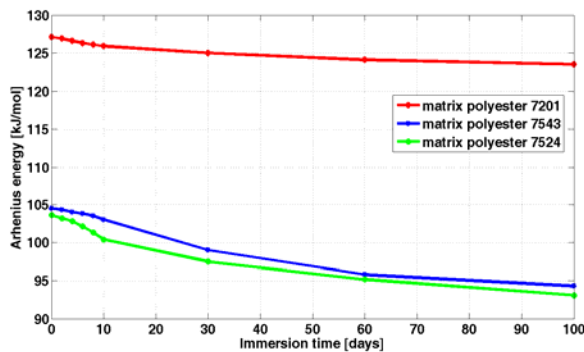
Fig. 6 – The dependency of Arrhenius activation energy
temperature by the immersion time.

The adsorption of water by the polyester matrix influences the elastic properties of the studied glass-polyester composites.

In Fig. 7 is presented the immersion time dependency of the in-plane elastic modulus, defined as:

$$|E| = \sqrt{E'^2 + E''^2} \tag{6}$$
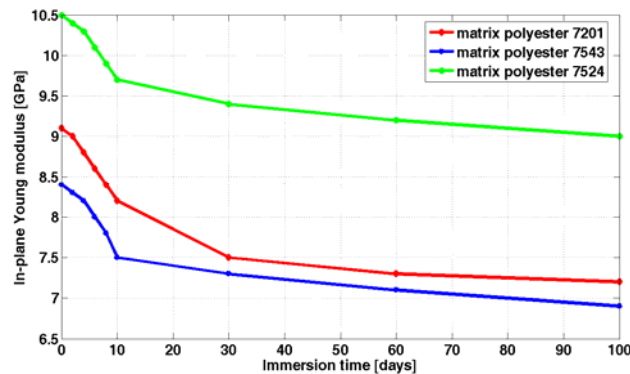
Fig. 7 – The immersion time dependency of the
in-plane elastic modulus.

Summarizing the obtained data, it can be observed that the water adsorption leads to a low importance decreasing of the Arrhenius activation energy and of the glass transition temperature T_g. This fact leads to the idea that the degradation of polyester due to water adsorption has small importance, which recommends their use in naval construction, pipes. Liquid storage tanks, etc. In the same time, the water adsorption leads to a much more importance decrease of the elastic modulus with the increasing of immersion time, thus of the concentration of adsorbed water.

5. Conclusion

The composites polyester-glass composites having fiberglass layers as reinforcement and different types of polyester resins as matrix adsorb water, the adsorption phenomenon being subdued to the second Fick's law. In the basis of experimental measurements, the diffusion constant for the temperature of thermal equilibrium (25±1°C) has been found.
The increasing of adsorbed water concentration leads to the diminishing of the glass transition temperature and of activation energy of this phase transition.

In the same time, the increasing of the adsorbed water concentration decrease the in-plane elastic modulus, the composite being practically isotropic in –plane.

REFERENCES

Erden S., Sever K., Seki Y., Sarikanat M., *Enhancement of the Mechanical Properties of Glass/Polyester Composite via Matrix Modification.* Fibers and Polymers, *11*, 732-737 (2010).

Krautkramer J., Krautkramer H., *Ultrasonic Testing of Materials.* 4th ed., Springer Verlag, 1990.

Lemaitre J., Chaboche J.L., *Mechanics of Solid Materials.* Cambridge University Press, NY, 1994.

Mayer R., *Design with Reinforced Plastics*, Spirnger, Berlin, 1993.

Menard K.P., *Dynamic Mechanical Analysis – A Practical Introduction.* CRC Press, Fl. 1999.

Schmerr L.W.,Jr., *Fundamentals of Ultrasonic Nondestructive Evaluation – A Modeling Approach.* Plenum Press, NY, 1998.

EFECTUL UMIDITĂȚII ASUPRA PROPRIETĂȚILOR MECANICE A
COMPOZITELOR POLIESTER STICLĂ

(Rezumat)

În această lucrare se prezintă rezultatele obținute la testarea probelor din compozit fibră de sticlă încastrate în diferite tipuri de poliesteri, produși de HELIOS GROUP Slovenia. Ranforsarea constă în fibre nețesute de sticlă produse de KURARAI – AMERICA Inc. Probele studiate au fost imersate în apă la temperatura de 25±1°C. A fost studiat efectul umidității asupra componentelor modului complex elastic și a tanδ, asupra energiei de activare Arhenius și a temperaturii de tranzitie vitroasă.

ENSURING RELIABLE OPERATION OF HYDRAULIC DRIVES WITH HYDRAULIC MOTORS

BY

V. SAVULIAK* and N. SEMICHASNOVA

Vinnytsia National Technical University

Abstract. According to their specific indices, hydraulic drives of modern mobile machines occupy leading positions among other types of drives. The majority of technological machines operate in the modes of relatively frequent starting, reversing and stopping. This requires consideration of the factors that influence the drive starting process at the design stage. Improvement of such machines involves higher requirements to the capacity, positioning accuracy, speed and quality of dynamic characteristics of the working equipment motion, which is impossible without further development of hydraulic drive, improvement of its starting characteristics and reliability.

The factors influencing reliability of hydraulic drive operation are determined and starting is shown to be the most significant among them. On the basis of system approach the factors ranking was performed. The following factors are demonstrated to be the most decisive ones: tribological perfectness of the design, rational distribution of the energy flows dissipated in the drive, constructive and organizational measures that help to reduce the load during starting and reversing processes.

Experimental studies and computer modeling were conducted taking info account non-linear characteristics of hydraulic drives. Main factors that influence the character of transient processes of starting are determined. It is shown that the following factors have the greatest influence: compliance of the hydraulic drive lines, presense of a rolling friction pair in the actuator, load value at the initial moment oil properties and influence of its active surface additives.

---

* Corresponding author; *e-mail:*

1. Introduction

In construction, agriculture and other engineering industries hydraulic drive has still prevails in the operation of excavators, bulldozers, cranes and other machines. A distinguishing feature of these machines is cyclicity in performing technological operations with relatively low cycle time that includes starting, acceleration, normal functioning, slowing and stopping of the mechanism. Hydraulic systems of such machines operate, most of the time, with the modes that have a significant influence on reliability of their operation.

If failures occur, they cause balance disturbances and are accompanied with high-speed, average-speed and slow processes.

High-speed processes influence mostly interlocution of the elements and disturb the drive operation process. These processes are characterized by high speeds and periodicity of parameter variations. They include vibration of the elements, pressure pulsation, etc. Average-speed processes lead to gradual failures. They occur mostly during the operating process. Average-speed processes are caused by environmental temperature variations as well as by changes of humidity, physical properties, of the working fluid, etc.

Slow processes occur during the entire period of the drive operation. They include wear of the friction pair elements, natural ageing and fatigue of the materials, seasonal changes of temperature and humidity.

According to the character of their manifestation, the failures are classified as gradual and sudden failures. Sudden failures are characterized by stepwise change in the values of one or several parameters of the drive. In this case the hydraulic system loses its operability. Seizure of the movable parts, cracking and damage of the elements are characteristic of sudden failures. Gradual failures are caused by natural wear of the elements, loss of tightness, fatigue damage accumulation, blocking of the filters and throttles. Reliable operation of any machine is ensured by timely detection of hydraulic system failures, monitoring the performance characteristics of the hydraulic drive during its operation.

The entire life cycle of the drive can be divided into the following stages:
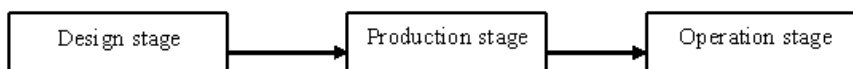
Fig. 1 – Stages of the drive life cycle.

In order to increase reliability, at the design stage (Fig.2) it is necessary, first of all, to optimize the principal hydraulic circuit in accordance with the specification, to minimize the number of hydraulic components that are included into the product design, to make a choice of the required hydraulic components taking into account the actuator loads, maximal speeds and acceleration, the required accuracy of operation and linear characteristics (Свешников *et al.,*2010). It is necessary to provide the hydraulic drive overload protection including that of separate hydraulic lines and components. A mathematical model is proposed that makes it possible to analyze the system dynamic behavior at the design stage taking into account inertial loads, the properties of the working fluid, to determine the conditions under which undesirable phenomena could occur and how reliability of the entire system could be further influenced.
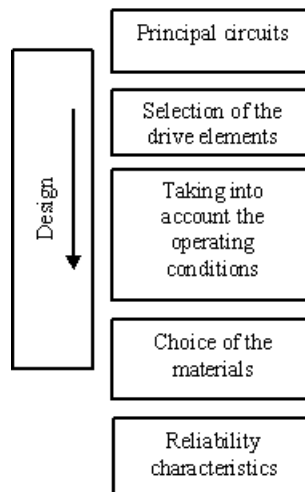
Fig. 2 – Factors of reliability ensurance at the design stage.

As a result of poor quality, the failures of hydraulic equipment could occur. Stability of technological processes, (Fig.3) availability of modern production equipment, special facilities and test rigs, qualification of the personnel have a significant influence on stability indices at the production stage. The quality of the materials being used and the hardware are also very important. Product quality management system monitors constantly all the stages of life cycle.

To achieve higher reliability, working fluids of the hydraulic system must have such chemical and physical properties that correspond to the operating conditions. It is desirable that optimal temperature range of the working fluid is maintained automatically according to the signals of temperature sensors.

Operation failures occur as a result of violating the rules of hydraulic drive operation and maintenance. At the operation stages the hydraulic drive reliability is influenced by various factors (Fig.4).

The climate factors include temperature, pressure, humidity, solar radiation and dust content (Сырицын, 1990). Hydraulic drives operate under different environmental conditions. As the temperature grows, mechanical properties of the most materials become worse, elasticity modulus is reduced as well as ultimate strength.
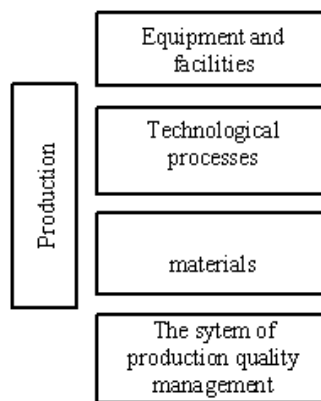
Fig. 3 – Factors of reliability ensurance at the production.

Temperature growth also leads to more intensive ageing processes of materials (especially of rubber materials). Lubricants and working fluids lose their viscosity, which causes leakage through the seals and gaps.
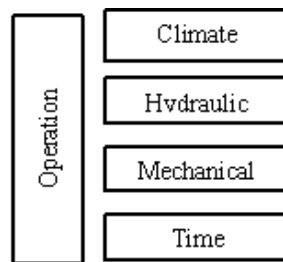
Fig. 4 – Factors of influence on operation.

Under low temperatures mechanical strength and plasticity of materials are reduced while fragility and viscosity are increased. Due to internal structural changes, additional local stresses emerge in the materials, which cause their damage.

The hydraulic factors include cleanliness, temperature, gas content and ageing of the working fluid. Failures of the machine drives are mostly caused by

the working fluid being contaminated with mechanical impurities during manufacturing and installation processes.

Temperature has a significant influence on all of the working fluid parameters that determine its characteristics. Increased viscosity caused by temperature reduction decreases leakage and increases volumetric efficiency. At the same time the friction force is increased and mechanical efficiency is reduced. Therefore, in order to provide high efficiency the fluid temperature must be optimal to ensure minimal total losses. Under negative temperatures the working fluid viscosity increases, which could lead to cavitations in the suction line that is one of the most undesirable factors contributing to the reduction of hydraulic pump resource and hydraulic drive reliability. If the hydraulic drive must operate in the conditions of negative temperatures of environmental air, it is necessary to arrange measures that would simplify starting, *i.e.* to provide the possibility of the working fluid pre-heating or additional starting facilities.

At the initial stage of testing frequent failures are observed which are caused by the defects of manufacturing and control. After revealed defects are eliminated, there comes a period when the failures occur only as a result of random factors. This period continues until the failures, caused by the wear of separate elements, emerge. Correct evaluation of failures depends on how typical the above-mentioned failures are.

While solving the problem of ensuring the hydraulic drive reliable operation, an important role is given to technical diagnostics that controls the hydraulic drive technical condition in the process of operation and allows making repairs within optimal periods. Optimal process of maintenance and repair during hydraulic drive operation can be built if you have statistical data obtained in the process of bench trials and field testing taking into account the conditions of hydraulic drive operation. To provide effective troubleshooting, hydraulic drive must be equipped with a sufficient number of elements to which measuring equipment could be rapidly connected, *i.e.* manometers, pressure pickups, etc.

Modern diagnosing facilities that include flow meters, strain-gauge transducers, their signal being stored in computer memory, enable effective analysis even of fast-going working processes, to reveal the reasons of failures and disorders and in some cases to predict possible failures.

Data on operation and failures of excavators (Бродский & Слесарев, 2002) has shown that idle periods occupy more that 10% of the total time of the machine operation. Expenses for materials and spare parts make 65% from the total expenses for the machine operation, including 30% of those spent on hydraulic drive.

Reliability of a hydraulic drive operation depends, to a great extent, on the reliability of hydraulic motors operation. For cyclic character of the hydraulic drive operation starting and speed-up losses occupy a significant place.

During cyclic operation with frequent stops and reversals the hydraulic machine assembly operates with undeveloped liquid films in the distribution end

pair (in axial-piston hydraulic motors) and in rolling bearings (in gear hydraulic motors) the losses will be much higher than during steady-state operation. In such cases special measures are recommended which make it possible to reduce mechanical losses during starting process.
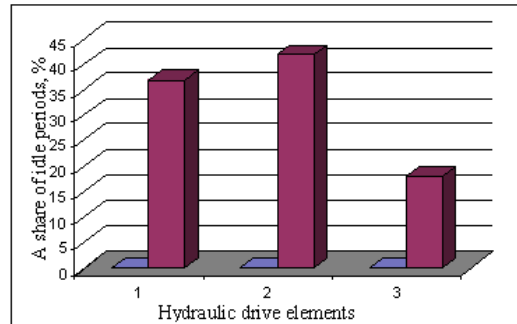
Fig. 5 – The part of a mobile machine idle periods caused by the failures
of its elements:1– hydraulic line elements; 2 – hydraulic pumps and hydraulic motors;
3 – hydraulic equipment.

It was determined that at the moments of starting and reversing the system pressure increases and could exceed considerably the nominal value (Савуляк & Семічаснова, 2010).

Such leading modes are the main reason for the failures of hydraulic system elements. Fig. 6 shows a typical transient process in hydraulic system during its starting.

In the machines with cyclic operation a significant factor of failure intensity in the hydraulic system elements is the form of pressure pulses, their duration and frequency. Quantitative data of the starting overload influence on reliability of the hydraulic system and its elements are limited and require further study.
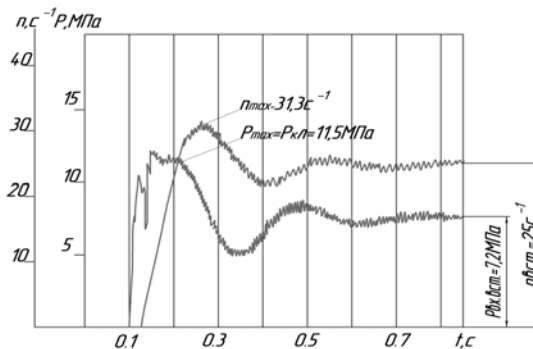
Fig. 6 – Typical transient process in a hydraulic drive during its starting.

Technical condition of the hydraulic motor starting system determines, to a great extent, operation reliability of the hydraulic motor itself and complex

dynamic processes, occurring in hydraulic motors during starting process, influence practically all the hydraulic system components. The analysis conducted on the reasons of the failures in hydraulic machines is presented in Fig.7.
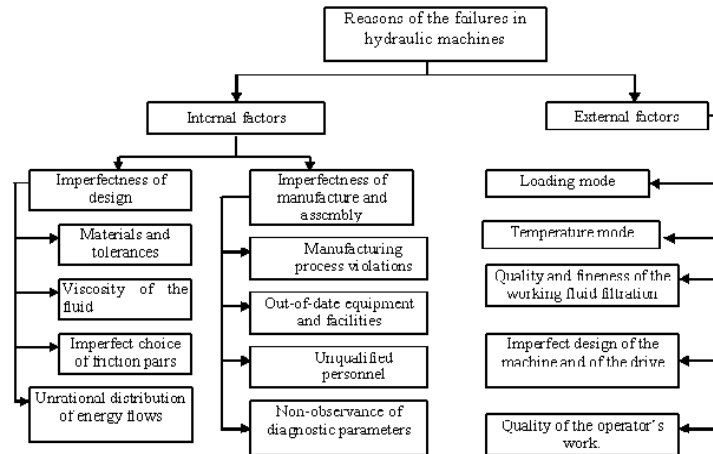
Fig. 7 – Reasons of the failures in hydraulic machines.

Hydraulic system failures can be divided into two groups: failures having no influence (to a certain time) on the machine operation, *e.g.* increased losses, temperatures and failures that influence the machine operation, for instance, by productivity reduction.

The algorithm of search and removal of failures includes, first of all, revealing the character of a failure (diagnostic signs: sharp variations of pressure in the system, insufficient speed of the working member, etc.); determination of the hydraulic drive parameters that could cause a failure (diagnostic parameters: pressure, flow rate, working fluid direction, motion); detection and analysis of hydraulic equipment that caused a failure in the system: pump station (pump) – high-pressure sleeves – hydraulic actuators (hydraulic motor, hydraulic cylinder) – control devices (valves, regulators, sensors); failure removal or replacement of the equipment (device) with a new one; analysis of the reasons that caused a failure.

3. Conclusion

1. Effectiveness of the planned preventive maintenance and repairs of the machine drives is insufficient. The flow of failures remains at a rather high level and the expenses are not always justified.

2. Combined systems show better results when maintenance and repairs are conducted taking into account actual technical condition of the drive.

3. Optimization of a range of activities in order to exclude the causes of

failures in hydraulic drives will make it possible to reduce the number of idle periods and their duration. Introduction of the system of the hydraulic drive continuous diagnostics will enable obtaining significant economic efficiency from optimization of the expenses for ensuring failure-free hydraulic system operation.

REFERENCES

Бродский Г.С., Слесарев Б.В., *Повышение надежности гидропривода - средство эффективного внедрения гидравлических экскаваторов на горных предприятиях СНГ*. "Горная промышленность", *2*, 54-57 (2002).

Савуляк В.І., Семічаснова Н.С., *Визначення пускових характеристик гідроприводів "Промислова гідравлика та пневматика"*. *4*, 2010.

Свешников В.К., Иванов А.О., *Дмитриевич Ю.В. Основные пути повышения надежности гидроприводов*. HPD. Гидравлика. Пневматика. Приводы, №1(3), 2010. – 4-7с.

Сырицын Т.А., *Эксплуатация и надежность гидро- и пневмоприводов*. Т.А. Сырицын, М.: Машиностроение, 247 (1990).

ASIGURAREA FUNCŢIONĂRII FIABILE A ACTIONĂRILOR HIDRAULICE CU MOTOARE HIDRAULICE

(Rezumat)

Conform indicaţiilor specifice acţionările hidraulice ocupă primele locuri printre alte tipuri de acţionări. Majoritatea utilajelor tehnologice operează în mod frecvent cu porniri, opriri, mers înapoi. Aceasta necesită considerarea factorilor care influenţează acţionarea hidraulică din etapa de proiectare. Îmbunătăţirea utilajelor implică cerinţe ridicate a capacităţii de poziţionare cu acurateţe, viteza sau calitatea proprietăţilor dinamice, îmbunătăţirea caracteristicilor iniţiale şi a fiabilităţii.

Factorii care influenţează fiabilitatea acţionărilor hidraulice sunt determinate şi sunt cele mai semnificative. Pe baza abordării sistemului a fost efectuat un clasament al factorilor. Următorii factori sunt dovedit a fi cei mai importanţi: corectitudinea proiectării tribologiei, distribuirea raţională a fluxurilor de energie disipată în acţionarea hidraulică, măsuri organizatorice şi constructive care ajută la reducerea sarcinii în timpul proceselor de pornire şi de mers înapoi.

Studii experimentale şi modelare pe calculator au fost realizate ţinând seama de caracteristicile non-lineare a acţionărilor hidraulice. Sunt determinaţi principalii factori care influenţează caracterul proceselor tranzitorii de pornire. Următorii factori au cea mai mare influenţă: respectarea liniei de acţionare hidraulică, prezenţa frecării de rulare în actuatori, solicitarea iniţială, proprietăţile uleiului şi influenţa aditivilor pe suprafaţa activă.

MODELLING OF THE PROCESS OF REGULAR PROFILES STAMPING FROM SHEET MATERIALS

BY

V. SAVULIAK[*]

Vinnytsia National Technical University

Abstract. Designing the technology of sheet blanks stamping is accompanied with the problems of limited plasticity of materials with high carbon content or alloys. As a result, damages of different types appear in the places of deformation and stress concentration. In general case they are caused by limited plasticity of the material. This problem is traditionally solved by experimental selection of the points of deformation process division into stages with plasticity restoration by intermediate annealing. At the same time there is a possibility to simplify the technological process in a number of cases by a rational choice of the deformation parameters. A limitation consists in the absence of sufficiently accurate calculation models and methods. This paper proposes a model and a calculation algorithm for this purpose. The models takes into account energy losses and additional stresses caused by the sheet slipping during deformation and the friction forces involved in this process. The measures on minimization of friction coefficient between the sheet and the stamping tool are shown to be feasible.

Key words: pressure, stamping, friction, calculation algorithm.

1. Introduction

Production efficiency depends, to a great extent, on the possibility to use resource-saving technologies. In particular, these include stamping

---

[*] Corresponding author; *e-mail:*

processes. A majority of them is based on the matrix–workpiece–punch interaction for sheet material forming. This technology requires studying the influence of friction parameters and geometrical characteristics of equipment on the workpiece strained condition in order to control it.

For modeling the process of forming regular profiles on sheet materials by stamping on presses it is feasible to consider the following stages: 1) working stroke of the punch up to its contact with the sheet; 2) from the beginning of the punch contact with the sheet to the moment when the punch stops; 3) idle stroke of the punch (unloading of the sheet). The second stage is a decisive one as it determines the process capabilities, tooling design and characteristics of the product. During the working stroke, at the moment when the punch – sheet – matrix surfaces come into contact, normal forces appear between the surfaces. As a result of elastoplastic deformation of the sheet, its slippage between the working surfaces of the matrix and the punch can be observed, which causes the emergence of friction forces. For slippage to occur, the tensile force value must be sufficient to overcome friction forces between the matrix – sheet and the sheet – punch elements (Fig.1).
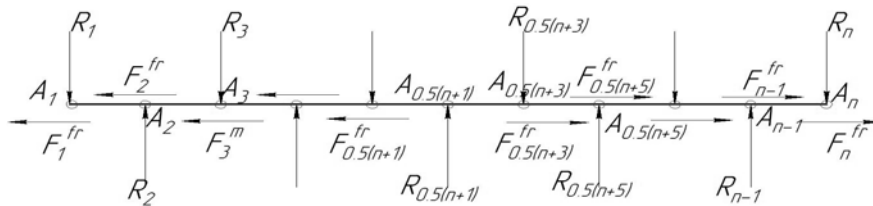
Fig. 1 – The scheme of action of forces on the sheet workpiece during stamping process.

It should be also noted that in the process of simultaneous creation of a large number of corrugations such tensile forces will be partially balanced relative to the symmetry axis and the workpiece will be subjected to bending with simultaneous extension.

Under real conditions, when the matrix and the punch have deviations from the ideal form whereas the sheet has deviations from homogeneity, pulling up of the sheet will not be necessarily directed to the symmetry axis of the workpiece. Therefore, workpiece dimensions must exceed the limit ones and after stamping the operation of cutting the sheet remains should be performed.
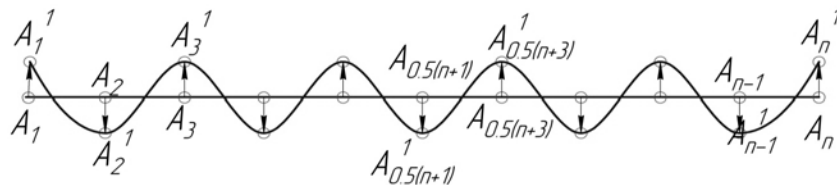
Fig. 2 – The scheme of the sheet form changes in the process of stamping.

At each of the points A_1, A_2, A_3, ...A_{n-1}, A_n (fig.3) apart from reactions R_1, R_2, R_3, ...R_{n-1}, R_n there emerge corresponding friction forces F_1^{fr}, F_2^{fr}, F_3^{fr}, ...F_{n-1}^{fr}, F_n^{fr}. They can be calculated by the simplified Coulomb formula:

$$F_i^{fr} = R_i \cdot f \tag{1}$$

where f is friction coefficient.

Friction force vector is always directed opposite to speed vector that coincides with the sheet slippage direction. Analysis of the action of forces during stamping process (the scheme is presented in Fig. 1) shows that in the middle of the workpiece at the contact point $A_{0,5(n+1)}$ ($n=5,7,9...$) balance of forces is observed and, therefore, the sheet can slip only in the direction of $A_{0,5(n+1)}$. As during deformation the length of the section $A_i^1 - A_{i+2}^1$ ($i=1, 2, 3... 0,5 \cdot (n-3)$) increases (Fig. 2) as compared to the distance between corresponding neighbouring points $A_i - A_{i+2}$, in the forming process the following three variants are possible: 1) as the length of $A_i^1 - A_{i+2}^1$ increases, the sheet slips between the matrix and the punch in the direction of the stamp centre at point $A_{0.5(n+1)}$ and, therefore, tension is reduced; 2) deformation takes places only due to the local forming of the regular profile separate part; 3) slippage of the material takes place with simultaneous local stretching. For the sheet to move (to slip) relative to point A_i it is necessary that:

1. the sheet tension force will exceed the total friction force $\sum_{k=1}^{i-1} F_k^{fr}$;

2. the energy of the sheet deformation at points $A_1 - A_{i-1}$ (bending and straightening) will be lower than the energy spent on the sheet extension.

Let us write the sheet slippage condition

$$E_{slip} \geq E_{def} + E_{fr} \tag{2}$$

where E_{slip} – the work, that would have been done during the sheet extension without slippage; E_{def} – work performed during bending-unbending of the sheet sections in the interval $A_1 - A_{i-1}$ (Fig. 3); E_{fr} – the work of friction forces in the interval $A_1 - A_{i-1}$. If bending deformation of the sheet section is elastic, then $E_{def} = 0$.

If the section with the length l_{i-1} moved through point A_{i-1} towards A_i, then the total work of the friction forces will be given by
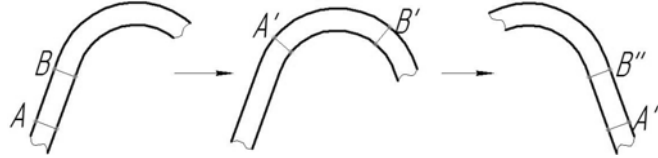
Fig. 3 – The scheme of the possible slippage of the sheet
section in the process of stamping.

$$E_{fr} = \sum_{k=1}^{i-1} \left(F_k^{fr} \cdot l_k \right), k=1, 2, 3, \ldots, 0{,}5 \cdot (n-3). \tag{3}$$

We can also write that

$$E_{def} = \sum_{k=1}^{i-1} E_k \tag{4}$$

where $E_k = 2E_{spec} \cdot l_k$; E_{spec} – plastic deformation work for bending the sheet
section of unit length to the radius of the curvature of internal surface r.

Work of the sheet tensile deformation is calculated by the formula

$$E_t = \sum_{k=1}^{i-1} l_k \cdot E_{spec.w.} \tag{5}$$

where $E_{spec.w.}$ –work performed for plastic extension of the sheet section with
unit length and constant values of width and thickness.

Proceeding from (3), (4), (5), condition (2) will take the form of

$$\sum_{k=1}^{i-1} l_k \cdot E_{spec.w.} > \sum_{k=1}^{i-1} \left(F_k^{fr} \cdot l_k \right) + 2E_{spec} \sum_{k=1}^{i-1} l_k \tag{6}$$

or

$$E_{spec.w.} > \frac{\sum_{k=1}^{i-1} \left(F_k^{fr} \cdot l_k \right)}{\sum_{k=1}^{i-1} l_k} + 2E_{spec} \tag{7}$$

When condition (7) stops to be satisfied, the stage of the sheet
deformation with its partial slippage begins. Then condition (2) will be
expanded to the form of

$$E_{slip} - E_t = E_{def} + E_{fr} \tag{8}$$

If we assume that the length of the neutral line in section $A_i A_{i-1}$ is equal to L, the length of the neutral line in section $A_{i-1}^1 A_i^1 - L^1$, the sheet extension value in the section $A_{i-1}^1 A_i^1 - l_{yk}$, the value of the sheet slippage in section $A_{i-1}^1 A_i^1 - l_{slipk}$, then from (8) and the equality of the motions and lengths of the sheet we write

$$\begin{cases} l_{yk} + l_{slipk} = L^1 - L, \\ \sum_{k=1}^{i-1} l_{yk} \cdot E_{spec.w.} + \sum_{k=1}^{i-1} \left(F_k^{fr} \cdot l_{slipk} \right) + 0{,}5\left(1 + \frac{1}{\beta} \right) E_{spec} \sum_{k=1}^{i-1} l_{slipk} = \\ = \left(L^1 - L \right) \cdot E_{spec.w.} \cdot (i-1), \end{cases} \qquad (9)$$

where β is Bauschinger coefficient.

On the other side, the length of the neutral line in section $A_{i-1}^1 A_i^1$ (provided that the sheet length is unchanged) is calculated as:

$$L^1 = 2(R+r+s) \, arctg \, \frac{h}{L} + \frac{L}{\cos(arctg(h/L))} - (R+r+s)\frac{h}{L}, \qquad (10)$$

where R and r – the radia of the punch and matrix curvatures; s – the sheet thickness; h – bending deflection of the sheet (Fig.4).
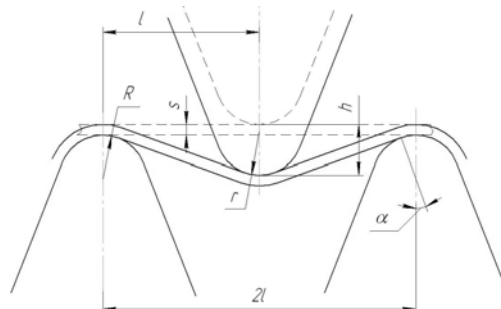
Fig. 4 – The scheme of the sheet deflection in the process of stamping.

Provided that deformation localization is absent, for the case of $\theta = \alpha$ (in the conjugation zone of rectilinear and curvilinear regions), the intensity of stresses σ_u could be conventionally considered equal to $\sigma_{\theta aver}$ and stresses and deformations to be distributed uniformly along the sheet thickness.

It can be assumed that in the rectilinear region between points $A_{i-1}^1 A_i^1$ the strained state corresponds to pure tension. Then, the degree of deformation is calculated as

$$e_u = \ln \frac{l_{yk}}{L}. \tag{11}$$

After solving system (9) we obtain the averaged value of the sheet deformation l_{yk} between points $A_{i-1}^1 A_i^1$. This solution, taking also into account (10), (11), can be used to determine boundary conditions and to calculate the strained state of the sheet in the curvature formation zone.

Mathematical model of the stamping process is based on the condition of elementary volume balance (Сивак & Савуляк, 2004; Савуляк, 2004):

$$2\sigma_{\theta aver} \cdot s \cdot \frac{\Delta \varphi}{2} = \sigma_{tool} \cdot \Delta \varphi \cdot (R_1 - s) - p \cdot R \cdot \Delta \varphi, \tag{12}$$

balance equations for flat strained state (Попов, 1977):

$$\begin{cases} \dfrac{\partial \sigma_\rho}{\partial \rho} + \dfrac{1}{\rho} \cdot \dfrac{\partial \tau_{\rho\theta}}{\partial \theta} + \dfrac{\sigma_\rho - \sigma_\theta}{\rho} = 0; \\[2mm] \dfrac{\partial \sigma_\rho}{\rho \partial \theta} + \dfrac{\partial \tau_{\rho\theta}}{\partial \rho} + 2\dfrac{\tau_{\rho\theta}}{\rho} = 0, \end{cases} \tag{13}$$

set of constraint equations:

$$\begin{cases} \sigma_\rho - \sigma = \dfrac{2}{3}\sigma_u \dfrac{\dot{\varepsilon}_\rho}{\dot{\varepsilon}_u}, \\[2mm] \sigma_\theta - \sigma = \dfrac{2}{3}\sigma_u \dfrac{\dot{\varepsilon}_\rho}{\dot{\varepsilon}_u}, \\[2mm] \sigma_z - \sigma = \dfrac{2}{3}\sigma_u \dfrac{\dot{\varepsilon}_\rho}{\dot{\varepsilon}_u}, \\[2mm] \tau_{\rho\theta} = \dfrac{1}{3}\sigma_u \dfrac{\dot{\gamma}_{\rho\theta}}{\dot{\varepsilon}_u}, \end{cases} \tag{14}$$

$$\sigma_u = A e_u^n \tag{15}$$

and the continuity condition

$$\dot{\varepsilon}_\rho + \dot{\varepsilon}_\theta + \dot{\varepsilon}_z = 0, \tag{16}$$

where $\sigma_{\theta aver}$ – average tangential stress ($\sigma_{\theta aver} = A\left(\ln \dfrac{l_{yk}}{L}\right)^n$); σ_{tool} – stress on the surface of contact with the tool; s – thickness of the sheet; R_1 – external radius

of the workpiece curvature correspondingly; p – distributed pressure on the sheet surface (for the case under consideration $p = 0$); $\Delta\varphi$ – angle of the marked region of the sheet; σ_ρ, σ_θ, σ_z, $\tau_{\rho\theta}$ – normal and tangential stresses; $\dot{\varepsilon}_\rho$, $\dot{\varepsilon}_\theta$, $\dot{\varepsilon}_z$ – deformation rates in the corresponding directions; $\dot{\gamma}_{\rho\theta}$ – shear deformation rate; $\sigma = \frac{1}{3}\sigma_{ij}\delta_{ij}$ – average stress (hydrostatic pressure); A and n – parameters of the material hardening curve; e_u – deformation degree.

Deformation rates are determined from:

$$\begin{cases} \dot{\varepsilon}_\rho = \dfrac{\partial \vartheta_\rho}{\partial \rho}; \\[2mm] \dot{\varepsilon}_\theta = \dfrac{\partial \vartheta_\theta}{\rho\partial\theta} + \dfrac{\vartheta_\rho}{\rho}; \\[2mm] \dot{\varepsilon}_z = \dfrac{\partial \vartheta_z}{\partial z}; \\[2mm] \dot{\gamma}_{\rho\theta} = \dfrac{\partial \vartheta_\theta}{\partial \rho} + \dfrac{\partial \vartheta_\rho}{\rho\partial\theta} - \dfrac{\vartheta_\theta}{\rho}. \end{cases} \tag{17}$$

To solve the set of equations (12-17) we accept the hypothesis that intensity of stresses $\sigma_u = \sigma_u(e_u)$ and $\sigma_u \neq \sigma_u(\rho,\theta)$ while functional dependence of the speeds υ_θ and υ_z of the material points movement is linear (Савуляк, 2006).

$$\begin{cases} \vartheta_\theta = a(\theta)\cdot(\rho - \rho_n) = a\cdot(\rho - \rho_n), \\ \vartheta_z = bz + k, \end{cases} \tag{18}$$

where ρ_n – radius of the neutral surface curvature

$$\rho_n = \sqrt{Rr\exp\dfrac{-\sigma_{tool}}{A\left(0.5\ln\dfrac{r+s}{r}\right)^n}}.$$

By substitution of (18) and (17) into (16) we obtain:

$$\vartheta_\rho = a'\left(\rho_n - \dfrac{\rho}{2}\right) - b\dfrac{\rho}{2} + \dfrac{c}{\rho} \tag{19}$$

where $a' = \dfrac{\partial a(\theta)}{\partial\theta} = \dfrac{\partial a}{\partial\theta}$; c – constant.

By substitution of (18) and (19) into (16) after reduction we obtain

$$\begin{cases} \dot{\varepsilon}_\rho = -\dfrac{a'}{2} - \dfrac{c}{\rho^2} - \dfrac{b}{2}; \\[2mm] \dot{\varepsilon}_\theta = \dfrac{a'}{2} - \dfrac{b}{2} + \dfrac{c}{\rho^2}; \\[2mm] \dot{\varepsilon}_z = b; \\[2mm] \dot{\gamma}_{\rho\theta} = a + \dfrac{a''(2\rho_n - \rho)}{2\rho}, \quad a'' = \dfrac{\partial^2 a}{\partial\theta^2}. \end{cases} \tag{20}$$

If we assume that deformation in the direction of the axis z is inconsiderable or constant we can take $b = 0$. Then (20) will be transformed into:

$$\begin{cases} \dot{\varepsilon}_\rho - \dot{\varepsilon}_\theta = -a' + \dfrac{2c}{\rho^2}; \\[2mm] \dot{\varepsilon}_\theta - \dot{\varepsilon}_z = \dfrac{a'}{2} + \dfrac{c}{\rho^2}; \\[2mm] \dot{\varepsilon}_z - \dot{\varepsilon}_\rho = \dfrac{a'}{2} + \dfrac{c}{\rho^2}. \end{cases} \tag{21}$$

Function $a(\theta)$ is determined from the system of equations (20) provided that deformations $\varepsilon_\rho = 0$, $\varepsilon_\theta = 0$, $\gamma_{\rho\theta} = 0$ for $\rho = \rho_n$. Deformations were found as a double integral of the corresponding deformation rates relative to the coordinates ρ and θ. Then function $a(\theta)$ will have the form of

$$a(\theta) = \frac{k_1}{\sqrt{\ln\rho_n - 0,5}}\cos\frac{\theta}{\sqrt{\ln\rho_n - 0,5}} - \frac{k_2}{\sqrt{\ln\rho_n - 0,5}}\sin\frac{\theta}{\sqrt{\ln\rho_n - 0,5}} \tag{22}$$

where $k1, k2$ – constants.
Taking into account (24), equation (22) will take the form of

$$\begin{cases} \dot{\varepsilon}_\rho = \dfrac{1}{2\ln\rho_n - 1}\left(k_1\cdot\sin\dfrac{\theta}{\sqrt{\ln\rho_n - 0,5}} + k_2\cdot\cos\dfrac{\theta}{\sqrt{\ln\rho_n - 0,5}}\right) - \dfrac{c}{\rho^2}, \\[3mm] \dot{\varepsilon}_\theta = \dfrac{-1}{2\ln\rho_n - 1}\left(k_1\cdot\sin\dfrac{\theta}{\sqrt{\ln\rho_n - 0,5}} + k_2\cdot\cos\dfrac{\theta}{\sqrt{\ln\rho_n - 0,5}}\right) + \dfrac{c}{\rho^2}, \\[3mm] \dot{\varepsilon}_z = 0, \\[3mm] \dot{\gamma}_{\rho\theta} = \left(k_1\cdot\cos\dfrac{\theta}{\sqrt{\ln\rho_n - 0,5}} - k_2\cdot\sin\dfrac{\theta}{\sqrt{\ln\rho_n - 0,5}}\right)\dfrac{\rho\ln\rho_n - \rho_n}{\rho(\ln\rho_n - 0,5)^{1,5}}. \end{cases} \tag{23}$$

For flat state of strain:

$$\dot{\varepsilon}_u = \frac{\sqrt{2}}{3}\sqrt{\left(\dot{\varepsilon}_\rho - \dot{\varepsilon}_\theta\right)^2 + \left(\dot{\varepsilon}_\theta - \dot{\varepsilon}_z\right)^2 + \left(\dot{\varepsilon}_z - \dot{\varepsilon}_\rho\right)^2 + \frac{3}{2}\dot{\gamma}_{\rho\theta}^2}. \tag{24}$$

After simple transformations, from (13) and (14) we obtain

$$\begin{cases} \dfrac{\partial \sigma_\rho}{\partial \rho} = -\dfrac{1}{\rho} \cdot \dfrac{\partial \tau_{\rho\theta}}{\partial \theta} - \dfrac{2}{3}\sigma_u \dfrac{\dot{\varepsilon}_\rho - \dot{\varepsilon}_\theta}{\rho\dot{\varepsilon}_u}; \\ \dfrac{\partial \sigma_\rho}{\partial \theta} = \dfrac{\partial \sigma_\theta}{\partial \theta} + \dfrac{2}{3}\sigma_u \dfrac{\partial}{\partial \theta}\left(\dfrac{\dot{\varepsilon}_\rho - \dot{\varepsilon}_\theta}{\dot{\varepsilon}_u}\right). \end{cases} \tag{25}$$

According to the formula of the total differential equation for the function of several variables

$$\sigma_\rho = \int \frac{\partial \sigma_\rho}{\partial \rho}\, d\rho + \int \frac{\partial \sigma_\rho}{\partial \theta}\, d\theta \tag{26}$$

By substitution of (15), (23), (24) and (25) into (26), taking into account boundary conditions (for $\rho = r$ $\sigma_\rho = \sigma_{tool}$ i $\sigma_\theta = \sigma_{tool} \cdot f$; for $\rho = R_1$ $\sigma_\rho = 0$; for $\theta=\alpha$ $\sigma_u = \sigma_{\theta aver}$) we can obtain characteristic of the strained state during stamping process, the sheet slippage and friction forces being taken into account.

3. Conclusion

1. Mathematical model of the workpiece forming from sheet material makes it possible to calculate permissible deformations and radia of the curvature in the points of localization of stresses and deformations.

2. Analysis of the stress change character for the flat state of stress has shown that normal stresses are practically independent from the taper angle when it value are in the range from 0 to 1 radian. At the same time the taper angle has a considerable on shear stress.

3. Application of stamping schemes with minimal friction coefficient between the workpiece–matrix–punch reduces tangential normal stresses and softens the stressed state scheme.

REFERENCES

Савуляк В.В., *Деформація і напружений стан тонколистових матеріалів в процесі формування гофрів*. Вісник Донбаської державної машинобудівної академії, *1* (*3*), 48-53 (2006).

Савуляк В.В., *Штампування гофрованих заготовок малих радіусів кривизни з використанням гідростатичного підпору*. Вісник ВПІ, *5*, 74-76(2004).

Сивак І.О., Савуляк В.В., *Штампування гофрованих заготовок з використанням гідростатичного підпору // Удосконалення процесів та обладнання обробки тиском в металургії і машинобудуванні*. Краматорськ: ДДМА, 331–335 (2004).

Попов Е.А., *Основы теории листовой штамповки*. М.: Машиностроение, 278 (1977).

MODELAREA PROCESULUI DE ŞTANŢARE A PROFILELOR REGULATE DIN TABLĂ

(Rezumat)

Proiectarea tehnologiei de ştanţare este însoţită de problemele provocate de limita de plasticitate a materialelor cu un conţinut ridicat de carbon sau elemente de aliere. Ca urmare, apar diferite tipuri de defecte în locurile de deformare şi de concentrare a solicitărilor În general, ele sunt cauzate de plasticitatea limitată a materialului. Această problemă este rezolvată în mod tradiţional prin selectarea experimentală a punctelor de divizare procesului de deformare în etape, cu îmbunătăţirea plasticităţii prin recoaceri intermediare. În acelaşi timp, există o posibilitate de a simplifica procesul tehnologic într-un număr de cazuri prin alegerea raţională a parametrilor de deformare. O limitare constă în lipsa unor modele şi a unor metodelor de calcul suficient de precise. Aceasta lucrarea propune un model şi un algoritm de calcul în acest scop. Modelele iau în considerare pierderile de energie, tensiunile suplimentare cauzate de alunecarea tablei în timpul deformării şi forţele de frecare implicate în acest proces. Măsurile privind reducerea de coeficientul de frecare dintre tablă şi ştanţă sunt fezabile.

CONSTRUCTION OF PLASTICITY DIAGRAMS ON THE BASIS OF LIMIT FORMING DURING UPSETTING PROCESS

BY

I. SIVAK[*], V. SAVULYAK and J. CHORNA

Vinnitsa National Technical University, Ukraine

Abstract. The analysis of processes of cold deformation requires knowledge of materials behaviour under forming. For this purpose curves and surfaces of plastic deformation are used. The paper considers the method of the plasticity diagram construction on the basis of experimental research of cylindrical samples upsetting with different friction conditions at their end surfaces. Three groups of experiments were conducted – with lubrication of the end surfaces, without their lubrication and with clamped edges. Intensity of deformation and index of the stressed state were calculated in accordance with the proposed dependencies. An inverse problem of finding the limit deformation was solved. Approximation of the limit deformation curves was conducted in accordance with the dependence proposed by V. Ogorodnikov.

Key words: plasticity, upsetting, limit deformation curve.

1. Introduction

For limit forming estimation in the process of plastic metal working deformability criteria are used to determine the boundaries of deformation

---

[*] Corresponding author; *e-mail:*

(Колмогоров, 1970; Дель, 1978; Огородников *et al.*, 2005). In most of such criteria plasticity diagrams are used to estimate the influence of the stress scheme on the plasticity of metals. A plasticity diagram describes experimental dependence of limit deformation e_p on the stressed state stiffness η determined by the formulas

$$\mathring{a}_{\partial} = \int\limits_{0}^{t_p} \dot{\varepsilon}_u d\tau, \tag{1}$$

$$\eta = \frac{3\sigma}{\sigma_u}, \tag{2}$$

where t_p – deformation time until macrocracks appear; $\dot{\varepsilon}_u$ - deformation rate intensity; $\sigma = \frac{1}{3}\sigma_{ij}\delta_{ij}$ - mean stress; σ_u - stress intensity.

The accuracy of the used plasticity resource calculation depends, to a great extent, on how accurately the dependence of e_p on η is constructed. This paper proposes a method to construct the plasticity diagram $e_p(\eta)$ in the value range of *-1≤η ≤0*. To achieve this, metal plasticity investigation procedure was developed for cylindrical samples upsetting tests. Let us determine limit deformation e_p during upsetting of the samples with the height and the diameter h_0 and r_0 in initial condition and h, r – in the deformed state. Let us assume that samples are compressed by two rigid plates that move one towards the other with relative velocity ϑ/r. If friction forces in the contact region of the samples and plates are ignored, deformation rate in the direction of the z-axis will equal:

$$\dot{\varepsilon}_z = -\frac{\vartheta}{h}, \tag{3}$$

where υ - the speed of one plate motion.

Radial and circular components of the deformation rate tensor are given by:

$$\dot{\varepsilon}_r = \frac{d\vartheta_r}{dr}, \quad \dot{\varepsilon}_\varphi = \frac{\vartheta_r}{r}. \tag{4}$$

Let us substitute (3) and (4) into incompressibility condition:

$$\dot{\varepsilon}_z + \dot{\varepsilon}_r + \dot{\varepsilon}_\varphi = 0 \tag{5}$$

Then:

$$\frac{d\upsilon_r}{dr} + \frac{\upsilon_r}{r} - \dot{\varepsilon}_z = 0, \tag{6}$$

Or:

$$\frac{d}{dr}(r\upsilon_r) = -\dot{\varepsilon}_z r \tag{7}$$

After integration of (6), taking into account that according to formula (3) $\dot{\varepsilon}_z$ does not depend on r, we obtain:

$$\upsilon_r = -\frac{\dot{\varepsilon}_z r}{2} + \frac{c}{r}. \tag{8}$$

We find integration constant from the condition that for solid cylindrical sample if $r = 0$, $\upsilon_r = 0$. From this we find that c = 0.

$$\upsilon_r = -\frac{\dot{\varepsilon}_z r}{2} \tag{9}$$

According to formula (4) we have:

$$\dot{\varepsilon}_r = \dot{\varepsilon}_\phi = -\frac{\dot{\varepsilon}_z}{2} \tag{10}$$

Then we obtain the expression for deformation rate intensity $\dot{\varepsilon}_u$:

$$\dot{\varepsilon}_u = -\dot{\varepsilon}_z = \frac{\upsilon}{h} \tag{11}$$

In accordance with formula (1) we obtain the formula for the limit value of deformation degree e_p:

$$e_p = \int_{h_p}^{h_0} \frac{\upsilon dt}{h} = \int_{h_p}^{h_0} \frac{dh}{h} = \ln\frac{h_0}{h_p} \tag{12}$$

where h_p - the sample height when a macrocrack appears.

In order to determine other experimental values of limit deformation e_p upsetting tests of cylindrical samples were performed with different friction

conditions on their end surfaces. In such tests, a bulge in the form of a barrel is known to emerge. In terms of destruction, the average-height region of the "barrelled" surface is the most dangerous one because due to considerable curvature of the barrelled surface tensile stresses could emerge. Curvature value could be changed by changing the friction conditions in the contact zone of the samples and plates. In this work the upsetting of samples was performed with lubrication, without lubrication and with clamped edges.

In order to determine the strained state in the sample dangerous zone, in the average-height part of its side surface we applied a grid with the step of (2 ± 0,005) mm in the direction of generator and (1±0,005) mm in the direction perpendicular to the generator (Fig. 1).
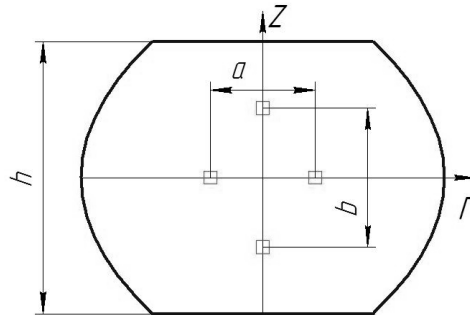
Fig. 1 – The sample with the grid after upsetting
without lubrication of the end surfaces.

The samples were subjected to upsetting in several steps until macrocracks emerged in the equator region. At the end of each step the values of a, b were measured using a toolmaker's microscope and logarithmic deformations were calculated by the formulas (13):

$$e_z = \ln \frac{a}{a_0}, \qquad e_\varphi = \ln \frac{b}{b_0}, \qquad (13)$$

where a_0, b_0, a, b – dimension of the elements of the applied grid in the initial and current states.

At the end of each step the degree of deformation was determined by the formula:

$$e_u = \frac{2}{\sqrt{3}} \sqrt{e_z^2 + e_z e_\varphi + e_\varphi^2} \qquad (14)$$

When cylindrical samples were subjected to upsetting on the free surface radial stress σ_r is zero.

$$\sigma_r = 0. \tag{15}$$

Therefore the stressed state index η at the sample side surface was determined by the formula:

$$\eta = -\frac{2e_r}{e_u} \tag{16}$$

In order to obtain this formula physical equation of deformation plasticity theory:

$$\sigma_r - \sigma = \frac{2}{3}\frac{\sigma_u}{e_u}e_r \tag{17}$$

and condition (15) were used.

To determine the rational component of deformation e_r, incompressibility condition (5) and equation (13) were used.

Experimental study was performed using cylindrical samples made from steel P6M5 with initial dimensions $d_0 = 10$ mm, $h_0 = 15$mm. Part of the samples were subjected to upsetting with lubrication of end surfaces until destruction started. Values of limit deformation e_p, obtained in these tests, were calculated by the formula (12). During upsetting process with lubrication a "barreled" region was not practically created and therefore, it was assumed that $\eta = -1$. For steel P6M5, if $\eta = -1$, limit deformation $e_p(-1)$=1,2. Another set of samples were subjected to upsetting with lubrication of the end surfaces and the third set - with clamped end surfaces (Fig. 2).

The samples of each set were subjected to upsetting to different deformation degrees until macrocracks appeared. According to the distortion of coordinate grid applied to the sample surfaces in the initial state, deformation degree e_u and deformation state index η were determined at each upsetting stage by formulas (14), (16).
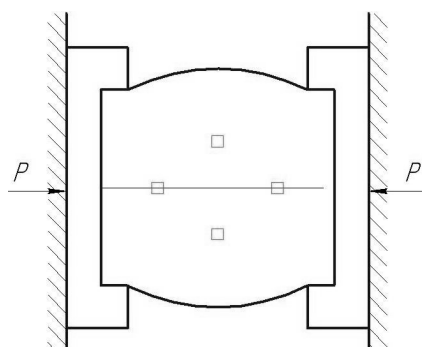
Fig. 2 – Upsetting of the cylindrical samples with clamped end surfaces.

Experimental results were processed using the method of least squares. The obtained relationships e_u and η for the cases of upsetting with friction (curves 1) and upsetting with clamped end surfaces (curves 2) are presented in Fig. 3. From the obtained results it follows that with growing η the plasticity of metal is reduced.

The obtained loading trajectories $e_u(\eta)$ 1 and 2 (see Fig. 3) were used for obtaining plasticity diagrams $e_p(\eta)$. Dependence of $e_p(\eta)$ was approximated by function (Огородников, 1989):

$$e_p(\eta) = e_p(0)\exp(-\lambda\eta) \qquad (19)$$

where $e_p(0)$ – limit deformation for $\eta = 0$; $e_p(-1)$ – limit deformation for $\eta = -1$;

$$\lambda = \ln\frac{e_p(-1)}{e_p(0)}$$

For plasticity diagram construction according to the known dependences $e_u(\eta)$ deformability criterion was used (Огородников *et al.*, 2005):

$$\psi = \int\limits_{0}^{e_p} \frac{de_u}{e_p(\eta)} \qquad (20)$$

and the inverse problem was solved, *i.e.* proceeding from the known values of limit deformation e_p^* and corresponding loading trajectories using formula (20), by the successive approximations method limit deformation e_p was determined, the value of which is plotted in plasticity diagram $e_p(\eta)$. In this way the location of six points that belong to the plasticity diagram was found. The obtained results were used to approximate dependence $e_p(\eta)$ in the range of $-1 \leq \eta \leq 0$ for steel P6M5 by the function.

$$e_p(\eta) = 0{,}21\exp(-1{,}74\eta) \qquad (21)$$

The obtained dependence of limit deformation e_p on the stressed state index η (21) is given in Fig. 3.

Thus, in this work the procedure of plasticity diagram construction is elaborated for value range $-1 \leq \eta \leq 0$ of the stressed state index on the basis of

experimental study of metal plasticity in the upsetting tests of cylindrical samples with different friction conditions at the end surfaces.
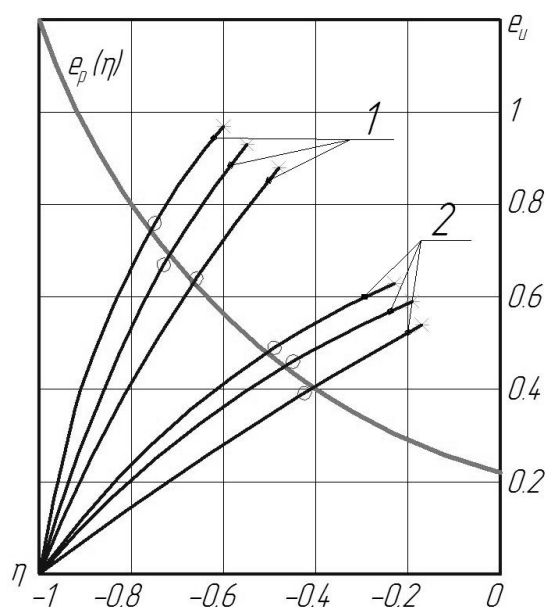
Fig. 3 – Dependence of limit deformation
from the index of the stressed state.

The dependence of e_p on η (21) is in good agreement with the same experimental plasticity diagrams of steel P6M5 obtained by other methods (Огородников, 1989). It should be noted that dependence $e_p(\eta)$ (21) can be also used for a wider range of values of the stressed state index η.

REFERENCES

Дель Г.Д., *Технологическая механика*. – М.: Машиностроение, 174 (1978).

Колмогоров В.Л, *Напряжения, деформации, разрушение*. М.: Металлургия, 229 (1970).

Огородников В.А., *Деформируемусти и разрушение металов при пластическом формоизменении*. К.: УМК ВО, 152 (1989).

Огородников В.А., Киселёв В.Б., Сивак И.О. *Энергия. Деформации. Разрушение.* (*Задачи автотехнической експертизы*). Винница: УНІВЕРСУМ-Вінниця, 204 (2005).

CONSTRUCŢIA DIAGRAMELOR DE PLASTICITATE PE BAZA
LIMITEI DE CURGERE ÎN PROCESUL DE REFULARE

(Rezumat)

Analiza procesului de deformare la rece solicită cunoaşterea comportării materialului la solicitare. Pentru aceasta se folosesc curbe şi suprafeţe de deformare plastică. Această lucrare foloseşte metoda de construcţie a diagramelor de plasticitate bazată pe cercetare experimentală a unor epruvete cilindrice refulate cu condiţii diferite de frecare la capetele acestora. S-au realizat trei grupuri de experimente: cu lubrifiere la capete , fără lubrifiere, şi cu capetele fixate. Intensitatea deformaţiei şi matricea stării de tensiuni au fost calculate în funcţie de dependenţele propuse. Astfel s-a rezolvat o problemă inversă, cea a găsirii limitei de deformare. Aproximarea curbei limitei de deformare a fost realizată în concordanţă cu dependenţa propusă de V. Ogorodnikov.

GLASS BEHAVIOUR AT ABRASIVE JET ENGRAVING

BY

**LAURENŢIU SLĂTINEANU∗, ŞTEFAN POTÂRNICHE,
LORELEI GHERMAN, MARGARETA COTEAŢĂ and NICOLAE POP**

"Gheorghe Asachi" Technical University of Iaşi,
Faculty of Machine Manufacturing and Industrial Management

Abstract. The abrasive jet engraving is applied in order to obtain various inscriptions or drawings on glass objects. This processing method is based on the removal of small quantities of the workpiece material in determined surfaces zones, under the action of the abrasive jet. In the case of the glass, the material removal could be especially generated by micro cracking phenomena. The paper presents some theoretical considerations concerning the base phenomena which develop at the contact of the abrasive jet with the surface layer of the glass workpiece. An experimental research was also developed to better highlight the aspects specific to the abrasive jet engraving of glass workpieces. A mathematical empirical relation was established to show the influence exerted by some work conditions on the roughness of the surface affected by the process of abrasive jet engraving. For the considered experimental conditions, the most significant influence was exerted by the average dimension of the abrasive particles.

Key words: engraving, abrasive jet, glass part, surface roughness, empirical model.

1. Introduction

Engraving is a processing method by which a text or a design is transferred on the surface of a metallic or non-metallic workpiece material.

∗ Corresponding author; *e-mail:* slati@tcm.tuiasi.ro

There are various procedures to achieve the engraving: there are engraving techniques based on chemical reactions, on the thermal material removal or material aspect changing by laser beam (Rusu & Găluşcă, 2010), electron beam, ion beam, on mechanical material removal or aspect changing when ultrasounds or cutting phenomena are used etc. Some of such techniques could be considered and approached as nonconventional machining techniques, especially when additional energy is directed to the work zone (Beşliu *et al.,* 2010).

One of the engraving methods based on the mechanical material removal or material aspect changing is the abrasive jet engraving; it could be efficiently applied especially in the case of brittle materials.

Thus, the abrasive jet engraving could be used to obtain various inscriptions or designs on glass workpieces, by considering the glass brittleness; it is known that the glass is a hard, brittle, translucent and transparent material, characterized by a conchoidal fracture. Just the conchoidal aspect of the fracture refers to a way that brittle materials break when the fracture does not follow any natural planes of separation. Of course, the glass is engraved to obtain inscriptions of designs, but it also could be engraved to diminish or to avoid the complete transparency; in both the cases, the problem of glass machinability by various machining techniques could be approached (Gherman, *et al.,* 2010).

Along the time, the abrasive jet engraving was used in order to apply engraving to the glass workpieces; the researchers tried to obtain additional information concerning this process in order to ensure an optimal development of the process. Thus, Park et al. studied the effect of the impact angle variation on the erosion rate when a powder blasting process is applied to the glass workpieces (Park, *et al.,* 2004). They established a fundamental basis that can be used when powder blasting is applied to obtain micro-mechanical parts of glass. In other paper, Park *et al*., (2004) described the results obtained in studying the micro-grooving of glass; they succeed to obtain grooves having a width of 80 μm and characterized by a surface roughness *Ra*=0.6 – 0.8 μm. They noticed that the machining depth is near proportional to the number of scanning time.

Fan *et al*., (2009) established predictive mathematical models valid for the material removal rate in the case of micro-hole drilling and micro-channel cutting on glasses; these models take into consideration the particle impact parameters, the properties of the target material and some major process parameters. They verified the model capability by experimental investigations.

Ghobeity *et al.,* (2009) studied two methods applicable in order to machine planar areas with increased sidewall slope by using target oscillation and an inclined direction of the abrasive jet; such an oscillation generates steeper sidewalls and it is convenient for application, but a significant mask under-etching could appear.

2. Theoretical Considerations

The abrasive jet is obtained by introducing abrasive particles in a jet of compressed air; this is achieved in a so-called blasting gun. A flexible tube ensures the connection of the gun to the compressor; the abrasive particles are absorbed in the blasting gun from a recipient due to the depression generated at the decrease of the cross section area of the tube by which the compressed air is sent to the nozzle (Fig. 1).
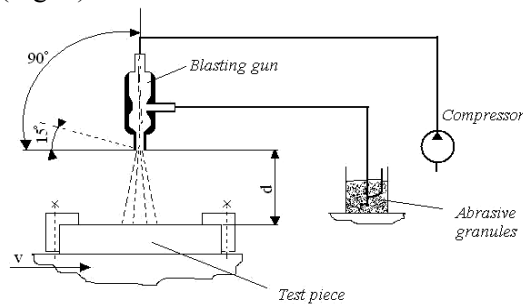
Fig. 1 – Obtaining the abrasive jet.

Initially, the abrasive jet has a cylindrical shape, but due to the decrease of the pressure from the axis of the abrasive jet to the atmospheric pressure found round of the jet, the abrasive particles transported by the compressed air change their direction and the jet becomes conical. The kinetic energy corresponding to a single abrasive particle having a mass m_g and a speed v is given by the relation:

$$W = \frac{m_g v^2}{2} \tag{1}$$

The abrasive particle having the kinetic energy W arrives in contact with the workpiece surface; by taking into consideration the particle energy and the properties of the workpiece surface layer, various effects could be generated; these effects could be the results of the elastic, plastic or fragile behaviour of the workpiece material.
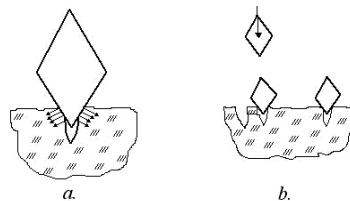
Fig. 2 – Phenomena at the impact of the abrasive particles with the test piece material:
a – microcracking phenomena; b – separating particles from the test piece material.

In the case of the glass workpiece, the main effect could be generated by the fragile behaviour of the material. It is expected that as results of the abrasive particle impact with the surface layer, initially many microcracks appear (Fig. 2 *a*) and, finally, by the joining of such microcracks, small particles are separated and removed from the workpiece material. The presence of the microcracks diminishes the resistance of the surface layer to the action of the abrasive jet and, thus, small particles could be separated from the test piece material (Fig. 2 *b*).

3. Experimental Results

In order to study the influence exerted by various factors on the results of glass engraving process, an experimental research was designed and developed. A blasting gun type 650R (Prodif Air comprimé - France) was used to obtain the abrasive jet; the blasting gun was connected to an air compressor which ensured a pressure of about 0.588 MPa. Sand particles having a known average dimension were absorbed in the compressed air from a recipient. The experiment developed in accordance with the request specific to a planned factorial experiment with three variables at two levels. The variables were the distance between the nozzle and the test piece (d_{min}=10 mm and d_{max}=40 mm), the angle of inclination between the axis of the abrasive jet and the plane surface of the test piece (α_{min}=15º and α_{max}=90º) and the average dimensions of the particles (g_{min}=0.35 mm and g_{max}=1.6 mm).

The experimental conditions and results are presented in table 1; the results were mathematically processed by means of software based on the method of the smallest squares (Creţu, 1992). Thus, the following empirical relation was established:

$$Ra = 3.66g^{0.385}d^{0.0246}\alpha^{0.131} \qquad (2)$$

Table 1
Experimental Conditions and Results

Exp. no.	Independent variables			Surface roughness parameter, Ra, µm			
	Average size of the particles, mm	Distance d, mm	Angle α, °	Ra_1	Ra_2	Ra_3	Average value
1	2	3	4	5	6	7	8
1	0.35	10	15	3.37	3.93	3.71	3.6700
2	0.35	10	90	4.48	3.83	3.98	4.0967
3	0.35	40	15	2.94	2.91	3.00	2.9500
4	0.35	40	90	4.20	4.05	3.61	3.9533
5	1.6	10	15	5.59	7.17	4.54	5.7667
6	1.6	10	90	5.81	7.53	7.62	6.9867
7	1.6	40	15	5.86	6.14	5.00	5.6667
8	1.6	40	90	6.59	8.96	8.44	7.9967

The empirical model defined by the relation (2) shows that among the three considered factors (average dimension g of the abrasive particles, distance d between the nozzle and the plane surface of the test piece and the angle α between the abrasive jet and the plane surface of the test piece), the most significant influence is exerted by the average dimension g of the abrasive particles, whose exponent in the relation (2) is maximum (0.385>0.131>0.0345).
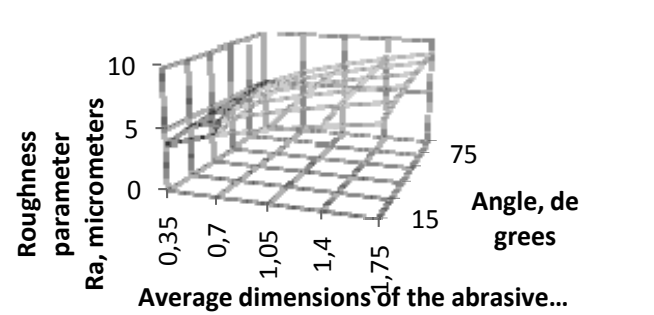
Fig. 3 − Influence exerted by the average dimension of the abrasive
particles and by the angle of inclination on the size of the roughness parameter Ra.

For the considered experimental conditions, the distance d practically does not exert influence on the surface roughness parameter Ra (the size of the exponent attached to the distance d is very low). A graphical representations corresponding to the relation (2) is shown in Fig. 3.

4. Conclusion

The abrasive jet engraving could be used to transfer drawings and inscriptions on parts made of hard enough materials. The abrasive jet is generally obtained by means of devices type blasting guns. Within the laboratory for non-conventional technologies from the "Gheorghe Asachi" Technical University of Iaşi, some theoretical researches were developed to explain the phenomena which develop during applying the abrasive jet engraving of glass parts. Experimental researches were performed to highlight the influence exerted by some parameters characterizing the work conditions (average dimension of the abrasive particles, distance between the nozzle and the test piece, angle between the direction of the abrasive jet and the plane surface of the test piece) on the surface roughness parameter Ra. By mathematical processing of the experimental results, an empirical model valid in the case of the surface roughness parameter Ra was established. One may notice that for the considered experimental conditions, the most significant factor able to influence the size of the surface roughness parameter Ra is the average dimension of the abrasive particles.

REFERENCES

Beşliu I., Schulze H.P., Coteaţă M., Amarandei D. *Study of the Dry Electrical Discharge Machining*. International Journal of Material Forming, **3**, Suppl., 1107-1110 (2010).

Creţu G., *Fundamentals of the Experimental Research. Handbook for the Laboratory Activities* (in Romanian). Institutul Politehnic din Iaşi (1992).

Fan J.M., Wang C.Y., Wang J., *Modelling the Erosion Rate in Micro-Abrasive Air Jet Machining of Glasses*. Wear, **266,** 968-974 (2009).

Gherman L., Petroi D., Iosub L., Isachi D., Coteaţă M., *Machinability Evaluation by the Constant Feed Force Method*. Bul. Inst. Polit. din Iaşi, **LVI** (**LX**), *2b*, S. Construcţii de Maşini, 243-250 (2010).

Ghobeity A., Papini M., Spelt J.K., *Abrasive Jet Micro-Machining of Planar Areas and Transitional Slopes in Glass Using Target Oscillation*. Journal of Materials Processing Technology, **209**, 5123-5132 (2009).

Park D.S., Cho M.W, Lee H., *Effects of the Impact Angle Variations on the Erosion Rate of Glass In Powder Blasting Process*. International Journal of Advanced Manufacturing Technology, **23**, 444–450 (2004).

Park, D.S., Cho M.W., Lee H., Cho W.S., *Micro-Grooving of Glass Using Micro-Abrasive Jet Machining*. Journal of Materials Processing Technology, **146**, 234–240 (2004).

Rusu S., Găluşcă D.G., *Laser Marking of Materials: Principles and Processes*. Bul. Inst. Polit. din Iaşi, **LVI** (**LX**), *4*, S. Ştiinţa şi ingineria materialelor, 71-84 (2010).

COMPORTAREA STICLEI LA GRAVAREA CU JET ABRAZIV

(Rezumat)

Gravarea cu jet abraziv se utilizează pentru a se obţine diverse inscripţii pe obiecte din sticlă. Această metodă de prelucrare se bazează pe îndepărtarea unor mici cantităţi din materialul semifabricatului, în zone de suprafaţă determinate, sub acţiunea jetului abraziv. În cazul sticlei, îndepărtarea materialului ar putea fi generată în special de fenomenele microfisurare. Lucrarea prezintă câteva consideraţii teoretice privind fenomenele de bază care se dezvoltă la contactul jetului abraziv cu stratul de suprafaţă al semifabricatului din sticlă. A fost de asemenea realizată o cercetare experimentală, pentru a sublinia mai bine aspectele specifice gravării cu jet abraziv a semifabricatelor din sticlă. A fost determinată o relaţie matematică empirică, pentru a evidenţia influenţa exercitată de unele condiţii de lucru asupra rugozităţii suprafeţei afectate de procesul de gravare cu jet abraziv.

INTER-BRANCH CONNECTIONS MODELING

BY

CRISTINA MARIA STOICA[∗]

University "PETRE ANDREI" from Iaşi

Abstract. Between the different branches of economy, there are production connections called inter-branch connections. Mathematical models which describe inter-branch connections are called inter-branch balance models, or "expenditures-production" models. These models are based on the inter-branch balance, represented by a table which delineates production and organization of production on different branches, inter-branch connections, use of material and workforce resources, creation and allotment on national income.

Key words: inter-branch balance, expenses coefficients, technological matrix, expenses matrix.

1. Introduction

Between the different branches of economy, there are production connections called inter-branch connections. Mathematical models which describe inter-branch connections are called inter-branch balance models, or "expenditures-production" models. These models are based on the inter-branch balance, represented by a table which delineates production and organization of production on different branches, inter-branch connections, use of material and workforce resources, creation and allotment on national income.

In order to devise the inter-branch connections' table, we need to formulate the list of branches which will be a part of the inter-branch balance.

[∗] Corresponding author; *e-mail:*

Let n be the number of branches in the inter-branch balance. The general image of the balance is pictured in Table 1. All branches are represented in the balance, each of them twice: as producer of goods and services and, at the same time, as consumer of goods and services.

The i line designates the i branch as producer (i = l, n), whereas the j column designates the j branch as consumer (j = l, n) in Table 1. At the intersection of line i and column j we find the $x_{i,j}$ variable which represents the cost of the product produced by branch i and consumed by branch j. Each one of the n columns which make up the inter-branch balance reflects the structure of material expenses and the amortization and net production for each branch. The total of material expenses, amortization and net production equals the global production x_j of the **j** branch, or:

$$\sum_{i=1}^{n} \mathbf{x}_{i,j} + \mathbf{s}_j + \mathbf{v}_j + \mathbf{m}_j = \mathbf{x}_j \qquad \left(i = 1, n\right) \tag{1}$$

The $v_j + m_j$ variable is the net production of the j branch, and s_j is the amortization. Each one of the n lines of the inter-branch balance reflects the distribution of production for each branch. For the i line, the following is true (balance):

$$\sum_{j=1}^{n} \mathbf{x}_{i,j} + \mathbf{y}_i = \mathbf{x}_i \qquad \left(i = 1, n\right) \tag{2}$$

Table 1
General *Representation* of the *Inter-Branch Balance*

Production branch	Consumer branches 1 2 ... j ... n	Final Production	Global production
1	$x_{11}, x_{12} ... x_{1j} ... x_{1n}$	y_1	x_1
2	$x_{21}, x_{22} ... x_{2j} ... x_{2n}$ 1st quarter	y_2 2nd quarter	x_2
...	....	...	...
i	$x_{i1}, x_{i2} ... x_{ij} ... x_{in}$	y_i	x_i
...	....	...	...
n	$x_{n1}, x_{n2} ... x_{nj} ... x_{nn}$	y_n	x_n
Amortization	$s_1, s_2 ... s_j ... s_n$ 3rd quarter	s 4th quarter	
Work remuneration	$v_1, v_2 ... v_j ... v_n$	v	
Net income	$m_1, m_2 ... m_j ... m_n$	m	
Global production	$x_1, x_2 ... x_j ... x_n$		

The y_i variable represents the production of the i branch, which is part of the national income and destined for consume, accumulation and export.

Hence, the analysis of the data in the inter-branch balance has the following endpoints:

1) the costs structure of the balance for a certain amount of time; 2) the distribution of this production among the different consumer branches.

2. The Mathematical Model of the Inter-Branch Balance

At the foundation of the mathematical model of the inter-branch balance lies the following equation system (2):

$$\sum_{j=1}^{n} x_{ij} + y_i = x_i \qquad (i = 1, n) \qquad (3)$$

In order to contrive the model, the following premises are considered:

1) the volumes x_{ij} of the production consumption are directly proportional to the x_j volumes, reflecting the production of the consumer branches:

$$x_{ij} = a_{ij} x_j \qquad (4)$$

2) one and the same product is produced by one branch only and each branch produces only one product. In other words, we are taking into account only those branches that we consider „pure". Let's indentify the meaning of the proportionality coefficient a_{ij}. From equation (1), we infer that:

$$a_{i,j} = \frac{x_{i,j}}{x_j}$$

Therefore, $a_{i,j}$ indicates *how many units of global production belonging to the i branch are spent in order to obtain one production unit of the consumer branch j.* These coefficients are called **direct material expenses coefficients.** They can be calculated using both a regular expression and a cost expression. Formula (2) (in monetary or regular expression), taking into account equation (4), becomes:

$$x_i = \sum_{j=1}^{n} a_{i,j} x_j + y_i \qquad (i = 1, n) \qquad (5)$$

If we introduce the matrix:

$$A = \begin{pmatrix} a_{11} & a_{12} \ ... \ a_{1n} \\ a_{21} & a_{22} \ ... \ a_{2n} \\ .... & .... \ .... \\ a_{n1} & a_{n2} \ ... \ a_{nn} \end{pmatrix}$$

Called the direct expenses matrix or ***the technological matrix***, the column vector of the global production volumes:

$$\mathbf{x} = \begin{pmatrix} \mathbf{x}_1 \\ \mathbf{x}_2 \\ ... \\ \mathbf{x_n} \end{pmatrix}$$

and the column vector of the final production volumes:

$$\mathbf{y} = \begin{pmatrix} \mathbf{y}_1 \\ \mathbf{y}_2 \\ ... \\ \mathbf{y_n} \end{pmatrix}$$

we can rewrite equation (5) under a matricial form like this:

$$x = Ax + y \qquad\qquad (6)$$

The linear system connects the volumes of global production to the volumes of final production and can be used calculations for every component. The building process of the model is not affected by the type of measurement units that are used for the expression of values x_i, a_{ij}, y_i, whether they are regular or cost units. If p_1, p_2,..., p_n are prices for the product (obtained from „pure" branches), then:

$$\bar{x} = p_i x_i \qquad i = 1, n$$

$$\bar{x}_{ij} = p_i x_{ij} \qquad i, j = 1, n$$

$$\bar{y}_i = p_i y_i \qquad i = 1, n$$

hence:

$$\bar{a}_{ij} = \frac{\bar{x}_{ij}}{\bar{x}_j} = \frac{p_i x_{ij}}{p_j x_j} = \frac{p_i}{p_j} a_{ij}$$

where the overline above a unit indicates that they are measured in cost expression. Let:

$$\bar{A} = \begin{pmatrix} a_{d11} & a_{d12} & \cdots & a_{d1n} \\ a_{d21} & a_{d22} & \cdots & a_{d2n} \\ .... & .... & .... \\ a_{dn1} & a_{dn2} & \cdots & a_{dnn} \end{pmatrix} \quad P = \begin{pmatrix} p_1 & 0 & \cdots & 0 \\ 0 & p_2 & \cdots & 0 \\ .... & .... & .... \\ 0 & 0 & & p_n \end{pmatrix}$$

$$\mathbf{P}^{-1} = \begin{pmatrix} \dfrac{1}{\mathbf{p}_1} & 0 & \cdots & 0 \\[2mm] 0 & \dfrac{1}{\mathbf{p}_2} & \cdots & 0 \\[2mm] \text{- - - - - - - - - - -} \\[2mm] 0 & 0 & & \dfrac{1}{\mathbf{p}_n} \end{pmatrix}$$

then the mathematical relation between matrices A and $\bar{\mathbf{A}}$ Is given by the formulas:

$$\bar{\mathbf{A}} = \mathbf{P}\,\mathbf{A}\,\mathbf{P}^{-1} \quad \text{and} \quad \mathbf{A} = \mathbf{P}^{-1}\,\bar{\mathbf{A}}\,\mathbf{P}$$

Whereas the relation between the models, using a regular and cost expression, respectively, can be written down as:

$$\mathbf{P}\,\mathbf{x} = \mathbf{P}\,\mathbf{A}\,\mathbf{x} + \mathbf{P}\,\mathbf{y} \quad \text{and} \quad \mathbf{P}^{-1}\,\bar{\mathbf{x}} = \mathbf{P}^{-1}\,\bar{\mathbf{A}}\,\bar{\mathbf{x}} + \mathbf{P}^{-1}\,\bar{\mathbf{y}}$$

The inter-branch balance model can be further extended to include restrictions regarding the use of the production factors (natural and work resources) and of the fixed funds (capital). Supposing that the expenses of the factors of production are proportional to the volumes of the production factors and that the volumes of the production factors are limited, we obtain the linear restrictions system:

$$\sum_{j=1}^{n} f_{kj} x_j \leq r_k \qquad (\,k = 1\,,\,m\,)$$

where f_{kj} is the direct expenses of the k factor in order to fabricate a j unit of production, whereas r_k is the volume of the k factor. The linear equations system (5) and the linear inequalities system (7) constitute the mathematical model of the inter-branch balance, when taking into account the limitations of the production factors.

3. Solving the Equation System of Inter-Branch Balance

Let's consider the problem regarding the existing solution of the linear systems (5) or (6) which have an economic interpretation. Let there be the matrix A of direct expenses coefficients. Based on the economic meaning of direct expenses, the a_{ij} coefficients of matrix A can only take non-negative values $a_{ij} > 0$. The problem that needs solving is: to find, for a fixed vector of final production **y,** a global production vector **x**; in other words, to solve the equations system:

$$\mathbf{x} = \mathbf{A}\,\mathbf{x} + \mathbf{y}$$

The components of vector **y** are non-negative on an economic basis ($y_i \geq 0(i = \overline{1,n})$). The requested solution **x,** also on an economic basis, must have only non0negative components ($x_i \geq 0(i = \overline{1,n})$).

If the a_{ij} components of matrix A are calculated in a cost expression manner, then $a_{ij} < 1$. In order to obtain only non-negative values for **x**, we must employ the so–called productivity of matrix A. *The non-negative A matrix is **productive** if there exists one, non-negative vector* **x**, *so that* **x** > **Ax**. Therefore, there exists one vector **y** > 0, so that $x = Ax + y$. The productivity of matrix A means that the economic system is able to ensure a certain volume of the final production for each and every product. The solution of the linear balance system can be written as follows:

$$x = (\mathbf{E} \text{ - } \mathbf{A})^{-1}y = \mathbf{B}y, \text{ where } \mathbf{B} = (\mathbf{E} \text{ - } \mathbf{A})$$

In order to solve the equation system $x = Ax + y$, we can also apply an approximate iterative method. If we want to ensure the final, required **y**, then we must initially fabricate the production $x_1 = y$, and this production requires spending some intermediary commodities in the volumes $x_2 = Ax_1 = Ay$. Moreover, the production of the x_2 commodities, presumes the spending of x_3 outturns, or $x_3 = Ax_2 = A^2 y$ etc. This leads to the acquirement of the approximate estimation of the general global volume of the x production, considering the first k items of the iterative process:

$$x \approx x_1 + x_2 + ... + x_k = y + \mathbf{A}y + \mathbf{A}^2y + .. . + \mathbf{A}^k y$$

For k —» ∞, we will retrieve the vectorial series:

$$x = y + \mathbf{A}y + \mathbf{A}^2y + ... \text{ or}$$
$$x = (\mathbf{E} + \mathbf{A} + \mathbf{A}^2 + ...)\, y$$

Beginning with this and comparing the last series and the expression x = (**E** −**A**)$^{-1}$y, we have **B** = (**E** - **A**)$^{-1}$ = **E** + **A** + **A**^{2} + **A**^{3} + ...This equality is the analogue matricial form of the Keynes multiplier. Consequently, the matrix (**E** - **A**)$^{-1}$ is called a matricial multiplier.

4. Total Matricial Expenses Coefficients

Let there be matrix **A**. In order to obtain one unit of production in the j branch, the expense of the following sort of product (direct expenses) is required:

$$\mathbf{a}_j = \begin{pmatrix} \mathbf{a}_{1j} \\ \mathbf{a}_{2j} \\ ... \\ \mathbf{a}_{nj} \end{pmatrix}$$

which is described in the j column of matrix $\mathbf{A}$. However, for the acquirement of the a_j sort of product, we must use the $a_j^{(1)}$ sort of product, which is calculated with the formula $a_j^{(1)} = \mathbf{A}\, a_j$. The elements of the $a_j^{(1)}$ vector are called first order indirect expenses coefficients of the corresponding product, for one unit of production of branch j. The matrix $\mathbf{A}^{(1)}$, made up of the $a_j^{(1)}$ columns (j = 1, 2, . ., n), is called **the first order indirect expenses matrix** and, as it may easily be observed, $\mathbf{A}^{(1)} = \mathbf{A} \cdot \mathbf{A} = \mathbf{A}^2$. The second order indirect expenses are called necessary expenses for the production of type $a_j^{(1)}$ commodities, and they represent the indirect first order expenses of the j branch, or $a_j^{(2)} = \mathbf{A}\, a_j^{(1)}$. In a matricial format:

$$\mathbf{A}^{(2)} = \mathbf{A} \cdot \mathbf{A}^{(1)} = \mathbf{A} \cdot \mathbf{A}^2 = \mathbf{A}^3$$

where $A^{(2)}$ is the second order indirect expenses matrix. The k order indirect expenses are the necessary expenses for the establishment of the product series $a_j^{(k-1)}$, which are the indirect, k -1 order expenses, or $a_j^{(k)} = \mathbf{A}\, a_j^{(k-1)}$; and in matricial format:

$$\mathbf{A}^{(k)} = \mathbf{A}\ \mathbf{A}^{(k-1)} = \mathbf{A}\ \mathbf{A}^k = \mathbf{A}^{k+1}$$

Total expenses are defined as the sum of every order, direct and indirect expenses; the $\mathbf{C}$ matrix of total expenses is the sum of the matricial series:

$$\mathbf{C} = \mathbf{A} + \mathbf{A}^{(1)} + \mathbf{A}^{(2)} + ... = \mathbf{A} + \mathbf{A}^2 + \mathbf{A}^3 + ...$$

The matrix $\mathbf{B}$:

$$\mathbf{B} = (\mathbf{E} - \mathbf{A})^{-1} = \mathbf{E} + \mathbf{A} + \mathbf{A}^2 + \mathbf{A}^3 + ...$$

therefore:

$$\mathbf{B} = \mathbf{E} + \mathbf{C}$$

We notice that, only in the case of the productivity of matrix $\mathbf{A}$ (and in this case only), the matricial series $\mathbf{A} + \mathbf{A}^2 + \mathbf{A}^3 + ...$ is convergent, and its sum represents the matrix of total material expenses. Based on the convergence of this matricial series:

$$\lim_{k \to \infty} \mathbf{A}^k = \mathbf{O}$$

where $\mathbf{O}$ is n order null matrix. Consequently, the $\mathbf{C}$ matrix can be approximated based on the following formula:

$$\mathbf{C} \approx \mathbf{A} + \mathbf{A^2} + ... + \mathbf{A^k}$$

taking into account the corresponding number of the first items in this matricial series. We will try to clarify the economic meaning of the b_{ij} elements of the matrix $\mathbf{B} = (\mathbf{E} - \mathbf{A})^{-1}$. In order to do this, we assume that it is necessary to fabricate only one unit of the final product of the j branch. Then the $\mathbf{y}$ vector of the final product is:

$$y = \begin{pmatrix} 0 \\ 0 \\ 1 \\ \cdots \\ 0 \end{pmatrix}$$

The required global production x is:

$$\mathbf{x} = \begin{pmatrix} \mathbf{x}_1 \\ \mathbf{x}_2 \\ \vdots \\ \mathbf{x}_n \end{pmatrix} = \mathbf{By} = \begin{pmatrix} \mathbf{b}_{11} \cdots \cdots \mathbf{b}_{1j} \cdots \cdots \mathbf{b}_{1n} \\ \mathbf{b}_{21} \cdots \cdots \mathbf{b}_{2j} \cdots \cdots \mathbf{b}_{nn} \end{pmatrix} \cdot \begin{pmatrix} 0 \\ \vdots \\ 1 \\ \vdots \\ 0 \end{pmatrix} = \begin{pmatrix} \mathbf{b}_{1j} \\ \mathbf{b}_{2j} \\ \vdots \\ \mathbf{b}_{nj} \end{pmatrix}$$

From this, the elements of the j column, belonging to matrix ***B*** *are the type of products by means of which we can obtain one unit of final production in the j branch.* Taking into account the interrelations between matrices **B** and **C**, we have:

$$\mathbf{b}_{ij} = \begin{cases} \mathbf{c}_{ij} + 1 & i = j \\ \mathbf{c}_{ij} & i \neq j \end{cases}$$

meaning that, in order to get one unit of production j, we must obtain the global production for all the other branches, which equals the total amount of expenses for the production of this unit, and, in branch j, it is required that we add one unit of this final product (product that we must fabricate). In order to do this it is easier that matrix **B**, and not matrix **C**, is named the matrix of total matricial costs, and we will use this from now on accordingly. Starting with:

$$x = \mathbf{B} y = (\mathbf{E} - \mathbf{A})^{-1} y$$

we deduce that the elements of matrix **B** show the interrelations between the global product and the final product. What kind of interrelations do the elements of matrix C show? To answer this question, we postulate the vector z = x - y, which emulates the intermediate products (the expenses). Using x = **B**y, we have:

$$z = x - y = \mathbf{B}y - y = \mathbf{B}y - \mathbf{E}y = (\mathbf{B} - \mathbf{E})y = \mathbf{C}y$$

Based on this, matrix **C** shows the connections between the intermediate product and the final product. Comparing the direct, indirect and material expenses, we surmise that:

1) the direct expenses are the expenses of products, used in a straightforward manner, in order to fabricate the given product;

2) the indirect expenses, of any order whatsoever, describe the expenses of previous stages of production;

3) total expenses include material, direct and indirect expenses of any order.

5. Total Expenses Coefficients of Production Factors

As previously mentioned, in order to obtain one unit of production j, we use:

1) products elaborated by the economic system – costs involving these products are equal to the direct material expenses coefficients a_{ij} (i,j = 1, 2,... ,n);

2) the primary factors (resources), which are not fabricated by the economic system (work, capital, land resources) – these costs are equal to the f_{kj} coefficients. Supposing we have m primary factors of production. Let r_{kj} be the volume of the k factor used by the j branch in order to obtain the global product in the x_j volume. Then the variable:

$$\mathbf{f_{kj}} = \mathbf{r_{kj}} / \mathbf{x_j} \ (k = 1,2,..., m)$$

is the **direct expenses coefficient** of the k factor. This coefficient describes the volume of the expenses of factor k, spent to fabricate one unit of global production. The direct expenses coefficients for the production factors compose the **F** matrix, of the dimensions m x n, which is called the **production factors expenses** matrix. If we have the volume x = $(x_1, x_2, ... , x_n)$ of global production, then we find the required r_k for the production factors in the following system:

$$r_k = \sum_{j=1}^{n} f_{kj} x_j \ (k = 1, 2, ...,m)$$

We can write this system in a matricial format: $\mathbf{r = F\,x}$

where: $\mathbf{r} = \begin{pmatrix} \mathbf{r_1} & \mathbf{r_2} & \cdots & \mathbf{r_m} \end{pmatrix}^{\mathbf{T}}$ is the vector of requirements for the production factors; $\mathbf{x} = \begin{pmatrix} \mathbf{x_1} & \mathbf{x_2} & \cdots & \mathbf{x_n} \end{pmatrix}^{\mathbf{T}}$ is the global production vector, and:

$$F = \begin{pmatrix} f_{11} & f_{12} \cdots f_{1n} \\ f_{21} & f_{22} \cdots f_{2n} \\ f_{m1} & f_{m2} \cdots f_{mn} \end{pmatrix}$$

is the primary factors expenses matrix.

We will, henceforth, analyze, total production factors' expenses coefficients. The coefficients of total expenses for factor k, for the j product, are the sums of total expenses for factor k and also the expenses made in order to produce this factor, expenses that are transferred to this product by means of products consumed by the economic system.

Let the coefficients of total expenses for factor k be $\varphi_{k1}, \varphi_{k2},..., \varphi_{kn}$. We formulate these coefficients using the following representation:

$$
\begin{array}{cccc}
a_{11} \cdot \phi_{k1} & a_{12} \cdot \phi_{k1} & \cdots & a_{1n} \cdot \phi_{k1} \\
a_{21} \cdot \phi_{k2} & a_{22} \cdot \phi_{k2} & \cdots & a_{2n} \cdot \phi_{k2} \\
\cdots & \cdots & \cdots & \cdots \\
a_{n1} \cdot \phi_{kn} & a_{n2} \cdot \phi_{kn} & \cdots & a_{nn} \cdot \phi_{kn} \\
\hline
f_{k1} & f_{k2} & \cdots & f_{kn} \\
\hline
\phi_{k1} & \phi_{k2} & \cdots & \phi_{kn}
\end{array}
$$

In this representation the products $a_{ij} \cdot \varphi_{ki}$ describe the expenses for the k factor, transferred on the j product by means of the spent product i, the expenses for the latter being equal to a_{ij}. According to the definition:

$$
\phi_{kj} = \sum_{i=1}^{n} a_{ij}\phi_{ki} + f_{kj} \qquad (j = 1, 2, \ldots, n)
$$

Evidently, this system has n equations. In a vectorial matricial format it can be written:

$$
\boldsymbol{\varphi}_k = \boldsymbol{\varphi}_k \, \mathbf{A} + f_k
$$

where $\varphi_k = (\varphi_{k1}, \varphi_{k2}, \ldots, \varphi_{kn})$ is the linear vector of the total expenses coefficients for factor k, $\mathbf{A}$ is the direct material expenses matrix, and $f_k = (f_{k1}, f_{k2}, \ldots, f_{kn})$ is the linear vector of the direct expenses coefficients for factor k. Considering the last system, we obtain $\varphi_k - \varphi_k \, \mathbf{A} = f_k$ or:

$$
\varphi_k \mathbf{E} - \varphi_k \, \mathbf{A} = f_k
$$

Thus, we have $\varphi_k (\mathbf{E} - \mathbf{A}) = f_k$. Hence:

$$
\varphi_k = f_k (\mathbf{E} - \mathbf{A})^{-1} = f_k \mathbf{B}
$$

Total expenses coefficients for all production factors form the matrix:

$$
\Phi = \begin{pmatrix}
\varphi_{11} & \varphi_{12} & \cdots & \varphi_{1n} \\
\varphi_{21} & \varphi_{22} & \cdots & \varphi_{2n} \\
\cdots & \cdots & \cdots \\
\varphi_{m1} & \varphi_{m2} & \cdots & \varphi_{mn}
\end{pmatrix}
$$

That we are going to refer to as the matrix of total expenses for the production factors. It is clear then, that:

$$
\boldsymbol{\Phi} = \mathbf{F(E - A)^{-1}} = \mathbf{FB}
$$

We will clarify the economic meaning of the total expenses coefficients for the production factors. It is postulated that $x = (\mathbf{E} - \mathbf{A})^{-1}y$. The resource requirements $r = \mathbf{F} \cdot x$. Consequently: $r = \mathbf{F}(\mathbf{E} - \mathbf{A})^{-1} y = \boldsymbol{\Phi} \, y$.

Therefore, the total expenses coefficients of the production factors are the expenses of the factors for one unit of the final production, so the φ_{kj}

element, of the $\mathbf{\Phi}$ matrix describes the expenses of factor k for the fabrication of one unit of final production belonging to the j branch.

Some of the most important production factors are work and capital (fixed assets). If l_j and k_j are the direct expenses coefficients for work and capital, respectively, and L_j and K_j, $(j = 1,2, ...,n)$ are the total expenses coefficients, then we have:

$$\mathbf{L} = \mathbf{l}(\mathbf{E} - \mathbf{A})^{-1} \text{ and } \mathbf{K} = \mathbf{k}(\mathbf{E} - \mathbf{A})^{-1}$$

where $\mathbf{L} = (L_1, L_2, . . . , L_n)$ and $\mathbf{K} = (K_1, K_2, . . . , K_n)$ are the linear vectors of total expenses coefficients for work and capital, while $\mathbf{l} = (l_1, l_2, ..., l_n)$ and $\mathbf{k} = (k_1, k_2, .., k_n)$ are the linear vectors of direct expenses coefficients for work and capital. Taking into consideration that $(\mathbf{E} - \mathbf{A})^{-1} = \mathbf{E} + \mathbf{A} + \mathbf{A}^2 + . . .$, we get: $\mathbf{L} = \mathbf{l} + \mathbf{l}\mathbf{A} + \mathbf{l}\mathbf{A}^2 + . . .$, and $\mathbf{K} = \mathbf{k} + \mathbf{k}\mathbf{A} + \mathbf{k}\mathbf{A}^2 + . . .$.

The $\mathbf{l}\mathbf{A}$ variables are first order indirect expenses for one unit of the j product; $\mathbf{l}\mathbf{A}^2$ are second order indirect expenses for work; $\mathbf{k}\mathbf{A}$, $\mathbf{k}\mathbf{A}^2$ etc. are first, second etc. order indirect expenses of the capital for one unit of production. The total expenses for work (as for any other production factor) represent the sum of direct and indirect expenses of work.

5.1. The Construction of the Price System Based on the Inter-Branch Balance

We will analyze how price is established with the help of the inter-branch balance. As it has already been mentioned, every fabrication unit of the global production j $(j = 1,2,... , n)$ is related to the product fabrication expenses and the production factors, which make up the expenses vector $z_j = (a_{1j}, a_{2j},..., a_{nj}; f_{1j}, f_{2j}, . . ., f_{mj})$.

Let the price of product i be p_i, and the price of factor k be q_k. Then, assuming that each product is sold for a price equal to the fabrication expenses, for the cost of one unit of the product j we have:

$$\mathbf{p}_j = \sum_{i=1}^{n} \mathbf{a}_{ij}\mathbf{p}_i + \sum_{k=1}^{m} \mathbf{f}_{kj}\mathbf{q}_k \quad (j = 1,2,..., \text{ n})$$

thus, the cost of one unit of the j product includes expenses of intrinsic products (produced by the economic system) and the expenses of the production factors. Including the price vectors $\mathbf{p} = (p_1, p_2, ..., p_n)$ and $q = (q_1, q_2, ..., q_m)$ and using matrix $\mathbf{A}$ of direct material expenses and matrix $\mathbf{F}$ of direct expenses of the production factors, the relations become:

$$\mathbf{p} = \mathbf{p}\,\mathbf{A} + \mathbf{q}\,\mathbf{F}$$

If we conjecture that the prices of the production factors are already known we have:

$$\mathbf{p} = \mathbf{q}\,\mathbf{F}\,(\mathbf{E} - \mathbf{A})^1 = \mathbf{q}\mathbf{\Phi}$$

Hence, the prices of commodities produced by the economic system are influenced by the prices and expenses of the production factors. On the other hand, for each product j, the following mathematical relations must be true (based on the first and third quarter of the inter-branch balance):

$$p_j = \sum_{i=1}^{m} a_{ij} p_i + s_j + v_j + m_j \qquad (j = 1, 2, \ldots, n)$$

where v_j represents the expenses for work remuneration, s_j represents the amortization and m_j represents the supplementary product involved in the total cost of one j-type unit of global production (these variables can be calculated starting from the third quarter of the inter-branch balance). The corresponding matricial format used for the model used to obtain the prices is:

$$\mathbf{p = pA + s + v + m}$$

where s is the amortization vector, v is the expenses for work remuneration vector, v is the supplementary product vector and p is the product's price vector. Hence:

$$\mathbf{p = (s + v + m)(E - A)^{-1}}$$

Comparing this result to the previous one, $\mathbf{p = q \cdot \Phi}$, we conclude that the prices $p = (p_1, p_2, \ldots, p_n)$ are identical to the expenses, rendered in a cost expression, of the production factors required for the fabrication of the products by the economical system; also, the vector s + v + m reflects the expenses of the production factors (especially, work). From:

$$p = (s + v + m) \ (\mathbf{E - A})^{-1} \ \text{ and } \ p = q\mathbf{F(E - A)}^{-1}$$

or:

$$p = p\mathbf{A} + q\mathbf{F} \ \text{ and } \ p = p\mathbf{A} + s + v + m$$

we obtain: $$s + v + m = q\mathbf{F}$$

In the coordinate-based distribution, we have:

$$\mathbf{s}_j + \mathbf{v}_j + \mathbf{m}_j = \sum_{k=1}^{m} \mathbf{q}_k \mathbf{f}_{kj} \qquad (j = 1, 2, \ldots, n)$$

The model we consider, in order to obtain the prices, determines these prices at the level of expenses of the production process. Quantitative estimation of the prices, using this method, enables us to avoid important errors, which

may come up when trying to obtain the price's system level for the products fabricated by the economic system. If the vectors **s**, **v**, **m** are variable according to Δs, Δv and Δm, then the price's variation Δp will be:

$$\Delta p = (\Delta s + \Delta v + \Delta m) \, (\mathbf{E} - \mathbf{A})^{-1}$$

According to this formula, we can determine, for example, the way in which the variation Δv of the expenses for work remuneration influences product prices.

REFERENCES

Blyte J., *Comportamentul consumatorului*. Editura Teora, Bucureşti, 1998.
Boris C-tin, *Metode numerice şi implementarea lor pe calculator*. Tehnopress, Iaşi, 2005.
Deaton A., *Understanding Consumption*. Oxford University Press, 1992.
Dussart C., *Comportement du consumateur et stratégie de marketing*. Monreale, Edition Mc-Graw-Hill, 1983.
Grill Ph., *Microéconomie. Interaction des acteurs économiques*. Edition Dunod, Paris, 1993.
Hyalmarsson L., Marin D., Oprescu Gh., Andrei A., *Microeconomie. O abordare cantitativă*. Editura Omnia, Braşov, 1995.
Imperato A., *Consumer Behavior for Labour Supply.* Conferinţă Internaţională de Cibernetică Economică, **A XII**, Bucureşti, 2004.
Kotler Ph., Duboi, B., *Marketing Management*. Publi-Union Edition, Paris, 1992.
Lambin, *Marketing Stratégique*. Edition McGraw–Hill, Paris, 1991.
Lilien L., Moorty, Ph., *Marketing Models*. Prentice-Hall, Inc., New Jersey, 1992.
Mihai Şt., Ioniţă I., Constantin B., Manole V., Găluşcă G., Bădărău Ghe., *Eroare, Compensare şi Aproximare în Experimentul Ştiinţific*. Tehnopress, 2005.
Mihut, I., Pop, M., *Consumatorul şi managementul ofertei*. Editura Dacia Cluj-Napoca, 1996.
Munteanu V.A., *Marketing. Concepte. Metode. Studii de caz*. Editura Fundaţiei Chemarea Iaşi, 1996.
Oprescu Gh., Imperato A., Andrei Ana, *Cibernetica consumatorului. Abordare statică şi dinamică*, Editura F.F. Pres, Bucureşti, 2005.
Oprescu Gh., Marin D., Andrei A., *Modele dinamice ale economiei de piaţă. Studii de caz*. Editura F.F. Pres, Bucureşti, 1996.
Scarlat E., Chiriţă N., *Cibernetica sistemelor economice*. Editura ASE, Bucureşti, 2003.
Stoica Cr.M., *Modelarea comportamentului consumatorului*. Editura Tehnopress, Iaşi, 2008.
Sviokla J., Shapiro P., *Keeping Customers*. Harvard Business Rewiew Book, Boston, 1993.
Tamaş V., Brânzei D., Moscovici J., *Modele matematice în economie*. Editura Graphix, Iaşi, 1995.

MODELAREA LEGĂTURILOR INTERRAMURI

(Rezumat)

Între diferite ramuri ale economiei există legături de producţie, numite legături interramuri. Modelele matematice care descriu legăturile interramuri se numesc modele de balanţă interramuri sau modele "cheltuieli-producţie". La baza acestor modele se află balanţa interramuri care reprezintă un tabel ce caracterizează producţia şi repartiţia producţiei pe ramuri, legăturile interramuri, utilizarea resurselor materiale şi de muncă, crearea şi repartizarea venitului naţional.

BIBLIOGRAFIA NU SE REGASESTE IN TEXT

[1]. (Blyte, 1998)
[2]. (Boris Ctin., 2005)
[3]. (Deaton, 1992)
[4]. Dussart, 1983)
[5]. (Grill, 1993)
[6]. (Hyalmarsson *et al.,* 1995)
[7]. (Imperato, 2004)
[8]. (Kotler & Duboi, 1992)
[9]. (Lambin, 1991)
[10]. (Lilien, 1992)
[11]. (Mihut & Pop, 1996)
[12]. (Mihai *et al.,* 2005)
[13]. (Munteanu, 1996)
[14]. (Oprescu & Marin, , 1996)
[15]. (Oprescu *et al.,* 2005)
[16]. (Stoica Cr.M., 2008)
[17]. (Scarlat & Chiriţă, 2003)
[18]. (Sviokla& Shapiro, 1993)
[19]. (Tamaş *et al.,* 1995)

ALGORITHM FOR SOLVING A MODEL DESCRIBED BY THE INTER-BRANCH BALANCE

BY

CRISTINA MARIA STOICA[∗]

University "PETRE ANDREI" from Iaşi

Abstract. The problem of building the inter-branch balances and the calculations we can make based on them is essentially to solve a linear system. When dealing with this problem, the calculations are made based on the inter-branch balance of direct material expenses and of production factors expenses for a certain period of time, usually the preceding one, taking into account the planned changes regarding the technological process of production. Also, the volume of final consumption (the demand for the final product) is fixed. It is convenient to represent the balance in the form illustrated in a table, where information is given in cost expression and satisfies the main relation of the balance model.

Key words: technology planning period, Gauss-Jordan elimination, SIMPLEX method, planned balance.

1. Introduction

The problem of building the inter-branch balances and the calculations we can make based on them is essentially to solve a linear system. In the general case, the following system must be solved:

[∗] Corresponding author; *e-mail:*

$$(\mathbf{E} - \mathbf{A})\, x = y \tag{1}$$

depending on the x variable.

In this system, the **A** matrix of direct material expenses and the **y** vector of final consumption are postulated.

We must solve the system for the **x** vector of global production and the **B** matrix of total material expenses:

$$B = \left(E - A \right)^{-1} = \begin{pmatrix} b_{11} & b_{12} & \cdots & b_{1n} \\ b_{21} & b_{22} & \cdots & b_{2n} \\ \cdots\cdots\cdots\cdots\cdots\cdots\cdots\cdots\cdots \\ b_{n1} & b_{n2} & \cdots & b_{nn} \end{pmatrix}$$

Concurrently with the calculations for problem (1), based on the **F** matrix of direct expenses, we must find the Φ matrix of total material expenses of the production factors:

$$\Phi = \begin{pmatrix} \phi_{11} & \phi_{12} & \cdots & \phi_{1n} \\ \phi_{21} & \phi_{22} & \cdots & \phi_{2n} \\ \cdots & \cdots & \cdots & \cdots \\ \phi_{m1} & \phi_{m2} & \cdots & \phi_{mn} \end{pmatrix}$$

as well as the requirements for the production factors.

When dealing with problem (1), the calculations are made based on the inter-branch balance of direct material expenses and of production factors expenses for a certain period of time, usually the preceding one, taking into account the planned changes regarding the technological process of production. Also, the volume of final consumption (the demand for the final product) is fixed. It is convenient to represent the balance in the form illustrated in Table 1, where information is given in cost expression and satisfies the main relation of the balance model:

$$x_i = \sum_{j=1}^{n} x_{ij} + y_i \qquad \left(i = 1, n \right) \tag{2}$$

In Table 1, the volume of production fabricated by each branch in the preceding period of time was used in the process of material fabrication of other production types, as well as with a view to the final consumption. Moreover, the following is true:

$$r_k = \sum_{j=1}^{n} r_{kj} \qquad (k = 1, m) \tag{3}$$

where r_{kj} is the volume of the k factor used by the j branch. After solving the problem for the inter-branch balance, a table similar to Table 1 is built, to be used only in the planning process. The algorithm that uses the inter-branch balance models (renewal of Table 1) comprises the following stages:

Stage I. Determination of the direct expenses coefficients

In order to do this, each column in Table 1 is divided by x_j, obtaining:
- the coefficients' values in matrix **A** of direct material expenses:

$$a_{ij} = \frac{x_{ij}}{x_j} \qquad (i = 1, n; j = 1, n)$$

- the coefficients' values in matrix **F** of direct expenses of the production factors:

$$f_{kj} = \frac{r_{kj}}{x_j} \qquad (k = 1, m; j = 1, n)$$

Table 1

i / j	1 2 ... n	y_i	x_i	p_i
1 2 ⋮ n	x_{11} x_{12} ... x_{1n} x_{21} x_{22} ... x_{2n} ⋮ ⋮ ⋮ x_{n1} x_{n2} ... x_{nn}	y_1 y_2 ⋮ y_n	x_1 x_2 ⋮ x_n	p_1 p_2 ⋮ p_n
k / j	1 2 ... n	r_k	q_k	
1 2 ⋮ m	r_{11} r_{12} ... r_{1n} r_{21} r_{22} ... r_{2n} ⋮ ⋮ ⋮ r_{m1} r_{m2} ... r_{mn}	r_1 r_2 ⋮ r_m	q_1 q_2 ⋮ q_m	
x_j	x_1 x_2 . . . x_n			
p_j	p_1 p_2 . . . p_n			

If the administration balance is represented in regular measurement units, then, taking into consideration the prices p_i and q_k, the a_{ij} and f_{kj} coefficients are also represented in a cost expression, according to the formulas:

$$\tilde{a}_{ij} = \frac{p_i}{p_j} \cdot \frac{x_{ij}}{x_j} \qquad i = 1, n ; \qquad j = 1, n$$

$$\tilde{f}_{kj} = \frac{q_k}{p_j} \cdot \frac{r_{kj}}{x_j} \qquad k = 1, m ; \qquad j = 1, n$$

According to the calculations performed in stage I, Table no. 2 is obtained. For Table no. 2 the following relations are true:

$$x_i = \sum_{j=1}^{n} a_{ij} x_j + y_i \qquad i = 1, n \tag{4}$$

$$r_k = \sum_{j=1}^{n} f_{kj} x_j \qquad k = 1, m \tag{5}$$

In order to check the accuracy of the calculations in stage I, we check that relations (4) and (5) are satisfied, and we also check the properties of direct expenses coefficients.

Table 2

i / j	1	2	n	y_i	x_i
1	a_{11}	a_{12} ...	a_{1n}	y_1	x_1
2	a_{21}	a_{22} ...	a_{2n}	y_2	x_2
⋮	⋮	⋮ ...	⋮	⋮	⋮
n	a_{n1}	a_{n2} ...	a_{nn}	y_n	x_n
k / j	1	2 ...	n	r_k	
1	f_{11}	f_{12} ...	f_{1n}	r_1	
2	f_{21}	f_{22} ...	f_{2n}	r_2	
⋮	⋮	⋮ ...	⋮	⋮	
m	f_{m1}	f_{m2} ...	f_{mn}	r_m	
x_j	x_1	x_2 ...	x_n		

Stage II. Corrections for coefficients a_{ij} and f_{kj}.

According to the changes envisioned for the technology planning period of time, and according to the expenses of production, the a_{ij} and f_{kj} coefficients are recalculated. The latterly obtained values are the ones that would be used in subsequent calculations. It must be noticed that for these new values, relations (4) and (5) are not satisfied.

Stage III. Determination of the inverse matrix

Two methods can be used to determine the inverse matrix. The first one consists in doing the calculations by hand with the help of, for example, Gauss-Jordan elimination. The second method is based on special numeric of matricial inversion, performed with the aid of an electronic calculator (refer to the

programming library SLATEC and IMSL), or on efficient algorithms that solve linear programming problems (the SIMPLEX method). At first, the coefficient of the matrix are determined using the formula:

$$\mathbf{D} = \mathbf{E} \cdot \mathbf{A}$$

from:

$$d_{ij} = \begin{cases} 1 - a_{ij}, & \text{from } i = j, \ i = 1, n, \ j = 1, n \\ - a_{ij}, & \text{for all the values so that } i \neq j, \ i = 1, n, \ j = 1, n \end{cases}$$

All d_{ij} coefficients of the D matrix, except those that are situated on the main diagonal, are negative or null, ($d_{ij} < 0$, $i = \overline{1, n}$, $j = \overline{1, n}$, $i \neq j$). The d_{ii} coefficients on the main diagonal are positive, or $d_{ii} > 0$, $i = \overline{1, n}$.

In order to obtain the coefficient of the inverse matrix we use an algorithm based on the Gauss-Jordan elimination. A characteristic of this algorithm is that, at each step, the pivotal elements are successively chosen from the diagonal elements of matrix D as they are always positive.

Another characteristic of this algorithm is that, after subsequent transformations, the coefficients of matrix D are gradually becoming non-negative at the left side of the pivotal column. We presume that, at the t step of the algorithm, the $\mathbf{D}^t$ matrix was obtained with its coefficients d^t_{ij}:

$$D^t = \begin{pmatrix} d^t_{11} & d^t_{12} & \cdots & d^t_{1t} & \cdots & d^t_{1n} \\ d^t_{12} & d^t_{22} & \cdots & d^t_{2t} & \cdots & d^t_{2n} \\ \cdots & \cdots & \cdots & \cdots & \cdots & \cdots \\ d^t_{t1} & d^t_{t2} & \cdots & d^t_{tt} & \cdots & d^t_{tn} \\ \cdots & \cdots & \cdots & \cdots & \cdots & \cdots \\ d^t_{n1} & d^t_{n2} & \cdots & d^t_{nt} & \cdots & d^t_{nn} \end{pmatrix}$$

At the step t + 1, we let the pivotal element be d^t_{tt}, so that the t line and t column are pivotal line and column, respectively. We do the calculations to determine the new values for the coefficients of the $\mathbf{D}^{t+1}$ matrix:

- instead of the pivotal element, we write its inverse value:

$$d^{t+1}_{tt} = \frac{1}{d^t_{tt}}$$

- the other elements of the pivotal line are divided by the pivotal element:

$$d^{t+1}_{tj} = \frac{d^t_{tj}}{d^t_{tt}}, \ j = \overline{1, m}; \ j \neq t;$$

- the other elements of the pivotal column are divided by the pivotal element and taken in their negative value:

$$d_{it}^{t+1} = -\frac{d_{it}^{t}}{d_{tt}^{t}}, i = \overline{1,n}; i \neq t;$$

- all the other coefficients of matrix $\mathbf{D}^{t+1}$ are calculated based on the triangle rule or the rectangle rule:

$$\mathbf{d}_{ij}^{t+1} = \frac{\mathbf{d}_{ij}^{t}\mathbf{d}_{tt}^{t} - \mathbf{d}_{it}^{t}\mathbf{d}_{tj}^{t}}{\mathbf{d}_{tt}^{t}}$$

$$= \mathbf{d}_{ij}^{t} - \frac{\mathbf{d}_{it}^{t}\mathbf{d}_{tj}^{t}}{\mathbf{d}_{tt}^{t}}$$

(the rectangle rule)

(the triangle rule)

for all $i = \overline{1,n}$; $j = \overline{1,n}$; $i \neq t$; $j \neq t$. After having performed the calculations for all the coefficients of the diagonal, after n steps, we obtain the inverse matrix:

$$\mathbf{D}^{n} = (\mathbf{E} - \mathbf{A})^{-1} = \mathbf{B}$$

The inverse matrix B, which is the total expenses matrix looks like this:

$$B = \begin{pmatrix} b_{11} & b_{12} & \cdots & b_{1n} \\ b_{21} & b_{22} & \cdots & b_{2n} \\ \ldots \ldots \ldots \ldots \ldots \ldots \ldots \\ b_{n1} & b_{n2} & \cdots & b_{nn} \end{pmatrix}$$

In order to check the correctness of the calculations, the following tests are performed:

1) all the coefficients of matrix B are positive, or $b_{ij} > 0$, $i = \overline{1,n}$; $j = \overline{1,n}$;

2) all the coefficients on the main diagonal of matrix B have values larger than one, or $b_{ii} > 1$, $i = \overline{1,n}$;

3) for the obtained B matrix, the following is true:

$$\mathbf{DB} = \mathbf{BD} = \mathbf{E}$$

Furthermore, calculations following the model in Table 3 can be performed, including coefficients from the matrices B and F. The second method that enables us to determine the inverse matrix is related to a linear programming problem looking like this:

$$z = u_1 + u_2 + \cdots + u_n \rightarrow \min \qquad (6)$$

$$\sum_{j=1}^{n} d_{ij} x_j + u_i = y_i \qquad i = 1, n \qquad (7)$$

$$u_i \geq 0, \qquad i = 1, n, \qquad x_j \geq 0, \qquad j = 1, n \qquad (8)$$

Table 3

i / j	1 2 n	y_i	x_i
1	b_{11} b_{12} ... b_{1n}	y_1	x_1
2	b_{21} b_{22} ... b_{2n}	y_2	x_2
⋮	⋮ ⋮ ... ⋮	⋮	⋮
n	b_{n1} b_{n2} ... b_{nn}	y_n	x_n
k / j	1 2 ... n		
1	f_{11} f_{12} ... f_{1n}		
2	f_{21} f_{22} ... f_{2n}		
⋮	⋮ ⋮ ... ⋮		
m	f_{m1} f_{m2} ... f_{mn}		
x_j	x_1 x_2 ... x_n		
y_j	y_1 y_2 ... y_n		

As system (1) can have only one valid solution, we can solve the problem using the SIMPLEX method, with the equality (6) - (8). At the same time, we obtain that $z_{min} = 0$; all x_j variables will be basic variables; the supplementary variables $u_1, u_2, ..., u_n$ are not basic variables and cannot take a null value. In the **last simplex table,** the coefficients related to the variables that are not basic ones compose the inverse matrix.

Stage IV. Determination of the global production volumes
If $y = (y_1, y_2...y_n)^T$ is the vector of the planned volumes belonging to the final production consumption, then, using the formula:

$$x_i = \sum_{j=1}^{n} b_{ij} y_j \qquad i = 1, n$$

we get the x_i volumes, of the global production of branch i for the planning period. The values x_i can be obtained from Table 3 by multiplying the respective coefficients of the i line of matrix **B** with the coefficients of line y_j. Adding the products, we get the values of the x_i coefficient.

Stage V. Determination of the inter-productive flows
Using the formula:

$$x_{ij} = a_{ij} \cdot x_j, \quad i = \overline{l,n}; \ j \ \overline{l,n}$$

we determine the production volumes for each branch, which will be used for material production by other branches. The results are noted in Table 4.

Stage VI. Determination of the total expenses of the production factors matrix
Taking into account the inverse matrix **B** that we obtained and matrix **F** of direct expenses of the primary production factors and the formula:

$$\phi_{kj} = \sum_{i=1}^{n} f_{ki} \cdot b_{ij} \qquad k = 1, m \qquad j = 1, n$$

We identify the total expenses coefficients of the production factors. The φ_{kj} coefficients are found by multiplying the respective coefficients of the line k in the **F** matrix and of column j in the **B** matrix, in Table 3.
When performing the calculations, in the last two steps of the algorithm, the initial values of the coefficients a_{ij} and b_{ij} are not used, instead, their new values are used; these new values are recalculated taking into the changes taking place in the production technology.

Stage VII. Determination of the expenses of the production factors
Owing to the fact that the f_{kj} coefficients represent the direct expenses of the production factor k for the fabrication of one unit of production of the j branch, the expenses of facto k for the whole volume of global production in the j branch are obtained using the formula:

$$r_{kj} = f_{kj} \cdot x_j, \quad k = \overline{l, \ m} \ ; \ j = \overline{l, \ n}$$

and with the help of: $r_k = \sum_{j=1}^{n} r_{kj}$ we can obtain the total volumes of the expenses of production factor k done to enable global production for all the branches. To calculate the values of r_{kj}, each column in matrix F, from Table 3, is multiplied by x_j. The results of the calculations are noted in Table 4.

Stage VIII. Testing the inter-branch balance
In table 4 are noted the coefficients for the production flows of material expenses x_{ij} and of the calculated volumes of global production x_j. In order to check the correctness of the illustrated balance we determine the subtractions:

$$v_i = x_i - \sum_{j=1}^{n} x_{ij} \qquad i = 1, n$$

that indicate the rest of the production for final consumption. If the following relation is true:

$$\left| v_i - y_i \right| \le \varepsilon \qquad i = 1, n$$

where ε is a small enough number, we can affirm that the calculations are accurate, with the precision of a given constant.

Table 4

i / j	1 2 n	y_i	x_i	p_i
1	x_{11} x_{12} ... x_{1n}	y_1	x_1	p_1
2	x_{21} x_{22} ... x_{2n}	y_2	x_2	p_2
⋮	⋮ ⋮ ... ⋮	⋮	⋮	⋮
n	x_{n1} x_{n2} ... x_{nn}	y_n	x_n	p_n
k / j	1 2 n	r_k	q_k	
1	r_{11} r_{12} ... r_{1n}	r_1	q_1	
2	r_{21} r_{22} ... r_{2n}	r_2	q_2	
⋮	⋮ ⋮ ... ⋮	⋮	⋮	
n	r_{m1} r_{m2} ... r_{mn}	r_m	q_m	
x_j	x_1 x_2 x_n			
y_j	y_1 y_2 y_n			
p_j	p_1 p_2 p_n			

Table 4 illustrates the planned balance of inter-branch connections for the planning period and can be used in order to take a decision regarding the direction of national economic development at a macro level.

REFERENCES

Blyte J., *Comportamentul consumatorului*. Editura Teora, Bucureşti, 1998.
Boris C-tin, *Metode numerice şi implementarea lor pe calculator*. Tehnopress, Iaşi, 2005.
Deaton A., *Understanding Consumption*, Oxford University Press, 1992.
Grill Ph., *Microéconomie. Interaction des acteurs économiques*. Edition Dunod, Paris, 1993.
Hyalmarsson L., Marin D., Oprescu Gh., Andrei A., *Microeconomie. O abordare cantitativă*. Editura Omnia, Braşov, 1995.

Imperato A., *Consumer Behavior for Labour Supply*. Conferinţă Internaţională de Cibernetică Economică, **A XII**, Bucureşti, 2004.

Kotler Ph., Duboi B., *Marketing Management*. Publi-Union Edition, Paris, 1992.

Lilien L., Moorty, Ph., *Marketing Models*. Prentice-Hall, Inc., New Jersey, 1992.

Mihut I., Pop, M., *Consumatorul şi managementul ofertei*. Editura Dacia Cluj-Napoca, 1996.

Munteanu V.A., *Marketing. Concepte. Metode*. Studii de caz, Editura Fundaţiei Chemarea Iaşi, 1996.

Oprescu Gh., Marin D., Andrei A., *Modele dinamice ale economiei de piaţă*. Studii de caz, Editura F.F. Pres, Bucureşti, 1996.

Oprescu Gh., Imperato A., Andrei Ana, *Cibernetica Consumatorului. Abordare Statică şi Dinamică*. Editura F.F. Pres, Bucureşti, 2005.

Stoica Cr.M., *Modelarea comportamentului consumatorului*. Editura Tehnopress, Iaşi, 2008.

Scarlat E., Chiriţă N., *Cibernetica sistemelor economice*. Editura ASE, Bucureşti, 2003.

Tamaş V., Brânzei D., Moscovici,J., *Modele matematice în economie*. Editura Graphix, Iaşi, 1995.

ALGORITM DE CALCUL UTILIZAT PENTRU REZOLVAREA UNUI MODEL DESCRIS DE O BALANŢĂ INTERRAMURI

(Rezumat)

Problema alcătuirii balanţelor interramuri şi efectuarea calculelor cu ajutorul lor, se reduce în esenţă, la rezolvarea unui sistem de ecuaţii lineare. În acest caz, calculele se efectuează în baza balanţei interramuri a cheltuielilor materiale directe şi a cheltuielilor factorilor de producţie pentru o perioadă oarecare, de regulă cea precedentă, luând în consideraţie modificările planificate ale tehnologiei de producere. De asemenea, se fixează volumele consumului final (cererea pentru produsele finale) al producţiei. Este convenabil ca balanţa să fie reprezentată sub forma unui tabel, în care informaţia este reprezentată în expresie de cost şi satisface relaţia principală a modelului de balanţă.

BIBLIOGRAFIA NU SE REGASESTE IN TEXT

[1]. (Blyte, 1998)
[2]. (Boris C-tin, 2005)
[3]. (Deaton, 1992)
[4]. (Grill, 1993)
[5]. (Hyalmarsson, *et al.,* 1995)
[6]. (Imperato, 2004)
[7]. (Kotler & Duboi, 1992)
[8]. Lilien & Moorty, 1992)
[9]. (Mihut & Pop, 1996)
[10]. (Munteanu, 1996)

[11]. (Oprescu *et al.,* 1996)
[12]. (Oprescu *et al.,* 2005)
[13]. (Stoica Cr. M., 2008)
[14]. (Scarlat & Chiriţă, N., *Cibernetica sistemelor economice*, Editura ASE, Bucureşti, 2003)
[15]. (Tamaş *et al.,* 1995)

CALCIUM PHOSPHATES DEPOSITED ON VARIOUS POROUS TITANIUM ALLOYS BY ELECTROCHEMICAL METHOD

BY

E. STOICA[1]*, C. FRATILA[2], E. VASILE[3], I. ROMAN[3], M. CORBAN[3] and M. NICOLAE[1]

[1] Politehnica University of Bucharest,
[2]Research and Development National Institute for Nonferrous and Rare Metals, Ilfov
[3]METAV Research and Development, Bucharest

Abstract. The paper purpose was to deposit calcium phosphates layer on porous titanium surfaces alloys using electrochemical method. The study started from the idea that soft tissue response and attachment strength is improved by a porous surface, and if the substrate is a very well known metallic biomaterial, which in the current paper is titanium alloy then the porous surface covered with calcium phosphate can be suitable for implants surface. The titanium alloy provides good mechanical proprieties while the porosity improves the attachment of calcium phosphates and also after surgery the tissue attachment, in the same time calcium phosphates gives the biocompatibility. In order to obtain calcium phosphates was used electrochemical method. Electrochemical deposition of calcium phosphates it is one of the most efficient method due to the low price.

Key words: calcium phosphates, porous titanium alloys, electrochemical deposition.

---

* Corresponding author; *e-mail:*

1. Introduction

Metallic materials are often used to replace structural components of the human body because they surpass plastic or ceramic materials in terms of tensile strength, fatigue strength, and fracture toughness. Consequently, 316L stainless steels; cobalt-chromium-molybdenum alloys, CP titanium, and titanium alloys gradually become the main biomedical materials used presently in orthopedic applications. Compared to stainless steels and cobalt-chromium alloys, titanium is superior in specific strength, corrosion resistance, and biocompatibility, but inferior in tribological properties (Theoh Swee Hin, 2002).

Titanium is non-ferrous - its elastic modulus is about half of those of stainless steels and cobalt-chromium alloys. In addition, a very stable passive film is formed at room temperature due to rapid reaction with oxygen (www.monographs.iarc.fr, 1999; Destefani, 1996; Nakayama *et al.,* 1989). The interest has focused on using porous implant materials, with lower elastic module that are closer to that of bone, instead of the traditional solid implants. Porous materials not only encourage more regular bone growth, but also allow the bone to grow into the implant itself, thereby improving the retention. Unfortunately, the corrosion rate of porous titanium in simulated body fluids has been reported to be significantly higher than that of solid titanium. Apparent increased corrosion rate is in part due to the much larger surface area that a porous structure exposes to the surrounding environment compared to its solid counterparts (Theoh Swee Hin, 2002). There are a lot of techniques to produce thin film, but a good one is electrodeposition which use lower temperatures and avoid the challenge associated with the structural instability of hydroxyapatite (HAp, $(CA_5(PO_4)_3(OH))$) at elevated temperatures. Using the process of immersion in alkaline solution is expected to accelerate bone formation on titanium in hard tissue (Theoh Swee Hin, 2002).

2. Methods and Materials

The surfaces on which were deposited calcium phosphates using electrochemical method were titanium alloys and commercial titanium porous surfaces manufactured by powder sintering technique. Titanium alloys are very well known as metallic biomaterials used in implantology, mainly in orthopedics. The using of porous substrate started from the idea that adherence of calcium phosphates and bone cells enhancement will be improved.

Electrochemical deposition was made using a potentiostat, a deposition cell, the auxiliary electrode was a spiral platinum wire and the work electrode was the sample. The electrolyte was a 250 ml solution of ammonium dihydrogen phosphate and calcium nitrogen. Other parameters were deposition temperature (room temperature, 37°C) an average of three cycles was applied starting on 10 V

voltages until a current of 20mA was reached. The deposition process was done with stirring using a magnetic stirrer. Concerning the samples, these looked as porous pills. The preparation samples procedure consisted of polishing with sandpaper, the surface was cleaned with HCl distillate water and ethanol on ultrasound. The repeated ultrasound cleaning was done for the deep pores cleaning. Brushite (formula, Ca $HPO_42(H_2O)$))), effective deposition consists in two important stage, particular anodic activation and deposition.

After the electrochemical deposition hydroxyapatite or calcium phosphates are obtained either a thermal treatment was followed in furnace at 300^0C for 3 hours or an immersion treatment in alkaline solution, NaOH. After these treatments were obtained calcium phosphates or hydroxyapatite. The treatments especially immersion treatments on different titanium alloys will be discuss in other study. As was mentioned upward the brushite (formula, $CaHPO_42(H_2O)$) deposition was done in two stages. First stage was the anodic activation of the sample surface which was performed in ammonium dihydrogen phosphate and calcium phosphate solution, the sample was the anode and the spiral platinum wire electrode was the cathode.

The sample was activated applying a voltage of 10-15V and the intensity was 60mA, without stirring. Inside the cell deposition there were certain reactions, including releasing of H_2 from the sample surface time when electrolyte pH was increasing. When H_2 bubbles are decreasing to no longer exist and the current intensity is decreasing can be considered as the first step, anodic activation. Therefore, the cathode is the sample and anode is the spiral platinum wire electrode, was required a 20V voltage and 20mA current intensity which represent the first cycle. There are three cycles used but the number of cycles depends on various factors and the cycle that is following is with 10V voltage. After the deposition process, the samples were removed from the deposition cell, washed with distilled water and ethanol and dried in the oven. For all the samples was performed the same stages. Samples anodic activation is useful because it helps the sample surface to be easily covered and in the same time it is cleaning the pores from the inside out. After the drying in oven the samples were immersed in alkaline solution 0.1 mol/L NaOH (Mukesh *et al.,* 1999), for 5 days and at 37°C. The samples were investigated on: Panalytical X' PERT MPD X-ray diffractometer using Cu Kα x-ray beam; QUANTA INSPECT F(Scanning Electron Microscope), equipped with FEG (Field Emission Gun), 1.4 nm resolution and Energy Dispersive X-ray Spectrometer (EDAX) with resolution at $MnK_α$ of 133 eV and TECNAI F30 G^2 STWIN(High-Resolution Transmission Electron Microscope), with 1Å line and 1.4 Å point resolution and the qualitative X-ray dispersion microanalysis in energy was performed using EDAX with resolution of 133eV.

3. Results and Discussions

Above mentioned, the samples were analyzed using Scanning Electron

Microscopy (SEM), Fig. 1, Energy Dispersive X-ray Spectrometry (EDX), Fig. 2, X-ray Diffraction (XRD), Fig.3, Transmission Electron Microscopy (TEM), Fig. 4. In this paper are presented the investigation results of the samples which were used as substrates for electrochemical deposition of calcium phosphates.

Scanning Electron Microscopy (SEM) investigations shows that the crystals have a needle aspect, rather longer then wide and slightly flattened. Also its have different orientation, because of the titanium alloys porous surface. The mesh networks sizes have various dimensions and different distributions.

Energy Dispersive X-ray Spectrometry (EDX) analysis shows that thin coating possesses has a high quantity of Ca, P, O and small amount of Na.
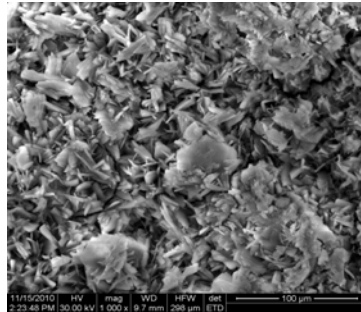
Fig. 1 − SEM micrograph of porous Ti6Al4V surface covered with hydroxyapatite using immersion in alkaline solution 0.1 mol/L NaOH.
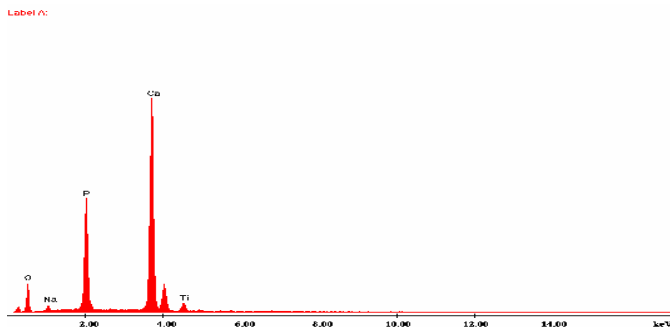
Fig. 2 − EDX spectra of HAp/porous Ti6Al4V.
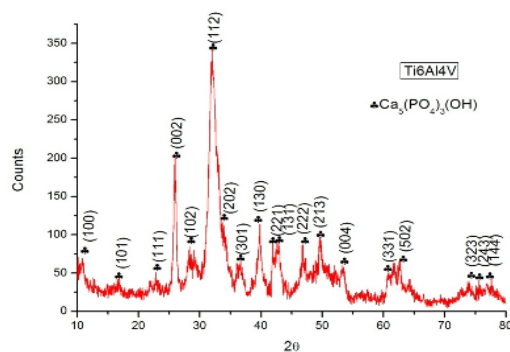
Fig. 3 − XRD spectra of porous Ti6Al4V covered with hydroxyapatite resulted from immersion treatment in alkaline solution 0.1 mol/L NaOH (Referince 00-024-0033).

The Na quantity is present due to the alkaline solution on which was immersed the porous Ti6Al4V substrate electrochemical covered with calcium phosphates. It is obvious that the Ti present is from the substrate and the small amount of it is the result of well covered surface with hydroxyapatite.

The X-ray Diffraction (XRD) pattern suggests that hydroxyapatite (HAp, $(CA_5(PO_4)_3(OH))$) was the major phase present in the sample. Indexing electron diffraction image shows the presence of a monophasic composition of sample: hydroxyapatite (HAp, $(CA_5(PO_4)_3(OH))$) with a hexagonal crystal lattice.

Transmission electron microscopy (TEM) bright field image shows that the sample surface is formed by needle-shaped nanoparticles with length around 7nm and can reach 100nm. The Selected Area Electron Diffraction image, (Fig.4, in the corner) shows different circles, characteristic of nanocrystalline sample which fit to hydroxyapatite compound.
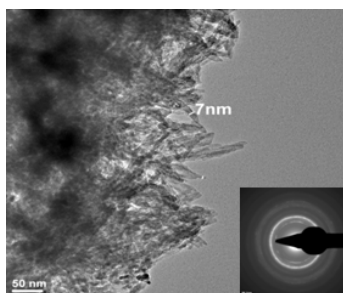
Fig. 4 – TEM analysis of porous Ti6Al4V covered with hydroxyapatite resulted from immersion treatment in alkaline solution 0.1 mol/L NaOH.

4. Conclusion

The conclusions of this study are focused not only on the surface which resulted from applying this method for obtaining calcium phosphates and also on the reactions which occur in the cell deposition. The current is decreasing slowly after the first cycle because on the surface is already a deposited brushite thin layer. Also the current is decreasing at the same time for each cycle (20mA) when the brushite deposition in on a fresh electrolyte solution. And actually, due to the different structure, slightly hydrophilic but also due to the sintering different materials it was notice that the cycle number varies from one sample to another.

When the surface as some issues is preferably to apply a lower voltage which is increasing slower with the purpose to obtain a thin layer. This is actually the purpose of electrochemical method, to obtain thin films of calcium phosphate. When the solution concentration decreases the removal of ions from the solution, such deposit is made possible by two manners: increasing the voltage with the purpose to stimulate the ions from solution and increasing the number of cycles.

The deposition in any dilution electrolyte solution is slower due to lower concentration of ions in solution. H_2 bubbles are more difficult to release from the metallic surface when the metals have a smaller potential then the H_2. It can be concluded that the method presented can be a particularly effective way in terms of cost to obtain nanometric hydroxyapatite structure.

REFERENCES

[*] www.monographs.iarc.fr, IARC Monographs on the Evaluation of Carcinogenic Risks to Humans: Surgical Implants and other Foreign Bodies. Lyon, 1999.

Destefani J.D., *Metals Handbook*. loth Edition, ASM International, 21586-605 (1996).

Fratila C., Roman I., Trusca Roxana, Vasile E., Prodan G., *(*IMNR) Titanium and TA6V4 Titanium Alloy Anodic Oxidation Aimed to Implantology Utility Nonconvetional Technologies Review*. Scientific Journal of the Timisoara, Romanian Accademy, Ed. BREN Bucharest, *2*, 61÷68 (2006).

Mukesh Kumar, Harani Dasarathy, *Clyde Riley-Electrodeposition of Brushite Coatings and Their Transformation to Hydroxyapatite in Aqueous Solutions*. John Wiley & Sons, Inc., 302-310 (1999).

Nakayama Y., Yamamura T., Kotoura Y., *Oka M., In Vivo Measurement of Orthopedic Implant Alloys: Comparative Study of in Vivo and Invim Experiments*. Biomaterials, 1989.

Theoh Swee Hin, *Engineering Materials for Biomedical Applications*. Biomaterials Engineering and Processing Series, **1**, *2*, 2-6 (2002).

DEPUNEREA FOSFAŢILOR DE CALCIU PE DIFERITE ALIAJE CU POROZITATE DE TITAN PRIN METODA ELECTROCHIMICĂ

(Rezumat)

Scopul lucrării a fost acela de a se depune fosfaţi de calciu pe suprafeţe poroase din aliaje de titan folosind metoda electrochimică. Studiu a pornit de la ideea că ţesutul moale şi rezistenţa adeziunii acestuia este îmbunătăţită de suprafeţele poroase, iar dacă este utilizat un substrat din biomaterial metalic foarte cunoscut, în cazul lucrării de faţă este aliajul de titan, atunci acoperirea suprafeţei poroase de titan cu fosfaţi de calciu poate fi potrivită pentru suprafeţele implanturilor. Aliajele de titan oferă bune proprietăţi mecanice, în timp ce suprafaţa poroasă îmbunătăţeşte adeziunea fosfatului de calciu (care oferă şi biocompatibilitate) şi mai apoi după implantare ataşamentul tisular. Pentru a se obţine fosfaţi de calciu s-a utilizat metoda electrochimică. Depunerea electrochimică a fosfaţilor de calciu este una din cele mai eficiente metode datorită preţului scăzut.

STUDY ON GLASS AND ANTIMONY SENSORS USED FOR MEASURING PH DURING THE BIOREMEDIATION PROCESS OF SOIL

BY

OCTAVIAN STOICA[*] **and VALER MICLE**

Technical University of Cluj-Napoca,
Faculty of Materials Science and Engineering

Abstract. Glass membrane electrode for pH measuring in aqueous media is the most commonly used in all laboratories. However those who have used this type of electrode in soils pH measurement have reported a number of shortcomings, and even its occasional breakage in heterogeneous soil texture and with hard impurities. Antimony electrode offers an alternative for measuring the pH of some soils subjected to bioremediation. This paper presents a study on the glass membrane electrode and on the antimony electrode, highlighting some advantages and some disadvantages of these electrodes. It is also presented the construction of antimony electrode and some tests made on this electrode in acidic and in alkaline environments similar to those found in a soil bioremediation process. Results of the study present the efficiency of using the antimony electrode in such a process (bioremediation process).

Key words: soil, bioremediation, pH, antimony.

1. Introduction

The meaning and measurement of pH in aqueous and non-aqueous media, plays an important role in many practical and scientific fields: in

_____

[*] Corresponding author; *e-mail:* Octavian.STOICA@im.utcluj.ro

chemical analysis, regulation and control of technological processes, medicine, in biological research etc.

The pH concept, was introduced in 1909 by Sorensen as the exponent of hydrogen, and now has became familiar to all chemists, engineers, biochemists, etc. Even today his significance is a relatively controversial topic.

The term pH is defined by:

$$pH = -\lg a_H^+$$

where: a_H^+ - is the activity of hydrogen ions [14].

2. Soils and pH

PH is probably one of the most used indicators to achieve a virtual image in ensemble of the processes occurring in soil. Several strategies for the characterization of soil pH have been described in (Thomas, 1996). A method often used include 10 g of dry soil mixed with 10 ml of deionized water, or its many variants, varying soil-deionized water ratio. To validate the lab results it is necessary a precise methodology for determining the pH in external environment. Some studies have focused on pore water in the soil, and used either dipwells or piezometers in waterlogged environments, or suction samplers that allow sampling of pore water from soil above the groundwater level (Elberling & Matthiesen). Direct measurements of pH on specific sites with waterlogged soils have been tested by (Caple & Dungworth, 1998) using electrodes installed at different depths, for 7-10 days.

Viewed in the context of bioremediation of polluted soils, pH is a key parameter for a successful site remediation. Thus, pH is a parameter included in monitoring programs of the soil. Currently, are developed a wide range of methods for measuring pH, methods presented in Fig. 1, (Vonau & Guth, 2006).
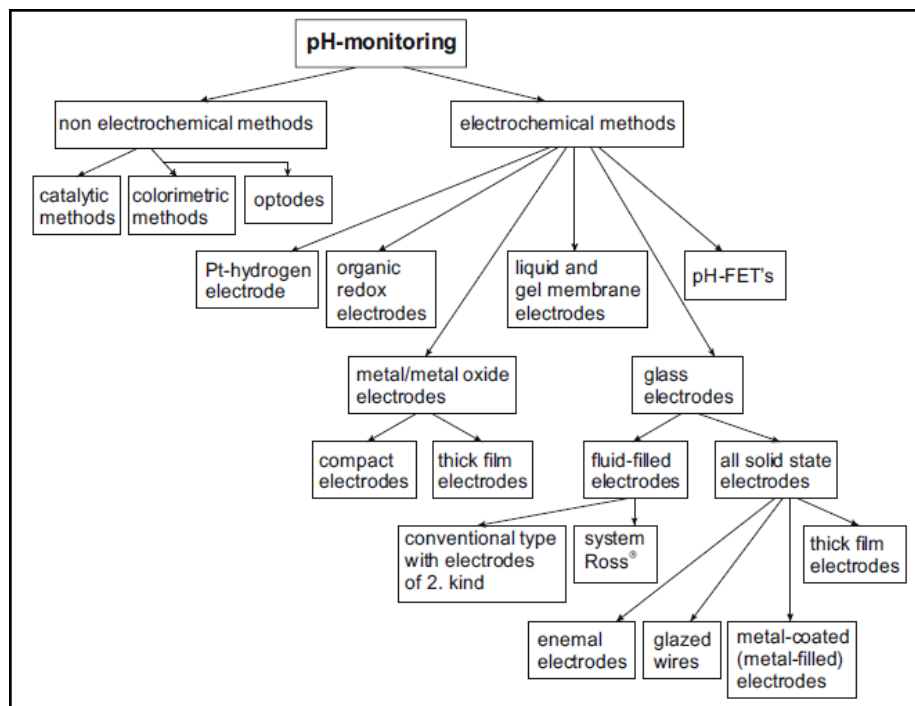
Fig. 1 – Experimental methods for measuring pH.

3. Glass electrode

Is the electrode which has a wide use, use barely occurred after 1950, due to the development of electrometers with electronic tubes. He belongs to the class of electrodes with membrane, its use in pH measurements is based on the fact that the potential which appears at the interface solution - glass-membrane is a function of hydrogen ion activity in solution. In Fig. 2 is a schematic representation of the function of the glass membrane (http://www.alliancets. com; Hopîrtean, 1988).

A 'gel layer' develops on the pH-sensitive glass membrane when a pH glass electrode comes into contact with an aqueous measuring solution. Such a 'gel layer' arises also on the inside of the glass membrane which is in contact with a defined buffer solution (the inner buffer). The H^+ ions either diffuse out of the gel layer, or into the gel layer, depending on the pH value of the measured solution. In the case of an alkaline solution the H^+ ions diffuse out and a negative charge is established on the outer side of the gel layer. Since the glass electrode has an internal buffer with a constant pH value, the potential at the inner surface of the membrane is also constant during the easurement. The total membrane potential is a result of the difference between the inner and outer charge.
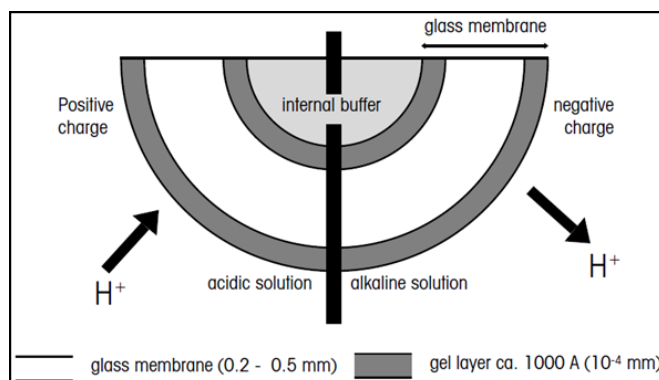
Fig. 2 – Schematic representation of the function of the glass membrane.

For usual electrodes the dependence of glass membrane potential in report with the hydrogen ions activity follow a defined law, in a range of pH values between 1 and 11. In strongly acidic and strongly basic medium, glass electrodes give erroneous indications of pH, but these errors can be corrected.

Until now, have been developed a wide range of technical processes to produce a wide range of pH glass electrode, whose basic functional elements are active glass membrane, the internal reference electrode and internal solution. General sketches of an combined, an reference and an simple glass electrodes for pH measuring are shown in Fig. 3 (http://www.alliancets.com; (Hopîrtean, 1988).
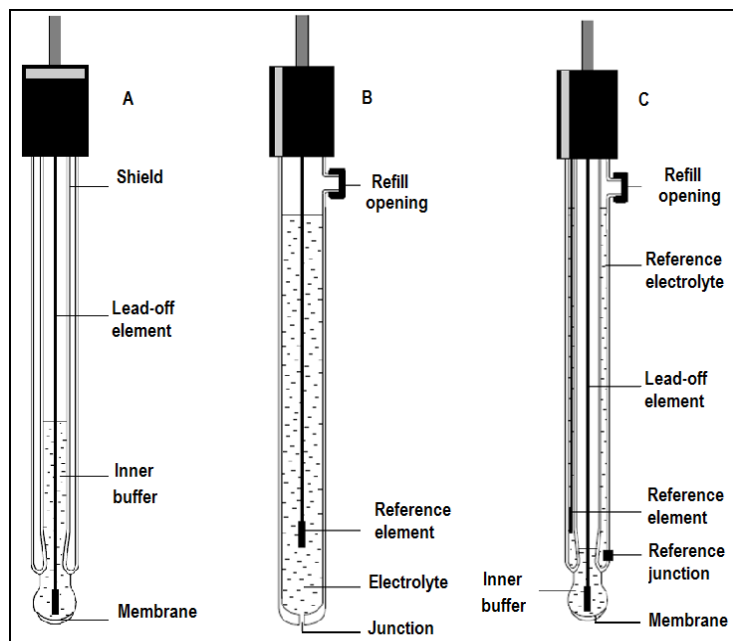
Fig. 3 – Structure of an: A – simple glass electrode; B – reference electrode;
C – combined electrode.

Electrodes are made from glass which has a number of qualities required: sensitivity to pH variation, time durable, high hygroscopicity and convenient electrical resistance reported with the possibilities of electronic measuring instruments. Generalizing, these glasses have a composition corresponding to 72.2% SiO_2, 6.4% CaO, Na_2O 21.4%, if sodium is replaced with lithium, can be achieved lithic glasses enabling precise measurements in the alkaline (pH up to 12-13). Uranium dioxide and germanium dioxide also gives to glasses a superior quality (Hopîrtean, 1988).

Advantages of using glass electrodes:

- It works with precision as electrodes which indicate hydrogen ion activity in a wide range of pH between 1 and 10 (or 1 and 13 in some special cases, *e.g.* lithic glass)

- Rapid is achieved a state of equilibrium, allow the execution of rapid tests in series (except for measurements in highly basic solutions)

- In analyzed solution it isn't necessary to introduce foreign substances, so does not contaminate the solution

- Measurements made with glass electrode are not influenced by oxidizing or reducing agents which are in solution; the presence of atmospheric air or other gases also does not affect the determinations

- It can make pH measurements in highly colored solutions in colloidal solutions, emulsions and suspensions, and generally in many heterogeneous systems

- Glass electrode measurements are not influenced by ions of elements positioned above hydrogen in the series of the electrode potentials

- Can be used for determining pH of un-buffered solution

- In comparison with the hydrogen electrode is not deteriorating so fast.

Disadvantages of glass electrodes:

- Must be handled carefully because of the fragility of membranes of glass (there are special glass electrodes with higher mechanical resistance);

- Having a high electrical resistance can't be used, generally in measurements with conventional potentiometric bridges, are required electronic devices;

- Glass electrode potential is influenced by the change in time of asymmetry potential, and this requires recalibration of the electrode from time to time;

- In strongly basic solutions, strongly acidic and high ionic strength, common glass electrodes have need some correction of positive and negative errors;

- In non-aqueous or partially aqueous solutions are obtained erroneous results, which also must be corrected.

4. Antimony Electrode

Where we meet, hydro-organics and aggressive environments for in-vivo measurements, the glass electrode can not be used due to slow response or membrane fragility of glass. In addition to general requirements, including rapid response, high sensitivity, long-term stability and ensuring reproducibility of pH measurements, the pH sensor must be easily manufactured in an appropriate size and shape without losing its mechanical strength. To maintain aseptic conditions, for example in the time when are realized some cultures, measuring electrodes should be treated at relatively high temperatures before making measurements. Add to this, is the high impedance of the membrane and instability in corrosive chemical system such as in hydrofluoric acid, which chemically attack the glass membrane (http://www.alliancets.com; da Silva *et al.,* 2008; Yang Ha & Min Wang, 2006).

These disadvantages of glass electrode leads our attention on antimony electrode which can be used for some of the cases mentioned earlier. The solution adopted is based on the fact that many bibliographic sources presents the use of antimony electrodes to measure soil pH of plant roots (Baghdady & Sommer, 1987), the pH of dental plaque (Jung-hoon *et al.,* 2007), in potentiometric determination of coke acidity and acetic acid content in vinegar

(Capelato *et al.,* 1996), attesting the fact that the use of antimony electrodes for on-line monitoring of pH proved to be a success.

Even if it is known as antimony electrode, it should be called right antimony - antimony trioxide electrode. The reaction that occurs on the antimony electrode can be written as follows:

$$Sb_2O_3(s) + 6H^+ + 6e \leftrightarrow 2Sb(s) + 3H_2O \tag{1}$$
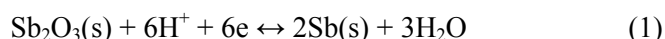
Antimony or antimony trioxide being found in solid phase are considered in their standard states of activity; in dilute aqueous solutions the activity of water may also be considered equal to unity. Considering these assignations, antimony electrode potential will be given by:

$$E = E^0 - \frac{2,3026 \cdot R \cdot T}{F} \cdot pH$$

Standard potential of antimony electrode does not show a very good reproducibility, and neither the slope of the curve E - pH is not constant in a field too wide of pH values. Antimony electrode sensitivity to pH can not be defined precisely because individual responses to pH electrodes are almost always very different from each other. Theoretical response to pH should of course follow the same function as for the hydrogen electrode, in fact, no part of the E-pH curve hasn't theoretical slope of -0.05916 V/pH (at 25°C). Moreover, the real slope varies from one region of curve to another. Izmailov and Pivnenko (1941) have established two areas where the curve E-pH is linear, between 2,5 - 9 and between 10 - 13. Generally, the values of real slope of the pH curve are lower than the theoretical values , and are ranging between 0.050 and 0.059 V/pH (at 25°C), which was mentioned also in (Galster, 1991). The low values of real slope are due to variation of standard potential of the electrode in function by pH of measured solution. Even if the theoretical values of the E-pH slope are different, the antimony electrode can be used in more precise measurements, with condition to prior calibrate it in several buffer solutions whose pH are already known.

4.1. Manufacturing Antimony Electrode

Antimony is heated to 750°C (Sb, mp 630°C, bp 1587°C) in an alumina crucible. After melting, the liquid metal is absorbed in a glass capillary tube, if is desired a miniaturization of such a sensor, or liquid metal is poured into a desired shape with dimensions previously made. In (Vonau & Guth, 2006) is presented that a centrifugal casting of molten antimony would lead to obtain sensors with a potential slope very close to the ideal slope. Antimony electrode

can be formed from: an antimony-piece molded, fixed into a rubber, plastic, or glass support as can be seen in Fig. 4, and a wire as part for connection.
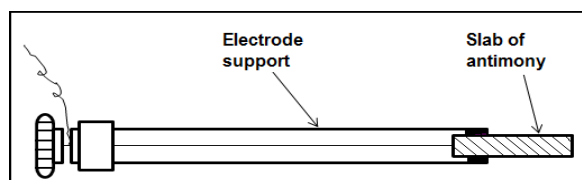
Fig. 4 – Antimony electrode [12].

Because no special precautions are taken, the metallic electrode surface is covered in humid air or aqueous solutions with a fine film of antimony trioxide. In (Yang Ha & Min Wang, 2006) is presented, oxidation of antimony electrode in a KNO_3 melting. After oxidation of the electrodes, they get a matte aspect having a high precision and reproducibility in comparison with the glossy electrodes.

Oxidizing and reducing agents, as well and complexing agents, such as tartrates, oxalates and citrates, make improper functioning of the electrode. Copper ions also influenced the use of this electrode.

Advantages of using antimony electrodes:
-Relatively low cost for electrode construction
-Robust (ideal for measurements in soil)
-Presents a relatively good linear response on soil pH interest range
-Quick response to low temperature
-Less errors in the alkaline domain in comparison with glass electrode
-Can be used in solutions containing hydrofluoric acid
-Acceptable measurements of pH even at a relatively low purity of antimony used in construction of electrodes
-Operational life time, can be said "unlimited"

Disadvantages of antimony electrodes:
-Major errors in measuring pH at values lower than 1
-Errors of measurement in the presence of copper ions
-Sensitive element is relatively brittle, when is mechanical processed.

5. Own Results Regarding the Construction of Antimony Electrodes used in pH Measurements

The main components of the electrodes are: sensitive part at H^+ made from antimony (electrode head), a plastic support, copper wire conductors (for the realization of electrical contacts), the cap of electrode, connection cable. According to the theoretical study presented in chapter .4.1, was cast from antimony with purity 99.65%, a metallic rod with a length of 20 mm and 4 mm

in diameter. This rod was caught in a previously designed polypropylene support (see Fig. 5).

Fig. 5 − Antimony electrode; A- sensible element, B- plastic support for electrode,
C- Antimony electrode assembly, D- Section through the body and an cap of electrode.

For the construction of a small electrode (miniaturization), as our case 1.5 mm (Fig. 6), this can be constructed as follows: The small piece of the prepared antimony rod was soldered to a copper lead for electrical contact; The metal rod was sealed into a short length of glass tubing of the same size with the help of fast setting epoxy glue.

Fig. 6 − Antimony electrode with glass support.

5.1. Testing of Antimony Electrodes in Acidic and Alkaline Solutions

Further will be presented the response of antimony sensors, made according bibliographical studies and presented in Fig. 5 (No. 1) and Fig. 6 (no.2), paired with a reference electrode Ag / AgCl purchased commercially, both immersed in standard buffer solutions with pH 1,68; 4,01; 6,88; 9,23.

Both electrodes present a fast and stable response toward pH change for aqueous solutions. The potential of the antimony electrodes have a linear relationship with the pH of the solution (fitting correlation coefficient R= 0,99 and R=0,99) with a sensitivity of 51,05 and 50,47 mV/pH.

Table 1

pH	Electrode no. 1, E [mV]	Electrode no. 2, E [mV]
1,68	-86	-83
4,00	-178	-176
6,88	-332	-334
9,23	-442	-443
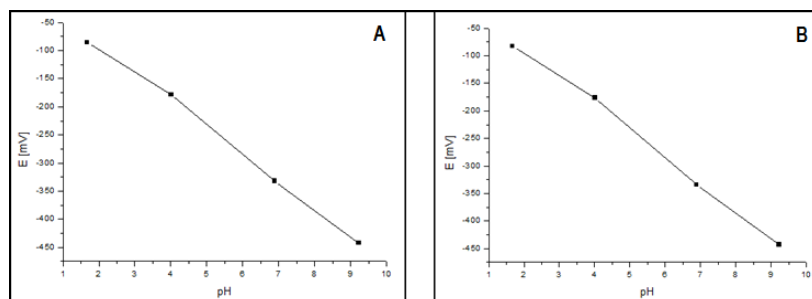
Fig. 7 – Curves of the potentials response of: A – antimony electrode presented in
Fig. 5, B – antimony electrode presented in Fig. 6, to pH change in multi-ion-buffers.

6. Conclusion

Because antimony electrode has a fast response and a stable potential at
all pH changes within the range 2-10, moreover, the response time was relative
reduced and response curves showed a good reproducibility, is reinforced the
claim that this type of electrode can be adapted to on-line monitoring of soil in
bioremediation process.

REFERENCES

* * *Alliance Technical Sales, Guide to pH Measurement*. http://www.alliancets.com
* * *ISA 48th *Analysis Division Symposium*., April 27 . May 1, 2003, Calgary, Alberta,
    Canada.
Baghdady H., Sommer K., *Improved Construction of Antimony Micro-Electrodes for
    Measuring pH-Changes at the Soil-Root Interface (Rhizosphere)*, Plant
    Nutrition, *10*, 1231 (1987).
Capelato M. D.,. dos Santos A. M, et al., *Flow Injection Potentiometric Determination
    of Coke Acidity and Acetic Acid Content in Vinegar Using an Antimony
    Electrode*. Analytical Letters, **29**, 5, 711-724 (1996).
Caple, C. & Dungworth, D., *Waterlogged Anoxic Archaeological Burial Environments*.
    Report 22/98. English Heritage. Ancient Monuments Laboratory, London
    1998.
da Silva G.M., Lemos S.G., et al., *Development of Low-Cost Metal Oxide pH
    Electrodes Based on the Polymeric Precursor Method*. Analytica Chimica
    Acta, *616*, 36–41 (2008).
Elberling B., Matthiesen H., *Methodologically controlled variations in laboratory and
    field pH measurements in waterlogged soils*, European Journal of Soil Science,
    58, 207–214.
Galster H., *pH Measurements-Fundamentals*, Methods, Applications, Instruments,
    VCH, New York, 176 (1991).

Hopîrtean Elena, *Prepararea si functionarea senzorilor electrochimici potentiometrici*, Electrodul de sticla de pH, Revista de chimie, **39**,*12*, 1133-1140 (1988).

Izmailov N., Pivnenko A., Ref. Jurnal, *4*, 65 (1941).

Jung-Hoon Ro, Soo-Young Ye, *et al., Development of Indwelling Wireless pH Telemetry of Intraoral Acidity*. World Academy of Science, Engineering and Technology *30*, 2007.

Luca C., *pH-ul şi aplicaţiile lui*. Ediţia a doua îmbunătăţită, Editura tehnică Bucureşti, 1973.

Michael Schirrmann, et. al., *Soil pH Mapping with an On-The-Go Sensor*. Sensors 011, *11*, 573-598 (2011).

Neniţescu C.D., *Chimie generală*. EDP Bucureşti 1985.

Thomas G.W., *Soil pH and Soil Acidity. In: Methods of Soil Analysis*. Part 3, Chemical Methods (ed. J.M. Bartels), Soil Science Society of America Book Series, *5*, 475–490 (1996)..

Vonau W., Guth U., *pH Monitoring: a Review, J Solid State Electrochem. 10*, 746–752 (2006).

Yang Ha, Min Wang, *Capillary Melt Method for Micro Antimony Oxide pH Electrode*. Electroanalysis, **18**, *11*, 1121 – 1125(2006).

STUDIUL SENZORILOR DE STICLĂ ŞI ANTIMONIU FOLOSIŢI PENTRU MĂSURAREA PH-ULUI ÎN TIMPUL PROCESULUI DE BIOREMEDIERE A SOLULUI

(Rezumat)

Electrodul cu membrană de sticlă pentru măsurarea pH-ului în medii apoase este cel mai frecvent utilizat în toate laboratoarele. Cu toate acestea cei care au utilizat acest tip de electrod au raportat o serie de neajunsuri, sau chiar spargerea ocazională a acestuia, în soluri cu textură neomogenă şi/sau cu impurităţi de dimensiuni mari. Electrodul de antimoniu oferă o alternativă pentru măsurarea pH-ului unor soluri supuse bioremedierii. Lucrarea prezintă un studiu asupra electrozilor cu membrană din sticlă şi din antimoniu, scoţând în evidenţă unele avantaje şi dezavantaje ale acestor electrozi. Este prezentată, de asemena, construcţia unui electrod de antimoniu şi testarea acestuia în medii acide şi alcaline asemănătoare cu cele întâlnite în cadrul unui process de bioremediere a solurilor. Rezultatele studiului efectuat arată eficienţa utilizării electrodului de antimoniu în cadrul unui astfel de proces (procesul de bioremediere).

SIMULATION OF THE FLAT CROSS-WEDGE ROLLING PROCESS USING THE METHOD OF FINITE ELEMENTS

BY

S. SUCHORUKOV[*], I. SYVAK and K. KOTZUBIVSKA

Vinnytsia National Technical University

Abstract. It is show, that during flat cross-wedge rolling simulation process using FEM of LS-DYNA package, re-division of the workpiece finite-element grid is required. This is determined by a sudden change of the metal flow direction during forming process. Application of r-adaptive finite-element grid re-division, in the places of big plastic deformation has made it possible to improve the mathematical model quality and to refine the values of strained state parameters.

Key words: flat cross-wedge rolling, finite-element grid, re-division.

1. Introduction

While designing and modeling different plastic metal working processes the simulation using the finite element method have found wide application as an alternative to experimental studies and analytic investigation.

When simulation data are prepared, it is necessary to have information about the workpiece material resistance to deformation, contact friction parameters, etc.

Calculation accuracy of numerical simulation will be determined not only by the validity of the initial date, but also by the correctness of the

----

[*] Corresponding autohor; *e-mail:* ssergeii@ukr.net

mathematical model construction (Сатонин, 2006; Матвийчук, 2009; Шпак, 2007; Алиев, 2008).

The goal of the paper is simulation of the flat cross-wedge rolling process (FCWR) using the finite element method (Fig. 1).

Cross-wedge rolling is a highly productive technology of the plastic metal working. Main advantages of this process are reduction in the consumption of materials and higher quality of the obtained workpieces. This process is distinguished by the material being subjected to large plastic deformation (Bartnicki, 2005; Pater, 2006).
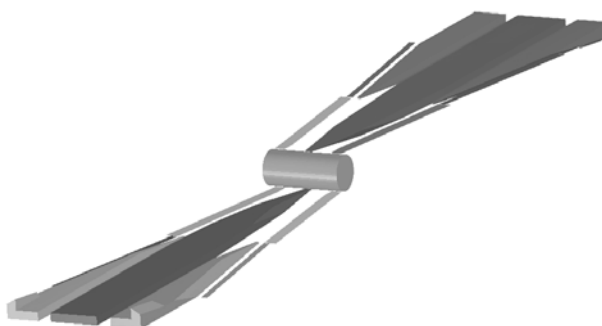
Fig. 1 − 3D model of the tool and the workpiece in the FCWR.

For model elaboration and further analyses of the simulation results pre-postprocessor LS-PREPOST Ver.3.0 that is included into LS-DYNA 971 package (Сухоруков, 2009).

For partitioning the model of the tool and the workpiece 8-node finite elements were used. If it was necessary, the system combined certain vertexes into one automatically, *i.e.* a finite element could be both of a cubic form and in a form of tetrahedron or a pyramid.

The tool was represented as an absolutely solid body with the following boundary conditions: it moves only in the direction of x-axis with constant speed; all other movements are forbidden.

The contact between the tool and the workpiece was set a contact algorithm of the "surface-surface" type.

In the process of simulation finite elements were strongly deformed in the place of intensive forming (Fig. 2) due to a sharp change of the metal flow direction. To prevent such phenomena, that have negative influence on the validity of the FCWR process simulation model, it is necessary to perform re-division of the finite element mesh during the calculation process.

In terms of calculation time and minimal size of the element, r-adaptive re-division of the finite-element mesh could be considered the most effective one, the possibility of setting the minimal element size being provided while rebuilding the mesh (LS–DYNA, 2006).
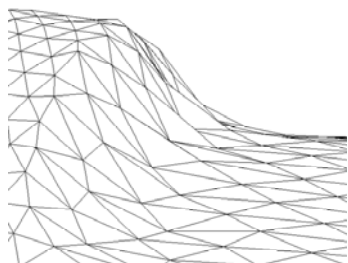
Fig. 2 − Deformation of finite elements in the place with the largest forming.

LS-DYNA program makes it possible to perform r-adaptive re-division of the finite-element mesh only in the places with deformations that achieved a certain value, and not trough the entire volume of the deformed workpiece (Fig. 3). That main parameters that influence the obtained mesh quality are included into the *CONROL REMESHING* and *CONROL ADAPTIVE* cards that are responsible for re-meshing. In the parameters included into these cards were used:
*CONTROL_REMESHING
$ rmin   rmax
  0.2   6
*CONTROL_ADAPTIVE
$ adpfreq adptol adpopt maxlvl tbirth tdeath lcadp ioflag
 0.10000 0.000   7   0   0.4   0.000   0   1
where rmin and rmax are minimal and maximal sizes of the finite element created after re-division; adpfreq – time interval between re-divisions; adpopt – r-adaptive re-division of the finite-element mesh a bar 3D element; tbirth – the time of launching the first re-division.
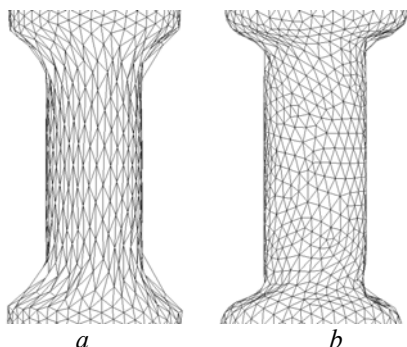
Fig. 3 − Finite-element grid of the workpiece at the calibration stage: *a* − without re-division; *b* − with re-division.

a   *b*

As result of calculations, the values of the main stresses and deformations in the dangerous point on the workpiece axis were obtained. No estimate the influence of the strained state on the workpiece plasticity, invariant characteristics were used:
    - Nadai-Lode parameter

$$\mu_\sigma = 2\frac{\sigma_2 - \sigma_3}{\sigma_1 - \sigma_3} - 1 \tag{1}$$

- the stressed state index

$$\eta = \frac{I_1(T_\sigma)}{\sqrt{3I_2(D_\sigma)}} = \frac{3\sigma}{\sigma_u} \tag{2}$$

where $I1(T_\sigma)$ – the first invariant of the stress tensor;

$I2(D_\sigma)$ – the second invariant of the diviator tensor;

σ_u – the intensity of stresses.

The analysis of the results of the FCWR process simulation using LS-DYNA 971 (finite element method) has shown that application of the option of r-adaptive finite-element mesh re-division improve geometric accuracy of the obtained model. If was also found that in FCWR process modeling without r-adaptive rearranging the values of the strained state parameters turned to be overestimated by 15-20%, which is determined by large deformations in the contact zone and strong distortion of the finite element mesh.

For steel 18ХГТ (workpiece material) the limit deformation ep dependence on the stressed state under the temperature of 950ºC was set by the surface of limit deformations:

$$e_p(\eta, \mu_\sigma) = 0,82 \exp(0,44\mu_\sigma - 0,54\eta) \tag{3}$$

To estimate the utilized plasticity resourse ψ for steel 18ХГТ in the temperature range – 950…1050 ºC deformability (fig. 4) criterion is proposed.

$$\psi = \int_0^{e_u} \frac{\exp[-\beta(T - 950)]}{0,82 \exp[0,44\mu_\sigma - 0,54\eta]} de_u , \tag{4}$$

which gives satisfactory description of the damage accumulation process, provided that the sign of curvature of the loading trajectory in the space of e_p, η, μ_0 remains unchanged. If the sign of curvature of the loading trajectory in chosen coordinates changes, for the utilized plasticity resource estimation it is necessary to use the criterion:

$$\psi = \int_0^{e_u} n \frac{e_u^{n-1} \exp[-\beta(T - 950)]}{(0,82 \exp[0,44\mu_\sigma - 0,54\eta])^n} de_u , \tag{5}$$

where T – temperature in Celsius, $n = 1 + a\dfrac{d\eta}{de_u} - b\dfrac{d\mu_\sigma}{de_u}$, a, b – empirical coefficients that were taken a = 0,04, b = 0,028 for steel 18ХГТ under the temperature 1000 ºC, β – coefficient.

In general case coefficient β depends on the temperature and the stressed state scheme, *i.e.* $\beta = \beta(\eta, \mu_\sigma, T)$. In this work β values were assumed to be constant and equal β = 0,0025 for the chosen temperature range – 950…1050ºC.
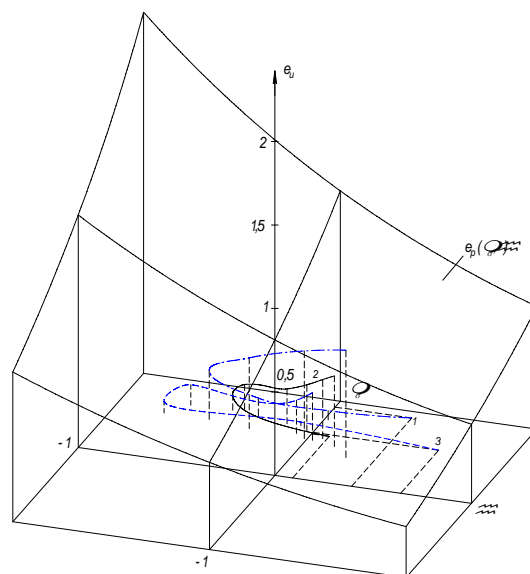
Fig. 4 – The surface of limit deformations.

Results of the stress-strain state calculation were used to build a loading trajectory for point 1, that is located in the point of workpiece axis intersection with its vertical surface of symmetry, and for points 2 and 3 located at the distance of Δr2 = 8 mm and Δr3 = 4 mm from the workpiece axis and at the distance of Δx2 = 3 mm, Δx3 = 6 mm from the vertical surface of symmetry (trajectories 2 and 3 Fig. 4). Fig. 4 also presents the limit deformation surface (3) for steel 18ХГТ under the temperature 950ºC.

The utilized plasticity resourse ψ in the points 1, 2 and 3 was calculated using the criterion (5).

3. Conclusion

The investigation of the flat cross-wedge rolling process using the finite-element method has shown that there is a dangerous (in terms of damage) point on the workpiece axis. When the wedge is introduced, the stressed state scheme in the area close to the deformation spread region is dangerous. If the workpiece is further deformed, in its axial region full is imposed on the pure shear deformation and loading path of point 1 is shifted into a more rigid zone, which leads to a fast increase of the utilized plasticity resourse.

REFERENCES

∗ ∗ LS–DYNA Keyword User's Manual version 970. Livermore Software Technology Corporation, 1564 (2006).

Алиев И.С., Жбанков Я.Г., Абхари П., *Решение проблемы формоизменения математическим моделированием в процессе радиально-прямого выдавливания на оправке*. Удосконалення процесів і обладнання обробки тиском в металургії і машинобудуванні: тем. зб. наук. праць. – Краматорськ: ДДМА, 26-36 (2008).

Bartnicki J., Pater Z., *Numerical Simulation of Three-Rolls Cross-Wedge Rolling of Hollowed Shaft*. J. of Mat. Processing Technology, **164**, 1154–1159 (2005).

Сатонин А.В., Александрова З.А, Стежкин П.М., Смолякова В.В., *Расчеты процессов листовой штамповки при помощи конечно-элементного комплекса LS-DYNA 3D*. Зб. наук. праць–Краматорськ: ДДМА, 11–16 (2006).

Сухоруков С.I., Коцюбівська К.I., Сивак І.О., *Оцінка деформуємості заготовок при поперечно-клиновій прокатці*. Наукові нотатки. Луцьк, *25*, 272-275 (2009).

Матвийчук В.А., Алиева Л.И., Сухоруков С.И. *Моделирование высадки торцевой раскаткой наружных буртов на трубных заготовках*. Обработка металлов давлением. – Краматорск, *2*, 46-51 (2009).

Pater Z., Bartnicki J., Samołyk G.*Numerical Modelling of Cross-Wedge Rolling Process of Ball Pin*. Journal of Materials Processing Technology, **164**, 1235–1240 (2006).

Шпак В.И., Сатонин А.А., Давыденко Е.С., *Конечно-элементное моделирование совмещенных процессов прокатки Зб*. наук. праць – Краматорськ: ДДМА, 420 – 424 (2007).

SIMULAREA FOLOSIND METODA ELEMENTULUI FINIT A PROCESULUI DE LAMINARE „FLAT CROSS-WEDGE"

(Rezumat)

În această lucrare, în care se realizează analiza cu element finit a procesului de laminare „flat cross-wedge", folosind pachetul de programe LS-DYNA, o rediscretizare a este necesară. Aceasta este determinată de schimbarea bruscă a direcţiei de curgere în timpul procesului de deformare. Aplicarea elementului finit „r-adaptive" şi rediscretizarea, în locul unei deformări plastice mari a făcut posibilă modificarea modelului matematic şi rafinarea parametrilor stării de tensiuni.

FRACTAL PATTERNS IMMUNOMODULATORY EFFECT OF THE VASCUM ALBUM IN THE EXPERIMENTAL EXPOSURE TO CHROMIUM

BY

DIDI SURCEL[1]*, MIOARA BUTAN[2], SEPTIMIU TOADER[3], CSABA SZANTO[2], OVIDIU ROTARU[4], SIMONA NITU[5] and CARMEN PONORAN[5]

[1] Blue Life Medical Center,
[2] Institutul de de Sanatate Publică,
[3] UMF Cluj,
[4] Institutul Agronomic,
[5] Plant Extract

Abstract. The aim of this paper is to demonstrate a possible protective effect of the vascum on the immune and oxidative response altered by chromium administered. In vivo experiment was carried out on the 80Wistar male rats divided in 4 groups following: 1. Control –group; 2. Vascum-group; 3 Chromium-group; 4. Vascum+chromium-group.Chromium was administered by intratracheally instillation and vascum per oral. A part of the each group was sacrificed after 60 days and the other part after 180 days. The following parameters were assessed: 1. 3HTdR incorporation test; 2. IL-1-assay; 3. TNF-assay; 4. Chemiluminiscence assay; 5. Morphological parameters. Chromium exposure is associated with alteration of the immune and oxidative response, evaluated by the modification of the immune response, cytokines and ROS' level. Partial reversibility of the parameters in the Vascum+chromium-group, suggest a protective effect of the Vascum on the dangerous effects induced by chromium.

Key words: immune response, Cr, Vascum, cytokins, ROL.

---

* Corresponding author; *e-mail:* didisurcel1@gmail.com

1. Introduction

Epidemiological studies pointed out those chromium (Cr) occupational exposure workers have increased risk for respiratory tract carcinoma. Cr-induced bronchial carcinoma has developed through a sequence of cellular alteration and has a long period of the reversible alteration. Many studies have associated the effect of the carcinogenic chemicals with immune functions.

The early pulmonary response to Cr is a dynamic one and includes an important influx and proliferation of alveolar macrophages (AM), with high level of the various cytokines (IL-1, TNF, IL-6) and proliferations of the type II cells. AM are thought to play a pivotal role in lung inflammatory and immune responses trough alteration in their ability to induce particles phagocytosis, antigen presentation, cytokines secretion and to produce toxic oxygen radicals. The inflammatory response is intrinsically destructive to the tissues surrounding area of the inflammation.

In the last years there is considerable interest on the antitumorous effects of the Vacuum Album plant extras. Various data point out those antitumor activities of the Vascum Album that could be ascribed to the combination of citotoxic and immunologic effects induced by industrial noxious substances.

The present study was undertaken to explore the effects of chronic exposure of the Cr with and without Vascum association on the immune, oxitative and morphological reactions in the Wistar rats.

2. Materials and Methods

In vivo experiment was carried out on the 80 Wistar male rats of 180-200g, that were divided into 4 groups as following: 1 Control-group; 2. Vascum Album-treated group (animals were given daily Vascum Album,4CH, 2ml / animl; 3. Chromium –treated group (animals were intra-tracheally instilled with 0.2mg K2Cr207 / animal; 4. Cr+ Vascum (animals were treated with Cr and Vascum in the same conditions as the animals from 2 and 3- groups. Half on animals from all the groups was sacrificed at 60 days after Cr instillation and the other half was sacrificed at 180 days after Cr instillation. The animals were sacrificed by tethal injection of sodium pentobarbital (250mg/kg body wt.) and bronchoalveolar lavage was carried out. For the investigation of the immune response were performed AM cultures preparation of splenic lymphocytes (Lys), co-cultivation of the AMs with Lys (1/40) for mitogen -induced lymphocyte proliferation. The following parameters were assessed: 1. 3HTdR incorporation test; 2. IL-1-assay; 3. TNF-assay; 4. Chemiluminiscence test; 5. Morphological parameters.

2.1. Mitogen-Induced Lymphocyte Proliferation

Mitogen-induced proliferation of spleen-derived lymphocytes (Ly) co-cultured with AMs was determined. Briefly, 1.10 spleen cells were cultured with authologous AMs (ratio40/1) in presence of phytohemaglutinin-p (PHA) in a total volume if 1mmlRPMI-1640 medium. supplemented with 10% FCS. After 48H a 0.5 fuci of 3HTdRwas added and the incubation was continuator for an additional 24 h. The 3HTdR incorporation was measured with a liquid scintillation counter. The results were presented as counts per minute (cpm) values ± standard error of means.

2.2. Interlukin-1 (IL-1) Assay

Interlukin-1 activity was assayed by measuring the capacity of dialyzed culture fluid to enhance the PHA–induced proliferation of mouse thymus cells in vitro. Thymuses from parathimic lymph nodes were aseptically removed from mice and were homogenized. After washing the cells were suspended at 3.10^7 cells /ml in RMPI-1460 medium, containing 10% FCS, 2 Mm l-glutamine and 5.10-5m2 mercaptoethanol, in 50 μl of medium. The cells were inculated for 72 h at 37^oC and pulsed for 3 h with 3HTdR (20Ci/mmol, 1uCi/well). The cells were collected and the uptake of 3HTdR was determined by scintillation counting. The result were presented as mean counts per minute (cpm) values ± standard error of means.

2.3. Tumor Necrosis Factor (TNF) Assay

Tumor necrosis factor (TNF) activity in culture of the bronchoalveolar cells was determined by 3 HTdR release in actinomicyn D-treatment L 929 target cells. Briefly, cells belonging to mouse L929 fibroblasts were incubated for 24 h with 1uCi/mol of 3HTdR in RMPI-1460 medium. The adherent cells were detached from the surface of the culture flask by gentile washing (three times) with media and were resuspended in RMPI-1460 medium, containing 3μg/ml actinomicyn D, at 3.10^5 cells. Five hundred microlites of target-cell suspension as added to 500 μl of macrophages culture supernatant and incubated 24h at 37°C.At the end of the incubation period tubes were centrifuged at 400 g for 10 min and 3HTdR release measured in a Beckman liquid counter. Results were expressed as mean counts per minute (cpm) values ± standard error of means.

2.4. Chemiluminiscence Assay

Luminal dependent chemiluminiscence (CL) assay evaluated the stimulated (zymosan) radical oxygen species (ROS) release of AMs. Briefly, the reaction mixture consisted of 100 μl freshly prepared luminol solution from

stock solution 10 mM luminol in dimethil sulfoxid was diluted 1:50 in aqua distillated; 100 µl RMPI- 1460 medium containing 10 mg/ml Zymosan and 100 µl cell suspension containing 2.10^5 AMs. The CL was measured over the next 30 min. in a Beckman liquid scintillation counter. Results were expressed as mean counts per minute (cpm) values ± standard error of means.

2.5. Statistical Analysis

Differences between groups of the experiment were analyzed for statistical significance by using student's "t" test.

3. Results and Discussions

3.1. 3HTdR Incorporation Test (Fig. 1)

PHA- induced splenic Ly proliferation in the co-cultures containing autologous AMs, showed differences in the investigated groups. In the Vacuum Album-treated group the 3HTdR incorporation was without statistically significant differences as compared to the control-group. The Chromium – treated group presented decreased level of the 3HTdR incorporation with statistically significant differences as compared to the control-group, in the animals sacrificed after 180 days. In the animals sacrificed at 60 days after Cr instillation, level of the 3HTdR incorporation is decreased, but without statistically significant differences as compared to the control-group. In the Cr+ Vascum-group level of the 3HTdR incorporation was increased as compared to the Cr-group, but without statistically significant differences in the animals sacrificed at 30 days after instillation and with statistically significant differences (ssd) after in the animal sacrificed after 180 days. These data showed that Vascum is able to ameliorate PHA-stimulated splenic Lys proliferation that was modified by Cr. exposure.
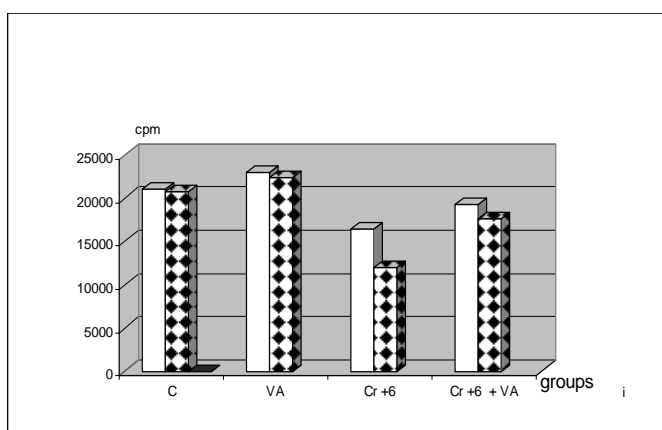
Fig. 1 – 3HTdR Incorporation Effect of the Vascum Album on the 3TdR incorporation by PHA – stimulated splenic Lys, in the presence of the autologous AMs, at 30 days and 180 days, after rats instillation with dichromate.

3.2. IL-1-Assay (Fig. 2)

IL-1production in supernatants from AMs obtained from investigated groups was assayed by measuring the capacity of the culture supernatants to co-stimulate the mitogen-induced tymocite proliferation. The differences in the generations of the

IL-1 production from investigated was observed. The production of the IL-1 in the Vascum treated group was very low and similar with control group. An important increase of the IL-1 production was detected in the Cr. treated – group and the differences were with high statistically significance versus to Controls. In the Cr+ Vascum-group, the IL-1 production was reduced as compared with cr.treated –group, (with ssd), but in comparison with Controls, the level of the cytokines was increased with ssd. These data suggest that Vascum may ameliorate IL-1 activity, altered by Cr.
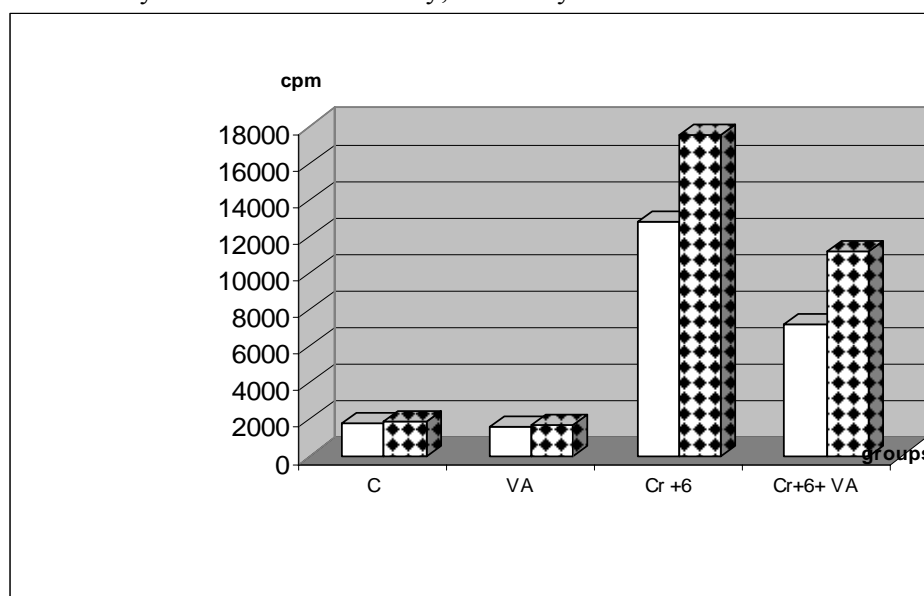
Fig. 2 – IL-1 release by AMs obtained by AMs by BAL,at 30 and 180 days after Cr and Vascum Album exposuhe rats.

3.3. TNF –Assay (Fig. 3)

The spontaneous TNF release was low in all the group. In the presence of the low concentrations of the LPS, AMs from Cr-treated-group pointed out very high TNF activity, with ssd as compared to Controls. In the Cr+ Vascum treted –group level of this cytokine was increased versus Controls (with ssd),

but decreased with ssd as compared to Cr-treated group. These results showed that Vascum interfere with the activity of the TNF and may induce attenuated values of this cytokine in the chromium instillation of the rats.
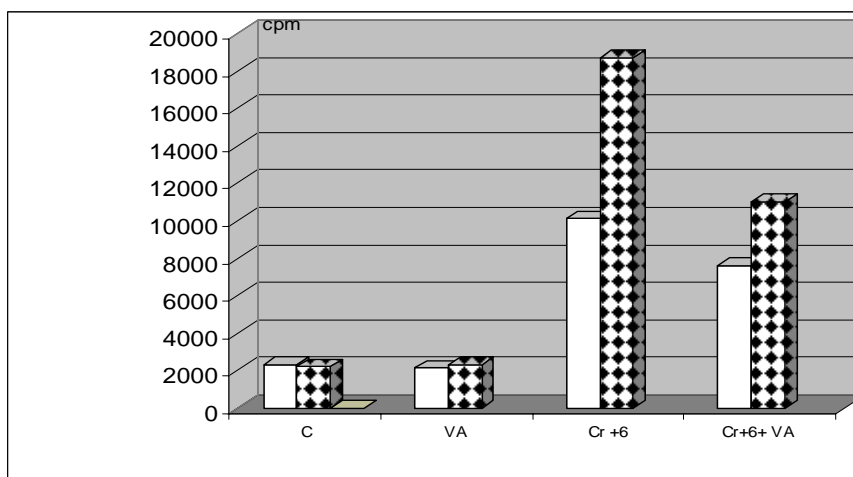
Fig. 3 – TNF release by AMs obtained by AMs by BAL, at 30 and 180 days after Cr and Vascum Album exposure rats.

3.4. Chemiluminiscence (CL) Assay (Fig.4)

The oxidative response of the AMs belonging to the investigated groups measured by luminal-dependent CL, shoved important differences in the investigated groups.
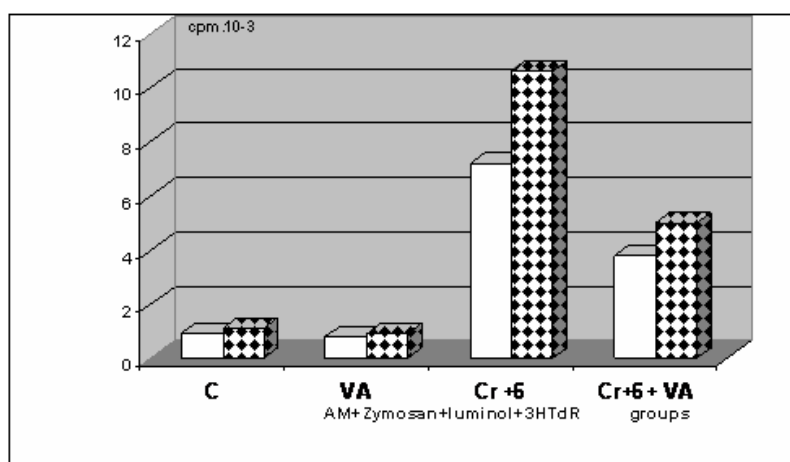
Fig. 4 – LUMINOL - DEPENDENT CHEMILUMINISCENCE ASSAY. Effect of the chronic exposure to on ROS release from the MAs, obtained by BAL, 30 and 180 days after Cr^{+6} and Vascum Album – exposed rats.

Vascum-group presented low levels of the ROS, generation similar with control group. A very important increase of the ROS production was detected in the all animals from Cr. instilled- group, with high ssd as compared to Controls. In the Cr + Vascum treated –group level of the ROS production was reduced as compared to Cr-treated group, with ssd. These data sugest that high level of the ROS induced by Chromium may be reduced by Vascum Album administration.

3.5. Morphological Parameters

The following histopathologically modifications were evidenced in investigated groups. In the Vascum Album were noted the same morphological aspects as in the Controls. In the Cr^{+6} group all the rats developed one or more metaplastic add dysplastic lesions in the bronchial epithelium, and 6 developed cacinomas. The Cr^{+6} and Vascum Album group, 6 rats develop metaplastic lesions, 2 displastic lesions and none developed lung cancer.

4. Conclusion

Cr interferes with immune reactions, were AMs play a pivotal role by releasing high levels of the IL-1, TNF and ROS. Morphological modifications consist in 5 carcinomas, and dysplastic and metaplastic lesions in all the rats.

VASCUM ALBUM administered simultaneous with Cr +6 is associated with partial reversible results of the 3HTdR incorporation, IL-1 and TNF activity and important decrease of the ROS. Morphological modifications are light and consist mainly in metaplastic lesions, reduced dysplastic lesions and anyone lung cancer.

LIPSA TRIMITERI IN TEXT A BIBLIOGRAFIEI

REFERENCES

Arunkumar R.I., Rajasekaran P., Michael R.D., *Differential Effect of Chromium Compounds on the Immune Response of the African Mouth Breeder Immunology.* **10**, *8*, 667-676 (2000).

Driscoll K.E., Higgins J.M., Leytart M.J., *Differential Effects of Mineral Dusts on the in Vitro Activation of Alveolar Macrophage Eicosanoid and Cytokine Release*, Toxic in vitro, **4**, *4/5*, 284-288 (1990).

Geir W., – *The mistletoe – preparation Isorel, in cases of carcinoma of the larynx-case report of a total remission- Krebsgeschehen. 1*, 4-79 (1982).

Jurin M., Zarkovic N., Hrzenjak M., Ilic Z., *Antitumorous and Immunomodulatory Effects of Viscum Albuml.* Preparation ISOREL, Oncology, *50*, 393-398 (1993).

Kissel D., *Infusion Therapy of Carcinomas with Vascum Album.* Annual Volume, *15*, 482-488 (1987).

Shrivastava R., Seth R.K., Chaturvedi U.C., *Effects of Chromium on the Immune System FEMS Immunology & Medical Microbiology*, **34**, *1*, 1–7 (2002).

Stohs Sidney J., Bagchi Debasis, Hassoun Ezdihar, Bagchi Manashi, *Oxidative Mechanisms in the Toxicity of Chromium and Cadmium Ions.* Journal of Environmental Pathology. Toxicology and Oncology 20(2), 77-88 (2001).

Wang J.Y., Wicklund B.H., Gustilo R.B., Tsukayama D.T., *Prosthetic Metals Impair Murine Immune Response and Cytokine Release in Vivo and in Vitro.* J. Orthop. Res. 15, 688–699 (1997).

Yucesoy B., Mirshahidi S., Yucesoy C., Karakaya A., *In Vitro Effects of Various Metals on Natural Killer Cell Activity in Cultured Human Lymphocytes.* Immunopharmacol. Immunotoxicol. 21, 599–607 (1999).

EFECTUL IMUNOMODULATOR AL PREPARATELOR DE VÂSC ÎN
EXPUNEREA PROFESIONALĂ LA CROM. STUDII EXPERIMENTALE

(Rezumat)

Subiectul acestei lucrări a fost de a demonstra un posibil efect protector al preparatelor de vâsc asupra răspunsului imun şi oxidativ, alterat prin instilarea animalelor de experienţă cu crom. Experimentul în vivo a fost realizat pe 80 şobolani, linia Wistar, împărţiti în 4 grupuri: 1. Lot -Martor; 2. Lot- Vâsc; 3. Lot-Crom; 4. Lot-Vâsc+Crom. Cromul a fost administrat prin instilare intratracheala, iar vâscul a fost administrat oral. O jumătate din fiecare lot a fost sacrificat la 30 zile după instilare, iar cealaltă jumătate la 180 zile.Au fost investigaţi următorii parametrii: 1.Incorporarea de 3HTdR; 2.Nivelul de IL-1; 3. Nivelul de TNF; 4.Testul de chemiluminiscenta; 5.Parametrii morphologici. Expunerea îndelungata la crom este asociată cu alterarea raspunsului imun si oxidativ, evaluat prin modificarea incorporarii de 3TdR, nivelul de citokine si mai ales de ROS. Reversibilitatea parţiala a parametrilor investigaţi în grupul Vâsc+crom a sugerat un efect protector al preparatului de vâsc asupra efectelor distructive, induse de crom.

[1]. (Arunkumar *et al.,* 2000)
[2]. (Driscoll *et al.,* 1990)
[3]. (Kissel, 1987)
[4]. (Geir, 1982)
[5]. (Jurin *et al.,* 1993)
[6]. (Stohs Sidney *et al.,* 2001)
[7]. (Shrivastava *et al.,* 2002)
[8]. (Wang *et al.,* 1997)
[9]. (Yucesoy *et al.,* 1999)

METAL COATINGS BY CHEMICAL METHODS OF SUBMISSION FLUIDIZED BED

BY

IRINA-ELENA SURDU[*], **DAN-GELU GĂLUŞCĂ, CARMEN NEJNERU, SANDA CREŢU and NECULAI AILENEI**

"Gheorghe Asachi" Technical University of Iaşi

Abstract. In many modern technologies in recent years, began to use metal powder coating, all inorganic polymer or to improve the surface properties of various materials. Most dye pigments containing metal core surrounded by a layer of atoms, well defined, which provides an index of refraction so that a particular color depth and brilliance that is simulated. Unlike pigments submission by wet processes, fluidized bed coating is much simpler (no need to separate solid / liquid, drying and dispersion of agglomerates).

Key words: c-CVD deposition, fluidized bed, precursor, tri-isobutyl-aluminum.

1. Introduction

Use of fluidized bed coating method has several advantages especially in the intimate mixture of solid highly efficient heat transfer and uniformity of temperature. Liu and others (2000) examined the thermal decomposition of tri-isobutyl-aluminum (TRI-ISOBUTYL-ALUMINUM) to cover the glass beads with high refractive index. The process could be used to obtain pigments whose color depends on the angle of contact and observation. Were tested in two ways:
  - injection in an conveyor vaporized precursor gas; -liquid-injection

---

[*] corresponding author; *e-mail:* irina.surdu@yahoo.com

spray directly into the fluidized tri-isobutyl-aluminum (Fig. 1).

To shorten the operating time necessary precursor supply flow high. In conventional CVD processes precursor is introduced into the reaction zone with a carrier gas. Precursor supply flow capacity is limited, however the saturation of the carrier gas with precursor vapor and this in turn depends on the relative volatility of the precursor, which until the entry into the reaction zone should be maintained at a temperature lower than reaction or decomposition.
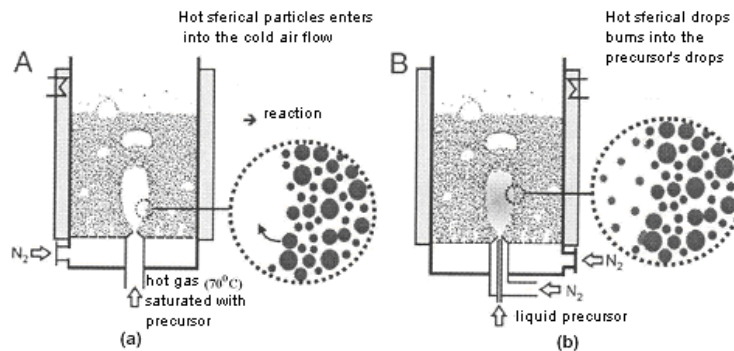
Fig. 1 – Precursor injection mechanisms: *a* – gaseous precursor; *b*– liquid precursor.

Inside the fluidized precursor in contact with hot particles which are driven by a carrier gas stream cooler (Fig. 1 *a*). In this way the precursor chemical reaction or decomposition occurs on the surface of hot particles, as long as the speed is greater than the mass transfer rate. By using such exclusions fluidized in the gas phase nucleation period. To increase the flow of precursor supply can be used directly injected by spraying liquid precursor in the reaction zone (Fig. 1 *b*).

Liquid droplets are driven jet hit the hot fluidized particles and vaporized, (Leclere *et al.,* (2004) found that a drop of 300 μm diameter is vaporized in 16 ms). Bruhns and Werther (2005) showed that a single drop can come in contact simultaneously with several hot fluidized particles and produce instant vaporization and the resulting vapor decomposes immediately neighboring particle surface (Fig. 2). Agglomerate formed in the spray mist is easily decomposed by evaporation and reaction.
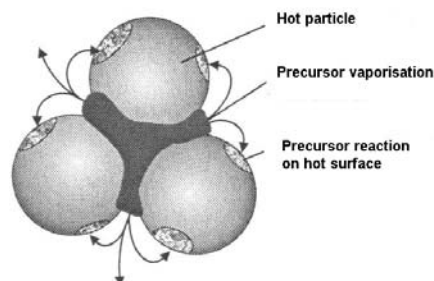
Fig. 2 – Reactions on hot surfaces

2. Stages of Chemical Vapor Deposition Process Are

1. Transport of reactants in the reaction: reactants + carrier gas;
2. Transfer of reactants to the substrate surface;
3. Adsorption of reactants;
4. Surface processes;
5. Desorption of reaction products;
6. Transfer of reaction products to the mainstream gas;
7. Transport of products outside of filing: carrier gas + unreacted reagents + reaction products.

For the reaction to take place, reactants are transferred from the gas mainstream substrate surface diffusion or convection and at the substrate surface are absorbed into the surface. The reaction takes place between the substrate and adsorbed molecules, resulting in thin surface layer containing the reaction with secondary products. A secondary product subsequently desorbs.

Technology for obtaining such layers on the surface of metal parts consists in passing over this area, heated in a sealed chamber at relatively high temperatures, a reactant gas mixture, which contains the chemical elements of the layer in the form of volatile compounds. C-CVD coatings can be formed from pure metals or their compounds of rough. Precipitation of C-CVD layer of the gas mixture can be held inside at normal pressure or under the atmospheric pressure.

In C-CVD processes, the phenomena of diffusion at the interface layer - the material are reduced in weight, they manifested especially by the retrieval of some alloy elements in the base material layer. Substrate that occurs submission must meet the condition that the structure does not change irreversibly depositing temperature and possess sufficient corrosion resistance to gas used in the process.

3. The Fluidized Bed

For the measurements we have constructed a microwave fluidized small. The oven is made of a quartz tube whit diameter 30 mm and length 300 mm, outer wrapped with resistance from kantal, isolated in asbestos and glass wool. Outside the oven is protected by another quartz tube diameter of 75 mm.

At the bottom of the outer tube are mounted two upper sites with stainless steel mesh sieve of 200 mesh/mm and 400-mesh sieve bottom having sighting/mm, the role of these sites was to allow the passage of carrier gas N_2 saturated with tri-isobutyl-aluminum reactant and to prevent leakage of Al_2O_3 grains used for fluidized bed.

Al_2O_3 layer of granules having a particle size dp <200 μ m occupies the lower third of the tube and the samples were suspended in their mass using nichelina yarn. Also at the bottom of the reactor is mounted under the site of the sprayer attachment.

Thermocouple to measure and regulate the temperature in the reactor is

placed at the top is a thermocouple type Cromel-Alumel, up to ¼ of the height of fluidized bed. The reactor is mounted vertically on a support by means of special clamps. At the top of the reactor during the measurement is attached a flexible aluminum pipe. To adjust the temperature using a thermostat this controls the supply voltage depending on oven thermocouple time to adjust the heating rate. Power through the oven was set between 0-220 V.
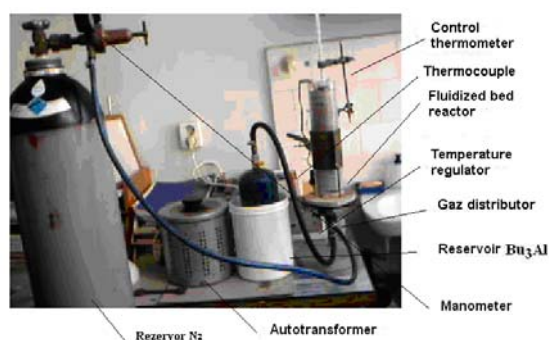
Fig. 3 – Installation of the fluidized bed.

Operating voltage during deposition ranged from 85-100 V. Oven temperature was read from an electronic millivoltmeter. Introduction of tri-isobutyl-aluminum in the furnace was made with dispenser of Fig. 5. It is constructed from an inner tube heads at the top to a diameter of 0.5 mm. It is vapor inlet tube tri-isobutyl-aluminum. The outer tube is inserted inert gas N_2. In order to standardize gas flow inside the outer tube train tri-isobutyl-aluminum, concentric inner tube is inserted to a distributor provided with external grooves. Tri-isobutyl-aluminum was directly supply the special cylinder was placed in a thermostat whose temperature was maintained at 800C.
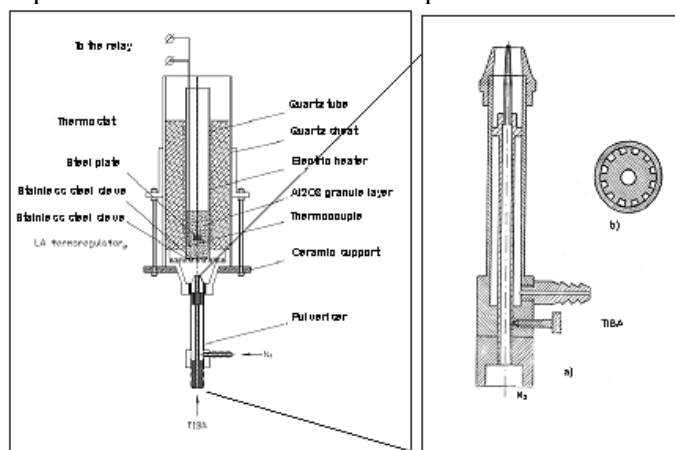
Fig. 4 – The principle scheme of fluidized   Fig. 5 – Scheme of the pulverizer;
                bed furnace.   *a*) pulverizer; *b*) distributor section.

Tri-isobutyl-aluminum is very reactive, and to be handled and stored should not be exposed to atmospheric moisture or oxygen. The cylinder Aldrich Sure / Pac is a convenient method of storage and distribution for research precusor quantities sensitive to the air so pure and in solution. Since tri-isobutyl-aluminum, tri-isobutyl-aluminum is highly reactive with water, oxygen, or both, the atmosphere should never be exposed.

Distribution of reagents required standard techniques (with needles). Flow of inert gas (nitrogen) was 1.2 bar, enough to ensure the functioning and fluidized bed was checked through a rotameters. Schematic diagram of the spray is shown in Fig. 5. The introduction of carrier gas mixture plus Tri-isobutyl-aluminum only after the reactor was under constant temperature. Oven temperature was maintained at 320C throughout the experiment. During measurement was 35 minutes. Aluminisation was performed in fluidized bed furnace. Samples were placed inside the furnace, ensuring a mix of aluminisation layer around them.nitrogen flow: 1.2 bar.
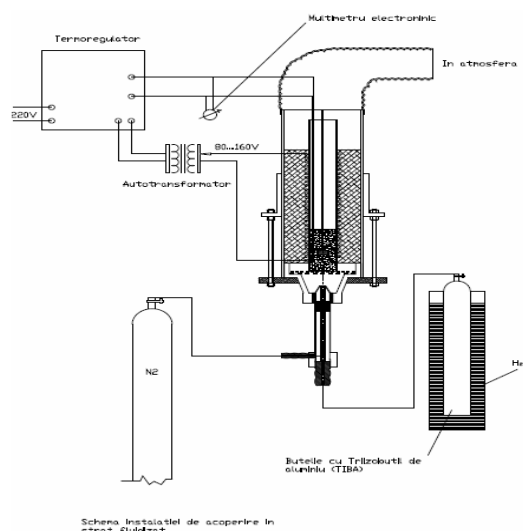
Fig. 6 – The principle scheme of fluidized bed deposition.

Tri-isobutyl-aluminum cylinder temperature: 80. Tri-isobutyl-aluminum thermal break down can be simplified by the reaction.
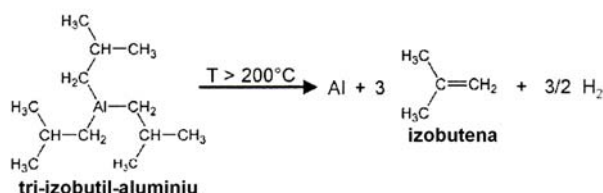
4. Conclusion

1. Installation was built respecting the conditions necessary for working with tri-isobutyl-aluminum protection with a high explosion hazard.

2. On the practical treatment of c-CVD chamber was the diameter of the primary enclosure which shall contain quartz thermocouple and heating medium (fine granular sand dp <200 μ m) in which samples are immersed.

3. Bubbling was carried out using a mixture of N_2 and Tiba, obtained in mixture through a distributor.

REFERENCES

Liu Shuqing, Shi Daxim, Cui Yihing, Cao Zhuyou, *Microstructure and Surface Topography of Aluminium Films Deposited on Glass Microspheres in a Fluidized bed CVD Reactor*. Chemicalş Journal of Chinese Universities, **21, 3**, 339 (2000).

Leclere K., Briens C., Gauthie T., Bayle J., Guigon P., Bergougnou M., *Experimental Measurement of Droplet Vaporization Kinetics in a Fluidized Bed*. Chemical Engineering and Processing, **43**, 693 (2004).

Bruhns S., Werther J., *An investigation of the Mechanism of Liquid Injection Into Fluidized Beds*. AIChE Journal, **51**, *3*, 766 (2005).

Yee K.K., *Protective Coatings for Metals by Chemical Vapor Deposition*. Review *226*, International Metals Reviews, **1**, 19–42 (1978).

Bryant W.A., *Review: The Fundamentals of Chemical Vapor Deposition*. J. Mater. Sci., **12**, 1285–1306 (1977).

ACOPERIRI METALICE PRIN METODE DE DEPUNERE CHIMICE ÎN STRAT FLUIDIZAT

(Rezumat)

În multe tehnologii moderne, în ultimii ani, a început să se utilizeze acoperirea cu pulberi metalice, polimerice sau anorganice, toate cu scopul îmbunătăţirii proprietăţilor superficiale ale diverselor materiale. Cei mai mulţi pigmenţi pentru colorarea metalelor conţin un nucleu care este înconjurat de un strat de atomi, bine definit, care asigură un indice de refracţie astfel încât o anumită culoare este simulată ca adâncime şi strălucire. Spre deosebire de depunerea pigmenţilor prin procedee umede, acoperirea în strat fluidizat este mult mai simplă (nu necesită separarea solid/lichid, uscarea şi dispersarea aglomeratelor).

MODIFICATION OF THE RESISTANCE AND PLASTICITY MECHANICAL CHARACTERISTICS DURING THE HIGH RESISTANCE WIRES DRAWING IN ULTRASOUND FIELD

BY

MIHAI SUSAN[1], VIOREL ILIESCU[2], ELENA CHIRILĂ[1], BOGDAN COJOCARIU[1]* and ORESTE CRISTODULO[1]

[1]"Gheorghe Asachi" Technical University of Iaşi,
[2] S.C. Cablero S.R.L

Abstract. The paper presents the modification of the resistance and plasticity mechanical characteristics, (R_m, $R_{p0,2}$, and A_{10}), depending on the relative rate of drawing ($v_{tr}/\overline{v}_v$, where v_{tr} - rate of drawing, $\overline{v}_v$ - vibratory rate of the die). This aspect goes to an eventual control of the strain hardness of the wires drawn in ultrasound field.

Key words: ultrasound field, wire, die, relative rate of drawing, strain hardness, plasticity and resistance mechanical characteristics.

1. Introduction

The paper presents the influence of the ultrasound field up to the resistance and plasticity mechanical characteristics of the high resistance

---

* Corresponding author; *e-mail:* bgdnlcn@yahoo.com

wires drawn with ultrasonic vibrations applied along the drawing direction to the die. In these conditions of ultrasonic drawing / UVD Technology, it takes place "the ultrasounds surface effect", the so called "reduction of the metal-tool contact friction", (Severdenko *et al.,* 1990; Susan & Bujoreanu, 1999).

The aim of the paper is to find a possible dependence between the parameters of the UVD Technology and the value of the resistance and plasticity characteristics of the so processed wires.

2. Material and Research Methodology

2.1. Researched Material

The research has used the samples made from hot rolled hardened wire Φ 3,00mm, C80, manufactured by S.C. CORD S.A. Buzau / www.cord.ro. The chemical composition of the steel C80 was determined using a spectrometer with optical emission DV6 – BAIRD type, made in USA, (belonging to S.C.ARCELOR MITTAL S.A. Iasi). The chemical composition of the steel C80 (mean values) is presented in Table 1.

Table 1
Chemical Composition of the Steel C80 (Mean Values), [%] [*)]

C	Mn	Si	P	S	Cu	Cr	Ni	Al	N	As	Sn
0,82	0,52	0,20	0,009	0,014	0,01	0,04	0,01	0,003	0,0026	0,001	0,001

[*)] The chemical composition is according to EN 10016 – 2 / 1994

2.2 Research Methodology

The objective of the experimental study is to give a characterization for the ultrasound drawing technology / UVD Technology, of the wires which have cylindrical symmetry and high resistance, through convergent conical dies, in comparison with the classic technology / CT (without ultrasound activation of the die). The researches were made based on the singular drawing principle / through one single die, on a drawing equipment UDZSA TO631 type.

The photo of the drawing equipment UDZSA TO631 type, based on the singular drawing principle, belonging to S.C. CABLERO S.R.L. Iasi / www.cablero.ro, is presented in Fig. 1.

There were used dies with cores made from metallic carbides, (WCr), belonging to S.C. MECHEL S.A. Campia Turzii, and which had the half-angle of the die cone α = 8°.

Fig. 1 – Photo of the drawing equipment UDZSA TO631 type,
the reels area – based on the singular drawing principle.

The scheme of the oscillator system / OS used in the research process is presented in Fig.2.
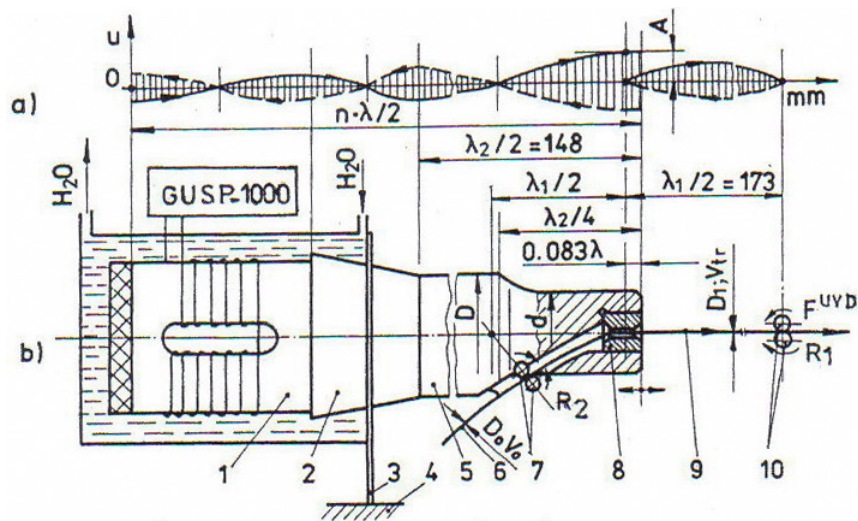
Fig. 2 – Scheme of the oscillator system / OS used in the research process:
a) waves oscillation; A – maximum oscillation of the die; b) properly scheme:
1- magnetostrictor transducer; 2- conical concentrator; 3- noduled flange; 4- frame of
the drawing equipment; 5- graded cylindrical concentrator; 6- semi-finished wire;
7, 10- ultrasonic energy reflectors, (R_1, R_2- presser rolls); 8- die; 9- processed wire.

The ultrasound activation of the die was realized at 15, 20 and 25 μm – values of the amplitude A – going to the following values of the vibratory rate,

$(\overline{v}_v)$: 1,64; 2,19 and 2,74 m/s; the load resonant frequency of the oscillator system, (f), was 17500Hz, $\overline{v}_v = 2 \cdot \pi \cdot f \cdot A$, (Iliescu, 2010).

The rate of drawing, (v_{tr}), registered at the command panel level of the drawing equipment, was 0,06m/s. The amplitude of the die oscillation, (A), was measured with the device of the amplitude measuring DMA – S.C. CABLERO S.R.L. Iasi type, after its calibration. For the researches, it was used the ultrasound generator GUS – CAB – 1000VA/220V – 50Hz, S.C. CABLERO S.R.L. Iasi type, (output power P_{iesire}= 1000VA, frequency f = 17500Hz, efficiency η = 0,60).

3. Determination of the Resistance and Plasticity Mechanical Characteristics, (R_m, $R_{p0,2}$, and A_{10})

The characterization of the plastic deformability for the hardened tyre cord C80, Φ3,00 mm – classic drawing technology / CT / A and ultrasonic drawing technology / UVD / B, C and D, (B / A = 15 μm; C / A = 20 μm; D / A =25 μm) was made based on the results obtained after the drawing rupture test; the test was made using the universal machine MTS 824.10, (the rate of stress was 20mm/s).

The diagrams of the drawing stress for the samples A, B, C and D and the cumulative diagram are presented in Fig.3…7 and Table 2.
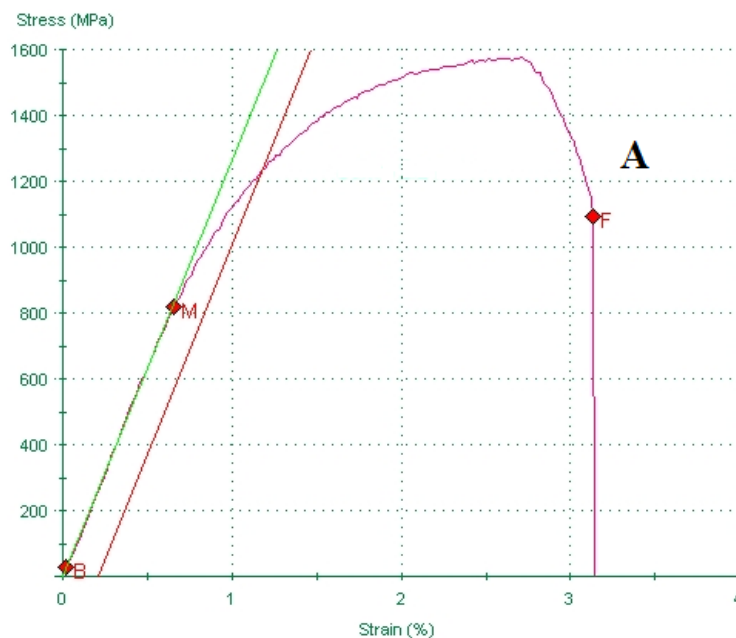
Fig. 3 – Diagram of the drawing stress / sample A, Classic Technology – CT.
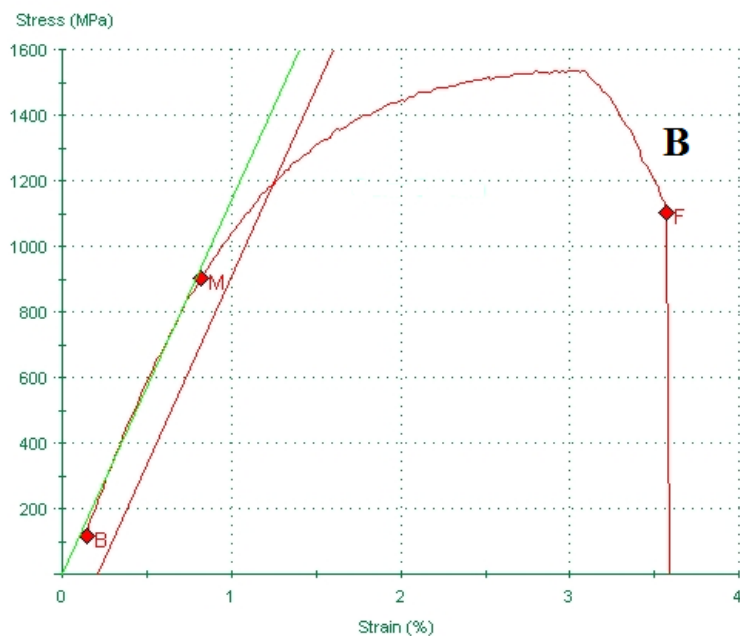
Fig. 4 – Diagram of the drawing stress / sample B, UVD Technology, A = 15 μm.

The test of the drawing stress is made according to SR EN 10002.
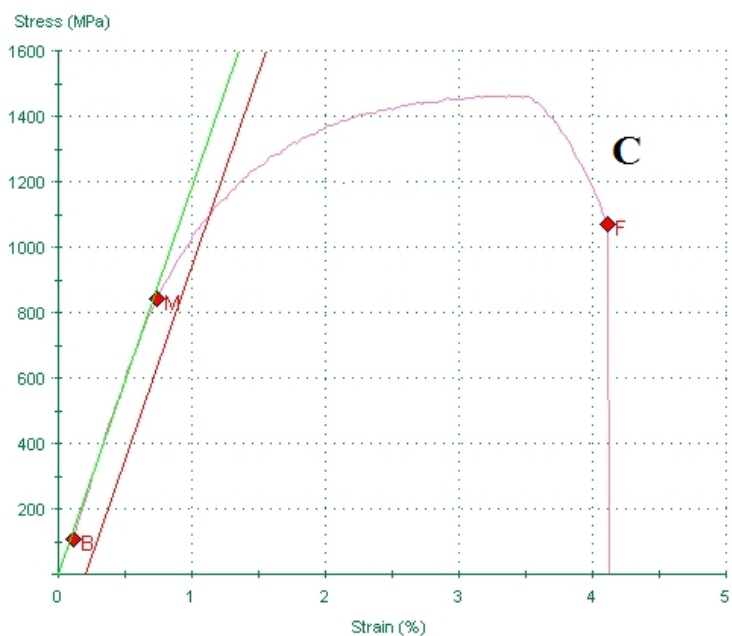
Fig. 5 – Diagram of the drawing stress / sample C, UVD Technology, A = 20 μm.
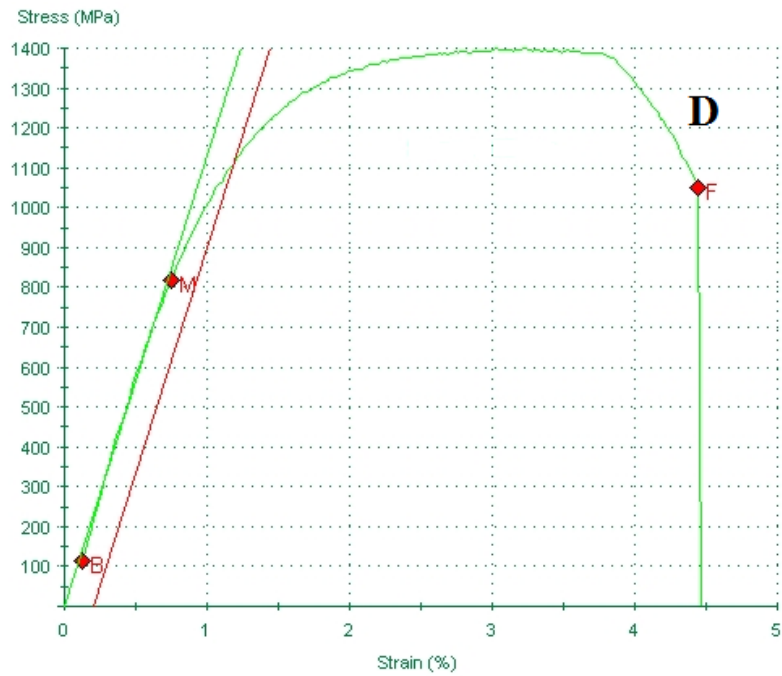
Fig. 6 − Diagram of the drawing stress / sample D, UVD Technology, A = 25 μm.
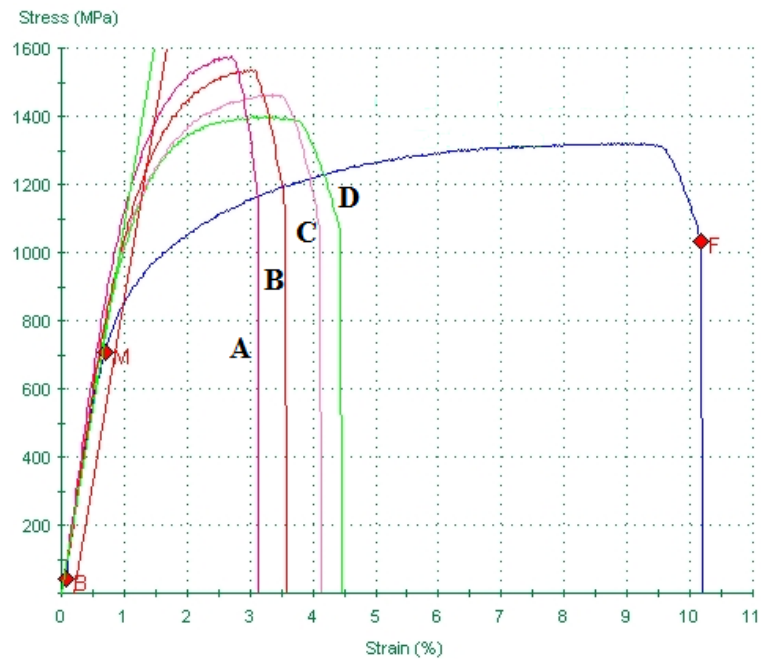
Fig. 7 − Cumulative diagram of the drawing stress, samples A, B, C and D.

Table 2[**)]

Variation of the Resistance and Plasticity Mechanical Characteristics, in the Case of the CT and UVD Technology Processed Samples, f = 17500Hz; D_0 = 3,50mm; D_1 = 3,00mm

Sample symbol	α [°]	δ [%]	λ -	$v_{tr}/\overline{v_v}$ -	R_m [MPa]	$R_{p0,2}$ [MPa]	A_{10} [%]
A/TC	8	19	1,18	-	1575	1485	3,60
B/UVD, 15 μm	8	19	1,18	0,036	1535	1425	3,66
C/UVD, 20 μm	8	19	1,18	0,027	1475	1356	3,84
D/UVD, 25 μm	8	19	1,18	0,021	1405	1255	4,04

[**)] Notations significance: α – half-angle of the die cone; δ – degree of deformation; λ – elongation

4. Conclusion

The modifications of the resistance and plasticity mechanical characteristics, (R_m, $R_{p0,2}$, and A_{10}), are analyzed in dependence with the relative rate of drawing, ($v_{tr}/\overline{v_v}$). It was observed that the values of the mechanical characteristics, (R_m and $R_{p0,2}$), decrease and the value of the plasticity characteristic (expressed by the elongation, A_{10}) increases in the same time with the decreasing of the relative rate of drawing. This means that, when both, v_{tr} and f, have constant values, the amplitude of the die oscillation must increase. The modification of the resistance and plasticity mechanical characteristics, depending on the relative rate of drawing, ($v_{tr}/\overline{v_v}$), goes to an eventual control of the strain hardness for the wires drawn in ultrasound field.

REFERENCES

Severdenko V.P., Klubovici V.V., Stepanenko A.V., *Prokatkia i volocenie c ulitrazvukom*, NAUKA I TEHNICA, Minsk, 1990.
Susan M., Bujoreanu L.G., *The Metal-Tool Contact Friction at the Ultrasonic Vibration Drawing of Ball-Bearings Steel Wires*. Revista Metalurgia de Madrid, Spain, **35**, *6*, 379-383 (1999).
Iliescu V., *Contribuţii privin modernizarea tehnologiilor şi utilajelor de trefilare a sârmelor pentru cabluri de oţel*. Universitatea Tehnică "Gheorghe Asachi" din Iaşi, 2010.

MODIFICAREA CARACTERISTICILOR MECANICE DE REZISTENŢĂ ŞI PLASTICITATE LA TREFILAREA SÂRMELOR DE ÎNALTĂ REZISTENŢĂ MECANICĂ ÎN CÂMP ULTRASONOR

(Rezumat)

Lucrarea pune în evidenţă modificări ale caracteristicilor mecanice de rezistenţă şi plasticitate (R_m, $R_{p0,2}$, şi A_{10}) în funcţie de viteza relativă de tragere, ($v_{tr} / \overline{v}_v$). Acest lucru conduce la un posibil control al ecruisării sârmelor trefilate în câmp ultrasonor.

EVALUATION OF ULTIMATE STRAIN DURING THE PROCESS OF LATERAL EXTRUSION WITH FURTHER UPSETTING

BY

R. SYVAK*, K. KOTSUBIVSKA, Y. BURENNIKOV and I. SYVAK

Vinnytsia National Agrarian University

Abstract. The paper studies metal plasticity in the process of lateral extrusion of the axially symmetric flange with its further upsetting. This process is distinguished by a non-monotonic loading. Therefore, calculation of the stress deviator components is performed using Bakhauz anisotropic strengthening model.

As the known tensors of the failure accumulation process model for non-monotonic loading are very cumbersome, this paper substantiates the transition from a tensor model to a 3D scalar model. Stressed state stiffness index and Nadai-Lode parameter are used as main characteristics of non-monotonic loading. Three components of the failure deviator in 3D space of the main stresses is introduced instead of 6 components of the failure tensor. Approximation of the function is proposed that describes the loading history influence on plasticity and takes into account the deformed metal sensitivity to the stressed state scheme. Stressed state influence on plasticity is given by the ultimate strain surface that describes the ultimate strain dependence on the two invariant indices of stressed state.

The developed model for evaluation of the metal plasticity under complex non-monotonic loading is used to evaluate the influence of the parameters of the flange lateral extrusion process on the ultimate strain. The proposed procedure of the combined extrusion design enables rational use of the extruded metal plasticity resource.

---

* Corressponding author; *email:*

Key words: plastic deformation, stress, nonmonotonic loading, deformation paths, failure.

1. Introduction

The main task of plastic metal working is obtaining workpieces of a definite form without continuity violation. Therefore, the problem of deformed metal plasticity evaluation has still been of current importance, especially for nonmonotonic deformation. The mechanism of failure accumulation and healing under nonmonotonic deformation is not fully understood at present. That is why there is no single view as to the evaluation of metal deformability under nonmonotonic loading (Дель, 1978; Огородников *et al.,* 2005; Колмогоров, 1970; Богатов *et al.,* 1984; Дель, 1982).

The model of failure accumulation under nonmonotonic loading is based on the hypothesis that failures have a directional character and are described by the second rank tensor. This tensor components are determined by the mechanics of plastic deformation in a definite manufacturing process as well as by material functions that describe phisico-mechanical properties of the material.

In accordance with (Ильюшин & Победря, 1970) and (Дель, 1982) we introduce failure tensor ψ_{ij}, the components of which are defined as follows:

$$\psi_{ij} = \int\limits_{0}^{e_u^*} F\left(e_u, \eta, \mu_\sigma\right) \beta_{ij} d e_u, \tag{1}$$

where $F(e_u, \eta, \mu_\sigma)$ – a positive function that characterizes the material sensitivity to the stressed state scheme.

Components of the guide tensor β_{ij} are given by (Дель, 1982).

$$\beta_{ij} = \sqrt{\frac{2}{3}} \frac{d\varepsilon_{ij}}{d e_u}. \tag{2}$$

From the relationships of the flow theory:

$$d\varepsilon_{ij} = \frac{3}{2} \frac{d e_u}{\sigma_u} S_{ij} \tag{3}$$

it follows that:

$$\frac{d\varepsilon_{ij}}{de_u} = \sqrt{\frac{3}{2}}\beta_{ij} = \frac{3}{2}\frac{S_{ij}}{\sigma_u} \qquad (4)$$

or

$$\beta_{ij} = \sqrt{\frac{3}{2}}\frac{S_{ij}}{\sigma_u} \qquad (5)$$

where: S_{ij} – stress deviator components,
        σ_u – stress intensity.
        Let us represent tensor σ_{ij} in the form of.

$$\sigma_{ij}=S_{ij}+\sigma\delta_{ij} \qquad (6)$$

where $\sigma = \frac{1}{3}\sigma_{ij}\delta_{ij}$ is mean pressure.

        Besides, we use the known relationships:

$$\mu_\sigma = \frac{2S_2 - S_1 - S_3}{S_1 - S_3} \qquad (7)$$

$$S_1+S_2+S_3=0, \ 2\sigma_u^2 = \left(S_1 - S_2\right)^2 + \left(S_2 - S_3\right)^2 + \left(S_3 - S_1\right)^2 \qquad (8)$$

where μ_σ is Nadai-Lode parameter.
        After solving system (7), (8), we find.

$$\frac{S_1}{\sigma_u} = \mp\frac{1}{3}\frac{\mu_\sigma - 3}{\sqrt{\mu_\sigma^2 + 3}}, \ \frac{S_2}{\sigma_u} = \pm\frac{1}{3}\frac{2\mu_\sigma}{\sqrt{\mu_\sigma^2 + 3}}, \ \frac{S_3}{\sigma_u} = \mp\frac{1}{3}\frac{\mu_\sigma + 3}{\sqrt{\mu_\sigma^2 + 3}} \qquad (9)$$

        From (5) and (9) it follows that main components of tensor β_{ij} are given by.

$$\beta_1 = \mp\frac{1}{\sqrt{6}}\frac{\mu_\sigma - 3}{\sqrt{\mu_\sigma^2 + 3}}, \ \beta_2 = \pm\frac{1}{\sqrt{6}}\frac{2\mu_\sigma}{\sqrt{\mu_\sigma^2 + 3}}, \ \beta_3 = \mp\frac{1}{\sqrt{6}}\frac{\mu_\sigma + 3}{\sqrt{\mu_\sigma^2 + 3}} \qquad (10)$$

It is assumed that under nonmonotonic loading failure occurs if a certain function of the invariants of tensor ψ_{ij} reaches a definite value. The first invariant of this tensor is equal to zero due to incompressibility of the material - $\beta_1+\beta_2+\beta_3=0$. Without taking into account the influence of the third invariant, failure condition can be written as.

$$\psi_1^2 + \psi_2^2 + \psi_3^2 = 1 \tag{11}$$

In order to determine the form of function $F(e_u,\eta,\mu_\sigma)$ that is included in (1), we consider a simple loading where β_{ij}, η, μ_σ remain constant. Then (Дель, 1982).

$$\psi_{ij} = \beta_{ij} \int\limits_0^{e_u^*} F\left(e_u,\eta,\mu_\sigma\right) d\,e_u = \beta_{ij}\phi\left(e_u,\eta,\mu_\sigma\right), \tag{12}$$

where

$$\phi\left(e_u,\eta,\mu_\sigma\right) = \int\limits_0^{e_u^*} F\left(e_u,\eta,\mu_\sigma\right) d\,e_u. \tag{13}$$

As $\beta_1^2 + \beta_2^2 + \beta_3^2 = 1$, it follows from (11) that under failure conditions if $e_u=e_p$, $\varphi(e_u,\eta,\mu_\sigma)=1$. Besides.

$$\varphi(0,\eta,\mu_\sigma)=0 \tag{14}$$

Satisfying these conditions, we assume that [5].

$$\phi = \sum_{k=1}^m b_k \left(\frac{e_u}{e_p\left(\eta,\mu_\sigma\right)} \right)^{n_k}, \quad \sum b_k = 1, \; n_k>0 \tag{15}$$

In accordance with (15) and (14) we will further adopt.

$$\phi = \left(1-a\right) \frac{e_u}{e_p\left(\eta,\mu_\sigma\right)} + a\, \frac{e_u^2}{e_p^2} \tag{16}$$

where $e_p(\eta,\mu_\sigma)$ is the surface of ultimate strain,
a – a constant that depends on the mechanical characteristics of the metal. Here a is adopted to be equal to a=0,48.
Satisfying relationships (1), (13), (16) we assume that in general case.

$$\psi_1 = \int\limits_0^{e_u} \left(1 - a + 2a \frac{e_u}{e_p(\eta, \mu_\sigma)} \right) \beta_1 \frac{d\,e_u}{e_p(\eta, \mu_\sigma)} \qquad (17)$$

Analogous expressions can be written for ψ_2 and ψ_3 that are included into the failure condition (11).

Failure criterion (11) is used for studying the process of lateral extrusion with further upsetting of a cylindrical billet made from steel 10. The process scheme is presented in Fig.1. At the first stage the lateral extrusion process is realized (Fig.1 *a*) and at the second stage – upsetting of the obtained flange (Fig. 1 *b*). The strained state calculation was performed by the method of coordinate grids using the procedure described in (Сивак *et al.,* 2000). The process of extrusion and the upsetting process were conducted in three stages. Deformation paths $\eta(e_u)$, $\mu_\sigma(e_u)$ were built taking into account the influence of the main technological parameters: relative thickness of the flange $h/2R_0$ and relative value of the curvature $r/2R_0$ of the transition edge. As deformation paths in e_u, η, μ_σ coordinates are not practically dependent on the material, for the strained state investigation samples (cut into halves), made from antimony lead were used ($d_0=28,2$mm, $l_0=60$mm). On the polished surface of one of the composite sample halves rectangular dividing grid with the base of 2mm was drawn with a sharpened cutting tool. Then the samples were soldered and extrusion of separate samples was performed to different deformation degrees within three transitions. After the last transition of the lateral extrusion 3 samples were used to realize three transitions of contour upsetting. Thus, each sample characterizes strained state at the end of the corresponding stage. After each stage the samples were unsoldered and coordinates of the deformed grid nodes were measured.
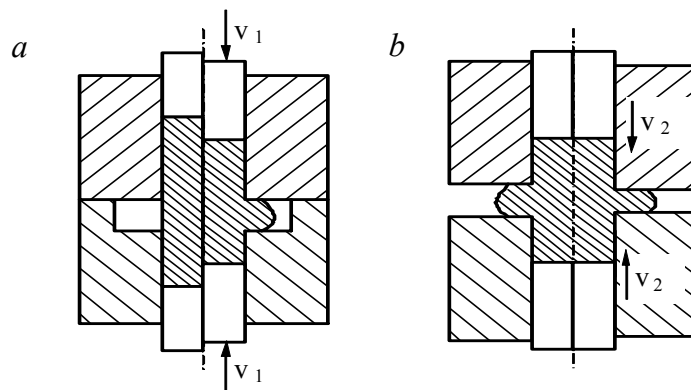
Fig. 1 - Scheme of the process of lateral extrusion with further upsetting of the obtained flange; *a* – lateral extrusion; *b* – upsetting.

Besides, a dividing grid was also drawn on the side surface of samples made from steel 10 and lateral extrusion with further contour upsetting was performed according to the same scheme as the samples made from lead were deformed.

Accumulated deformation was found by the formula:

$$e_u = \int\limits_0^t \dot{\varepsilon}_u d\tau$$

where $\dot{\varepsilon}_u$ - intensity of the deformation rates,

t - deformation time.

Stress deviator components were calculated using relationships that enable taking into account the influence of plastic deformation non-monotony [8] which is observed in the process under consideration.

$$S_{ij} = \frac{2}{3}\sigma_u\left(e_u\right)\frac{\dot{\varepsilon}_{ij}}{\dot{\varepsilon}_u} - \frac{1}{3}\int\limits_0^{e_u}\left(1 - \beta\left(e_u^*\right)\right)\sigma\left(e_u^*\right)\cdot\phi\left(e_u^* - e_u^0\right)\frac{d^2\varepsilon_{ij}}{de_u^2}\left(e_u^*\right)de_u^* \quad (18)$$

Dependences $\beta(e_u)$, $\phi\left(e_u - e_u^0\right)$ for steel 10 were obtained experimentally using the procedure (Хван *et al.,* 1996). Experimental results were approximated by functions.

$$\beta = 0{,}34 + 0{,}66\exp(-62e_u) \qquad\qquad (19)$$

$$\phi = 0{,}19 + 0{,}81(-22{,}3(e_u - e_u^0)^{0,806}) \qquad\qquad (20)$$

Constants included in (19) and (20) were determined by the method of least squares.

The stress tensor components were found by integration of the balance differential equations.

$$\frac{\partial\sigma_r}{\partial r} + \frac{\partial\tau_{rz}}{\partial z} + \frac{\sigma_r - \sigma_\phi}{r} = 0$$

$$\qquad\qquad\qquad\qquad\qquad\qquad (21)$$

$$\frac{\partial\tau_{rz}}{\partial r} + \frac{\partial\sigma_z}{\partial z} + \frac{\tau_{rz}}{r} = 0$$

using the integral equation:

$$P = 2\pi \int\limits_{0}^{R} \sigma_z r \, dr \tag{22}$$

where R – the radius of the workpiece to be deformed,

P – the force that is measured in the process of the investigated workpiece deformation.

The obtained results of the stresses and deformation calculation were used for building loading paths $\eta(e_u)$, $\mu_\sigma(e_u)$ and also for β_I values calculation.

The surface of ultimate strain for steel 10 was approximated by the relationship obtained in (Сивак et al., 2000).

$$e_p(\eta,\mu_\sigma)=0{,}68 \exp(0{,}43\mu_\sigma-0{,}91\eta) \tag{23}$$

Calculation of the used plasticity resource according to criterion (11) has made it possible to give satisfactory description of the experimental results. Discrepancy with the experimental result does not exceed 20%. It should be noted that application of the distinguishing features of plastic deformation non-monotony makes it possible to obtain flanges with the diameter that exceeds by 60-80% the flange diameter under usual lateral extrusion.

REFERENCES

Богатов А.А., Мижирицкий О.И., Смирнов С.В., *Ресурс пластичности металлов при обработке давлением*. М.: Металлургия, 144 (1984).

Дель Г.Д., *Пластичность деформированного металла*. Физика и техника высоких давлений. *11*, 28 – 32 (1982).

Дель Г.Д., *Технологическая механика*. М.: Машиностроение, 174 (1978).

Ильюшин А.А., Победря Б.Э., *Основы математической теории термовязкоупругости*. М.: Наука, 280 (1970).

Колмогоров В.Л., *Напряжения, деформации, разрушение*. М: Металлургия, 229 (1970).

Огородников В.А., Киселёв В.Б., Сивак И.О., *Энергия. Деформации. Разрушение.* (задачи автотехнической экспертизы) / Винница: УНІВЕРСУМ - Вінниця, 204 (2005).

Сивак И.О., Сивак Р.И., Алиев И.С., *Деформируемость заготовок при радиальном выдавливании с контурной осадкой*. Механика деформируемого твёрдого тела и обработка металлов давлением. – Тула: ТулГУ, 278-284 (2000).

Хван Д.В., Томилов Ф.Х., Корольков В.И., *Экспериментальная механика конечных деформаций*. Воронеж: Издательсьво «ЭЛИСТ», 248 (1996).

EVALUAREA STĂRII DE TENSIUNI FINALE ÎN TIMPUL PROCESULUI DE EXTRUDARE LATERALĂ URMATĂ DE REFULARE

(Rezumat)

Lucrarea studiază plasticitatea metalului în procesul de extrudare laterală a unei flanşe simetric axial urmată de refulare. Acest proces se distinge prin solicitare non-monotonă. Astfel, calculul componentelor tensiunilor este realizat folosind modelul anizotropic Bakhauz.

Datorită faptului ca tensorii din modelul procesului de rupere prin acumulare sunt foarte complicaţi, această lucrare fundamentează tranziţia de la un model tensor la un model scalar 3D. Matricea stării de tensiuni şi parametrul Nadai-Lode sunt folosite ca şi caracteristici principale a solicitarilor non-monotone. Trei componente ale deviatorului rupturii în spaţiul 3D a tensiunii pricipale sunt folosite în locul celor 6 componente ale tensorilor rupturii. Este propusă aproximarea funcţiei care descrie influenţa înregistrării solicitărilor asupra plasticităţii şi ia în calcul sensibilitatea metalului deformat asupra stării de tensiuni. Influenţa stării de tensiuni asupra plasticităţii este data de suprafaţa solicitării la rupere ce descrie ultima dependenţă a solicitării faţă de cei doi invarianţi ai stării de tensiuni.

Modelul dezvoltat pentru evaluarea plasticităţii la acţiunea unei solicitări complexe non-monotone este folosit pentru a evalua influenţa unor parametri ai procesului de extrudare laterală a flanşei asupra tensiunii de rupere. Procedura propusă de proiectare a extrudării combinate permite folosirea raţională a resurselor de plasticitate a materialului extrudat.

STUDY ON SOIL WASHING WITH CHELATING AGENTS OF THE METAL CONTAMINATED SOILS

BY

MARIA SZANTO (PRODAN)*, VALER MICLE and CĂLIN VASILE PRODAN

Technical University of Cluj-Napoca,

Faculty of Materials and Environmental Engineering

Abstract. Soil contamination by metals is one of the most difficult problems to fix because of the toxicity and mobility of metals in the soil and their bio-accumulation potential. One of the ways this problem can be solved is soil washing. Soil washing is a process that uses physical and/or chemical methods for extracting metals from soil. The washing solution may contain water or water with various additives (acids, surfactants, bases, or chelating agents) to facilitate the extraction of metals from soil. Among the most commonly used chelating agents are EDTA, NTA, DTPA, PDTA, EDDS. Lately there research was done about using biodegradable chelating agents such as EDDS ([S,S]-ethylenediaminedisuccinic acid) to preserve as much as possible of the original structure and properties of the soil under remediation. Choosing a specific chelating agent for soil remediation is done taking into account several factors: pH, quantity of major extracted cations, chelating agent-metal ratio. Through this study we want to summarize the recent data obtained in remediation of contaminated soils with metals by soil washing.

Key words: soil washing, chelating agents, metal.

---

* Corresponding author; *e-mail:* prodan.mari@gmail.com

1. Introduction

Resistance of soil to pollution by heavy metals varies according to nature of the soil. Thus, clay soils retain pollutants more, neutral and carbonate soils have a strong retention and sandy soils retain the least. Also, the finer the soil texture is the more pollutants are retained in the soil, where they are absorbed by plants. The pH has an important role in the availability or immobilization of heavy metals. Thus, soil retention capacity of heavy metals increases with pH, reaching maximum values around neutral value, and availability for plants decreases for Cu, Mn and Zn when the pH increases in the range 5-8 (Dude *et al.,* 2001).

Soil washing is a process that uses physical and/or chemical methods to separate contaminants from soil and sediments. The contaminants are concentrated in a smaller volume of contaminated waste, which is also recycled and disposed. The washing water may contain only water or may include additives such as acids, bases, surfactants, chelating agents witch are used to facilitate the separation of contaminants from soil or sediments. The water resulting from the process is usually recycled and brought back into the process (Sogorka, *et al.,*; www.epa.gov).

2. Soil Washing Using Chelating Agents

Soil washing's (Fig. 1) principle is to remove pollutant from soil matrix by solubilizing it into the washing solution. Soil washing technology can be applied for remediation of sites contaminated with heavy metals, hydrocarbons and semi-volatile organic compounds. In the case of pollutants with low solubility in aqueous solution it's required the presence of additives such as acids, bases, surfactants, solvents, chelating agents to achieve an efficient remediation (Moutsatsou *et al.,* 2006).

The soil washing process involves: excavating the contaminated soil; size sorting process for separating the fine fraction of coarse; treatment of fine fraction (soil washing); water treatment; residue management (Lina *et al.,* 2008; (www.epa.gov; Litao *et al.,* 2010).

Chemical extraction is basically using a fluid containning a chemical reagent (acids/bases, surfactants, salts or redox agents) to extract metals from contaminated soil by transfering them into aqueous solution. Remediation of soil through chemical washing is done by dissolving the metal contaminant or convert metal compounds to more soluble forms (*e.g.* The conversion of soluble metal salt by changing valency) (Dermont *et al.,*, 2008).

Extraction of metals from soil by chemical washing depends on soil geochemistry (soil texture, cation exchange capacity, buffering capacity and organic matter content), dosing and chemistry of extraction agent and extraction

conditions (pH, residence time, number of successive steps of extraction, how the reagent is added, the ratio liquid/solid, etc.) (Dermont *et al.,*, 2008).
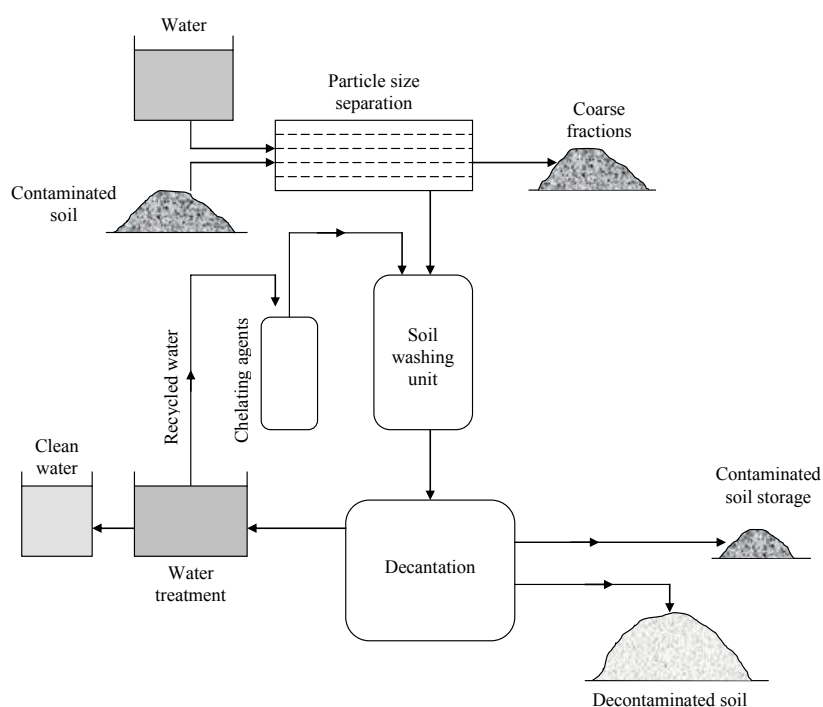
Fig. 1 – Scheme of the soil washing process.

Speciation and fractionation of metals are very important parameters in determining the efficiency of extraction of metals from soil, chemical extraction, but these factors are not sufficient to determine extraction efficiency as it depends on other factors such as metal concentration, soil geochemistry, metal type, metal valence (Dermont *et al.,*, 2008).

Usually the ability to extract metal cations increases with decreasing pH. In soil metal cations absorption decreases with decreasing pH, and dissolved metal components increases (Dermont *et al.,*, 2008).

The ability of chelating agents to form stable metal complexes makes them confidently used to extract metals from contaminated soils. When choosing the chelating agents for remediation of contaminated soil as a solution the following factors must be taken into account:

  ➢ chelating agents can form stable complexes on a wide range of pH;
  ➢ metal complexes that form must not be adsorbed by the soil matrix;
  ➢ chelating agents needs to be less biodegradable when they are recovered for reuse in the process;
  ➢ reagents used must be efficient in economic terms;

> metal recovery must have a low cost (Dermont *et al.,*, 2008; Mulligan *et al.,* 1999; Abumaizar & Smith, 1999; Peters, 1999; Sun *et al.,* 2001).

Table 1 presents the main chelating agents used in decontamination of soil polluted with metals by soil washing.

The great advantage of using the chelating agents (eg EDDS, EDTA) compared with strong acids (*e.g.* HCl) is that chelating agents affect the soil structure in a very small measure. However using EDTA in the rehabilitation of polluted soils also has disadvantages compared to using HCl, such as higher costs and that it produces serious environmental problems if it's not recovered from soil treatment, EDTA being less biodegradable and having a high potential to remobilize the metals (Dermont *et al.,*, 2008).

EDTA is among the best synthetic chelating agents because:

> it has a strong capacity for chelating metal cations;
> soil washing with EDTA can be applied to a wide range of soils;
> can be recovered and reused in the washing process(Dermont *et al.,*, 2008).

Table 1

Types of Chelating Agents (http://en.wikipedia.org; http://www.benbest.com/nutrceut/ EDTA.html; http://kelatox.com/EDTA; Paul W. Jones & David R. Williams, 2001; Lina *et al.,* 2008; Litao *et al.,* 2010; http://en.wikipedia.org/wiki/EDDS; http://en. wikipedia.org/wiki/Pentetic_acid; http://www.hc-sc.gc.ca; http://monographs.iarc.fr).

Chelating agent	Characteristics
EDTA (EthyleneDiamineTetraAcetic Acid), $C_{10}H_{16}N_2O_8$	EDTA is a solid chelating agent, crystaline, colorless, slightly soluble in water and behave as a weak organic acid. EDTA retains di- and trivalent metal ioans. $EDTA^{4-}$ binds the metal through the two amine and four carboxylates. EDTA is one of the most commonly used chelating agent because of its strong metal-complexing ability. This is an effective chelating agent for metals in soil that have a low availability, such as Pb, Cu and Cr. EDTA disadvantages are: high cost, toxicity and low biodegradability.
EDDS (EthyleneDiamineDiSsucinic Acid), $C_{10}H_{16}N_2O_8$	EDDS is a structural isomer of EDTA. EDDS is used instead of EDTA due to its higher biodegradability. EDDS has two chirality centers and, as such there are three stereoisomers: the enantiometric (R,R) and (S,S) isomers and the achiral meso (R,S) isomer, but only the (S,S) stereoisomer is of interest and the others are less biodegradable. The efficiency of (S,S) stereoisomer proved to be high even when heavily polluted soils.

Continuation Table 1

Chelating agent	Characteristics
DTPA (DiethyleneTriaminePentaAcetic Acid), $C_{14}H_{23}N_3O_{10}$	DTPA is a white crystalline powder. DTPA has a high affinity for metal cations, and as a chelating agent it wraps a metal ion through the formation of up to eight ties.
NTA (NitriloTriAcetic Acid), $C_6H_9NO_6$	NTA is a compound in the form of needles or prismatic crystals. NTA retain metal ions forming complexes soluble in water. NTA is similar with EDTA but is comparatively less biodegradable. NTA is highly toxic and was considered to be part of class II products of carcinogens. For these reasons it is not recommended for rehabilitation of contaminated soils.

Efficiency of metal extraction with EDTA is highly dependent on soil characteristics and metal fractionation. EDTA in generally effective in the removal of the metal cations bound to exchange fractions, carbonate and organic, but is less effective in metal fractions related to reducible Fe-Mn. Low selectivity of EDTA leads to high reagent consumption due to the fact that there is potential for chelating other cations too, such as Ca^{2+}, Fe^{3+} dissolved in the washing solution (Dermont *et al.*,, 2008).

Extraction of metals depends on a number of parameters such as: EDTA/metal molar ratio, soil washing method (column or bach), how the reagent is added (a single washing step or successive steps), pH, liquid/solid ratio, washing time. The best results were obtained when applying a multi-step soil washing, at lower reagent concentrations and pH in the range 4-8, at lower pH values of metal complex that is formed it can be re-adsorbed in the soi (Dermont *et al.*, 2008; Finzgar & Lestan, 2007).

An important issue is the recovery and reuse of EDTA, avoiding its disposal in the environment. Recovery of EDTA and metals from washing solution can be achieved through several variants:

➢ EDTA recovery and metal precipitation by adding chemical agents;
➢ electrochemical process;
➢ using ion exchange resins;
➢ nano-filtration;
➢ EDTA degradation by oxidation and metal recovery by absorption (Dermont *et al.*,, 2008). Lately, another highly studied chelating agent is EDDS because most metal-EDDS complexes proved to be biodegradable in the soil. Resulting complexes are biodegradable and because of these they have a much

lesser environmental alteration and they are less toxic for plants and fungi. The high value of stability constants and the high efficiency of extraction of metals has advantages for the use of EDDS. The studies conducted so far have shown that by the usage of EDDS metals are extracted from the soil by forming metal-chelating agent complexes. Soil washing with EDDS like chelating agent is influenced by soil organic matter as it forms strong bounds with the metals and inhibits their extraction (Dickson *et al.,* 2011).

Organic matter dissolved in the soil forms complexes with some metals such as Cu, Pb even in the presence of free EDDS (http://www.hc-sc.gc.ca).

Studies by E. Meers and collective showed that metal complexation affinity for soil remediation with EDDS is as follows:

$$Cu > Fe > Zn > Ni > Mn > Al > Cd > Pb > Mg > Ca \qquad (1)$$
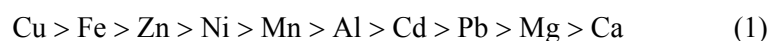
E. Meers and colective did tests on three soil types: a type of clay soil, calcareous and moderately polluted (A1), a different type of soil with similar characteristics with privious but more strongly polluted with Cd, Cr and Zn (A2) and finally a third type of soil which is sandy and moderately contaminated (A3). They highlighted EDDS degradation by measuring dissolved organic carbon (DOC) and metals mobilized from the soil solution, the results obtained by them are presented in Fig. 2 and 3, (Meers *et al.,* 2008).
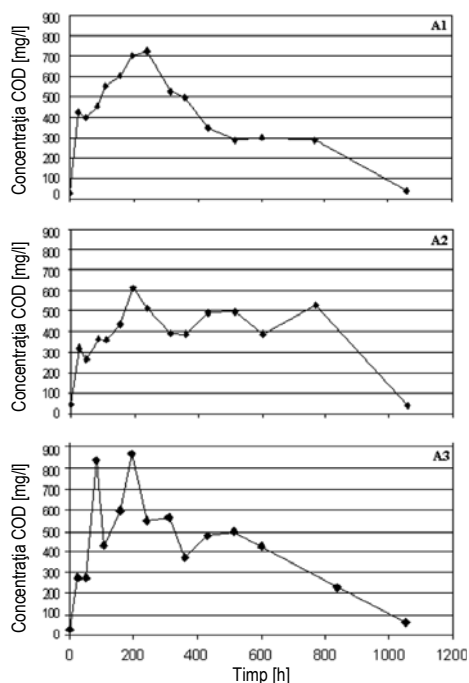
Fig. 2 – Evolution of dissolved organic carbon (DOC) over the course of the experiment (mg/l); experiment conducted in triplicate for the three soils tested (Meers *et al.,* 2008).
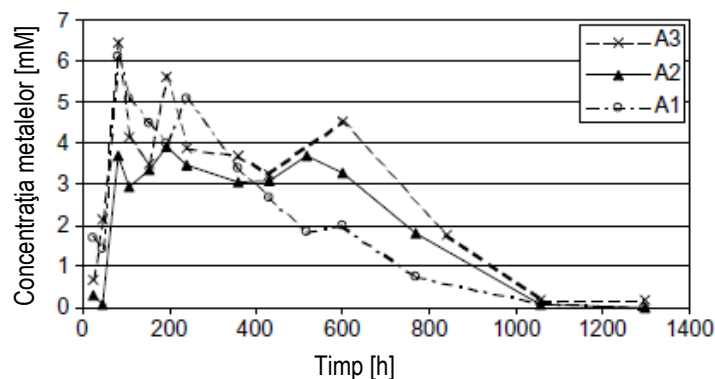
Fig. 3 – Evolution of total dissolved metals (Σ [Al, Fe, Mn, Cd, Cu, Cr, Ni, Pb, Zn])
over the course of the experiment (mM); experiment conducted in triplicate
for the three soils tested (Meers *et al.,* 2008).

Initial increase of dissolved organic carbon and metal concentration in the first 200-240 h is due to EDDS treatment. After this increase a delay takes place in the degradation of EDDS for A2 and A3 soil types. For A1 soil type, clay and moderately polluted, there was a decrease from day 10. A2 soil showed no signs of degradation of EDDS in the first 32 days of the experiment after wich it has been mineralized. A3 was found to have a similar behavior like A2 soil type, without showing a significant decrase in metal mobilization within the first 25 days. However in all soils EDDS was degraded within 50 days according to the authors. EDDS was degraded differently in the three soils the delay period having a special importance. It follows that to obtain good results for EDDS degradation it depends very much on the time of adjustment (Meers *et al.,* 2008).

Advantages: adsorbed metal forms in soil particle can be treated; some metal compounds can be dissolved; in certain cases even fine-grained soils can be treated; the metals extracted can be easily recovered using various methods (Dermont *et al.,,* 2008).

Disadvantages: chemical agents increase the costs of treatment; treated soil can become unsuitable for revegetation due to loss of physical-chemical and biological properties; the reagents that remain in the treated soil can pose problems in its disposal; chemical agents from the washing water can pose problems in water recycling and treatment, thereby increasing the cost of treatment; treatment of sludge with high metal content can be difficult (Dermont *et al.,,* 2008).

3. Conclusion

Unlike other methods that immobilize metals into the soil this soil washing process has the advantages that it offers the possibility to extract them,

supervision and monitoring of contaminated areas after decontamination not being necessary anymore.

Using soil washing for remediation of contaminated soils with metals requires a very thorough analysis of site's characteristics (soil type, soil chemistry, horizontal and vertical extent of pollutant, particle size analysis etc.) and of the pollutant (metal speciation and fractionation, the bounds between metal particles and soil matrix etc.).

Soil washing has a high efficiency for sandy soils and at a low pH. In case of usage of chelating agents to extract metals from soil the washing time is lower than with acids. A high importance in the washing process has the concentration of chelating agents, which is chosen depending on the characteristics and properties of the pollutant.

Chelating agents are recommended for remediation of the soils contaminated with metals due to the fact that they allow the extraction of metals from the soil without greatly affecting the soil's properties. The biodegradable chelating agents are the most recommended for soil remediation for reducing the treatment costs by the fact that they no longer pose problems related to recovery and treatment of the water resulting from the washing process.

Soil washing is used also for heavily contaminated soils where the pollutants can not be removed completely by this process. In this case it follows to concentrate the pollutants in a lower volume of soil which is then subjected to decontamination by other methods, resulting in a significant reduction in remediation costs.

REFERENCES

∗∗ http://en.wikipedia.org., *Ethylenediaminetetraacetic Acid.*

∗∗ http://en.wikipedia.org/wiki/EDDS, *EDDS.*

∗∗ http://en.wikipedia.org/wiki/Pentetic_acid. *Pentetic Acid.*

∗∗ http://kelatox.com/EDTA, *Ethylenediaminetetraacetic acid (EDTA) Definition.*

∗∗ http://monographs.iarc.fr/ENG/Monographs/vol73/mono73-19.pdf
       Nitrilotriacetic acid and its salts.

∗∗ http://www.benbest.com/nutrceut/EDTA.html, *Ben Best–Chelation Therapy with EDTA.*

∗∗ http://www.epa.gov; *A Citizen`s Guide to Soil Washing*. 2001.

∗∗ http://www.hc-sc.gc.ca/ewh-semt/alt_formats/hecs-sesc/pdf/pubs/water-eau/
        nitrilotriacetic_acid/nitrilotriacetic_acid-eng.pdf.*Nitrilotriacetic acid*, 1990.

∗∗ www.epa.gov, *Soil Washing as a Cleanup Method*. TOSC, 1996.

Abumaizar R.J., Smith E.H., *Heavy Metal Contaminants Removal by Soil Washing*.
        J. Hazard. Mater. **B70**, 71–86 (1999).

Dermont G., Bergeron M., Mercier G., Richer-Lafleche M., *Soil Washing for Metal
        Removal: A Review of Physical/Chemical Technologies and Field
        Application*, Journal of Hazardous Materials, *152*, 1-31 (2008).

Dickson Y.S. Yan, Irene M.C. Lo, *Enhanced Multi-Metal Extraction with EDDS of
        Deficient and Excess Dosages Under the Influence of Dissolved and soil
        Organic Matter*. Environmental Pollution, *159*, 2011.

Dude A., Zbytniewski R., Kowalkowski T., *Adsorbtion and Migration of Heavy
        Metals in Soil.* Polish Journal of Environmental Studies, **10**, *1*, 2001.

Finzgar N., Lestan D., *Multi-Step Leaching of Pb and Zn Contaminated Soils with
        EDTA*. Chemosphere, *66*, 824–832 (2007).

Jones Paul W., Williams David R., *Chemical Speciation Used to Assess [S,S`]-
        Ethylenediaminedisuccinic Acid (EDDS) as a Readily-Biodegradable
        Replacement for EDTA in Radiochemical Decontamination Formulations*.
        Applied Radiation and Isotopes, *54*, 2001.

Litao Chen, Ting Liu *et al*., *Metal Complexation and Biodegradation of EDTA and
        S,S-EDDS: A Density Functional Theary Study*. J. Phys. Chem., *114*, 2010.

Mann Michael J., *et al.*, *Innovative Site Remediation Technology Soil Washing/Soil
        Flushing*. **3**, American Academy of Environmental Engineers, 1993.

Meers E., Tack F.M.G., *et al.*, *Degradability of Ethylenediaminedisuccinic Acid
        (EDDS) in Metal Contaminated Soils: Implication for its use Soil
        Remediation*. Chemosphere, *70*, 2008.

Moutsatsou A., Gregou M., Matsas D., Protonotarios V., *Washing as a Remediation
        Technology Applicable in Soils Heavily Polluted by Mining*-Metallurgical
        Activities, Chemosphere, *63*, 1632-1640 (2006).

Mulligan C.N., Yong R.N., Gibbs B.F., *On the use of Biosurfactants for the
        Removal of Heavy Metals from Oil-Contaminated Soil*. Environ. Prog. *18*,
        50–54 (1999).

Ortega L.M., Labrun R., Blais J.-F., Hausler R., Drogui P., *Effectiveness of Soil
        Washing, Nanofiltration and Electrochemical Treatment for the Recovery
        of Metal Ions Coming from a Contaminated Soil*. Water Research, *42*,
        1943-1952 (2008).

Peters R.W., *Chelant Extraction of Heavy Metals from Contaminated Soils*. J.
        Hazard. Mater. **66**, 151–210 (1999).

Sogorka Brian, Gombert Dirk, *et al., – Technical and Regulatory Guidelines for Soil Washing.*

Sun B., Zhao F.J., Lombi E., McGrath S.P., *Leaching of Heavy Metals from Contaminated Soils Using EDTA*, Environ. Pollut. *113*, 111–120 (2001).

STUDIU ASUPRA SPĂLĂRII CU AGENŢI DE CHELARE A SOLURILOR
CONTAMINATE CU METALE

(Rezumat)

Contaminarea solurilor cu metale este una dintre cele mai dificile probleme de remediere datorită toxicităţii, mobilităţii metalelor în sol precum şi a potenţialului lor de bio-acumulare. Una dintre metodele prin care poate fi soluţionată această problemă este spălarea solurilor. Spălarea solurilor utilizează metode fizice şi/sau chimice pentru a extragere metalele din sol. Soluţia de spălare poate să conţină apă sau apă cu diverşi aditivi (acizi, surfactanţi, baze sau agenţi de chelare) pentru a favoriza extragerea metalelor din sol. Dintre agenţii de chelare cei mai utilizaţi sunt EDTA, NTA, DTPA, PDTA, EDDS. În ultima perioadă s-au făcut cercetări cu privire la utilizarea agenţilor de chelare biodegradabili cum este EDDS ([S,S]-ethylenediaminedisuccinic acid) pentru a păstra pe cât posibil structura şi proprietăţile iniţiale ale solului supus remedierii. Alegerea unui anumit agent de chelare pentru remedierea solului se face ţinând cont de o serie de factori: pH, cantitatea de cationi extraşi, raportul agent de chelare-metal. Prin lucrarea de faţă se doreşte sintetizarea datelor recente obţinute în domeniul reabilitării prin spălare a solurilor contaminate cu metale.

INFLUENCE OF FORGING TEMPERATURE ON THE MECHANICAL PROPERTIES OF MICROALLOYED STEELS

BY

MIHAELA TACA[1]*, EUGENIU VASILE[1] and ELVIRA ALEXANDRESCU[2]

[1] Metav-Cercetare Dezvoltare S.A.,
[2] INCDI Comoti

Abstract. Micro alloyed steels have been developed for forged or cast components used in the automotive industry due to their mechanical strength in as forged condition. The addition of alloying elements (such as niobium and/or vanadium) in small amounts was used to increase the resistance of carbon steels and thus eliminate the necessity of thermal treatment. This represents a very effective method of reducing the cost and energy saving. A further step in reduction of the forging process costs is lowering the forging temperature. Since the increasing of the strength of medium carbon steels is given by primary precipitation of vanadium and/or niobium carbides and by the size and distribution of these precipitates during the cooling, it is necessary to evaluate the influence of lowering the forging temperature on the micro alloyed steels mechanical characteristic. Tests were conducted in order to study the effect of the temperature reduction on the mechanical and structural characteristics of the slugs forged at temperatures ranged between 1200 and 900°C.

Key words: microalloyed steels, semi-hot forging, mechanical properties.

---

* Corresponding author; *e-mail:* taca@metav-cd.ro

1. Introduction

The strengthening of the microalloyed steels is related to the interphasic precipitation and the volume fraction and dimensions of precipitates are the main factors responsible for their increased mechanical properties (Honeycomber, 1986). Addition of microalloying elements such as vanadium, niobium, titanium and nitrogen ensures the strengthening through precipitation hardening and grain refinement (http://www.vanitec.com). The final mechanical properties depend on the complete solution of any microalloy precipitates at a forging temperature. The solution process is temperature dependent as presented in equation 1, (Garcı́a-Mateo *et al.,* 2001):

$$\ln[M\,][N\,] = A - \frac{B}{T} \tag{1}$$

where 1 [M][N] represents the solubility product, A and B are constants for a given reaction, and T is the temperature in K. The precipitates formed by the alloying elements as vanadium, niobium and titanium have different solubility in the solid-solution. The vanadium nitrides and carbonitrides dissolve readily at lower forging temperatures compared with niobium or titanium and therefore the vanadium alloyed steels might be forged at lower temperatures without significant loss of properties. Lowering of the final forging temperature is associated with a slight decreasing of tensile strength and improvement of the toughness. The accurate selection of the finish forging temperatures allows the achievement of specified mechanical properties.

When forged at lower temperatures (in warm working range) the recrystallization kinetics of microalloyed steels changes due to the presence of undissolved small precipitates that have a retarding effect. The interaction between precipitates and recrystallization is different to that observed for hot working conditions where strain-induced precipitation takes place during recrystallization (Gawne *et al.,* 1985).

The present research aims to evaluate the effect of lowering finish forging temperature on the mechanical characteristics of two microalloyed steel grades.

2. Experimental

Mechanical tests and metallographic analyses were conducted in order to study the effect of the temperature reduction on the mechanical and structural characteristics of the microalloyed slugs forged at temperatures ranged between 1200 and 900°C.

The chemical composition of the two steel grades is presented in Table 1.

Table 1

Chemical Composition of the Preformed Billets

%	C	Si	Mn	P	S	Cr	Mo	Ni	V	Cu	N
Steel grade											
C70S6BY	0.72	0.19	0.51	0.08	0.05	0.11	0.01	0.06	0.00	0.10	
38MnSiVS5	0.38	0.68	1.51	0.02	0.06	0.18			0.11		0.00

Two preformed parts (Fig.1) made of 38MnVSi (cross wedge rolled) and C70S6 (forge rolled) have been chosen. The rolling tests for C70S6 samples were performed at four different temperatures 1250, 1050, 950 and 900°C. The rolling of 38MnVSi5 samples was carried out at three temperatures: 1220-1230, 1078-1088, 900-908°C.

Fig. 1 – Shape of the preformed sample
1,2,3 position of the impact testing bars.

2.1 Mechanical Characteristics

The rolled and warm forged pieces were tested and compared with the given requirements on hot forged pieces. The mechanical characterization was done by tensile test, impact test and hardness test. Tensile test was performed using an universal testing machine EU40tf type. 10 mm diameter tensile test bars were cut from the preformed sample and tested at 20°C. Charpy U bending impact test (EN 10045-1) was done on Impact testing machine WPM30 type. The test bar has a 3 mm notch (KCU 3). For every forging temperature three test bars were cut from the preformed billets according to Fig. 1. Hardness values were measured on cross section of the preformed billet, after polishing according to EN 10003-1, on Instron-Wolpert equipment.

2.2. Microstructural Analysis

The microstructural analysis was performed on cross section of forged parts. The sample surface was prepared by polishing and etching. Etching

reagent was Nital 2%. The microstructural analysis was done using a field emission gun scanning electron microscope (FEGSEM) Quanta Inspect FEY equipped with energy and wavelength dispersive X-ray spectrometers.

3. Results

3.1. Mechanical Tests

The results of mechanical tests for the two steel grades are given in Table 2 and 3.

Table 2

Results of Mechanical Tests for the 38MnVSi5 Cross Rolled Billets

	38MNVS5					
	Rm	$Rp_{0,2}$	A5	Z	KCU3	Hardness
	N/mm^2	N/mm^2	%	%	J	HB
Standard Values	820- 1000	min 550	min 12	min. 45	min. 40	
Billet preformed at 1220-1230°C					42	269
	866.2	573.2	18	51	42	270
					44	272
Billet preformed at 1078-1088°C					58	245
	872.6	598.7	17	48	52	242
					56	240
Billet preformed at 900-908°C					82	231
	796.1	560.5	21	51	94	234
					78	238

Table 3

Results of Mechanical Tests for the Forge Rolled Billets

	38MNVS5					
	Rm	$Rp_{0,2}$	A5	Z	KCU3	Hardness
	N/mm^2	N/mm^2	%	%	J	HB
Standard mechanical properties	850-1000	min 560	min 10			248-302
Billet preformed at 1250-°C					14	307
	955.4	789.8	7	10	16	301
					14	305
Billet preformed at 1050-°C					20	277
	929.9	764.3	11	19	14	270
					16	272
Billet preformed at 950-°C	910.8	726.1	6	13.5	18	283
					14	252
					16	260
Billet preformed at 900-°C					12	256
	923.5	700.6	12	36	18	247
					14	240

3.2. The Microstructural Analysis

38MnVSi5 samples. The microstructure of the analysed samples is fine lamellar pearlite with outlined ferrite. The amount of ferrite is within the limits for this steel grade (10-30%). The structure is generally fine grained with grain size ranging from 5-7 (samples formed at 1220-1230°C), 7-8 (samples formed at 1078-1088°C) to 8-9 (samples formed at 900-908°C) (Fig. 2 *a*, *b*, *c)*. The microstructural examination of samples did not reveal significant modifications due to different heating temperatures other than slight differences in grain size.
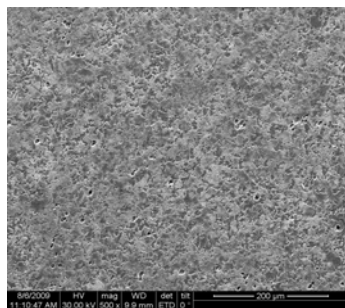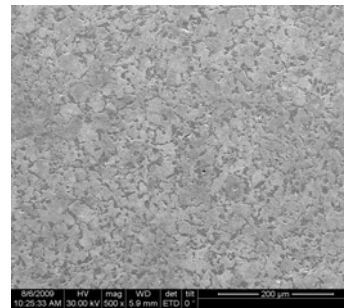
a − Cross rolled at 900-908°C   *b* −Cross rolled at 1078-1088°C
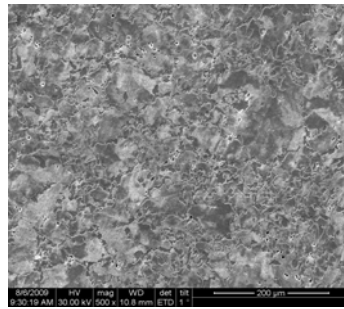
c − Cross rolled at 1220-1230°C

Fig. 2 − General aspect of microstructure for the samples cross rolled (VIVA): lamellar pearlite and ferrite. Material 38MnVS5.
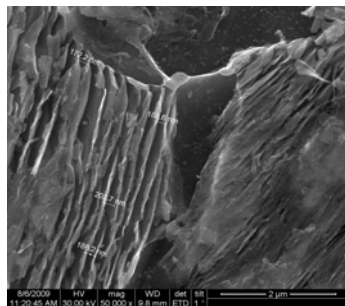
a − Cross rolled at 900-908°C, (x 50000)   *b* − Cross rolled at 1078-1088°C, (x 40000)
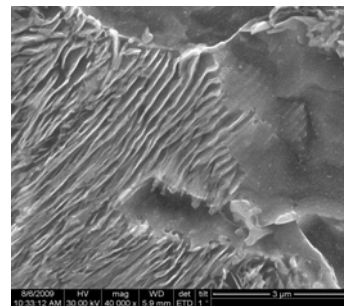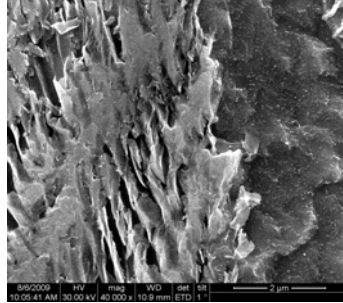
c − Cross rolled at 1220-1230°C, (x 40000)
Fig. 3 − Detail of the microstructure showing lamellar
pearlite morphology, Material: 38MnVS5, (Reagent Nital 2%).

The morphology of the pearlite and interlamellar distances as well as ferrite aspect are rather similar for all the forming temperatures (Fig. 3 *a*, *b*, *c*).

C70S6 Forge rolled billet. The structure of the specimens is pearlite with small amounts of ferrite, with very fine grains. For the temperatures below 1250°C ferrite is outlining the pearlite grains in a fine discontinuous network (Fig. 4 *a*, *b*, *c*, *d*). The outlining ferrite network is finer as forming temperature is higher.
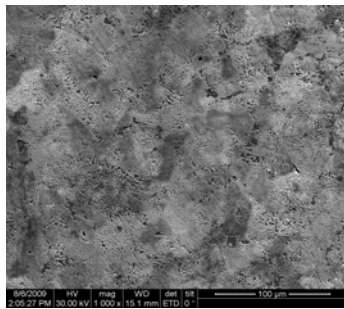
a − Forge rolled at 900°C, (x 1000)
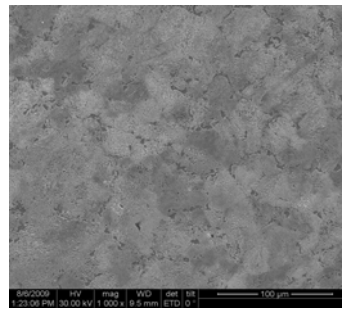
b − Forge rolled at 950°C, (x 1000)
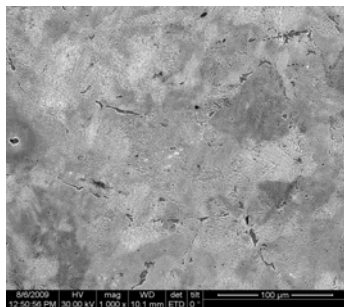
c − Forge rolled at 1050°C, (x 1000)
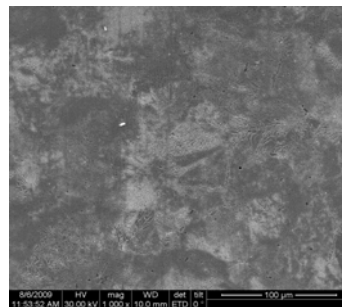
d − Forge rolled at 1250°C, (x 1000)

Fig. 4 − Microstructure of forge rolled samples − general aspect fine lamellar pearlite and ferrite. Material C70S6, (Reagent Nital 2%).

Pearlite morphology was analysed at orders of magnification of 40000. The interlamellar distances varied with temperature variation. The interlamellar distances decreased with the temperature increasing from 650-950 nm to 150-250 nm (Fig. 5 *a*, *b*, *c*, *d*).
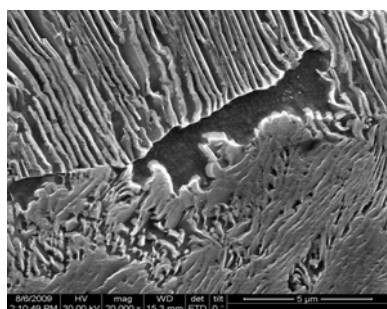
a − Forge rolled at 900°C, (x 20000)   b − Forge rolled at 950°C, (x 40000)
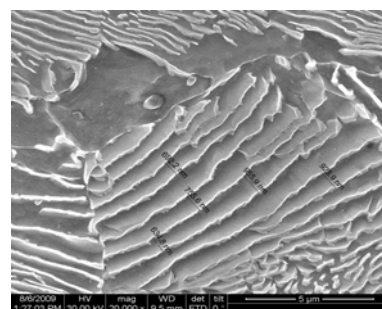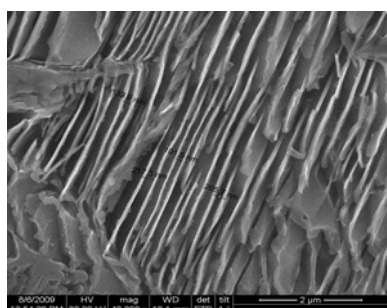
c − Forge rolled at 1050°C, (x 20000)   d − Forge rolled at 1250°C, (x 40000)
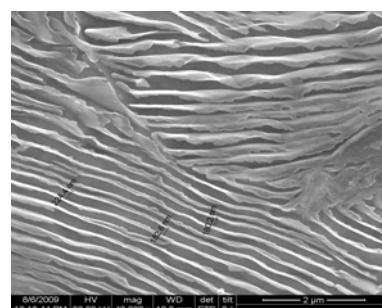
Fig. 5 − Detail of microstructure at higher magnification – showing the modification of interlamellar distances with temperature (Reagent Nital 2%).

Pearlite morphology was analysed at orders of magnification of 40000. The interlamellar distances varied with temperature variation. The interlamellar distances decreased with the temperature increasing from 650-950 nm to 150-250 nm (Fig. 5 *a*, *b*, *c*, *d*).

4. Conclusion

The effect of lower forging temperatures on mechanical properties was evaluated. The tensile strength decreases as forging temperature decreases. The plasticity and toughness of the samples improve with decreasing of the forging temperature.

Forging at 900°C seems to be the lower limit for both 39MNVS5 and C70S6 if the standard mechanical properties are required (Fig. 6).
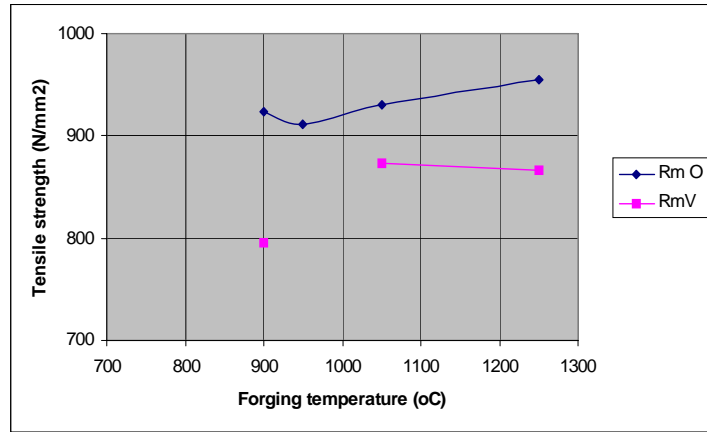
Fig. 6 – Variation of the tensile strength with forging temperature;
Rm O – tensile strength of forge rolled –C70S6 billet;
Rm V – tensile strength of cross rolled –38MnVS5 billet.

The strengthening mechanism in microallied steels as 39MNVS5 and C70S6 consists in dispersion of precipitates formed by microalloying elements as vanadium (carbides and nitrides). If the soaking temperature is not high enough to dissolve the microalloying constituents, their reprecipitation during cooling will be affected. The lower strength values at lower forging temperatures could be explained by the diminished strengthening effect of those precipitates.
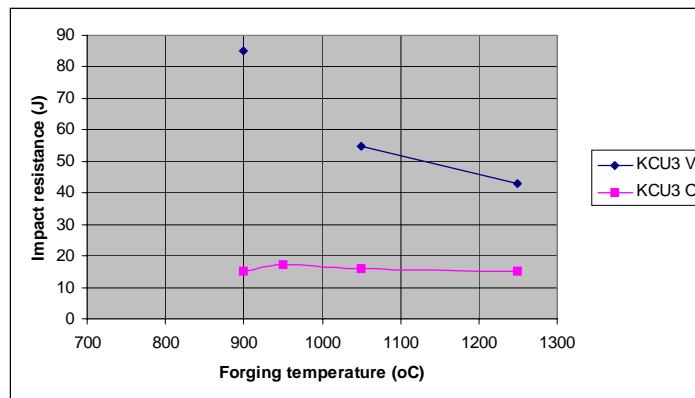
Fig. 7 – Variation of impact resistance with forging temperature;
KCU3 O – Impact resistance of forge rolled C70S6 billet;
KCU3 V – Impact resistance of cross rolled 38MnVS5 billet.

Tensile strength of 38MNVS5 billets forged at 900°C is slightly below the standard prescribed values. For the final forged part, higher values

of tensile strength could be attained by slightly raising the forging temperature and probably by an increase of the cooling speed. For the steel C70S6 the mechanical characteristics are still within the standard required interval. Due to the same effect the toughness and plasticity of materials are improved with decreasing of the forging temperature. The fracture occurs at higher impact energy for the billets forged at lower temperature (Fig. 7). The structure of the analysed samples is rather similar for all forging temperatures. The samples forged at lower temperature have a finer grain size but the amount of outlining ferrite is higher, which is also affecting the strength. The values of impact resistance for C70S6 steel are within 14-20 J; the ability to crack splitting of the forged material will be not affected by warm forging at 900°C.

The tests performed proved that the forging temperature for the two steel grades considered (38MnVS5 and C70S6) could be lowered up to 900°C. The decreasing of the tensile strength and hardness is within standard limits for C70S6. The mechanical properties and structural characteristics of grade 38MnVS5 are more affected at the lower forging temperature (900°C) and probably a slight raising of the final forging temperature should be considered if tensile strength above 820N/mm^2 is required.

REFERENCES

Garcı́a-Mateo, C., Ló pez, B., Rodriguez-Ibabe, J.M., *Static Recrystallization Kinetics in Warm Worked Vanadium Microalloyed Steels*. Mat. Sci. and Eng. **A303**, 216–225 (2001).

Gawne D.T., Lewis G.M.H., *Strengthening Mechanisms in High-Strength Microalloyed Steels*. Mat. Sci and Techn., **1**, *3*, March 1985, 183-191.

Honeycomber R.W.K., *Fundamental Aspects of Precipitation in Microalloyed Steels*. in HSLA Steels: Metallurgy and Applications, J. M. Gray et al., Editors, ASM International, 243-250 (1986).

Krauss G., *Vanadium Microalloyed Forging Steels*. http://www.vanitec.com/pdfs /3773c705e2eb9b89209d05f45b320a09.pdf

INFLUENŢA TEMPERATURII DE FORJARE ASUPRA PROPRIETĂŢILOR OŢELURILOR MICROALIATE

(Rezumat)

Oţelurile microaliate au fost realizate pentru realizarea componentelor forjate şi turnate destinate industriei auto datorită rezistenţei lor mecanice ridicate în stare normalizată. Adaosul unor elemente de aliere cum ar fi niobiul sau vanadiul în compoziţia unor oţeluri carbon a fost efectuat în scopul creşterii rezistenţei materialului, eliminându-se astfel necesitatea tratamentelor termice de călire şi revenire. Utilizarea acestor oţeluri permite realizarea unor importante reduceri de preţ pentru repere auto care nu lucrează în condiţii de impact. Reducerea în continuare a costului de fabricaţie se poate face prin deformarea plastică la semicald. Totuşi, reducerea temperaturii de deformare poate afecta procesul de durificare prin precipitare primară a carburilor sau carbonitrurilor de vanadiu şi niobiu şi implicit şi caracteristicile mecanice finale ale produsului. Din acest motiv, prezenta lucrare a avut ca scop evaluarea influenţei temperaturii de forjare (în intervalul 1200-900°C) asupra caracteristicilor mecanice ale unor oţeluri microaliate.

THE IMPORTANCE OF THE METALLIC MATERIALS IN THE PROTECTION EQUIPMENTS PRODUCTION

BY

GEORGE DANIEL TANASIEVICI[∗] **and GABRIELA CĂLDĂRESCU**

Territorial Labour Inspectorate Iaşi

Abstract. The present work focuses on the importance of the metallic materials the personal protection equipment (PPE) are made of and on the relation between their properties, the technologic and economic development dynamics and the maintenance of their protection features in regard to the risk factors which are continuously changing and affecting the human body.

Key words: personal protection equipment, metallic materials.

1. Introduction

The research and studies in the field of occupational safety and health pointed out that the personal protection equipment (PPE), are placed on the last hierarchic level, when the intrinsic prevention measures, the group protection or organizational measures do not succeed to eliminate completely the risk and may contribute significantly to the prevention of the professional illnesses or to the diminution of the physical stress, when they are appropriately chosen.

The criteria any personal protection equipment (PPE) should comply with are stipulated in the national and European legislation by the Government Decision no. 1048/2006 and the European Directive 89/656/EEC and they are:

[∗] Corresponding author; *e-mail:* george.tanasievici@expertssm.ro

a. To be appropriate for the risks involved, without leading itself to a an increased risk;

b. To be appropriate for the work place conditions;

c. To take into consideration the ergonomic requirements and the worker's health condition;

d. To fit the person wearing it, after all the appropriate adjustments have been made.

Currently in Romania, the standards according to which the PPE are designed have been harmonized with the European ones and appear in the specialty literature as SR EN Standard.

The SR EN 13291:2007 (EN 13921:2007) Standard "Personal protection equipment. Ergonomics principles" represents a guideline on the ergonomic features of these products.

This should be applied both by the certification bodies, the manufacturers and the users in order to identify the features necessary for a PPE to be considered risk, work place and bearer appropriate.

The following factors should be considered in establishing the ergonomic requirements:

- Integration of the current ergonomic performances and requirements;

- Establish the optimum level to be ensured by protection;

- Practical use: understand the specifications, the possibility of making specific moves etc.;

- Measure the PPE physiological impact: oxygen consumption, respiratory debit, body temperature modifications, sweating, fatigue or muscle contraction etc.;

- The adaptability of PPE and body fitting: adjustment, stability of adjustments, body fitting;

- Agents which ensure that PPE does not cause irritations or discomfort;

- The anthropometric factors of PPE;

- Biomechanical features: mass distribution, the dynamics of the inertial forces on the human body, moves limitation or prevention, tegument and muscle abrasion or compression, vibration increase etc.;

- Thermal features of PPE: heat insulation, water vapour permeability, water absorption and desorption;

- Effects on the senses: sight, hearing, taste, smell, tactile sense.

An important element in the PPE certification procedure is the features verification and it may suppose:

➢ Technical performance tests (in the laboratory);
➢ Ergonomic specific tests;
➢ Bearer/subject tests.

In terms of time, it is worth mentioning that the features control should be performed:

I. Before the market introduction, usually by the model certification (tests + examinations), for the application of the EC mark (in accordance with the GD no. 115/2004 with the subsequent amendments, that is, the European Directive 89/686/EEC), by a notified body;

II. Before acquisition – by the employers – by testing, specification charts and selection of the optimum model, experimental wearing.
Starting from the idea that: "There is no universal equipment – to fit any risk, any level of risk, work place, or bearer" the specialists in the field of labour security and health, the engineers, technologists, study permanently and struggle to find improvement solutions for the PPE.

Of all the PPE special interest should be paid to the PPE which are made totally or partially of metallic materials.

Within this context, the present work approaches the topic of the metallic materials which are part of the PPE structure; it focuses on their influence and the necessity of further research in order to replace some metallic materials in certain personal protection equipment.

Nevertheless there are a series of PPE which do not correspond entirely to the bearer's requirements and their long term use may cause not only discomfort but also some specific diseases (dermatitis, allergies etc.).

2. PPE Made of Metallic Materials – Description and Features

The technological development imposed a certain dynamics in the research of PPE and metallic materials of which they are made.

Both the scientific studies and the industrial practice demonstrated that the same product may be made of various materials but only one can satisfy best all the requirements imposed for that product.

New models of protective clothing generally comply with the increasing requirements of the bearers regarding the assurance of:

✓ The bearer protection against the cumulated action of the risks at the work place depending on the level, strength and duration of the exposure to each specific risk;

✓ The general requirements regarding particularly the non-noxious nature of the materials used in the PPE production, the hygiene and comfort features;

✓ A reasonable service life, considering the fact that for most work places, the main risks (heat and/or fire, chemical, biological etc.) are associated with mechanical risks (abrasion, catching, tearing, cutting etc.) which lead to the rapid usage of the protection outfit.

An PPE classification made entirely of metallic materials points to a less studied type of PPE which are destined to the meat processing industry (metallic aprons and gloves).

Table1
*PPE Made of Metallic Materials Which are Destined
to the Meat Processing Industry*

PPE	Metallic material	PPE features
	Anodized aluminium plates	**Size**: 55x60 cm, **Weight**: 0,8-1,1 kg, **Quality**: waterproof, **Purification**: by washing and sterilization, **Protection function**: against stitching and cutting caused by the portioning knife, **Destination**: butchers' protection.
	Coat of stainless steel wire	**Size**: 55x60 cm, **Weight**: 0,9-1,3 kg, **Protection function**: against stitching and cutting caused by the portioning knife.
	Gloves of stainless steel wire	Stainless steel gloves, **Shackle diameter**: 4 mm, **Glove top length**: 80 mm, **Protection function**: against stitching and cutting caused by the portioning knife.
	Gloves of stainless steel wire	Stainless steel gloves, **Shackle diameter**: 4 mm, **Glove top length**: 120 mm, **Protection function**: against stitching and cutting caused by the portioning knife.
	Gloves of stainless steel wire	Stainless steel gloves, **Shackle diameter**: 4 mm, **Glove top length**: 190 mm, **Protection function**: against stitching and cutting caused by the portioning knife.

Continuation Table 1

	Gloves of stainless steel wire	Stainless steel gloves, Fastening accessory made of plastic. **Protection function**: against stitching and cutting caused by the portioning knife.
	Gloves of stainless steel wire	Stainless steel gloves, **Shackle diameter**: 4 mm, **Glove top length**: 24 mm, **Protection function**: against stitching and cutting caused by the portioning knife.

3. Technical Fabrics Within Metallic Materials - Definition – Basic Terms

The technical term „fabric" designates all the products made of rectangular crossed metallic wire or plastic wire which compose the final gauze. This processing and formation method gives the possibility of stylizing the fabric in various ways for instance for filters, sieves, classifiers, protection equipment, consolidations, supports etc.

Warp and weft

1. Warp - the wires which go along the fabric.

2. Weft - cross wires

Shackle shape - The square shackle fabrics or the so called "zero shackle" are created according to various arrangements of the cross wires.

- zero shackle– the wires of the warps are stretched at certain distances close to each other but it is possible to stretch the wires of the weft at certain free distances.

Fabric parameters - Shackle width, thickness, pace

- The „w" shackle width for rectangular shackles is the warp or weft distance. The distances are given in mm or micrometres.

- Shackle thickness –„d" wire thickness is given for the round diameter wires.

- Pace- „t" is the warp or weft distance to the next wire.

$t=w+d$ - is used to calculate the number of necessary wires for a given distance.

- Open surfaces - % - the open screening surface, which indicates the percentage of holes on the entire fabric surface.

- Number of shackles – The number of shackles indicates the number of holes per inch (n/2.54 mm).

4. Standardization - Certification of PPE Made of Metallic Materials

The standard is a document approved by an acknowledged standardization body. In Europe these bodies are: CEN, CENELEC and ETSI. This document contains rules, instructions or features of the products and activities or of their results.
There are several types of standards: fundamental standards, testing standards, product standards etc.

Most of the standards used in Europe are European standards. The number of international standards increases continuously for national standards are rarely elaborated. The European standards played a major role in building the Internal Market of the European Union, by the elimination of the trade barriers which were caused by the disparities between the national standards and the introduction of the product certification process.

The common use of the European standards in the European Union eliminates several national testing and certification requirements. Companies require common standards in order to diminish the components acquisition costs and make sure that networks remain functional. Standards create a common commercial language while tests and certificates are seen as a way of building trust between business partners. The certification aims to demonstrate the conformity with a certain reference system, through a certificate, mark or label. This applies to products, services, organizations and persons. The conformity   with certain reference systems (*i.e*. standards, specifications or technical regulations, conditions, norms, levels of competence) is being assessed. Depending on the situation and on the reference system different techniques are used: tests, auditing, inspections, exams etc.

The certification may be compulsory, required by the law, or voluntary and the manufacturers opt for certification mostly for commercial reasons. The entire certification process is carried on through conformity evaluation procedures.

The directives set forth these conformity evaluation procedures, considering the potential risks identified. The conformity evaluation is performed by the testing and certification bodies ("notified organisms"), nominated by the Member States under their jurisdiction and responsibility.
The EC mark indicates the conformity with all the relevant rules of the Community – the Member States acknowledge the fact that a product marked EC traded on the Community Market complies with the national rules.
The directives are based on the following principles:

✓   The harmonization refers strictly to essential requirements;

✓   Only the products which comply with the essential requirements may be traded or commissioned;

✓   The harmonized standards whose reference numbers have been published in the Official Gazette and which have been transposed in the national standards comply with the correspondent essential requirements;

✓   The application of the harmonized standards or of other technical specifications remains voluntary, and the producers are free to choose any technical solution which ensures the observance of the essential requirements;

✓   Manufacturers may choose one of the conformity evaluation procedures corresponding to the applicable directive.

Thus, considering these legal provisions, standards for all types of PPE have been created. As regards our study we point out the protective clothing standard – gloves and arm protectors against cutting and injuring with hand knifes, wire gloves, arm protectors and metallic materials aprons: SR-EN 1082-1:2004.

Currently the PPE manufacturers have designed and manufactured this equipment (which have metallic materials in their structure) out of stainless steel wire and anodized aluminium plates considering that these materials are the most appropriate for this type of equipment, but involving high costs.

A study may be developed regarding the features of these materials, their influence on the human body as well as on the economic agent.

5. Conclusions

Considering that the compliance with the essential safety and health requirements represents a must in order to ensure human safety we understand the major role of personal protection equipment which function as a barrier between the risk action and the human factor.

That is why more research regarding the structure of the metallic materials which are part of the PPE should be done in order to keep the pace with the technological and economic development worldwide and maintain the protection function in regard to risk factors which are continuously changing.

REFERENCES

Dobrescu E., Poruschi F., Henţulescu V., *Prevention of Musculo-Skeletal Disturbances by Ergonomic or Special PPE*. I.N.C.D.P.M., 2000.
Katrine I., Bontea A., *Standardization and Certification*, Training Module.
Personal protection equipment Guideline, version July 3rd, 2008.
Tanasievici G., Căldărescu G.*, Security Conformity Evaluation for the Work Equipments and Personal Protection Equipment*, postgraduate course, UTI, 2010.

IMPORTANŢA MATERIALELOR METALICE LA PRODUCEREA
ECHIPAMENTELOR DE PROTECŢIE

(Rezumat)

Lucrarea de faţă face referire la importanţa studiului asupra materialelor metalice din care sunt confecţionate echipamentele individuale de protecţie (EIP) şi corelarea proprietăţilor acestora cu dinamica dezvoltării tehnologice şi economice şi menţinerea funcţiilor de protecţie faţă de factorii de risc care sunt în permanentă transformare şi acţionează asupra organismului uman.

[1]. (Katrine, I., Bontea, A., *Standardization and Certification*, Training Module.
[2]. (Dobrescu, E., Poruschi, F., Henţulescu, V., *Prevention of Musculo-skeletal Disturbances by Ergonomic or Special PPE*, I.N.C.D.P.M., 2000.
[3]. (*Personal protection equipment Guideline*, version July 3rd, 2008.
[4]. Tanasievici, G., Căldărescu, G., *Security Conformity Evaluation for the Work Equipments and Personal Protection Equipment*, postgraduate course, UTI, 2010.

THE TURNING INTO ACCOUNT OF SANDS FROM THE HARTOP-SUCEAVA AREA IN FOUNDRIES

BY

NASTACA TIMOFTE[*]

"Gheorghe Asachi" Technical University of Iaşi

Abstract. The paper present experimental research concerning Hartop sands used on preparation of moulding mxture and manufacture of core.

Key words: sand, core, mould.

1. Introduction

The deposit of Hârtop is situated in the district of Suceava, at six kilometers NE from Fălticeni city.

In the mentioned area, exist very good natural openings, at altitudes between 400 and 470 meter.

In the depth of sands of Hârtop between approximately 400-450 m exists frequent intercalation of sand clays and argillaceous sands as well as sandstone of fossiliferous limestone.

2. Grading Composition

The histograms of analyzed samples proved a unilinear asymmetrical

---

[*] Corresponding author; *e-mail:* nastacatimofte@yahoo.com

distribution of the dimensions of granules, for the raw samples and for the one that was washed with water and NaOH (sodium hydroxide) and then treated with HCL (hydrochloric acid).

From the viewpoint of grading, Hârtop sands are situated in the category of fine sands, which are sorted very well and uniform. There are noted N10(M50)015(Gu)75b.

3. Chemical Composition

The variation of SiO2 are show in Table 1.

Table 1
Variation of SiO2

	Variation boundary %	Mean %
Crude sand	77,8-86,6	82,54
Washed sand	88,3-91,2	88,62
Treated sand	93,0-95,7	93,66

4. Mineralogical Composition

Hârtop sands are constituted of quartz, siliceous rocks and pieces of lune spar, muscovite and glaucovite. The levigable components are removed by washing with water and it varieties between 2,82-5,30.

5. Experimental Results

5.1. Experiments Regarding the Moulding of Pieces from Ferrous Alloy

Core sands were used because, as a consequence of the contraction, which accompanies the solidification, the dimensions that correspond to the previous diameter are diminished. The following mixtures have been used (Table 2).
The first core has dimensions of Ø 50x100.

It was mounted on a bigger core and was stiffened of the mixture by means of foundry nails.

The moulding was made by uphill casting in order to ensure a good moulding.

For the big core a moulding sand with Aghires sand has been used with 8% Na_2SO_3. sodium silicate.

Table 2

No. recipe core	Sand		Moulding mixture	Binder, %				
	Sand of Hârtop	Quartz sand double washed		Sodic Bentonite	Dextrin	Linseed oil	Na silicate	Water
1.	53,5	-	36,0	-	-	8	-	3,5
2.	35,0	60,0	-	-	-	4,5	-	4,5
3.	66,5	17,0	-	-	-	5,0	-	5,0
4.	35,0	51,0	-	6,0	6,0	4,0	-	4,0
5.	66,3	17,0	-	6,5	6,5	5,0	-	5,0
6.	51,5	34,0	-	2,5	-	-	7,0	5,0
7.	66,5	17,0	-	2,5	-	-	7,0	4,0
8.	31,0	57,0	-	-	-	-	7,0	5,0

There was moulded six technological sample at diverse temperatures:

First sample: - steel OT 50;
        -temperature: 1590ºC
        -composition: 0,3%- C (carbon); 0,49% Si (silicium); 0,69% Mn (manganese); 0,010% S (sulfur); 0,015% P (phosphorus).

The second sample: -   steel OT 50;
- temperature: 1510ºC
- the same composition as first sample.

The third sample: - cast iron- Fe 200;
- temperature: 1290ºC
- composition: 3,15% C; 2,45% Si; 1,2 % Mn; 0,12% S.

The fourth sample: - cast iron Fe 200;
- temperature: 1460ºC
- the same composition as the third sample;

The fifth sample: - cast iron - Fe 200;
 - the same composition.

The sixth sample: - cast iron- Fe 200;
- temperature: 1235ºC;

- the same composition.

Note: The temperature was measured with the optic pyrometer.

The first, the fourth, the fifth, the sixth, the seventh and the eight core was dried by a temperature about 200ºC in half past and one hour, but second and the third cores was dried at an temperature about 100ºC, two hours in time.

For the third and the fifth sample the cores were dyed with a dye which was prepared from 75% graphite, 5% dextrin, 3% bentonite and 17% water.

After moulding and solidification, the technological samples were treated with oxyacetylene flame longitudinal and transversal in order to suitable microscopic studies. The technological samples were oxidized the lathe.

The undertaken studies proved the fact that at the third and the fifth technological samples did not mould any adherents in the core area.

The conclusion is that all the preparation mixture could be used for core execution but only in dying mode. The smallest adherents were noticed at the samples number two which used dextrin as a binder.

In conclusion, the Hartop sands could be used for core sands preparation in anyone of the eight suggested mixture abynding the following conditions:

- it has to be mode the protection with dye on the basic of graphite for moulding of cast iron;

- the pieces must be thinner tha 30 mm and slighter than 100 kg.

5.2. Experimentation Regarding the Moulding of Pieces from Non-Ferrous Alloy

In order to experiments non-ferrous alloy were chosen CuAl 19T-STAS 1982/75 which present the following composition: 88% Cu, 9% Al, 0,3% Pb, 0,3% Sn, 5% Ni, 0,2% Si.

This bronze with aluminum has the temperatures of eutectic transformations of 1037ºC.

In the Table 3 we propose four composition of core.

Table 3

No. recipe core	Sand		Moulding mixture	Binder, %				
	Sand of Hartop	Quartz sand double washed		Sodic bentonite	Dextrin	Linseed oil	Na silicate	Water
1	35,0	-	-	-	6,0	4,5	-	4,5
2	66,5	17,0	-	-	6,5	5,0	-	5,0
3	53,5	-	36,0	-	-	8,0	-	3,5
4	69,5	17,0	-	2,5	-	-	7,0	4,0

The cores prepared with the first, second and the third composition was dried with a mobile drier about 25 minutes in time.

The rugosity of moulded pieces was measured with the electronic surtronical rugosimetre. The best rugosities were obtained with the fourth compostion which is based on (Na2SiO3) sodium silicate.

The macroscopic and microscopic analyses did not show thermic and chemical adherence.

For the mixture for filling the following composition was used:

- double refined quartz sand 12%

- recycled moulding sand 80%;

- bentonite 4%;

- water 4%.

Uphill casting made the moulding. There was moulded sixteen technological samples at 1140ºC, 1210ºC, 1260ºC, 1290ºC for cores which was executed according to proposed composition.

After moulding and solidification, it was result good pieces; the casting mould was knockout normally.

As adherence, it was remarked only mechanics adherence at couplings of surfaces.

The metallostatic pressure did not influence significantly the formation of adherence.

The results of these experiments guide us at the conclusion that the Hârtop sands could be used for moulding of nonferrous alloy, which are based on copper and aluminum.

REFERENCES

Ciorchină C., Andrei E. *et al.*, *Cercetări privind formarea aderenţelor la turnarea pieselor din aliaje feroase, folosind pentru amestecurile de formare nisipuri de Hârtop*. Creaţia tehnică şi fiabilitatea in construcţia de maşini, Iaşi, 15-16 apilie, 1983.

Ciorchină C., Andrei E. *et al., Cercetări privind formarea aderenţelor la turnarea pieselor din aliaje neferoase, folosind pentru amestecurile de formare nisipuri de Hârtop.* Creaţia tehnică şi fiabilitatea in construcţia de maşini, Iaşi, 15-16 apilie, 1983.

VALORIFICAREA NISIPURILOR DIN ZONA HÂRTOP-SUCEAVA ÎN TURNĂTORII

(Rezumat)

Lucrarea abordează un subiect important în metalurgie şi anume cel al utlizării unor noi zăcăminte de nisip care să fie utilizat în turnătorii pentru prepararea amestecurilor de formare şi de miez.

Cercetările experimentale efectuate asupra nisipurilor din zona Hârtop-Suceava au pus în evidenţă faptul că aceste nisipuri se pot folosi atât la prepararea amestecurilor de formare cât şi pentru confecţionarea miezurilor. Experimentările care au condus la aceste concluzii s-au efectuat atât la turnarea pieselor din aliaje feroase cât şi la aliaje neferoase.

THE EFFECT OF SPRAYING NOZZLE GEOMETRY ON THE PARTICLES SIZE DISTRIBUTION SPRAYED IN ELECTRIC ARC

BY

ŞT. L. TOMA[1]*, C. BACIU[1], C. BEJINARIU[1], DIANA GHEORGHIU[1] and GABRIELA TOMA[2]

[1] "Gheorghe Asachi" Technical University of Iaşi,
[2] Grup Scolar Econmic de Turism Iaşi

Abstract. This paper presents the analyze of material particles size detached from the anode, respectively cathode during the thermal spraying process, by using as adding material different kind of wires (steel and copper) – insoluble in liquid phase. The differentiated detaching, atomization and acceleration of material particles with average diameters can be modify by increasing the atomization pressure gas and by using a closed nozzle system with a converging – diverging orifice (CD/CL). The microstructure analyze of deposition, shows that this kind of nozzle produces coatings with a fine microstructure, a reduced porosity and a raised amount of oxides.

Key words: arc spray, particle size, nozzle geometry.

1. Introduction

In researches concerning wire arc spray process, many works were devoted to better understanding of the droplet formation, in flight particle

---

* Corresponding author; *e-mail:* xpower1903@yahoo.com

properties such as particle size, temperature, and velocity, and the effects of spray parameters, *e.g*., nozzle configuration and atomising gas pressure, as they contribute to coating properties to a great extent. For example, the effect of nozzle configuration, gas pressure and gas type on coating properties were studied by Wang et al. In-flight particle properties were measured by using phase Doppler anemometer. The pheonmenon of particle cross-over trajectories in twin wire arc spraying was demonstrate by Zhu et al. Investigation of the asymmetric melting behavior of the anode and cathode wires was traced back to 1966. These works gave insight into the origin of the droplet forming process. However, few work discussed how this asymmetry was retained after atomization and acceleration. In addition, literatures state that the bimodal size distribution of the particles collected is due to the asymmetric melting of the electrodes. But the properties of particles from individual wires remain to be tackled to reveal the very fundamentals of the arc spray process so as to help spray process control, nozzle design and explanation of coating microstructure characters. The problems in studying particle properties of individual wires lies in that neither can we trace a specific particle from its birth to its impact with the substrate/coating surface nor can we distinguish between particles from different wires. In this study, two consumable wires of different magnetic properties were used as anode and cathode and the corresponding particles were separated with the help of a magnetic field. Another concern of this paper is the effect of nozzle geometry on particle characteristics and coating microstructures. As an influential factor, nozzle geometry has a profound effect on the atomizing performance of a nozzle system when other operational parameters are given. In this paper, three different nozzle shapes were studied, namely the standard spray nozzle corresponding to a closed nozzle whidt converging orifice (C/CL), a closed nozzle with a converging-diverging orifice (CD/CL), and an open nozzle with a converging-diverging orifice labelled as CD/OP. In order to correlate nozzle geometry and coating microstructure in a quantitative way, a numerical model incorporate with experimental data was used to predict particle velocity distribution and splat diameter distribution.

2. Experimental Procedure

2.1. Spray Conditions

While all the spray operations were performed electric arc spray system – de conceptie proprie, three different spray nozzles were studied to evaluate the effects of different nozzle geometries as shown in Fig. 1.
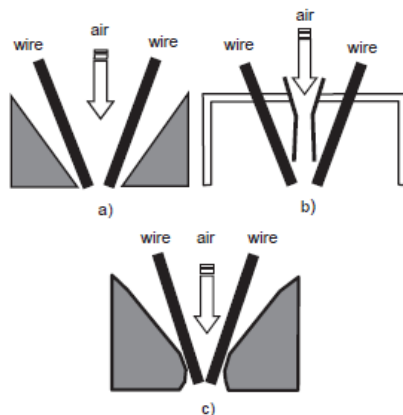
Fig. 1 − Schematic configuration of the different nozzles:
a − C/CL, *b* − CD/ OP, *c* − CD/CL.

The first nozzle, referred to as C/CL, a closed nozzle and a converging orifice. The second one, labeled as CD/CL, is a closed nozzle with converging-diverging (de Laval) orifice.

The last one is an open nozzle with a converging-diverging orifice which was referred to as CD/OP. Commercially available is steel - 30 T and copper - 05 T, wires - 1.6 mm diameter, were used for the spray operations.

2.2. Collection and Analysis of Particles

Particles were collected by directing spray jet onto water with a standoff distance of 300 mm, an arc current of 200 A, and an arc voltage of 30 V. After proper evaporation and drying of water, particles were made separated using a magnetic field. To make it clear whether the steel and copper particles were fully distinguished or not, SEM and EDS analyses were performed on the separated particles. The size distribution of the collected particles was then analyzed using a an optical microscope IM 7000.

2.3. Microstructure Analysis

Polished cross-sections of the sprayed deposits were examined using an IM 7000® optical microscope with a digital camera Evolution QImaging VF product by Media Cybernetics.

3. Results and Discussion

3.1. Chemical Analysis of the Copper and Steel Particles

When using dissimilar materials as anode and cathode in an arc spray gun one question that could arise is to investigate the attribute of particles from

individual wires, and one of the concerns is whether molten particles from the two wires will dissolve each other. Copper and iron are nearly insoluble and it might then be difficult to form solid solution between them. In addition, during the initial stage of melting and detaching from the wire tips, droplets from the two wires have little contact thanks to the strong blowing of the atomising gas stream. Meanwhile, after atomization, the particles may come in contact one with each. The question is then whether such a contact between copper and steel particles would join them together to form a single particle afterwards. This remains to be clarified to make sure that the collected copper and steel particles can be made seperated via a magnetic field. Therefore, the collected particles were randomly sampled for EDS analysis after magnetic separation. Fig. 2 shows a typical energy spectrum of a steel particle, which indicates that only vanishingly small amount of copper can be found in the steel particle. In fact, the element analysis shows there is 1.27 wt.% of copper in iron particles. Similarly, Fig. 2 *b* presenting an energy spectrum of a copper particle shows quite small amount of iron: only 1.9 wt.% of iron in copper particles according to the analysis. However, on the surface of some of the copper particles, dark grey contamination corresponding to an iron rich compound (about 20 wt.%) was found (indicated by the arrows in Fig. 3). In fact, this contamination is limited to very thin layers of iron or iron oxide adhered to the surface of some copper particles. No similar phenomenon was found for the steel particles. The above analysis indicates that the overall interaction between the two materials is quite small and the solubility of the two materials is quite small and the coalescence and mixing of the copper and the steel particles after separation are negligible.
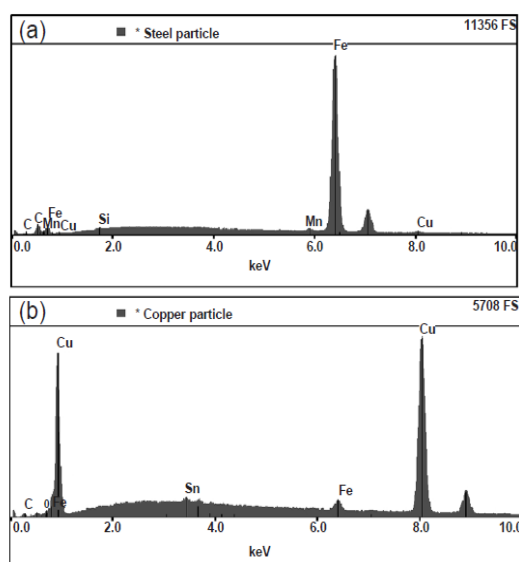
Fig. 2 – Chemical Analysis of separated copper and steel particles from group 6 with copper and steel wires as cathode and anode, respectively: *a* – steel particle, *b* – copper particle.
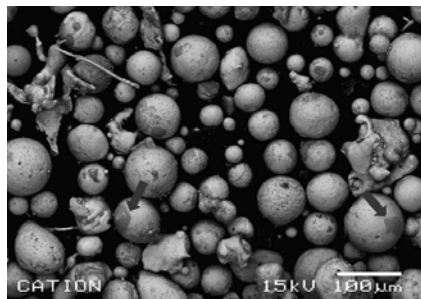
Fig. 3 – SEM micrograph of copper particles showing
dark grey contaminations on some of the particle surface

3.2. Particles Size Distribution for Individual Wires

By using two wires of different magnetic properties, *e.g.* one ferromagnetic and the other non-ferromagnetic, as anode and cathode, or inversly, the resulting collected particles can readily be separated by applying a magnetic field with a magnet. In this way, particles from each wire can be collected and analyzed to obtain information concerning the melting and atomizing behaviors of each wire. Fig. 4 shows the volume percentage versus particle size histogram of copper particles sprayed by the C/CL nozzle with atomizing gas pressures of 0.28/0.28 MPa (premier/arc-jet pressure).
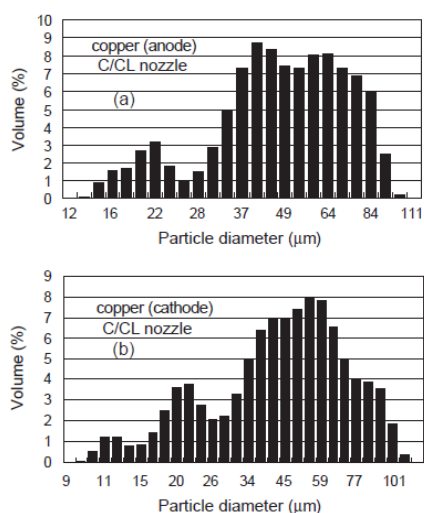
Fig. 4 – Copper particle size histogram (C/CL nozzle with atomizing gas pressure: 0.28/0.28 MPa): *a*– copper wire as anode; *b*– copper wire as cathode.
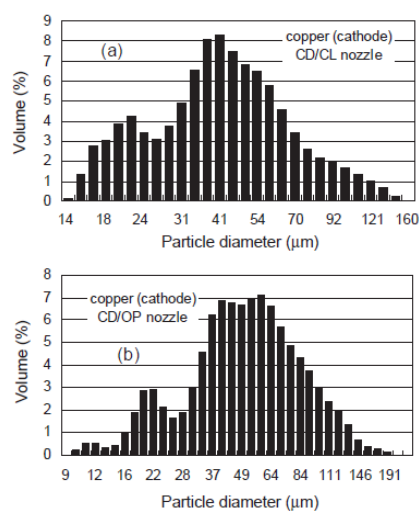
Fig. 5 – Cathode (copper) particle size histogram (atomizing gas pressure: 0.32/0.32 MPa): *a*– CD/CL nozzle; *b* – CD/OP nozzle.

Whether as anode or as cathode, the particles from the copper wire exhibits a bimodal size distribution. Previous researches have attributed the bimodal size distribution to the nonsymmetrical melting of the anode and cathode wires. However, Fig. 4 clearly indicates that with the given gas pressure, particles from a single wire also present a bimodal size distribution.
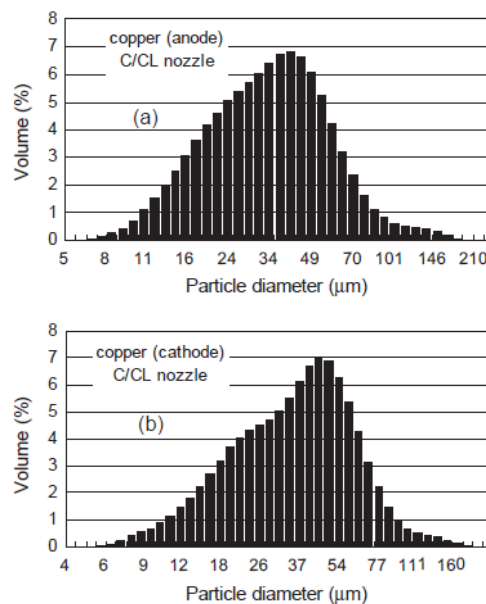
Fig. 6 – Copper particle size histogram (C/CL nozzle
with atomizing gas pressure: 0.46/0.49 MPa):
a − copper wire as anode; *b* − copper wire as cathode.

A bimodal size distribution can also be observed when using the CD/CL or the CD/OP nozzles (Fig. 5) with a slightly attenuated effect in the case of the CD/CL nozzle. Increasing atomizing gas pressure tends to reduce the bimodal size distribution of particles from an individual wire. Fig. 6 shows that with atomizing gas pressure approaching 0.46/0.49 MPa, the bimodal size distribution has nearly disappeared. The bimodal size distribution for particles from a single wire is likely the result of the periodical fluctuation of arc length and arc voltage and hence videographs and oscillographic voltage recordings and was related to particle formation and particle size variations qualitatively. In the literatures, it was stated that during spraying, the arcing and melting of the consumable wire tips are unstable. The wire melting rate are not equal, forcing a periodic variation of arc length and arc voltage. The consequence is a periodic variation of the molten droplet size. For the case of steel wire, although the bimodal particle size distribution can still be observed, its intensity is substantially reduced relatively to the case of copper wire (Fig. 7), which tells

that the bimodal particle size distribution is material property dependent, e.g., viscosity and surface tension of the molten particles

Another interesting result observed is the average size difference between the particles produced from the anode and the ones from the cathode. While it has already been observed, through high speed video camera imaging, that the initial droplets from the two wires are quite different in size because of the more constricted arc attachment compared to the more diffuse arc attachment at the anode, the questions remain to be clarified is that how far this difference will affect the final particle size after secondary atomization.
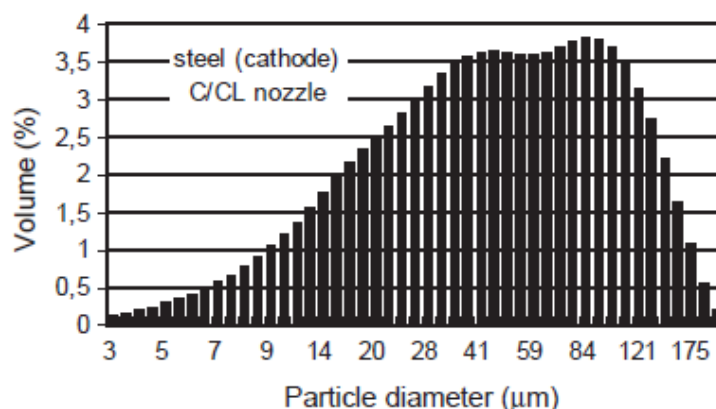
Fig.7 −Steel particle size histogram (C/CL nozzle with atomizing gas pressure: 0.28/0.28 MPa).

Fig. 8 shows the average size of particles from individual wires when using different nozzles and atomizing gas pressures. It can be seen that even if there is the difference between the average diameter of the particles coming from each wires, this difference is quit small (between 6% and 14%), and certainly smaller than it was at the moment of droplet formation as the literature stated. Results in Fig. 8 also suggest that by using a closed nozzle system with converging-diverging orifice (group 5) the difference can further be reduced, whereas, more difference were preserved when using the open nozzle system (group 6). This is probably due to the better atomizing performance of the CD/CL nozzle over that of the CD/OP nozzle, which will be explained further below.

Fig. 8 also shows that the CD/CL nozzle produced the smallest particles and the CD/OP nozzle produced the largest ones. With the same atomizing gas pressure the average particle size of group 5 is merely half of that in group 6, and with much lower atomizing gas pressure the average particle size in group 5 is comparable to those in group 3 and group 4 obtained with a much higher atomizing gas pressure, which indicates that the closed

nozzle system with CD orifice tends to produce better atomization and more uniform particle size distribution.
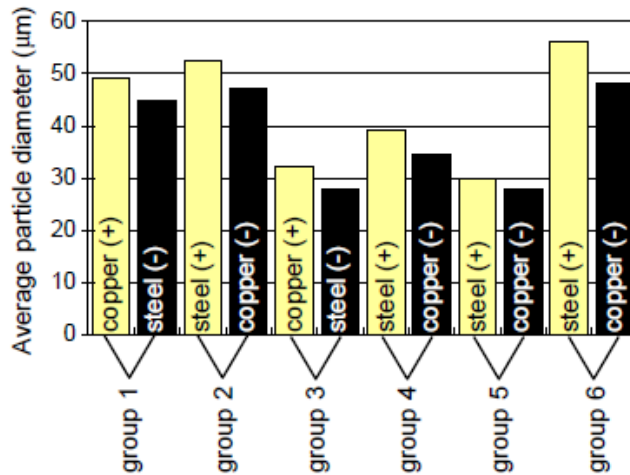
Fig. 8. Average particle size of individual wires with different nozzle configuration and atomizing gas pressure (stand-off distance: 300 mm); group 1—C/CL nozzle, 0.28/0.28 MPa; group 2—C/CL nozzle, 0.28/0.28 MPa; group 3—C/CL nozzle, 0.46/0.49 MPa; group 4—C/CL nozzle, 0.46/ 0.49 MPa; group 5—CD/CL nozzle, 0.32/0.32 MPa; group 6—CD/OP nozzle, 0.32/0.32 MPa.

3.3 Coatings Microstructure Analysis

Fig. 9 shows the microstructure of steel coatings sprayed by using the different nozzles. It is evident from this figure that with identical process parameters, the coating sprayed by the CD/OP nozzle (Fig. 9 *a*) exhibits the coarsest microstructure due to poor atomization and relatively lower particle velocities. Large particles with low velocity and hence reduced temperature will result in poor deformation and calking upon impact with the substrate so that many interlaminar cracks can be found (Fig. 9 *a*), which implies poor bonding between the flattened particles and hence a lower cohesive strength. A dense and fine microstructure revealing a better atomization and higher particle velocities was obtained by using the CD/CL nozzle (Fig. 9 *c*).
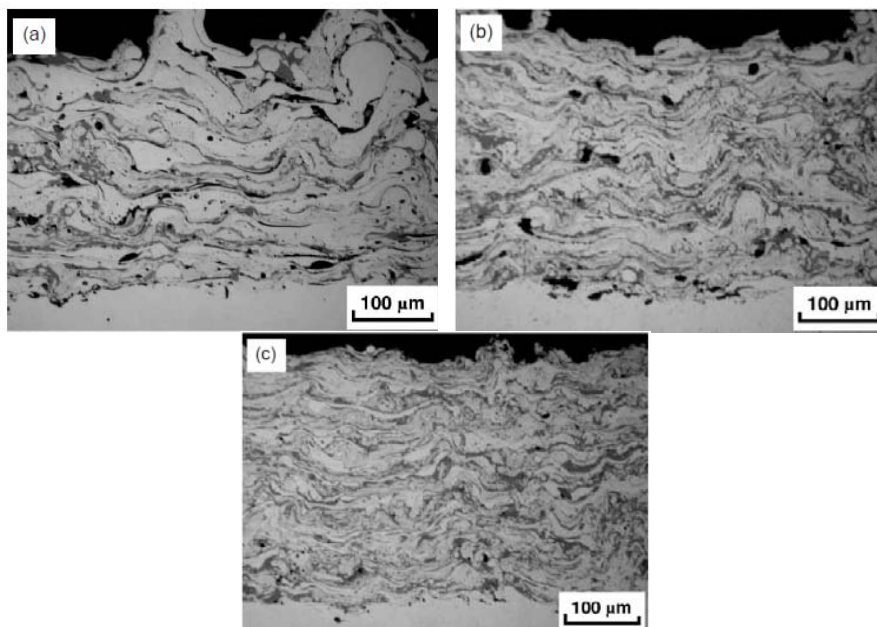
Fig. 9 – Optical microscope of steel coatings sprayed by different nozzles with arc current: 200 A, stand-off distance: 200 mm, atomizing gas pressure: 0.38/0.38 MPa. *a* – CD/OP nozzle; *b* – C/CL nozzle; *c* – CD/CL nozlle.

4. Conclusions

By separating particles coming from the anode and the cathode wires, the particle properties of each wire of the arc spray process were investigated. A bimodal particle size distribution was found for particles from each wire. This bimodal particle size distribution is probably due to the periodical fluctuation of the arc length and arc voltage leading to a varying particle size. Meanwhile, after second atomization, the difference between average particles size for particles coming from the anode and cathode becomes very small. This difference gets smaller when increasing the atomizing gas pressure and/or when using a closed nozzle system with a converging-diverging orifice. Microstructure analysis also indicates that the closed nozzle system with a converging-diverging orifice tends to produce coating with finer microstructure, lower porosity and higher oxide content, than the open nozzle which leads to very coarse coating microstructure with high porosity but low oxide content because of its poorer atomising performance. They show that one of the major drawbacks of an open nozzle system is its relatively longer distance between the wires intercept point and the nozzle exit where the gas velocity attains its maximum value. Results show a smaller average splat diameter and a narrower

splat diameter distribution for the CD/CL nozzle, which is in close agreements with microstructure observations.

REFERENCES

[1]. Wang X., . Heberlein. Pfender J, E, Gerberich W., Therm. Spray J. Technol. 8 (1999) 565.

[2]. Wang X., Zhuang D., . Pfender E, Heberlein J., . Gerberich W, *Effect of atomizing gas pressure on coating properties in wire arc spray*, Proc. 7th National Thermal Spray Conference, 20-24 June 1994, Boston, Massachusetts, 1994, p. 587.

[3]. Watanabe T., Wang X., Heberlein J., . Pfender E, . Herwig W, *Voltage and Current Fluctuations in Wire Arc Spraying as Indications for Coating Properties*, in: C.C. Berndt (Ed.), 9th National Thermal Spray Conference, 1996, Cincinnati, Ohio, ASM International, Materials Park, 1996, p. 577.

[4]. Sheard J.S., *Diagnostic Developments for control of Wire Arc Spraying, MS The*se, University of Minnesota (1997).

[5]. . Kelkar M, . Hussary N, Schein J., Heberlein J., *Optical diagnostics and modelling of gas and droplet flow in wire arc spraying,* in: C. Coddet (Ed.), Thermal Spray: Meeting the Challenges of the 21st Century, ASM International, Materials Park, OH, 1998, p. 329.

EFECTUL GEOMETRIEI DUZEI DE PULVERIZARE ASUPRA DISTRIBUŢIEI MĂRIMII PARTICULELOR PULVERIZATE ÎN ARC ELECTRIC

(Rezumat)

Lucrarea prezintă analiza mărimii particulelor de material desprinse din anod, respectiv din catod în timpul procesului de pulverizare termică, prin utilizarea ca material de aport sârme de natură diferită (oţel şi cupru) - insolubile în stare lichidă. Desprinderea, atomizarea şi accelerarea diferenţiată a particulelor de material de diametre medii poate fi modificată prin creşterea presiunii gazului de atomizare şi folosirea unui sistem de duză închis cu un orificiu convergent – divergent (CD/CL). Analiza microstructurală a depunerii, indică faptul că acest tip de duză produce învelişuri cu microstructură fină, porozitate scăzută şi conţinut ridicat de oxizi.

FERRO-CHROME-ALUMINUM LAYERS DEPOSED BY THERMAL SPRAYING AND USED IN CRANKSHAFTS RECONDITIONING

BY

ŞT.L. TOMA[1]*, D.G. GĂLUŞCĂ[1], V. CAŢARSCHI[1], O. CALANCIA* and GABRIELA[2] TOMA

[1] "Gheorghe Asachi" Technical University of Iaşi,
[2] Grup Scolar Econmic de Turism Iaşi

Abstract. This paper presents the structure of ferro- chrome-aluminum layers obtained from wire by thermal spraying in electric arc – used in crankshafts reconditioning. The scientific data concerning on ferro - chrome-aluminum layers structure obtained offers informations regarding the instability of thermal spraying process in electric arc and to the strict requirements for crankshafts reconditioning.

Key words: arc spray, layers, ferro- chrome-aluminum.

1. Introduction

One of the most important directions of the elevation of the quality of crankshafts reconditioned by the method of electric-arc metallization is the use of powder wires.

---

* Corresponding author; *e-mail:* xpower1903@yahoo.com

The use of a metallic shell with various fillers makes it possible to vary the chemical composition, structure, and service properties of the grown surface within a wide range.

It is interesting to estimate the special features of formation of layers in such treatment, the uniformity of the distribution of components in them, the composition of the formed phases, and the presence of discontinuities.

We studied the structure of coatings obtained from powder wires on a substrate of ferro- chrome-aluminum with additional alloying elements added into the charge in different proportions (Mo, Si, V).

2. Methods of Study

In order to bring the deposition of the coating under laboratory conditions as close as possible to commercial conditions, we chose specimens of steel 45 cut from a worked out crankshaft of an SMD-60 engine.

Before the metallization the specimens were cleaned and annealed at 200 - 250°C for 1 - 1.5 h in order to stabilize the structure of the working layer and remove the stresses. The annealed specimen was subjected to shot blasting by a mechanical mixture of cast iron shot and quartz sand at a pressure of 0.5 + 0.05 MPa and an air flow rate of 2.5 m3/min.

The treatment distance was 130 - 150 mm. The slope of the incidence of the mixture onto the treated surface was 55 - 70°. The time between the metallization and the shot blasting was chosen, proceeding from the conditions of the fullest possible recrystallization on the deformed surface and avoiding the appearance of a coarse oxide film that would hamper strong cohesion between the particles and the reconditioned surface.

The optimum interval was 1.5 - 2 h. The layer was grown in a stationary EM-17 apparatus at an arc voltage U = 25 - 30 V, an air pressure p = 0.7 - 0.75 MPa, and a rate v = 2.0 - 2.5 m/min of feeding the wire. The spraying distance was 170 - 190 mm. In this case the substrate was heated to a temperature not exceeding 90°C. The coating was formed on the specimen in six passes with time intervals in which the temperature fell to 30°C. We studied a thin layer (without the substrate), which was deposited on inconsiderably worn parts (up to 1 mm over the diameter).

The special features of structure formation in the coating were studied by metallographic (MIM-8M microscope) and x-ray diffraction (DRON-3M diffractometer) methods and chemical analysis. The spectra of the characteristic x-ray radiation were measured using an REMMA-101A electron probe unit that included a combined scanning electron microscope, a microanalyzer, and a computer.

In order to estimate the porosity and discontinuity of the coating the initial image of the polished section of the analyzed specimen (magnified by x

100) was converted to an electron form in a 1-to-1 scale and processed with the help of standard software.

The visualized surface of the deposited layer was conventionally divided into several sectors 10 |im2 in size.

A sample consisting of 10 elements was examined. The criterion for the evaluation was a visually determined black gradient of unpolished black zones. For each sector we determined the percent of its filling with such black color. The result was determined as an arithmetic sum.
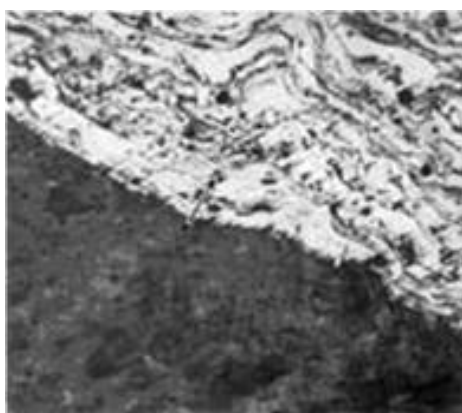
Fig. 1 – Microstructure of a crankpin of an
SMD-60 engine with a coating deposited by the
method of electric-arc metallization (x 100).
The arrow indicates aluminum oxide.

In order to determine the layer-by-layer distribution of the elements and the phases formed in the coating the scanning was performed over the thickness of the deposited layer automatically with a step of 7 |im. We used a magnification of x 7000 and x 10,000 with focusing of the primary electron beam at a point. Based on the intensities of the characteristic x-ray radiation from the zone of deceleration of the probe electrons at the studied points of the specimen the computer performed (with the help of specially developed programs) qualitative and quantitative estimation of the distribution of t he components. The energy dispersion method of detection of the x-ray radiation is not suitable for determining the concentration of elements with low atomic weights (like carbon, oxygen, boron).

The phase composition of the specimens was determined by x-ray diffraction analysis in a DRON-3M diffractometer. The computer isolated the diffraction intensity in the range of low angles and processed it for reducing the error of the experiment. Carrying out the x-ray diffraction analysis we used focusing from a flat specimen (an area 1.2 x 2 cm in size) according to the Bragg - Brentano method and used copper Ka radiation.

The computed values of the slip angle 29 were compared with the experimental data with allowance for the relative intensity of the diffraction maximum I/I1 (Table 1).

Table 1
Values of the Angles 29 Obtained by Computation and Experimentally

Probable phase	HKL	29	I/I\	Spinning type
Fe$_\alpha$	110	44.72/44.31	100/100.00	Cubic
	200	65.09/64.31	30/13.91	
	211	82.43/81.52	40/31.90	
	220	99.08/97.87	20/9.84	
	310	116.57/114.86	20/15.80	
Fe$_\delta$	212	45.08/44.31	100/100	Tetragonal
	721	80.62/81.52	80/31.90	
Fe$_\gamma$	111	43.09/44.31	100/100.00	Cubic
	222	95.56/97.87	50/8.84	
	400	117.56/114.86	20/15.80	
(Cr, Fe)$_{21}$Mo$_2$C$_6$	333	44.35/44.31	100/100.00	Cubic
	753	82.88/81.52	60/31.90	
	10.6.0	115.82/114.86	20/15.80	
α-Al$_2$O$_3$	113	43.32/44.31	100/100	Hexagonal
	124	66.47/64.31	32/13.91	
	226	95.17/97.87	11/8.84	

Note. The numerators present the computed data; the denominators present the experimental data.

3. Results and Their Discursion

We established that as the power wire was sprayed, the motion of the molten particles in the air jet substantially increased the content of oxygen in the deposited coating. A metallographic analysis showed that oxygen was present in the layers in the form of thin light- and dark-gray oxide films distributed over grain boundaries and inside the grains in the form of round well-polished inclusions. A complex study combining metallographic, electron microscopic, and x-ray spectral microanalysis and x-ray analysis confirmed the assumption that these formations were primarily iron and aluminum oxides. Figure 1 presents a typical microstructure of the deposited layer. The porosity and the discontinuity of the layer is about 12%.

The coating is represented by a layered structure consisting of flat deformed particles. Upon the impact against the surface a spherical particle with diameter d is strongly deformed and acquires a shape with a volume equal to

that of a thin cylinder with diameter D1 and height h. We assume that splashing of the material is inconsiderable. Due to the high deformation rate of a fully molten drop the conditions of stable spreading are violated and its crystallized edges are somewhat raised with respect to the substrate. As a result, the particles are strongly welded to the substrate only in the interaction spot.

The violation of the condition of stable motion of the boundary of the spreading particle is estimated by the Weber criterion:

$$We = \frac{\rho \cdot v^2 \cdot d}{\sigma}$$

where: - ρ is the density of the material of the particle, [kg/m3];
 - v is the speed of the particle, [m/sec];
 - d is the diameter of the particle, [m];
- σ is the coefficient of surface tension of the material of the particle, [J/m2].

Table 2
Distribution of Elements Over The Thickness of the Sprayed Layer

Points of measurement	Distance from the surface	Fe	Cr	Al	Si	Mo	V	Formed phase
0	0	55.793	33.369	8.240	1.682	0.916	0.000	Fea + M$_4$C
1	7	58.850	30.579	9.360	0.742	0.469	0.000	Fea + M$_4$C
2	14	45.991	49.072	3.766	0.435	0.736	0.000	Cr + M$_4$C
3	21	33.780	59.527	5.423	0.717	0.179	0.373	Fe$_a$ + FeCr + M$_4$C
4	28	44.106	47.909	6.788	1.005	0.193	0.000	FeCr + M$_4$C
5	35	38.285	58.002	2.013	0.334	0.932	0.414	Fe$_a$ + FeCr + M$_4$C
6	42	79.393	11.981	8.006	0.370	0.250	0.000	Transition zone

We determined the mean diameter of the particles metallographically by the method of statistical processing of the measured values of D1 and h on a prepared microsection etched with a 4% solution of picric acid in ethyl alcohol. Then, proceeding from the equality of the volumes of the drop before and after the deformation, we calculated the value of d. For the used process

regimes it turned out to be 21 |im. The density of the coating was determined with allowance for the coefficient of porosity. For the given material it was 0.96.

Substituting the appropriate data: $p = 8 \times 10^3$ kg/m3, and $v = 30 - 150$ m/sec, into the formula presented above we established that We ranged within 151 and 3.780×10^3. By the data of, the stability of the radial spreading of the material of the drop upon an impact in the absence of wetting is disturbed at We > 80. If this value is exceeded considerably, the probability of dispersion of the molten particles increases markedly. According to the performed metallographic study with use of computer, the mean thickness of the sprayed layer amounted to 42 μm.

The results of the general chemical analysis showed that the carbon content in the coating was 0.12%, which corresponded to a 35% melting loss. The results of a quantitative analysis performed layer-by-layer by x-ray spectral micro- analysis are presented in Table 2.

Analyzing the obtained data we established that the elements were no uniformly distributed over the layers. The variation of the concentration of the components over the thickness of the grown layer obeyed no rule, which seems to be connected with the formation of various phases.

The high content of chromium at a low carbon concentration in the coating determined the crystallization of a small amount of special carbides, the most probable of which is M23C6. According to the data of the formation of a (Cr, Fe)23C6 carbide is possible even at 0.19% C in the coating. However, it is known from that the solubility of Fe in this carbide is at most 30%, whereas in the presence of Mo the solubility of iron in the given phase increases. This allows us to presume the formation of the complex (Cr, Fe)21Mo2C6 in the coating.

The considerable in homogeneity of the distribution of the elements over the layers is responsible for the appearance of regions depleted of and enriched with carbon. Therefore, due to the special features of the crystal lattice of the composite (Cr, Fe)21Mo2C6 carbide, even its inconsiderable de-carbonization results in transformation either to a b.c.c. structure or to a structure of the FeCr type (σ-phase).

Basing ourselves on an analysis of the phase equilibrium diagrams and on experimental data we can assume that the predominant phase in the coating is an a-phase with an inconsiderable content of Cr (from 30.58 to 59.53%) and a FeCr compound (σ -phase) with a mean chromium content of 48.22% (according to Table 1 its experimentally determined concentration was 47.91%). When crystallization occurs at a high rate, as in hardening of the particles, the widening of the solubility range in the solid state can be accompanied by formation of unstable intermediate phases, in particular, a narrow region of a γ-phase.

Since the solubility of carbon in the α- and σ -phases is inconsiderable, its displacement may be accompanied by segregation of disperse special carbides in the formed layer.

Proceeding from the facts described above and from the diagram of phase equilibria of the Fe - Cr - C system at 20°C we determined the presence of presumable phases for every point (Table 1).

According to the solubility of Al in the α -phase can attain 30% and more. Therefore, we can presume that the major part of aluminum is dissolved in this phase. Ordering of the a-solid solution may give rise to the appearance of a α1-phase (Fe3Al) with 13.87% Al.

The results of an x-ray diffraction analysis of the phase composition of the grown layer showed (Table 2) that the matrix phase of the coating was an iron a-phase with a considerable content of chromium and aluminum plus a certain amount of a FeCr compound (a-phase). The amount of the y-phase turned out to be inconsiderable. We determined a high content of composite carbides of the (Cr, Fe)21Mo2C6 type and traces of Al2O3. It seems that the determination of other special carbides lies outside the sensitivity range of the used method.

4. Conclusion

We recommend reconditioning of worn crankshafts by depositing a coating from powder wires based on ferro- chrome-aluminum with Mo, Si, and V alloying additives on their surface by the method of electric arc metallization. This promotes the formation of a heterogeneous structure and phases providing the requisite hardness in the sprayed layer due to the segregation of dispersed special carbides and oxides, and the presence of an alloyed matrix a-phase. According to the data of the performance tests the recommended coating is wear-resistant.

REFERENCES

Goldschmidt D.H., *Interstitial Alloys*. Butterworths, London, 1967.
Gudtsov N.T. (ed*.), Physical Metallurgy and Heat Treatment of Steel and Cast Iron*. Gos. Nauch.-Tekh. Izd. Chern. Tsvetn. Met., Moscow, 1956.
Kurdyumov G.V., Utevskii L.I., Entin R.I., *Transformations in Iron and Steel*.Nauka, Moscow , 1977.
McPherson R., *The Relationship Between the Mechanism Formation of Microstructure and of Plasma-Sprayed Coatings*. Thin Solid Films, *83*, 297 - 310 (1981).

STRATURI DE FERO-CROM-ALUMINIU DEPUSE PRIN PULVERIZARE TERMICĂ UTILIZATE ÎN RECONDIȚIONAREA ARBORILOR COTIȚI

(Rezumat)

Prezenta lucrare prezintă structura straturilor de fero-crom-aluminiu obținute din sârmă, prin pulverizare termică în arc electric - utilizate la recondiționarea arborilor cotiți. Datele științifice referitoare la structura straturilor de fero-crom-aluminiu obținute oferă informații cu privire la instabilitatea procesului de pulverizare termică în arc electric și la cerințele stricte pentru recondiționarea arborilor cotiți.

MATHEMATICAL MODEL AND COMPUTER PROGRAM FOR DEVELOPING ENERGY BALANCES IN HEAT TREATMENT FURNACES

BY

UDRISTE MIHAI[*], MUŞAT DORIAN[*], GABA AUREL[*]

Abstract.
This study presents the mathematical model to calculate actual and optimal energy balances for heat treatment furnaces used in the metallic materials industry.

In order to optimise the operation of these types of furnaces, the following measures that fall into two categories are considered:

A. Measures that do not require investments, such as:
• operation with optimal productivities, for which energy consumptions are minimum;
• conducting thermal treatments diagrams according to those set by technology;
• operation with minimum excess air coefficients;
• follow up of furnace operation under actual operation conditions and respectively after updating activities.

B. Measures that require investments, such as:
• replacement of the recovering device so as to obtain increased temperatures for preheating the combustion air and respectively the fuel, if appropriate;
• introduction of a gas-dynamic sealing system for the working openings of the furnace;
• replacement of the burner installation with higher performance burners to allow operation with excess air coefficients as low as possible, reducing pollutant emissions at the same time;
• update of the burning process management system and of the furnace automation system.

The quantification of these measures within the energy balance requires laborious calculations, which lead to mathematical model transcription into a calculation program in Microsoft EXCEL. Using this program, we can quantify the effect of each measure with a view to reducing furnace energy consumption.

An application of this computer program for a heat treatment furnace is presented for operation both under actual conditions and under conditions where various optimization measures are implemented.

Key words: mathematical model, computer program, energy balance, furnace, heat treatment

1. Introduction

The metallic materials industry is one of the high energy consuming branches, and the highest part of the energy is required as thermal energy. Efficient energy use in metallurgy is not a simple issue because of high production capacities of industrial installations, as well as because of the complexity of the technological processes that take place. As natural energetic resources are not renewable and more and more expensive, their use needs reconsideration by saving methods, methods to reduce loss and to update energy consuming installations and technologies.

An analysis study of energy consumptions can be conducted based on energy balances, developed for installations, aggregates, technological processes. This analysis, named *energetic audit* as well, aims to set the necessary directions and measures, technical and organizational, to eliminate and reduce loss and to value secondary energetic resources as efficiently as possible [1, 2].

The sector of heat treatment furnaces is included among those with high energy consumptions in the metallic materials industry. In order to reduce the energetic consumptions of heat treatment furnaces, the following measures are considered, falling into two categories in terms of investments:

A. Measures that do not require investments:
- operation with optimal productivities, for which energy consumptions are minimum;
- conducting thermal treatments diagrams according to those set by technology;
- operation with minimum excess air coefficients;
- follow up of furnace operation so as the working openings should be closed as long as possible.

B. Measures that require investments:
- introduction of an air pre-heater or its updating, so as to obtain increased temperatures for pre-heating the combustion air and respectively the fuel, if appropriate;
- introduction of a material pre-heater;
- introduction of a gas-dynamic sealing system for the working openings of the oven;
- replacement of the burner installation with high performance burners (e.g. recuperative), to allow operation with lower excess air coefficients, reducing pollutant emissions at the same time;
- update of the burning process management system and of the furnace automation system;
- replacement of thermal insulation systems based on massive masonry made of refractory bricks by using ceramic fibre-based materials [1].

As thermal treatment furnaces are high energy consuming installations, with high fuel consumption and low efficiency, it is necessary to develop a

more detailed analysis for the possibilities to improve operation systems using modern technologies.

The most used analysis method for the processes taking place in a thermal-energetic system is based on energy balance. The purpose of the energy balance is to know the energy flows within the boundaries of the analysed process, in order to find out energy consumptions, useful energy flows and energy losses. By finding out these energy flows, it is possible to set measures to rationalise consumptions or losses, by saving energy for components that allow for proper technical and organizational measures to be applied [1, 2, 3, 4].

Optimization of each technological process is based on a mathematical model that must reproduce the respective process as truthful as possible, the mathematical model is the main element in conducting the process, characterized by two variable values: energy input and output flows [1].

2. Mathematical model description

As the energy balance sets the heat quantities and the technical and economical indexes in detail, it represents the most efficient method to identify ways to save and rationalize the fuel consumption.

The mathematical model of the energy balance for heat treatment furnaces expresses the conservation of energy principle, according to the relation:

$$\sum_{i=1}^{a} Q_{i_i} = \sum_{j=1}^{b} Q_{e_j}$$

(1)

where Q_{i_i} and Q_{e_j} are input, respectively output heat quantities, as related to the framework set for the balance. The heat quantities Q_{i_i} and Q_{e_j} are calculated with relations found in the specialised literature [1, 2, 3, 4, 5], depending on certain parameters.

By applying the mathematical model, using the parameters measured directly on the operational heat treatment furnace, the actual energy balance is obtained.

The technical and organizational measures resulted following the analysis of the actual energy balance lead to energy saving which, deducted from the energy loss components set in the actual balance, set part of the heat quantities of the optimal energy balance. The other components are obtained from the relation (2):

(2)
$$\sum_{k=1}^{c} Q_{i_k}(C_0) + \sum_{l=1}^{a-c} Q_{i_l} = \sum_{m=1}^{d} Q_{em}(C_0) + \sum_{n=1}^{b-d} Q_{e_n}$$

where C_0 is the optimal fuel flow.

The quantification of these measures within the energy balance requires laborious calculations, as not only the characteristics of the furnace, but also the characteristics of thermally treated materials should be considered.

An optimal balance mathematical model for all heat treatment furnaces can be used only if the particularities of each separate furnace are taken into account. This condition is met by the model shown below by using generally valid relations, where certain parameters are found out directly by the model, and the others are found out by each separate furnace by the energetic and technology specialists supervising the respective furnace.

The mathematical model has been designed so as to be used for both continuous and discontinuous running furnaces. Also, the mathematical model takes into account the situations where heat treatment furnaces are provided or not with air-preheating devices, developing both separate balances for the furnace and the recovery device, as well an on the boundary including the furnace and the recovery device together. Based on the data from the measurements performed for the operational furnace and recovery device (if available) and of the other parameters in the calculations, using relation (1), the actual energy balances are developed for the furnace, recovery device and the general balance, setting in detail the input and output heat quantities, the amount of input heat, the amount of output heat and technical and economical indexes, for each separate boundary.

Following the analysis of the actual energy balance, the energetic and technology specialists supervising the respective installation develop an action plan. The measures and actions to save energy are usually proposed in stages, because of financial limits [1].

Following these measures, there are new values resulted for certain characteristic parameters for each installation, which will serve as calculation data for the optimal energy balance, namely:
- excess air coefficients in the burning installation, at furnace exit, at pre-heater entry, at pre-heater exit;
- preheated air temperature;
- preheated material temperature;
- maximum admitted temperature of the burning gases at pre-heater entry;
- number of open holes;
- opening duration for each hole.

On the other hand, in order to develop the optimal energy balance, the mathematic model contains certain generally valid relations; some of them resulted from the following assumptions:

- burning is complete;
- the air flow introduced in the burning installation is equal to the one exited from the air pre-heater and is found out from the equations of complete burning at the imposed excess air coefficient when entering the burning installation.

Based on these assumptions and on the values of the parameters modified following the analysis of the actual energy balance, the optimal fuel flow is found out from a relation type (2), where the temperature of the burned gas at furnace exit is assumed to be equal to the one in the actual energy balance.

The mathematical model has been transposed into an electronic calculation sheet in Microsoft EXCEL and tested for various types of heat treatment furnaces. The development of this model took into account the possibility to be used for a number of types of heat treatment furnaces as large as possible, as well as the adaptation possibility, by small changes, so as their use for other heating furnaces should be possible. The mathematical model presented allows reduction of the necessary time to develop and analyse the energy balances in order to save energy.

An example of using the energy balance calculation program is presented for a heat treatment furnace.

3. Results of the program for developing energy balances for heat treatment furnace

A heat treatment furnace is a continuously running annealing furnace, with roll hearth, for wire coils made of various types of low carbon steels. The entire installation is made of loading table, actual furnace, cooling area and extraction table. All roll transportation systems are operated by chain wheels and roll chains. The wire coils are transported with craned on grids, places on the stationary rolls of the loading table. They pass through the three areas of the furnace, areas with temperatures adjusted according to the provided annealing program. The furnace is heated by radiant tube burners placed above and below the transportation rolls. The exhaust gases are aspirated from each area by the collecting channel passing above the furnace. The burned gas exhaust control is made by the manually handled valves, installed in intermediate channels and a main valve controlled in an automated way by the pressure command. The measurement and adjusting installation has to produce and maintain in an automated way the temperatures adjusted by the reference value, related to the prescribed thermal treatment diagrams. Also, the prescribed report for the natural gas – air mixture is maintained in an automated way. The natural gas pressure is adjusted using the pressure adjusting device.

Between the two doors of the oven, protection gas made of: 6% CO, 6% H_2 and 88% N_2 is introduced.

The heating is made by radiant tube burners with natural gas. The maxim natural gas flow for the furnace is 100 Nm^3/h. The maximum combustion air flow is 1 200 Nm^3/h, and the quantity of the burned gas is about 1300 Nm^3/h. The temperature of the exhausted flue gases is about 600 °C. The automation installation adjusts the furnace temperature and the gas-air ratio in each area of the furnace. The furnace casing is made of a profiled steel framework with metal sheet covering.

An overview of this thermal treatment furnace is shown in fig.1.

Fig. 1 - Overview of a heat treatment furnace.

Fig. 2 - Structure, as a screenshot of the EXCEL program, of the actual energy balance,

for the maximum operation system for the actual heat treatment furnace.

The actual energy balances have been calculated using the mathematical model, based on the measurements performed for the operational heat treatment furnace. Fig.2 shows, as a screenshot of the EXCEL program, the structure of the actual energy balance, for the maximum operation system for an actual thermal treatment oven (without cooling area, as we meant to highlight the effectiveness of the mathematical model use in analysing energy saving measures).

Also, the structure of the actual energy balance for the maximum operation system is shows in fig. 3,in the graphic form developed by EXCEL, and in fig. 4 the actual energy balance for the minimum operation system is shown, where various quantities of heat entered [in % of total heat input] and exited [in % of total heat output] are:

Q1- fuel chemical heat; Q2- fuel sensitive heat; Q3- load physical heat; Q5- total heat introduced by the combustion air; Q7- sensitive heat of the protection gas at the entry; Q10- sensitive heat of the main product at the exit of the actual furnace; Q11- heat lost through walls and hearth; Q13- radiant heat through non-tightened parts; Q14- heat lost at the chimney; Q17- the sensitive heat of the secondary products and auxiliary devices; Q24- sensitive heat of the protection gas at the furnace exit; Qeroare- error when closing the energy balance.
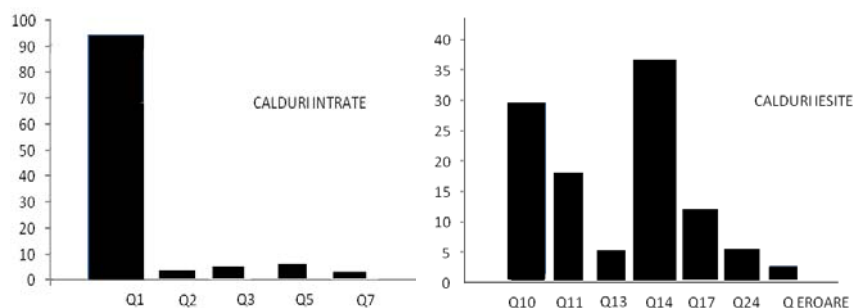
Fig. 3 - Structure of the actual energy balance for the maximum operation system, in the graphic form developed in EXCEL program.

The analysis of the operation of heat treatment furnace leads to the application of certain measures to reduce fuel consumption that we can quantify by mathematical model application.

Therefore, by mathematical model application, under different operation conditions with different excess air coefficients, beginning with the actual situation up to a minimum value of the excess air coefficient obtained with the highest performance radiant tube burners, optimal energy balances are developed, from where specific fuel consumptions shown in fig. 5 result.

Similarly, by introducing a material pre-heater, optimal energy balances are developed for various material pre-heating temperatures, from where specific fuel consumptions shown in fig. 6.
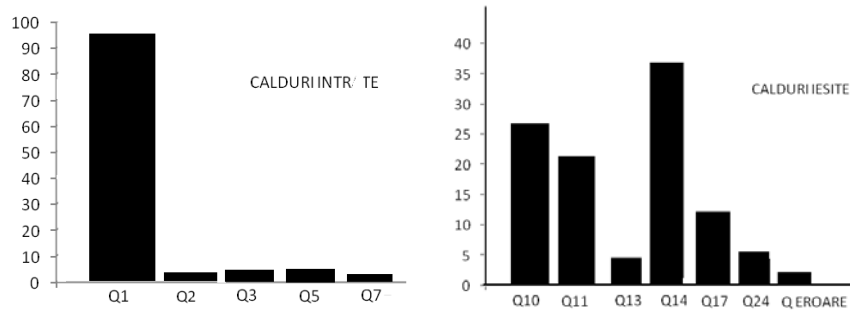
Fig. 4 - Structure of the actual energy balance for the minimum operation system, in the graphic form developed in EXCEL program.
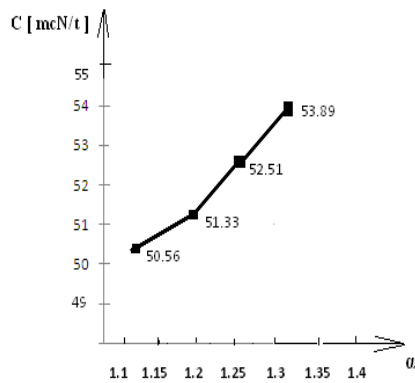
Fig. 5 - Specific fuel consumption , C,depending on the excess air coefficient α.
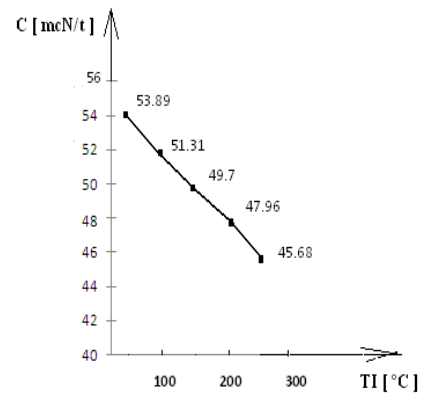
Fig. 6 - Specific fuel consumption ,C, depending on the material pre-heating temperature TI.

4. Conclusion

The mathematical model for calculating actual and optimal energy balances of heat treatment furnaces, used in the metallic materials industry, allows the development of actual energy balances based on data measured during operation and of optimal energy balances, based on measures to reduce fuel consumption. The mathematical model has been transposed into an EXCEL program, in order to automate calculations and applied for various

types of heat treatment furnaces for validation. An application for a continuously running annealing furnace presents actual energy balances, based on the data measured during operation, in maximum and minimum system respectively. Also, by applying the mathematical model under different operation conditions with different excess air coefficients, starting from the actual situation up to a minimum value of the excess air coefficient obtained with the highest performance radiant tube burners, optimal energy balances are developed, from where specific fuel consumptions result.

Similarly, by introducing a material pre-heater, optimal energy balances are developed for various material pre-heating temperatures, from where specific fuel consumptions result.

Therefore the mathematical model usefulness for performing energetic audits for heat treatment furnaces used in metallic materials industry is fully justified.

R E F E R E N C E S

[1]. Gaba, A., Vâlceanu S., Catangiu, A., Paunescu, L., Auditul energetic în metalurgie (Energetic Audit in Metallurgy), Ed.Bibliotheca, Targoviste, 2003.
[2]. Răducanu, C., Pătraşcu, R., Paraschiv, D., Gaba, A., Auditul energetic (Energetic Audit), Ed. AGIR, Bucuresti, 2000.
[3]. Berinde, T. a.a., Întocmirea şi analiza bilanţurilor energetice în industrie (Development and Analysis of Energy Balances in Industry), Ed. Tehnică, Bucuresti, 1976
[4]. Carabulea, A. a.a , Modele de bilanţuri energetice reale şi optime (Actual and Optimal Energy Balances Models), Ed. Academiei, Bucuresti, 1962.
[5]. Carabogdan, I.G. a.a., Bilanţuri energetice. Probleme şi aplicaţii pentru ingineri (Energy Balances. Problems and Applications for Engineers), Ed. Tehnică, Bucuresti, 1986.

MODEL MATEMATIC ŞI PROGRAM DE CALCULATOR PENTRU ELABORAREA BILANŢURILOR ENERGETICE LA CUPTOARELE DE TRATAMENTE TERMICE

(Rezumat)

Lucrarea prezintă modelul matematic de calcul al bilanţurilor energetice reale şi optime ale cuptoarelor de tratamente termice utilizate în industria materialelor metalice.Cuantificarea acestor măsuri în cadrul bilanţului energetic necesită calcule laborioase, ceea ce a condus la transcrierea modelului matematic, într-o foaie

electronică de calcul sub programul Microsoft EXCEL. Cu ajutorul acestui program putem cuantifica efectul fiecărei măsuri în vederea reducerii consumului de energie al cuptorului. O aplicaţie a acestui program de calculator pe un cuptor de tratamente termice se prezintă pentru funcţionarea în condiţii reale, cât şi în condiţiile în care sunt realizate diverse măsuri de optimizare.

STUDY ON THE SIMULATION SOFTWARE OF THE BIOREMEDIATION PROCESS THROUGH BIOPILE TECHNIQUE

BY

ALINA MONICA URS (NEDELCU)[*]**, VALER MICLE and FLORIN POTRA**

Technical University of Cluj-Napoca,
Faculty of Materials and Environmental Engineering

Abstract. In this article preliminary studies for a software design used to control parameters in a bioremediation process are presented. The biopile technique is proposed to achieve bioremediation. This technology has proven effectiveness in the remediation of soils contaminated with hydrocarbons, having lower operating costs and less pollutant than other methods. The parameters considered are: O_2, pH, soil moisture and soil temperature. The high effectiveness requires good knowledge of the changes of parameters during the bioremediation process. The purpose of this research reflects the description of SCADA system used in the design of the software which allows the control of parameters with direct influence on the bioremediation process.

Key words: biopile, bioremediation, automation control system.

1. Introduction

Environmental issues are very important, mainly because of local pollution produced in the sectors of petroleum and mining holdings, in the ore

---

[*] Corresponding author; *e-mail:* Alina.URS@im.utcluj.ro

and the oil processing industries, chemical industry, wood and pulp processing industry, metallurgy, electrical and mechanical engineering, cement industry, transportation and agriculture (Constantinescu, (2008).

Biodegradation has proved to be an adequate technique for the following groups of pollutants: petroleum hydrocarbons, waste oil from petroleum exploitation, sludge and oil residues, waste products and basic organic chemicals, halogenated organic compounds, complex compounds and polycyclic aromatic hydrocarbons, pesticides, nitrates and sulphates, heavy metals (RESOLMET – etapa II 2008).

The aim of the bioremediation process is to achieve optimal conditions and favorable treatment of the hydrocarbons contaminated soil using microbial strains.

2. SCADA System (*Supervisory Control and Data Acquisition*)

SCADA, an acronym for "*Supervisory Control and Data Acquisition*" may be called the Human-Machine Interface (operator interface) through which an operator can monitor and / or control a particular technological process. Also an important function of this system is the continuous acquisition of data, through which can be achieved the effective analysis of the technological process as well the implementation of prediction algorithms through which the development of the process in time may be described.

The SCADA system structure is complex, encompassing from the supervisory system (also called process computer), the communication system, a central host computer server (with role of local data centralizer) to the sensors and field data interface devices required to monitor the technological process. All components which implement SCADA system are very important because they affect the operations of monitoring and control the process, and the data acquisition function of the process.

The technological process is influenced by many variables; therefore these should be monitored and controlled so that they fall within a prescribed range of values, known as technological recipes.

The SCADA systems are generally operated in three types of working conditions. These are:

- Manual operating mode in which commands are given directly to actuators and the process computer only keeps track of the facility parameters;
- Automatic operating mode in which the process computer controls the process based on the technological recipes;
- User operating mode in which the human makes use of sequential logic wired of the conventional automation facilities, working under controlled condition by prescribed reference.

Given the large number of variables needed to be controlled, two solutions are proposed:

• First in which each control loop includes a numeric direct-action controller that communicates with the PC directly on the serial interface;

• Second that uses a programmable logic controller that takes values from sensors and transducers of the process, communicates with the PC, and has implemented control algorithms required for the commands' synthesis of controlled facility.
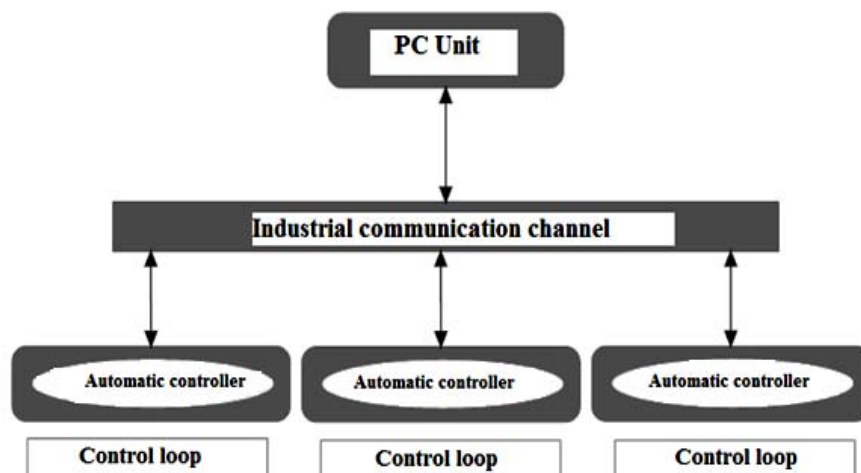

Fig. 1 – The SCADA system with numeric direct-action controllers.
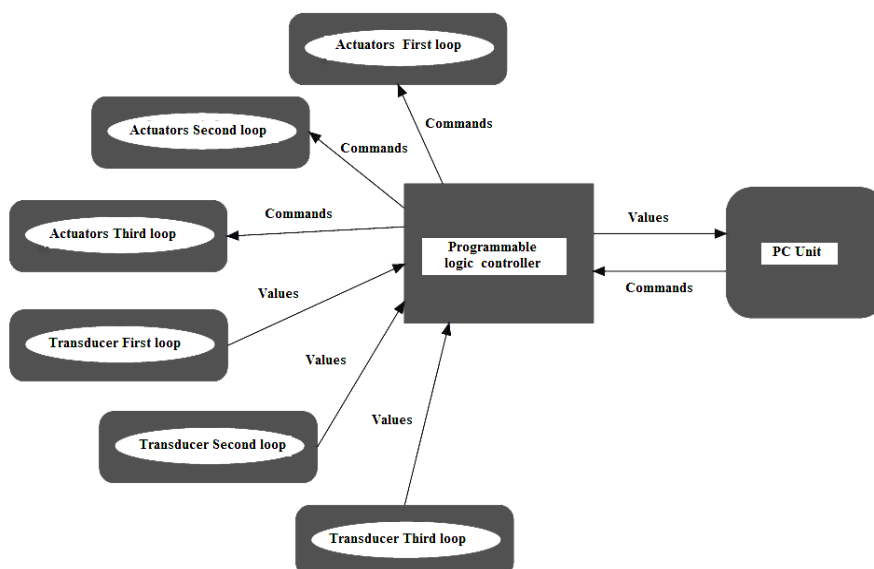
Fig. 2 – The SCADA system with programmable logic controller.

The inclusion of SCADA systems into system configuration has major benefits as flexibility, reliability, safety and high performance.

Data collection and the provision of an interface to control specific equipment are the main functions of SCADA systems.

The main functions of SCADA system that will be implemented for the bioremediation facility are:

- processing signals from sensors and transducers;
- signal filtering;
- generating of the measurements database;
- generating reports of events that occurred at the technological facility;
- post-processing of acquired data;
- the commands' synthesis at the actuators;
- implementation of the control loops;
- communication management;
- generation of the technological networks.

Transducers will be used for the monitoring and control of the facility. The transducers or smart sensors convert electrical and non-electrical signals by transforming the measured signal in a unified electrical signal typically 4-20 mA or 0-10V. Functions will be implemented in the programmable logic controller or PC. These functions transform the signals transmitted by transducers in values that can be retrieved and processed by the programmable logic controller or PC.

3. Control Loops of the Facility

The bioremediation process is influenced by the following parameters: the flow nutrient supply of the soil irrigation system, the level of water in the drainage basin used for the storage of water discharged by the drainage system, the compressor pressure of the ventilation system.

Because this process is continuous and long process, the parameters that maintain the pile unaffected must be monitored constantly as for no damage of the pile taken for analysis to occur. The steady supplies of both air, assured by an aeration system, as well as water, used by the irrigation system, are also needed. Also, the irrigation system should be performed in conjunction with the drainage system to avoid failures which would result in the failure of the bioremediation facility.

The water supply will be performed from a 50 L tank, with a constant flow assured by a metering pump.

The systems of irrigation and aeration affect both the drainage system and the analyzed soil pile. The pile of soil, proposed for analysis, and the dynamic of the drainage system can be rated by the amount of water introduced into the soil and the efficiency of aeration system. Since each variable that determines the quality of the desired pile is influenced by several disturbing

elements, for each parameter a control loop is recommended.

Control loops must be achieved for the automatic control of the following process parameters: flow, temperature and pressure.

The control loop for each parameter is shown in Fig. 3, which has as elements:

- controller;
- actuators;
- technological process;
- measuring element (transducer).

Since the system requirements are very high, the optimal controller is a PID controller. The controller is provided with a function in the programmable logic controller.

Each parameter should be maintained within a certain range of values, because too high variation of those parameters could cause more damage to the finished product or even more damage to the facility. The transfer function of the PID controller is given by the following differential equation:

$$u(t) = K_p \left[e(t) + \frac{1}{T_i} \int_0^t e(t)dt + T_d \frac{de(t)}{dt} \right] \qquad (1)$$

where: u (t) – the controller output

e (t) – tracking error

K_p – proportional coefficient

T_i – integer time constant

T_d – derivative time constant
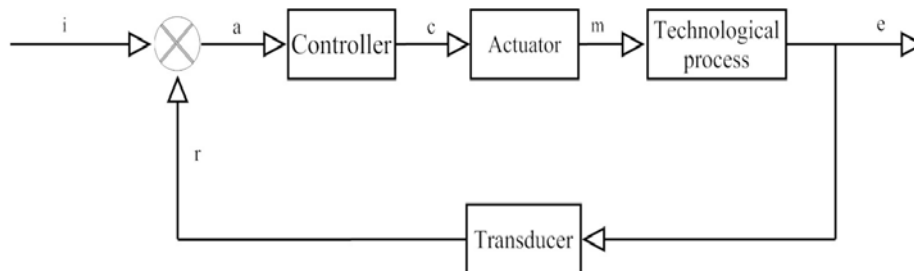

Fig. 3 – The control loop of each parameter; i – Input; a – error;
c – control input; m – output regulator; e – output.

The automation system of the biopile bioremediation process consists of three subsystems:

- ***The irrigation subsystem*** will provide the irrigation of soil with clean water or water laden with different bacteria, at a certain temperature depending on

soil characteristics. This subsystem will be used for further analysis.

• ***The drainage subsystem*** will provide the soil drainage by collecting the effluence in the drainage basin. This subsystem is closely related to the irrigation subsystem, as the proper functioning of the facility to not be damaged.

• ***The aeration subsystem*** will provide the continuous or delayed aeration of the pile of soil depending on the analysis carried out later. This subsystem is freestanding being independent of the other two subsystems. To maintain a constant temperature of the water, circulated through the irrigation subsystem, two temperature transducers, that provide a voltage signal proportional to temperature, will be used. The circulated water temperature will be measured at two points: the water basin and the ambient environment. The sensors are:

• T-type thermocouple, for the water basin;
• LM35, for the ambient environment.

In the water basin is also introduced a level transducers to detect at any time if the water in the basin drops to a critical level. If this drop level is notified, the water supply of the basin is controlled through a controlled charging valve. This terminal transducer is very useful because with its help the water level is constantly maintained in the basin. This is extremely necessary in this lengthy ongoing process which runs at the desired temperature depending on the type of analysis performed. The water is circulated through the irrigation subsystem by a centrifugal pump with a maximum flow of 10 L/min.

Based on the data taken from the temperature transducers, the programmable logic controller via the software implemented in it, is able to send commands to the actuators. The programmable logic controller determines which actuators should be controlled so that the circulated water temperature remains constant. In this case the following elements are operated:

• thermally sensitive resistance element, if the circulated water must be heated;
• the controlled charging valve available in the water-supply network (5-15ºC), if the circulated water must be cooled;
• the controlled charging valve available in the water-supply network (5 – 15ºC), if the water level in the basin is below 90 % of rated capacity.

The programmable logic controller controls the water supply of the basin by a controlled charging valve, with the help of the level sensor placed in the drainage basin of the drainage subsystem. A mismatch between the two sensors could cause malfunction of the entire automation system.

The adequate aeration of soil is obtained by air flows between 0.93 and 12.28 m^3/min and pressures between 5.5 and 15 bars performed by the aeration subsystem. Depending on the time that soil aeration is expected, the programmable logic controller will send commands to actuators in order to effectuate their tasks.

Table 1

Input Sensors

Cur. no.	Measured signal	The domain of the signal measured by PLC	Sensor	Sensor type	Characteristics
I1	Temperature of the cold water	0-5V	integrated	LM35	Linear transmittance 10mV/C, domain of measure -55-+150C, accuracy 0,5C
I2	Irrigation water tank level	discrete contact	Liquid Level Float switches	a-07188-90 Cole-Parmer	domain of measure -23-105C, assemblage 3/8", 24Vdc
I3	Water tank temperature	80mV	thermocouple	R(or T)	accuracy 0,1C , domain of measure -200+100C
I4	Collected water tank level	discrete contact	Liquid Level Float switches	a-07188-90 Cole-Parmer	domain of measure -23-105C, assemblage 3/8", 24Vdc
l5	Ambient temperature	0-5V	integrated	LM36	

Table 2

Actuators

Cur. no.	Controlled signal / part of the facility	Output type from PLC	Actuator	Type	Characteristics
E1	Coolant of the irrigation water basin	contact	Electromagnetic valve	solenoid	24Vca, 10W, operating range 0-52C
E2	Temperature of the irrigation water basin	contact	Thermally sensitive resistance element	immersion	500W, 24Vca, isolated
E3	Irrigation water basin level	contact	Electromagnetic valve	solenoid	24Vca, 10W, operating range 0-52C
E4	Water irrigation circuit	contact	Pump	centrifugal	maximum 10l/minute, 24Vca
E5	Water drainage basin level	contact	Electromagnetic valve	solenoid	24Vca, 10W, operating range 0-52C
E6	Compressor command	contact	Electromagnetic valve	solenoid	24Vca, 10W, operating range 0-52C

The programmable logic controller is the basic element that continuously checks the data received from the facility transducers. Based on these elements the programmable logic controller establishes priorities and

operational parameters (modulation time) of the actuators. The programmable logic controller performs the auto-test operation besides taking the signal of the transducers and establishing of commands for the actuators. Through this operation it can be determined whether the measuring and control components of the facility are working properly. The auto-test of the facility is initialized at start-up.

   The automation diagram of the bioremediation facility and the location of measuring and control elements are presented in Fig. 5. The details of the input sensors and the actuators are presented in Table 1 and Table 2.
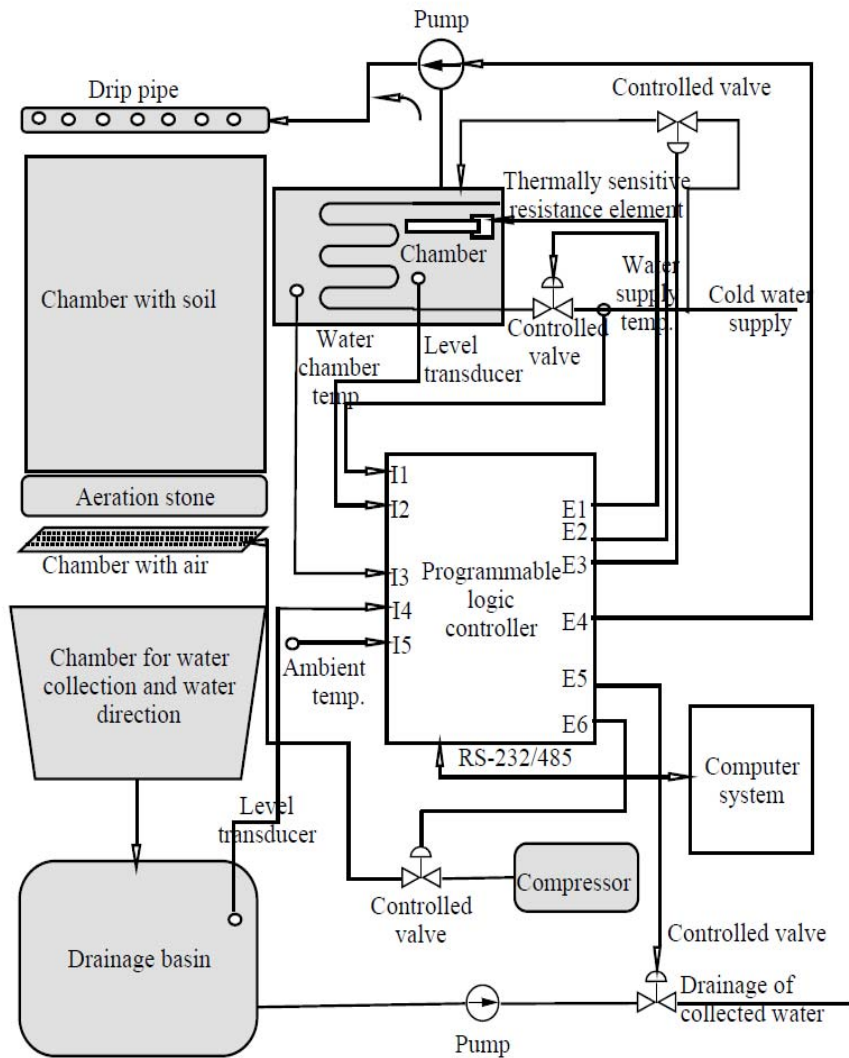

Fig. 4 – Automation diagram.

4. Conclusion

This paper present the solutions currently available, their advantages and disadvantages in designing the software used to simulate the bioremediation process through biopile technique. The monitoring and controlling of the facility is performed by SCADA system (Supervisory Control and Data Acquisition). This system allows continuous monitoring and control of both the parameters tracked by the facility, and its functional parameters. The system allows the permanent access of the users to the parameters, the intervention in case of malfunctions and to obtain relevant statistical data for further studies.

Future research will include a software application of cost estimation, which will allow the configuration of the facility components through update operations (add / edit / delete). This application will be useful to achieve a calculation of cost estimation for facilities of any scale.

REFERENCES

* * Raport ştinţific şi tehnic al proiectului, *Tehnologie inovativă de remediere a solurilor contaminate prin activităţile specifice industriei metalurgice – acronim RESOLMET* – etapa II 2008.

Constantinescu L., *Soil Pollution With Heavy Metals In Critical Areas*. Bulletin UASVM, Agriculture Series, **65**, *2*, 2008.

Ilaş C., Priboiana M., *Teoria sistemelor de reglare automată*. Îndrumător de laborator, Ed. Matrix Rom, Bucureşti, 2004.

Kodres C.A., *Coupled Water and Air Flows Through a Bioremediation Soil Pile*. Naval Facilities Engineering Service Center, Port Hueneme, USA, 1998.

STUDIU PRIVIND REALIZAREA UNUI SOFT PENTRU SIMULAREA PROCESULUI DE BIOREMEDIERE PRIN METODA BIOPILE

(Rezumat)

În acest articol se prezintă studii preliminare pentru realizarea unui soft utilizat pentru controlul parametrilor într-un proces de bioremediere. Se propune metoda „Biopile" pentru realizarea bioremedierii. Această tehnologie s-a dovedit eficientă în procesul de depoluare a solurilor contaminate cu hidrocarburi, înregistrând costuri de

funcţionare şi depoluare mai mici faţă de alte metode. Parametrii luaţi în considerare sunt: O_2, pH, umididate şi temperatura solului. Obţinerea unui randament ridicat necesită cunoaşterea variaţiei parametrilor în timpul procesului de bioremediere. Finalitatea cercetării reflectă crearea unui soft prin care se permite controlul parametrilor cu influenţă directă asupra procesului de bioremediere.

THE CHARACTERIZATION (SURFACE ANALYSIS, NANOINDENTATION, TRIBOLOGY) OF SOME MAGNETRON-SPUTTERED TUNGSTEN CARBIDE COATINGS DEPOSITED ON A LOW CARBON ALLOY STEEL

BY

**MIHAI-IONEL URSU[1]*, CRISTIAN-FLORIAN IONESCU[2]
and CONSTANTIN DUMITRU[3]**

[1]"Gheorghe Asachi" Technical University of Iaşi,
[2]University of Piteşti,
[3]SC Automobile DACIA SA of Piteşti

Abstract. The goal of this paper is to present aspects concerning the surface analysis (profilometry and SEM), the mechanical (hardness and elastic modulus) and tribological (friction, wear) behaviour of some tungsten carbide coatings, deposited by magnetron sputtering on a low carbon alloy steel (previously thermochemically treated). The surface analysis was done using a Mitutoyo SJ401 Profilometer and a FEI Scanning Electron Microscope with EDX. The nanoindentation and tribological tests were performed using a CSM Instruments type Nanoindenter, respective a Ball-on-disk tribometer and a Profilometer Surtonic S25 (Taylor Hobson). The results of the profilometer analysis revealed an improvement of the roughness state (0.36 → 0.30 microns), while the SEM analysis was done to investigate the surface before and after the tribological tests. The nanoindentation and the tribological tests showed a much better behaviour of the coated sample (higher hardness and better wear) compared with the characteristics of the un-coated (thermochemically treated) sample.

---

* Corresponding author; *e-mail:* mihai-ionel.ursu@daciagroup.com

1. Introduction

Over many decades, a large amount of research has been given over to the study of different solutions / equipments destined to the coatings characteristics measurements. This has been driven by the importance of mechanical devices (presenting coatings) within the modern era. A reliable observable technological trend is toward the miniaturization and, therefore, many discussions have been held among scientists, technologists and non-specialists, about the possibility to produce mechanical devices with dimensions measured at the micro/nano-scale, and the term 'nanotechnology' has evolved to encompass a whole range of research focused in this general area (Cao, 2004). But, there is still a limited relevance to the use of macro-scale testing for predicting nano-scale behaviour (Achanta *et al.,* 2005).

The purpose of this work is to investigate the behavior of the surface using the profilometer and the scanning electron microscopy analysis, the mechanical (hardness and elastic modulus) behaviour using an equipment with high precision, a nanoindenter, capable of achieving indentation to order of nano or micro, and tribological (friction, wear) behaviour of some tungsten carbide coatings, deposited by magnetron sputtering on a low carbon alloy steel.

2. Surface Analysis

2.1. Roughness Analysis (Profilometry)

The roughness test was done taking into account that this characteristic of the deposited layers has a big influence over the friction and wear behaviour. For this test, a profilometer Mitutoyo SJ400 - type, with a regular-conic tip, was used. The testing conditions were:

Standard	ISO 1997	Evaluation length	7.0mm
Profile	R	Cut-Off	2.5mm
Range	800um	Filter	GAUSS

The environmental conditions were: Temperature $24 \pm 3°C$; Humidity 18 ± 2 %. For each sample, more measurements (five) of the surface roughness, on different areas, were realized.

The measurements revealed that the average roughness value of the uncoated sample (before deposition) was $Ra=0.36\mu m$.

After deposition, even if the thickness of the layer is lower than 10 microns, and in this way it follows the shape of the substrate, an improvement

(meaning roughness reduction) was observed. The results of the tests show an average roughness of the coated sample Ra=0.30μm.

a   *b*
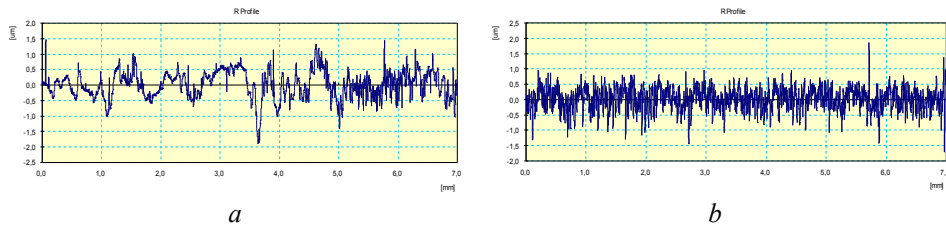
Fig. 1 – The surface of the sample before (*a*) and after (*b*) deposition.

2. 2. SEM EDX Analysis

The SEM analysis was done in order to investigate the surface of the coated sample before and after the tribological tests. The tests were realized at a magnification of 3000x, using both the secondary electron microscope, for analyzing the surface (morphology), and the EDX technique for mapping the surface elements.
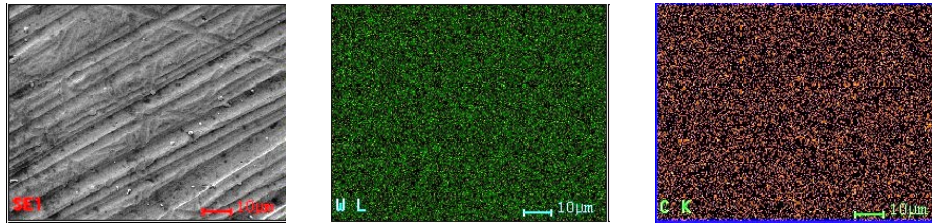
Fig. 2 – The Morphology and EDX analysis before tribological tests.
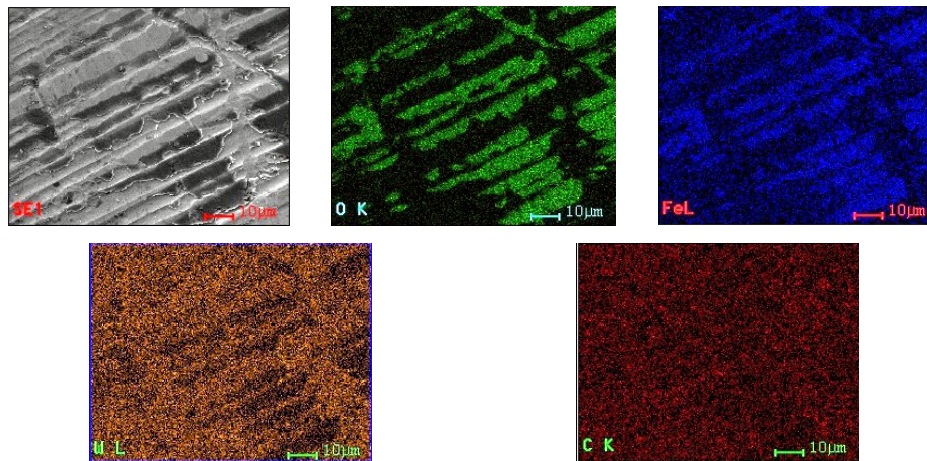
Fig. 3 – The Morphology and EDX analysis after tribological tests.

The morphology of the coated sample surface shows the same in both cases, before and after the tribological tests.

An EDX analysis was realized, using the mapping function to check the distributions of the elements on the analyzed surface. In the case of the sample analyzed before the tribological tests, a concentration of tungsten and carbon was determined, confirming the composition of the coating. But, in case of the sample analyzed after the tribological tests, it is interesting to observe that, on the wear track caused by the tests, there have been detected some traces of the elements (iron oxide) of the ball used for the wear tests. This proves that the material of the ball was removed / deployed, probably because of the high hardness of the coating.

3. The Mechanical and Tribological Characteristics

3.1. The Mechanical Characteristics - Nanoindentation Tests

The Nanoindentation tests were performed using a CSM Instruments Nanoindenter (Micro-Combi Tester + NHT with Berkovich diamond tip). The testing conditions were: Load → 263 mN; Max. penetration depth → 804 nm; Frequency of data acquisition → 5 Hz; The method of data calculation → Oliver & Pharr; Environmental conditions → Temperature 22 ± 3ºC, Humidity 18 ± 2 %.

Five indentations were done for one sample. The results of the tests are presented in Table 1.

Table 1
Results of the Nanoindentation Tests

Indenta tion no.	$F_{max.}$* [mN]	$h_{max.}$* [nm]	HV * [kgf/mm^2]	E_r* [GPa]	$HV_{med.}$* [kgf/mm^2]	$E_{r\ med.}$* [GPa]
1	223,23	802,91	2281,17	257,96		
2	223,47	803,70	2268,71	259,59		
3	233,10	801,88	2460,05	261,88	**2550,20**	**264,04**
4	262,81	801,08	2952,61	277,85		
5	247,92	801,53	2788,45	262,92		

where: * Fmax. = Maximum load [mN]; hmax. = Maximum penetration depth [nm]; HV = Vickers hardness [kgf/mm^2]; Er = Young's modulus [GPa], HVmed. = Medium hardness [kgf/mm2], Er med. = Medium Young's modulus [GPa]

The nanoindentation test revealed that the hardness of the tungsten carbide coated sample (1550,20 HV) is much higher than the one of the un-coated, thermochemically treated sample (~ 800 HV).
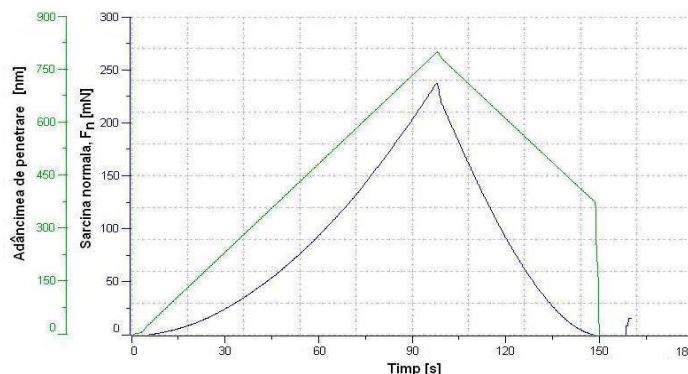
Fig. 4 – The variation of the penetration depth and of the normal load,
as a function of the time – tungsten carbide coated sample.

This high hardness value of the tungsten carbide coated sample is corroborated with relatively high value of the Young's modulus (264,04).

3.2. The Tribological Characteristics

The Testing Equipment was a Ball-on-disk tribometer with rotative module (CSM Instruments) and a Profilometer Surtonic S25 (Taylor Hobson) with standard tip.

The Testing conditions were: Normal load → 10 N; Linear speed → 0,5 cm/s; Radius → 8 mm; Frequency of a rotation → 6 rot / min.; Duration / Distance covered / no. of testing cycles → 1 h / 18,2 m / 362 cycles; Frequency of data acquisition → 5 Hz; Static partner → 100Cr6 steel ball, 6 mm diameter; Environmental conditions → Temperature 22 ± 3ºC, Humidity 18 ± 2 %.

The results of the tests are presented in table 2:

Table 2
Results of the Tribological Test

Sample	Medium friction coeff. med	Maximum friction coeff. max	Wear rate [mm^3/N·m]	Wear track
After coating	**0,587**	0,725	**144,5 x 10^{-6}**	
Before coating	**0,767**	0,865	**247,1 x 10^{-6}**	

The tribological test revealed that the coated sample presents better wear and friction behaviour compared with the un-coated sample. It is interesting to remark that the coated sample exhibits a much better wear behaviour than the un-coated, thermochemically treated sample.

Fig. 5 – The variation of the friction coefficient and penetration depth, as a function of the duration, distance and testing cycles number – sample before coating.
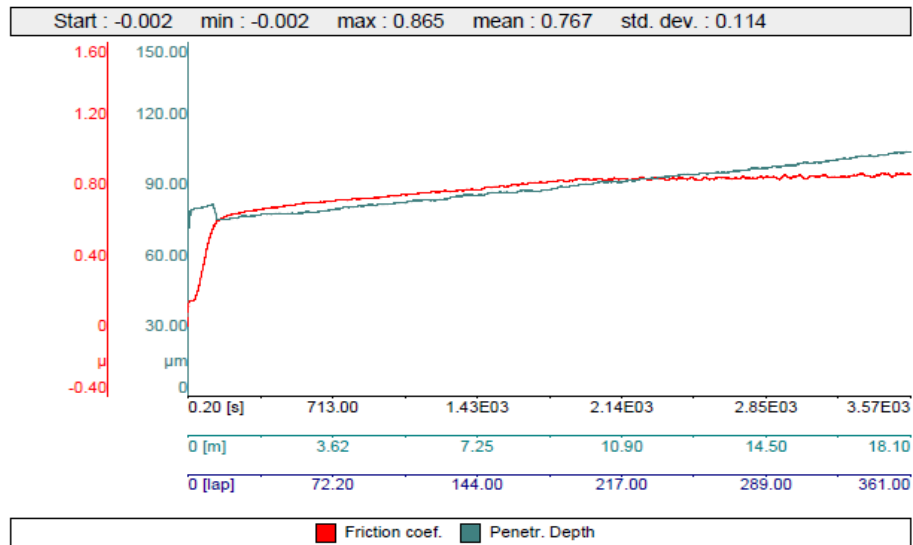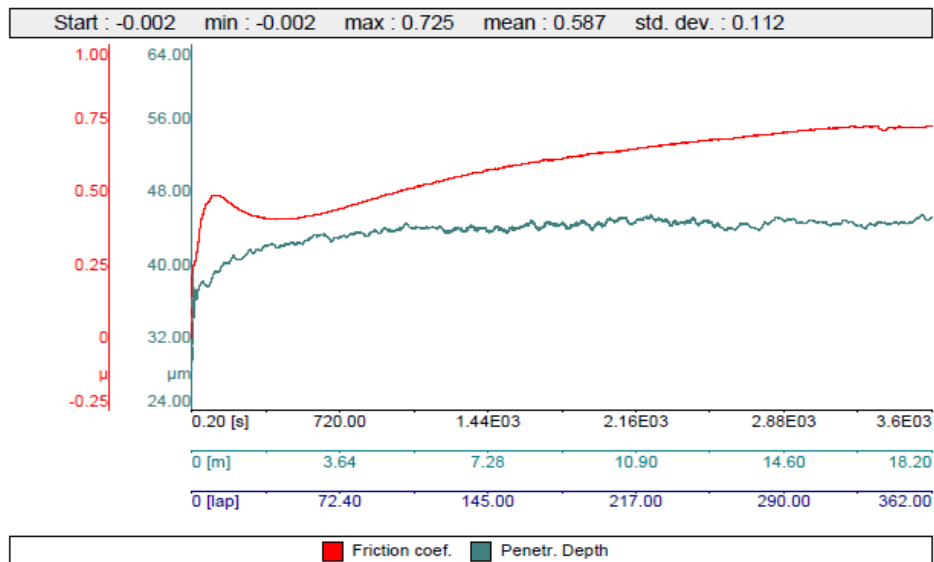

Fig. 6 – The variation of the friction coefficient and penetration depth, as a function of the duration, distance and testing cycles number – tungsten carbide coated sample.

3. Conclusion

This paper investigated the surface characteristics (profilometry and SEM), mechanical and tribological behavior of some magnetron sputtered tungsten carbide coatings, deposited on low-carbon alloy steel (previously thermochemically treated).

After deposition an improvement (meaning roughness reduction) was observed, from Ra=0.36μm to Ra=0.30μm, decreasing in this way the friction coefficient.

The morphology of the coated sample surface shows the same in both cases, before and after the tribological tests. Following the EDX analyses was detected some traces of the elements of the ball used for the wear test, this show a superior hardness of the coating.

Analyzing both the nanoindentation and tribological results, it can be noticed that the tungsten carbide coated sample presents better characteristics than the un-coated (only thermochemically treated) sample, associating a lower friction coefficient with good wear behaviour and high values of the hardness (2550 HV, compared with ~800 HV – the sample in thermochemical treatment state) and elastic modulus (264 GPa).

REFERENCES

Cao G., *Nanostructures and Nanomaterials*. Hackensack: World Scientific Publishing Company Inc., 2004.

Achanta S., Drees D., Celis J.-P., *Friction and Nanowear of Hard Coatings in Reciprocating Sliding at Milli-Newtons Loads*. Wear 2005; 259:719–29.

CARACTERIZAREA (ANALIZA SUPRAFEŢEI, NANOINDENTAŢIE, TRIBOLOGIE) UNOR STRATURI DE CARBURI DE WOLFRAM PULVERIZATE CU MAGNETRON, DEPUSE PE UN OŢEL SLAB ALIAT

(Rezumat)

Scopul acestei lucrări este prezentarea unor aspecte în ceea ce priveşte analiza suprafeţei (profilometrie şi SEM), proprietăţilor mecanice (duritate şi modulul de elasticitate) şi tribologice (frecare şi uzură) a unor straturi de carbură de titan, depuse prin pulverizare cu magnetron pe un oţel slab aliat (tratat termochimic anterior).

Analiza suprafeţei a fost realizată cu profilometrul Mitutoyo SJ401 şi microscopul electronic cu scanare de electroni cu EDX. Nanonidentarea şi testele tribologice s-au realizat utilizând instrumentul „CSM Instruments type Nanoindenter" respectiv tribometrul cu bilă pe disc „Profilometer Surtonic S25 (Taylor Hobson)". Rezultatele obţinute la analizele pe profilometru au arătat o îmbunătăţire a rugozităţii (0,36→0,30 microni) iar analiza SEM a fost utilizată pentru investigarea suprafeţei înainte şi după testele tribologice. Nanoindentarea şi testele tribologice au arătat o mult mai bună comportare a stratului depus (duritate mai mare şi rezistenţă la uzură mai bună), comparativ cu proprietăţilor epruvetelor neacoperite (tratate termochimic).

INFLUENCE OF THE TITANIUM DIBORIDE ON THE PROPERTIES OF Al/TiB$_2$ IN SITU COMPOSITES

BY

EMILIA-MARIA UŞURELU[*], **MIHAI BUŢU** and **PETRU MOLDOVAN**

University "Politehnica" Bucharest

Abstract. The aim of this paper is to present the mechanical properties of in-situ Al/TiB$_2$ metal matrix composites variation. Mechanical properties in terms of ultimate strength, yield strength, elasticity module, hardness and microhardness have been improved by composite containing 2.5, 5 and 7.5 wt.% TiB$_2$. The in-situ formed TiB$_2$ particles are very fine – nanometers and micrometer order – and thermodynamically more stable than other particles from the Al-Ti-B system. TiB$_2$ particle size and quantity from the aluminum alloy matrix leads to a meant variation of mechanical properties of composites obtained.

Key words: mechanical properties, in situ composites, titanium diboride.

1. Introduction

In-situ fabrication of metal matrix composite is a process, in which reinforcing phase is formed in the matrix as a result of precipitation from the melt during its cooling and solidification. Dispersed phases of in-situ metal matrix composite may consist of borides, carbides or intermetallic compounds, and ensuring a strong connection at the interface between particles and matrix. The interfaces matrix/reinforcement material thus obtained are much more stable and content of impurities is reduced to the maximum. In the last years

---

[*] Corresponding author; *e-mail:*

have been realized an important number of researches concerning the processing of Al/TiB$_2$ composite materials through in-situ methods.

TiB$_2$ particles obtained from the reaction of KBF$_4$, K$_2$TiF$_6$ and liquid aluminum alloy can have nanometer or micrometer dimensions depending on the duration of maintaining the melt at temperature at which the forming reaction of borides occurs. TiB$_2$ particle size and quantity from the aluminum alloy matrix leads to a meant variation of mechanical properties of composites. (Moldovan, 2008; Wood *et al.*, 1993; Kumar *et al.*, 2009; Fjellstedt & Jarfors, 2005a; Dezhi Zhu *et al.*, 2007; Fjellstedt & Jarfors, 2005b; Daniel *et al.*, 1997; Uşurelu *et al.*, 2010; Tjong & Ma, 2000).

The objective of this paper is to presents the properties variation of Al/TiB$_2$ composites depending on the content of nanometer and micrometer particles of titanium diboride in the base matrix. Depending on the amount of salts used for the reaction, also the reaction time, composites obtained are different compositions, different physical and mechanical properties.

2. Methods and Results

In the process proposed in this paper, TiB$_2$ particles result by aluminothermique reduction of hexafluorotitanate (K$_2$TiF$_6$) and of tetrafluoroborate (KBF$_4$) with liquid aluminium:

$$3K_2TiF_6 + 6KBF_4 + 10Al = 3TiB_2 + 12KF + 10AlF_3 \qquad (1)$$
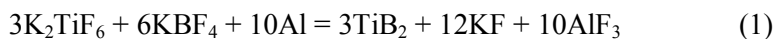
To determine the reaction time and quantity of newly created stage influence on the evolution of mechanical properties, the experiments were produced composite containing 2.5%, 5% and 7.5% by weight of TiB$_2$ particles.

Mechanical properties in terms of ultimate strength, yield strength, elasticity module, hardness and microhardness have been improved with increasing of TiB$_2$ amount.

Fig. 1 shows the SEM micrografs of the Al/TiB$_2$ composites and Fig. 2 shows percent of TiB$_2$ particles obtained in the Al/TiB$_2$ in situ composites.
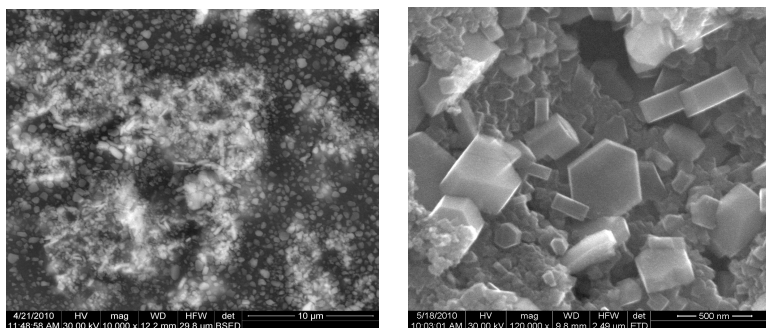
Fig. 1 – SEM micrographs of the Al/TiB$_2$ composites.
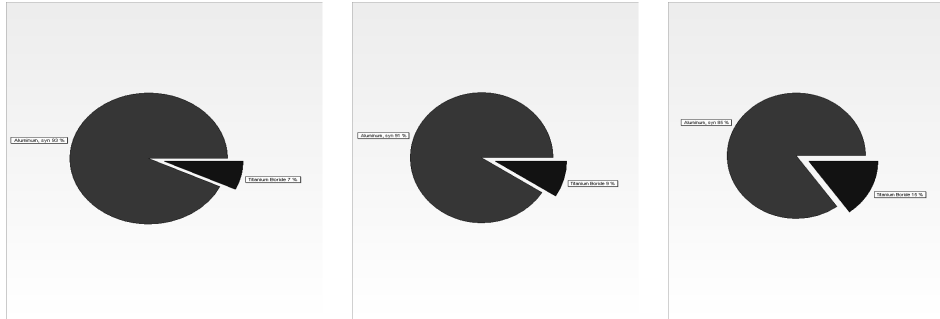
Fig. 2 – Percentage of TiB_2 particles obtained in the Al/TiB_2 in situ composites.

Fig. 3 shows an X-ray diffraction (XRD) pattern of the Al/TiB_2 composite. The pattern reveals the presence of aluminum and TiB_2 peaks, indicating that TiB_2 particles are formed in the composite, only.
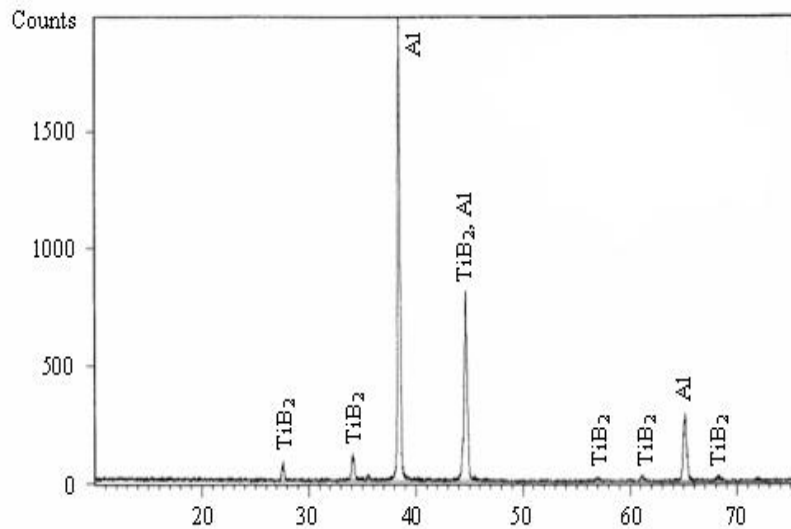
Fig. 3 – XRD pattern of Al/TiB_2 in-situ composite.

For the Al/TiB_2 composite specimens were tested to determine mechanical properties. Thus were determined breaking strength, yield strength, elasticity module, hardness and microhardness of the material.

Table 1 presents the mechanical properties values for the samples development, and Fig. 4 presents the evolution of mechanical properties vs TiB_2 percent.

B0-aluminum alloy; B1-in situ composite-2.5% TiB2, 60 min reaction time; B2-in situ composite-5%TiB2, 60 min reaction time; B3-7.5% TiB2, 60 min reaction time;B32-7.5% TiB2, 90 min reaction time; B33-7.5% TiB2, 1200 min reaction time.

Table 1

Mechanical Characteristics for the Samples

		σ_r MPa	σ_c MPa	E GPa
Alloy sample	B0	89,6	48,3	68,9
Experimental samples of composites	B1	95,99	33,21	27,7
	B2	78,34	25,88	22,24
	B3	90,11	42,39	27,38
	B32	146,6	55,39	30,07
	B33	61,63	36,08	27,04
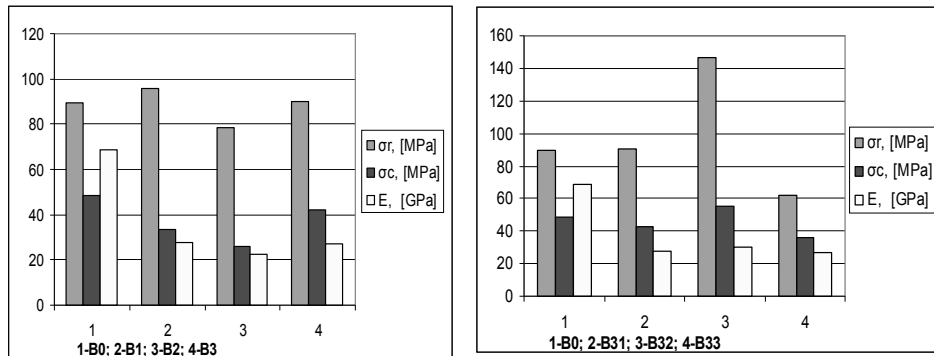
Fig. 4 – Mechanical properties vs TiB$_2$ percent.

Table 2 presents the hardness (HB) and microhardness (HV) values for the samples.

Table 2

Hardness (HB) and Microhardness (HV) Values for the Samples

Sample	B0	B1	B2	B31	B32	B33
Brinell hardness, HB	45	45.6	51.3	64.7	95	66.5
Vickers microhardness, HV	48	47	77.8	67.7	106	70.9

3. Discussions and Conclusions

From the results obtained, the following may be concluded:

Experimental research revealed an important influence of TiB$_2$ particle amount on the mechanical properties of aluminum alloy/TiB$_2$ in situ composites.

TiB$_2$ particles are hexagonal with average size between 1 and 1.20 m.

TiB$_2$ particle percentage have an important influence on the mechanical properties of Al/TiB$_2$ composites, with direct influence on the hardness, mechanical strength and elasticity module of composites obtained by in-situ. TiB$_2$ particles are situated at the grain boundary or in interdendritic regions.

REFERENCES

Daniel B.S.S., Murthy V.S.R., Murty G.S., *Metal – Ceramic Composites Via in Situ Methods*. Journal of Materials Processing Technologz, *68*, 132 – 155 (1997).

Dezhi Zhu, Gaohui Wu, Longtao Jiang şi Guoqin Chen, *Microstructures and Dynamic Compression Properties of a High Reinforcement Content TiB2/Al Composite*. Materials Science Forum, **546-549**, 639-642 (2007).

Fjellstedt J., Jarfors A.E.W., *Materials Science and Engineering*. **A413-414**, 527 (2005a).

Fjellstedt J., Jarfors A.E.W., *On the Precipitation of TiB$_2$ in Aluminum Melts from the Reaction with KBF$_4$ and K$_2$TiF$_6$*, ELSEVIER. Materials Science and Engineering, **A 413-414**, 527-532 (2005b).

Kumar S., Subramanya Sarma V., Murty B.S., *Metallurgical and Materials Transaction A*, **40A**, 223 (2009).

Moldovan P., *Compozite cu matrice metalică*. Editura Printech, Bucureşti, 2008.

Tjong S.C., Ma Z.Y., Mater. Sci. Eng., **A 29**, 49-113 (2000).

Uşurelu E., Buţu M., Moldovan P., Hadăr A., Cojocaru D., *Influence of TiB$_2$ Nano and Microparticles Obtained in Situ on the Mechanical Properties of Composite Materials*. 4th International Conference "Biomaterials, Tissue Engineering & Medical Devices" BiomMedD'2010, 238.

Wood J.V., Davies P., Kellic J.L.F., *Properties of Reactively Cast Aluminum – TiB2 Alloys*. Mater.Sci.technol., *9*, 833-840 (1993).

INFLUENŢA DIBORURII DE TITAN ASUPRA PROPRIETĂŢILOR
COMPOZITELOR IN SITU AL/TiB$_2$

(Rezumat)

Scopul acestei lucrări este de a prezenta variaţia proprietăţilor mecanice ale compozitelor in-situ cu matrice metalică Al/TiB$_2$. Proprietăţi mecanice din punct de vedere al rezistenţei la rupere, rezistenţei la tracţiune, modulul de elasticitate, duritate şi

microduritate au fost puse în evidenţă în materiale compozite care conţin 2,5%, 5% şi 7,5% procente TiB_2. Particulele TiB_2 formate in situ sunt foarte fine – de ordinul nano şi micro - şi termodinamic mult mai stabile decât alte particule din sistemul Al-Ti-B. Dimensiunile particulelor TiB_2 din aliajul de aluminiu matrice conduce la o variaţie semnificativă a proprietăţilor mecanice ale compozitelor obţinute.

SOFTWARE FOR THE OCCUPATIONAL HEALTH AND SAFETY INTEGRATED MANAGEMENT SYSTEM

BY

GABRIEL VASILESCU[1], VALERIU PLEŞEA[2], ANGELICA DRĂGHICI[1], MARIUS-EREMIA VLAICU-POPA[3], RADU TOMA[4] and CONSTANTIN BACIU[5]*

[1] INSEMEX Petroşani,
[2] SC ICPM S, Petroşani,
[3] Constantin Brancusi University of Tg. Jiu,
[4] Roşia Montană, Gold Corporation (România),
[5] "Gheorghe Asachi" Technical University of Iaşi

Abstract. This paper intends to present the design and the production of a software for the Occupational Health and Safety Integrated Management System with the view to a rapid drawing up of the system documents in the field of occupational health and safety. This software has been produced in compliance with the provisions stated by NUCLEU program, Project no. PN-07-45-01-03.

Key words: occupational safety, complex system, software, OHSAS standard.

1. Introduction

History has shown that a correct implementation and maintenance of a Occupational Health and Safety Integrated Management System can bring about several benefits both to the employers and tot o employees (Program NUCLEU, Faza V/2009):

− an easier way for an organized evaluation of risks, hazards and incidents;

---

* Corresponding author; *e-mail:* cbaciu@tuiasi.ro

  − a better awareness of hazards and of risks;
  − improving the transparency of internal processes;
  − improving communication among employees;
  − improving the motivation and identification of the employees with the intrests of the undertaking where they work;
  − a suitably integrated approach of the working environment;
  − a better quantisizing of the OHSAS.

In order to provide a good implementation of the Occupational Health and Safety Integrated Management System, a software specific for diagnosis of occupational safety could prove its usefulness; there have taken into consideration the notice on the implementation guide for the model of the Occupational Health and Safety Integrated Management System and the tools used for auditing this type of system with the view to drawing up the system documents in compliance with the principles and practices used by the quality system.

Consequently, there had been drawn up 15 system documents (checklist with the management requirements in the field of OHSAS, a handbook for the management of OHSAS and 13 system procedures); these documents were transposed into an expert software that can provide certain major benefits derived from the facilities determined by the use of professional computers: high capability for the storage of information, rapid search of information, high data, processing speed etc.

2. Theoretical and Practical Approach of the Occupational Health and Safety Integrated Management System

An integrated management system represents a logic and organized managing − type approach; it allows to take the best possible operating and strategic decision that takes into consideration all the essential aspects that lead to an efficient operation of an undertaking, both from a qualitative point of view and from the point of the surrounding environment, or of food safety and hygiene (Cotigă *et al.,* 2009) etc.

The integrated management systems display several advantages:
  − they provide a higher coherence;
  − they provide an optimization of operations;
  − they provide a diminuation of overlaps and of dissipation of responsibilities;
  − the common requirments are being fulfilled in an efficient manner;
  − a joint approach of the future development with the diminuation of costs related to the certification process.

An integrated management system is made of at least two different management systems:

− OMS+EMS (quality management system + environment management system);

− OMS+OHSAS (quality management system + occupational health and safety management system);

− OMS+EMS+OHSAS (quality management system + environment management system + occupational health and safety management system).

An advanced management system shall have to have a modular structure so as to allow the entrance of new elements into the current system.

OHSAS covers a set of elements bearing a decision like, organizational, information and motivator character within the undertaking; it is being used for the implementation of the processes and relations inside the occupational health and safety integrated management system with the view to getting the required occupational health and safety level.

The implementation of an OHSAS in accordance, with SR OHSAS 18001:2008 provides several advantages that strengthen the idea that the economic agents:

− shall observe the legal and regulating requirments;

− shall possess an OHSAS at a very high standard, included in the general management of the company.

Consequently, the following aspects shall have to be settled for a suitable development of the activities at the level of the national economy (Vasilescu, 2008; Simion *et al.,* 2004; Toma, 2009):

− accident risks;

− manner used to diminish the occupational diseases as much as possible;

− manner used to measure, monitor and evaluate the implementation of the OHSAS.

An improved occupational health and safety shall cover:

− a well planned and well-documented approach of the issues related to the OHS;

− procedures related to OHS that define the areas of responsability;

− a familiarization with the issues related to the OHS and a stable social climate favorable to high performances in the undertaking;

− issues related to the improvement of the OHSAS with quantized results;

− a diminuation of risks related to occupational diseases and accidents;

− inspections and operations bearing a preventive type charcter;

− exercises and practical operations that have proven their efficiency in emergency situations;

− analyses audits and recordings of the OHS management;

− a periodical evaluation regarding the application of the legal and regulating requirements that also provides a diminuation of probability for the

payment of legal and compensatory penalities;

    − a good motivation of the working perssonel and a diminuation of operating costs;

    − a dissemination of the efforts with respect to the compliance with SR OHSAS 18001:2008 to all the interested parties;

    − an improvement in the image of the economic agent by increasing competitivennes and improving the relations with the public authorities.

3. Documentation of the Quality System in the Field of OHSAS

There have been devised the models of the documents that belong to the quality system in the field of OHSAS Ffor a suitable implementation of the principles listed in the model of the OHSAS proposed in application guidelines.

The production of the system documents in the field of OHSAS has taken into consideration the tailoring of the requirments stated for the proposed model to the organizational particular aspects of the production specific to economic agents that carry on their activities in atmospheres with hazard of explosion and for in toxic atmospheres and the requirments stated by the legislation in force in the field of OHS, especially the Law no. 319/2006 of OHS and the Methological Norms for the implementation of this law.

Basically, the documentation of the OHSAS includes the following items (Plesea & Vlaicu -Popa, 2009; Program NUCLEU, Faza V/2009):

    − checklist with the requirments of the OHSAS;

    − handbook of the OHS management; the main document of the system that is the basis for all the other documents;

    − the procedures of the system that provide details on certain provisions stipulated by the handbook; there are also established concrete aspects on responsibilities, functions, competences, actions, informations flows, recording of information so that the system should work in compliance with the requirements stated by the legislation in force and by the model and all the general objectives related to OHSAS should be reached.

Checklist with the requirments of the OHSAS. This checklist is a working document that comprises the description of the requirments stipulated in SR OHSAS 18001:2008 and provides the possibility to check the observance of the corresponding requirements from the above mentioned standard, with the view to a correct and complete drawing up of the system documents (MC-SSM şi PS-SSM).

Model for the management handbook of OHS. The model of the basic document for the OHSAS has been drawn up by taking into consideration the following issues:

    − the requirments of the legislation in force related to the OHS;

    − the requirments valid for the model for OHSAS proposed in the paper;

− correlation between the OHSAS and the quality management system existing at the officies of economic agents;

− particular aspects related to the organization of the economic agents.

The handbook starts with the ″Political statement of the managing board in the field of OHS″; this document covers the approach and the objectives of the managing board.

The introductory part of this model comprises a general presentation of the economic agent, the scope and the targets and the drawing up and the management of the handbook.

The subseqvent clauses in the handbook present the structure of the model of OHS and basic issues that correspond to each element of the system that provides the observance of the requirements for the model, together with the implementation, maintenance and improvement of the system.

Models of the procedures for the OHSAS. The system procedures provide detailson certain provisions stipulated by the handbook; there are also established concrete aspects on responsibilities, functions, competences, actions, information flows, recording of information with the view to providing compliance with the requirements of the model and efficiency in the operation of the OHSAS.

The drawing up the models for the system procedures has taken into consideration two main requirments for the model that might seen in opposition one from another:

− the volume of the documentation shall be maintained to necessary minimum in order to provide the efficiency of the system;

− the documents shall cover a general and detailed description of the basic elements of the system and of the relations from among them.

To this end, there have been determined the models of the following system procedures: PS-SSM–01 "Identification of hazard, risk evaluation and establishing the verification"; PS-SSM–02 "Evaluation of compliance with the legal requirements and other requirments"; PS - SSM – 03 "Competence, training and raising awareness"; PS-SSM–04 "Communication"; PS-SSM–05 "Participation and advisory operations"; PS-SSM–06 "Control of document-tation"; PS-SSM–07 "Preparedness for emergency situations and capability for answering back"; PS-SSM–08 "Monitoring and measuring the performances of OHSAS"; PS-SSM–09 "Investigating the incidents"; PS-SSM–10 "Non-compliances, corrective and preventive actions"; PS-SSM–11 "Control of recordings"; PS-SSM–12 "Internal audit"; PS-SSM–13 "Management Analysis".

4. Software for the Occupational Health and Safety Integrated Management System

This software is in EXE format and it has been designed in Visual Basic. Fig. 1 shows the logical diagram of the mathematical algorithm proposed for the

drawing up documents related to the OHSAS.

MSSM.EXE 01 software represents a working tool that is being used for the drawing up the system documents for the OHSAS. The input data covers the following issues: objectives of the OHS, the targets, the scope, the responsibilities with respect to the drawing up and the management of the handbook for OHS, the implementation, maintenance and improvement of the system related to OHS, action means, information flow, means used to record the information with the view to providing compliance with the requirements of the model and an efficient operation of the OHSAS. Fig. 2 shows the start page of MSSM.EXE 01 software.
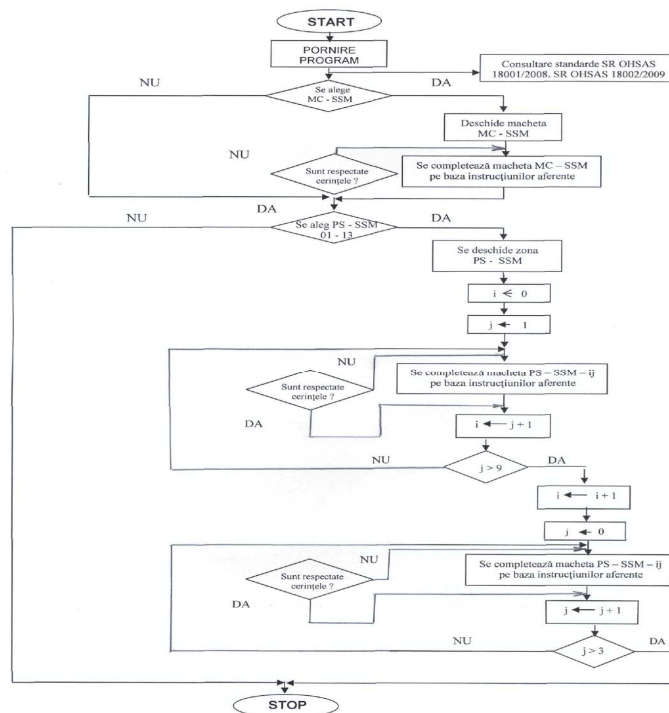

Fig.5. Schema logică a programului MSSM.EXE 01

Fig. 1 − Logical diagram of the mathematical algorithm.

Fig. 2 − MSSM.EXE 01 - Te start page of software.

By pressing the button *"Pornire program/Start software"* the application is being launched and the main window that contains 4 distinct areas is displayed. Fig. 3 shows the working window where the user shall select from among the 4 areas.
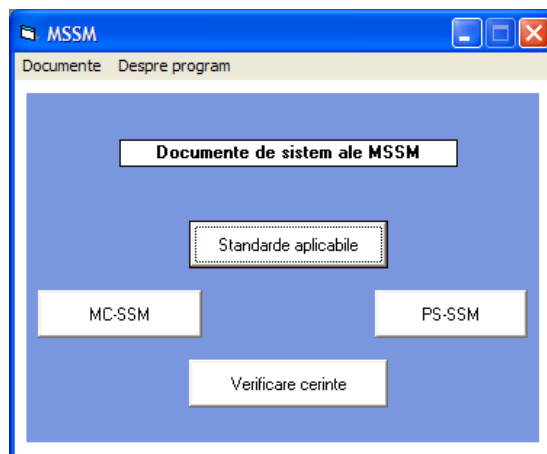

Fig. 3 – Working window in MSSM.EXE.01software.

These areas provide the following facilities:

1. The area *"Standarde aplicabile/Applicable standards"*, comprises the applicable standards for the domain of OHSAS. They can be visualized as pdf. These standards are the following ones: SR OHSAS 18001:2008 ″Occupational health and safety management systems. Requirments″ and SR OHSAS 18002:2009 ″ Occupational health and safety management systems. Guidelines for the implementation of OHSAS 18001:2007″ (Fig.4).
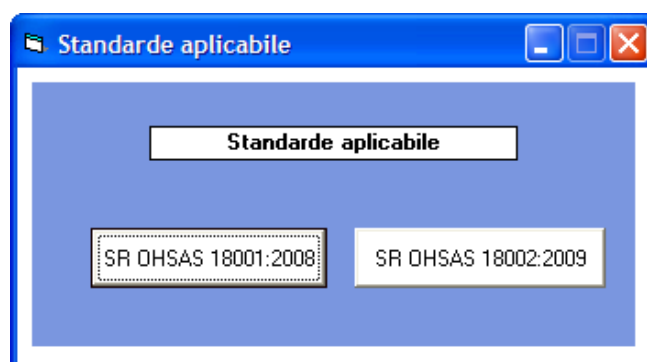

Fig. 4 – Working window for the visualization of the applicable standards.

2. The area of *"MC-SSM"*, is used to visualie the model of the handbook for the management of OHS. It comprises the instructions for the

filling in of each clause in this structure. The model of the system document has been produced with the help of hyperlinks which help the browing of the working areas of the document with the view to reading the instructions and to filling in correctly the handbook for the management of the OHS;

3. The area of *"PS-SSM"*, allows the acces to the list with the 13 system procedures, making easier the acces to these models, which also include instructions for their filling in. The reading and the filling in of these models are similar to those valid for the above said handbook for the management of the OHS. By taking into consideration the design of the software, the 13 models for the system procedures can be opened/filled in both one by one or randomly, depending on the option of the user (Fig.5).
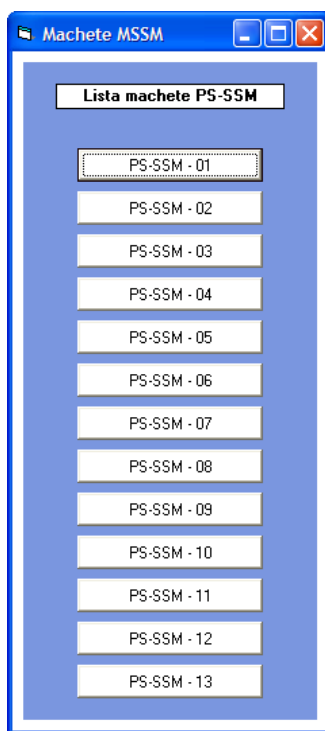
Fig. 5 –Working window with the list of the models for
the 13 system procedures of OHSAS.

4. The area for the *"Verification of requirments"*, provides the possibility to verify/self-check the observance of the requirements stated by the SR OHSAS 18001:2008, with the view to getting correct and full system documents (MC-SSM şi PS-SSM). This area comprises the document with the description of the requirments stipulated in the above-said standard. It has been designed based on the same system with hyperlinks that help the visualization of the corresponding requirments.

Fig. 6 – Window with the access password to
MSSM.EXE 01 software.

For providing the safety of information introduced into MSSM.EXE 01, the access to the application and to the models of the system documents is made with the help of a password (fig.6).

Subsequently, all data and information comprised by the documents are provided protection as it follows:
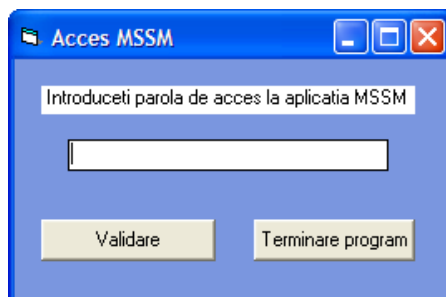
− during the reading of the standards applicable for the OHS domain, *i.e*: SR OHSAS 18001:2008 and SR OHSAS 18002:2009, available in pdf format;

− during the reading and typing in the checklist with the requirements for the OHSAS and the models of the system documents (MC-SSM, PS-SSM-01 ÷ PS-SSM-13).

5. Conclusion

MSSM.EXE 01 software can provide rapid and accurate system documents in the field of OHS based on the evaluation of the specific features displayed by all the occupational health and safety and manages by the economic agents involved in hazardous and/or toxic activities.

The use of this software is not limited and it needs a minimum configuration, together with the use of the suitable operating system. All data and information which are to be introduced are stipulated by the requirements of the guideline for the implementation of the model for the occupational health and safety integrated management system.

This software is the first version and it allows the updating of information and the upgrading of the application whenever significant changes are being made to its documents.

Subsequently, MSSM.EXE 01 can represent a reliable solution for a rapid and accurate solving of the issues in the field of OHS, more exactly through:

− a well-planned and well-documented approach of OHS issues;
− underilng the domains of responsibilities;

- becoming more familiar with the aspects related to OHS and increasing awareness on the issues raised by the OHS;

- providing a stable, favorable and highly performant climate for the assignet humain resources;

- improving the OHSAS by quantized results.

REFERENCES

Cotigă F., Drăghici A., Vasilescu G., *Baze teoretice şi practice privind auditul securităţii şi sănătăţii în muncă*. Editura PROMUN, Arad, 2009.

Vasilescu G.D., *Metode de calcul probabilistic utilizate în diagnoza şi prognoza riscului industrial*. Editura INSEMEX, Petroşani, 2008.

Vasilescu G.D., *Metode neconvenţionale de analiză şi evaluarea riscului profesional*. Editura INSEMEX, Petroşani, 2008.

Simion S., *et al., Reducerea riscurilor profesionale în din industria extractivă*. **1- 2**, Editura Europrint, 2004.

Plesea V., Vlaicu Popa M.E., *Consideraţii privind obiectivele şi studiul optimilor de reabilitare economică şi dezvoltare a locurilor de muncă în zonele monoindustriale afectate de restructurare*. Analele Universităţii „Constantin Brâncuşi", Tg Jiu, Seria Inginerie, *2*, 2009.

Toma R., *Stadiul actual al cunoaşterii în domeniul evaluării riscurilor de accidentare şi îmbolnăvire profesională*. Referat de doctorat,Universitatea din Petroşani, *1*, 2009.

* * Program NUCLEU: *Sistem integrat de management al riscului profesional generat de aplicaţiile industriale desfăşurate în medii cu pericol de explozie şi/sau toxicitate*. Aplicaţie informatică privind sistemul de management integrat al securităţii şi sănătăţii în muncă, Studiu INSEMEX, Faza V/2009.

SOFTWARE PENTRU SISTEMUL DE MANAGEMENT INTEGRAT A SĂNĂTĂŢII ŞI SIGURANŢEI ÎN MUNCĂ

(Rezumat)

Lucrarea de faţă se referă la conceperea şi realizarea unei aplicaţii informatice a sistemului de management integrat al securităţii şi sănătăţii în muncă, în vederea asigurării elaborării operative a documentelor de sistem în domeniul securităţii şi sănătăţii în muncă, care a fost efectuată în baza Programului NUCLEU, Proiect nr.PN-07-45-01-03.

OBTAINING OF COPPER NANOPOWDERS BY REDUCTION IN POLYOLS

BY

LIANA MARIA VLADUTIU[1]*, D. SOTCA[2], A. PREDESCU[1], ROXANA TRUSCA[3] and S. IORGA[1]

[1] POLITEHNICA University of Bucharest,
[2] Institutul Naţional de Cercetare Dezvoltare pentru Industria Chimică şi Petrochimică,
[3] METAV CD Bucharest

Abstract. Particles of nanometer-sized metallic copper, were prepared by reducing copper oxide in ethylene glycol. Synthesis of nanometer copper particles in liquid polyols is a simple method of obtaining pure copper powder. Reaction conditions: temperature, stirring rate, pH, reaction time, determine the size of copper particles. The obtained sizes of the copper particles are in the range of 10 to 30 nm.

Key words: copper nanoparticles, reduction in polyols.

1. Introduction

Pure copper powder is increasingly required for applications in electronics, solar cells, etc. Pure copper metal price is a material with low cost and high electroconductive properties. It has high catalytic activity therefore it is used in organic synthesis industry (Anzlovarm *et al.,* 2007). Copper can be easily obtained by electrolytic refining or hydrometallurgical processes, often by reducing copper compounds (oxides, acetates, sulfates).

---

* Corresponding author: *e-mail:*

A relatively simple method for obtaining copper, is the reduction of copper compounds in polyols (Anzlovarm *et al.,* 2007; Fievet *et al.,* 1993). The paper presents research results obtained in the reduction of black copper oxide (CuO) in ethylene glycol ($C_2H_6O_2$). The reaction takes place in two stages, there is an intermediate form of Cu_2O (Chen *et al.,* 2005). Stirring speed of reaction mass is an influential parameter on the particle size of powder (Predescu *et al.,* 2009; (Vladutiu *et al.,* 2007). The obtained copper powder is between 10 to 30 nm in size. Investigative methods used to characterize the copper powder were X-ray diffraction, scanning electron microscopy (SEM) and transmission electron microscopy (TEM).

2. Experimental Procedure

2.1. Materials

It was used copper oxide (CuO) with concentration $\geq$ 98% (FLUKA), ethylene glycol ($C_2H_6O_2$) with boiling point at 196°C (FLUKA), sodium hydroxide (NaOH) 99% (Merck), D-sorbitol ($C_6H_{16}O_6$) $\geq$ 98% (Sigma), ethanol (C_2H_6O) (Merck).

2.2. Synthesis Process

In a glass baloon approx. 500 ml, equipped with stirrer, reflux condenser, thermometer and dropping funnel were added the copper oxide, ethylene glycol and D-sorbitol. Stirrer speed was kept constant at 900 rpm. Molar ratio CuO: ethylene glycol = 0.07 and D-sorbitol: ethylene glycol = 0.06. With the help of an electrical resistance, the temperature inside the balloon was adjusted to the boiling point of the solvent. The black colour of the content becomes slowly, reddish brown, as an evidence of the formation of metallic copper. An important role in determining the particle size of the formed copper has the addition of sodium hydroxide solution. An addition of 0.01% sodium hydroxide favors the formation of small particles with nano size dimensions. After approx. 1.5 hours of reaction at reflux, the mass is separated, washed with ethanol and dried in oven at approx. 40°C. Identification of metallic copper was done by XRD, SEM and TEM.

3. Results and Discussions

Reduction of copper oxide (II) in ethylene glycol occurs according to the equation:

$$2CH_2OH\text{-}CH_2OH \xrightarrow{-2H_2O} 2CH_3CHO \xrightarrow{CuO} \boldsymbol{Cu} + CH_3CO\text{-}COCH_3 + H_2O \quad (1)$$
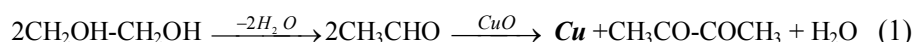
The reaction is complex and consists of an oxide-reduction, which takes place between black oxide copper and ethylene glycol. In the first stage of the reaction, acetaldehyde is produced by dehydration of ethylene glycol. Then the redox reaction occurs between copper oxide (Cu^{+2}) and acetaldehyde (CH_3CHO). Copper oxide is reduced to metallic copper and acetaldehyde oxides to dibutanone. The temperature range in which metallic copper can be achieved is between 150-170°C. The reaction time for complete conversion is 3-4 hours. If the reaction takes place at reflux (ca. 197°C), reaction time is only 1-1.5 hours. Lower temperatures is bad for crystallite growth, while extending the reaction time is beneficial to the formation of copper clusters. A solution containing sodium hydroxide increases the reaction kinetics, the transformation of CuO in metallic copper is almost total. This sodium hydroxide reaction mass at concentrations of approx. 0.01% copper favors the decreasing of the copper particle size.

The obtained metallic copper powder was investigated by X-ray diffraction on a Shimadzu diffractometer type, working in Bragg-Brentano geometry in 2θ. It was used a CuK_α characteristic X-ray beam with a wavelength of 1.54065 A. It were identified the peaks characteristic for the metallic copper, as represented in Fig. 1.
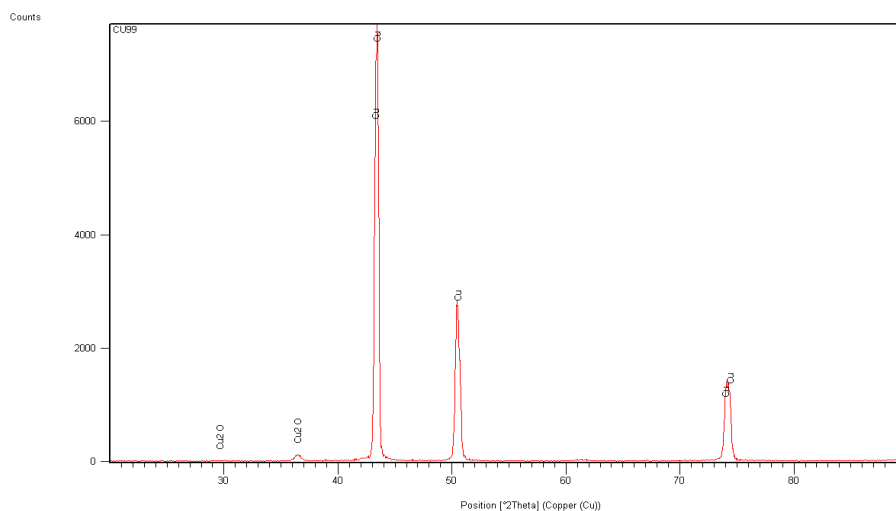

Fig. 1 – X-ray spectrum of copper powder synthesis.

The semi-quantitative analysis performed on a sample of synthesized copper powder, shows a metallic copper concentration of 99.9% ±. At a reaction time of 1 hour at reflux, the content in Cu_2O, intermediate product of incomplete reduction of CuO, is below 1%.

Copper particle size determined by TEM, is between 10 to 30 nm. BET specific surface of the powder is 12-36 m^2/gr. Fig. 2 represents a TEM image where is to see the spherical form of the copper particles and their size.
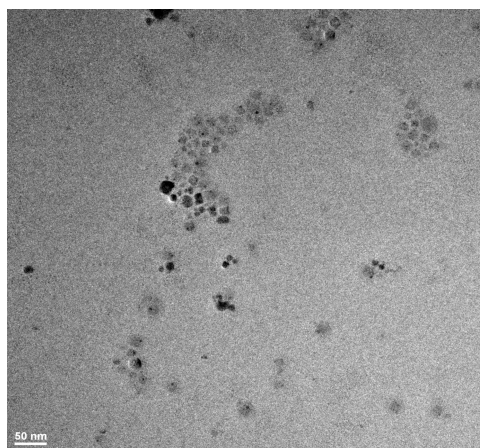

Fig. 2 – TEM image of nano-copper powder.

If the reaction temperature is 150-170°C, and the synthesis time is prolonged to approx. 3 hours, the copper particles agglomerate to form aggregates of 200-400 nm size. SEM image of such particle is shown in Fig. 3*a*. Over time, the nanometric copper agglomerates, get a polyhedral shape as can be seen in a SEM images in Fig. 3 *b*.
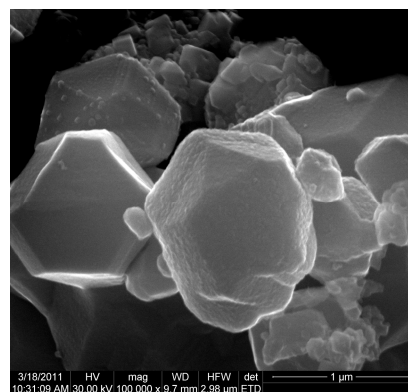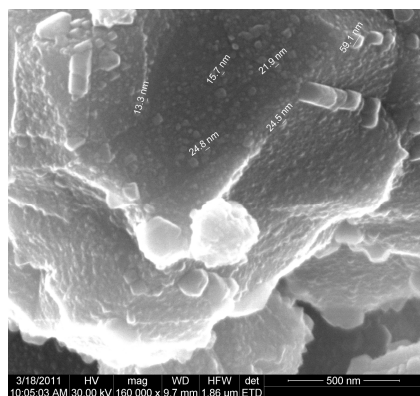

Fig. 3 – SEM image of agglomerated copper powder; *a* – nanometric agglomerate;
b – formation of polyhedral.

If the oxide-reduction reaction of CuO occurs in the presence of a dispersant, D-sorbitol, or sodium dodecilbenzen sulfur (DDBSNa), then are obtained dispersed and individual copper powder particles as presented in Fig. 4.
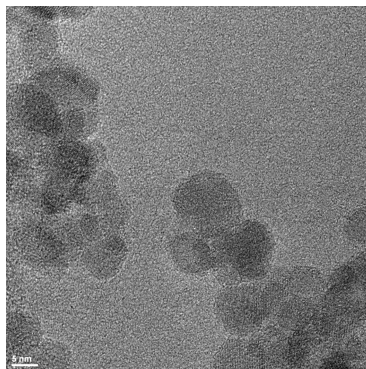
Fig. 4 – TEM image of the obtained copper powder
in the presence 2% D-sorbitol dispersant.

The dispersant content of the reaction mass does not exceed 2-3%. Although the tendancy to agglomerate of the nanoscale particles is high, there is a good dispersion in the presence of D-sorbitol used in the synthesis in a concentration of 2%.

4. Conclusion

The results show that it is possible to obtain nanometric particles of copper in the range of 10-30 nm by reducing the copper oxide polyols (CuO). The reaction is fast and almost total. The obtained copper powder has a concentration of approximate 99.9%. The time and the stirring rate of the reaction mass, the addition of dispersant and sodium hydroxide influence the particle size.

REFERENCES

Anzlovarm Alojz, Crnjak Orel Zorica, Zigon Majda, *Copper (I) Oxide and Metallic Copper Particles Formed in 1,2- Propane Diol.* Journal of the European Ceramic Society, **27**, 987-991(2007).

Chen Y.T., Zang W. Zhou, Xu B.Z., Fan X.Q., *et al., Polyol Process to Large-Scale Synthesis of Cu₂O with Disk-Like Structure*. Chinese Chem. Lett., **16**, *2*, 245-248 (2005).

Fievet F., *et al., Controlled Nucleation and Growth of Micrometre-size Copper Particles Prepared by Polyol Process*. J. Mater. Chem., **3**, *6*, 627-632(1993).

Predescu A., Vladutiu L., Moldovan P., *Researche on the Characteristics Nanopowders Based on Magnetic Iron Oxide.* ICSAAM, Tarbes Franta Ecole Nationale d`Ingenieurs de Tarbes (2009).

Vladutiu Liana Maria, Taloi D., Constantin I., Sotca D.., *Prepararea pulberii de cupru de dimensiuni micrometrice prin reducere cu polioli.* Buletinul Institutului Politehnic Iasi, **LIII**, *4*, s. Stiinta si Ingineria Materialelor, 329 (2007).

OBȚINEREA NANOPULBERILOR DE CUPRU PRIN REDUCERE ÎN POLIOLI

(Rezumat)

Particule de cupru metalic de dimensiuni nanometrice, au fost preparate prin reducerea oxidului de cupru în etilenglicol. Sinteza particulelor nanometrice de cupru în polioli lichizi, este o metodă simplă de obținere a pulberii de cupru pure. Condițiile de reacție: temperatura, viteza de agitare, pH-ul, timpul de reacție, determină dimensiunea particulelor de cupru. S-au obținut particule de cupru cu dimensiuni cuprinse între 10 - 30 nm.

SIMULATED MULTILAYER INTERFERENTIAL FILTERS FROM NATURAL INORGANIC CRYSTALS

BY

**BEATRICE CARMEN ZELINSCHI*, CARMEN FELICIA DASCĂLU
and DANA ORTANSA DOROHOI**

"Al. I. Cuza" University of Iaşi,
Faculty of Physics

Abstract. Multilayer interferential filters from Maramures area quartz were simulated using the optical data previously obtained by interferometric procedure. The simulations permits identification of the maximum transmission factor of a device containing 1 - 5 anisotropic layers of the same thickness placed between crossed polarizers. Results were analyzed as function on the layers thickness and the number of anisotropic elements. Quartz is a hardly manufactured mineral so, the simulation is necessary in order to avoid the experimental trials for given optical characteristics of the interferential filters.

Key words: quartz, transmission factor, layers between crossed polarizers.

1. Introduction

Materials crystallize into different crystal forms as a function of the conditions of growth (temperature, pressure, impurity content, growth rate, etc.) (Meyerson, 2002). Crystals are classified in two groups: isotropic (cubic system) and anisotropic (birefringent) crystals (Ladd & Palmer, 2003; Born & Wolf, 1999).

---

* Corresponding author; *e-mail:* carmen_beatrice_zelinschi@yahoo.com

Anisotropic crystals are divided in two categories: uniaxial and biaxial crystals (Born & Wolf, 1999). Uniaxial crystals have one optically section and include tetragonal, hexagonal and trigonal crystals systems (Ladd & Palmer, 2003; Born & Wolf, 1999; Dorohoi, 2010). Biaxial crystals have two optically isotropic sections and include triclinic, monoclinic and orthorhombic crystals systems (Ladd & Palmer, 2003; Born & Wolf, 1999; Dorohoi, 2010).

Quartz is a chemical compound consisting of one part silicon and two parts oxygen (trigonal system SiO_2). It is the most abundant mineral found at Earth's surface and its unique properties make it one of the most useful natural substances.

Quartz is a uniax crystal and it is are characterized by two values of the refractive index: the ordinary value (n_o) measured for radiation having the electric field intensity perpendicular to the optical axis and the extraordinary value (n_e) measured for radiations having electric field intensity parallel to the optical axis (Dorohoi, 2010). The birefringence of the uniax crystals can be estimated by using the formula (Dumitraşcu *et al.,* 2007):

$$\Delta n = n_e - n_o \qquad (1)$$

Let's consider a device (D_1) consisting of a quartz layer between two crossed polarizers (P and A) Fig. 1. When in Fig. 1 the transmission directions of the polarizers are perpendicular and the main axes of the anisotropic layer are at 45 degrees related to the polarizers (see Fig. 2), the transmission factor of the device depends on the phase difference between the ordinary and extraordinary rays. If the losses by reflection at the separation surfaces are neglected the transmission factor of the device is (Dumitraşcu & Dorohoi, 2009):

$$T(\lambda) = \frac{1}{2} sin^2 \frac{\pi \cdot (n_e - n_o) \cdot L}{\lambda} \qquad (2)$$

where n_e - n_o is the birefringence of the anisotropic layer, L is the thickness of the quartz layer and λ is the light wavelength.
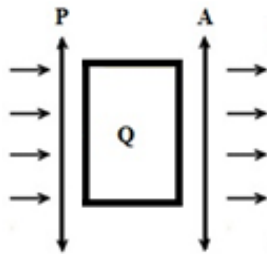

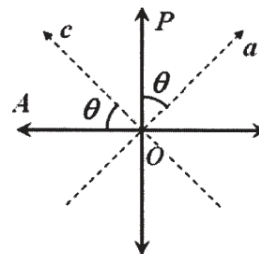Fig. 1 – Device (D_1) consisting from a quartz layer between crossed polarizers.

Fig. 2 – Reciprocal orientation of the main directions of the quartz and of the transmission directions of the polarizers in the device (D_1).

When two or more quartz layers with the same thickness are introduced in device (D_m) see Fig. 3, the transmission factor is (Dumitraşcu & Dorohoi, 2009):

$$T_m(\lambda) = \frac{1}{2}\, sin^{2m}\, \frac{\pi \cdot (n_e - n_o) \cdot L}{\lambda} \quad (m=2, 3, 4, ...) \tag{3}$$

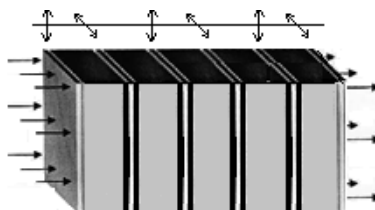where m is the number of anisotropic layers from device.

Fig. 3 – Device with 5 quartz layers (D_5).

The device from Fig. 3 made up from 5 quartz layers with the same thickness are orientated in such a way that the transmission direction of the polarizer at the entrance in every layer is parallel with the transmission direction of the polarizer at the exit from the precedent layer. In order to diminish the losses by reflection only one polarizer is kept between two consecutive anisotropic layers.

2. Experimental Part

In a previous paper (Dascălu *et al.,* 2010) it was established that, the quartz crystal from Maramureş area can be used for the construction of optics components, due to its high purity.

The main refractive indices of quartz crystal were determined with Rayleigh interferometer at three wavelengths (546.07nm, 589.3nm, 656.27nm). The experimental data were used to simulate the dispersion of the birefringence in visible range using Cauchy formula with three coefficients (Zelinschi *et al.,* 2011). In this paper the transmission factor of a device consisting of 1-5 quartz layers with the same thickness is simulated.

3. Results and Discussions

The transmission factor (T) vs. thickness (L) of the quartz layer at $\lambda=550$nm for device with one quartz layer (D_1), three layers (D_3) and five layers (D_5) is given in Fig. 4 (*a, b, c*).

From Fig. 4 one can be see that at $\lambda=550$nm the transmission factor is maximum when the thickness of the quartz layer is approximately 270, 328, 390, 449μm. The half bandwidth decrees when the number of anisotropic layers increases.
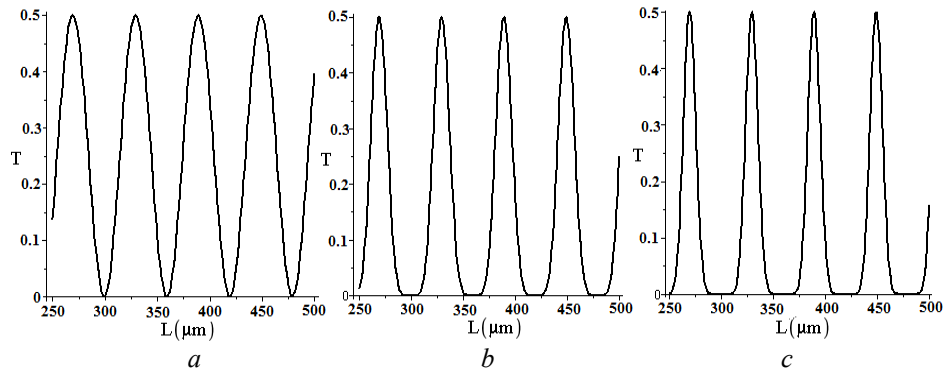
Fig. 4 – Transmission factor (T) vs. thickness (L) of the quartz layer
at λ=550nm for *a*) D_1, *b*) D_3 and *c*) D_5.

The thickness of the anisotropic layer for which the transmission factor is maximum at a given wavelength can be estimated by simulations achieved in Maple program.

The transmission factor (T) vs. wavelength (λ) when the thickness of the anisotropic layer is L=1750μm is represented in Fig. 5 for device D_1 and D_5.
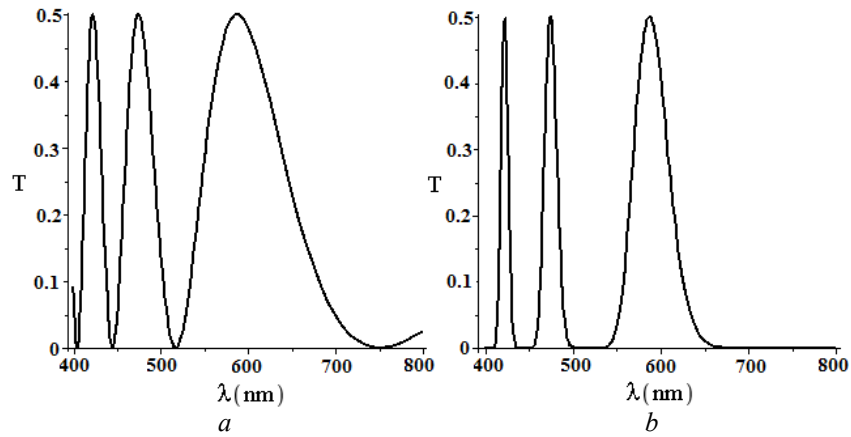
Fig. 5 – Transmission factor (T) vs. wavelength (λ) for *a*) D_1 and *b*) D_5.

In the channeled spectra are three transmission bands with different half bandwidth when the thickness of the quartz layer is 1750μm. The half bandwidth increases when the light wavelength increases. The half bandwidth also decreases when the number of the layers increases.

The 3D graph from Fig. 6 was obtained for L ∈ (300, 500)μm, λ ∈ (400, 800)nm in the case of device D_1, containing only one quartz layer.

From Fig. 6 one can be identify the thickness of the anisotropic layer for which the transmission factor at a given wavelength is maximum.
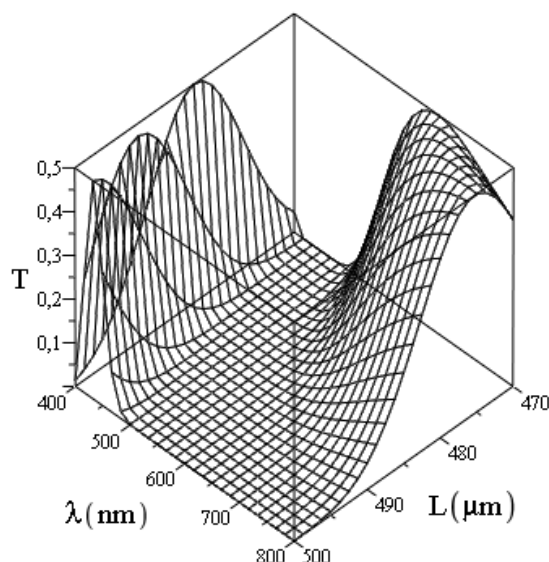
Fig. 6 – Transmission factor (T) vs. wavelength (λ)
vs. thickness (L) of the quartz layer.

4. Conclusion

In a device with quartz layer between crossed polarizer the transmission factor depends by the crystal characteristics (thickness, birefringence, dispersion of the birefringence etc.). From these simulations can be estimated the thickness of the anisotropic layer for which the transmission factor is maximum at a given wavelength. The half bandwidth increases when the wavelength increases. The half bandwidth decreases when the number of the layers increases. The representations are useful in order to design interferential filters with specific optic characteristics.

REFERENCES

Born M., Wolf E., *Principles of Optics*. 7th Ed., Cambridge University Press, 1999.
Dascălu C.F., Zelinschi B.C., Iustain C., Dorohoi D.O., *Electro-Optical Parameters of Mica Crystals*, Bull. Polyt. Inst., **4**, *56*, 2010.
Dorohoi D.O., *Fundamental Optics*. Addleton Academic Publisher, New York, 2010.

Dumitrascu L., Dorohoi D.O., *Elemente de optica mediilor anizotrope*. Aplicaţii, Editura Tehnopress, Iaşi, 2009.

Dumitrascu L., Dumitrascu I., Dorohoi D.O., Dimitriu D., Aflori M., Apreutesei G., *Complemente de fizică pentru studenţii şcolii doctorale*. **I**, Ed. TehnoPress, Iaşi, 2007.

Ladd M., Palmer R.A., *Structure Determination by X-Ray Crystallography*. Mark Ladd, Rex Alfred Palmer, Kluwer Academic/Plenum Publishers, New York, 2003.

Meyerson Allan S., *Handbook of Industrial Crystallization*. 2nd Ed., Butterworth-Heinemann, 2002.

Zelinschi B.C., Dascălu C.F., Stanculescu R., Dorohoi D.O., *Simulation of the Main Refractive Indices of Quartz Crystal From Maramures Area*. Annals of "Dunarea de Jos" University of Galati, Fascicle II, 2011, accepted.

SIMULAREA UNOR FILTRE INTERFERENŢIALE CU GEOMETRIE
MULTISTRAT DIN CRISTALE NATURAL

(Rezumat)

În lucrare au fost simulate filtre interferenţiale cu geometrie multistrat, din cuarţ din zona Maramureş, utilizând date experimentale obţinute anterior prin metoda interferometrică. Simulările permit să se indentifice factorul de transmisie maxim a unui dispozitv care conţine 1 - 5 straturi anisotrope cu aceeaşi grosime, aflate între doi polarizori în cruce. Rezultatele au fost anlizate în funcţie de grosimea stratului şi de numărul de elemente anisotrope. Cuarţul este un mineral greu de prelucrat astfel încât simularea este necesară pentru a evita încercările experimentale pentru a obţine caracteristici optice ale filtrelor interferenţiale.

IMPROVING WORKERS SAFETY AND RELIABILITY BY APPLYING RISK BASED MAINTENANCE ON THE BLACK LIQUOR PUMP

BY

DANIELA FULOP*, **TIBERIU RUSU and ISTVAN FULOP**

Technical University Cluj-Napoca-Romania,
Department of Environmental Engineering

Abstract. The paper present the main aspects for application of Risk Based Maintenance concept, at S.C. SOMES Dej Company for the black liquor pump used in pulp industry. The constructive and technological aspects regarding the maintenance of this unit are presented using this case study, proving the real advantages of this concept as compared to the classical concept of maintenance.

Key words: black liquor pump,risk based maintenance,workers safety, reliability.

1. Introduction

Black liquor pump is the supplier pump of the Kamyr kettle from the Pulp division (Fig. 1). The pump retrieve the black liquor resulted after the boiling of the wood chops in the kettle, the liquor is stored in a tank of 100 m³ and send it on the top of the kettle at 54 m, where is heated with steam at 16 at., contributing then to the boiling process of the chopped wood. The circulated fluid temperature is 70-80ºC.

* Corresponding author; *e-mail:* daniel.fulop@gmail.com

The risk based maintenance and continuous monitory of equipments stage are in close interdependence, which is the only counterwork solution of unexpected breakdowns appearance (Barratt, 2004). The determination produced risk of damage and technical unexpected breakdowns are realized with the risk matrix depending on gravity and probability of damages appearance (Tischuk, 2002).

The risk analysis of damages is based on equipment analyze and the following components of society integral management (Wintle *et al.*, 2001):

- the security and health of workers;
- the process safety of installations equipments;
- the actual environment legislation;
- the technological aspects;
- the economic-financial aspects.

The implementation stages of risk based maintenance at the Black liquor pump are the following (Fulop *et al.,* 2009):

- identified the component elements and functions of the equipments;

- identified the probability that this component element functions not accomplished, and the possible damages of the equipment elements;

- the analysis of probability and risk produce at the equipment elements of paper machine;

- identified the causes of damage risk appearance and solutions to avoid the risk appearance;

- establish maintenance process for equipments protection avoiding the failure risk appearance and planning the specific demands for avoiding risks.

Fig. 1 – Liquor supply pump.

2. Components of the Evaluated System

Black liquor supply pump:
- Pump type: NK 125/100;

- Impeller: open;
- Pump housing material: cast iron;
- Bearings:
    − in direction of the electric engine: series 6313 NR-1 pc;
    − in direction of the impeller: series NU313 ECP-1 pc;

Electric engine:
- Electric engine type: ASI 350-80-4;
- Bearings:
    − in direction of the pump: series NU 317 C3-1 pc;
    − in direction of the fan: series 6317 C3-1 pc;
- Engine power: 55KW;
- Engine speed: 1500 rpm;

The clutch between electric motor and pump is a clutch with rubber claws and jaws.

Risk factors that are in the range of unacceptable are the folowings:
- Deterioration of the bearing series 6313 NR;
- Deterioration of the bearing series NU 312 ECP;
- Wear of the pump impeller due to erosion;
- Wear of the pump casing due to erosion;
- Soft sealing problems due to leaks between the housing and pump shaft;
- Destruction of coupling between the electric motor and pump;
- Sprinkling the workers with hot liquor due to the pump leaks;
- Sprinkling the workers with hot liquor due to leaks between the pump and the suction line;
- Sprinkling the workers with hot liquor due to leaks between the pump and the discharge pipe;
- Sprinkling the workers with hot liquor due to unsiling of pump by closing the pump inlet valve in case of pump removal;
- Sprinkling the workers with hot liquor due to unsiling of pump by closing the pump discharge valve in case of pump removal;
- Sprinkling the workers with hot liquor due to overpressure existance in the pump during it's removal;
- Failure to follow work instructions, maintenance instructions and operating instructions for specific health and safety at work;
- Deterioration of the bearing series NU 317 C3;
- Deterioration of the bearing series 6317 C3;

The distribution of risk factors by the generating sources are as follows:
    − 51,11 %, specific factors due to own dameges of the analized system;
    − 24,45 %, factors specific to the workers health and security;
    − 4,44 %, specific factors of the environment;

− 20,00 %, specific factors fow the own economical and financial environment;

To reduce or eliminate the 15 risk factors (which lies in the unacceptable), are necessary the folowing generic measurs presented in the „*Sheet of the proposed measures*" presented in the table 1.

Table 1
Sheet of the Proposed Measures

Line No.	Risk factor	Proposed measures nomination of the measure
1	Deterioration of the bearing series 6313 NR	1.1. The bearing appropriate lubrication 1.2. Compliance with the regime and technical parameters of the pump 1.3. Dynamic balancing of the pump impeller after each restoration of the impeller 1.4. Changing the type of seal between the shaft and pump housing 1.5. Surface treatment of seating and fixing of the pump casing in a single set 1.6. Replacing bearing a row radial ball bearings 6313 No two angular contact ball bearings mounted in a row set with 7313 series BECBP 1.7. Checking the condition of pump by thermography
2	Deterioration of the bearing series NU 313 ECP	2.1. The bearing appropriate lubrication 2.2. Compliance with the regime and technical parameters of the pump 2.3. Dynamic balancing of the pump impeller after each restoration of the impeller 2.4. Changing the type of seal between the shaft and pump housing 2.5. Surface treatment of seating and fixing of the pump casing in a single set 2.6. Checking the condition of pump by thermography
3	Wear of the pump impeller due to erosion	3.1. Fitting a send trap between liquor storage tank and pump for retaining the solid particles from liquor
4	Wear of the pump casing due to erosion	4.1. Fitting a send trap between liquor storage tank and pump for retaining the solid particles from liquor
5	Soft sealing problems due to leaks between the housing and pump shaft	5.1. Replacement of mechanical seals with a soft seal between the shaft and pump housing
6	Destruction of coupling between the electric motor and pump	6.1. Replacing claw coupling between electric motor and pump with a flexible coupling venetian 6.2.Properly balance the electric motor and pump assembly

Continuation Table 1

7	Grip clothes, drive hand or body organs by rotating transmission	7.1. Regular briefing at work ; 7.2. Any intervention to the machinery will be performed by qualified and trained people for this purpose 7.3. Periodical inspection of the psycho-physiological status of the employees 7.4. Assignment of employees and medical inspection at the moment of hiring and then regular in accordance with Law 319/2006, completed by GD 1425 / 2006 7.5. Mounting a protective device on the coupling between electric motor and pump
8	Sprinkling the workers with hot liquor due to the pump leaks	8.1. Stop pump immediately and change the seal when there is loss of liquor 8.2. Any intervention at the pump will be done only based on a work permit 8.3. Maintenance personnel will wear personal protective equipment required for such work set
9	Sprinkling the workers with hot liquor due to leaks between the pump and the suction line	9.1.Stop of the pump immediately and change the sealing between the suction line and pump when loss of liquor is found 9.2. Any intervention at the pump will be done only based on a work permit 20.3. Maintenance personnel will wear personal protective equipment required for such work set 9.3. Mounting a protective device on the flange joint between the pump and the suction line
10	Sprinkling the workers with hot liquor due to leaks between the pump and the discharge pipe	10.1.Stop of the pump immediately and change the sealing between the discharge line and pump when loss of liquor is found 10.2. Any intervention at the pump will be done only based on a work permit 21.3. Maintenance personnel will wear personal protective equipment required for such work set 10.3. Mounting a protective device on the flange joint between the pump and the discharge line
11	Sprinkling the workers with hot liquor due to unsiling of pump by closing the pump inlet valve in case of pump removal	11.1. Before removing the pump it is mandatory to close the inlet valve of the pump 11.2. Any intervention at the pump will be done only based on a work permit 22.3. Maintenance personnel will wear personal protective equipment required for such work set

Continuation Table 1

12	Sprinkling the workers with hot liquor due to unsiling of pump by closing the pump discharge valve in case of pump removal	12.1. Before removing the pump it is mandatory to close the discharge valve of the pump 12.2. Any intervention at the pump will be done only based on a work permit 23.3. Maintenance personnel will wear personal protective equipment required for such work set
13	Sprinkling the workers with hot liquor due to overpressure existance in the pump during it's removal	13.1. Before removing the pump it is mandatory to open the discharge valve of the pump 13.2. Any intervention at the pump will be done only based on a work permit 24.3. Maintenance personnel will wear personal protective equipment required for such work set
14	Interventions at the pump during its operation	14.1. Any intervention on the pump will be made after the pump is stopped and based on a working permit 14.2. Compliance with the work instructions specific to the pump 14.3. Following the instructions of their occupational safety and health
15	Failure to follow work instructions, maintenance instructions and operating instructions for specific health and safety at work	15.1. Compliance with the work instructions specific to the pump 15.2. Compliance with the maintenance and operating instructions specific to the pump 15.3. Following the instructions of their occupational safety and health
16	Deterioration of the bearing series NU 317 C3 at the electric motor	16.1. Proper lubrication of the electric motor bearing 16.2. Compliance with the regime and technical parameters of the pump 16.3. Periodical vibration measurements 16.4. Checking the condition of the electric motor by thermography
17	Deterioration of the bearing series 6317 C3 at the electric motor	17.1. Proper lubrication of the electric motor bearing 17.2. Compliance with the regime and technical parameters of the pump 17.3. Periodical vibration measurements 17.4. Checking the condition of the electric motor by thermography

Based on the assessment of risks to pump for the black liquor and the measures proposed in the *Sheet of the proposed measures* was prepared a sample pump NK 125/100 with the following modifications :

- replacing bearing a row radial ball bearings 6313 NR two angular contact ball bearings mounted in a row set with 7313 series BECBP;

- dynamic balancing of the rotor speed of 1,500 rpm;
- processing a single set of the feet for positioning the pump and the interface between body and frame pump rotor;
- a new solution for achieving electric motor pump coupling, replacing the coupler with a coupling jaw slats, which are able of the take some of the existing system misalignments;
- soft sealing type replacement cord with mechanical seal: in this sense has been dropped wear sleeve mounted on the pump shaft and pump shaft was modified to achieve optimum mechanical seal assembly;

To eliminate erosion of the pump impeller, pump casing wear, mounting flange wear on the inlet and outlet of the the pump, it was purchased a sand trap in the amount of EUR 30000, and a washing plant for wood chops in the amount of EUR 20000.

These facilities are designed of the remove dirt (gravel, sand and other solid particles) resulting from the kettle Kamyr of liquor and liquor stored in the reservoir, where the pump carrying NK 125-100 on top of the kettle black liquor.

During the planned stop in September 2006 the classic black liquor pump have been change to the new modified pump.

In this sense the concrete foundation of the pump has recovered completely and changed of the pump pedestal.

The electric motor and pump have been aligned with the laser alignment device. Replacing pipes pump inlet and outlet pipes so as to be perpendicular to the surface, for positioning of the pump flange connection has been restored and hardening of pipe clamp and media.

3. Conclusion

Analyzing the black liquor pump for a period of six months after commissioning, and have obtained the following advantages over a similar period before the commissioning of the modified pump:
- crash reduction due to damage pump bearings by 80%;
- crash reduction due to wear of theimpeller and pump housing by 73%;
- accidental shutdowns due to pump leakage reduction by 78%;
- crash reduction due to coupling damages by 64%;
- reduce costs of spare parts and repairs by 40%;
- reduce the length of accidental stops by 67%;
-increase the workers safety;

Following changes made to the black liquor pump, duration of black liquor pump average increased from 1.5 months to 6 months.

Expenses related to the investment required to change the pump, and construction works have been amortized after four months of operation of black

liquor pump, cost savings with maintenance and spare parts, without taking into account production losses stoppages due to accidents.

Applying the risk based maintenance, after identifying and evaluating the risks of faults, damages or accidents, the maintenance team can focus their efforts for finding technical solutions in order to reduce or eliminate the unacceptable risks, to grow the reliability and safety during the paper machines equipments and installations functioning.

REFERENCES

* * *Guide to Risk Assessment Requirements*. HSE Books, 1996.
* * *The Guide to Asset Efficiency Optimization for Improved Profitability*. SKF, Denmark, 2004.
Barratt M., *Risk Based Inspection*. SKF Engineering and Research Center, San Diego, 2004.
Fulop I., *et al., Some Practical Aspects of Risk Based Maintenance Implementation in Paper Industry*. 9th MTeM International Conference, Cluj-Napoca, 2009.
Gyenge Cs., *et al.*, *Main Aspects Regarding the Maintenance of Echipments for Paper and Pulp Industry*. Procedings of 9th International TMTM 2005 Conference, Turkey, 2005.
Tischuk J.L., *The Application of risk Based Approaches to Inspection Planning*. Tischuk Enterprises, Aberdeen, 2002.
Wintle J.B., *et al.*, *Best Practice for Risk Based Inspection as a Part of Plant Integrity Management*. TWI and Royal &SunAlliance Engeneering for the Health and Safety Executiv, 2001.

ÎMBUNĂTĂŢIREA SECURITĂŢII ŞI SĂNĂTĂŢII LUCRĂTORILOR ŞI A FIABILITĂŢII POMPEI DE LEŞIE NEAGRĂ PRIN APLICAREA MENTENANŢEI PE BAZĂ DE RISC

(Rezumat)

Lucrarea de faţă prezintă aspectele principale cu privire la aplicarea mentenanţei pe bază de risc la societatea S.C. Someş S.A. Dej pentru pompa de leşie neagră din procesul de fabricaţie a celulozei.

Aspectele constructive şi tehnologice cu privire la mentenanţa acestui utilaj sunt prezentate printr-un studiu de caz, fiind evidenţiate avantajele reale ale acestei metode de abordare comparativ cu metoda clasică de mentenanţă.

MICROSTRUCTURAL AND COMPOSITIONAL INVESTIGATION OF Al-alloy-Al$_2$O$_3$ CERAMIC-METALLIC COMPOSITES SYNTHESIZED BY REACTIVE MELT PENETRATION

BY

ANTHONY YURCHO[1][*]**, KLAUS-MARKUS PETERS**[2]**, BRIAN HETZEL**[2]**,
MATTHIAS ZELLER**[3]**, TIMOTHY R. WAGNER**[3]
and VIRGIL C. SOLOMON[4]

[1] Chemical Engineering, Youngstown, Ohio
[2] Fireline TCON, Youngstown, Ohio
[3] Chemistry Youngstown, Ohio
[4] Youngstown State University
[5] Mechanical & Industrial Engineering

Abstract. Al alloy-Al$_2$O$_3$ based ceramic-metallic interpenetrating phase composites (IPC's) have gained significant interest in the scientific community because of their unique mechanical characteristics. An ongoing study conducted in coordination with Youngstown State University and Fireline TCON, Inc. (Youngstown, Ohio, USA) aims to examine the composition and microstructural properties of such compounds. IPC's produced using pure Al and an Al-7.5wt.%Fe alloy were investigated using optical and electron microscopy and X-ray diffraction. Material produced using pure Al exhibited a co-continuous network of Al and Al$_2$O$_3$, while the IPC produced using Al-7.5wt.%Fe shows the same basic Al-Al$_2$O$_3$ structure with the addition of multiphase metallic regions. The results indicate that the microstructural characteristics of IPCs can be altered by changing the composition of the starting material, which is beneficial for producing materials used in a wide variety of applications.

---

[*] Corresponding author; *e-mail:*

1. Introduction

Interpenetrating phase composites belong to a class of materials that have interconnected networks of two or more continuous phases. The physical properties of IPC's are determined by the individual components that comprise their three-dimensional microstructure (Clark, 1992). The majority of research focuses on IPC's that contain a hard, thermal resistant ceramic phase toughened by a ductile metal phase. The most common ceramic-metallic composite is the alumina-aluminum system (San Marchi *et al.*, 2003). Several processes have been developed to produce such materials. Examples of processing techniques include: liquid phase displacement reactions (Breslin *et al.*, 1995), *in situ* combustion synthesis (Feng *et al.*, 1995), and pressurized metal infiltration (Zhou *et al.*, 1998).

TCON materials are produced by a unique process utilizing reactive melt penetration, Fig. 1. The standard process involves immersing a sacrificial SiO_2 preform into a molten aluminum bath. The SiO_2 is transformed into the Al-Al_2O_3 composite according to Equation 1. As the preform undergoes transformation its shape and size remains essentially unchanged, resulting in net-shape or near net-shape products. It is believed that changes or additions to the metal bath can tailor the final properties of the material. For example, it has been proposed that metallic additions to the melt can enhance mechanical properties by forming inter-metallic compound phases. This is useful because it can increase the number of applications for IPC's (Hemrick *et al.*, 2010). The objective of this experiment is to characterize and contrast the microstructures of TCON materials transformed in pure Al and Al-7.5%Fe alloy.
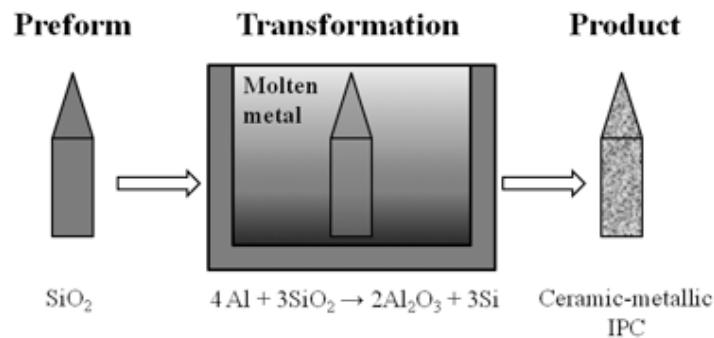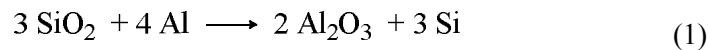
$$3\ SiO_2 + 4\ Al \longrightarrow 2\ Al_2O_3 + 3\ Si \qquad (1)$$

Fig. 1– Schematics of the reactive melt penetration (RMP) process.

2. Experimental

Fireline TCON, Inc. provided two IPC materials for analysis. The samples were produced via reactive metal penetration using a clear fused quartz preform, approximately $2 \times 2 \times 0.25$ in^3. Information regarding the metal bath and transformation times is displayed in Table 1.

Necessary sectioning was performed using a precision saw (Buehler IsoMet^{TM} 1000) equipped with a water-cooled diamond-impregnated cut off wheel. Due to the unique metal penetration process, each sample was examined in both longitudinal and latitudinal directions.

Table 1
Transformation Conditions

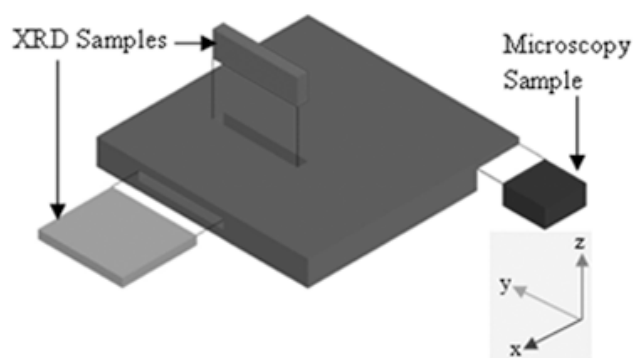| Name	Starting Material	Metal Bath	Transformation Time
Sample 1	Clear fused quartz	Pure Al	6 hours
Sample 2	Clear fused quartz	Al-7.5%Fe	4.63 hours

Fig. 2 – A graphical representation of the transformed material showing the areas examined by microscopy and X-ray analysis. A Cartesian coordinate system is used to indicate the investigated surface.

Fig. 2 illustrates the areas removed and examined. The sectioned samples were prepared for microscopy investigations using metallographic techniques including grinding and fine polishing steps. Initial analysis was performed using stereo and bright field optical microscopy (OM). Powder X-ray diffraction (XRD, Cu Kα radiation) was also performed on the samples using a Bruker-Nonius D8 Advance Powder Diffractometer. A JEOL JIB-4500 Multi Beam FIB/SEM System equipped with an X-ray energy dispersive detector was utilized for electron microscopy investigations. Samples for transmission electron microscopy (TEM) investigations were prepared by ion milling in the FIB/SEM system. TEM investigations were carried out in a JEOL 2100 Scanning/Transmission Electron Microscope (S/TEM). The high resolution S/TEM has a 0.2 nm point-to-point resolution and it is equipped with EDAX^{TM} Sapphire EDX, bright and dark field scanning detectors and two CCD cameras for micrograph and electron diffraction acquisition.

3. Results and Discussion

Fig. 3 shows optical stereo micrographs of the cross-sectioned samples. Initial observation reveals that both samples exhibit two distinct features: a Y-shaped boundary-like feature symmetrically positioned relative to the edges and corners of the rectangular-shaped cross-section, and alternating columnar-shaped bright/dark regions with the long axes orthogonal to the sample surface. The symmetry of Y-shaped feature is broken due to the fact that the top surface was partially removed for microscopy investigation. Since these features were not observed in the clear fused quartz starting material it is reasonable to assume that they are a result of the transformation process. Higher magnification optical microscopy as well as SEM investigation reveals the boundary-like feature to consists of interconnected micrometer sized voids, Fig. 4.
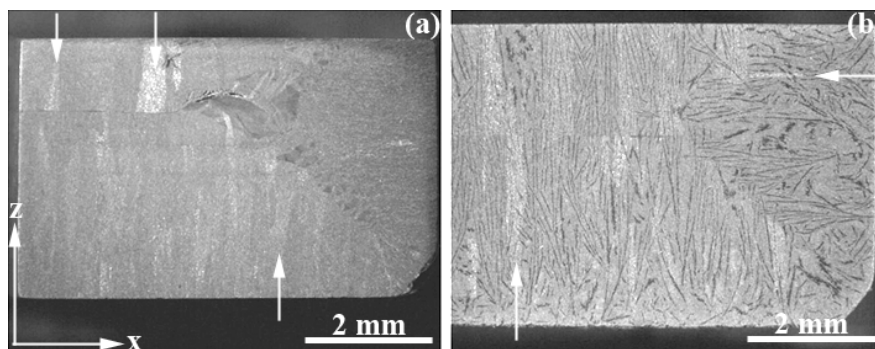

Fig. 3 – Stereo optical micrographs of polished cross-sectioned Sample 1 (a) and Sample 2 (b). The cross-section is parallel with the x–z plane.

The columnar-shaped bright regions are indicated by white arrows in Fig. 3. The regions can be revealed by manipulating the light source in the stereo optical microscope. These regions are related with the preferential orientation of the Al_2O_3 ceramic phase, in agreement with the results of the XRD experiments described below. The formation of the central-positioned voids (Fig. 4) can be explained in relationship with the transformation process during reactive melt penetration and growth of preferentially oriented Al_2O_3 regions. By immersing the preform into molten metal, SiO_2 transforms into Al_2O_3 as described in Equation (1). The transformation proceeds from exterior toward the interior of the sample following a mechanism described by Liu *et al*., 1996. Both Al_2O_3 ceramic and metal phases grow from the exterior toward the interior of the sample. Due to the sample symmetry and identical transformation velocity (about 2 mm/hr) at any point on the sample surface, the reaction fronts from two opposite surfaces will meet at the center of the sample, where the pore accumulation is observed, Fig. 3. From these observations, it appears that a direct relationship exists between the interaction of two reaction fronts and pore

accumulation (Murthy *et al.*, 2005), but the exact mechanism of porosity formation needs further clarification.
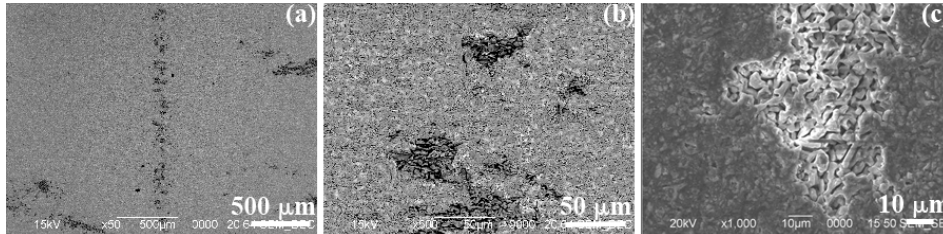

Fig. 4 – (*a*), (*b*) Backscattered electron micrographs and (*c*) secondary electron micrograph of the central Y-shaped feature observed on the x–z cross-section of Sample 1. The Y-shaped feature morphology is readily visible at higher magnification.
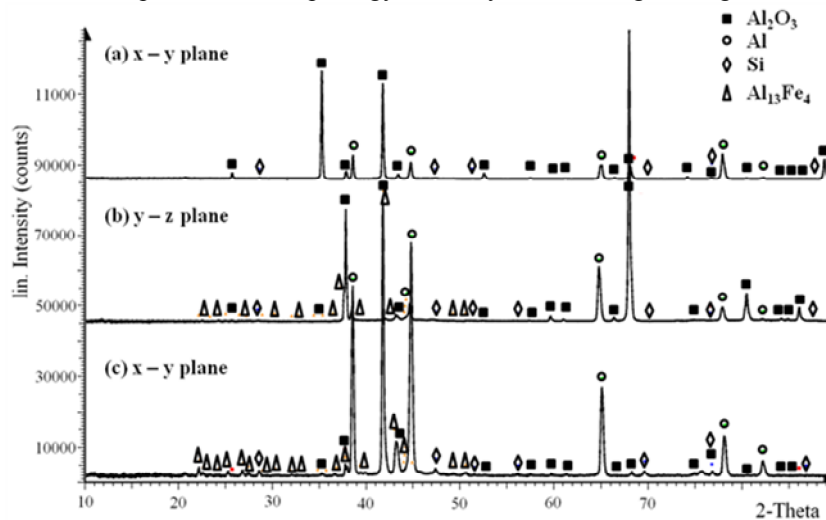

Fig. 5 – Powder XRD patterns from sample 1 (a) and sample 2 (b and c). Sample 1 was examined in the x-y plane and Sample 2 was examined in the x-y (c) and y-z (b) planes. Both samples show preferential orientation of Al_2O_3 (■ ICDD: 00-010-0173, rhombohedral R-3c, a: 4.758Å, c: 12.991Å) and Al (● ICDD: 00-004-0787, cubic Fm-3m, a: 4.049Å). The data also show the presence of small amounts of Si (♦ ICDD: 04-001-7247, cubic Fd-3m, a: 5.429Å) in both samples. The pattern suggests the presence of $Al_{13}Fe_4$ (▲ICDD: 00-050-0797, orthorhombic Bmmm, a: 7.751Å, b: 23.771Å, c: 4.034Å) in sample 2, but other Fe-Al alloys showed similarly well fitting patterns and further analysis is needed for an unambiguous assignment of the type of Fe-Al alloy. See References for ICDD files information.

Powder XRD performed on the samples indicates the presence of Al, Al_2O_3, and Si in samples 1 and 2, Fig. 5. In sample 2, additional diffraction lines point towards the presence of one or more Al-Fe-alloy phases, but a clear assignment to a specific alloy is not possible based on the diffraction pattern alone. XRD analysis did not show the additional phases suggested by electron

microscopy investigations (see below), probably due to the poor resolution of XRD at nano-scale. The mismatch between the experimental and theoretical intensities of the aluminum and especially the corundum peaks can be explained by preferential orientation of the Al_2O_3 phase and, to a lesser extent, of the Al phase along the z-axis as had been already seen in the optical micrographs. In the Al-transformed material, the Al_2O_3 peaks are well defined (Fig. 5 *a*), but the intensity mismatch is obvious for nearly all of the peaks. Correlating this observation with the bright columnar regions observed by stereo microscopy (Fig. 3), it can be concluded that the ceramic phase of the transformed material shows preferential orientation along the z axis.
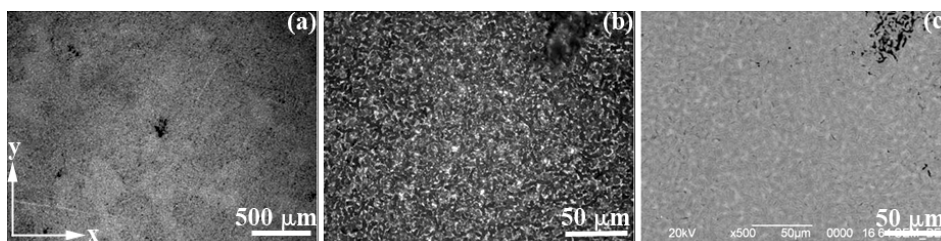

Fig. 6 – (*a*), (*b*) Optical bright field micrographs of the x-y cross-section of sample1 showing a homogeneous structure consisting of two phases and some isolated voids. (*c*) Backscatter electron micrograph of the same area confirming the presence of two distinct phases.

Determining the nature of the Al-Fe-alloy phase is difficult, and a clear assignment of the peaks not assigned to Al, Al_2O_3 or Si to one or several specific Al-Fe alloys was not possible. An $Al_{13}Fe_4$ phase (ICDD entry number 00-050-0797) was tentatively selected as the best match, but other Fe-Al alloys with different compositions did show similar agreement with the experimental patterns (for most diffraction patterns of Fe-Al alloys deposited to the ICDD database, no structural data are reported, and they might also be phase mixtures of two or more components). However, the presence of the Al_2O_3 and Al-Fe phases in the Al-Fe-transformed material was confirmed by electron microscopy analysis, as described below. XRD did not show a recognizable preferential orientation for the Si phase.

Further investigation of the cross-sectioned samples was performed using medium magnification optical microscopy and low magnification SEM, and the results are presented in Figs. 6, 7. Isolated voids can be observed throughout the bulk of both samples. Sample 1 shows a homogenous structure consisting of two phases, depicted as gray and white areas in the backscattered electron micrograph presented in Fig. 6 *c*. By comparison, sample 2 exhibits regions similar to that of sample 1 plus striated regions observed in both optical and electron micrographs,
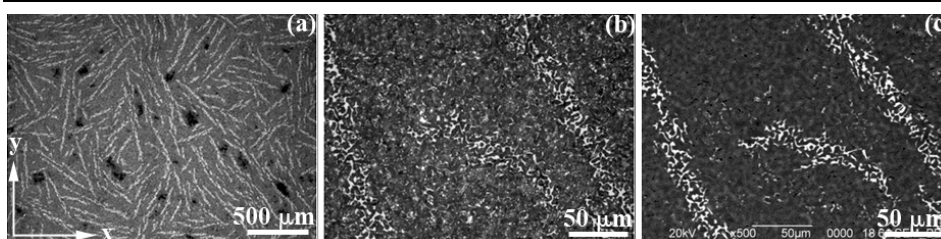
Fig. 7 – (*a*), (*b*) Optical bright field micrographs of the x-y cross-section of sample 2 showing striations and voids throughout the sample. (*c*) Backscatter electron micrograph of the same area confirming the presence of stripe-like features with a different composition than the two-phase matrix.

Fig. 7. In this (x-y) planar view of sample 2, the striated regions seem to have a random orientation. Investigation of the polished (y-z) and (x-z) surfaces shows preferential/columnar orientation of the striated regions along the z axis. A 3D reconstruction of a $1.5 \times 1.5 \times 1.5$ mm^3 volume is presented in Fig. 8. From the reconstructed volume it seems that the stripes are oriented perpendicular to the (x-y) plane and the morphology of the striated regions are plate-like with the long side parallel to the z axis and the short side contained in the (x-y) plane. Since the reactive melt penetration proceeds from the exterior toward the interior of the sample, it seems that the plate-like stripes are oriented in the same direction as the transformation gradient.
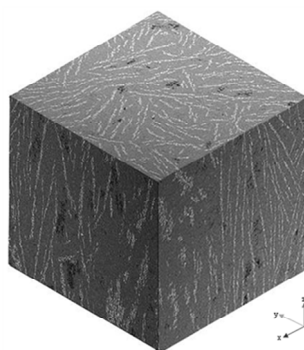

Fig. 8 – Three-dimensional reconstruction of an Al-7.5wt.%Fe sample volume with dimensions approximately $1.5 \times 1.5 \times 1.5$ mm^3. The iron-rich phases (white stripes) tend to propagate along the z axis with notable edge effects present.

The chemical composition of the phases present within the samples, as well as the morphology and distribution of the phases was investigated by combining high resolution SEM, EDX and XRD techniques. In order to obtain high quality cross-sections, the samples were polished using the ion beam of the JEOL JIB-4500 FIB instrument. Fig. 9 *a* shows the typical morphology of a stripe-like feature, while Fig. 9 *b* shows the matrix (an area devoid of 'stripes')

morphology of an Al-Fe-transformed sample (sample 2). The micrograph in Fig. 9 b reveals two interpenetrating co-continuous networks of Al metal and Al_2O_3 ceramic. A similar morphology was observed and reported in various Al-transformed composites [2]. Using spot EDS analysis it was determined that the dark gray areas (C) correspond to Al metal, while the light gray areas (D) correspond to Al_2O_3 ceramic. Small particles of precipitated silicon were also observed, as indicated by black arrows. The silicon particles are an expected by-product from the reaction. It is understood that the displaced Si from the SiO_2 preform diffuses away from the reaction front through the aluminum channels (Breslin *et al*., 1995). It should be noted that no iron was observed in the investigated volume illustrated in Fig. 9 b.
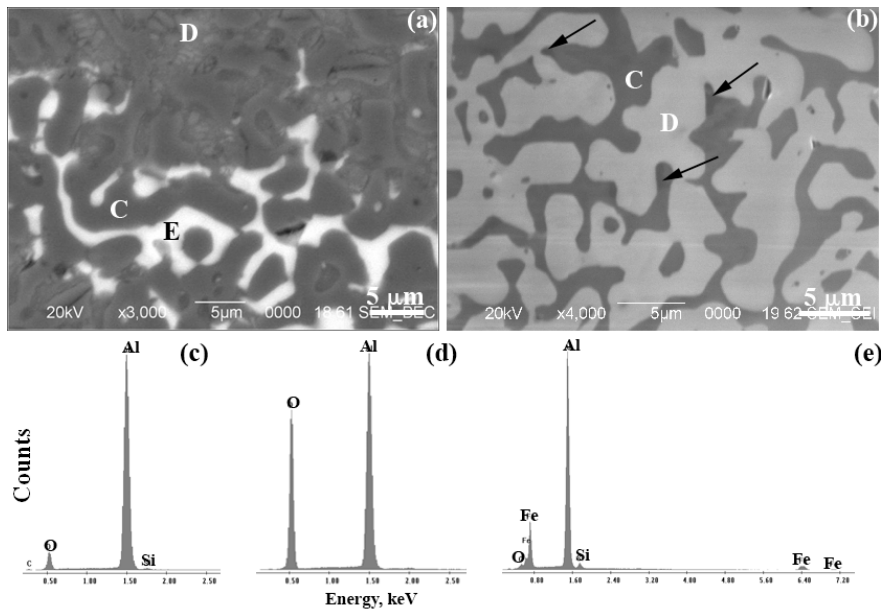

Fig. 9 − (a), (b) High resolution SEM micrographs of a sample 2 cross-section taken from a stripe-like feature and from the matrix, espectively. (c) − (e) EDX spectra from volumes C, D and E in (a).

The EDX analysis of areas identical to that presented in Fig. 9 a indicate the presence of Fe-rich phases besides the expected aluminum, alumina, and precipitated silicon phases. Sample 2 stripes are an Fe-Al phase surrounded by small amounts of Fe-Al-Si and Fe-Al-Si-O phases. The existence of nano-scale sized Fe-Al-Si and Fe-Al-Si-O phases is confirmed by TEM analysis, Fig. 10. Based on the electron microscopy analysis, it is concluded that the plate-like stripes observed in the Al-Fe-transformed sample consist of two phases: Fe-Al and Fe-Al-Si, while the matrix consists of two networks, Al metal and Al_2O_3 ceramic, as reported above.

Examination of the silicon distribution in the EDS maps shows that silicon appears as concisely defined particles in the ironless regions. Whereas, in the iron-rich regions, the silicon is more dispersed and individual particles are not observed. This suggests that the iron may have reacted with diffused silicon to form nano-scale phases. Other studies have shown that Fe, Al and Si can form intermetallics such as α-Al_8Fe_2Si, β-Al_5FeSi, or δ-Al_3FeSi_2 (Timpel *et al.,* 2010).
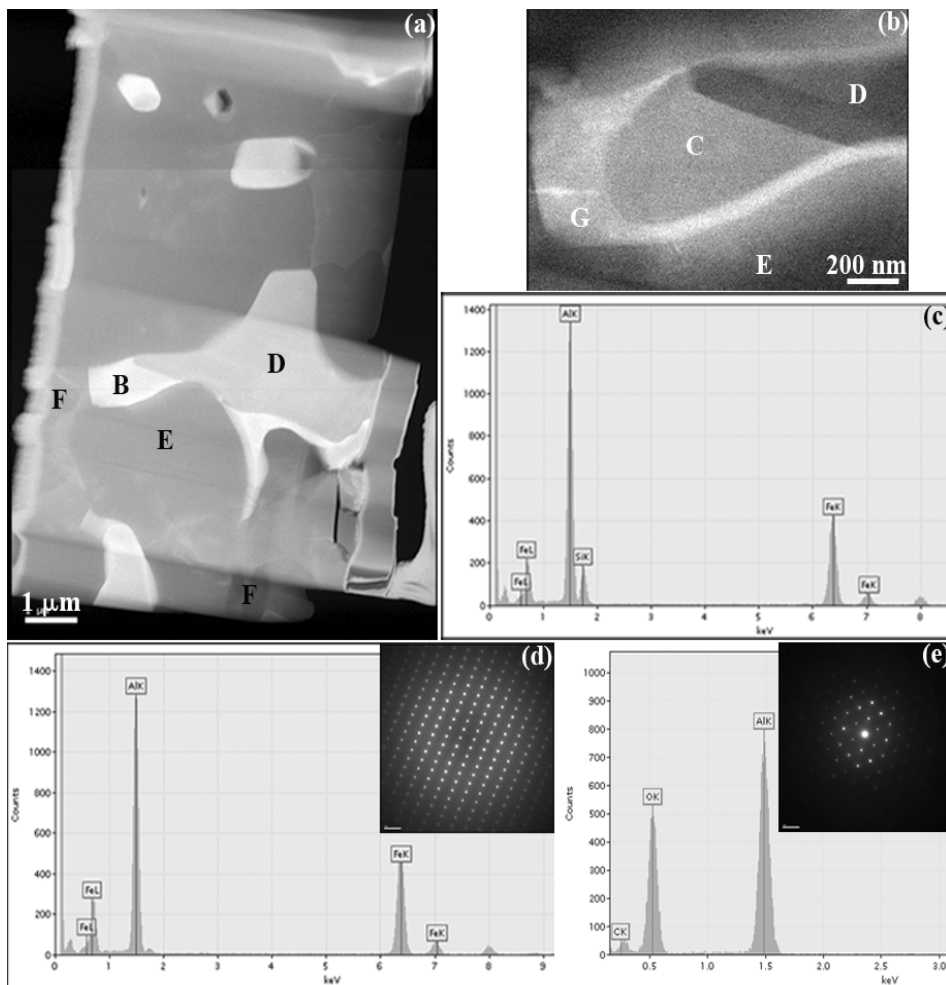

Fig. 10 – (a) Dark-field scanning-transmission electron micrograph from a striated (Fe-rich) volume of sample 2. (b) High magnification dark-field scanning-transmission electron micrograph of area B in (a). (c) EDS spectra of area C in (b). (d), (f) Electron diffraction patterns and EDS spectra from an Al-Fe phase (area D in (a) and (b)), and Al_2O_3 phase (area E in (a) and (b)), respectively. F denotes pure Al regions.

Fig. 10 shows the results of S/TEM investigation of an Fe-rich volume of the Al-Fe-transformed sample. Four different micrometer-sized phases plus several nanoscale features are observed in the dark field STEM micrograph in Fig. 10 *a*. By combining the results of EDS analysis with the information provided by XRD investigation the micron-sized volumes were identified as Al-Fe-Si phase (C in Fig. 10 *b*), Al-Fe intermetallic (D in Figs. 10 *a*, *b*), Al_2O_3 ceramic (E) and Al (F). A nano-scale transition layer (G) is readily observed at the ceramic-metal boundary, Fig. 10 *b*. Based on EDS analysis the chemical composition of the transition layer is was identified as Al-Fe-Si-O. The formation of nano-scale phases may contribute to the superior flexural strength of the Al-alloy-Al_2O_3 composite, as reported by Hemrick *et al.,* 2010. Future work involving high resolution TEM combined with electron crystallography will aim to determine the exact composition and structure of these phases.

4. Conclusion

The interpenetrating phase composites (IPC's) investigated in the present research were produced by reactive melt penetration using pure Al and Al-7.5wt.%Fe alloy as molten metal baths. Analysis showed that the addition of 7.5wt.% Fe to the molten Al bath adds iron-rich regions that contain multiple phases, but the addition does not change the basic Al-Al_2O_3 structure. Analytical electron microscopy investigations showed that the interaction between Fe and Si during processing formed nano-scale intermetallic compounds. This experiment proves that the microstructure of IPC's produced by reactive melt penetration can be tailored by altering the molten metal bath composition.

REFERENCES

Aluminum Iron Powder Diffraction File; International Centre for Diffraction Data (ICDD): Newtown, PA, 2011; PDF# 00-010-0173 (accessed 10 Feb 2011). Aluminum Oxide Powder Diffraction File; International Centre for Diffraction Data: Newtown, PA, 2011; PDF# 00-010-0173 (accessed 10 Feb 2011). Aluminum Powder Diffraction File; International Centre for Diffraction Data: Newtown, PA, 2011; PDF# 00-004-0787 (accessed 10 Feb 2011). Silicon Diffraction File; International Centre for Diffraction Data: Newtown, PA, 2011; PDF# 00-010-0173 (accessed 10 Feb 2011).

Breslin M.C., Ringnalda J., Xu L., Fuller M., Seeger J., Daehn G.S., Otani T., Fraser H.L., *Processing, Microstructure, and Properties of Co-Continuous Alumina-Aluminum Composites*. Mat. Sci. Eng., **A195**, 113-119 (1995).

Clark D.R., *Interpenetrating Phase Composites*. J. Am. Ceram. Soc., **75(4)**, 739-759 (1992).

Feng H.J., Moore J., *In Situ Combustion Synthesis of Dense Ceramic and Ceramic-Metal Interpenetrating Phase Composites*. Metall. Mat. Trans. B-Process Metallurgy and Materials Processing Science, **26(2)**, 265-273 (1995).

Hemrick J.G., Hu M., Peters K.M. and Hetzel B., *Nano-Scale Interpenetrating Phase Composites (IPC's) for Industrial and Vehicle Applications*. ORNL/TM-2010/80, DOE contract DE-AC05-00OR22725, Oak Ridge, Tennessee, USA (2010).

Liu W., Koster U., *Criteria for Formation of Interpenetrating Oxide/Metal-Composites by Immersing Sacrificial Oxide Performs in Molten Metals*. Scripta Materialia, **35(1)**, 35-40 (1996).

Murthy V. S. R., Kawahara K., Saito Y., Matsuzaki T.,Watanabe T., *Orientation and Grain Boundary Microstructure of Alumina in Al/Al₂O₃ Composites Produced by Reactive Melt Penetration*. J. Am. Ceram. Soc., **88(10)**, 2902-2907 (2005).

San Marchi C., Kouzeli M., Rao R., Lewis J.A., Dunand D.C., *Alumina-Aluminum Interpenetrating-Phase Composites with Three-Dimensional Periodic Architecture*. Scripta Materialia, **49(9)**, 861-866 (2003).

Timpel M., Wanderka N., Murty B.S., Banhart J., *Three-Dimensional Visualization of the Microstructure Development of Sr-Modified Al-15Si Casting Alloy Using FIB-EsB Tomography*. Acta Materialia, **58**, 6600-6608 (2010).

Zhou Wei, Hu Wenbin, Zhang Di, *Study on the Making of Metal-Matrix Interpenetrating Phase Composites*. Scripta Materialia, **39(12)**, 1743-1748 (1998).

STUDIUL STRUCTURII FINE ŞI A COMPOZIŢIEI CHIMICE A MATERIALELOR COMPOSITE AL₂O₃-ALIAJE PE BAZĂ DE Al OBŢINUTE PRIN REACŢIA TOPITURII METALICE CU MODELUL CERAMIC

(Rezumat)

Materialele composite Al₂O₃-aliaje pe bază de aluminiu prezintă interes ştiinţific şi ingineresc datorită proprietăţilor mecanice şi fizice pe care le posedă. Univetsitatea de Stat din Youngstown în colaborare cu compania Fireline TCON, Inc. (Youngstown, Ohio, SUA) efectuează în present un studiu de cercetare a acestor materiale obţinute în urma reacţiei dintre topitura metalică şi modelul ceramic fabricat din SiO₂. Până în prezent au fost studiate două materiale composite: Al₂O₃-Al şi Al₂O₃-Al7.5wt.%Fe. Studiul compoziţiei chimice, precum al structurii acestor materiale la scară micro- şi nano-metrică a fost efectuat cu ajutorul microscopiei optice, electronice şi a difractiei de raze X. În urma cercetării s-a stabilit ca materialul compozit produs în Al topit prezintă o structură alcatuită din două reţele microscopice, una metalică de Al şi

altă cermică de Al_2O_3, care se întrepătrund. În cazul materialului produs în urma reacţiei dintre modelul ceramic şi topitura aliajului Al-Fe, pe lângă reţelele microscopice de Al, Al-Fe şi Al_2O_3, a fost observată şi faza ternară Al-Fe-Si, de dimensiuni nanometrice, distribuită neuniform la graniţa dintre faza intermetalică Al-Fe şi cea ceramică. Rezultatele obţinute în urma acestui studiu ajută atât la înţelegerea relaţiei dintre structura fină şi proprietăţile fizico-mecanice ale materialelor composite, precum şi la controlul acestor proprietăţi prin modificarea corespunzătoare a parametrilor technologici ai procesului de fabricare.